Cellulose nanocrystals : From gels to solid materials

Lise Morlet-Decarnin

UNIVERSITÉ DE LYON

ENS DE LYON

THÈSE

en vue de l'obtention du grade de Docteur, délivré par

l'École Normale Supérieure de Lyon

École Doctorale N°52
École Doctorale de Physique et Astrophysique de Lyon (PHAST)

Discipline : Physique

Soutenue publiquement le 8 Juillet 2024, par :

Lise MORLET-DECARNIN

Cellulose nanocrystals:
From gels to solid materials

Les nanocristaux de cellulose :
Des gels aux matériaux solides

Devant le jury composé de :

RAMOS, Laurence	Directrice de recherche	Laboratoire Charles Coulomb, Univ. de Montpellier	Rapporteur
LENZ, Martin	Directeur de recherche	LPTMS, Univ. Paris-Saclay	Rapporteur
ANGELINI, Roberta	Directrice de recherche	Institute for complex systems, Univ. de Rome	Examinatrice
ROYALL, C. Patrick	Directeur de recherche	ESPCI Paris	Examinateur
OGAWA, Yu	Chercheur	Max Planck Institute of Colloids and Interfaces	Examinateur
MANNEVILLE, Sébastien	Professeur	Laboratoire de Physique de l'ENS de Lyon	Directeur
DIVOUX, Thibaut	Chargé de recherche	Laboratoire de Physique de l'ENS de Lyon	Examinateur

Acknowledgments

First of all, I would like to thank the jury for accepting to evaluate my work. In particular, I would like to thank the rapporteurs, Laurence Ramos and Martin Lenz, for taking the time to read this quite long and dense manuscript. I hope it was not too painful and you could find some interest for your own research topics. Thank also to the examinators, Roberta Angelini, Patrick Royall and Yu Ogawa, for your interest into my work, for your very constructive questions and discussions, and for the trip you made to come in person to attend my defense. I hope the "after party" was a good reward!

Second, I would like to deeply thank my supervisors, Sébastien Manneville and Thibaut Divoux. Thibaut, even if you were not officially my supervisor, unofficially, you were as much my supervisor as Sébastien. Both of you, thanks to your hundreds of ideas per minute and to your constant enthusiasm, you have always maintained me very motivated. Moreover, I would like to thank you both for the freedom and the trust that you have placed in me. Indeed, you were very opened for new ideas and I really enjoyed being able to propose and test my own ideas, even when it was involving a different field of physics, or deviating a bit from the initial subject. Furthermore, you have allowed me to participate in many conferences in many different countries. Besides the wonderful travels that it initiated, it was a great opportunity for me to present my work to different scientific communities, to learn a lot about various subjects, and to meet very interesting people and build my own network. Actually, one person that I have met during my last conference in Japan gave me my future job, and another the potential next one! All in all, thanks to both of you, my three years of PhD went very fast and it was a great experience. You have helped me to confirm my interest for physics and for research. Even more than a simple interest, you have succeeded to transmit me your passion for research in general and for this subject more particularly, and I am very grateful for that. Indeed, the proof is that I will continue to do research on a closely related subject for the next few years at least!

I would also like to thank Jean-Baptiste Salmon and Sylvain Deville for the collaborations that they have agreed to establish. Working with you have allowed me to extend my knowledge to other fields of physics, to explore new topics and to carry out new types of experiments. I agree Thibaut, rheology is great, but I really enjoyed being able to bring some diversity in my PhD. Thank also to Bruno Jean for helping us to know more about the constituents of our gels, i.e., the cellulose nanocrystals.

Third, I would like to thank the secretaries without whom it would have been much more difficult to travel as much as I did. Thank you very much Laurence, Erika and Nadine for your patience, your persistence and your adaptability when the administrative tools where not always on your side to make your life easier. Always in good spirits and with a smile!

Finally, I would like to sincerely thank all the colleagues and friends of the lab and of outside the lab, as well as my whole family, for putting up with me during these 3 years, especially when I was too stressed or fed up with my work. Thank you all for the very good moments that we have shared, which were sometimes very helpful for my moral well-being (when writing my manuscript for example, but not only). Some friends have always been here for me, from the beginning of my PhD, and others arrived right when they were needed most. I am not giving any names, but I am sure you will all recognize yourselves, and you are already aware of your importance to me.

CONTENTS

CHAPTER

1

INTRODUCTION

Contents

CHAPTER 1. INTRODUCTION

From our earliest classes of physics in primary school, we learn that a dense material, under normal temperature and pressure conditions, is either a solid or a liquid. A solid has it own shape, and it can maintain its own weight. It can be slightly deformed, but as soon as the deformation is too large, it breaks. On the contrary, a liquid does not have its proper shape: it cannot maintain its own weight, and it adopts the shape of the container in which it is poured. It can be infinitely deformed, and does not break.

Nevertheless, we are confronted to many materials in our everyday life that we cannot classify into either of these two categories. Let us start our investigation in the kitchen. We open the fridge and here are the strange materials that we find: custard, yogurt, mayonnaise, jelly, etc. Are those materials solid or liquid? Custard, yogurt and jelly can bear their own weight and maintain their own shape, so we would say that they are solid. However, when we begin to mix one of those materials, it flows like a liquid. When we put the mayonnaise dish upside down, it does not flow, yet we can spread it easily on a piece of bread, or mix it with salad and it does not break into pieces like a solid. Let us continue our investigation in the bathroom. Take the shaving cream, it behaves similarly to mayonnaise: you can shape it in your hands easily without breaking it, yet it keeps the shape you give it, and does not collapse under its own weight. You can also spread it on you face and it stays there without leaking. Two other examples: shampoo and toothpaste. Both do not flow when you turn the bottle or the tube upside down, so we would say that they are not liquids. Yet, as soon as you press a bit on the bottle, shampoo flows outside of the bottle like a liquid. Concerning toothpaste, it is even more impressive: it flows to settle on your toothbrush, and once it is there, it keeps the cylindrical shape given by the tube end, like a solid! There are plenty of other materials that you could think of, such as modeling clay, which you can deform as much as you like without breaking it, like a liquid, and which will maintain the shape you have given it, like a solid ; or slime which remains in the shape you have given it at short times, like a solid, but which will spontaneously flow like a liquid at long times. What is important to keep in mind is that there is no change of temperature and no drying involved in the change of behaviors observed here. The only two culprits are deformation and time. A final example to make this last point clear: everyone has already played at home with corn starch mixed with water, or seen videos of people running on swimming pools filled with this mixture. When pushing fast on the mixture, it behaves like a solid, allowing people to run on it by bouncing on its surface without drowning. However, at rest, it behaves like a liquid and flows.

All those materials, which lie between solids and liquids, have been gathered in an additional category named “soft materials" by de Gennes [de Gennes, 1992], and also referred to as complex or non-Newtonian fluids, i.e., fluids which do not behave like water. The present PhD work is devoted to the study of one specific class of such soft materials.

In this introductory chapter, we first present some generalities about soft materials, such as their microstructural organization and the origin of their unusual mechanical behaviors. Then, we give a quick overview of rheology, the science that describes the mechanical properties of soft materials. For the rest of the introduction, we focus on the study of a specific class of soft materials, referred to as “gels”. In particular, we explore the typical mechanical response of gels in their linear and in their non-linear regimes of deformation, as well as their flow properties. In a third section, we concentrate on the dynamics of formation and aging of gels (i) by exploring how to determine the “gelation time”, i.e., the time for a gel to form, (ii) by uncovering some universality in the gel dynamics through “superposition principles”, and (iii) by establishing mechanical models, namely fractional models, to capture the gel viscoelastic properties. Finally, we focus on a specific type of soft gels, i.e., gels constituted of cellulose nanocrystals. After describing the individual properties of those natural colloids, their interest, and the various phases they can lead to by self organizing once suspended in water in the presence of salt, we review previous studies on the rheological properties of these colloidal suspensions.

Figure 1.1: Examples of soft materials at the macroscopic scale (upper raw) and at the microscopic scale (lower raw). From left to right: mayonnaise, yogurt, paint, toothpaste, beaten egg whites. The scale bars on the upper corner of the microstructure images correspond to 150 μm. Adapted from [Dagès, 2021].

A Generalities on soft materials

A.1 What are soft materials made of?

Soft materials are very rich, both in their microstructural organization as they include emulsions, foams, gels, glasses, liquid crystals, and even granular media, and in their composition, as they can be constituted of small solid particles and/or polymers, which are either synthesized or natural products, either organic or inorganic. This great diversity leads to a great variety of mechanical properties and therefore to a great variety of applications in many different fields, such as the food, the construction or the pharmaceutical industries. Many of those soft materials are also indirectly used as precursors to the design of solid materials, through 3D printing or molding for instance. A good understanding of the mechanical behavior of those soft materials is therefore key for applications.

Besides the great variety in the nature of the constituents, their size, and their microstructural organization, soft materials do show some similarities. First in their structure, which is responsible for their original properties: they all present a disorganized mesoscopic structure of large characteristic size compared to the atomic size, contrasting with the very organized microstructure at small scale constituting a crystalline solid material (see the examples given in Fig. 1.1). Second, in their mechanical response to an external solicitation, as seen at the beginning of this introduction. The study of those mechanical behaviors has raised increasing interest since the beginning of the last century, and continues to be a very fruitful field nowadays. In this thesis, we put aside the granular materials and the multiphases materials such as emulsions and foams, and we focus on soft materials composed of Brownian constituents suspended in a solvent. Those constituents can be either polymers, colloids, or a mix of both. While polymers are long and flexible chains of molecules, colloids are solid particles of size ranging between a few nanometers and a few micrometers. Both constituents can have very different shapes and individual mechanical properties: polymers can be linear or branched, of various length and flexibility, while colloids can be spherical, disk-like, rod-like, etc, monodisperse or polydisperse, and totally rigid or deformable.

A.2 How are soft materials organized microscopically?

When the particles, whether polymers or colloids, are dispersed in a solvent and interact through repulsive forces, such as electrostatic repulsion, they form a stable suspension. However, upon

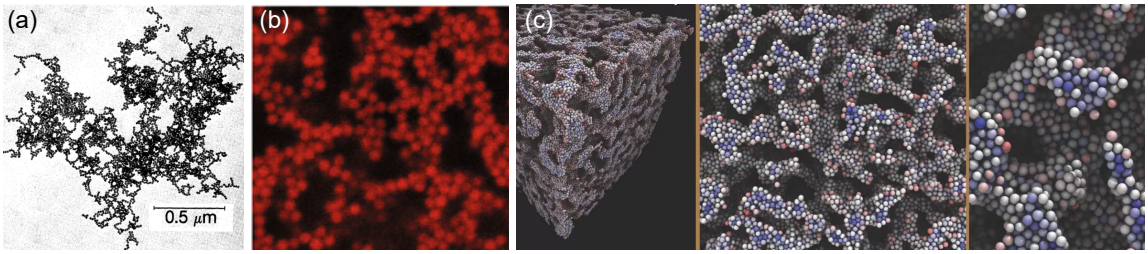

Figure 1.2: Microscopic organization of colloidal gels. (a) Transmission electron microscopy image of a gold colloidal aggregate showing a fractal organization [Weitz and Oliveria, 1984]. (b) Confocal image of a polymethylmethacrylate (PMMA) depletion gel. One particle has a 1.11 μm diameter [Whitaker et al., 2019]. (c) Gel simulation. From left to right: part of one periodic cell, 2× magnification, and 4× magnification. The colors codes for the number of contacts per particle (red: few contacts, to blue: many contacts) [Zia et al., 2014].

modification of those interaction forces from repulsive to attractive, e.g., by adding salt to screen the repulsive electrostatic interactions, by changing the pH or temperature, or by inducing a chemical reaction for instance, particles may aggregate and form a network which spans over long distances, from several hundreds of micrometers to the whole sample volume (see Fig. 1.2). This network is either formed by individual particles or by clusters of particles, which interact either through the formation of covalent bonds in the case of "chemical gels" for instance, or through non-covalent interactions such as hydrogen bonding, van der Waals interactions, hydrophobic interactions, etc. in the case of what is referred to as "physical gels" for instance. The latter physical gels constitute the subject of the present thesis.

The precise organization of a gel network, both at the microscopic scale and at the mesoscopic scale, depends on the nature of its constituents and on their concentration. At small concentration, there are not enough particles to form a network spanning over the whole sample volume. Particles are organized into clusters, or several small networks that are not interconnected. When the concentration increases, particles can organize to form a percolated network that spans over the whole sample volume, and which presents some self-similarity over a range of length-scales. This establishes the definition of a "gel phase", and the first instant when the percolated network is formed, i.e., when there exists at least one continuous path of particles to go from one point of the suspension to another, defines the "gelation time", associated to the "gel point". At even larger concentrations, each particle is trapped in a "cage" formed by its neighboring particles, and in order for this particle to escape this cage, the displacement of several layers of neighboring particles is necessary, which can only be achieved over long time-scales. This kinetically arrested disordered state is called a "glass". While a gel can only form when inter-particle interactions are attractive, a glass can form through either attractive or repulsive interactions, as it results from crowding effects, for which aggregation of particles is not necessary. Nevertheless, the glass microstructure and properties might differ depending on the inter-particle interactions. Therefore, we distinguish between a glass formed with attractive interactions, referred to as an "attractive glass", and a glass formed with repulsive interactions, referred to as a "repulsive glass". However, the distinction between a gel and a glass is not always clear. In particular, it has been shown that some colloidal gels present a glass-like microstructure within the strands that constitute the overall gel network [Johnson et al., 2019].

The specific disordered mesoscopic structures of soft materials are responsible for their original mechanical behaviors. In the rest of this Introduction, we will focus more particularly on the gel phase.

A.3 Where does the gels solid-like behavior and elasticity come from?

One of the particularity of colloidal gels is that, with a very small amount of solid particles dispersed in a liquid, only a few percents in volume, a gel presents some solid-like properties: it can maintain its own weight and shape, and deforms elastically.

In dense crystalline solids, the origin of rigidity and elasticity are well understood: while the former comes from the contact between particles, the latter emerges from broken symmetry in the particle crystalline organization.

In colloidal gels, which are low density materials, the origin of rigidity is far from obvious. Those gels are constituted of a sparse network of colloidal particles in contact, which is sustained through attractive interactions. This geometric percolation is certainly necessary to form a gel, but it is not sufficient to explain alone the emergence of mechanical rigidity. In fact, the onset of rigidity requires a mechanically stable spanning cluster, able to transmit stresses. However, it has been observed that this rigidity percolation, which occurs when mechanical stability emerges in disordered networks as constraints or components are added, actually occurs at a larger density than the one associated with geometric percolation. How does one reconcile this aspect of rigidity percolation with the appearance of mechanically rigid structures in suspensions of colloidal particles at volume fractions of just a few percents? The basic theories of rigidity percolation ignore structural correlations: bonds or sites are randomly removed from a lattice, with no correlation between them, until the structure loses its rigidity. While this simple approach gives good predictions for colloidal glasses, which are high density soft materials [He and Thorpe, 1985], it cannot explain the small value of this threshold observed in colloidal gels. Actually, it has been shown that spatial correlations are crucial to understand the onset of rigidity in materials like colloidal gels [Zhang et al., 2019]. In fact, the rigidity of a network comes from the coordinated organization of many interacting particles rather than from the fact that each single cluster is rigid. Therefore, unlike connectivity, rigidity is inherently a non-local property: whether a region of a network is floppy or rigid generally depends upon structural details that are far away. Simply put, the role of structural correlations is to organize particles, via inter-particle attractive interactions, into "smart" thin structures that transmit stress, hereby shifting the rigidity percolation threshold to small volume fractions. Therefore, colloidal gelation can be understood as a rigidity percolation transition, but the rigidity of this percolated network does not come from connectivity and from the fact that each single cluster is rigid, but rather from the coordinated organization of many interacting particles. This theory is consistent with experiments, both for the predicted values of particles volume fraction at which rigidity appears, and for capturing the decrease of this threshold when increasing inter-particle attraction, which leads to an increase of structural correlations [Zhang et al., 2019].

In summary, colloidal gels are rigid materials that can deform elastically. The origin of this elasticity has long been attributed to the stretching stiffness of the strands constituting the network microstructure. However, it has been shown recently that, in colloidal gels, rather than this stretching stiffness, it is the bending stiffness of those strands that dominates and accounts for the material elastic properties [Gado et al., 2016].

B Rheology: a tool to study the mechanical behavior of soft materials

Soft materials can be studied and characterized using many different methods. In particular, the mechanical behavior of those materials is most often characterized experimentally using rheology.

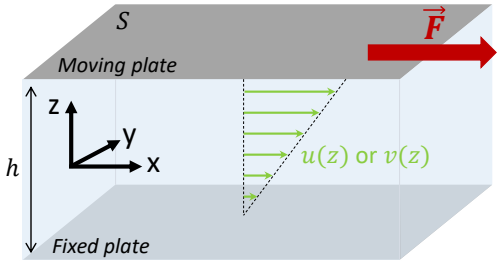

Figure 1.3: Deformation or flow of a material confined between two plates, induced by a force applied on the upper moving plate.

B.1 Rheological physical quantities

Let us first introduce some relevant physical quantities to describe the mechanical response of a soft material to external solicitations.

a Stress and strain

Let us consider a surface element $\mathrm{d}\vec{S} = \mathrm{d}S\vec{n}$ at position $\vec{r}$ in the orthonormal basis $(\vec{e}_i)_{i=1,2,3}$, where $\vec{n}$ is the unit vector orthogonal to the surface. This surface element undergoes a force $\vec{F}$ from the material, given by:

$$\vec{F}(\vec{r}) = \underline{\underline{\sigma}}(\vec{r}) \cdot \mathrm{d}\vec{S} = \sum_{i,j} \sigma_{ij} n_j \mathrm{d}S \vec{e}_i. \tag{1.1}$$

This relationship defines the stress tensor $\underline{\underline{\sigma}}(\vec{r})$: $\sigma_{ij}(\vec{r})$ is the surface force applied along the direction $\vec{e}_i$ to a surface perpendicular to $\vec{e}_j$, at position $\vec{r}$. The equilibrium of torques in the sample volume leads to the symmetry of the stress tensor.

The stress applied locally results in a deformation of the material, and therefore to the development of a strain field in its volume. The deformation at time t and position $\vec{r}$ is described by the Lagrangian field $\vec{u}(\vec{r},t)$: a small volume of the material at position $\vec{r}$ and time t will shift to position $\vec{r} + \vec{u}(\vec{r},t)$ at time $t + \mathrm{d}t$. The resulting strain tensor $\underline{\underline{\gamma}}$ is defined as the symmetric part of the deformation field gradient:

$$\gamma_{ij} = \frac{1}{2}\left(\frac{\partial u_i}{\partial x_j} + \frac{\partial u_j}{\partial x_i}\right). \tag{1.2}$$

The stress can also induce some flow within the material. This flow is described by the velocity field $\vec{v}(\vec{r},t) = \partial_t \vec{u}(\vec{r},t)$, and one introduces the shear rate tensor $\dot{\underline{\underline{\gamma}}}$ as the time derivative of the strain tensor, corresponding to the symmetric part of the velocity gradient:

$$\dot{\gamma}_{ij} = \frac{1}{2}\left(\frac{\partial v_i}{\partial x_j} + \frac{\partial v_j}{\partial x_i}\right). \tag{1.3}$$

b Application to simple shear

Let us apply this theoretical framework to a simple example which is particularly relevant in rheology. We consider a soft material which is sheared between a fixed and a moving plate, separated by a distance h, as represented on the diagram of Fig. 1.3. The two plates are parallel and both have a surface area S. In the stationary regime, the application of a force $\vec{F} = F\vec{e}_x$ tangential to the upper plate causes a deformation of the material along the same direction $\vec{e}_x$. If the material has a solid behavior, this force induces a deformation $\vec{u}(\vec{r}) = u(z)\vec{e}_x$ in the sample volume. If this material is liquid, the material flows with a stationary and laminar velocity profile $\vec{v}(\vec{r}) = v(z)\vec{e}_x$.

In this simple unidirectional deformation, known as "simple shear", the three tensors that we have defined above all have a single non-zero value, which are used to describe the mechanical behavior of a soft material: $\sigma_{xz} = \sigma_{zx} = \sigma$ is referred to as the shear stress (or the stress), $\gamma_{xz} = \gamma_{zx} = \gamma$ is referred to as the shear strain (or the strain), and $\dot{\gamma}_{xz} = \dot{\gamma}_{zx} = \dot{\gamma}$ is referred to as the shear rate.

The above relationships therefore simplify as follows:

- The stress σ corresponds to the surface force applied on the material in the direction perpendicular to the surface $\vec{e}_z$:
$$F = \sigma S. \tag{1.4}$$
- The strain γ corresponds to the amplitude of the material deformation with respect to the sample thickness:
$$\gamma = \frac{\partial u}{\partial z} = \frac{u(h)}{h}. \tag{1.5}$$
- The shear rate $\dot{\gamma}$ corresponds to the temporal derivative of the strain:
$$\dot{\gamma} = \frac{\partial v}{\partial z} = \frac{v(h)}{h}. \tag{1.6}$$

c Viscoelastic moduli

In the linear regime of deformation, i.e., for deformations that are not large enough to induce irreversible plastic deformations in the case of a solid, or to induce flow instabilities in the case of a liquid, the mechanical response of a material is proportional to the external stimulation:

- In the case of an elastic solid, Hooke's law links strain and stress, through the introduction of the static elastic modulus G:
$$\sigma = G\gamma. \tag{1.7}$$
- In the case of a simple fluid, Newton's law links strain and shear rate:
$$\sigma = \eta\dot{\gamma} \tag{1.8}$$
where η is the dynamic viscosity of the liquid.

A soft material is a material that shows both liquid and solid behaviors depending of the time-scale that we consider, as highlighted at the beginning of this introduction. Therefore, for those particular materials, we cannot apply this permanent regime description, instead, we need to consider the time-scale associated to the mechanical stimulation. Therefore, if the mechanical response of the material is linear, this response is properly characterized by the application of a periodic stimulation.

Let us consider the application of an oscillatory stress of angular frequency ω to the material:

$$\sigma(\omega, t) = \sigma_0(\omega)\cos(\omega t). \tag{1.9}$$

In the linear regime of deformation, this stress induces a strain response of the material which is also an oscillatory function, of same frequency, but with a phase shift $\delta(\omega)$:

$$\gamma(\omega, t) = \gamma_0(\omega)\cos(\omega t - \delta(\omega)). \tag{1.10}$$

In complex notations, we can write $\sigma^*(\omega, t) = \sigma_0(\omega)e^{i\omega t}$ and $\gamma^*(\omega, t) = \gamma_0(\omega)e^{i(\omega t - \delta(\omega))}$. We can now generalize both the Hooke's law and the Newton's law into a generalized Hooke's law for soft materials:

$$\sigma^*(\omega) = G^*(\omega)\gamma^*(\omega) \tag{1.11}$$

where $G^*(\omega)$ is the complex modulus of the material. Its real part, which characterizes the in-phase response of the material to the periodic deformation and does not dissipate any energy, is called the elastic modulus:

$$G'(\omega) = \frac{\sigma_0}{\gamma_0} \cos\delta. \tag{1.12}$$

It accounts for the solid-like behavior of the material. The imaginary part of the complex modulus, which characterizes the response of the material that is in phase-quadrature with the applied stress and is strictly dissipative, is called the viscous modulus:

$$G''(\omega) = \frac{\sigma_0}{\gamma_0} \sin\delta. \tag{1.13}$$

It accounts for the liquid-like behavior of the material. The ratio of those two so called viscoelastic moduli defines the loss factor:

$$\tan\delta(\omega) = G''(\omega)/G'(\omega) \tag{1.14}$$

with δ the phase of the complex modulus G^*. This quantity provides additional information on the state of the material: if $\tan\delta > 1$, then the viscous modulus is larger than the elastic modulus $G'' > G'$, therefore viscous dissipation dominates over elasticity, meaning that the material is in a liquid-like state ; on the contrary, if $\tan\delta < 1$, then the elastic modulus is larger than the viscous modulus, $G' > G''$, meaning that the material is in a solid-like state. It is important to note that those three quantities do depend on the excitation angular frequency ω, or frequency $f = \omega/2\pi$.

In the limit of a purely elastic solid of static elastic modulus G, we have $G'(\omega) = G$, $G''(\omega) = 0$ and $\tan\delta(\omega) = 0$ whatever the frequency. In the case of a simple fluid, which is purely viscous, we have $G'(\omega) = 0$, $G''(\omega) = \eta\omega$ and $\tan\delta(\omega) \to \infty$. In the case of soft materials, which present both solid-like and liquid-like behaviors, both the elastic modulus G' and the viscous modulus G'' are non-zero. Therefore, those materials are also called viscoelastic materials.

Finally, one should remember that this description is only valid if the material response to a mechanical load is linear, i.e., if the amplitude and the shear rate of the deformation applied to the sample are small enough not to probe some non-linearities in the material microscopic dynamics.

B.2 Linear viscoelasticity

As seen in the previous section, the viscoelastic properties of a colloidal gel depend on the frequency at which it is deformed. Indeed, deforming a material at different frequencies allows us to probe the various relaxation times associated to the material microstructure. The measurement of the frequency dependence of the elastic and viscous moduli is called a viscoelastic spectrum. Such a spectrum is measured by applying an oscillatory strain signal of small amplitude, in order to stay in the linear regime of deformation, and of varying frequency.

a Macroscopic models

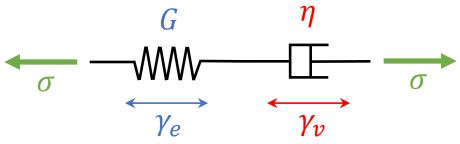

Figure 1.4: Maxwell model.

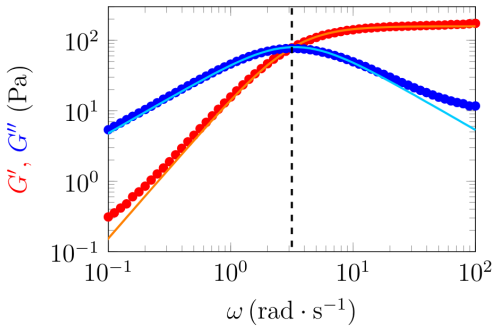

Figure 1.5: Elastic modulus G' (red) and viscous modulus G'' (blue) as a function of the frequency ω for surfactant worm micelles (CTAB/$NaNO_3$), measured with an amplitude γ = 1 %. The solid lines show the best fit of the data with a Maxwell model with G = 160 Pa and τ = 0.3 s. The dashed line highlights the characteristic time $\tau = 1/\omega_c$. Reproduced from [Lidon, 2016].

Figure 1.5 shows the viscoelastic spectrum of a surfactant solution, namely cetyltrimethylammonium bromide at c_{CTAB} = 0.3 mol.L^{-1}, and salt, namely sodium nitrate at c_{NaNO_3} = 0.4 mol.L^{-1}, in distilled water. The surfactant molecules spontaneously organize into cylindrical micelles which are responsible for the non-Newtonian properties of the material. We clearly observe that this material is a viscoelastic material in which both the elastic and the viscous moduli are simultaneously non-zero, and strongly depend on the frequency at which they are measured, or equivalently on the angular frequency $\omega = 2\pi f$. A critical frequency ω_c appears, at which both moduli crossover: at small frequency, for $\omega < \omega_c$, the viscous modulus is much larger than the elastic modulus, and the material response resembles that of a liquid, i.e., $G^* \approx iG''$. On the other hand, at large frequency, for $\omega > \omega_c$, the elastic modulus dominates, and the response is mainly solid-like, i.e., $G^* \approx G'$.

This frequency dependence is well captured by a simple empirical model: the Maxwell model [Maxwell, 1867] (see the solid lines in Fig. 1.5). The mechanical behavior of this material is modeled by two mechanical elements assembled in series, as represented in Fig. 1.4: a purely elastic element of elastic modulus G, represented by a spring, and a purely viscous element of viscosity η, represented by a dashpot. When this material is subjected to a stress σ, its resulting total deformation is the sum of the deformations undergone by both elements: $\gamma = \gamma_e + \gamma_v$. The same stress is applied to both elements, and each element has its own constitutive relationship linking stress and strain: $\sigma = G\gamma_e = \eta\dot{\gamma}_v$. Using those two relationships, we obtain $\dot{\gamma} = \dot{\sigma}/G + \sigma/\eta$. Using complex notations and the definition of G^* given by Eq. (1.11), we obtain:

$$G^* = \frac{G\eta i\omega}{\eta i\omega + G}. \tag{1.15}$$

Taking the real and imaginary parts of G^* leads to:

$$\begin{cases} G'(\omega) = \dfrac{G(\omega\tau)^2}{1+(\omega\tau)^2} & (1.16) \\ G''(\omega) = \dfrac{G\omega\tau}{1+(\omega\tau)^2} & (1.17) \end{cases}$$

where $\tau = \eta/G = \omega_c^{-1}$ corresponds to a characteristic relaxation time.

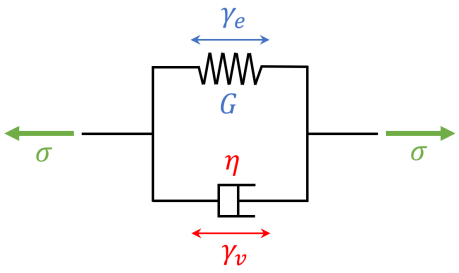

Figure 1.6: Kelvin-Voigt model.

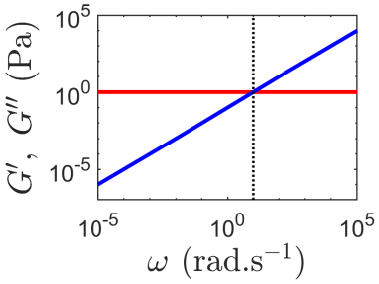

Figure 1.7: Schematic representation of the viscoelastic spectrum predicted by a Kelvin-Voigt model with $G = 1$ Pa and $\eta = 0.1$ Pa.s. Elastic modulus G' (red) and viscous modulus G'' (blue) as a function of the frequency ω. The dashed line highlights the characteristic time $\tau = 1/\omega_c$.

Another very simple mechanical model can be obtained by assembling the same two mechanical elements in parallel, as represented in Fig. 1.6: this model is known as the Kelvin-Voigt model [Voigt, 1890]. In this model, when this material is subjected to a stress σ, its resulting deformation is the same in both elements: $\gamma = \gamma_e = \gamma_v$. The stress is distributed to both elements $\sigma = \sigma_e + \sigma_v$, and each element has the same constitutive relationship linking stress and strain as described in the previous paragraph. In this case, we obtain $\sigma = \gamma G + \dot{\gamma}\eta$ and:

$$G^* = G + \eta i\omega. \tag{1.18}$$

Taking the real and imaginary part of G^* leads to:

$$\begin{cases} G'(\omega) = G & (1.19) \\ G''(\omega) = \eta\omega. & (1.20) \end{cases}$$

Here again, we can define a characteristic relaxation time $\tau = \eta/G = \omega_c^{-1}$. A schematic of the viscoelastic spectrum for a material following this model is represented in Fig. 1.7. The dependence of the viscoelastic moduli with frequency is reversed compared to the previous model: the material is in a solid state ($G' > G''$) at small frequency, for $\omega < \omega_c$, while it is in a liquid state ($G' < G''$) at large frequency, for $\omega > \omega_c$.

b Spectrum of relaxation times

The Maxwell and the Kelvin-Voigt models, which present a single relaxation time, fail to capture the viscoelastic spectrum of most soft materials. Indeed, soft materials generally present a microstructure characterized by multiple length-scales, associated to a wide range of relaxation times. Therefore, the complex modulus G^*, which characterizes the viscoelastic properties of soft materials, does not involve a single relaxation time, but rather a continuous range of time-scales. In the discrete limit, such a wide range of relaxation times can be obtained by considering the association of multiple Maxwell or Kelvin-Voigt models in series or in parallel. However, such a description involves a very large number of adjustable parameters in order to capture the full viscoelastic spectrum of the soft material under study.

Actually, an accurate, general description is achieved by taking the continuous limit and by introducing the spectrum of relaxation times $H(\tau)$ [Wagner and Mewis, 2021]. Indeed, Boltzmann's equation allows one to calculate the stress response $\sigma(t)$ of a soft material from its shear history $\dot{\gamma}(t')$, for $-\infty < t' < t$, through the relaxation modulus $G(t)$ [Boltzmann, 1874]:

$$\sigma(t) = \int_{-\infty}^{t} G(t-t')\dot{\gamma}(t')dt'. \tag{1.21}$$

The complex modulus is linked to the Fourier transform $\hat{G}(\omega)$ of the relaxation modulus through:

$$G^*(\omega) = i\omega\hat{G}(\omega). \tag{1.22}$$

Furthermore, the relaxation modulus can also be expressed as a weighted time integral over all relaxation modes in the soft material [Tschoegl, 2012]:

$$G(t) = \int_0^{\tau_{max}} H(\tau)\mathrm{e}^{-t/\tau}\frac{d\tau}{\tau} \tag{1.23}$$

where τ_{max} is the longest relaxation time of the material. The above relationship defines the relaxation time spectrum $H(\tau)$ which accounts for the continuum of relaxation times within the material microstructure. In general, fast relaxation processes, leading to short τ, correspond to some structural relaxation over small length-scales. Conversely, long time relaxations, leading to long τ, are indicative of relaxation processes over large length-scales within the material microstructure. Eq. (1.23) shows that the relaxation modulus and the ratio of the relaxation time spectrum over the relaxation time $H(\tau)/\tau$ are linked by a Laplace transform. In other words, the ratio $H(\tau)/\tau$ accounts for the contribution of Maxwell elements of relaxation times ranging between τ and $\tau + d\tau$, to the elastic modulus of the material.

Using Eq. (1.22), the viscoelastic moduli of a soft material can be calculated from the relaxation time spectrum through a Fourier transform of Eq. (1.23):

$$\begin{cases} G'(\omega) = G_e + \displaystyle\int_0^{\tau_{max}} H(\tau)\frac{(\omega\tau)^2}{1+(\omega\tau)^2}\frac{d\tau}{\tau} & (1.24) \\ G''(\omega) = \displaystyle\int_0^{\tau_{max}} H(\tau)\frac{(\omega\tau)}{1+(\omega\tau)^2}\frac{d\tau}{\tau} & (1.25) \end{cases}$$

Therefore, probing a material viscoelastic properties at large frequencies, corresponding to short time-scales, allows one to probe the material microstructure at short length-scales, while focusing on the viscoelastic moduli at small frequencies provides information on structural relaxation over large length-scales.

B.3 Soft material failure: from the linear to the non-linear regime of deformation

The description of the viscoelastic properties of a gel given in the previous sections is valid only at small strain amplitude, in the linear regime of deformation of the material. There, the goal was to characterize the material mechanical properties at rest, without damaging it or affecting its mechanical properties. The question is: how does one determine the strain amplitudes corresponding to this linear regime of deformation?

Upon increasing the strain amplitude, plastic deformations are induced in the material microstructure: some bonds can break, others may be created, and some clusters or particles may deform and align along the shear direction. One can study this transition from the linear regime of deformation, where only elastic deformations are induced, to the non-linear regime of deformation, where plastic deformations are induced, together with the gel failure and fluidization that follows, through two different rheological measurements.

a From small to large amplitude oscillatory deformation

First, one can apply an oscillatory strain signal of increasing amplitude to deform the sample, and probe how its viscoelastic properties evolve with the strain amplitude. Such an experiment, referred to a strain sweep experiment, allows one to switch from small amplitude oscillatory shear (SAOS) to large amplitude oscillatory shear (LAOS). At large strain amplitudes, in the non-linear

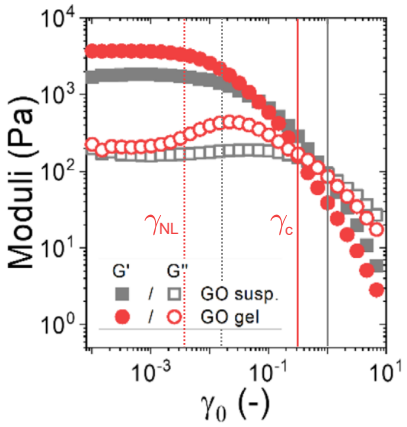

Figure 1.8: Viscoelastic moduli as a function of the strain amplitude during a strain sweep measurement at ω = 1 rad.s^{-1}. In gray: for a suspension containing 4.2 wt % graphene oxide colloids dispersed in water. In red: for a gel containing 0.86 wt % graphene oxide colloids and 0.12 wt % $CaCl_2$. The gray and red dashed lines highlight the strain γ_{NL} corresponding to the transition from the linear to the non-linear regime of deformation, for the suspension and for the gel respectively. The gray and red solid lines highlight the yield strain γ_c of the suspension and of the gel respectively. Adapted from [Shim and Rogers, 2023].

regime of deformation, the response of the material is no longer linear: unlike the applied strain signal, the stress is not a simple oscillatory function at frequency ω. Instead, several harmonics develop, and a full study of the stress response should include such harmonics. In practice, the viscoelastic moduli G' and G'' are extracted from the fundamental mode of the stress response. In this thesis, we shall only focus on a simple analysis based on G' and G'' measured under LAOS.

Figure 1.8 presents an example of results obtained for two dispersions of graphene oxide (GO) colloids: one at large GO concentration, 4.2 wt % GO, without any salt, referred to as a suspension ; and one at small GO concentration, 0.86 wt %, in the presence of salt, 0.12 wt % $CaCl_2$, which acts as a cross-linker to form a gel through coordination interactions with oxygenated functional groups on the GO surface. At small strain amplitudes, the elastic and the viscous moduli of both suspensions do not evolve with the strain amplitude, corresponding to the linear regime of deformation of the material. In this regime, the material undergoes no plastic deformation and thus no damage of its microstructure. Therefore, its viscoelastic properties are not impacted by the imposed deformation, and the material response is linear: the resulting stress is proportional to the applied strain. As the strain amplitude increases, the elastic modulus decreases and deviates from its plateau value at small strain amplitudes. Similarly, the viscous modulus deviates from its plateau value at small strain amplitudes by either decreasing for the suspension, or by increasing for the gel. This deviation is due to the development of some non-linearities in the material response to the large amplitude oscillatory shear: some plastic events may occur, hereby impacting the material microstructure and therefore modifying its viscoelastic properties. This transition from SAOS to LAOS corresponds to the transition from the linear to the non-linear regime of deformation. The strain amplitude at which this transition is observed is denoted γ_{NL}. In this type of measurement, this critical strain amplitude can be arbitrarily set as the position where either G' or G'' deviates by 10 % from their plateau value, as represented by the dashed lines in Fig. 1.8. The precise value of γ_{NL} is not necessarily meaningful, but it gives a criteria to choose the strain amplitude used for the measurements in the linear regime of deformation, which must be much smaller than this critical value γ_{NL}.

Besides the similarity of the moduli at small and large strain amplitudes, the suspension and the gel present a very different behavior at intermediate strain amplitudes. Those different behav-

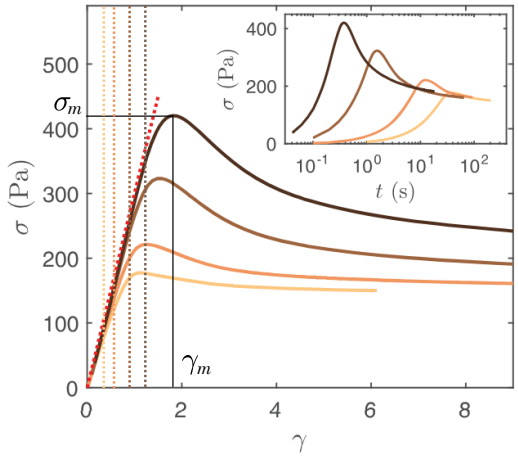

Figure 1.9: Shear start up experiments in a Carbopol microgel. Stress as a function of strain $\gamma = \dot{\gamma}t$ during continuous shear at $\dot{\gamma} = 5,\ 1,\ 0.2,\ 0.03\ \mathrm{s}^{-1}$ from top (darker color) to bottom (lighter color). The red dashed line highlights the linear response at short times $\sigma = G_0\gamma$ with $G_0 = 300$ Pa. The vertical dashed lines highlight the deviation from the linear response at $\gamma = \gamma_{NL}$ for each shear rate. The black solid lines highlight the coordinates (γ_m, σ_m) of the stress overshoot for $\dot{\gamma} = 5\ \mathrm{s}^{-1}$. Inset: same data plotted as a function of time. Reproduced from [Benzi et al., 2023].

iors have been classified [Hyun et al., 2002, Hyun et al., 2011]: for the gel, the viscous modulus presents an overshoot at intermediate strain amplitudes, before decreasing at larger strain amplitudes, while the elastic modulus simply decreases. This behavior is referred to as a "type III" behavior (weak strain overshoot). As for the suspension, both moduli simply decrease with increasing strain amplitude, with no overshoot. This is referred to as a "type I" behavior (strain thinning). Some materials, such as a solution of PVA and Borax [Hyun et al., 2002], present a strain hardening behavior, where both the elastic and the viscous moduli increase or overshoot with the strain amplitude, referred to as a "type II" behavior.

At large strain amplitudes, the elastic modulus becomes smaller than the viscous modulus: this solid-like to liquid-like transition is referred to as the yielding transition, and the strain amplitude γ_c at which it occurs is called the yield strain (see the continuous line in Fig. 1.8). The yield strain can also be taken as a reference for the measurements in the linear regime of deformation, with $\gamma \ll \gamma_c$. For a strain amplitude above the yield strain, too many bonds have been broken in the material microstructure for it to maintain its solid-like behavior. At even larger strain amplitude, the material remains in a liquid-like state, with $G'' > G'$, and both viscoelastic moduli decrease with the strain amplitude as the material microstructure continues to break down.

It is important to note that there are some limitations to the strain sweep experiments. First, they are performed at a single frequency, while we have seen that the viscoelastic moduli depend on the frequency. Second, they may not be stationary as each strain amplitude step is applied during a certain time. Yet, the material may evolve during this measurement time, in particular if it recovers or rearranges under oscillatory shear.

b Yielding under continuous shear: shear start up experiments

Another way to probe the transition from linear to non-linear behavior, which avoids sweeping the amplitude of an oscillatory deformation, is to apply a continuous shear to the material. This is referred to as a shear start up experiment. Figure 1.9 shows a typical example of the results obtained by continuously shearing a gel of Carbopol at four different shear rates [Benzi et al., 2023]. As the material is sheared at a given shear rate $\dot{\gamma}$, it first deforms elastically at short times, corre-

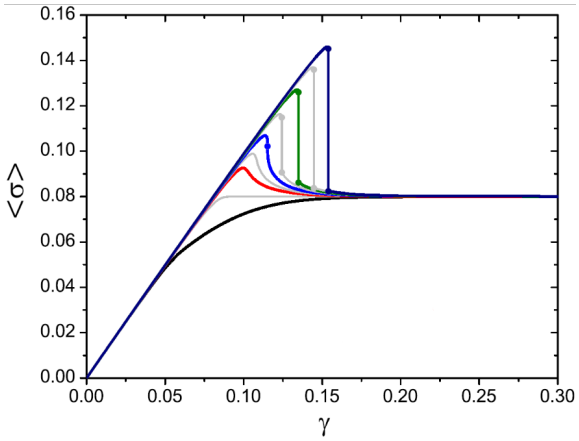

Figure 1.10: Numerical computations of shear start up experiments. Stress as a function of strain calculated through a mean-field elasto-plastic model for increasing degree of annealing from bottom to top. Adapted from [Ozawa et al., 2018].

sponding to small strains $\gamma = \dot{\gamma} \times t$, and follows the linear response predicted by Hooke's law for an elastic solid and given by Eq. (1.7) (see the red dashed line in Fig. 1.9), where the static elastic modulus $G = G_0$ is estimated by extrapolating the small frequency plateau of the elastic modulus $G'(f)$ to $f = 0$. The strain γ_{NL} at which the gel stress response deviates from the linear prediction corresponds to the onset of plasticity, and therefore sets the transition between the linear and the non-linear regime of deformation of the material. As visible from Fig. 1.9 (see the vertical dashed lines), this critical strain does depend on the shear rate, and may also depend on other parameters. Moreover, depending on the shear rate, on the material and on its age, the stress response may differ. In Carbopol gels for instance, at small shear rate $\dot{\gamma} = 0.03\ s^{-1}$, the stress increases at small strains and plateaus at larger strain, while at large shear rate $\dot{\gamma} = 5\ s^{-1}$, the stress overshoots before decreasing and eventually reaching a plateau at large strains. This stress overshoot corresponds to the material yielding, when the network constituting the gel microstructure cannot deform anymore without breaking a significant part of bonds. The coordinates of this overshoot define another characteristic strain γ_m and the corresponding critical stress σ_m (see the black solid lines in Fig. 1.9).

In recent years, the phenomenology of the stress overshoot during yielding and its theoretical modeling have attracted a lot of attention [Park and Ahn, 2013, Colombo and Del Gado, 2014, Ozawa et al., 2018, Barlow et al., 2020, Benzi et al., 2021a, Divoux et al., 2023]. In particular, predicting whether a soft material yields in a brittle or ductile way is difficult, since yielding depends on a variety of factors, including the material properties, the system preparation, the geometry confining the material, and boundary conditions. The ductile to brittle transition refers to a clear qualitative change of the material behavior when subject to an external deformation. This transition is typically observed by monitoring the stress dynamics under imposed deformation, as represented in Fig. 1.9 and in Fig. 1.10, and is linked to a change in the material rigidity. The ductile to brittle transition can be achieved by changing the density of the material, the temperature, the pressure, or simply the initial preparation of the sample. Such a transition in the yielding behavior of a material is well known in many areas of material sciences, ranging from metallic glasses [Lu et al., 2003, Schuh et al., 2007, Gu et al., 2009] to biological materials [Meyers et al., 2006, Peterlik et al., 2006, Barthelat et al., 2016]. An example of numerical computations of the yielding behavior of a soft amorphous material is showed in Fig. 1.10 [Ozawa et al., 2018]. A ductile to brittle transition is observed when increasing the "degree of annealing" of the system. In experiments, this can generally be achieved by letting the sample age spontaneously over a longer waiting time, also referred to as the "age" of the sample. For a ductile

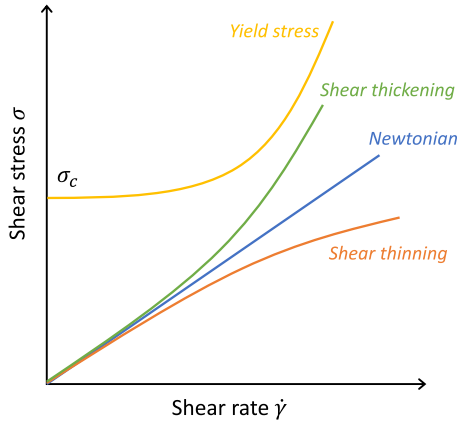

Figure 1.11: Schematic representation of the stress response of a Newtonian, shear thinning, shear thickening and yield stress fluid when sheared at various shear rates.

failure, the initial linear increase of the stress with applied strain, which corresponds to the material elastic response as detailed in the previous paragraph, is followed by a continuous crossover towards a stress plateau or by a smooth stress overshoot over a large strain range, associated to the viscoplastic response of the material (see the bottom curves in Fig. 1.10). On the other hand, in the case of a brittle failure, the short-time elastic response is followed by an abrupt stress drop at small strains (see the top curves in Fig. 1.10). The ductile to brittle transition is continuous. Indeed, in between these two extreme cases, there exists a wide range of responses with a stress overshoot which is more or less abrupt, that are referred to as brittle-like or ductile-like respectively, as observed in Fig. 1.9. The yielding behavior of a soft material strongly depends on the system preparation, as observed in Fig. 1.10, but also on how fast it is deformed, as observed in Fig. 1.9.

The ductile to brittle transition has been mainly studied in the case of dense amorphous systems such as colloidal glasses, through both experiments [Koumakis and Petekidis, 2011, Koumakis et al., 2012, Benzi et al., 2023] and theoretical modeling [Park and Ahn, 2013, Colombo and Del Gado, 2014, Ozawa et al., 2018, Barlow et al., 2020, Benzi et al., 2021a, Divoux et al., 2023]. Yet, only a few studies have reported such a transition in colloidal gels [Persello et al., 1994, Wei et al., 2019, Koumakis and Petekidis, 2011, Dimitriou and McKinley, 2014]. In this thesis, we will show that cellulose nanocrystal gels present a ductile to brittle transition when decreasing the shear rate or when increasing the sample age.

B.4 Flow behavior

In order to further characterize a soft material, we can investigate its liquid-like behavior by studying its flow properties and by comparing it to Newton's law, given by Eq. (1.8). Newton's law correlates the stress σ to the shear rate $\dot{\gamma}$ via the viscosity η. It is verified by simple fluids such as water or honey, that are called Newtonian fluids, and for which the viscosity is independent of how fast or of how strong the fluid is sheared. For non-Newtonian fluids, the viscosity does depend on the shear rate, and Newton's law can be generalized through the following phenomenological relationship:

$$\frac{\sigma}{\dot{\gamma}} = \eta(\dot{\gamma}). \tag{1.26}$$

Therefore, in order to probe the flow behavior of a soft material, one needs to measure its stress response to various shear rates. This resulting $\sigma(\dot{\gamma})$ curve is referred to as the material "flow curve".

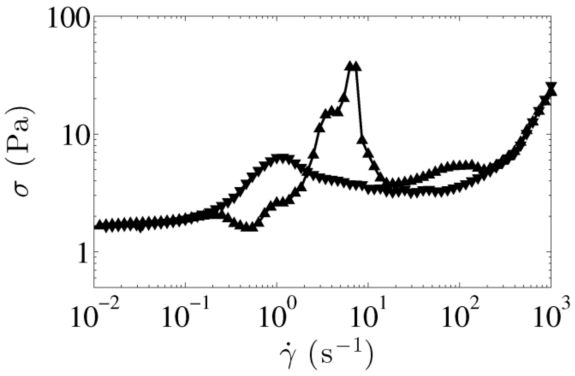

Figure 1.12: Flow curve σ versus $\dot{\gamma}$ obtained by first decreasing the shear rate continuously from 10^3 to 10^{-2} s^{-1} in 75 logarithmically spaced points of duration 8 s (▼) and then increasing the shear rate over the same range (▲). Experiments performed on a colloidal gel of silica particles. Reproduced from [Kurokawa et al., 2015].

Because of the dependence of the viscosity with the shear rate, the stress measured in a non-Newtonian material is not simply proportional to the shear rate, as represented in Fig. 1.11. If the viscosity of the material decreases with the shear rate, resulting in a slower increase of the stress when compared to a Newtonian material, the material is called "shear thinning". It is the case of yogurt and mayonnaise for example. If the viscosity of the material increases with the shear rate, resulting in a faster increase of the stress than in a Newtonian material, the material is called "shear thickening". It is the case of slime and dense corn starch suspensions for example. Some materials do not flow until a critical force is applied to them, resulting in a non-zero stress at vanishingly small shear rates. Such materials are called "yield stress" materials, and the value σ_c of the stress plateau in the limit $\dot{\gamma} \to 0$ is called the yield stress. It is the case of shampoo and toothpaste for example. Finally, some materials present a flow behavior which is a combination of the three phenomena: they may have a yield stress σ_c, and they can be shear thinning over a range of shear rates, and shear thickening over a different range of shear rates.

In order to measure the flow curve of a material, we can either ramp down or ramp up in shear rate. If the material evolves under shear, the two responses do not superimpose, and some hysteresis appears, as represented in Fig. 1.12. In this case, the shape of the flow curves and the area of the hysteresis depend on the time during which each shear rate is applied. This complex behavior may result from a sensitivity of the material to shear history due to the evolution of the material properties through time during measurement. For instance, the competition between aging at small shear rate and shear rejuvenation at larger shear rate can lead to a stress overshoot when ramping up in shear rate, as observed in Fig. 1.12. Such a competition usually leads to "thixotropic properties". Strictly speaking, a thixotropic material is a material whose viscosity decreases (resp. increases) over time following a step from a given shear rate to a larger (resp. smaller) shear rate.

In the literature, the hysteresis observed in flow curves is generally interpreted as the signature of thixotropy. However, while thixotropic materials indeed show a hysteresis in their flow curve, such a hysteresis is not necessarily the signature of thixotropy. In particular, it has been shown that other types of time-dependence, different from thixotropy, can account for the hysteresis observed in their flow curves. First, purely viscoelastic effects might come into play during the shear rate ramps leading to some hysteresis [Radhakrishnan et al., 2017, Puisto et al., 2015]. Second, instabilities may develop along the flow curve measurement [Bonn et al., 2017, Divoux et al., 2016]. For instance, shear bands may appear, in which part of the material is sheared at a larger shear rate than its surrounding, and might coexist with arrested bands where the material is not sheared at all. Such heterogeneities of the local shear rate in the bulk of the material results from the

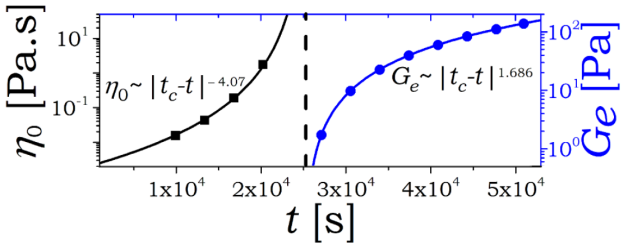

Figure 1.13: Time evolution of the zero-shear viscosity η_0 prior to gelation, and of the equilibrium modulus G_e after gelation of a colloidal suspension of hectorite clay. The vertical dashed line highlights the gelation time t_g. Adapted from [Suman and Joshi, 2020].

competition between aging and shear rejuvenation of the time-dependent material. Third, the material may slip on the geometry walls through lubrication layers that may develop in different way whether the shear rate is increased or decreased. Finally, all these effects may combine and contribute to the hysteresis of the flow curve.

Note that, due to wall slip and/or shear banding, the local shear rate in the bulk material may actually differ from the imposed one. In particular, in the limit of total slip, the bulk material is not sheared at all. Therefore, one should remain cautious when interpreting rheological measurements under steady or transient shear. Local measurements of the flow field under shear allows one to complement the macroscopic rheology. In this work, ultrasound velocimetry will be briefly used to get some insight into the local flow scenario in cellulose nanocrystal gels under shear.

C Gelation dynamics and aging of colloidal suspensions

All rheological approaches and mechanical characterizations introduced so far assumed that the material is in a stationary state. However, the rheological properties of a soft material may evolve in time, as its microscopic constituents assemble and its microstructure evolves through small rearrangements driven by thermal fluctuations. In the case of gels, we can rationalize the effect of time by probing the gelation dynamics, i.e., the kinetics of formation of the percolated network constituting the gel microstructure, and by probing their subsequent aging dynamics. The gelation and aging dynamics can be studied by following the time evolution of the gel viscoelastic properties thanks to rheometry.

C.1 Pioneering approaches of gelation

In order to study the gelation dynamics through rheological measurements, we first need to determine a criterion indicating the point at which the gel, i.e., the percolated network, is actually formed, corresponding to the gelation time.

a Liquid to solid transition versus true gelation

First, we can assume that the liquid to solid transition during the gel build up coincides with gelation, i.e., with the formation of a percolated network, as already mentioned in Sec. 1.A.2. This statement, which is consistent with the percolation theory accounting for the rigidity of a gel, is the most commonly used to determine the gelation time of many different polymer and colloidal soft materials.

Historically, this liquid to solid transition was first probed by measuring the time evolution of the material viscosity by applying a continuous shear with a small shear rate, and by assimilating this viscosity to the zero shear viscosity η_0. At the liquid to solid transition, the zero-shear viscosity

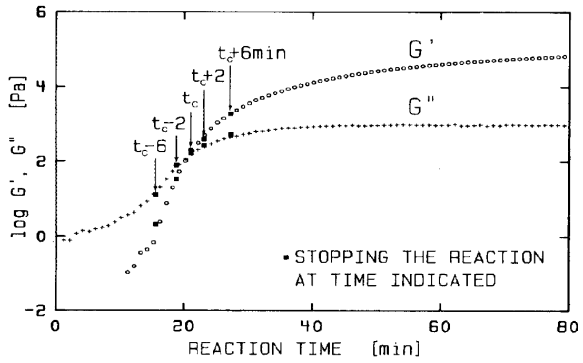

Figure 1.14: Time evolution of the elastic modulus G' and of the viscous modulus G'' of a polydimethylsiloxane polymer gel, measured by application of an oscillatory strain of frequency $\omega = 0.5$ rad.s^{-1} and amplitude varying from 3.0 %. to 0.005 %. Reproduced from [Winter and Chambon, 1986].

diverges, as a solid has an infinite viscosity. The subsequent aging dynamics of the solid-like material were probed by applying an oscillatory shear of small amplitude and small frequency in order to measure the time evolution of the elastic modulus, assimilated to the equilibrium modulus G_e, i.e., to the elastic modulus at zero frequency. Figure 1.13 shows an example of such measurements for a colloidal suspension of hectorite clay [Suman and Joshi, 2020]. The liquid to solid transition occurs at about 2.5×10^4 s. However, this method presents several drawbacks. First, measuring the viscosity at small shear rate and measuring the elastic modulus at small frequency involves long measurements times. Therefore, this method can only apply to materials with slow gelation and aging dynamics, in order for its time evolution not to interfere with the measurement. Moreover, applying a continuous shear to measure viscosity induces large strains, and may therefore impact the material microstructure, its viscoelastic properties and their gelation dynamics. Finally, this method does not allow one to define precisely a transition time and to resolve the dynamics around the transition point due to the divergence of the viscosity and to the emergence of the equilibrium modulus, and to the requirement to switch from one measurement to another.

A second method to probe the liquid to solid transition is to measure the time evolution of both the elastic and the viscous moduli at a single frequency, by applying a small amplitude oscillatory strain signal. Figure 1.14 presents the results of such a measurement for a polydimethylsiloxane polymer gel [Winter and Chambon, 1986]. At short times, both moduli increase with time, and the viscous modulus G'' is larger than the elastic modulus G', indicating that the material is in a liquid-like state. At time $t_c \approx 22$ s, referred to as the crossover time, both moduli are equal. At longer times, the elastic modulus is now larger than the viscous modulus, indicating that the material is in a solid-like state. This method allows one to precisely define the liquid to solid transition time t_c and to resolve correctly both the transition point and the pre- and post-transition dynamics, without impacting the material microstructure. However, since G' and G'' depend on the frequency, the crossover time t_c should also depend on the frequency. Therefore, t_c does not in principle correspond to a well-defined "gel point" and to a frequency-independent "gelation time". Moreover, even if the crossover time t_c usually turns out to be a good approximation of the gelation time t_g, t_c may strongly differ from t_g, as will be discussed more precisely in the following.

b Critical gel point

Actually, it has been shown that the true "gel point" corresponds to the point at which both the elastic and the viscous moduli evolve as a power-law with the frequency, with the same exponent

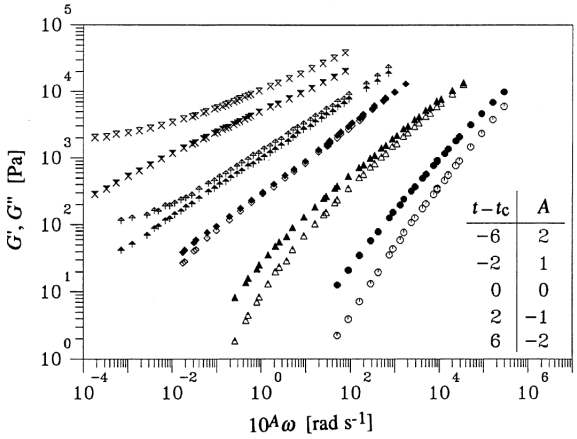

Figure 1.15: Time evolution of the viscoelastic spectrum $G'(\omega)$ and $G''(\omega)$ of a polydimethylsiloxane polymer gel. The curves are shifted sideways by a factor A to avoid overlap. Reproduced from [Winter and Chambon, 1986].

[Winter and Chambon, 1986, Winter, 1987, Suman and Joshi, 2020]:

$$G'(\omega) \sim G''(\omega) \sim \omega^{\beta}. \tag{1.27}$$

Such a power-law behavior is the signature of a continuum of time-scales in the relaxation spectrum of the gel microstructure, associated to a continuum of length-scales. It has been attributed to the formation of a fractal microstructure within the critical gel with no characteristic length-scale, i.e., to a microstructure which is self-similar over a wide range of length scales, associated to the time-scales probed by ω [Forrest and Witten Jr, 1979, Lin et al., 1989]. As a result, the loss factor is independent of the frequency at the gel point:

$$\tan\delta(\omega) = G''(\omega)/G'(\omega) \sim \omega^{0}. \tag{1.28}$$

The exponent β is called the "critical relaxation exponent", the gel formed at this point is referred to as the "critical gel", and the time at which we measure this critical behavior is the gelation time t_g. Such a definition of the gelation time is independent of the frequency, as previously mentioned.

It has been shown for polymer gels in the limit of fully screened hydrodynamic and excluded-volume interactions in three dimensions, that the critical relaxation exponent β is linked to the fractal dimension d_f of the critical gel network through the relationship [Muthukumar, 1989]:

$$d_f = \frac{5}{2}\frac{(3-2\beta)}{(3-\beta)}. \tag{1.29}$$

Experimental characterizations of the critical gel microstructure have been shown to agree with the above relationship in some colloidal gels [Eberle et al., 2012, Keshavarz et al., 2021].

Besides the power-law dependence of the viscoelastic moduli with the frequency, it has been shown experimentally that at the gel point, the growth rates of the logarithm of both moduli also evolve as a power-law with the frequency, with the same exponent (see Fig. 1.16) [Scanlan and Winter, 1991]:

$$\left.\frac{\partial \ln G'}{\partial t}\right|_{t_g}(\omega) = C\left.\frac{\partial \ln G''}{\partial t}\right|_{t_g}(\omega) \sim \omega^{-\kappa} \tag{1.30}$$

The exponent κ is called the "dynamical critical exponent", and C is a proportionality constant. This relationship suggests that, as the system approaches the critical gel point, the rates of change

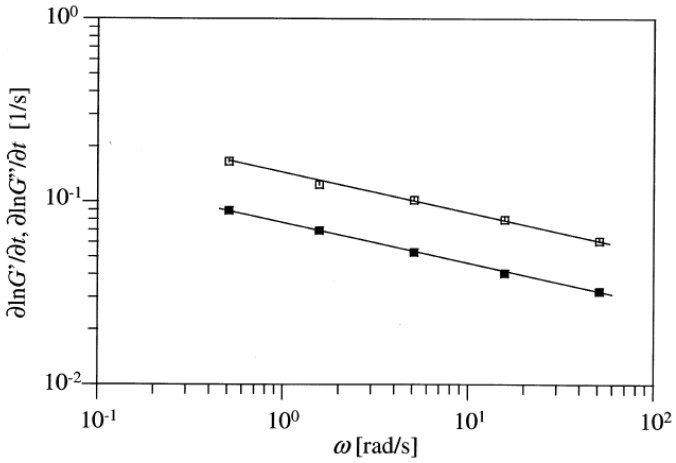

Figure 1.16: Frequency dependence of the elastic and viscous moduli growth rates at the gel point, for a polydimethylsiloxane polymer gel. Adapted from [Scanlan and Winter, 1991].

of both the elastic and the viscous moduli decrease in a similar way with increasing frequency. Based on experimental data, it has been hypothesized that both the exponent κ and the proportionality factor C might be universal constants, with $\kappa = 0.2$ and $C = 2$, for systems in which mechanical percolation and gelation is observed [Suman and Joshi, 2020].

Thereby, in order to properly determine the gelation time, one needs to measure the viscoelastic spectrum of the gel at different point in time. In the case of the chemical polydimethylsiloxane gel mentioned above, it is possible to stop the cross-linking reaction at a given point in time, and measure the corresponding viscoelastic spectrum of the material at rest. Figure 1.15 presents the viscoelastic spectra measured at different points in time on both sides of the gel point, which appears very clearly as the point where the elastic and the viscous spectra are parallel in a log-log representation. For this polydimethylsiloxane gel, the gelation time t_g coincides with the crossover time t_c highlighted in Fig. 1.14. However, depending on the system, the approximation $t_c \approx t_g$ is not always verified. In particular, it has been shown experimentally in polyurethane gels that, at small stoichiometry ratio between the monomer and the cross-linker, the solution presents a gelation time which is shorter than the crossover time by about 300 s [Winter et al., 1988]. Conversely, we will see in this thesis that, in cellulose nanocrystal gels, the gelation time can become as much as one order of magnitude longer than the crossover time, hence the necessity to determine the true gel point through time-resolved measurements of the suspension viscoelastic spectra.

In the case of colloidal physical gels however, it is not possible to stop the aggregation process at a given point in time in order to measure the corresponding viscoelastic spectrum at rest. Therefore, one needs to measure the suspension viscoelastic spectra through time during gelation, fast enough compared to the characteristic time-scale over which the suspension viscoelastic properties evolve, in order to obtain measurements that are not affected by the time evolution of the suspension. Such measurements of viscoelastic spectra resolved in time are referred to as "time-resolved mechanical spectroscopy". However, measuring a viscoelastic spectrum one frequency after the other takes time, especially for small frequencies. There are several ways to overcome this issue, and we will only present two of such techniques here. First, one can apply a series of pulses of a small-amplitude oscillatory strain signal, whose frequency is swept up between two predefined values. Each pulse results in a measurement of one viscoelastic spectrum at a given point in time. This technique is referred to as the "chirp" technique [Ghiringhelli et al., 2012, Geri et al., 2018]. Second, one can apply a periodic strain signal of small amplitude that results from the sum of several sinusoidal strain signals with different frequencies. Each period of the total strain signal results in the measurement of one viscoelastic

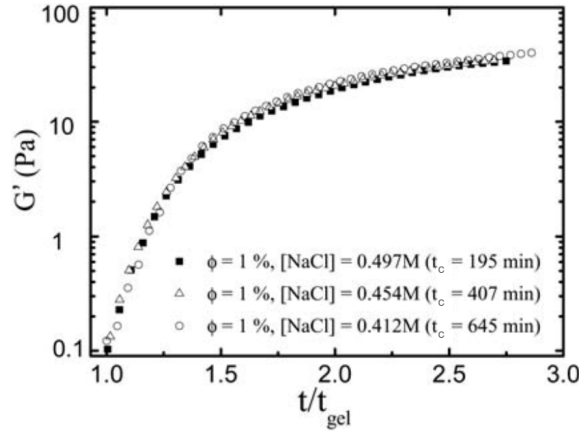

Figure 1.17: Time-composition superposition in colloidal gels of silica particles in the presence of salt. Time evolution of the elastic modulus rescaled by the crossover time t_c of each suspension containing ϕ = 1 % of silica particles and various NaCl concentrations. Measurement obtained by applying an oscillatory strain signal of frequency 1 Hz and amplitude 1 %. Adapted from [Cao et al., 2010].

spectrum at a given point in time. This technique is referred to as the "multiwave" technique [Heyes et al., 1994, Mours and Winter, 1994]. Both techniques allow one to measure a viscoelastic spectrum every few fraction of a second to a few seconds depending on the range of frequencies chosen. Besides offering the potentiality of measuring the viscoelastic spectra of a fast time-evolving gel in quasi-static conditions, these techniques also provide a good time-resolution, hereby providing a precise determination of the gelation dynamics and of the gelation time. An example of results for an aluminosilicate gel using chirp is given in Fig. 1.18(C) and (D) and will be detailed in the next section.

C.2 Superposition principles in gels

The gelation dynamics of polymer and colloidal gels present some universality, which is conveyed by the construction of master curves for the time evolution of their viscoelastic properties. Such master curves are obtained by rescaling the viscoelastic properties of a system whose composition, age, or some external control parameters such as the temperature (as commonly done for polymers), is varied. Such superposition principles are established by rescaling the suspension viscoelastic properties measured either at a single frequency, or at multiple frequencies, i.e., by rescaling its viscoelastic spectra. The construction of such master curves reveal the existence of an underlying superposition principle which reflects a certain universality in the viscoelastic properties of the material.

a Rescaling of single frequency measurements

Master curves can be obtained by rescaling the time evolution of the viscoelastic properties, measured at a single frequency, of suspensions whose composition is varied for instance. Figure 1.17 presents an example of such master curve for the time evolution of the elastic modulus of silica suspensions containing various salt concentrations [Cao et al., 2010]. In this case, every time responses are superimposed by rescaling time by the crossover time t_c of each suspension. In this example, the controlling parameter is the NaCl concentration, i.e., the suspension composition. Therefore, the superposition principle associated to the construction of the master curve is referred to as a "time-composition superposition principle". We will see in this thesis that a similar

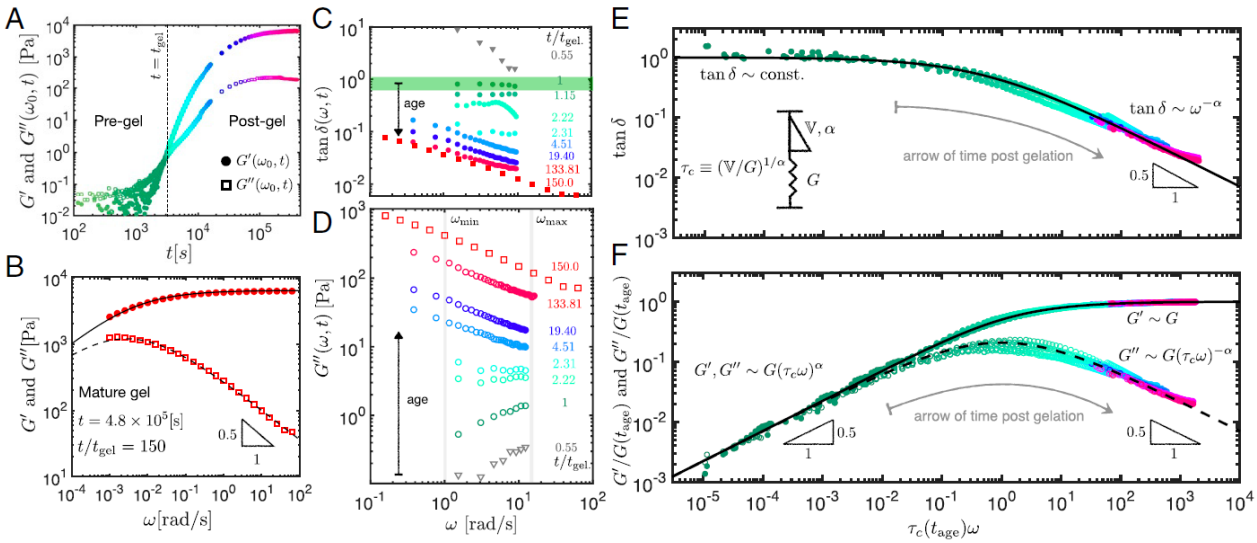

Figure 1.18: Time-resolved mechanical spectroscopy measurements and time-connectivity superposition on an aluminosilicate gel. (A) Time evolution of the linear elastic and viscous moduli measured at a single frequency $\omega_0 = 10$ rad.s^{-1}. (B) Viscoelastic spectrum of the aged gel measured at time $t = 4.8 \times 10^5$ s. The black lines show the best fit of the data by a fractional Maxwell model, represented in (E). (C) Loss factor and (D) viscous modulus spectra measured at various times during the sample gelation. The gel point is highlighted by the green band in C. (E and F) Master curves for the time evolution of the viscoelastic spectra. The black lines shows the best fit of the data by a fractional Maxwell model. Reproduced from [Keshavarz et al., 2021]

superposition principle can be established for cellulose nanocrystal gels of various salt concentrations.

b Rescaling of viscoelastic spectra

Another type of master curves can be obtained by rescaling the viscoelastic properties of a suspension measured at several frequencies. Figures 1.18(E) and (F) show an example of such master curves, obtained by rescaling the time evolution of the viscoelastic spectra of an aluminosilicate gel during aging [Keshavarz et al., 2021]. The master curve for the loss factor $\tan\delta$, represented in Fig. 1.18(E), is constructed by shifting along the horizontal axis the $\tan\delta(\omega)$ curves measured at several points in time, represented in Fig. 1.18(C), in order to maximize their overlap. The corresponding frequency shift factor $a(t) = \tau_c(t_{age})$ depends on time, i.e., on the sample age. The two master curves for the elastic modulus and for the viscous modulus respectively, represented in Fig. 1.18(F), are constructed (i) by applying the same frequency shift $\omega \times \tau_c(t_{age})$ as for the loss factor to the viscoelastic spectra measured through time, represented in Fig. 1.18(D) for the viscous modulus, and then (ii) by shifting vertically the resulting curves in order to maximize their recovery. The same vertical shift factor $b(t) = 1/G(t_{age})$, that depends on time, is applied for both the elastic and the viscous moduli.

In this example, gelation is fast, therefore, only the aging, or post-gel, dynamics for $t > t_g$ are captured. Figure. 1.19 shows an example of similar master curves where both the pre-gel and the post-gel dynamics are probed using micro-rheology on a peptide polymer gel [Larsen et al., 2008]. Indeed, rescaling the mean square displacement $\langle \Delta r^2 \rangle$ versus the lag time τ is equivalent to rescaling the complex modulus G^*, and therefore the viscoelastic moduli G' and G'', versus the frequency ω, as evidenced by the generalized Stokes-Einstein relationship [Mason and Weitz, 1995b,

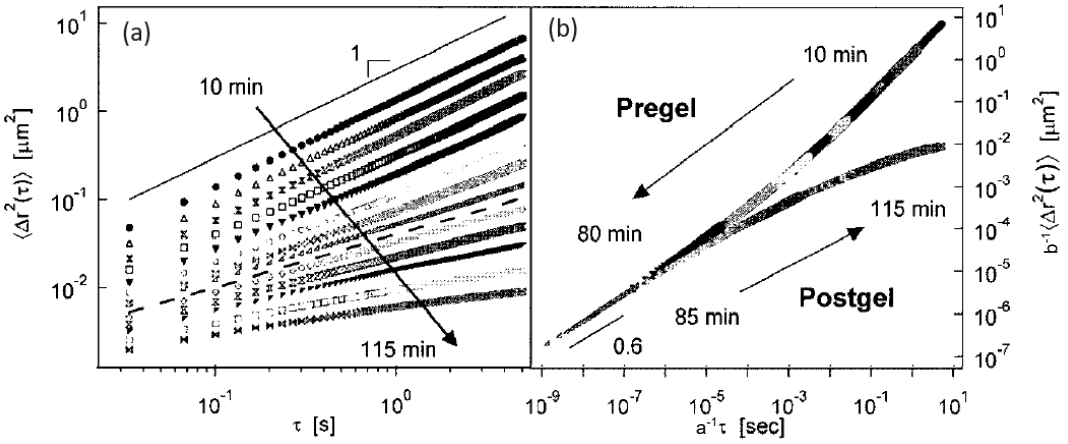

Figure 1.19: (a) Time evolution of the ensemble averaged mean-square displacement of embedded polystyrene microspheres versus lag time in a 0.15 wt % peptide solution, where gelation is provoked by addition of a buffer at time $t = 0$. The dashed line indicate the gel point. (b) Superposition of the mean-square displacement data by rescaling in time and in mean-square displacement by factors $a(t)$ and $b(t)$ respectively. Adapted from [Larsen et al., 2008].

Segre et al., 1995, Imhof et al., 1994]:

$$G^*(\omega) = \frac{k_B T}{\pi a i \omega \mathcal{F}\{\langle \Delta r^2(\tau) \rangle\}}. \tag{1.31}$$

Two master curves are obtained, for the pre-gel and for the post-gel dynamics respectively [see Fig. 1.19(b)], by shifting the $\langle \Delta r^2(\tau) \rangle$ curves measured at different points in time during gelation [see Fig. 1.19(a)] both horizontally, by a factor $1/a(t)$, and vertically, by a factor $1/b(t)$.

During gelation and aging, the gel microstructure evolves. In particular, the connectivity of the gel network changes through time. Therefore, the superposition principle evidenced by the construction of master curves for the time evolution of the suspension viscoelastic spectra during gelation is referred to as a "time-connectivity" superposition principle. In the literature, this superposition principle is also referred to as "time-cure" superposition. In this thesis, we show that time-connectivity superposition applies on gels of cellulose nanocrystals in the presence of salt.

c Critical exponents

Some useful information can be extracted from the time evolution of the rescaling parameters $a(t)$ and $b(t)$ used to horizontally and vertically shift the viscoelastic spectra and construct the master curves corresponding to the time-connectivity superposition principle. We illustrate this point using the example of the peptide polymer gel, where both the pre-gel and the post-gel dynamics are captured. Indeed, colloidal gels usually form too fast to be able to capture properly their entire gelation dynamics (both the pre-gel dynamics for $t < t_g$ and the post-gel dynamics for $t > t_g$), as observed in the previous section. Figure 1.20 shows the time evolution of the rescaling parameters $a(t)$ and $b(t)$ used to construct the master curves presented in Fig. 1.19(b). Both parameters diverge at the gel point, hence justifying the denomination "critical" gel point. The shift factors a and b evolve as power laws with the distance to the gel point $\varepsilon = |t - t_g|/t_g$, with exponents y and z respectively. Note that this divergence is symmetrical with respect to the gel point, i.e., the exponents y and z are the same for $t < t_g$ and for $t > t_g$.

Relationships, called hyper-scaling relations, have been established in polymer gels, and verified in some colloidal gels, to link all the different exponents extracted from time-connectivity su-

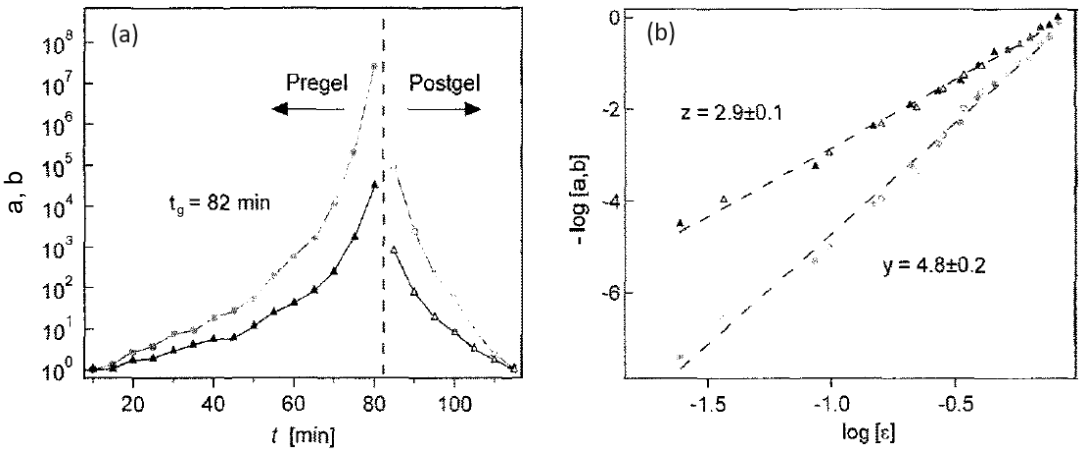

Figure 1.20: Time evolution of the rescaling factors a (circles) and b (triangles), plotted (a) as a function of time, and (b) as a function of the distance to the gel point $\varepsilon = |t - t_g|/t_g$. Filled symbols are for the pre-gel ($t < t_g$) and empty symbols are for the post-gel ($t > t_g$). The dashed line in (a) highlight the gelation time, while the ones in (b) represent a linear fit of the logarithmic data of exponents y and z. Adapted from [Larsen et al., 2008].

perposition [Winter, 1987, Stauffer et al., 1982]. First, at the critical gel point, both the non-rescaled and the rescaled viscoelastic moduli evolve as a power law of exponent β with the frequency or the rescaled frequency respectively: $G'(\omega, t_g) \sim G''(\omega, t_g) \sim \omega^{\beta}$ and $b(t)G'[a(t)\omega, t_g] \sim b(t)G''[a(t)\omega, t_g] \sim [a(t)\omega]^{\beta}$. By using those two relationships and the power law dependence of the shift factors to the distance to the critical gel point $a \sim \epsilon^y$ and $b \sim \epsilon^z$, one can show that the critical relaxation exponent β characterizing the gel point is equal to the ratio of the two exponents y and z characterizing the divergence of the horizontal and vertical shift factors at the gel point:

$$\beta = z/y. \tag{1.32}$$

Then, assuming that, in the vicinity of the critical gel point, for $t < t_g$, the relaxation modulus evolves as a stretched exponential $G(t) \propto \exp -(t/\tau)^{\kappa}$ of exponent κ similar to the one defined in Eq. (1.30), a second hyperscaling relation can be established:

$$\kappa = (1 - \beta)/(y - z). \tag{1.33}$$

Moreover, assuming the symmetry of the gelation dynamics with respect to the gel point, i.e., a similar value for the exponents y and z on both sides of the gel point, one gets a similar hyperscaling relation for the post-gel dynamics:

$$\kappa = \beta/z. \tag{1.34}$$

Finally, combining the first hyperscaling relation Eq. (1.32) with Eqs. (1.33) and (1.34), one gets:

$$\kappa = 1/y \tag{1.35}$$

One of the key goals of research on gelation is to uncover some universality classes among the different gel forming systems. Establishing hyperscaling relationships is a step forward in this direction. While they have been widely verified in many polymer systems, their validity has been tested on only few colloidal systems. In particular, we will see in this thesis that the hypothesis of symmetry of the gelation dynamics with respect to the critical gel point, assuming that the exponents y and z for the divergence of the rescaling parameters a and b are equal on both sides of the critical gel point, is not verified in gels of cellulose nanocrystals.

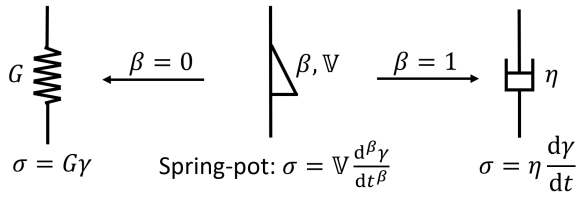

Figure 1.21: Diagram of a fractional element, or spring-pot.

C.3 Fractional models for gelation dynamics of colloidal gels

The evidence of time-connectivity superposition principles and the construction of the corresponding master curves spanning over several orders of magnitude in rescaled frequency, show gelation dynamics in colloidal gels that involve multiple time-scales. Such a broad relaxation dynamics cannot be captured by simple Maxwell or Kelvin-Voigt models which present a single time-scale τ. Instead, in order to properly capture such multiple time-scale gelation dynamics, it is necessary to complicate the previous models by adding a large number of springs or dashpots assembled in series or in parallel, hereby introducing a large number of parameters to the model. A way to simplify those complex models with a minimum number of parameters, and still account for the gels broad relaxation dynamics, is to use fractional elements [Keshavarz et al., 2021, Geri et al., 2018, Bonfanti et al., 2020, Bouzid et al., 2018]. The simplest fractional element, referred to as a "spring-pot", is a mechanical element which lies in between a spring and a dashpot. Its schematic representation is showed in Fig. 1.21. This mechanical element is defined by a constitutive equation that relates the stress σ to the strain γ through a fractional derivative [Blair and Coppen, 1943, Jaishankar and McKinley, 2013]:

$$\sigma = \mathbb{G}\frac{d^\beta \gamma}{dt^\beta} \tag{1.36}$$

where $\mathbb{G}$ is the element "quasi-property" with dimension Pa.s$^\beta$, and $\beta \in [0,1]$ is the order of the derivative. The fractional derivative is defined using the Caputo derivative [Podlubny, 1999]:

$$\mathrm{D}_t^\beta f(t) \equiv \frac{d^\beta}{dt^\beta} f(t) = \frac{1}{\Gamma(n-\beta)} \int_0^t (t-t')^{n-\beta-1} f^{(n)}(t') dt' \tag{1.37}$$

where $n-1 < \beta \leq n$, n is an integer, and $f^{(n)}(t)$ is the standard derivative of order n of the function $f(t)$.

From the relationship given by Eq. (1.36) and the definition of the complex modulus G^* given by Eq. (1.11), using complex notations, the complex modulus G^* associated to a spring-pot is given by:

$$G^* = \mathbb{G}(i\omega)^\beta. \tag{1.38}$$

Using $i = e^{i\pi/2}$ and taking the real and imaginary parts of G^*, the corresponding elastic modulus and viscous modulus are given by:

$$\begin{cases} G' = \mathbb{G}\omega^\beta \cos \beta\pi/2 & (1.39) \\ G'' = \mathbb{G}\omega^\beta \sin \beta\pi/2 & (1.40) \end{cases}$$

and the loss factor is given by:

$$\tan\delta = \tan(\beta\pi/2). \tag{1.41}$$

In the limit $\beta \to 0$, the spring-pot corresponds to a simple spring: $G' = \mathbb{G}$ and $G'' = 0$, with $\mathbb{G} = G$. In the limit $\beta \to 1$, the spring-pot corresponds to a simple dashpot: $G' = 0$ and $G'' = \mathbb{G}$, with $\mathbb{G} = \eta$. For $0 < \beta < 1$, the spring-pot gives rise to a power-law viscoelastic spectrum $G' \sim G'' \sim \omega^\beta$,

and to a frequency-independent loss factor and phase angle $\delta = \beta\pi/2$. Therefore, a single spring-pot captures the viscoelastic behavior of a critical gel of critical relaxation exponent β.

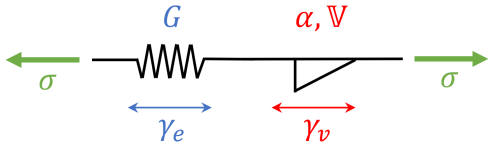

Figure 1.22: Fractional Maxwell model.

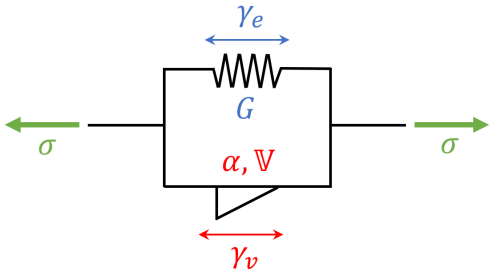

Figure 1.23: Fractional Kelvin-Voigt model.

A fractional model that is commonly used to describe the viscoelastic behavior of a gel is the Maxwell fractional model. It consists in replacing the dashpot in the classical Maxwell model by a fraction element, as represented in Fig. 1.22. Similarly to the calculations performed for the classical Maxwell model, detailed in Sec. 1.B.2, one can calculate the complex modulus associated to this fractional model. Using complex notations, the additivity of strain and the definition of the complex modulus G^* given by Eq. (1.11), we obtain:

$$G^* = \frac{G\mathbb{V}(i\omega)^\alpha}{(i\omega)^\alpha\mathbb{V} + G} \tag{1.42}$$

Using $i = e^{i\pi/2}$ and taking the real and imaginary parts of G^*, the elastic and viscous moduli are given by:

$$\begin{cases} G' = \dfrac{G\mathbb{V}^2\omega^{2\alpha} + G^2\mathbb{V}\omega^\alpha\cos(\alpha\pi/2)}{G^2 + \mathbb{V}^2\omega^{2\alpha} + 2G\mathbb{V}\omega^\alpha\cos(\alpha\pi/2)} & (1.43) \\ G'' = \dfrac{G^2\mathbb{V}\omega^\alpha\sin(\alpha\pi/2)}{G^2 + \mathbb{V}^2\omega^{2\alpha} + 2G\mathbb{V}\omega^\alpha\cos(\alpha\pi/2)} & (1.44) \end{cases}$$

and the loss factor is given by:

$$\tan\delta = \frac{G\sin(\alpha\pi/2)}{\mathbb{V}\omega^\alpha + G\cos(\alpha\pi/2)}. \tag{1.45}$$

This model captures perfectly well the aging, post-gel dynamics of a silicate gel as showed in Fig. 1.18(E) and (F). Similarly to the classical Maxwell model, the fractional Maxwell model allows one to capture the elastic plateau at large frequency ($G' \underset{\omega\to+\infty}{\longrightarrow} G$). Moreover, contrary to the classical model, the fractional Maxwell model allows to account both for the slow G'' power-law decrease at large frequencies ($G'' \underset{\omega\to+\infty}{\sim} \omega^{-\alpha}$), and for the power-law dependence of G' and G'' with the frequency at the gel point, with an exponent α which is smaller than one ($G', G'' \underset{\omega\to0}{\sim} \omega^\alpha$).

Similarly to the fractional Maxwell model, one can define a Kelvin-Voigt fractional model by replacing the dashpot by a fractional element, as represented in Fig. 1.23. Using the additivity of stress, the complex modulus G^* is defined by:

$$G^* = G + \mathbb{V}(i\omega)^\alpha \tag{1.46}$$

The resulting elastic and viscous moduli are given by:

$$\begin{cases} G' = G + \mathbb{V}\omega^\alpha\cos(\alpha\pi/2) & (1.47) \\ G'' = \mathbb{V}\omega^\alpha\sin(\alpha\pi/2) & (1.48) \end{cases}$$

and a loss factor given by:

$$\tan\delta = \frac{\mathbb{V}\omega^{\alpha}\sin(\alpha\pi/2)}{G + \mathbb{V}\omega^{\alpha}\cos(\alpha\pi/2)} \tag{1.49}$$

As the classical Kelvin-Voigt model, this fractional model allows one to capture the elastic plateau at small frequencies ($G' \underset{\omega\to 0}{\longrightarrow} G$). Moreover, contrary to the classical model, the fraction Kelvin-Voigt model allows to account for a power-law evolution of both the elastic and the viscous moduli at the gel point, at large frequency, with an exponent smaller than one ($G', G'' \underset{\omega\to+\infty}{\sim} \omega^{\alpha}$).

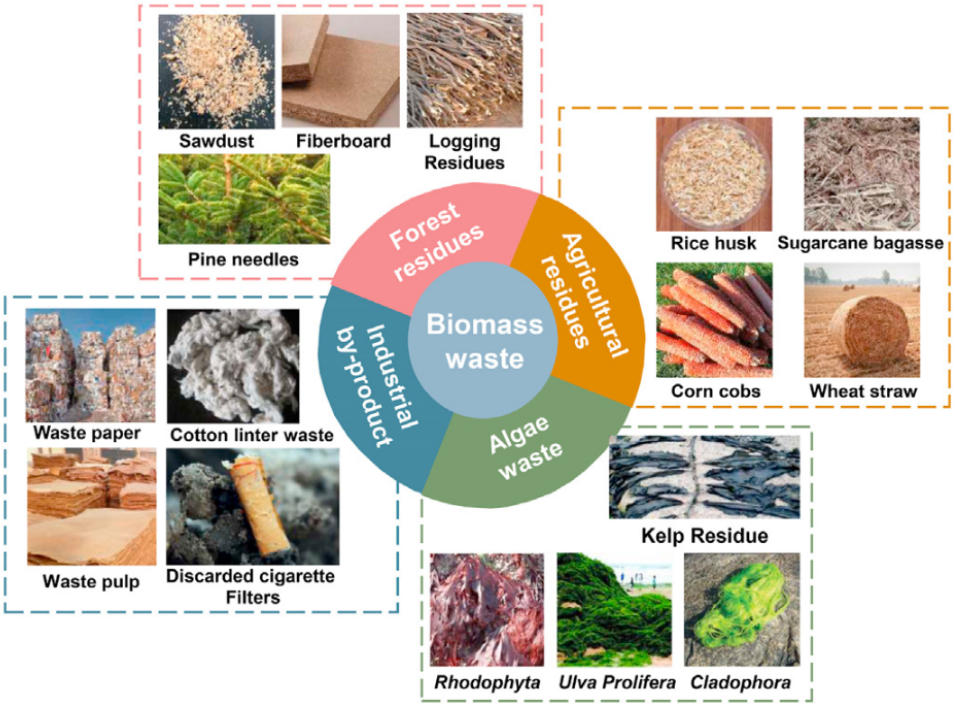

Figure 1.24: The various sources of biomass waste from which cellulose can be extracted. Reproduced from [Yu et al., 2021].

D Structure and rheology of cellulose nanocrystals

Cellulose is the most abundant bio-polymer on Earth. It is synthesized by plants, such as wood, cotton or algae, as one of the constituents of their cell walls, but also by some bacteria and by tunicate, a small marine invertebrate [Klemm et al., 2018, Li et al., 2021]. Plants alone produce between 50 and 100 billions of tons of cellulose every year, which represents over 50 % of the biomass, therefore constituting an abundant and sustainable resource [Li et al., 2021, Trache et al., 2020]. Moreover, cellulose can be extracted from a great variety of biomass wastes (see Fig. 1.24), such as derivatives from the food and paper industries, which may be key to address waste reduction [Yu et al., 2021, Danial et al., 2015, Neto et al., 2013].

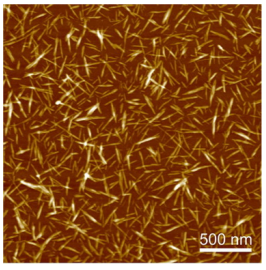

Figure 1.25: Atomic force microscopy image of CNCs. Reproduced from [Klemm et al., 2018].

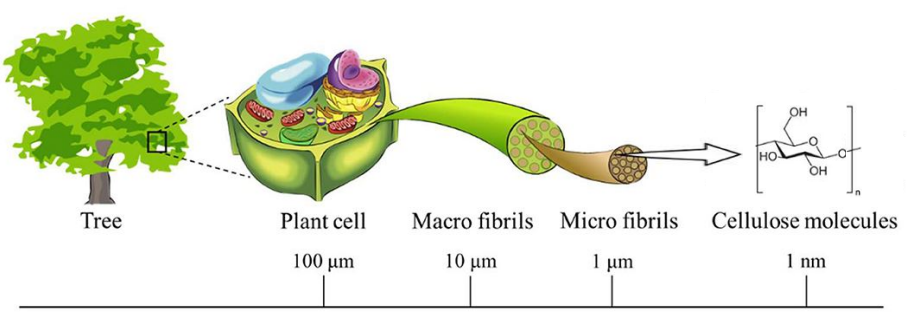

Figure 1.26: Hierarchical structure of cellulose in plant cells. Extracted from [Miyashiro et al., 2020].

Cellulose is a polysaccharide which monomer is represented in Fig. 1.26. In nature, cellulose does not exist as an individual particle, but rather takes the form of a macrofibril, constituted of microfibrils which result from the arrangement of several chains of monomers assembled together via hydrogen bonds and van der Waals interactions, as represented in Fig. 1.26 [Habibi et al., 2010]. This arrangement results in both crystalline regions, where the chains of monomers are assembled in a very organized crystalline order, and disordered regions in a cellulose fibril [Rowland and Roberts, 1972]. The crystalline regions are the building blocks of the cellulose nanocrystals (CNCs) (see Fig. 1.25).

D.1 Cellulose nanocrystals extraction and individual properties

In order to isolate cellulose nanocrystals from a cellulose fiber, one needs to separate the crystalline regions from the disordered regions. To do so, several techniques can by used, such as (i) mechanical treatments involving ultra-sonication, high-pressure homogenization or ball milling, (ii) biological treatments involving an enzymatic hydrolysis, (iii) chemical treatments involving an acid or alkali hydrolysis, or (iv) a combination of the three, as shown in Fig. 1.27 [Yu et al., 2021]. Each technique has its own advantages and drawbacks: the chemical method is the most widely used and the cheapest, leading to CNCs of large aspect ratio and high crystallinity. However, it involves long reaction times with low yield, high energy and the use of corrosive chemicals. Mechanical methods have a high yield, but are more energy consuming and lower the degree of cristallinity and the purity of the extracted CNCs. Finally, the biological method consumes very little energy and eliminates the use of harmful chemicals. However, it is highly sensitive to experimental parameters such as the precise composition of the culture medium. It is also expensive, with low efficiency, and involves long reaction times. In this thesis, we use CNCs which are extracted through the chemical method, namely through an acid hydrolysis.

The individual properties of cellulose nanocrystals differ depending on the extraction process, and depending on their source. In particular, the conditions of the hydrolysis such as the acid used, its concentration, the reaction time and the temperature, affect the individual particle shape, i.e., its length L and diameter D, and its surface chemistry. The acid penetrates more easily the disordered regions of the cellulose fiber than the crystalline ones, and it therefore destroys the disordered parts of the fibers first, leaving the crystalline parts intact (several days are necessary for the acid to affect the crystalline parts, i.e, much longer than the typical few hours over which the acid hydrolysis is performed) [Davidson, 1943, Nickerson and Habrle, 1947]. Furthermore, depending on the acid used, the hydrolysis of the cellulose fibers can result in the introduction of a chemical group on the CNCs surface, hereby modifying the particle surface chemistry. For instance, sulfuric acid leads to the presence of negatively charged sulfate groups on the CNCs surface (see the schematic representation of Fig. 1.28), while hydrochloric acid leads to

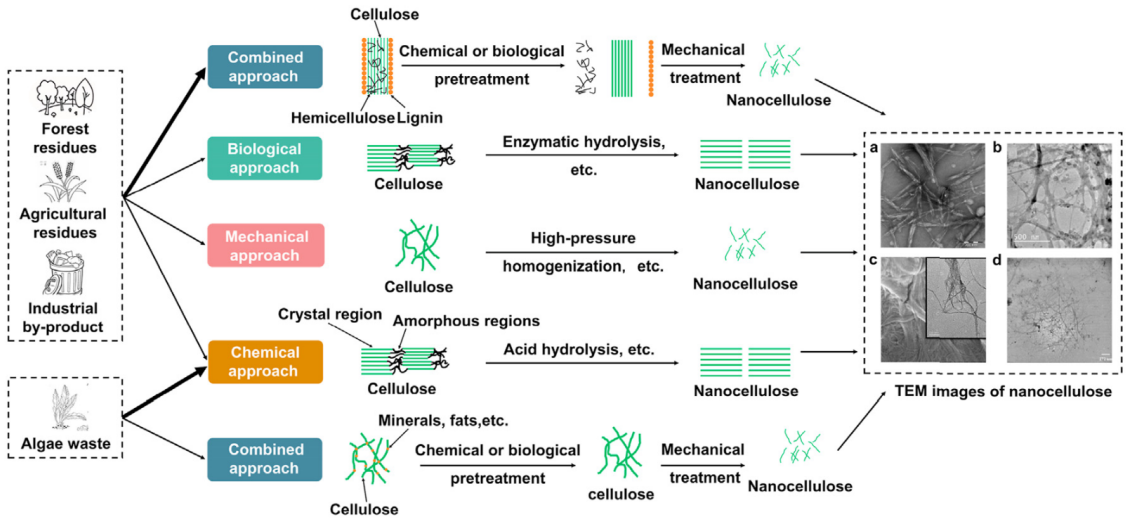

Figure 1.27: Schematic diagram of biomass waste-based processing for cellulose nanocrystals extraction. Transmission electron microscopy images of cellulose nanocrystals extracted with (a) chemical, (b) biological, (c) mechanical and (d) combined approach. Reproduced from [Yu et al., 2021].

no negative surface charges, hence to a more poorly dispersed suspension [Eichhorn et al., 2010]. Besides the surface chemistry of CNCs, the extraction protocol also influences their length and polydispersity. For instance, a long or high temperature hydrolysis leads to shorter CNCs than a short or low temperature hydrolysis (L varies from 120 nm to 141 nm for a reaction time decreasing from 45 min to 25 min, and L varies from 70 nm to 120 nm for a temperature decreasing from 72°C to 45°C) [Beck-Candanedo et al., 2005, Elazzouzi-Hafraoui et al., 2008]. The natural source from which cellulose is extracted also impacts the size and aspect ratio of CNCs, whose length L can vary between 100 nm and 1300 nm, and diameter D between 5 nm and 30 nm [Li et al., 2021, Lahiji et al., 2010, Elazzouzi-Hafraoui et al., 2008]. For instance, CNCs extracted from bacteria and tunicates are much longer and thinner than the ones extracted from wood or cotton [Battista, 1975]. In this thesis, we use cellulose nanocrystals which are extracted from wood through strong sulfuric acid hydrolysis, hereby introducing negatively charged sulfate groups $-O-SO_3^-$ on their surface.

Whatever the extraction process and their source, cellulose nanocrystals are very rigid colloids which cannot be easily deformed or broken into pieces: they have a compression elastic modulus of about 100 GPa to 200 GPa, and a flexion elastic modulus of about 10 GPa to 50 GPa [Li et al., 2017, Rao et al., 2022]. Besides those interesting individual mechanical properties, CNCs present the advantage to have a small density, of about 1.5 g.cm^{-3}, which is similar to that of water. Therefore CNCs do not sediment once suspended into water.

D.2 Interest of cellulose nanocrystals

Cellulose nanocrystals have raised great interest in the last few years, both for their original physical properties, and for their natural origin. Moreover, they are biodegredable and biocompatible, i.e., non-toxic, what further contribute to their great value for the elaboration of new materials which would be more environmentally friendly.

Moreover, CNCs have particularly interesting individual mechanical properties, their surface chemistry is easily modified during the extraction process or during post treatment, and their

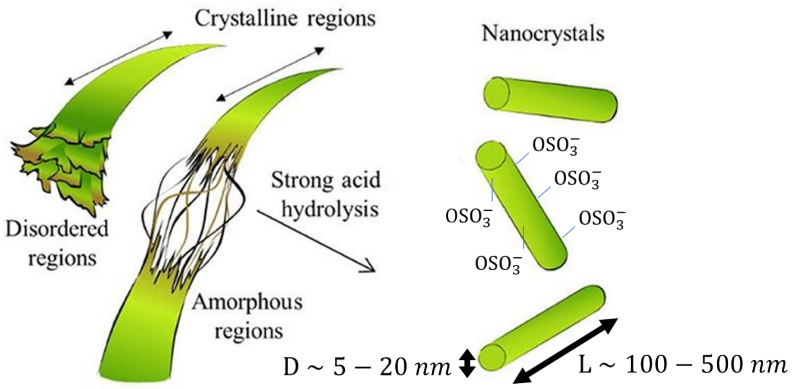

Figure 1.28: Schematic representation of CNCs extraction from a cellulose fiber through a sulfuric acid hydrolysis. Adapted from [Miyashiro et al., 2020].

capacity to arrange into a great variety of phases, including liquid crystal phases with original optical properties, contributes to their many advantages, which could lead to many applications in a wide range of domains [Lagerwall et al., 2014, Trache et al., 2020, Grishkewich et al., 2017, George and Sabapathi, 2015].

First, CNCs can be used as a soft material when suspended in a solvent or added to an already existing solution. Their rheological properties make them particularly interesting for applications in the food industry or in any other domain involving soft materials, as a thickener, gelling agent, texture enhancer and even suspension and emulsion stabilizer [Perumal et al., 2022, Mu et al., 2019]. Those soft materials can also be used as precursors to the elaboration of solid materials through molding or 3D printing [Klemm et al., 2018, Rao et al., 2019, Li et al., 2021].

Second, CNCs can also be used as a solid material. Their rod-like shape can be utilized to design materials with specific microstructural arrangement leading to specific mechanical or optical properties. For example, it has been shown that CNCs microstructural organization, such as the length-scale associated to the cholesteric arrangement or the orientation of a liquid crystal cluster, can be controlled by the application of shear, mechanical compression, magnetic field, or through planar anchoring [Frka-Petesic et al., 2014, Parker et al., 2018]. Using these methods, band gap photonic films [Shopsowitz et al., 2010] and holograms [Parker et al., 2018] can be designed. Furthermore, the great rigidity of CNCs individual particles allows one to form materials which can be very rigid both at small and at large scales. For example, razor blades have been made out of CNCs (Gillette Company LLC).

Finally, CNCs display good thermal properties and can be used to increase the thermal stability of many polymeric materials [Xie et al., 2018, Habibi et al., 2010]. Furthermore, the original chemical properties of CNCs can lead to many other applications in the food and pharmaceutical industries, where the antioxidant, antimicrobial and gas barrier properties of CNCs can be utilized to elaborate packaging reducing or inhibiting microbial spoilage of food products or medicines. It has also been shown that CNCs have good encapsulating and carrier agent properties to deliver active compounds such as active substance in drugs or vitamins, minerals and probiotics naturally present in aliments. Therefore, CNCs can be used to design drug capsules, or added to food products to help digestion and delivery of the bioactive compounds into the biological system [Perumal et al., 2022].

This list of applications is not exhaustive. Many other applications of cellulose nanocrystals exist, from the construction industry [Aziz et al., 2021, Rahmawati et al., 2021] to wound dressing and tissue engineering in medicine [Du et al., 2019]. To conclude, cellulose nanocrystals present a great potential for the elaboration of more environmentally friendly materials, and could replace

some petrochemical products.

D.3 Suspension of cellulose nanocrystals in water: phase diagram

The different phases formed by cellulose nanocrystals suspended in water in the presence or in the absence of salt have been widely studied [Xu et al., 2020, Moud and Moud, 2023, Parker et al., 2018, Hirai et al., 2009, Oguzlu et al., 2017]. A qualitative phase diagram is represented in Fig. 1.30 [Xu et al., 2019].

Sulfated cellulose nanocrystals suspended in water form a stable suspension thanks to the inter-particle electrostatic repulsion induced by the negative surface charges. At small concentration and in the absence of salt, i.e., at very small ionic strength (see upper part of Fig. 1.30), this suspension is an isotropic liquid where CNCs are randomly dispersed. At intermediate concentrations, CNCs organize into helicoidal structures to form a cholesteric liquid crystal [Revol et al., 1992]. Those helicoidal structures are made of CNCs which are aligned parallel to each other in a same plane, with a small angle rotation between the orientation of each plane, as illustrated in Fig. 1.29. This spontaneous mesoscale self-organization of CNCs does not arise directly from the twisted morphology of individual cellulose crystallites at the microscale, as usually observed in other biological systems such as DNA [Tortora et al., 2020]. Rather, in CNC suspensions, it was recently shown that the chirality observed at the mesoscale through the presence of cholesteric arrangements, is induced by a sub-population of bundles formed by a few CNC particles assembled parallel to each others [Parton et al., 2022]. This liquid crystal phase is easily identified under polarized light thanks to its optical properties: the helicoidal structures formed by CNCs induce a rotation of the polarization direction, responsible for the suspension birefringence [Revol et al., 1992]. At large concentration, this suspension forms a repulsive glass constituted of liquid crystals domains, in which CNCs are aligned, confined into cages formed by their neighboring domains due to crowding effects.

Figure 1.29: Schematic representation of the CNCs arrangement in the cholesteric liquid crystal phase. Reproduced from [Barrett, 2021].

Upon addition of salt, i.e., upon increasing the ionic strength (see lower part of Fig. 1.30), part of the CNCs negative surface charges are screened, resulting in a weakening of the electrostatic repulsion forces. Attractive forces such as van der Waals interactions and hydrogen bonding may then come into play and induce particle aggregation. At intermediate CNC content, CNCs organize into a percolated network of particles, i.e., an isotropic gel where no liquid crystal arrangement is present. At large CNC content, crowding effects leads to the formation of an arrested state, i.e., an attractive glass.

Figure 1.31 presents a quantitative phase diagram which has been established for suspensions of CNCs at various NaCl concentrations (the vertical axis representing the NaCl concentration is reversed compared to the previous phase diagram pictured in Fig. 1.30) [Xu et al., 2020]. In this phase diagram, the CNC volume fraction ϕ is replaced by the reduced concentration $c = \phi r$, where $r = L/D$ is the particle aspect ratio (L is the CNC length and D its diameter), in order to get rid of the effect of the CNC morphology, due to a change of source or of extraction protocol. The boundaries have been established relying on various experimental data reported in the literature. At small salt concentration, the presence of liquid crystal phases is evidenced optically by the appearance of birefringence, upon increasing the CNC volume fraction (biphasic phase). At larger CNC volume fraction, the transition from a liquid to a repulsive glass is predicted theoretically to occur for $c_{\text{glass}} = \phi_{\text{glass}} r = 0.7$. This prediction has been confronted to simulations and experimental data where the glass transition is evidenced by a transition from a liquid-like state to a solid-like state, in which elasticity becomes measurable and a yield stress is measured. The boundary is not perfectly vertical as it has been observed that the CNC volume fraction corresponding to this glass transition increases with the ionic strength, i.e., with the salt concentration. When increasing the

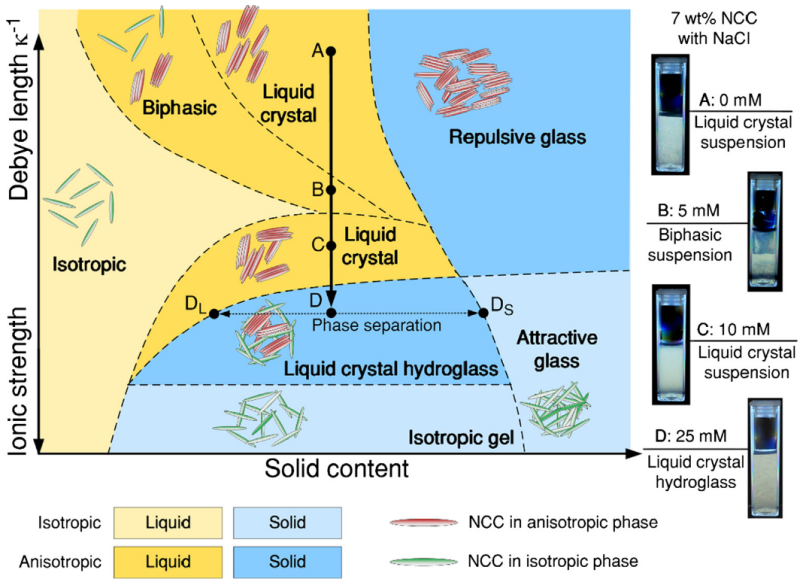

Figure 1.30: Qualitative phase diagram for CNCs suspended in water at various concentrations and for various salt contents. An increasing ionic strength and a decreasing Debye length correspond to an increasing salt concentration. Reproduced from [Xu et al., 2019].

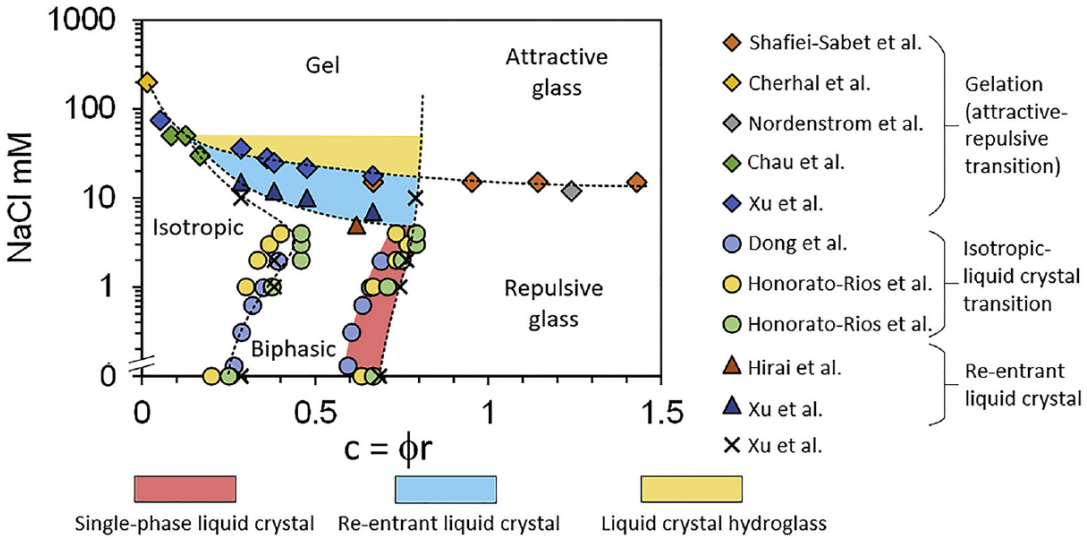

Figure 1.31: General phase diagram for CNCs suspended in water in the presence of NaCl. The vertical axis is reversed compared to Fig. 1.30. The reduced concentration c is defined as the product of the CNC volume fraction ϕ by the particle aspect ratio $r = L/D$, with L the particle length and D its diameter. Diagram established relying on experimental data from CNCs of different aspect ratio. Reproduced from [Xu et al., 2020].

salt concentration from the isotropic liquid or biphasic phases, i.e., for $c < c_{glass}$, rheological measurements show that the suspension goes from a liquid-like state to a solid-like state: the elastic modulus becomes larger than the viscous modulus over a range of measured frequencies. In this phase diagram, this liquid-to-solid transition is associated to the gel transition. Yet, as shown in Sec. 1.C.1.b such a criterion may fail if the true gelation occurs before or after the liquid to solid transition. The distinction between the gel phase and the attractive glass phase upon increasing the CNC content at large salt concentration cannot be evidenced through standard rheological measurements. The attractive to repulsive glass boundary at large CNC content upon decreasing the salt concentration can be determined using rheology through the presence of a discontinuity in the suspension yield stress as a function of the NaCl concentration. Moreover, two samples in the two phases have a different response to dilution: while a repulsive glass leads to a stable suspension of well dispersed individual CNC particles, an attractive glass leads to a dispersion of flocs of CNCs.

By taking into account the particle aspect ratio, such a phase diagram is assumed to be universal, whatever the CNC source and extraction protocol. However, the positions of the boundaries may vary with the density of surface charges on a CNC particle, with its surface chemistry and with the polydispersity of CNC particles. All these properties depend on the cellulose source and on the CNC extraction protocol, and influence the inter-particle interactions, and therefore their microstructural arrangement leading to the formation of the different phases. Moreover, this phase diagram has been established at a given point in time. However, we shall show in this thesis that CNC suspensions in the presence of salt evolve over very long time-scales, without reaching any stationary state. Therefore, the validity of such a static phase diagram can be questioned, and in particular the positions of its boundaries may depend on time. Finally, such a phase diagram has been established for the addition of sodium chloride in the CNC suspensions, and it would be interesting to determine how it depends on the salt nature.

D.4 Rheology of aqueous suspensions of sulfated cellulose nanocrystal

Besides the rationalization of the microstructural organization of CNCs in suspension, investigating and understanding the mechanical behavior of such suspensions is an important step towards potential applications.

a Rheology of cellulose nanocrystals in the absence of salt

The rheology of aqueous suspensions of cellulose nanocrystals in the absence of salt, hence in the isotropic, liquid crystal or repulsive glass phases, has been the subject of many studies. In particular, the dependence of CNC suspensions linear viscoelastic properties with the frequency and the dependence of their dynamic viscosity with the shear rate have been widely studied [Li et al., 2015, Wu et al., 2014, Buffa et al., 2019, Xu et al., 2024, Fazilati et al., 2021, Shafiei-Sabet et al., 2014, Qiao et al., 2016, Kádár et al., 2020, Keyvani et al., 2021, Wojno et al., 2023]. Figure 1.32 shows an example of viscoelastic spectra and flow curves measured for CNC suspensions at different concentrations, after a 60 min recovery period following a strong pre-shear at $\dot{\gamma} = 100\ s^{-1}$ during 5 min [Xu et al., 2024]. At rest, when the CNC concentration increases, the suspension goes from a liquid state in which $G'' > G'$, to a solid-like state in which $G' > G''$, at all frequencies [see Fig. 1.32(a)]. The concentration at which this transition occurs depends on the size of the CNC particles, and therefore on their source [Wu et al., 2014, Buffa et al., 2019], on the hydrolysis time [Li et al., 2015], and on their surface chemistry [Keyvani et al., 2021] as already mentioned. Moreover, at a given frequency, both the elastic and the viscous moduli increase with the CNC weight fraction, and the frequency dependence of the viscoelastic moduli varies with the CNC content: both G' and G'' increase with the frequency, but this increase is less and less pronounced as the CNC weight fraction increases, until they become almost independent of the frequency for a weight fraction of 7.5 wt % CNC. When flowing under shear, CNC suspensions show a shear thinning behavior

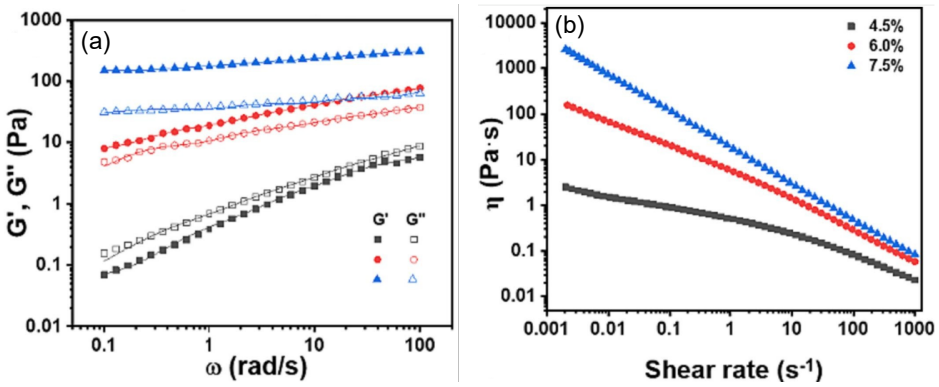

Figure 1.32: (a) Linear viscoelastic spectra (measured at γ = 1 %) and (b) viscosity as a function of the shear rate, of CNC suspensions of various weight fractions: 4.5 wt % CNC (■), 6.0 wt % CNC (•) and 7.5 wt % CNC (▲). Sulfated CNCs extracted from wood (CelluForce) suspended in water. Experiments performed after a 60 min recovery period following a strong pre-shear at $\dot{\gamma}$ = 100 s^{-1} during 5 min. Adapted from [Xu et al., 2024].

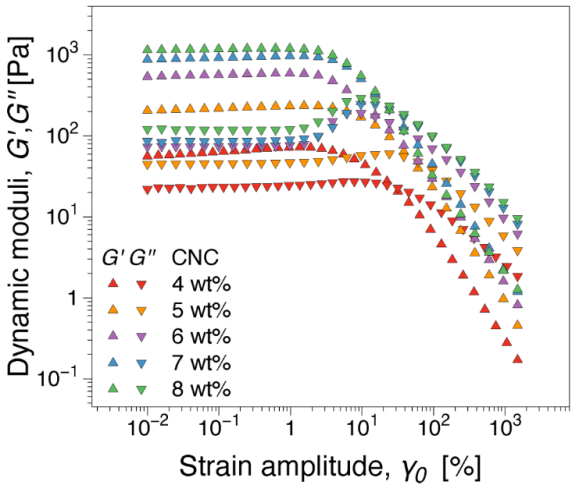

Figure 1.33: Strain sweep experiments. Viscoelastic moduli as a function of the strain amplitude, measured at ω = 2 rad.s^{-1} for suspensions containing various CNC weight fractions. Sulfated CNCs extracted from wood (CelluForce) suspended in water. Experiments performed after a 4 min relaxation period following loading in the rheometer. Reproduced from [Fazilati et al., 2021].

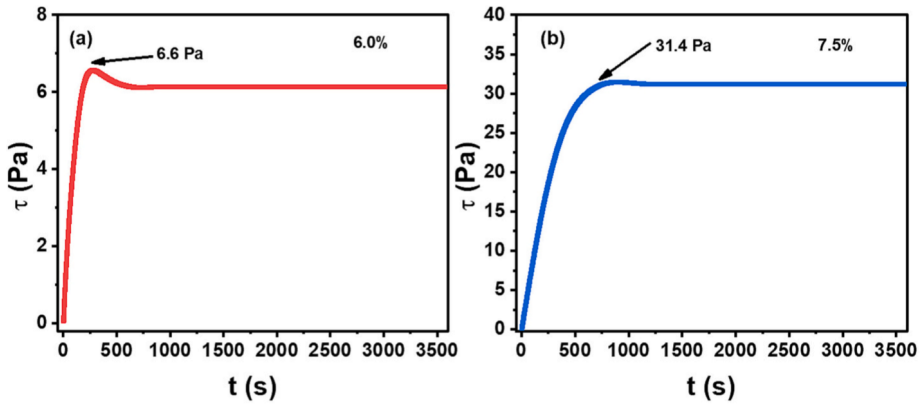

Figure 1.34: Shear start up experiments. Stress as a function of time of two suspensions containing (a) 6.0 wt % CNC and (b) 7.5 wt % CNC continuously sheared at 0.01 s^{-1}. Sulfated CNCs extracted from wood (CelluForce) suspended in water. Experiments performed after a 60 min recovery period following a strong pre-shear at $\dot{\gamma}$ = 100 s^{-1} during 5 min. Reproduced from [Xu et al., 2024].

over a wide range of shear rates, whatever the CNC concentration: the viscosity decreases with the shear rate [see Fig. 1.32(b)]. However, the way the viscosity decreases with the shear rate depends on the CNC concentration. Indeed, the rate of decrease of the viscosity with the shear rate increases with the CNC weight fraction, and for CNC weight fractions smaller than 6.0 wt %, the η versus $\dot{\gamma}$ curves present two regimes, separated by a critical shear rate for $\dot{\gamma} \approx 5$ s^{-1}. Moreover, the viscosity of a suspension at a given shear rate increases with the CNC weight fraction.

Despite those two characterizations of a CNC suspension viscoelastic properties at rest and under flow, only a few studies have reported on the yielding transition of those suspensions [Wu et al., 2014, Xu et al., 2024, Fazilati et al., 2021, Keyvani et al., 2021]. Figure 1.33 shows strain sweep experiments performed on suspensions containing various CNC weight fractions [Fazilati et al., 2021], and Fig. 1.34 shows shear start up experiments performed by shearing two suspensions of different CNC weight fractions, with the same shear rate $\dot{\gamma}$ = 0.01 s^{-1} [Xu et al., 2024]. Depending on the CNC concentration, the yielding behavior of the suspension is very different. At a CNC weight fraction smaller than 5 wt %, the suspension yields following a type I scenario when submitted to an oscillatory strain of increasing amplitude (see Fig. 1.33). At larger CNC weight fractions, above 6 wt % here, an overshoot of the viscous modulus develops and increases in amplitude with an increasing CNC content, indicating that the CNC suspension yields following a type III scenario (see Fig. 1.33). Such a change in the yielding behavior of a suspension depending on its CNC content is also evidenced in shear start up experiments. Indeed, at a CNC weight fraction of 6 wt %, the stress response to a continuous shear presents an overshoot [see Fig. 1.34(a)], whereas at a CNC weight fraction of 7.5 wt %, the yielding transition becomes more ductile-like and the stress overshoot almost totally disappears [see Fig. 1.34(b)].

Finally, only a few studies have reported time-dependence in CNC suspensions [Xu et al., 2024, Fazilati et al., 2021]. Figure 1.35 shows flow curves measured by ramping down and up in shear rate, for suspensions containing various CNC weight fractions, and for various times spent measuring the stress response for each shear rate [Xu et al., 2024]. At w_{CNC} = 4.5 wt %, the flow curves present no hysteresis: the ramping down and up curves superimpose. When the CNC content increases, an hysteresis appears and the loop area associated to this hysteresis increases with the CNC weight fraction. When the sweeping time is increased from 2 min to 20 min, the loop area decreases. Such observations prove that CNC suspensions in the absence of salt present a time-dependent behavior suggesting that their viscoelastic properties evolve over time. However, to our knowledge, only one study has investigated the time evolution of the viscoelastic properties of a CNC suspension and evidenced the suspension aging [Derakhshandeh et al., 2013]. Figure 1.36

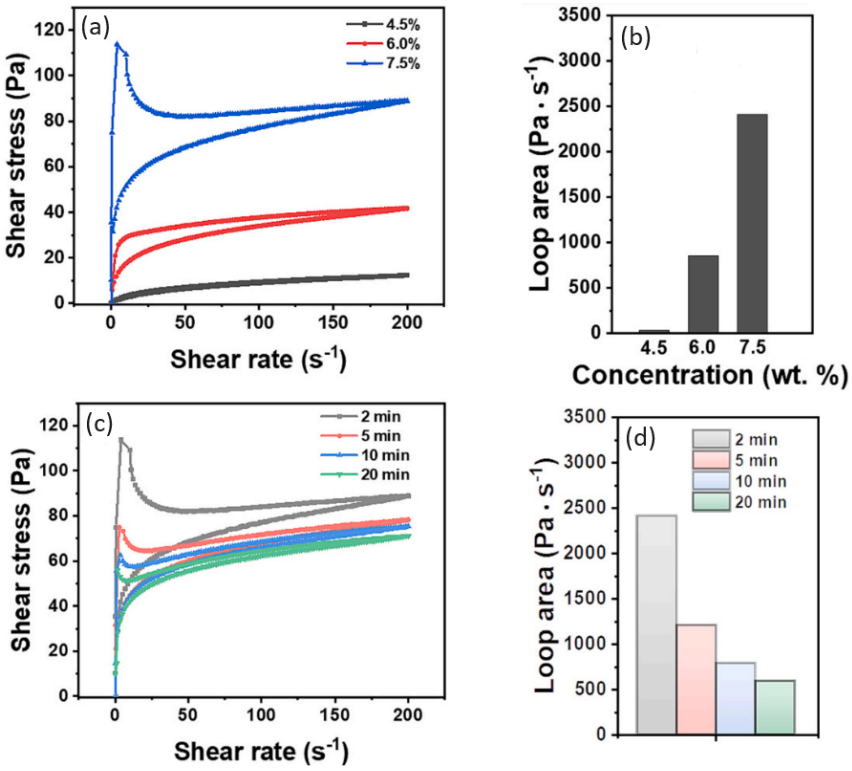

Figure 1.35: (a),(c) Hysteresis in the flow curves measured ramping down and up in shear rate, when varying (a) the CNC weight fraction with a sweep time of 2 min and (b) when varying the sweep time on a suspension containing 7.5 wt % CNC. (b),(d) The corresponding loop area. Sulfated CNCs extracted from wood (CelluForce) suspended in water. Experiments performed after a 60 min recovery period following a strong pre-shear at $\dot{\gamma}$ = 100 s^{-1} during 5 min. Adapted from [Xu et al., 2024].

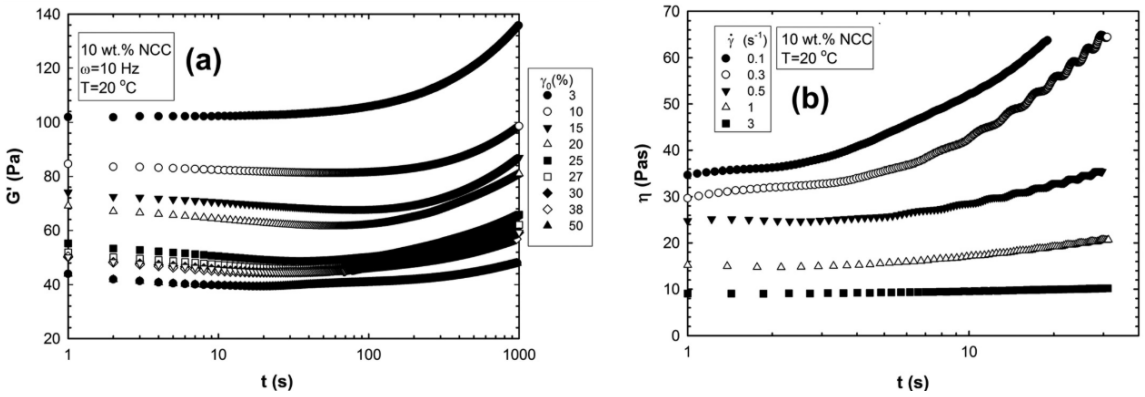

Figure 1.36: Time evolution of the viscoelastic properties of a CNC suspension (a) at rest and (b) under continuous shear. (a) Elastic modulus as a function of time measured by applying an oscillatory strain signal of various amplitude and fixed frequency f = 10 Hz. Sulfated CNCs extracted from wood (FPInnovation) suspended in water. Experiments performed after a 1000 s oscillatory pre-shear at large strain γ = 200 % and frequency f = 10 Hz followed by a rest period of 300 s. Reproduced from [Derakhshandeh et al., 2013].

presents the results obtained for a suspension containing 10 wt % CNC. Figure 1.36(a) shows that whatever the strain amplitude at which the suspension elastic behavior is probed, either in the linear or in the non-linear regime of deformation, G' is constant at short times and begins to increase after about 100 s of rest. This aging is more pronounced at small strain amplitudes. The CNC suspension also ages under continuous shear, but only when the shear rate is small enough, i.e., smaller than 3 s^{-1} [see Fig. 1.36(b)]. Furthermore, the time at which the viscosity begins to increase, and so time-dependent effects begin to appear, increases with the shear rate.

Such evidence for aging suggests that all the rheological results presented in this section may depend on time, and more precisely on the age of the suspension. Therefore, future work on the mechanical behavior of CNC suspensions should focus on rationalizing their aging dynamics.

b Rheology of cellulose nanocrystals in the presence of salt

The rheology of CNC suspensions in the presence of salt, i.e., in the gel or attractive glass phase, has been even less studied. Once again, many studies report the viscoelastic spectra of CNC suspensions measured in the linear regime of deformation, as well as their flow behavior given by the viscosity dependence with the shear rate, at a given point in time, as a function of the salt concentration, for different CNC weight fractions and for different types of salts [Danesh et al., 2021, Chau et al., 2015, Shafiei-Sabet et al., 2014, Qiao et al., 2016, Lu et al., 2024, Xu et al., 2019]. Figure 1.37 shows an example of results at various NaCl concentrations, ranging between 0 and 15 mM, and for two CNC weight fractions: w_{CNC} = 7 wt % and w_{CNC} = 15 wt %. As the NaCl concentration increases, both the elastic and the viscous moduli increase at a given frequency and CNC weight fraction, as attractive interactions become stronger due to an enhanced screening of repulsive negative charges. Simultaneously, the viscosity measured at a given shear rate, for a given CNC weight fraction, increases with the salt concentration, as shown in Fig. 1.38. At w_{CNC} = 7 wt % for this type of CNCs, both the elastic and the viscous moduli increase with frequency, but the viscous modulus remains larger than the elastic modulus at all frequencies, indicating that the suspension is in a liquid-like state [see Fig. 1.37(a)]. However, the difference between both moduli decreases with increasing salt concentration, until G' and G'' become almost equal for [NaCl]=15 mM in this case. At larger CNC weight fraction, w_{CNC} = 15 wt % in this case, the suspension is in a solid-like state whatever the NaCl concentration, and both moduli are almost independent of the frequency.

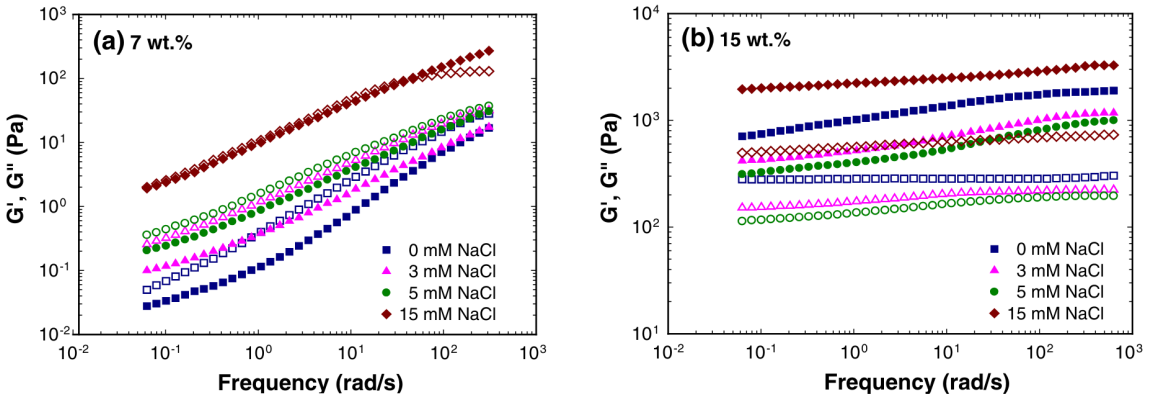

Figure 1.37: Viscoelastic spectra of CNC suspensions containing various NaCl concentrations, ranging from 0 mM to 15 mM, and (a) 7 wt % CNC and (b) 15 wt % CNC. Sulfated CNCs extracted from black spruce kraft pulp suspended in salty water. Experiments performed with a strain amplitude $\gamma = 1 - 3$ %. No precision is given on the recovery period duration following the sample preparation after which those measurement are performed. Adapted from [Shafiei-Sabet et al., 2014].

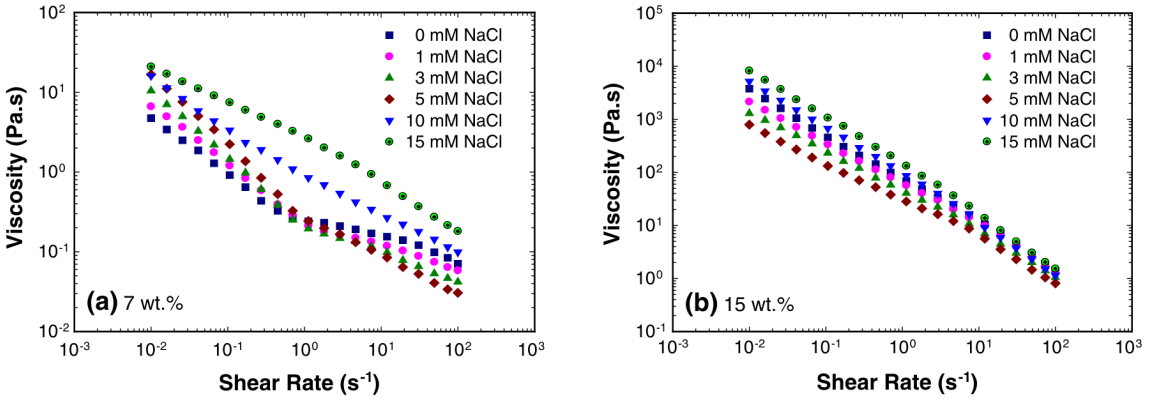

Figure 1.38: Viscosity as a function of the shear rate of CNC suspensions containing various NaCl concentrations, ranging from 0 mM to 15 mM, and (a) 7 wt % CNC and (b) 15 wt % CNC. Sulfated CNCs extracted from black spruce kraft pulp suspended in salty water. No precision is given on the sweeping time and on the recovery period duration following the sample preparation after which those measurement are performed. Adapted from [Shafiei-Sabet et al., 2014].

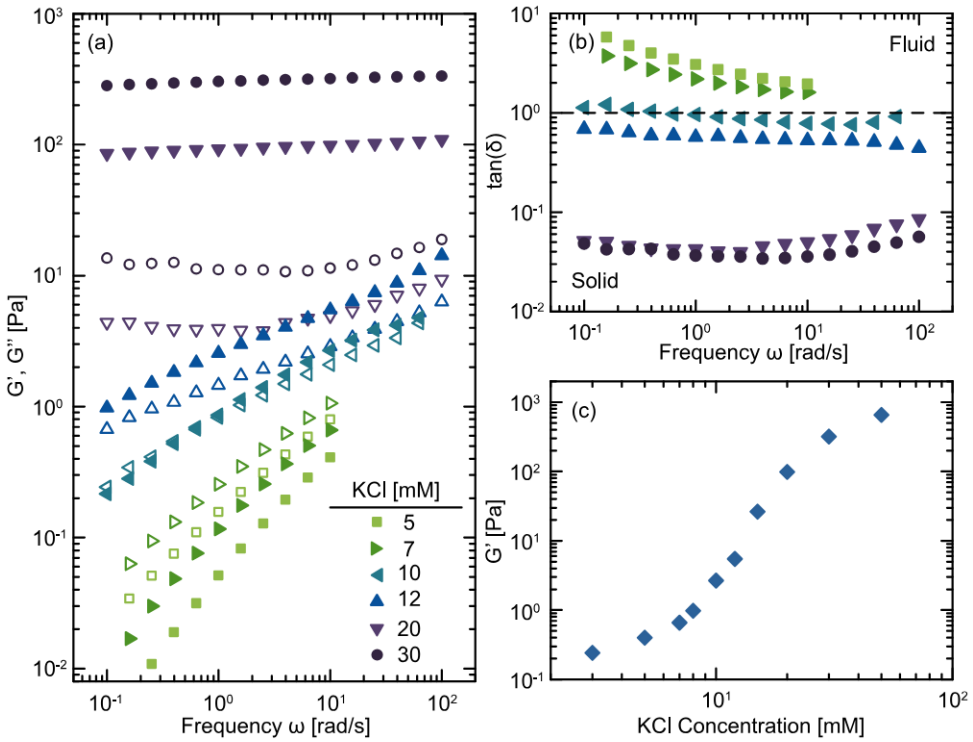

Figure 1.39: (a) Viscoelastic spectra (G': filled symbols, G'': empty symbols) of CNC suspensions containing 3 wt % CNC and various KCl concentrations, ranging from 5 mM to 30 mM, measured in the linear regime of deformation by applying an oscillatory strain signal of amplitude γ = 0.1 %. (b) Corresponding frequency dependence of the loss factor $\tan\delta$. (c) Elastic modulus measured at ω = 10 rad.s^{-1} and extracted from (a), as a function of the KCl concentration. Experiments performed following an oscillatory pre-shear of amplitude γ = 100 % and frequency ω = 10 rad.s^{-1} during 1 min. Sulfated CNCs extracted from wood (CelluForce), suspended in salty water. Reproduced from [Nikoumanesh and Poling-Skutvik, 2023].

This liquid to solid transition corresponds to the phase transition from an isotropic liquid to a gel upon increasing the salt content, as highlighted by Fig. 1.39 where the critical gel point, at which $G' \sim G'' \sim \omega^{\beta}$ and the loss factor $\tan\delta$ becomes independent of frequency, appears clearly [see the horizontal dashed line in Fig. 1.39(b)].

Similarly to CNC suspensions in the absence of salt, only a few studies have reported the yielding behavior of CNC suspensions in the presence of salt using strain amplitude sweep measurements, for various salt concentrations and CNC contents [Danesh et al., 2021, Moud et al., 2020, Lu et al., 2024]. An example of results is presented in Fig. 1.40 for a CNC suspensions containing 2 wt % CNC and between 1.72 mM and 172 mM NaCl [Moud et al., 2020]. For this CNC content and over this range of NaCl concentrations, the suspensions present a type III yielding behavior, with an amplitude of the viscous modulus overshoot which does not seem to depend on the NaCl concentration. However, both the strain amplitude corresponding to the transition from the linear to the non-linear regime of deformation γ_{NL}, and the yield strain γ_c decrease with the salt concentration [see Fig. 1.40(f)]. A type I yielding behavior has been reported at salt concentrations small enough for the suspension to be in a liquid-like state, with $G'' > G'$ at all strain amplitudes [Danesh et al., 2021].

To our knowledge, no shear start up experiments have been performed in CNC suspensions in the presence of salt, and very little evidence of time-dependent properties has been reported

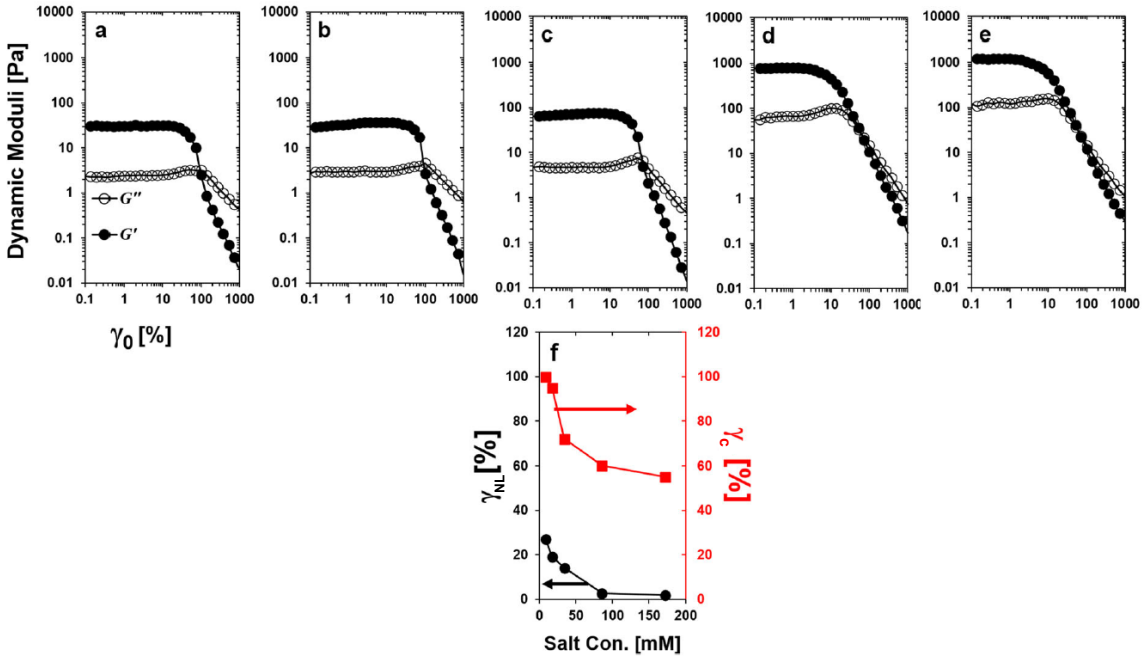

Figure 1.40: Strain sweep experiments on CNC suspensions containing 2 wt % CNC and (a) 1.72 mM, (b) 17.2 mM, (c) 34.4 mM, (d) 85.5 mM and (e) 172 mM NaCl. (a)-(e) Viscoelastic moduli as a function of the strain amplitude. (f) Strain amplitude γ_{NL} (black •) corresponding to the transition from the linear to the non-linear regime of deformation, and yield strain γ_c (red ■) as a function of salt concentration. Experiments performed at a frequency ω = 1 rad.s^{-1}, after a 10 min rest period following sample loading into the rheometer. Sulfated CNCs extracted from wood (InnoTech Alberta) dispersed in salty water. Adapted from [Moud et al., 2020].

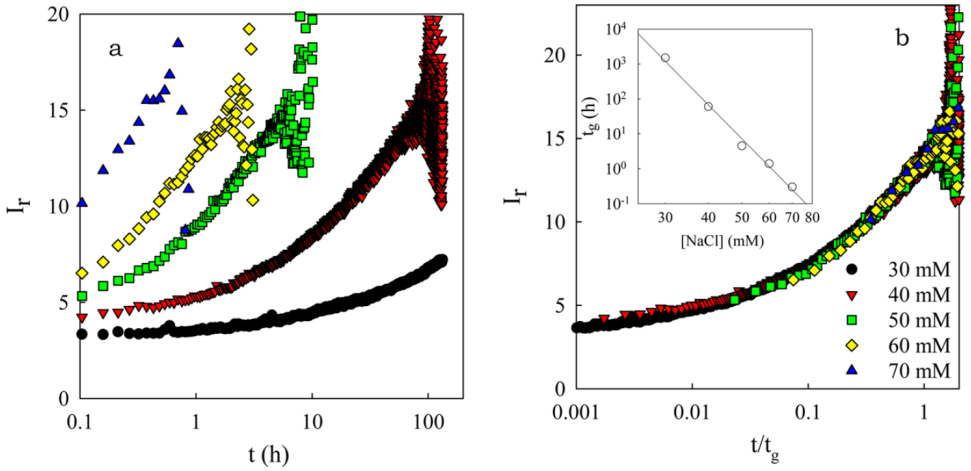

Figure 1.41: (a) Evolution of the scattered light intensity as a function of time during the suspension gelification following its preparation, for suspensions containing 0.5 wt % CNC and various NaCl concentrations. (b) Master curve for the time evolution of the light scattering intensity, rescaled in time by the characteristic time t_g at which large fluctuations appear in the measured scattered intensity. Inset: Characteristic time t_g as a function of the NaCl concentration. The black line represent the power-law fit $t_g = 18[\mathrm{NaCl}]^{-10}$. Sulfated CNCs extracted from cotton, suspended in salty water. Reproduced from [Peddireddy et al., 2016].

[Nikoumanesh and Poling-Skutvik, 2023], yet without any determination of a characteristic time associated to the time evolution of the viscoelastic properties. Indeed, all the previously described studies have been made at a given point in time, without considering the possible aging of CNC suspensions. Yet, we show in this thesis that the viscoelastic properties of CNC suspensions in the presence of salt do strongly depend on time, which most certainly affects the conclusions drawn in these previous studies.

Evidence for such aging dynamics have been reported at the microscale by following the aggregation dynamics of CNCs using light scattering [Peddireddy et al., 2016], confocal microscopy [Moud et al., 2019, Moud et al., 2021] and by measuring the time evolution of the particle hydrodynamic diameter [Danesh et al., 2021]. In particular, a time-composition superposition principle has been established for the scattered intensity as a function of time, upon varying the NaCl concentration, as shown in Fig. 1.41 [Peddireddy et al., 2016]. The master curve attesting for this superposition principle has been constructed by shifting the time evolution of the scattered intensity by the time when large fluctuations appear in the measured scattered intensity, which depends on the salt concentration [see the inset of Fig. 1.41(b)]. The authors identify this time to the gelation time t_g at which a network is formed. The only measurement of the time evolution of the viscoelastic moduli of CNC suspension in the presence of salt that we are aware of has been reported using interfacial rheometry [Bertsch et al., 2018]. This study reports that both the elastic and the viscous moduli increase with time without reaching a stationary state after 14 hours of measurements, as shown in Fig. 1.42.

E Objectives of the thesis and outline of the manuscript

The mechanical behavior of polymeric gels has been widely studied, and some universality have been established thanks to, e.g., superposition principles. More precisely, several theories have been developed to rationalize and predict a significant part of the experimental results. In contrast, the field of colloidal gels is much younger and more systematic studies are required to draw

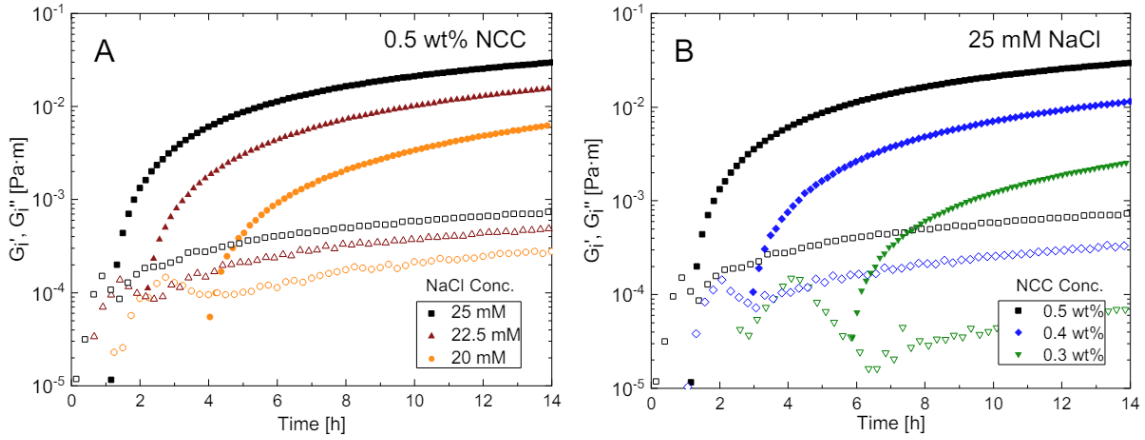

Figure 1.42: Time evolution of the interfacial elastic modulus G_i' (filled symbols) and of the the interfacial viscous modulus G_i'' (empty symbols) for suspensions containing (A) 0.5 wt % CNC and various NaCl concentrations ranging between 20 mM and 25 mM NaCl, and (B) various CNC weight fractions ranging between 0.3 wt % and 0.5 wt % CNC and 25 mM NaCl. Measurement performed by applying an oscillatory strain signal of amplitude γ = 1 % and frequency ω = 1 rad.s^{-1}. Sulfated CNCs extracted from wood (CelluForce). Reproduced from [Bertsch et al., 2018].

a general picture of their mechanical behavior, including the gelation process. Moreover, theories are missing to confront with experimental studies. Therefore, the mechanical behavior of colloidal suspensions are often compared to the one of polymeric soft materials, although both materials do not always behave similarly. In this thesis, we enrich the general understanding of the mechanical behavior of colloidal gels by studying a suspension of rod-like colloids, namely cellulose nanocrystals.

The self-assembly of cellulose nanocrystals into different phases, in particular into cholesteric liquid crystal phases, has been widely studied. Many studies have focused on the rheology of suspensions of cellulose nanocrystals without any salt. In the presence of salt, most previous studies have performed rheological measurements at a given point in time, without considering the possible time-dependent properties of such suspensions. Only a few microstructural studies have reported a time evolution of CNC suspensions in the presence of salt. The aim of the present work is to provide an extensive study of the rheology of suspension of cellulose nanocrystals in the presence of salt. In particular, we rationalize the gelation and aging dynamics of such suspensions, and we explore their rheological properties both at rest, in their linear regime of deformation, and during failure and flow, in their non-linear regime of deformation. The present thesis manuscript is organized as follows.

The second chapter presents the experimental techniques used to obtain the results presented in this thesis. More precisely, chapter 2 contains a description of the rheometers and the corresponding geometries used, as well as a description of the ultrasound velocimetry setup, which will be coupled to rheological measurements, in order to get some insight into the local scenario during suspensions yielding. Then, the main characteristics of the cellulose nanocrystals used in this thesis are detailed. Finally, a preparation protocol is proposed, which allows us to obtain homogeneous CNC suspensions in the presence of salt.

In the third chapter, we focus on the recovery dynamics of CNC suspensions in the presence of salt, following fluidization by a strong shear. In particular, we demonstrate a time-composition superposition principle for the time evolution of the viscoelastic properties of such suspensions, probed at 1 Hz. Then, using time-resolved spectroscopy, we show that CNC suspensions in the presence of salt form a critical gel at a time t_g, which can be up to one order of magnitude longer

than the crossover time t_c. We also evidence a time-connectivity superposition principle which remains valid over a wide range of CNC and salt concentrations. Furthermore, by dynamically characterizing the critical gel point, we highlight a change of regime upon increasing the CNC content, which we interpret as the signature of a phase transition from a gel to an attractive glass. Finally, we show that the time-composition and the time-connectivity superposition principles can be generalized into a time-connectivity-composition superposition by rescaling the time-resolved spectroscopy data of suspensions with various salt concentrations.

The fourth chapter focuses on the non-linear rheological properties of CNC suspensions in the presence of salt, and more precisely on their yielding and flowing properties. First, we show that their flow curves show complex features that depend on the suspension composition and on the experimental protocol. In particular, we demonstrate the presence of an hysteresis between the ramping down and the ramping up responses, whose characteristics, such as its area, depend on the ramping rate. Then, shear start up experiments allow us to reveal a ductile to brittle transition upon decreasing the shear rate or increasing the sample age. By quantitatively characterizing this transition, we extract phenomenological laws that capture the yielding behavior of CNC suspensions in the presence of salt, and we propose a general rescaling parameter that accounts for the effect of both the shear rate and the sample age. We also evidence shear memory effects in suspensions with the largest salt contents. Third, using ultrasound velocimetry coupled to rheological measurements, we uncover the development of shear bands and wall slip during the flow curves measurements, as well as the existence of an elastic recoil, which coincides with the stress maximum upon shear start up and brittle-like yielding. Finally, strain sweep experiments provide evidence for a transition from a type I to a type III yielding behavior under oscillatory strain for CNC suspensions with increasing salt concentration. Moreover, by varying the type of salt, the CNC content and the solvent isotope, we highlight the existence of a time-composition superposition principle valid in the non-linear regime of deformation for CNC suspensions in the presence of salt.

Finally, the concluding chapter summarizes the main results of this thesis, and presents some perspectives opened by this work. In particular, microstructural characterizations are needed to complete our understanding of the gelation dynamics of CNC suspensions, and some attempts using a variety of microscopic techniques are described. Another important perspective concerns the transition from a soft material to a solid material. We present preliminary experiments based on two different solidification processes: drying and freezing.

CHAPTER

2

MATERIALS AND METHODS

Contents

This chapter presents the material and methods used to perform the experiments detailed in this thesis. In the first part, after presenting the various rheometers and geometries used along this thesis, we describe the ultrasound velocimetry setup. In the second part, we detail some characterizations of the cellulose nanocrystals used to elaborate the samples. Finally, in the third part, we determine a preparation protocol that allows to obtain homogeneous CNC suspensions in the presence of salt.

A Rheometry

A.1 Rotational rheometer

Rheometry is an experimental technique used to characterize the mechanical properties, also referred to as the "rheological properties", of a soft material, as previously mentioned in Sec. 1.B. The device commonly used to make those measurements is a rotational rheometer. It consists of a rotor and a stator between which the studied material is squeezed. The application of a torque $\vec{\Gamma}$ on the rotor induces its rotation by an angle $\theta(t)$, with a corresponding rotational velocity $\dot{\theta}$, leading to the deformation of the sample. The advantage of this rotational configuration compared to the translational one described in Sec. 1.B to introduce rheology, is that one can apply very large deformations in a limited space, while requiring a smaller amount of material. The torque $\vec{\Gamma}$, the rotation angle $\theta(t)$ and the rotational velocity $\dot{\theta}$ of the rotor are related, respectively, to the stress σ, the strain γ, and the shear rate $\dot{\gamma}$ in the sample:

$$\sigma = F_\sigma \Gamma \tag{2.1}$$

$$\gamma = F_\gamma \theta \tag{2.2}$$

$$\dot{\gamma} = F_\gamma \dot{\theta}. \tag{2.3}$$

The constants F_σ and F_γ are calibration parameters that depend on the rotor geometry.

There are two types of rotational rheometers: stress-controlled or strain-controlled. For a stress-controlled rheometer, the motion of the rotor is dictated by the torque applied on the sample, and the resulting displacement of the rotor is measured. In this case, the rotor constitutes the upper element on the rheometer. For a strain-controlled rheometer, the motion of the rotor is dictated by the imposed rotational velocity of the rotor, and the resulting torque induced by the sample deformation is measured. In this case, the rotor constitutes the lower element on the rheometer. Both types of rheometers can be used to impose either a stress or a strain thanks to a feedback loop. However, the stress-controlled rheometer will be able to precisely impose the required stress faster than the strain-controlled one, whereas the strain-controlled rheometer will be able to precisely impose the required strain faster than the stress-controlled one. In this thesis, both types of rheometers are used depending on the rheological measurements to be performed. The stress-controlled rheometers are an MCR 301 (Anton Paar), an MCR 302 (Anton Paar) and an ARG2 (TA Instruments). The strain-controlled rheometer is an ARES G2 (TA Instruments).

For both types of rheometers, there exists various rotor and stator geometries that have their own advantages and drawbacks. In this thesis, two configurations are used.

In the first configuration, referred to as a "cone-and-plate" configuration, the lower element of the rheometer is a plate, while the upper element is a cone of angle α. The tip of the cone is truncated over a height Tr. This upper geometry is positioned at height Tr, from the center of the cone, above the bottom plate, such that the virtual position of the tip would be in contact with the bottom plate, as represented in Fig. 2.1. The volume defined by the free space between the two geometries, which is filled by the sample, is called the "gap ". Both the upper and the lower geometries have the same radius R. In this thesis, two different cone-and-plate geometries are used, whose characteristics are detailed in Table 2.1.

Let us calculate the shear rate in the gap volume when the rotor, say the upper geometry, rotates by an angle θ with a rotational velocity $\vec{\Omega} = \dot{\theta}\vec{e_z}$ and a corresponding torque $\vec{\Gamma} = \Gamma\vec{e_z}$ (see Fig.2.1). We assume that the flow induced in the sample is laminar, i.e., $\vec{v}(r,\theta,z) = v(r,z)\vec{e_\theta}$, and that there is no slip on the geometries surfaces, i.e., $\vec{v}(r,z=0) = \vec{0}$ and $\vec{v}(r,z=h) = r\dot{\theta}\vec{e_\theta}$. Therefore, the velocity profile of the sample in the volume defined by both geometries is:

$$\vec{v}(r,z) = \frac{z}{h} r\dot{\theta}\vec{e_\theta} \tag{2.4}$$

and the resulting shear rate is:

$$\dot{\gamma}(r) = \frac{\partial v_\theta}{\partial z} = \frac{r\dot{\theta}}{h}. \tag{2.5}$$

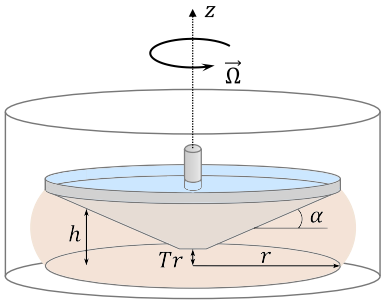

Figure 2.1: Diagram of a cone-and-plate configuration.

In the cone-and-plate configuration, the height h is a function of the radial position in the gap volume:

$$h(r) = r\tan\alpha \tag{2.6}$$

with α the cone angle. This angle is always very small: in our case, $\alpha = 2°$. Therefore, we can consider with a good approximation $\tan\alpha \approx \alpha$, leading to:

$$h(r) = r\alpha \tag{2.7}$$

As a result, in this configuration, the shear rate is uniform in the whole sample volume:

$$\dot{\gamma}(r) = \frac{\partial v_\theta}{\partial z} = \frac{r\dot{\theta}}{r\alpha} = \frac{\dot{\theta}}{\alpha} \tag{2.8}$$

This is the main advantage of this configuration.

The rotor geometry, i.e., the upper cone in the case of the stress-controlled rheometer and the bottom plate in the case of the strain-controlled rheometer, have a sand-blasted surface in order to avoid slip of the sample on the boundaries. The bottom plate is controlled in temperature thanks to a Peltier module. Moreover, in order to prevent solvent evaporation and sample drying during the rheological measurements, we fill a small reservoir on top of the upper geometry with the same solvent as the one used in the sample, i.e., water in this study, and we confine both geometries, including the reservoir and the sample, under an airtight dome, thereby saturating the atmosphere surrounding the sample with its solvent. Finally, a force sensor allows to measure the normal force applied on the upper cone during rheological measurements.

In the second configuration, referred to as a "Taylor-Couette" configuration (or concentric cylinder configuration), the lower element of the rheometer is a cylindrical cup of radius R_{ext} that contains the sample. The upper element is a cylinder with either a flat or a conic bottom end, of radius R_{int} smaller than the cylindrical cup, that is inserted into the cup. The sample fills the whole volume in between both cylinders and below the inner one, as illustrated in Fig. 2.2. The difference of radius between the inner and the outer cylinders defines the gap e. Three different Taylor-Couette geometries are used in this thesis, whose characteristics are detailed in Table 2.1. The outer cylinder is controlled in temperature, either thanks to a Peltier module in the case of the strain-controlled rheometer, or by being immersed in a heated

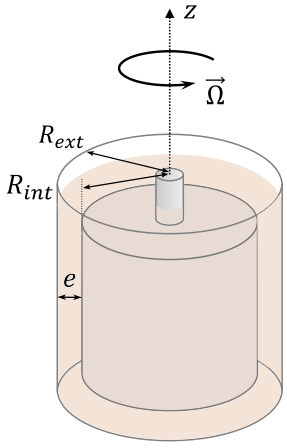

Figure 2.2: Diagram of a Taylor-Couette configuration.

bath in the case of the stress-controlled rheometer. Here again, in order to prevent solvent evaporation and sample drying, we close the cup with a lid. Such a Taylor-Couette configuration requires a larger volume of sample compared to the cone-and-plate configuration: between 10 and 25 mL for the Taylor-Couette configuration versus less than 1 mL for the cone-and-plate configuration. This can be a limitation, but it can also be an advantage depending on the type of experiments. For instance, it allows to average measurements over a larger volume, and thus reduces noise or confinement effects. Moreover, a larger sample volume is less sensitive to solvent evaporation and therefore enables one to realize longer experiments. Finally, this configuration can allow one to get some insight into the local phenomena occurring during rheological measurements using ultrasound velocimetry, as detailed in Sec. 2.A.3.

A.2 Rheological measurements

In this thesis, two main types of measurements are performed using a rotative rheometer: the rotor is set in motion either in an oscillatory or in a continuous way.

Oscillatory shear If the rotor is set to oscillate at a rotational velocity of angular frequency ω, the resulting strain γ is also an oscillatory function of the same frequency: $\gamma(t) = \gamma_0(\omega)\cos(\omega t)$. As recalled in the Introduction in Sec. 1.B.1.c, in the linear regime of deformation of the material, if $\gamma_0(\omega)$ is small enough, the stress induced on the material is also an oscillatory function of the same frequency with a possible phase shift δ: $\sigma(t) = \sigma_0(\omega)\cos(\omega t + \delta)$. Using complex notations, the generalized Hooke's law can be written as follows:

$$\sigma_0(\omega) = G^*(\omega)\gamma_0(\omega) \tag{2.9}$$

where $G^*(\omega) = G' + iG''$ is the complex modulus of the material, from which we extract the elastic modulus G', the viscous modulus G'', and the loss factor $\tan\delta$:

$$\begin{cases} G' = \dfrac{\sigma_0}{\gamma_0}\cos\delta & (2.10) \\ G'' = \dfrac{\sigma_0}{\gamma_0}\sin\delta & (2.11) \\ \tan\delta = \dfrac{G''}{G'}. & (2.12) \end{cases}$$

Therefore, an oscillatory motion of the rotor allows one to estimate the viscoelastic properties of a soft material by measuring both its viscous modulus and its elastic modulus. However, both moduli depend on the frequency at which they are measured. A first estimation can be made by applying an oscillatory strain or stress at a frequency of 1 Hz. We can also estimate their dependence over the frequency by sequentially varying the frequency of the applied signal. Each measurement at a given frequency f takes a certain amount of time δt_{exp}: in order to be able to estimate the phase shift δ, a measurement at a given frequency f must last at least one period. In order to get a more precise result, the measurement is usually averaged over few periods, leading to $\delta t_{\text{exp}} \propto 1/f$. During this period of time, the viscoelastic properties of the sample may evolve, hereby distorting the measurement. The mutation number is a quantity that allows one to quantify this effect by comparing the measurement time to the typical time-scale over which the sample viscoelastic properties evolve:

$$N_{\text{mu}} = \frac{\delta t_{\text{exp}}}{X}\frac{\partial X}{\partial t}, \tag{2.13}$$

with X the variable of interest, such as the elastic modulus G' or the viscous modulus G''. If $N_{\text{mu}} \ll 1$, the system does not evolve much during the measurement time. Therefore, the measurement can be considered as valid. However, if $N_{\text{mu}} \gg 1$, the system does evolve during the measurement time, therefore, the measurement is biased.

To tackle this issue, we can use time-resolved mechanical spectroscopy, as introduced in Sec. 1.C. To do so, in this thesis, we apply a multiwave strain signal which is a periodic signal composed of the sum of a discrete number of sinusoidal strain signals of various frequencies. A Fourier transform of the resulting stress signal allows one to decouple the response of the material at the different frequencies, and therefore obtain a measurement of the elastic modulus G' and of the viscous modulus G'' at several frequencies simultaneously, within a small measurement time δt_{exp}.

Besides varying the frequency of the rotor motion, we can also vary its amplitude by changing either γ_0 or σ_0. This type of experiment allows one to determine the transition from a the linear regime of deformation of the material to its non-linear regime, and to study its viscoelastic properties in both regimes through strain sweep experiments, as introduced in Sec. 1.B.3.

Continuous shear For this second type of measurement, the rotor rotates continuously at a given speed $\dot{\theta}$, without oscillating. This type of experiment allows us to investigate how a soft material breaks down and flows under shear, through shear start up experiments, as introduced in Sec. 1.B.3, or by measuring its flow curve, as introduced in Sec. 1.B.4. The resulting shear rate $\dot{\gamma}$ and stress σ are recorded by the rheometer, which also computes the apparent viscosity as $\eta = \sigma/\dot{\gamma}$.

Device limitations Like every device, a rheometer has its limitations which are important to keep in mind in order to adjust properly the various measurement parameters and to avoid biased data [Ewoldt et al., 2015]. First, the torque sensor sets the lower and upper limits for the torque and the motor controlling the rotor sets the lower and upper limits for the rotational velocity. Those limits can be transcribed into limits on the rheological quantities that can be applied or measured, using the calibration parameters F_σ and F_γ. The corresponding limits are reported in Table 2.1. Second, concerning the oscillation mode, two sources of inertia need to be considered: (i) the inertia of the rotor geometry, and (ii) the inertia of the sample loaded in between the two geometries, which is set into motion. Inertia becomes predominant at high frequency, typically above 10 Hz. In the present thesis, we ensure that this high frequency limitation is never reached.

Finally, the way the sample is loaded may have a strong impact on the rheological measurements, more specifically in the cone-and-plate configuration where the free surface on the edges of the rotor is quite important in front of the sample volume [Ewoldt et al., 2015]. This effect is overcome by cleaning carefully the edges of the sample once it has been squeezed between the rotor and the stator, hereby enabling the formation of a well defined meniscus leading to reproducible and non-biased data. Moreover, in any configuration, one must also take care not to introduce bubbles when loading a sample.

A.3 Ultrasound velocimetry

In this thesis, ultrasound velocimetry is used to get insight into the local breakdown and flow behavior of CNC suspensions under shear in a Taylor-Couette configuration. The experimental setup, sketched in Fig. 2.3, has been developed by Sébastien Manneville and is described in details in Refs. [Manneville et al., 2004, Gallot et al., 2013]. An ultrasound scanner, constituted of 128 independent electronic channels, each of them made of a transmitter and a receiver, is used to emit an ultrasound plane wave, and to record the waves reflected by the soft material. The plane wave is emitted by the simultaneous transmission to the 128 transmitters of a single impulsion signal. The transducers operating at a center frequency $f = 15$ MHz, the wavelength of the plane wave in water is $\lambda = c_w/f \approx 100$ μm, with $c_w = 1480$ m.s^{-1} the sound velocity in water at 20 °C. The emission of the pulsed plane wave is repeated N times with a repetition frequency f_{PRF}. If ultrasound scattering from the microstructure of the soft material itself is too weak, the sample can be seeded by tracers that act as acoustic contrast agents. The interferences of all the waves reflected by the tracers (or by the soft material itself) result in a complex acoustic signal referred to

Table 2.1: Geometries characteristics, minimum and maximum stresses, and minimum and maximum shear rates that each rheometer and corresponding geometries can apply or measure.

Rheometer	Geometries	Shear mode	σ_{min} (Pa)	σ_{max} (Pa)	$\dot{\gamma}_{min}$ (s^{-1})	$\dot{\gamma}_{max}$ (s^{-1})
MCR 301 (Anton Paar)	Cone-and-plate R = 40.0 mm Tr = 176.0 μm α = 2.0 ° sand-blasted cone (surface roughness 30 μm)	Oscillatory	6.0×10^{-4}	1.2×10^{4}	1.9×10^{-6}	5.6×10^{3}
		Continuous	3.0×10^{-3}	1.2×10^{4}	1.9×10^{-6}	5.6×10^{3}
MCR 302 (Anton Paar)	Cone-and-plate R = 40.0 mm Tr = 176.0 μm α = 2.0 ° sand-blasted cone (surface roughness 30 μm)	Oscillatory	3.0×10^{-5}	1.4×10^{4}	0	5.6×10^{4}
		Continuous	6.0×10^{-5}	1.4×10^{4}	0	5.6×10^{4}
ARG2 (TA Instruments)	Taylor-Couette R_{int} = 48.0 mm R_{ext} = 50.0 mm H = 58.0 mm gap e = 1.0 mm	Oscillatory	1.4×10^{-5}	9.2×10^{2}	3.4×10^{-8}	7.4×10^{3}
		Continuous	4.6×10^{-5}	9.2×10^{2}	3.4×10^{-8}	7.4×10^{3}
ARG2 (TA Instruments)	Taylor-Couette R_{int} = 46.0 mm R_{ext} = 50.0 mm H = 60.0 mm gap e = 2.0 mm	Oscillatory	1.4×10^{-5}	9.3×10^{2}	1.7×10^{-8}	3.6×10^{3}
		Continuous	4.6×10^{-5}	9.3×10^{2}	1.7×10^{-8}	3.6×10^{3}
ARES G2 (TA Instruments)	Cone-and-plate R = 40.0 mm Tr = 46.0 μm α = 2.0 ° sand-blasted cone (surface roughness 1 μm)	Oscillatory	3.0×10^{-9}	1.2×10^{4}	2.8×10^{-5}	8.5×10^{3}
		Continuous	6.0×10^{-9}	1.2×10^{4}	2.8×10^{-5}	8.5×10^{3}
ARES G2 (TA Instruments)	Taylor-Couette R_{int} = 27.7 mm R_{ext} = 30.0 mm H = 41.5 mm gap e = 1.2 mm	Oscillatory	8.4×10^{-10}	3.4×10^{3}	1.2×10^{-5}	3.7×10^{3}
		Continuous	1.7×10^{-9}	3.4×10^{3}	1.2×10^{-5}	3.7×10^{3}

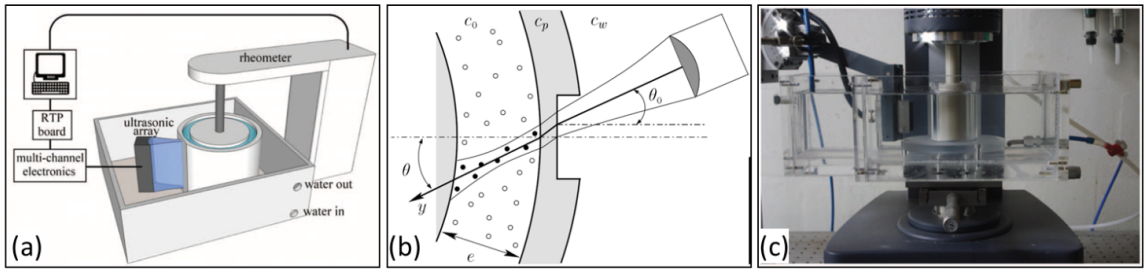

Figure 2.3: (a) Experimental setup. (b) Top view of the path of the ultrasound beam across the Taylor-Couette and the sample. c_0, c_p and c_w indicate, respectively, the sound velocity in the soft material, in the Plexiglas forming the outside cup of the Taylor-Couette geometry, and in water. (c) Picture of the experiment setup. Reproduced from [Sudreau, 2022].

as an "ultrasonic speckle". If one neglects the echoes resulting from multiple reflections, there is a direct correlation between the travel time of the ultrasound wave and the position of the reflecting particle.

Thereby, the signal recorded by a given channel $s_i(t,z)$ corresponds to the sum of the echoes induced by the reflecting particles at various positions in the image. The ultrasound image $S_i(y,z)$ is obtained by summing up the ultrasound signals, with delay laws:

$$S_i(y,z) = \sum_{z_0} s_i(t(y,z,z_0),z) \tag{2.14}$$

with y the axis distance to the ultrasound transducer along the propagation axis of the ultrasound wave, and z the vertical position. The travel time $t(y,z,z_0)$ corresponds to the travel time of the ultrasound wave between the position (y,z) and the transducer located at latitude z_0. Using the sound velocity c_0 in the soft material, the travel time is given by:

$$t(y,z,z_0) = \frac{y + \sqrt{y^2 + (z-z_0)^2}}{c_0}. \tag{2.15}$$

The local displacement in the material at a point (y,z) along the y direction between two successive pulses is calculated by estimating the maximum, with respect to the increment δy, of the following correlation function:

$$C_i(y,z,\delta y) = \sum_{y'=y-\Delta y/2}^{y'=y+\Delta y/2} S_i(y',z) S_{i+1}(y'+\delta y,z) \tag{2.16}$$

with $\Delta y = 2\lambda \sim 200$ μm the width of the correlation window.

The axial velocity field is then easily deduced from the displacement field using: $v_{y,i}(y,z) = \delta y_i(y,z)/\delta t$, where $\delta t = 1/f_{PRF}$ is the time interval between two successive pulses, and v_y is the projection of the local velocity $\vec{v} = (v_r, v_\theta, v_z)$ on the ultrasound propagation axis y. A calibration on water, sheared in the laminar regime, inducing a purely tangential flow, allows one to convert the axial velocity $v_y(y,z)$ into an apparent tangential velocity $v(r,z)$. In the limit of a small gap, this tangential velocity is given by:

$$v(r,z) \approx \frac{v_y(y,z)}{\sin\theta} \tag{2.17}$$

with $r = e - \sin\theta(y - y_0)$ the distance to the rotor, and θ the incidence angle of the ultrasound wave.

More generally, in the case of a three dimensional flow, the tangential velocity v is given by:

$$v(r,z) \approx v_\theta(r,z) + \frac{v_r(r,z)}{\tan\theta}. \tag{2.18}$$

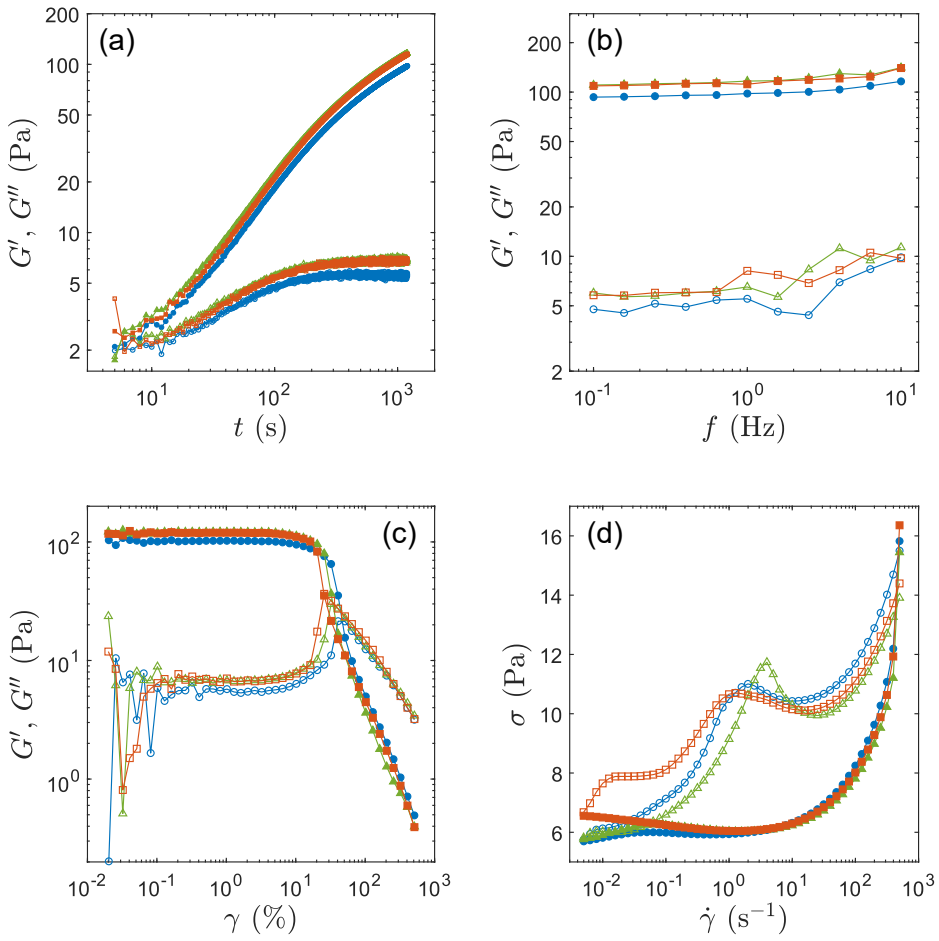

Figure 2.4: Comparison of the rheological properties of a suspension containing 3.2 wt % CNC, 18 mM NaCl, without any beads (blue •), with 1 wt % polyamide beads (orange ■) and with 1 wt % polystyrene beads (green ▲). (a) Time evolution of the elastic modulus G' (filled symbols) and of the viscous modulus G'' (empty symbols) following a 20 s pre-shear at $\dot{\gamma}$ = 500 $^{-1}$. Measurements performed by applying an oscillatory strain of amplitude γ = 0.2 % and frequency f = 1 Hz. (b) Elastic modulus G' (filled symbols) and viscous modulus G'' (empty symbols) as a function of frequency f following the 1000 s recovery plotted in (a). Measurements performed by applying an oscillatory strain of amplitude γ = 0.2 %. (c) Elastic modulus G' (filled symbols) and viscous modulus G'' (empty symbols) as a function of strain amplitude γ, measured following the recovery and frequency sweep steps. Measurements performed by applying an oscillatory strain of frequency f = 1 Hz. (d) Stress σ as a function of shear rate $\dot{\gamma}$ when ramping down (filled symbols) and then up (empty symbols) in shear rate.

Due to the small size of the nanocrystals compared to the ultrasound wavelength and to their weak acoustic contrast with water, CNC suspensions do not scatter ultrasound efficiently. Therefore, in order to use ultrasound velocimetry, we seed the CNC suspensions with spherical beads that strongly scatter the ultrasound signal, and which play the role of tracers for the CNC suspension deformation and flow. In order to check for the influence of such tracers on the rheology of CNC suspensions, 1 wt % of polyamide beads of diameter 30 μm (Orgasol, Arkema) are added to a CNC suspension with 3.2 wt % CNC and 18 mM NaCl in one set of experiments, and 1 wt % of polystyrene beads of diameter 20 μm (Dynoseeds, Microbeads) was added to the same suspension in another set of experiments. As shown in Fig. 2.4, the addition of tracers does not significantly modify the mechanical properties of the CNC suspension under study.

B Cellulose nanocrystals

The cellulose nanocrystals (CNCs) used for this thesis are bought from CelluForce in the form an aqueous dispersion containing 6.4 wt % CNC. They are extracted from wood through an acid hydrolysis during which part of the hydroxyl groups (OH) on a CNC particle surface are substituted with negatively charged sulfate groups $^{-}SO_3^{-}$.

Bruno Jean from CERMAV (Gières, France) has helped us to characterize the individual CNC particles. On the one hand, a conductiometric titration of the sulfate groups in the commercial suspension reveals a sulfur rate between 0.02 and 0.03 %, which is very small compared to the typical 0.7 % sulfur rate measured on cotton CNC dispersions produced at CERMAV. On the other hand, measurements on the commercial suspension reveals a zeta-potential of the CNC particles between -36.0 mV and -41.7 mV, which is consistent with measurements performed on their homemade suspensions. The contradiction between the sulfate titration and the zeta-potential measurements can be explained as follows: sodium ions may have been introduced into the commercial suspension during its fabrication process, and they might have condensed on the surface of the CNC particles, hereby screening part of the negatively charged sulfate groups, and thereby distorting the conductiometric measurements which are based on charge counting. On the contrary, zeta potential measurements are based on charge mobility and therefore are not affected by the presence of sodium ions. Finally, our CNC particles carry a surface charge of about 0.2 e.nm^{-2}, what is similar to other CNCs extracted from similar sources and under similar conditions.

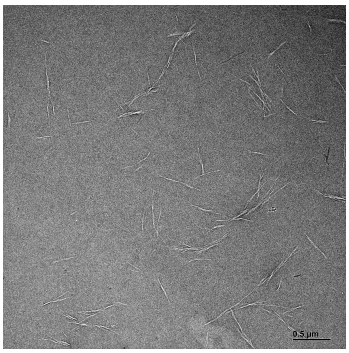

Figure 2.5: Transmission electron microscopy image of a dilution of the commercial CNC suspension. The scale bar corresponds to 0.5 μm.

Transmission electron microscopy (TEM) images of dilutions of the commercial suspensions show that CNC particles are quite well dispersed, with no large aggregates and only few bundles (see Fig. 2.5). This observation is in agreement with the fact that these CNC particles are charged enough to induce inter-particle electrostatic repulsion. From an analysis of the TEM images, we deduce that individual CNC particles are quite polydisperse, with an average length of about 131 ± 44 nm, and an average diameter of about 4 ± 1 nm. TEM images have also revealed an atypical arrangement of CNCs: some CNCs assemble end to end to form lines made of few individual CNC particles, leading to large characteristic sizes in our system. This observation is confirmed by dynamic light scattering (DLS) measurements. Indeed, the obtained size distribution, shown in Fig. 2.6, present a single peak at 130.4 nm, which is quite broad, with a standard deviation of 84 nm. Such a large standard deviation is the signature of polydispersity, and the mean size of 130.4 nm is consistent with the mean length deduced from the TEM images.

Finally, there exists four types of cellulose, which differ in the location of the hydrogen bonds between and within the polymer

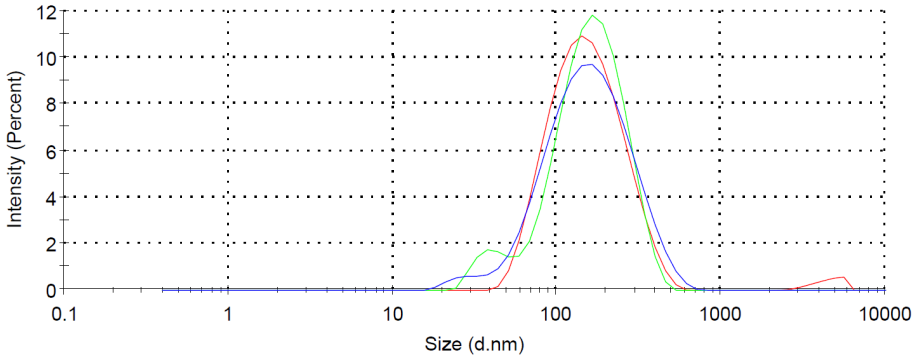

Figure 2.6: Size distribution of the commercial CNC suspension, which has been diluted 100 times, obtained through dynamic light scattering. The three curves correspond to three different measurements on the same sample.

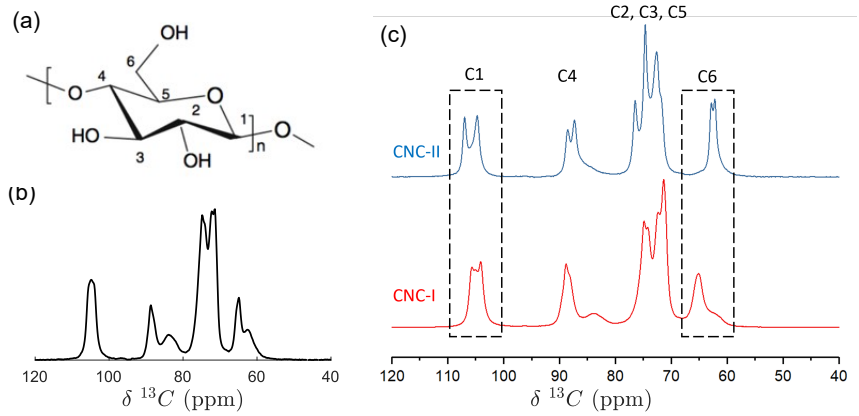

Figure 2.7: ^{13}C spectra of CNCs using nuclear magnetic resonance (NMR). (a) Monomere of cellulose. (b) Spectrum of CNCs from the commercial suspension. (c) Spectra of CNCs constituted of cellulose I (red) and of cellulose II (blue). The label of the carbon atoms corresponds to the one indicated in (a).

strands: cellulose I, II, III and IV. Cellulose I, also referred to as native cellulose, is the one found in nature, while cellulose II can be formed during its extraction from the cell walls. Cellulose III and IV results from a transformation of cellulose I and II in the lab. Nuclear magnetic resonance (NMR) analysis of the commercial suspension reveals that the CNCs used for this thesis are made from cellulose I only: there are two single peaks around 105 ppm, corresponding to the carbon C1, and around 88 ppm, corresponding to the carbon C4, instead of double ones for cellulose II, and the peak corresponding to the carbon C6 is located around 66 ppm instead of 62 ppm for cellulose II and has a different shape (see Fig. 2.7).

C Sample preparation protocol

In this section, we determine a protocol that allows to prepare homogeneous suspensions when adding salt to the initial commercial CNC suspension. Indeed, adding salt directly into the commercial suspension would lead to the immediate aggregation of CNCs through screening of the inter-particle electrostatic repulsion, resulting in a heterogeneous suspension. The resulting in-

(a) Non-polarized white light.

(b) Polarized white light.

Figure 2.8: CNC suspensions containing 3.2 wt % CNC and 25 mM, 50 mM, 100 mM and 240 mM NaCl respectively, from left to right, prepared using protocol 2.

homogeneities might influence its viscoelastic properties and the reproducibility of the measurements.

In order to establish a well controlled and reproducible protocol to prepare our samples, we use mechanical stirring. Mechanical stirring is induced using a IKA RW 20 Digital mixer equipped with an R1402 blade dissolver. We have established two preparation protocols.

In protocol 1, we first homogenize the commercial CNC suspension under strong shear using mechanical stirring at 2070 rpm during 5 min. Then, we add a solution of NaCl (Merck) dissolved in distilled water, and we shake the sample by hand. Finally, we store it in the refrigerator for at least 24h before using it.

In protocol 2, we first homogenize the commercial CNC suspension under strong shear using mechanical stirring at 2070 rpm during 5 min like in protocol 1. Then, while shearing, we slowly add a solution of NaCl (Merck) dissolved in distilled water, and we continue to shear the sample for 5 min. Finally, we store it in the refrigerator for at least 24h before using it.

In both protocols, as soon as salt is added, the suspension thickens, becomes pasty, and turns whitish. This is indicative of the formation of CNC clusters and, eventually, of gelation (see Fig. 2.8a). Moreover, the suspensions are birefringent under polarized light (see Fig. 2.8b).

We test those two protocols on two different suspensions: one containing 3.2 wt % CNC and 50 mM NaCl, and one containing 3.2 wt % CNC and 100 mM NaCl. The samples are then characterized using polarized light microscopy and using rheometry, with a stress-controlled rheometer (MCR 301, Anton Paar). The samples mechanical properties are probed using the following rheological protocol: each sample is first rejuvenated by the application of a strong shear $\dot{\gamma}$ = 500 s^{-1} during 20 s in order to ensure a reproducible initial state, with no influence of the sample loading. After this pre-shear, an oscillatory strain of small amplitude γ = 1 % and frequency f = 1 Hz is applied during 200 s in order to probe the time evolution of the viscoelastic properties of the sample in the linear regime of deformation (γ = 1 % $\ll \gamma_{NL}$, with γ_{NL} the onset of the non-linear regime, estimated through an amplitude sweep experiment as described in Sec.2.A.2). Figure 2.9 shows polarized light microscopy images of the four samples, and Fig. 2.10 shows the corresponding time evolution of their viscoelastic properties following pre-shear.

First, we observe that the addition of salt without shearing the suspension, corresponding to protocol 1, leads to the formation of large millimetric aggregates [see Fig.2.9 (a) and (c)]. Such aggregates result from the screening of the inter-particle electrostatic repulsion by the Na^+ ions. Once repulsive interactions are screened, CNCs move closer to one another and form bonds through the action of some attractive forces such as hydrogen bonding or van der Waals interactions. This mechanism is very fast and CNCs are strongly bonded to each other. Therefore, mixing the sample by hand after the addition of salt is not enough to break these large aggregates. On the other hand, we observe that the addition of salt under strong mechanical shear, corresponding to protocol 2, considerably improves the sample homogeneity [see Fig.2.9 (b) and (d)]: we observe no large ag-

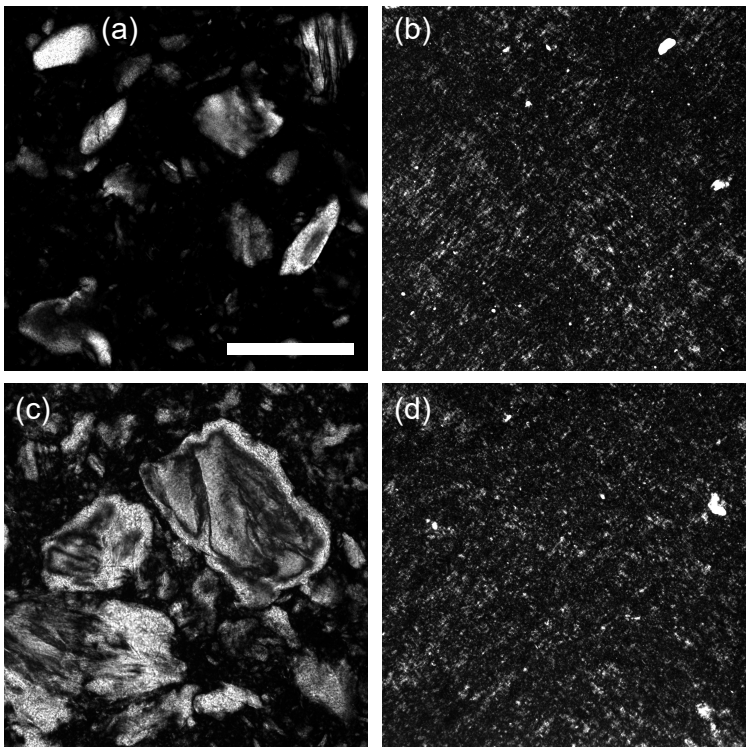

Figure 2.9: Microscope images under polarized light of CNC suspensions containing 3.2 wt % CNC and (a),(b) 50mM and (c),(d) 100 mM NaCl, prepared using (a),(c) protocol 1 and (b),(d) protocol 2 respectively. The scale bar in (a) corresponds to 1 mm and the magnification is the same in all figures.

gregate anymore, only small ones of size 150 μm maximum, even for the sample containing the largest salt content.

This homogeneity difference affects the sample rheological properties, as seen in Fig. 2.10. Indeed, we observe that both the elastic modulus G' and the viscous modulus G'' are larger for samples resulting from protocol 1 (G'_1, G''_1), where salt is added without mechanical shear, compared to samples from protocol 2 (G'_2, G''_2), where salt is added under mechanical shear. Moreover, the larger the aggregates, the greater the difference in the sample viscoelastic properties: the sample containing 50 mM NaCl has aggregates up to 0.7 mm large and a G' relative difference of about $(G'_1 - G'_2)/G'_2$ = 11.6 %, whereas the sample containing 100 mM NaCl has aggregates up to 1.6 mm large and a G' relative difference of about $(G'_1 - G'_2)/G'_2$ = 114.8 %. However, the recovery kinetics are very similar with or without addition of salt under shear, as $G'(t)$ and $G''(t)$ evolve the same way for both samples.

In addition, DLS measurements performed by Bruno Jean on the commercial suspension show that there is no effect of the strong mechanical shear on the CNC individual particles as both the size distribution (see Fig. 2.12) and the zeta potential (-41.2 mV for the mechanically sheared commercial suspension) remain the same.

Such results show that an addition of salt under strong mechanical shear allows us to obtain homogeneous samples, without altering the individual CNC particles. In order to determine the optimal mechanical shear time, we prepare a series of samples, containing 3.2 wt % CNC and 50 mM NaCl, using protocol 2 in which we vary the shearing time after salt addition between 5 min and 60 min. The time evolution of the viscoelastic properties of the resulting samples following shear-rejuvenation is plotted in Fig. 2.11. We observe that for all shearing times longer than 5 min,

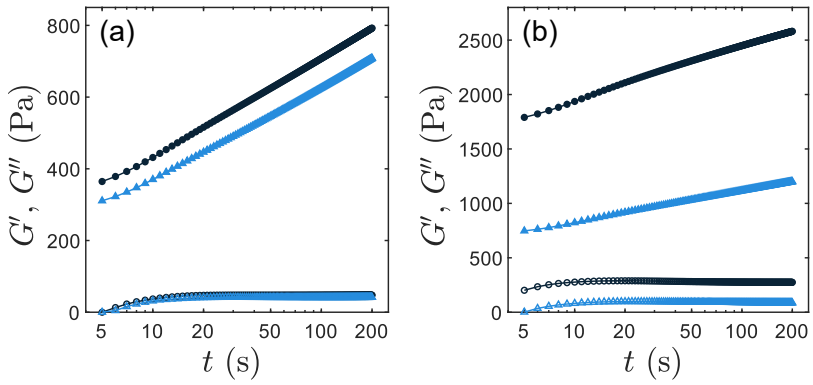

Figure 2.10: Time evolution of the elastic modulus G' (filled symbols) and of the viscous modulus G'' (empty symbols) following a 20 s pre-shear at $\dot{\gamma} = 500\ ^{-1}$, for suspensions containing 3.2 wt % CNC and (a) 50 mM NaCl or (b) 100 mM NaCl, prepared using protocol 1 (dark blue ▲) or using protocol 2 (light blue •). Measurements performed by applying an oscillatory strain of amplitude $\gamma = 0.2$ % and frequency $f = 1$ Hz.

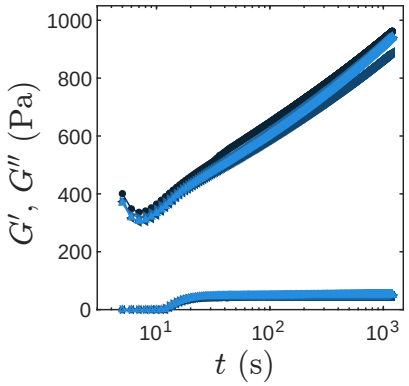

Figure 2.11: Time evolution of the elastic modulus G' (filled symbols) and of the viscous modulus G'' (empty symbols) following a 20 s pre-shear at $\dot{\gamma} = 500\ \text{s}^{-1}$, for a suspension containing 3.2 wt % CNC and 50 mM NaCl, prepared using protocol 2, with a mechanical shearing time following salt addition of 5 min (darkest blue •), 10 min (◂), 30 min (▸), and 60 min (lightest blue (▲). Measurements performed by applying an oscillatory strain of amplitude $\gamma = 0.2$ % and frequency $f = 1$ Hz.

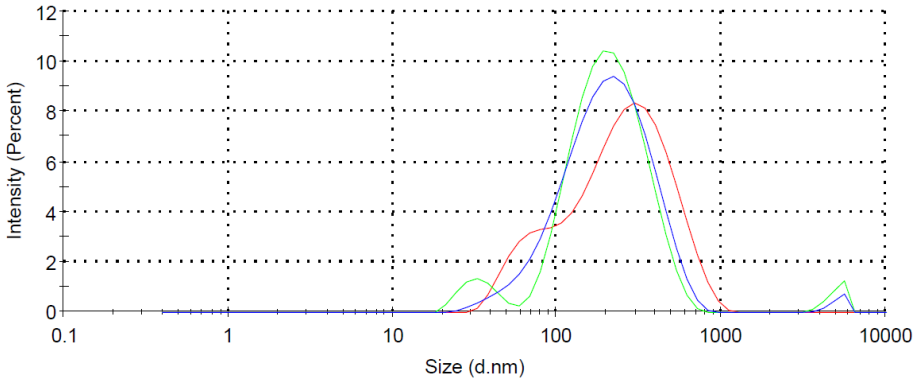

Figure 2.12: Size distribution of the commercial CNC suspension which has been mechanically sheared at 2070 rpm during 5 min, and diluted 100 times. Results obtained through dynamic light scattering. The three curves correspond to three different measurements on the same sample. To be compared with Fig. 2.6.

the rheological response of the sample is very similar. This observation suggests that, above 5 min, there is no significant effect of an increase of the shearing time on the sample microstructure and on the size and proportion of the remaining aggregates. Therefore, we deduce that shearing the sample for 5 min after salt addition is enough to obtain a homogeneous sample.

We could have applied high-power ultrasound in order to better disperse CNCs by breaking down the aggregates. However, we show that sonication of CNC suspensions might also break down the CNC particles themselves (see the Appendix for a detailed study of the effect of sonication on CNC particles and on the rheology of CNC suspensions).

To conclude, mechanical shear provides an easy way to make well-controlled homogeneous samples, without altering the CNC particles themselves. For this reason, all the samples used in this thesis are made following protocol 2, as described in the following box.

Sample preparation protocol:

1. Homogenization of the aqueous commercial CNC suspension under strong mechanical shear: 2070 rpm during 5 min.
2. Slow addition under shear of a solution of salt dissolved in distilled water.
3. Continuation of the strong mechanical shear at 2070 rpm during 5 min.
4. Storage of the sample in the refrigerator for at least 24 h.

This protocol allows us to obtain samples containing between 1 and 5.5 wt % CNC dispersed in water, and between 5 and 240 mM of salt of different types: NaCl, KCl, LiCl, NH_4Cl and $MgCl_2$.

D Appendix

Effect of sonication on CNC suspensions rheological properties

We study the effect of sonication on the indiviual CNC particles and on the rheology of CNC suspensions. In Sec. 2.B, we have seen that in the commercial CNC suspension, CNCs form aggregates. Sonication is a technique that has been widely used to break such aggregates in colloidal suspensions. It consists of applying high-power ultrasound to the suspension. To do so, we use an ultrasonic processor (VCX 750, Sonics), equipped with a 13 mm probe tip. We vary the acoustic energy applied between 1 kJ and 17 kJ while adjusting the sonication time to keep a total power of 200 W. During sonication, the sample is placed in an ice bath in order to avoid over-heating it, and ultrasound is applied as pulses of 2 s separated by 2 s breaks. The suspension mechanical properties are then characterized using a stress-controlled rheometer (MCR 301, Anton Paar). The sample is first rejuvenated by the application of a strong shear $\dot{\gamma} = 500\ \mathrm{s}^{-1}$ during 20 s in order to ensure a reproducible initial state, with no influence of the sample loading. After this pre-shear, an oscillatory strain of small amplitude $\gamma = 1\ \%$ and frequency $f = 1$ Hz is applied during 200 s in order to probe the time evolution of the viscoelastic properties of the sample in the linear regime of deformation ($\gamma = 1\ \% \ll \gamma_{NL}$, with γ_{NL} the onset of the non-linear regime, estimated through an amplitude sweep experiment as described in Sec.2.A.2).

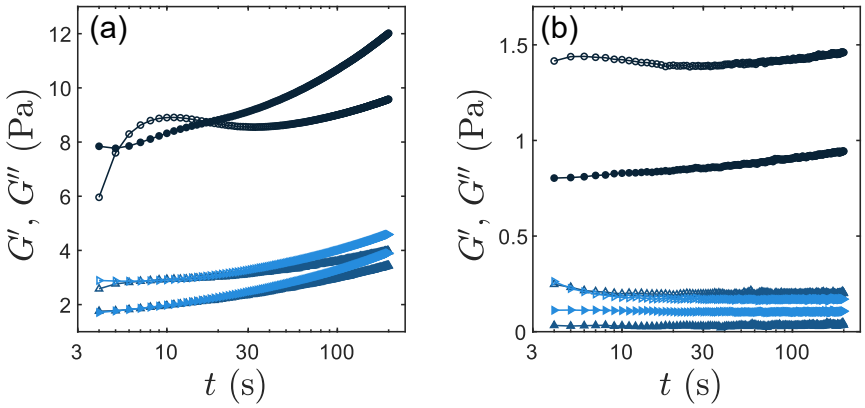

Figure 2.13: Time evolution of the elastic modulus G' (filled symbols) and of the viscous modulus G'' (empty symbols) following a 20 s pre-shear at $\dot{\gamma} = 500\ ^{-1}$, for suspensions containing (a) 6.4 wt % CNC or (b) 3.2 wt % CNC, having received an acoustic energy of 0 kJ (darkest blue •), 1 kJ (▲), or 17 kJ (lightest blue ▸). Measurements performed by applying an oscillatory strain of amplitude $\gamma = 0.2\ \%$ and frequency $f = 1$ Hz.

Figure 2.13(a) compares the time evolution of the viscoelastic properties of the commercial suspension containing 6.4 wt % CNC after it has received an acoustic energy of 0 kJ, 1 kJ and 17 kJ. Both the elastic modulus G' and the viscous modulus G'' decrease by a factor 3 when the suspension has been sonicated. However, above 1 kJ, an increase of the received acoustic energy has no influence on the sample viscoelastic moduli. Indeed, the time evolutions of the viscoelastic moduli of the suspension which has received 1 kJ and of the suspension which has received 17 kJ are superimposed at short times. This result shows that sonication results in a weakening of the viscoelastic properties. Therefore, it suggests that high-power ultrasound breaks down some of the CNC aggregates that were initially present in the commercial suspension, and which are responsible for these viscoelastic properties. This hypothesis is confirmed by DLS measurements performed by Bruno Jean: after sonication of the commercial suspension, the mean size of the objects in the CNC suspension is decreased from 130.4 nm to 81.5 nm (see Fig. 2.14, to be com-

pared with Fig. 2.6). This decrease of the mean size indicates a decrease of the length of either the CNC clusters or the CNC particles themselves. Therefore, sonication most breaks down the CNC clusters, but it might also affect the individual CNC particles.

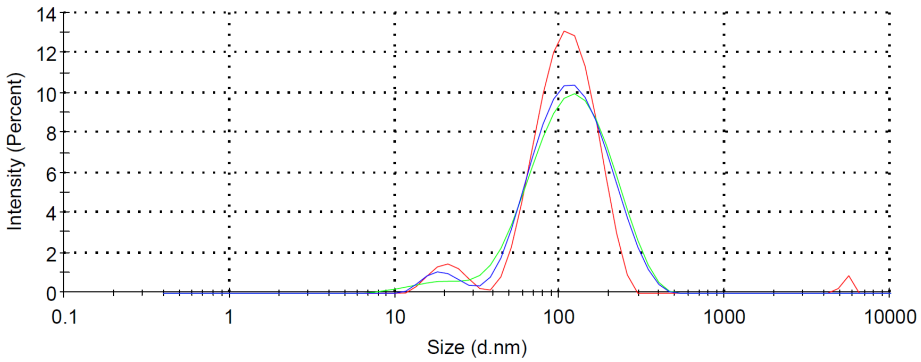

Figure 2.14: Size distribution of the commercial CNC suspension which has been sonicated for 90 s at an acoustic energy of 2.25 kJ, and diluted 100 times. Results obtained through dynamic light scattering. The three curves correspond to three different measurements on the same sample. To be compared with Fig. 2.6.

Besides this change in the absolute values of the viscoelastic moduli, their time evolution is also affected by sonication and we observe an effect of the acoustic energy received by the suspension. In fact, at long times, there is a sharper increase of both G' and G'' for the suspension having received an acoustic energy of 17 kJ compared to the one having received an acoustic energy of 1 kJ. This result shows that the re-organization kinetics of CNCs following a strong shear are affected by sonication, therefore suggesting that the inter-particle interactions might also have changed.

We now investigate the effect of sonication on CNC suspensions in the presence of salt. The introduction of salt into the commercial suspension leads to particle aggregation and to the formation of a soft material. To prepare such salty CNC suspensions, we first dilute a precise quantity of NaCl (Merck) into 25 g of distilled water. Then, we pour this solution into 25 g of the commercial suspension of CNC at 6.4 wt %, and we shake it strongly. We obtain a CNC suspension containing 3.2 wt % CNC and a given NaCl concentration. As soon as salt is added, the suspension becomes much "thicker", more like a paste than a viscous liquid, and turns whitish. This is indicative of the formation of CNC clusters and, eventually, of gelation.

Figure 2.15 presents the time evolution of the viscoelastic properties of suspensions containing 3.2 wt % CNC and 25 mM NaCl [Fig. 2.15(a)] and 55 mM NaCl [Fig. 2.15(b)], which have been sonicated with acoustic energies ranging between 0 kJ and 17 kJ. Interestingly, the effect of sonication is reversed compared to the one observed in Fig. 2.13 for the commercial suspension. Indeed, both the elastic modulus G' and the viscous modulus G'' increase with the acoustic energy. However, we observe the same trend as for the commercial suspension concerning the recovery kinetics: the rate of increase of the elastic modulus G' becomes faster when increasing the acoustic energy. This observation suggests that the suspension recovery kinetics accelerate with an increasing acoustic energy. Finally, in the range of energies explored here, we do not reach an acoustic energy threshold above which we observe no impact anymore on the suspension viscoelastic properties.

Previous studies on the effect of ultrasound on CNC suspensions have shown that, besides breaking down large CNC aggregates, sonication similar to the one we have applied to our suspensions may also have a great influence on the morphology of the CNC particles themselves. Indeed, it has been shown that such treatment can shorten the CNCs length, as observed above, destroy part of their crystalline structure, and affect the network of inter-particle hydrogen bonds [Sumari et al., 2013, Shojaeiarani et al., 2020]. These results may explain part of the behavior we

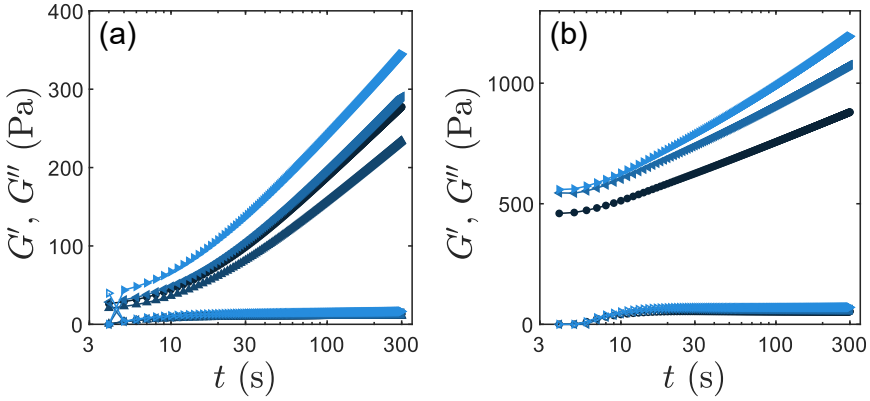

Figure 2.15: Time evolution of the elastic modulus G' (filled symbols) and of the viscous modulus G'' (empty symbols) following a 20 s pre-shear at $\dot{\gamma} = 500\ ^{-1}$, for suspensions containing 3.2 wt % CNC and (a) 25 mM NaCl or (b) 55 mM NaCl, having received an acoustic energy of 0 kJ (darkest blue •), 1 kJ (▲), 9 kJ (◂) or 17 kJ (lightest blue ▸). Measurements performed by applying an oscillatory strain of amplitude $\gamma = 0.2$ % and frequency $f = 1$ Hz.

observe in this study.

To conclude, this preliminary study show that sonication has a complex impact on CNC suspensions: besides breaking down the particle aggregates, high-power ultrasound also affects the CNCs morphology such as their length and their crystalline structure. Moreover, for a reasonable sonication time and limited heating of the sample, there is no acoustic energy threshold above which we observe no impact anymore on the suspension viscoelastic properties. For these reasons, we decided not to use sonication in our sample preparation protocol.

CHAPTER 2. MATERIALS AND METHODS

CHAPTER

3

GELATION DYNAMICS UPON FLOW CESSATION

Contents

In the Introduction, we have seen that CNC suspensions form a soft solid in the presence of salt through screening of electrostatic repulsion forces, leading to particle aggregation 1.D.3. This soft solid is characterized by its viscoelastic properties that are measured through rheological measurements. It can be broken down and turned into a viscoelastic liquid when submitted to a strong shear which breaks part of the inter-particle bonds. Interestingly, after being fluidized, CNC suspensions in the presence of salt reconstruct and recover their initial solid-like viscoelastic properties.

In this chapter, we rationalize the recovery dynamics following shear cessation for suspensions containing various CNC and salt concentrations. By establishing two superposition principles, we highlight a certain universality of these dynamics which holds across part of the CNC versus NaCl phase diagram, and we provide experimental evidence for a gel to attractive glass phase transition.

A Recovery dynamics at a single frequency

In order to investigate the recovery dynamics following shear cessation, we measure the time evolution of the viscoelastic properties of CNC suspensions in the linear regime of deformation. Those viscoelastic properties depend on the frequency, as explained in Sec. 1.B.1.c in the Introduction. In this first section, we focus on the time evolution of the suspensions viscoelastic moduli $G'(t)$ and $G''(t)$ measured at a single frequency $f = 1$ Hz. Part of the work presented in this section has been published in L. Morlet-Decarnin, T. Divoux and S. Manneville, J. Chem. Phys., 2022, 156, 214901 [Morlet-Decarnin et al., 2022].

A.1 Rheological protocol

We use a stress-controlled rheometer (either MCR 301 or MCR 302, Anton Paar), equipped with a cone-and-plate geometry. The cone is sand-blasted, with a surface roughness of 30 μm as provided by the manufacturer, in order to avoid slip of the sample along the cone surface. The cone has a 40.0 mm diameter, a 2° angle, and a 176.0 μm truncation. The smooth bottom plate is connected to a Peltier module, which sets the sample temperature to $T = 23.0 \pm 0.1$ °C. In order to avoid evaporation, we use a home-made solvent trap made of a Plexiglas cylindrical dome covering the geometry, and we saturate the atmosphere surrounding the sample with water. The rheological protocol is the following:

(1) We strongly shear the sample in order to fully fluidize it and break down its microstructure. This so called "pre-shear" step allows us to obtain a reproducible initial state by minimizing the influence of previous mechanical history including the loading of the sample into the shear cell. It consists of imposing a shear rate $\dot{\gamma} = 500$ s^{-1} during 20 s. Fig. 3.2a shows a typical example of the time evolution of the shear stress σ during this initial step, for a sample containing 3.2 wt % CNC and 12 mM NaCl. After 10 s, the stress is almost constant, indicating that a stationary state is reached, therefore confirming that a 20 s pre-shear is sufficient to rejuvenate the sample and get a reproducible state.

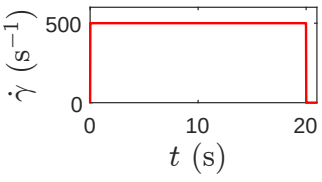

(2) The pre-shear is stopped abruptly by setting $\dot{\gamma} = 0$, which defines the time origin $t = 0$, and we subsequently measure the linear viscoelastic moduli, i.e., the elastic modulus G' and the viscous modulus G'', every second for 1200 s by imposing small-amplitude oscillatory shear (SAOS) with a strain amplitude $\gamma = 0.2$ % at a frequency $f = \omega/2\pi = 1$ Hz.

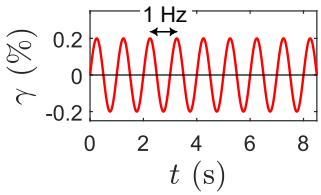

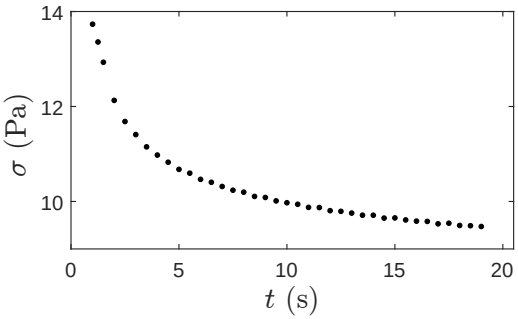

(a) Temporal evolution of the stress σ during the 20 s pre-shear at $\dot{\gamma} = 500\ s^{-1}$.

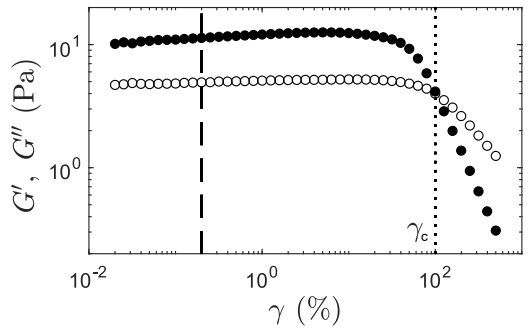

(b) Elastic modulus G' and viscous modulus G'' as a function of strain amplitude γ following 1470 s of rest after a 20 s preshear at $\dot{\gamma} = 500\ s^{-1}$. The black dashed line at $\gamma = 0.2$ % highlights the strain amplitude used in steps (2) and (3) of the protocol, while the one at $\gamma \approx 100$ % defines the yield strain γ_c.

Figure 3.2: Example of rheological measurements during (a) step (1) and (b) step (4) of rheological protocol detailed in Sec. 3.A.1, for a suspension containing 3.2 wt % CNC and 12 mM of NaCl.

(3) The viscoelastic spectrum G' and G'' versus f is measured at $t_w = 1200$ s after cessation of shear through a SAOS measurement, consisting of applying an oscillatory strain signal of amplitude $\gamma = 0.2$ % and sweeping down logarithmically the frequency f from 10 Hz to 0.1 Hz with 5 points per decade over a total duration of 270 s. Each frequency is applied for six periods, and the recorded data are averaged over the five last periods.

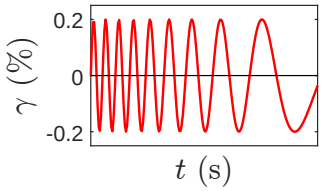

(4) Finally, starting 1470 s following shear cessation, we determine the yielding properties of the sample through a large-amplitude oscillatory shear (LAOS) measurement, consisting in sweeping up logarithmically the oscillatory strain amplitude from $\gamma = 0.02$ % to 500 % at $f = 1$ Hz, with 10 points per decade and a waiting time of 18 s per point, leading to a total duration of 790 s. This duration is small enough to avoid artifacts due to solvent evaporation. For each strain amplitude, the recorded data are averaged over the last 9 s of application of the given strain amplitude. This last step of the protocol allows us to determine the yield strain γ_c and to check that a strain amplitude of 0.2 % lies within the linear viscoelastic regime for all samples, i.e., $\gamma = 0.2\ \% \ll \gamma_c$, so that the measurements of G' and G'' versus t in step (2) and of G' and G'' versus f in step (3) do not interfere with the structural build-up and aging processes. An example of such a measurement is given in Fig. 3.2b for a sample containing 3.2 wt % CNC and 12 mM NaCl. The first black dashed line represents the strain amplitude $\gamma = 0.2$ % used in steps (2) and (3), and the second black dashed line represents the yield strain $\gamma_c \approx 100$ %, defined by $G'(\gamma_c) = G''(\gamma_c)$.

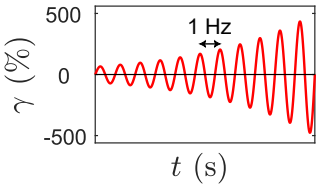

A.2 Typical evolution of the viscoelastic moduli at 1 Hz

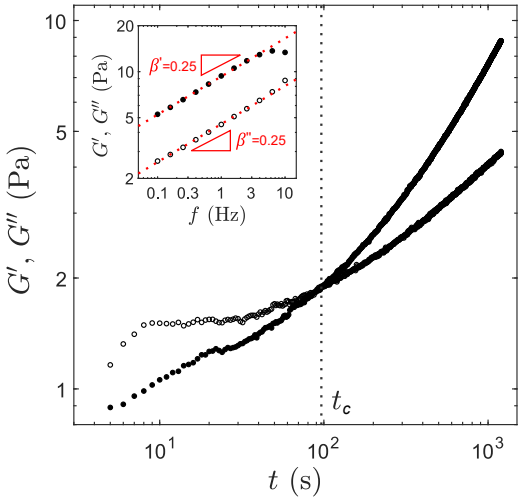

Figure 3.3: Temporal evolution of the elastic modulus G' (•) and viscous modulus G'' (◦) measured at 1 Hz following a 20 s pre-shear at $\dot{\gamma} = 500\ \mathrm{s}^{-1}$. The vertical dashed line at $t = t_c = 96.5$ s defines the G'-G'' crossover time t_c at 1 Hz. Inset: Viscoelastic spectrum G' and G'' as a function of frequency f for a strain amplitude of 0.2 %, measured 1200 s after cessation of shear. The red dashed lines represent fits of $G'(f)$ and $G''(f)$ by power-laws of exponent $\beta' = \beta'' = 0.25 \pm 0.01$. Experiment performed on a 3.2 wt % CNC suspension containing 12 mM of NaCl.

Figure 3.3 illustrates the temporal evolution of the viscoelastic properties measured at 1 Hz for a suspension containing 3.2 wt % CNC and 12 mM NaCl. Both the elastic modulus G' and the viscous modulus G'' increase with time as the sample recovers following shear rejuvenation, without reaching a steady state within the 1200 s measurement. At short times, the viscous modulus G'' is larger than the elastic modulus G' meaning that the sample is in a viscoelastic liquid state. At time $t_c = 96.5$ s, hereafter called the crossover time, both moduli become equal: $G'(t_c) = G''(t_c)$ [see the vertical dashed line at $t = 96.5$ s in Fig. 3.3]. At longer times, the elastic modulus becomes larger than the viscous modulus: the sample is therefore now in a viscoelastic solid state.

To further characterize the mechanical state of the sample, the inset of Fig. 3.3 shows the viscoelastic spectrum G' and G'' versus f measured after the rest period of 1200 s, i.e., during step (3) of the rheological protocol described in Sec. 3.A.1. While both the elastic and viscous moduli increase with frequency, the elastic modulus remains larger than the viscous modulus over the whole range of measured frequencies, confirming the observation made at $f = 1$ Hz that the sample is in a solid-like state after $t_w = 1200$ s of recovery. The frequency dependence of both the elastic and the viscous moduli can be fitted by power-laws $G' \sim f^{\beta'}$ and $G'' \sim f^{\beta''}$ respectively. For this sample, after $t_w = 1200$ s following shear cessation, we observe that both exponents are the same over the frequency range [0.1–10 Hz], which is characteristic of a critical gel [Winter, 1987]: $\beta' = \beta'' = 0.25 \pm 0.01$. Such a power-law dependence of G' and G'' with the frequency suggests the presence of a continuum of time-scales corresponding to multiple length-scales in the suspension microstructure. Note, however, that due to the strong impact of the salt concentration on the kinetics reported below (see Sec. 3.A.3), some samples may undergo significant aging over the 270 s duration of the viscoelastic spectrum measurement, so that one should remain cautious when interpreting those viscoelastic spectra.

This first analysis allows us to identify:

(1) remarkably slow recovery dynamics following flow cessation without any apparent steady-state, involving long time-scales before the sample may reach a steady-state if it exists

(2) a transition from a liquid-like state to a solid-like state occurring at time t_c, measured at $f = 1$ Hz

(3) a power-law dependence of the elastic modulus with the frequency at the end of the recovery period: $G' \sim f^{\beta'}$.

A.3 Time-composition superposition

We now study how these recovery dynamics depend on the NaCl concentration introduced in the CNC suspension.

a Time evolution of the viscoelastic moduli at 1 Hz

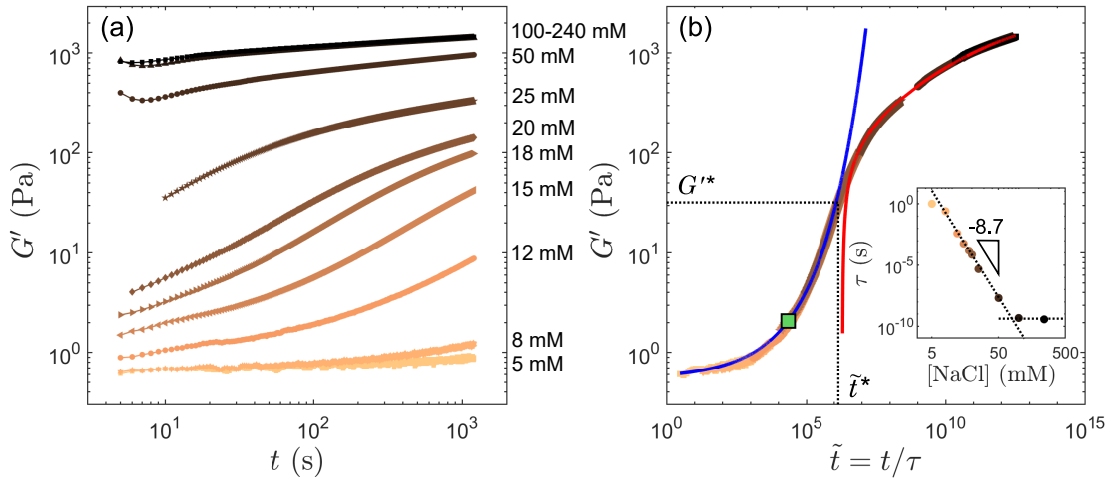

Figure 3.4: (a) Temporal evolution of the elastic modulus G' following a 20 s pre-shear at $\dot{\gamma} = 500$ s^{-1}. Experiments performed on 3.2 wt % CNC gels with NaCl concentrations ranging from 5 mM to 240 mM (from yellow to black). (b) Master curve obtained by shifting the $G'(t)$ data in (a) along the time axis by a factor $1/\tau$. The response $G'(t)$ of the gel with 5 mM of NaCl is used as a reference ($\tau = 1$ s). The gray dashed lines indicate the inflection point of coordinates ($\tilde{t}^*$,G'^*). The green square shows the point where $G'(\tilde{t})$ and $G''(\tilde{t})$ cross. The blue and red lines show stretched exponential fits, respectively, $G'(\tilde{t} \lesssim \tilde{t}^*) = G'_0 \exp[(\tilde{t}/T_p)^p]$ and $G'(\tilde{t} \gtrsim \tilde{t}^*) = G'_\infty(1 - A \exp[-((\tilde{t} - \tilde{t}^*)/T_q)^q])$ with $G'_0 = 0.55$ Pa, $T_p = 8 \times 10^3$, $p = 0.28$, $G'_\infty = 2200$ Pa, $A = 1.11$, $T_q = 8 \times 10^{11}$, and $q = 0.16$. Inset: Shift factor τ as a function of salt concentration. The black dashed line for [NaCl]<50 mM shows the best fit of the data by a power-law of exponent -8.7, and the one for [NaCl]>50 mM shows the mean value of the data.

Figure 3.4(a) gathers the temporal evolutions of the elastic modulus $G'(t)$ for 3.2 wt % CNC suspensions with NaCl concentrations ranging from 5 mM to 240 mM and following the same protocol as above, described in Sec. 3.A.1. The corresponding viscous moduli $G''(t)$ are shown

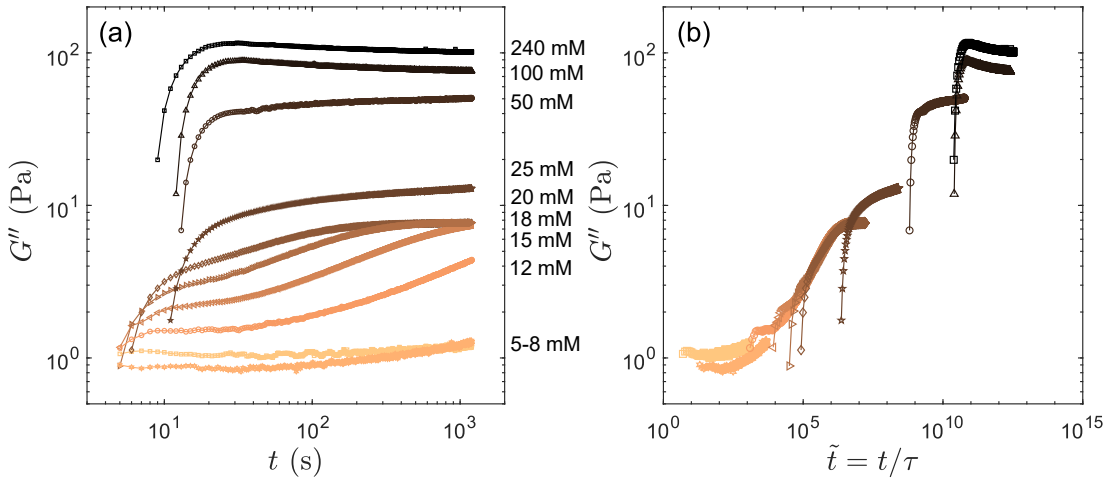

Figure 3.5: (a) Temporal evolution of the viscous modulus G'' following a 20 s preshear at $\dot{\gamma}$ = 500 s^{-1}. Experiments performed on 3.2 wt % CNC gels with NaCl concentrations ranging from 5 mM to 240 mM (from yellow to black). (b) Master curve obtained by shifting the $G''(t)$ data in (a) along the time axis by the same factor $1/\tau$ as used for the construction of the $G'(\tilde{t})$ master curve.

in Fig. 3.5(a). For all the NaCl concentrations explored, both the elastic and the viscous moduli increase with time following shear cessation. However, the elasticity and the viscosity of the sample at a given time strongly depend on the salt concentration: the larger the salt concentration, the larger the initial elasticity and viscosity. The recovery kinetics also strongly depend on the salt concentration: for both [NaCl] < 12 mM and [NaCl] > 50 mM, the elastic modulus slowly increases, while we observe a sharper increase at intermediate salt contents over the time window chosen for the experiments. For salt concentrations larger than 100 mM, the evolution of the elastic modulus appears to become independent of the NaCl content: both the $G'(t)$ curves corresponding to samples containing 100 mM and 240 mM NaCl are superimposed. This influence of the salt content on the sample recovery kinetics is also highlighted by the time evolution of the viscous modulus: G'' increases slowly with time at small salt concentrations, for [NaCl] < 12 mM, and accelerates at intermediate salt contents, for 12 < [NaCl] < 20 mM. At larger salt concentrations, for [NaCl] > 20 mM, we observe a very fast increase of $G''(t)$ at short times, followed by a plateau. Such a change in the viscous response of the sample must be linked to a modification of the dissipation process upon flow cessation. Moreover, we note that for the two largest salt concentrations, above 50 mM NaCl, $G''(t)$ shows an overshoot before decreasing at long times. This non-monotonic response, which is absent from $G'(t)$, could be related to the syneresis of the gels, i.e., the spontaneous expulsion of solvent that is observed when these two specific samples are left at rest. Finally, contrary to what we have observed for the elastic modulus, the time-responses of the viscous modulus do not superimpose for [NaCl] > 50 mM, because of the fast increase of $G''(t)$ at short times, the presence of the overshoot and because $G''(t)$ plateaus while the value of G'' at a given time does not plateau but rather increases with the salt concentration.

We now focus on the time evolution of the elastic modulus $G'(t)$ of our series of samples following shear cessation. The shape of the elastic responses for different salt concentrations prompts us to construct a master curve from the data in Fig. 3.4(a). By translating the $G'(t)$ curves in time by a factor $1/\tau$, which depends on the salt concentration, we obtain the master curve shown in Fig. 3.4(b). We arbitrarily take τ = 1 s for the smallest salt concentration of 5 mM, which thus constitutes a reference concentration. The corresponding data for the viscous modulus G'' are

presented in Fig. 3.5. Remarkably, the elastic modulus increases over 13 decades of relative time $\tilde{t} = t/\tau$, and follows a sigmoidal curve in logarithmic scales with a clear inflection point, whose coordinates are denoted $\tilde{t}^*$ and G'^* in the following. Over the 1200 s rest period investigated here, the inflection point is only observed for salt concentrations in the range 15–20 mM [see middle curves in Fig. 3.4(a)].

This master curve provides clear evidence for a "time-composition superposition" principle underlying the kinetics of the elastic modulus: for any salt content, the time evolution of $G'(t)$ after shear rejuvenation can be mapped onto a segment of the master curve by simply rescaling the time by a factor that strongly decreases with the salt concentration. Thus, increasing the salt content corresponds to an increase of the effective age of the sample. In practice, our results imply that, provided one waits 3.2×10^{12} s or about 10^5 years, a 3.2 wt % CNC suspension containing 5 mM of NaCl should reach the same elastic modulus as a 3.2 wt % CNC suspension with 240 mM of NaCl after 1200 s of rest. This suggests that the salt concentration only controls the kinetics of formation of a microstructure which is very similar whatever the salt content. Time-resolved measurements of the suspensions viscoelastic spectra will allow to confirm this hypothesis (see Sec. 3.B).

We note that the master curve cannot be fitted in logarithmic scales by a symmetric function with respect to the inflection point. Rather, similar $G'(t)$ master curves for the recovery of isotropic colloidal gels have been fitted to exponential functional forms [Rueb and Zukoski, 1997, Negi and Osuji, 2010, Mahmoudi and Stradner, 2017]:

$$G'(t) = G'_\infty(1 - \exp[-\lambda(t/t_g - 1)^q]) \tag{3.1}$$

where λ quantifies the rate of increase of connectivity of the gel, and t_g is the "gelation time," defined as the time when a critical gel is first observed [Winter and Mours, 1997] or sometimes more pragmatically as the time when the sample becomes solidlike, i.e., when $G' > G''$, for a given frequency [Negi et al., 2014] (see Fig. 3.3). Note that this expression implies that $G'(t_g) = 0$, which is *a priori* not compatible with the definition of t_g, but still leads to realistic fits of the data, since the elastic modulus at the gel point usually takes very small values. The exponent $q = 1$, i.e., a simple exponential function, was reported to fit the evolution of $G'(t)$ in the above-mentioned thermoreversible silica gels [Negi et al., 2014, Rueb and Zukoski, 1997, Guo et al., 2011], while salt-induced gels of Ludox silica particles yielded values of $q = 1.6$–2.1, i.e., *compressed* exponentials, depending on the colloid volume fraction [Cao et al., 2010].

In the case of CNC suspensions, we show that a *stretched* exponential with $q \simeq 0.16$ accounts well for the $G'(\tilde{t} \gtrsim \tilde{t}^*)$ master curve, although with a slightly different form:

$$G'(\tilde{t} \gtrsim \tilde{t}^*) = G'_\infty\ (1 - A\ \exp[-((\tilde{t} - \tilde{t}^*)/t_q)^q]) \tag{3.2}$$

involving an additional fitting parameter A, and provided the characteristic time is taken as $\tilde{t}^*$ rather than the much smaller relative crossover time t_c/τ, which might depend on the NaCl concentration. This fit is drawn as a red line in Fig. 3.4(b). However, a single exponential form only captures the later stages of the aging dynamics for $\tilde{t} \gtrsim \tilde{t}^*$ and cannot reproduce the sigmoidal shape of the master curve as observed in logarithmic scales in Figs. 3.4(b). In order to capture the initial growth of the elastic modulus, for $\tilde{t} \lesssim \tilde{t}^*$, we need to introduce another exponential form, different from the one accounting for the $G'(\tilde{t} \gtrsim \tilde{t}^*)$ master curve:

$$G'(\tilde{t} \lesssim \tilde{t}^*) = G'_0\ \exp[(\tilde{t}/t_p)^p] \tag{3.3}$$

with $p = 0.28$ [see the blue line in Fig. 3.4(b)]. Although we could fit both the initial recovery and the aging regime by two stretched exponential growths, a single functional form fitting the whole dynamics is still lacking. In particular, the fact that $G'(t)$ does not tend to 0 at short times is indicative of some non-negligible initial elasticity immediately after pre-shear. Consistently, such a sigmoidal shape, with a non-zero limit at small salt concentrations, corresponding to short

times, has been reported in another study, for the elastic modulus measured at a given time and frequency, as a function of the KCl concentration [Nikoumanesh and Poling-Skutvik, 2023]. This small level of elasticity could be due to the incomplete disaggregation of the CNC clusters by shear or to some intrinsic viscoelasticity of the fully dispersed CNC suspension that could result from partial liquid-crystalline order. More experiments are needed to clarify the origin of the initial elastic modulus upon flow cessation, e.g., by systematically varying the pre-shear value $\dot{\gamma}$. The physico-chemical parameters that control the amplitude and the steepness of the sigmoid in the master curve also remain to be uncovered.

Finally, the above discussion raises the question of the interpretation of the stretching exponents observed here, $p \simeq 0.28$ and $q \simeq 0.16$, which contrast with the compressed exponentials of Ref. [Cao et al., 2010]. Stretched exponentials are typically reported from the relaxation of correlation functions measured in glassy systems where particles escape from the cages formed by their neighbors due to thermal fluctuations [Cipelletti and Ramos, 2002, Bouzid et al., 2017]. On the other hand, systems where thermal fluctuations are weak rather display dynamics governed by compressed exponentials due to the local elastic relaxation of frozen-in stress heterogeneities [Cipelletti et al., 2003, Guo et al., 2007, Madsen et al., 2010, Bouzid et al., 2017]. In our case, whether or not the stretched exponentials reported here in $G'(\tilde{t})$ result from the glassy-like dynamics of clusters of CNCs remains to be investigated, e.g., through time-resolved spectroscopy.

The shift factor τ, used to construct the master curve and reported as an inset in Fig. 3.4(b), decreases as a power-law of the salt concentration with an exponent -8.7 ± 0.2, until a plateau is reached for salt concentrations above 50–100 mM. This plateau suggests that all the negative surface charges of the CNCs have been screened beyond 50–100 mM, and that any supplemental addition of salt only weakly affects the viscoelastic properties of the CNC suspension. However, the most salted samples still undergo significant aging since no saturation is reached in $G'(t)$ at the longest accessible times.

Applying this shift factor τ to rescale the time evolution of the viscous moduli $G''(t)$ following shear cessation leads to the data displayed in Fig. 3.5(b). At small salt concentrations, for [NaCl] < 20 mM, the rescaled viscous modulus $G''(\tilde{t})$ follows a master curve similar to the one reported for the rescaled elastic modulus. However, at larger salt concentrations, the individual responses deviate from the general master curve due to a change of shape of $G''(t)$ from a continuous increase to a sharp increase at short times followed by an overshoot and a plateau at longer times, as described above. This difference in the viscous modulus response suggests a modification of the gel network reconstruction scenario for salt concentrations above 50 mM. Indeed, in this very fast recovery regime, CNCs aggregation could become dominated by diffusion of the particles, which are not slowed down by repulsive electrostatic repulsion.

b Frequency spectra after recovery

The time-composition superposition principle illustrated in Fig. 3.4(b) shows that, within the range of samples investigated here, the suspension properties are the same for a given position along the master curve $G'(t)$ versus $\tilde{t}$, whatever the NaCl concentration. However, those properties have been measured at a single frequency $f = 1$ Hz. Therefore, in order to explore the frequency dependence of a CNC suspension viscoelastic properties at various points in time during its recovery, we can consider the viscoelastic spectra G' and G'' versus f of every sample containing various salt content, measured $t_w = 1200$ s after shear cessation by applying an oscillatory strain of small amplitude, $\gamma = 0.2$ %, and frequency sweeping down logarithmically from 10 Hz to 0.1 Hz [see step (3) of the protocol described in Sec. 3.A.1]. A selection of those viscoelastic spectra for suspensions containing 3.2 wt % CNC and 5, 15, 25 and 100 mM NaCl are plotted in Fig. 3.6(a). We note that, at large salt concentrations, the viscous modulus $G''(f)$ does not follow such a clear power-law behavior as the elastic modulus, and even seems to go through a minimum. This behavior is rather unexpected as it is a feature typical of soft glassy

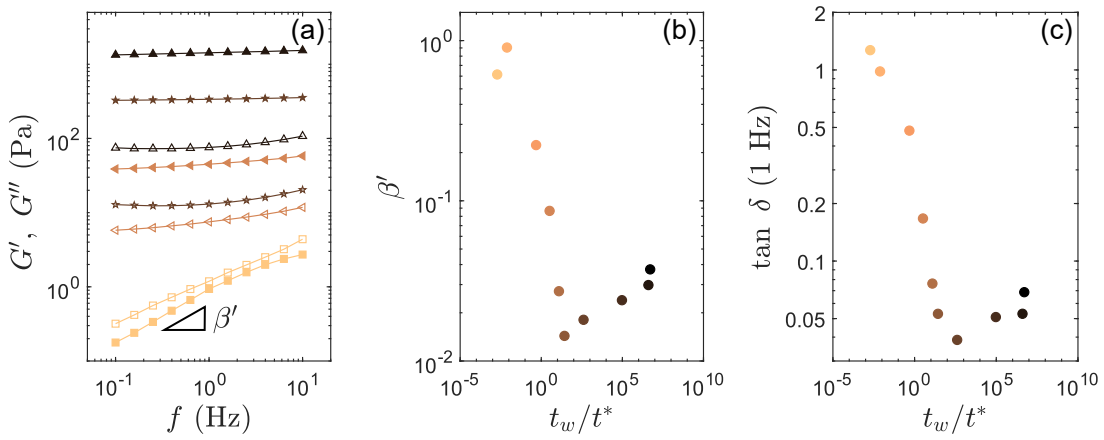

Figure 3.6: (a) Elastic modulus G' (filled symbols) and viscous modulus G'' (open symbols) versus frequency f measured following t_w = 1200 s of rest [step (3) of the rheological protocol detailed in Sec. 3.A.1]. Experiments performed on 3.2 wt % CNC gels with 5, 15, 25, and 100 mM NaCl. (b) Exponent β' extracted from power-law fits of the elastic modulus, $G'(f) \sim f^{\beta'}$, over the whole frequency range, and (c) loss factor $\tan\delta$ at f = 1 Hz versus the effective sample age t_w/t^* at the beginning of the frequency sweep test. Experiments performed on a series of samples containing 3.2 wt % CNC and various NaCl concentrations.

materials [Mason and Weitz, 1995a, Mason et al., 1995, Purnomo et al., 2006], although glassy features have been inferred in colloidal gels at the level of the strands constituting the gel network from rheological measurements [Keshavarz et al., 2021]. Yet, as already emphasized above, the time-dependence and aging of the sample may affect the measurements of the viscoelastic spectra, especially at small frequencies, which take longer to record. Therefore, in this section, we only focus on the exponent β' inferred from the power-law fit of $G'(f)$, and introduced above in Sec. 3.A.2.

Another parameter of interest to characterize a sample is the loss factor $\tan\delta = G''/G'$. It indicates the sample state, liquid-like for $\tan\delta > 1$ or solid-like for $\tan\delta < 1$, by quantifying the ratio of the viscous contribution over the elastic contribution to its mechanical properties. The resulting exponents β' and values of the loss factor $\tan\delta = G''/G'$ measured at f = 1 Hz for the various samples are plotted in Fig. 3.6(b) and (c) as a function of the normalized time t_w/t^*, where t_w is the waiting time (or recovery time) at rest after shear cessation, here t_w = 1200 s, and $t^* = \tilde{t}^* \times \tau$ is a characteristic time of the sample recovery, extracted from the master curve from Fig. 3.4(b). Note that $t_w/t^* = \tilde{t}_w/\tilde{t}^*$ corresponds to the location of the start of the frequency sweep, namely to the end of the 1200 s rest period, along the master curve of Fig. 3.4(b) relative to the inflection point. In other words, t_w/t^* measures the "effective age" of the sample relative to the inflection time.

Interestingly, Fig. 3.6(b) and (c) shows that both β' and $\tan\delta(1\,\text{Hz})$ follow a very similar dependence on the effective sample age relative to the inflection time, with a change of behavior around $t_w/t^* = 50 - 500$. More precisely, the exponent β' strongly decreases from about 1 at the early stages of the effective dynamics, down to about 0.012 for $t_w \simeq 50\,t^*$ [see Fig. 3.6(b)]. This evolution of β' shows that, at large salt concentrations, the suspensions are approaching a state that resembles a Hookean solid, for which $\beta' = 0$. Concomitantly with the decrease in β', the loss factor measured at f = 1 Hz drops with t_w/t^* by more than one order of magnitude, from values slightly above 1 indicative of a viscoelastic liquid, down to about 0.035 for $t_w \simeq 500\,t^*$, signaling a clear solid-like behavior [see Fig. 3.6(c)]. Finally, both observables change behavior rather abruptly around $t_w \gtrsim 50 - 500\,t^*$: both β' and $\tan\delta(1\,\text{Hz})$ seem to increase weakly with t_w/t^* for $t_w \gg t^*$.

Table 3.1: Coordinates $(\tilde{t}^*, G'^*)$ of the inflection point of each master curve [see Figs. 3.7(a) and (b) for the corresponding normalized master curves] and parameters I_0 and γ of the best power-law fits $t^* = I_0 \times I^{-\gamma}$ of the inflection time $t^* = \tau \times \tilde{t}^*$ versus ionic strength I for $I < 100$ mM.

w_{CNC} (wt %)	Salt	G'^* (Pa)	$\tilde{t}^*$	I_0	γ
3.2	NaCl	17.0 ± 0.5	$63 \pm 2 \times 10^4$	13.1	8.9
3.2	KCl	17.0 ± 1.0	$16 \pm 1 \times 10^5$	12.1	8.7
3.2	$MgCl_2$	24.5 ± 1.0	$19 \pm 2 \times 10^2$	14.6	8.8
2	NaCl	6.4 ± 1.0	$24 \pm 1 \times 10^1$	13.0	8.1
3.2	NaCl	17.0 ± 0.5	$63 \pm 2 \times 10^4$	13.1	8.9
4.8	NaCl	22.0 ± 1.0	$14 \pm 1 \times 10^3$	11.2	8.5
5.5	NaCl	17.7 ± 1.0	$80 \pm 1 \times 10^1$	10.7	8.7

Interestingly, the NaCl concentration corresponding to this change of regime coincides with the emergence of an abrupt increase of G'' at short times visible in Fig. 3.5. This observation strengthens our hypothesis that a change of scenario for the recovery dynamics of CNC suspensions occurs above about 20 mM NaCl. More precisely, at small salt concentration, or equivalently short effective time $\tilde{t}$, the response of the CNC suspension at $f = 1$ Hz corresponds to that of a gel, whereas at larger salt concentrations, or equivalently long effective time $\tilde{t}$, the same frequency reveals a more glassy-like behavior of the CNC suspension, which could originate from a microstructure composed of locally packed –and therefore glass-like– rods.

A.4 Robustness of time-composition superposition principle to salt nature and CNC weight fraction

In order to probe the robustness of the time-composition superposition principle, we now vary both the nature of the salt and the CNC weight fraction, allowing us to explore various positions in the CNC versus salt phase diagram. In particular, the same pre-shear and rest protocol is used on suspensions containing 3.2 wt % CNC and various concentrations of NaCl, KCl or $MgCl_2$, and on suspensions containing 2, 3.2, 4.8, or 5.5 wt % CNC and various NaCl concentrations. For all series of samples, using the same procedure as in Sec. 3.A.3 and described in Sec. 3.A.1, the temporal evolution of the elastic modulus can be rescaled onto a master curve similar to the one presented above in Fig. 3.4(b). Note that, for each series of suspensions, we take the sample with the smallest salt concentration as the reference for the time shift factor $\tau = 1$ s. Further normalizing each $G'(\tilde{t})$ data set based on the coordinates of the inflection point $(\tilde{t}^*, G'^*)$ leads to the general master curves reported in Figs. 3.7(a) and (b). The three series of suspensions with various salt cations, and the four series of samples with various CNC weight fractions w_{CNC} fall onto two single master curves, whose shape does not depend on the nature of the salt cation or on the CNC weight fraction, hence on the position in the phase diagram over the range explored. This demonstrates the robustness of the time-composition superposition principle, both to the salt nature and to the CNC content, for the recovery and aging dynamics of CNC suspensions, measured at a single frequency.

The coordinates of the inflection point used to normalize the various master curves are gathered in Table 3.1. For the three series containing various salt cations, the values of G'^* are similar for the two monovalent cations Na^+ and K^+, while it is much larger for the divalent cation Mg^{2+}, suggesting that the microstructure formed by CNCs through the interaction of a divalent cation is stronger than the one formed through the interaction of a monovalent cation. This observation is consistent with previous works [Chau et al., 2015, Lu et al., 2024], and it has been shown that this increase in the network stiffness is due (i) to a reduced Debye length of CNCs by ad-

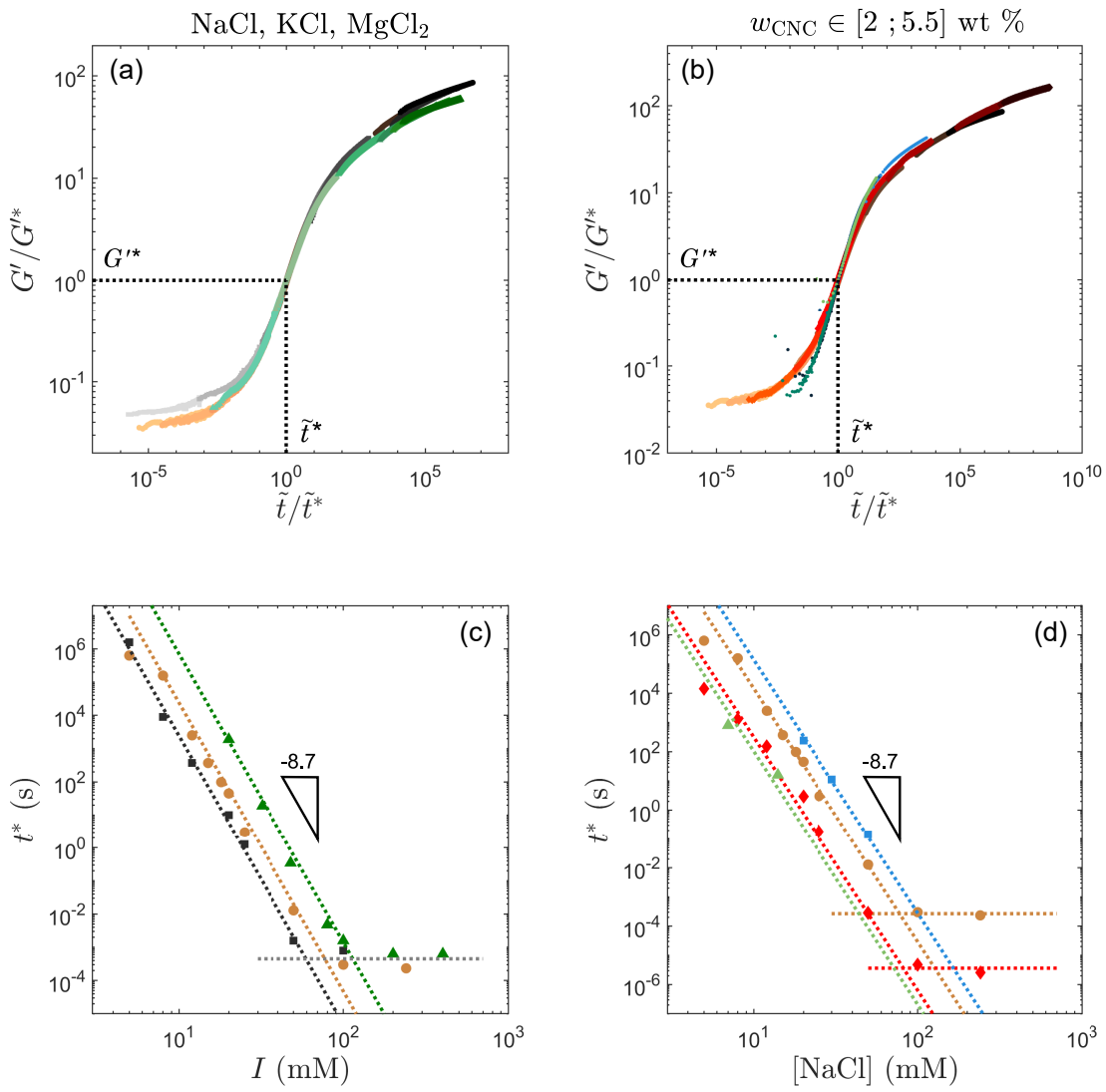

Figure 3.7: Time-composition superposition in CNC suspensions, generalized to a change of type of salt and to a change of CNC weight fraction. (a),(b) Normalized elastic modulus G'/G'^* versus normalized time $\tilde{t}/\tilde{t}^*$ during recovery and aging following shear cessation. Experiments performed (a) on three series of samples containing 3.2 wt % CNC and different types of salt, namely NaCl (orange •), KCl (gray ■) and $MgCl_2$ (green ▲) ; and (b) on four series of samples containing w_{CNC} = 2 wt % CNC (blue ■), 3.2 wt % CNC (orange •), 4.8 wt % CNC (red ♦) and 5.5 wt % CNC (green ▲) and various NaCl concentrations. The black dashed lines highlight the inflection point. (c),(d) The corresponding inflection time $t^* = \tau \times \tilde{t}$ for each series of samples, as a function of (c) the ionic strength I, and (d) the NaCl concentration. The dashed lines show the best fits of the data with a power-law of exponent -8.7. The horizontal dashed line highlights the plateau reached beyond $I \simeq 50 - 100$ mM and [NaCl]$\simeq 50 - 100$ mM.

dition of a cation with an increased number of charges, thereby reducing the inter-particle distance and favoring the formation of a denser network with thicker strands and greater stiffness [Chau et al., 2015, Lu et al., 2024], and (ii) to the formation of electrostatic bridges between CNC particles in the presence of divalent cations [Lopez and Richtering, 2019]. For the four series containing various CNC weight fractions, the values of G'^* seem to increase weakly with w_{CNC}, suggesting a reinforcement of the suspension microstructure with the CNC weight fraction, at a given point in time, or, equivalently, for a given salt concentration. This observation is consistent with the fact that an increase of the weight fraction leads to more inter-particle interactions, and therefore to the formation of a tougher network resulting in an increase of the sample elastic modulus. However, this consideration does not hold for the series containing 5.5 wt % CNC for which G'^* is smaller than the one estimated for the series containing 4.8 wt % CNC.[1]

In order to quantitatively compare the different series of suspensions, we consider the (dimensional) time $t^* = \tau \times \tilde{t}^*$ as a function of the ionic strength in Figs. 3.7(c) and (d). Here, the ionic strength I is defined considering only the charges brought in solution by the introduction of salt, i.e., $I = C \times z^2$, where C is the salt concentration, and z is the salt valency. Multiplying τ by $\tilde{t}^*$ allows us to remove the possible influence of the different references used in the rescaling from one series to another. Actually, $t^* = \tau \times \tilde{t}^*$ corresponds to the time it would take for each gel to reach the inflection point in its $G'(t)$ curve. Therefore, we shall refer to t^* as the "inflection time" in the following. Strikingly, Figs. 3.7(c) and (d) show that the inflection times all evolve in a similar manner with I: whatever the cation type and the CNC weight fraction, t^* decreases as a power-law of I with an exponent of about -8.7 ± 0.2, until it reaches a plateau beyond a critical ionic strength $I_c \simeq$ 50–100 mM, most likely when all negative CNC surface charges have been screened by the cations of the salt. For the sake of completeness, the parameters of the best power-law fits:

$$t^* = I_0 I^{-\gamma} \tag{3.4}$$

below 100 mM are listed in Table 3.1, although only power-laws of exponent −8.7 are shown in Figs. 3.4(b) and 3.7(c) and (d) for clarity. The mere difference between the various series is thus a vertical translation.

Hofmeister Series

Classification of ions in order of their lyotrophic properties, i.e., their ability to solubilize proteins, through a modulation of the hydrophilic interactions. It has been shown to be also relevant for colloids.

From the more chaotropic (or "structure-breaking") to the more kosmotropic (or "structure-forming"):

$NH_4^+ > K^+ > Na^+ > Li^+ > Mg^{2+} > Ca^{2+}$

For the series with various salt cations, I_0 increases from K^+ to Na^+ and Mg^{2+}, or equivalently, the inflection time t^* increases from K^+ to Na^+ and Mg^{2+} for a given ionic strength I. This result shows that the kinetics become slower following the Hofmeister series [Kunz et al., 2004b, Lyklema, 2009]. The enhanced "efficiency" of divalent cations to induce CNCs aggregation, reflected by the reduced amount of salt necessary to obtain the same viscoelastic properties and the same t^* with a divalent cation when compared to a monovalent one, has already been evidenced in suspensions of cellulose nanocrystals [Phan-Xuan et al., 2016, Nyamayaro et al., 2023, Moud et al., 2019, Cao and Elimelech, 2021].

However, ionic valency alone is not enough to explain the difference observed when varying the salt nature. The slowing down of the gelation kinetics following the Hofmeister series in CNC suspensions has already been reported too [Prathapan et al., 2016, Cao and Elimelech, 2021], and results in a combination of electrostatic, hydration and hydrophobic effects. In fact, to explain such a dependence, one must complement the classical DLVO potential with an additional

[1] We will see later in Sec. 3.B.3 that this series actually corresponds to a different region of the CNC versus NaCl phase diagram: the suspensions containing 5.5 wt % CNC form an attractive glass, while the three other series of samples are in the gel phase.

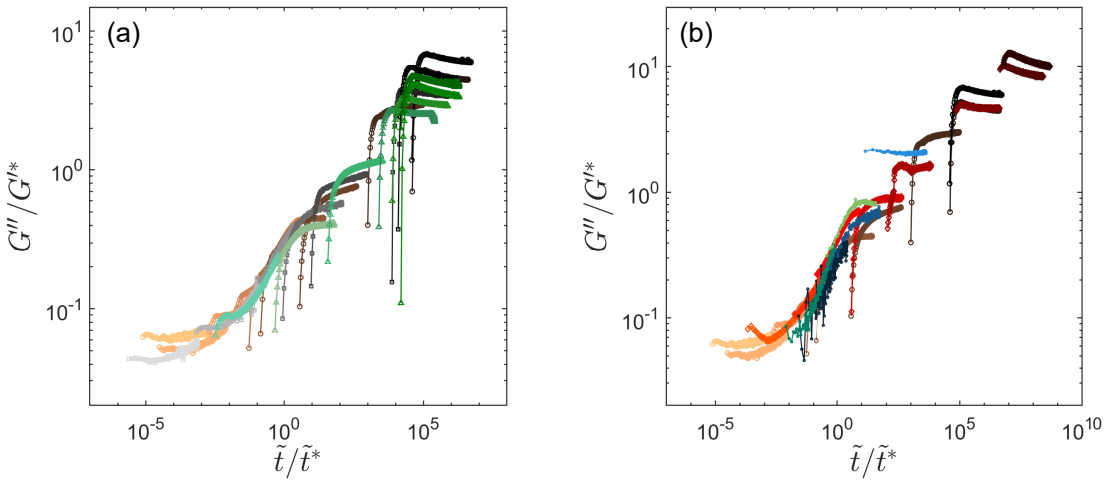

Figure 3.8: Master curves for the viscous modulus of the same series of samples as the one presented in Fig. 3.7, containing (a) 3.2 wt % CNC and different types of salt, namely NaCl (orange •), KCl (gray ■) and $MgCl_2$ (green ▲), and (b) w_{CNC} = 2 wt % CNC (blue ■), 3.2 wt % CNC (orange •), 4.8 wt % CNC (red ♦) and 5.5 wt % CNC (green ▲) and various NaCl concentrations. The shift factor τ applied to construct those master curves is the same as the one used for the construction of the corresponding $G'(\tilde{t})$ master curves.

ion-specific repulsive potential [Israelachvili and Wennerström, 1996] due to the hydration shell that surrounds ions adsorbed on the CNC surfaces, as proposed for silica particles not only for the gelation times [van der Linden et al., 2015] but also for the rheological properties of the resulting gels [Franks, 2002, Okazaki and Kawaguchi, 2008]. The more kosmotropic (or "structure-forming") ions, such as Mg^{2+}, surround themselves with a greater number of water molecules [Kunz et al., 2004b, Kunz et al., 2004a], making their adsorption on the CNC surface more difficult and weaker, therefore leading to a larger effective hydration repulsion between CNC particles [Cao and Elimelech, 2021]. On the contrary, the more chaotropic (or "structure-breaking") ions, such as K^+, are less hydrated, therefore reducing their hydration diameter. As a result, those ions absorb more strongly on the oppositely charged CNC surface, leading to an acceleration of the network reconstruction dynamics. For the series at various CNC weight fractions, we observe a vertical translation of the t^* versus I curves, which follows the order of w_{CNC}: I_0 decreases with the CNC content, as indicated in Table 3.1, and t^* decreases by about three orders of magnitude from 2 wt % to 5.5 wt % CNC. This result suggests that the recovery kinetics accelerate with the CNC weight fraction, which is expected due to the decrease of the inter-particle distance with w_{CNC}, and has already been reported in many other colloidal systems, such as gels of latex particles [Wu et al., 2013, Cao et al., 2010].

Following the same data processing as described above in Sec. 3.A.3, we now rescale the time evolution of the viscous modulus during recovery for each series of samples by applying the horizontal shift factor τ used to construct the master curves presented in Figs. 3.7(a) and (b). By further normalizing the resulting $G''(\tilde{t})$ master curves by the inflection point coordinates (G'^*, $\tilde{t}^*$) of each $G'(\tilde{t})$ master curves, we obtain the two sets of master curves for the viscous modulus plotted in Fig. 3.8. Similarly to what we have observed in Sec. 3.A.3, the various master curves, corresponding to different salts or to different CNC weight fractions, rescale properly onto a single general master curve for small to intermediate salt concentrations. However, here again, in both cases, the individual viscous responses diverge from a general master curve at large salt content, due to the appearance of the very fast increase of $G''(t)$ at short times, followed by a plateau which

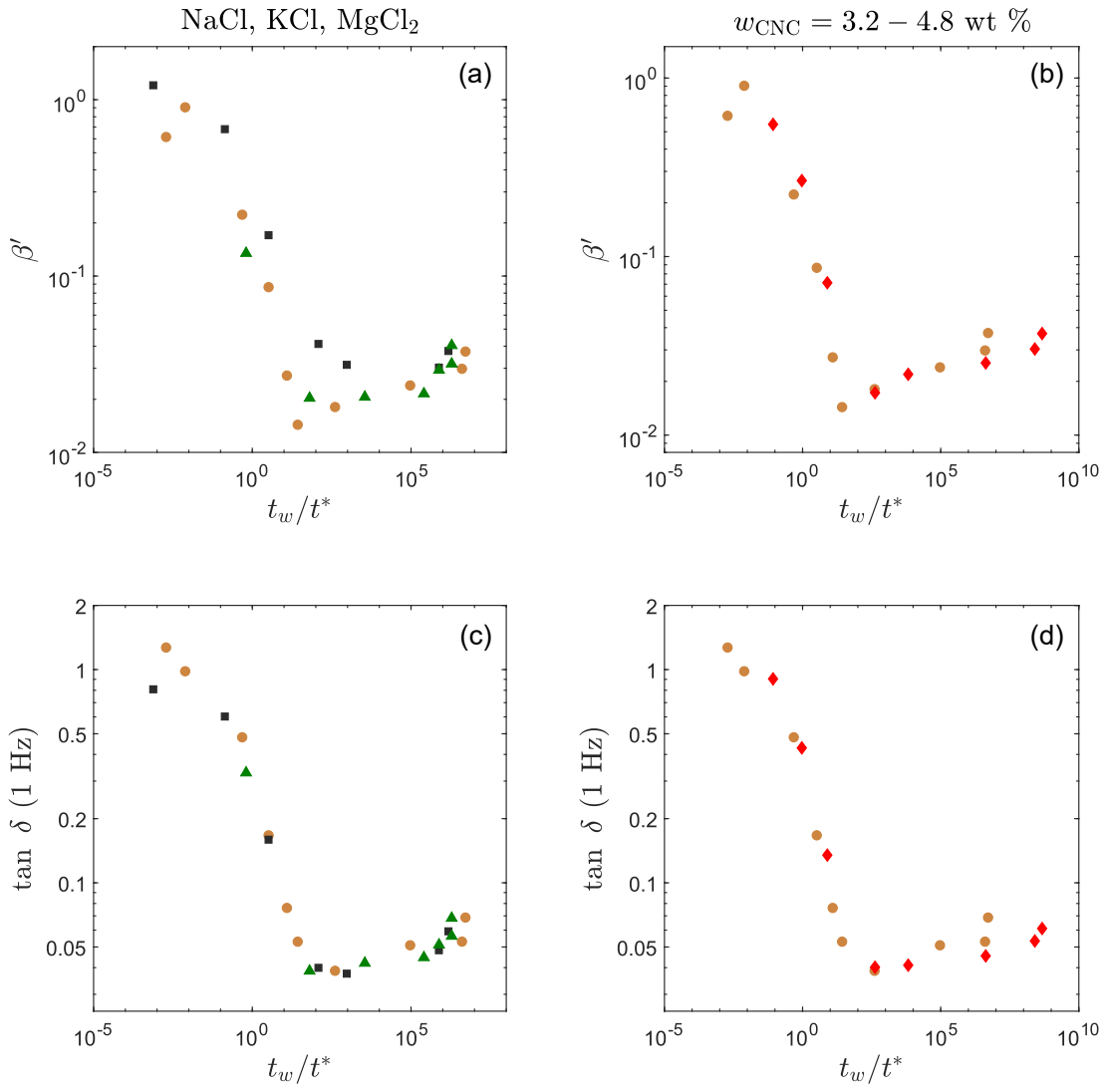

Figure 3.9: (a),(b) Exponent β' extracted from the power-law fit of $G'(f)$ measured at time t_w = 1200 s following shear cessation, and (c),(d) loss factor $\tan\delta$ measured at f = 1 Hz at time t_w = 1200 s following shear cessation as a function of the effective sample age, for the series of samples containing (a),(c) 3.2 wt % CNC and different types of salt, namely NaCl (orange •), KCl (gray ■) and $MgCl_2$ (green ▲) ; and (b),(d) two series of samples containing w_{CNC} = 3.2 wt % CNC (orange •) and 4.8 wt % CNC (red ⧫) and various NaCl concentrations.

value strongly depends on the salt concentration, its nature and on the CNC weight fraction.

The time-composition superposition principle generalized to a change of salt nature and to a change of the CNC weight fraction, illustrated in Figs. 3.7(a) and (b), suggests that, within the range of samples investigated here, the CNC suspension properties should be the same for a given position along the general master curve $G'(t)/G'^*$ versus $\tilde{t}/\tilde{t}^* = t/t^*$, whatever the ionic force, the type of salt or the CNC content. In order to test this hypothesis further, we investigate the viscoelastic spectra G' and G'' versus f measured after the t_w = 1200 s rest period following the cessation of shear (step (3) in the protocol of Sec. 3.A.1). In particular, for all series of samples, we extract the exponent β' from the power-law fit of $G'(f)$, and the value of the loss factor $\tan\delta = G''/G'$ at f = 1 Hz. As done previously in Sec. 3.A.3, both parameters are plotted as a function of the effective sample age relative to their corresponding inflection time t_w/t^* in Figs. 3.9(a),(b) and (c),(d) respectively. Remarkably, for both observables, the data for the series of samples containing various salt cations and for the series of samples containing CNC weight fractions of 3.2 wt % and 4.8 wt %[2] nicely collapse onto single curves, proving that both β' and $\tan\delta(1\,\text{Hz})$ follow a universal dependence on t_w/t^*. This result provides very strong support for the generality of the time-composition superposition principle revealed through Fig. 3.7, which is valid at least for the linear viscoelastic properties of CNC suspensions. In particular, the master curve for the exponent β' confirms that whatever the salt nature and the CNC weight fraction, a similar microstructure is formed, which evolves following the same path.

A.5 Robustness of time-composition superposition principle to solvent nature: deuterated water versus hydrogenated water

In this section, we explore the effect of the solvent nature (here D_2O) on the recovery dynamics of CNC suspensions. Indeed, CNCs suspended in water interact with the solvent through different types of interactions such as van der Waals interactions, but also by forming hydrogen bonds. Yet, the strength of those interactions may vary depending on the isotope constituting the water molecules. For example, it has been shown for biomolecular complexes that deuterium tends to induce the formation of more stable complexes, through hydrogen bonding, than hydrogen at temperatures lower than room temperature, while this tendency is reversed at higher temperatures, and almost no difference is observed at room temperature [Kjaersgaard et al., 2020]. Therefore, a change of the solvent nature could provide some information on the interactions between CNCs and the water molecules.

CNC suspensions in deuterium oxide D_2O cannot be made from the commercial aqueous suspension where CNCs are suspended in H_2O. Therefore, to prepare such suspensions, we use dried CNCs from CelluForce, which come in the form of a powder, that we suspend in D_2O using the protocol described in Sec. 3.C in Appendix. We obtain homogeneous suspensions containing 3.2 wt % CNC and NaCl concentrations varying between 2.25 and 100 mM. According to the supplier (CelluForce), the dried CNCs are exactly the same as the CNCs constituting the commercial aqueous suspension.

Once again, we have applied the same rheological protocol as described in Sec. 3.A.1 to both series of samples, containing either H_2O or D_2O and various NaCl concentrations, and we have observed that the temporal evolution of the elastic modulus of each series of samples can be rescaled onto a master curve similar to the one presented in Fig. 3.4(b). However, when further normalizing each $G'(\tilde{t})$ data set based on the coordinate of the inflection point $(\tilde{t}^*, G'^*)$, as represented in Fig. 3.10(a), the two master curves do not superimpose. Instead, the change of curvature in the sigmoidal shape of the master curve seems more abrupt for the series of CNCs suspended in H_2O than for the series of CNCs suspended in D_2O. Therefore, time-composition superposition is robust to a change of solvent from H_2O to D_2O, as we find a master curve for both series of sam-

[2] The spectra for w_{CNC} = 2 wt % and 5.5 wt % CNC were not recorded, as the protocol described in Sec. 4.B.1.a was used for these samples.

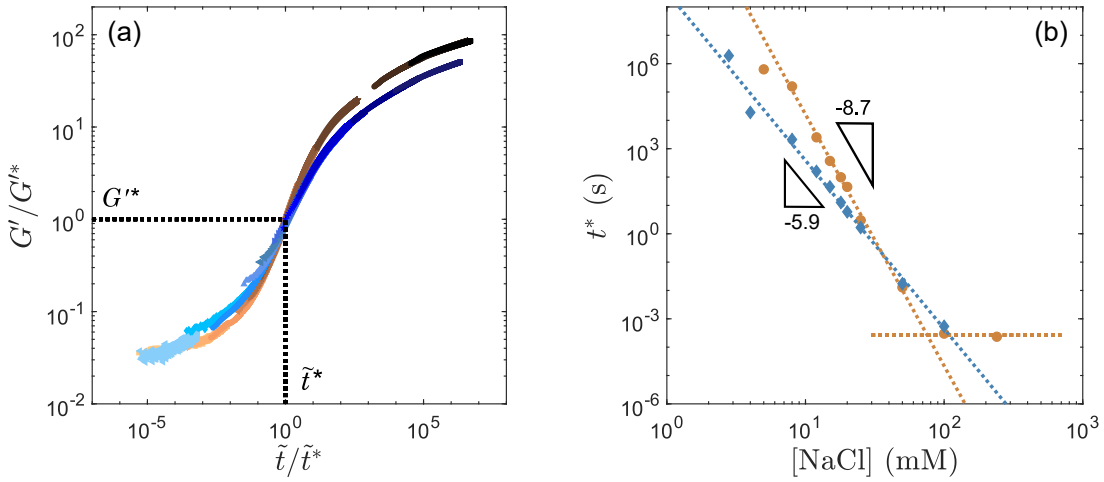

Figure 3.10: Time-composition superposition in CNC suspensions in H_2O and D_2O. (a) Normalized elastic modulus G'/G'^* versus normalized time $\tilde{t}/\tilde{t}^*$ during recovery and aging following shear cessation. The black dashed lines highlight the coordinates of the inflection point ($\tilde{t}^*$,G'^*). Experiments performed on two series of samples containing 3.2 wt % CNC and various NaCl concentrations, suspended in H_2O (orange •) or D_2O (blue ♦). (b) The corresponding inflection time $t^* = \tau \times \tilde{t}$ for each series of samples as a function of the NaCl concentration. The dashed lines show the best fits of the data with power-laws of exponents -8.7 and -5.9 for the series suspended in H_2O and D_2O respectively. The horizontal dashed line highlights the plateau reached beyond [NaCl]≃ 50 – 100 mM.

Table 3.2: Coordinates ($\tilde{t}^*$,G'^*) of the inflection point of each master curve [see the normalized master curves in Fig. 3.10(a)] and parameters I_0 and γ of the best power-law fits $t^* = I_0 \times I^{-\gamma}$ of the inflection time $t^* = \tau \times \tilde{t}^*$ vs. ionic strength I for $I < 100$ mM.

Solvent	G'^* (Pa)	$\tilde{t}^*$	I_0	γ
H_2O	17.0 ± 0.5	$63 \pm 2 \times 10^4$	13.1	8.9
D_2O	35.0 ± 1	$19 \pm 2 \times 10^8$	8.5	5.9

ples. However, the fact that we cannot construct a general master curve gathering the data from both series of samples in H_2O and in D_2O demonstrates that this time-composition superposition principle cannot be generalized to a change of the solvent nature, unlike what we have observed previously when varying the salt nature and the CNC weight fraction.

The impact of the solvent on CNC suspensions is also highlighted by the coordinates of the inflection point used to normalize the two master curves, reported in Table 3.2. The value of G'^* is about twice larger for the D_2O series than for the H_2O series, indicating the formation of a stiffer suspension microstructure in the presence of D_2O at a given time, or equivalently for a given salt concentration. This observation suggests stronger interactions between CNC particles in the presence of D_2O than in the presence of H_2O. This difference could result (i) from the formation of inter-particle hydrogen bonds mediated by water molecules, which would be stronger in the case of D_2O than in the case of H_2O or (ii) from a difference in the water structuration around CNC particles.

Finally, the evolution of the inflection time t^* with the salt concentration plotted in Fig. 3.10(b) shows that the solvent has a great influence on the recovery kinetics of CNC suspensions. In both cases, the inflection time decreases as a power-law with the salt concentration, indicating an accel-

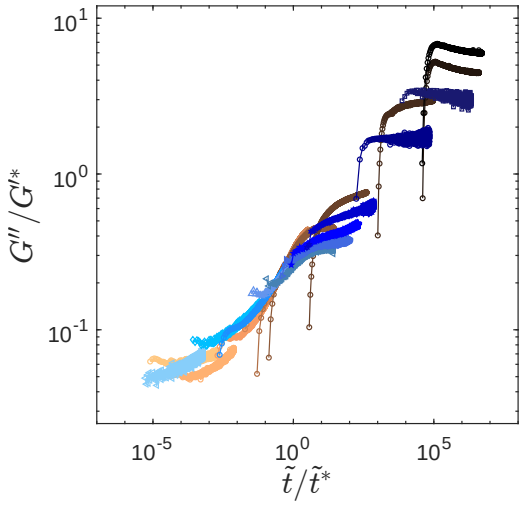

Figure 3.11: Master curves for the viscous modulus of the same series of samples as the one presented in Fig. 3.10, containing 3.2 wt % CNC and various NaCl concentrations, suspended in H_2O (orange •) or D_2O (blue ⧫). The shift factor τ applied to construct those master curves is the same as the one used for the construction of the corresponding $G'(\tilde{t})$ master curves.

eration of the recovery kinetics, as observed in the previous sections. However, this acceleration is slower for D_2O suspensions than for H_2O suspensions, as reflected by the smaller exponent γ extracted from Eq. (3.4) and reported in Table. 3.2. This remarkable dissimilarity suggests a difference in the recovery kinetics of CNC suspensions depending on the isotope.

As in the previous Section 3.A.4, we now rescale the time evolution of the viscous modulus following flow cessation for the two series of samples using the rescaling factor τ determined through the construction of their respective $G'(\tilde{t})$ master curves. Further normalizing those $G''(\tilde{t})$ data by the inflection point coordinates $(G'^*, \tilde{t}^*)$ of each $G'(\tilde{t})$ master curve, we obtain the general master curve plotted in Fig. 3.11. Here again, the time evolutions of the viscous modulus corresponding to each series of samples rescale onto a master curve for small to intermediate salt concentrations. At large salt content, we recover the same behavior as described in the previous sections: the individual viscous responses deviate from a general master curve due to the apparition of the very fast increase of $G''(t)$ at short times, followed by a plateau whose value strongly depends on both the salt and the solvent nature. These observations are consistent with a significant effect of the solvent isotope on the recovery dynamics and on the inter-particle interactions.

Despite a noticeable difference between the master curves and the recovery kinetics of the series of CNCs dispersed in H_2O and D_2O, at long aging time, for $\tilde{t} > \tilde{t}^*$, corresponding to large salt concentrations, both suspensions have similar viscoelastic properties in the linear regime of deformation. Indeed, Fig. 3.12(a) shows that the viscoelastic spectrum G' and G'' versus f is very similar for a suspension of CNCs dispersed in H_2O and a suspension of CNCs dispersed in D_2O, both containing 3.2 wt % CNC and 100 mM NaCl: both the $G'(f)$ responses are parallel, as well as the $G''(f)$ responses. We only observe a vertical shift towards larger G' and G'' values for the viscoelastic spectrum of the sample containing D_2O, which is consistent with the observation that G'^* is larger for this series than for the series containing H_2O. This result suggests that the microstructure formed during the sample recovery is very similar in the presence of H_2O or D_2O, but that the strength of the inter-particle bonds forming this microstructure depends on the isotope.

Finally, we extract the exponent β' from the power-law fit of $G'(f)$ and the value of the loss factor $\tan\delta = G''/G'$ at $f = 1$ Hz, both measured after the $t_w = 1200$ s rest period [step (3) in the protocol of Sec. 3.A.1]. Both parameters are plotted as a function of the effective sample age relative to their corresponding inflection time t_w/t^* in Figs. 3.12(b) and (c) respectively. Interestingly,

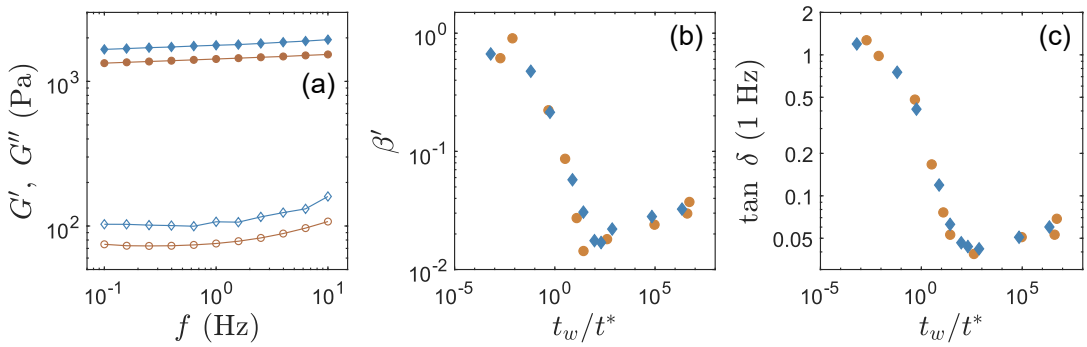

Figure 3.12: (a) Viscoelastic spectra $G'(f)$ (filled symbols) and $G''(f)$ (open symbols) measured at time t_w = 1200 s following shear cessation. (b) Exponent β' extracted from the power-law fit of $G'(f)$ measured at time t_w = 1200 s following shear cessation, and (c) loss factor $\tan\delta$ measured at f = 1 Hz at time t_w = 1200 s following shear cessation as a function of the effective sample age, for the series of samples containing 3.2 wt % CNC and various NaCl concentrations, suspended in H_2O (orange •) and D_2O (blue ♦).

even if the time-composition superposition principle could not be generalized to a change of solvent, as illustrated in Fig. 3.10(a), both observables collapse onto a single curve, proving that both β' and $\tan\delta(1\,\text{Hz})$ follow a universal dependence on t_w/t^*, independently of the solvent isotope. This result confirms the hypothesis proposed in the previous paragraph suggesting that the microstructure of samples made in H_2O or D_2O is very similar, and that only the strength of the inter-particle bonds forming this microstructure differs.

A.6 Discussion and open questions

Master curves for the evolution of the elastic modulus during gelation have been reported in other colloidal systems, such as isotropic silica particles at various temperatures [Negi et al., 2014], and at various salt concentrations [Cao et al., 2010], or in suspensions of CNCs mixed with an epoxide oligomer at various accumulated strain [Rao et al., 2019], with shapes that are similar to the one that we obtain [see Fig. 3.4(b), Fig. 3.7(a) and Fig. (b)3.10(a)]. For instance, in some thermoreversible gels of sterically stabilized silica particles, it has been deduced from time-temperature superposition that the elastic modulus at infinitely long times is independent of the temperature [Negi et al., 2014]. Here, we may deduce from time-composition superposition that the final elastic modulus $G'(t = \infty)$ of CNC suspensions is independent of the salt concentration. The results reported so far raise the following open questions.

a How may one interpret the inflection time?

The remarkable master curves followed by $G'(t)$ during recovery are based on the scaling of the inflection time t^*, which so far essentially appears as a phenomenological parameter. We will demonstrate in Sec. 3.B.2 that this characteristic time t^* for the suspensions recovery dynamics following pre-shear, coincides with the gelation time t_g, defined as the time needed for CNCs to organize into a "critical gel", i.e., a percolated network spanning over the whole sample volume. Therefore, we consider $t^* = t_g$ for the following discussion.

b How may one rationalize the influence of salt on the dynamics?

We have shown that, for an ionic strength below $I_c \simeq 50$–100 mM, the inflection time t^* decays as a power-law of the ionic strength I with an exponent $\gamma = 8.7 \pm 0.2$ independent of the nature of the cation and of the CNC weight fraction for CNCs suspended in H_2O, and an exponent $\gamma = 5.9 \pm 0.2$ for CNCs suspended in D_2O. Interestingly, a similar, very steep exponent of about 10 has been found in gels of cotton CNC in H_2O for the dependence upon salt concentration of the gelation time t_g inferred from light scattering experiments [Peddireddy et al., 2016]. Moreover, rough estimations of the sol-gel transition time in Ludox silica suspensions have reported power-laws $t_g \sim I^{-\gamma}$ with $\gamma = 5.9$–8.4 depending on the type of salt and on the colloid volume fraction [van der Linden et al., 2015]. Power-law behaviors with exponents in the range $\gamma = 6$–11 for the stability ratio W, or equivalently for the inverse of the coagulation rate, as a function of salt concentration have been predicted theoretically for monodisperse spherical particles and indeed found in pioneering experiments on AgI colloids through turbidity measurements [Reerink and Overbeek, 1954]. Since the gelation time is directly proportional to the stability ratio [Zaccone et al., 2014, van der Linden et al., 2015], similar exponents are expected for t_g vs I. The theory, however, predicts that the exponent should depend on the salt, in particular on the valency z of the counterion [Reerink and Overbeek, 1954, van der Linden et al., 2015], whereas we do not observe any significant variation in β with the type of salt. This discrepancy could be ascribed to the non-spherical nature and/or to the polydispersity of CNCs. To the best of our knowledge, a complete theory that would account for the specific characteristics of CNCs, both in terms of geometry and of surface charges, and for their interactions in the presence of salt is yet to be devised. Furthermore, the change of exponent γ when varying the solvent isotope points to a strong influence of the particle-solvent and the solvent-solvent interactions in the gel recovery dynamics, which therefore should be taken into account for the establishment of a complete theory.

Another striking observation on the effect of salt is the plateau observed in t^* above $I_c \simeq 50$–100 mM [see Figs. 3.7(c),(d) and Fig. 3.10(b)]. Such a critical ionic strength may be accounted for through the following rough charge balance between the negative charges borne by the CNCs and the positive charges brought by counterions. The latter is easily computed per unit volume as:

$$q_{\text{ion}} = \mathcal{N}_A I \tag{3.5}$$

where $\mathcal{N}_A$ is the Avogadro number and the ionic strength I is expressed in mM. Assimilating CNCs to cylinders of large aspect ratio $r = L/D \gg 1$, with L the length of a CNC and D its diameter, and bearing a surface charge σ, the former charge per unit volume simply reads:

$$q_{\text{CNC}} = 4\sigma\phi/D \tag{3.6}$$

where ϕ is the CNC volume fraction, given by the ratio of the CNC weight fraction to the density $d \simeq 1.5$ of CNCs relative to water for a dilute dispersion. Equating q_{ion} and q_{CNC} then leads to:

$$I_c \simeq 4\sigma\phi/(\mathcal{N}_A D) \tag{3.7}$$

expressed in mM. With $\phi = 2$–3 %, $D = 2$–8 nm, and $\sigma = 0.2$–0.8 charge.nm^{-2} as the typical range of charge surface density reported in the literature for CNCs [Reid et al., 2017, Abitbol et al., 2013, Jiang et al., 2010], one gets $I_c \simeq 4$–90 mM, which is compatible with the experimentally observed $I_c \simeq 50$–100 mM. Although the above estimate of I_c is subject to strong approximations, it suggests that the plateau in t^* indeed results from full screening of the charges at the CNC surface for $I > I_c$.

Furthermore, in the large ionic strength regime, the aggregation process is likely to be dominated by the self-diffusion of the CNC nanorods. For a sharp-ended cylinder in a Newtonian solvent of viscosity η_s, the rotational and translational diffusion coefficients are respectively given by[Brenner, 1974, Doi and Edwards, 1988, Aragon and Flamik, 2009, Lee and Cognet, 2020]:

$$\begin{cases} D_r \simeq 3k_BT(\ln r - 0.49)/(\pi\eta_s L^3) & (3.8) \\ D_t \simeq k_BT(\ln r + 0.38)/(3\pi\eta_s L) & (3.9) \end{cases}$$

up to corrective terms of order $r^{-1/2}$. Considering the average length and diameter of the present CNC nanorods and η_s = 1 mPa.s, we estimate the corresponding rotational and translational diffusion times $\tau_r = 1/D_r \simeq 0.27$ ms and $\tau_t = L^2/D_t \simeq 0.13$ ms respectively. These time-scales are consistent with the plateau values reached by t^* around 4×10^{-4} s for $I > I_c$ in suspensions containing 3.2 wt % CNC and various types of salt [see Fig. 3.7(b)-3.10(b)]. The much smaller plateau value, $t^* \approx 4 \times 10^{-6}$ s, reported in Fig. 3.7(b) for the 4.8 wt % CNC dispersions suggests that rods only need to diffuse over angles or distances about 10 times smaller than for 3.2 wt % CNC for aggregation to occur. Although a more complete model would be needed to fully account for the aggregation kinetics in the presence of crowding effects [Solomon and Spicer, 2010, Zaccone et al., 2013], this simplified approach supports the idea that aggregation becomes diffusion-limited for $I > I_c$.

c How may one rationalize the effect of a change of the solvent isotope?

We have shown that a change of the solvent isotope from hydrogen to deuterium results in a slowing down of kinetics for the recovery of CNC suspensions, along with a strengthening of the suspension microstructure reflected by the increase of the elastic modulus G'^*. Despite those discrepancies, we have not evidenced any rheological signature of a change of microstructure in the suspensions, suggesting that a change of solvent from H_2O to D_2O does not influence the local arrangement of CNC particles, but only the inter-particle interaction strength.

Effects of H_2O versus D_2O isotope have already been reported on the kinetics of chemical reactions [Wade, 1999], on the structuration of proteins and other biomolecules [Giubertoni et al., 2023] as well as on their solvatation dynamics on the surface of ZrO_2 nanoparticles [Pant and Levinger, 1999]. In all cases, the variations between deuterated and hydrogenated water are attributed to a change of the zero-point vibrational energy (the difference between the equilibrium energy and the energy of the vibrationless energy level) of bonds involving hydrogen or deuterium atoms, due to their difference of mass [Scheiner and Čuma, 1996]. However, a general rationalization of those effects is missing. In particular, while it is well-known that a substitution from hydrogen to deuterium affects a chemical reaction kinetics, these kinetics can be slowed down or accelerated depending on the reaction and the chemical compounds involved [Wade, 1999]. Similarly, this substitution from hydrogen to deuterium affects the kinetics of assembly of proteins, but whether it accelerates it or slows it down depends on the protein [Giubertoni et al., 2023]. Nevertheless, those observations are consistent with the change of dynamics that we observe for the reconstruction of CNC suspensions.

Several explanations could account for both the change of recovery kinetics and the change of elasticity that we observe in our CNC suspensions when switching from H_2O to D_2O. First, it has been shown that O–H bonds are longer than O–D bonds, and that the average hydrogen bond length increases in the presence of D_2O compared to H_2O [Soper and Benmore, 2008]. Considering the solvent alone, it has been demonstrated that the topology of the hydrogen bond network differs from H_2O to D_2O: in the presence of D_2O, the network is more tetrahedral, the coordination number is larger, and the hydrogen bonds are stronger. This leads to a stronger hydrogen bond network [Whalley, 1957, Scheiner and Čuma, 1996, Soper and Benmore, 2008, Giubertoni et al., 2023]. Moreover, the change of dipole moment between those two molecules may also play a role in the network strength: μ_{H_2O} = 1.8546 D< μ_{D_2O} = 1.8558 D [Clough et al., 1973, Whalley, 1957]. This difference in the solvent alone is important and might have a great influence on the interactions between CNC particles. In fact, it has been shown that CNCs induce a particularly strong structuring of water molecules around them, creating a hydration layer constituted of several layers of water molecules, which strongly influences the inter-particle interactions [Sinko and Keten, 2014, Sinko et al., 2015, Wei et al., 2018].

Moreover, a change from H_2O to D_2O also has direct effects on the constituents dispersed in the solvent and their interactions, both due to hydrogen bonds involving the constituent and the solvent molecules, and due to proton exchanges between the constituent and the solvent molecules. In the case of hydrogen bonds involving an anionic complex, as might be the case

in our CNCs due to the presence of negatively charged sulfate groups on their surface, it has been shown that hydrogen bonds involving an hydrogen atom are stronger than the one involving a deuterium atom. On the contrary, it has been observed in the case of a neutral complex that hydrogen bonds involving an hydrogen atom are weaker than the one involving a deuterium atom, which is consistent with what we have described in the previous paragraph for the solvent alone [Scheiner and Čuma, 1996]. Furthermore, it has been shown that a change of the solvent isotope also has an influence on the binding affinity, hydrophobicity and polarity of biomolecules [Wade, 1999, Turowski et al., 2003, Giubertoni et al., 2023]. However, this behavior cannot be rationalized as it strongly depends on the molecule.

All in all, those observations provide potential explanation for the observations that we have made on suspensions of CNCs. Yet, a deeper investigation of the isotope effect in this particular system is necessary to determine the precise origin of the dissimilarities that we have reported above.

d How does the microstructure evolve during recovery and aging?

Besides the influence of salt, the volume fraction of CNCs plays a crucial role in the recovery and aging dynamics, since an increase of 175 % in the CNC content from 2 wt % to 5.5 wt % accelerates the kinetics by a factor of about 1000 (see Sec. 3.A.4). Such an acceleration when increasing the CNC volume fraction has also been reported from turbidity measurements, although these were limited to the recovery phase [Peddireddy et al., 2016]. This suggests that the more particles, the more interactions, and the sooner the equilibrium configuration is reached. This also questions the role of interactions at the molecular scale between CNC clusters, including hydrogen bonds as recently emphasized in Refs. [Rao et al., 2019, Wohlert et al., 2021].

From the mechanical measurements presented in Fig. 3.6, Fig. 3.9 and Fig. 3.12, we may further elaborate on the potential structure reached by the suspension along the $G'(t)$ master curve. In particular, in the framework of critical gels, originally developed for branched polymer gels [Winter and Mours, 1997, Muthukumar, 1989, Ng and McKinley, 2008] and later extended to silica polymers [Ponton et al., 2002], protein gels [Ikeda and Nishinari, 2001, Ikeda, 2003], fibrin-thrombin gels [Curtis et al., 2013], thermoreversible gels of silica nanoparticles [Eberle et al., 2012], or aluminosilicate and Ludox gels [Keshavarz et al., 2021] among others, the exponent β' that characterizes the frequency-dependence of the viscoelastic spectrum has been linked to the fractal dimension d_f of the particulate network through [Muthukumar, 1989]:

$$d_f = \frac{5}{2}\frac{(3-2\beta)}{(3-\beta)} \tag{3.10}$$

under the assumption that hydrodynamic and excluded-volume interactions are fully screened. In our case, this relationship leads to a fractal dimension that increases from about $d_f = 1.25$ to 2.5 with the salt content, or, equivalently, with the effective sample age. These estimates are fully consistent with previous results on similar suspensions of charged cotton CNC rods in H_2O in the presence of salt, which report fractal dimensions $d_f \simeq 1.6$ for a moderate salt concentration (70 mM NaCl) using light scattering [Peddireddy et al., 2016] and $d_f \simeq 2.1$ at large ionic strength (200 mM NaCl) through small-angle neutron scattering [Cherhal et al., 2015]. Moreover, if this relationship between the exponent β' and the fractal dimension d_f remains valid throughout the whole recovery of the suspension, the existence of master curves for β' versus t_w/t^* suggests that the topology of the skeleton of the percolated network formed during recovery is very similar, independent of the counterion nature, the CNC weight fraction, and the isotope composing the solvent. Structural measurements along the master curves are required to validate such deductions, as well as to confirm the fractal nature of the present CNC suspensions and the evolution of d_f with the effective sample age.

(1) The time evolution of the viscoelastic properties of CNC suspensions in the presence of salt following shear cessation obeys a time-composition superposition principle, suggesting that time is equivalent to salt concentration.

> → Similar microscopic organization of CNCs whatever the salt concentration, only the kinetics of formation of this microstructure vary.

(2) This time-composition superposition principle is robust to a change of the salt nature, CNC weight fraction and solvent nature.

(3) Further rescaling of the master curves into general master curves shows that this time-composition superposition principle can be generalized to a change of the salt nature and of the CNC weight fraction.

> → Similar microscopic organization of CNCs and similar evolution path for this microstructure whatever the salt nature and the CNC weight fraction. Only the kinetics of formation of this microstructure vary.

But there is no generalization of this principle to a change of the solvent nature.

(4) The recovery kinetics accelerate with the salt concentration: $t^* \propto I^{-\gamma}$. $\gamma = 8.7 \pm 0.2$ is independent of salt nature and CNC weight fraction, but it is affected by the solvent nature.

B Recovery dynamics at several frequencies: time-resolved mechanical spectroscopy

Following the recovery of a CNC suspension at a single frequency, as described above in Sec. 3.A, has allowed us to identify a transition from a liquid-like to a solid-like state occurring at time t_c following fluidization by a strong shear. Based on a time-composition superposition principle, we have deduced a characteristic time for this recovery dynamics: the inflection time t^*, which decreases as a power-law of the ionic strength. However, this simple one-frequency measurement does not give us any insight into the physical meaning of this characteristic time. In particular, it does not allow us to identify a sol-gel transition and the corresponding gelation time t_g, defined as the time required for CNC particles to aggregate into a percolated network spanning over the whole sample volume. In order to properly identify a gel point and its corresponding gelation time t_g, we need to consider the time evolution of the sample viscoelastic properties measured at several frequencies, or equivalently, at several angular frequencies $\omega = 2\pi f$. Indeed, the "true" gel point is defined as the point where both the elastic and the viscous moduli evolve as the same power-law of the frequency [Winter and Chambon, 1986, Winter, 1987, Suman and Joshi, 2020]:

$$G'(\omega) \sim G''(\omega) \sim \omega^{\beta} \tag{3.11}$$

Such a power-law dependence is associated to the existence of a fractal microstructure, i.e., a microstructure which is self-similar over a vast range of length scales, associated to the time-scales probed by ω. The exponent β is called the critical relaxation exponent. Consequently, at the gel point, the loss factor $\tan\delta$ becomes independent of the frequency:

$$\tan\delta(\omega) = G''(\omega)/G'(\omega) \sim \omega^{0} \tag{3.12}$$

However, estimating the frequency dependence of a sample viscoelastic properties by probing it one frequency after the other takes a significant amount of time. Thus, if the system is not in a stationary state, as observed above in Sec. 3.A, the resulting viscoelastic spectra might be affected by the sample aging during measurement. In order to avoid artifacts, we need to reduce the measurement time so that the time needed to record one viscoelastic spectrum is smaller than the typical time over which the sample viscoelastic properties evolve significantly. In other words, as previously explained in Sec. 2.A.2, we need to ensure that the mutation number N_{mu} remains much smaller than one. We have shown in the previous section that, over the range of concentrations and measurement times explored, CNC suspensions do not reach any stationary state, and that their evolution gets faster as the salt concentration is increased. Therefore, in order to enforce $N_{\mathrm{mu}} \ll 1$, we use time-resolved mechanical spectroscopy, which allows us to reduce the measurement time of a viscoelastic spectrum down to 5 s to 8 s per spectrum. This technique thereby provides an in-depth study of gelation dynamics and an unambiguous determination of the critical point by probing the viscoelastic moduli at different frequencies as a function of time, sufficiently fast compared to the suspension aging and with sufficient resolution. It has been widely used on both chemical and physical polymer gels [Mours and Winter, 1994, Filippone et al., 2015, Kruse and Wagner, 2016, Arrigo et al., 2020, Geri et al., 2018, Suman and Joshi, 2020, Scanlan and Winter, 1991].

B.1 Protocol for time-resolved mechanical spectroscopy

The rheological protocol used throughout this section to measure the time evolution of a CNC suspension viscoelastic spectrum through time-resolved spectroscopy is detailed below. Part of the work presented in this section has been published in L. Morlet-Decarnin, T. Divoux and S. Manneville, ACS Macro Letters, 2023, 12, 1733–1738 [Morlet-Decarnin et al., 2023].

For these measurements, we use a stress-controlled rheometer (ARG2, TA Instruments), equipped with a smooth cylindrical Taylor-Couette geometry of height 58 mm, inner rotating cylinder of

radius 24 mm, outer fixed cylinder of radius 25 mm, and gap e = 1 mm. In order to prevent evaporation, the cell is closed by a home-made lid, and the temperature is controlled to $T = 23.0 \pm 0.1$ °C, thanks to a water circulation around the cell. The rheological protocol is similar to the one used for the previous section, described in Sec. 3.A.1, except for the recovery step, corresponding to step (2):

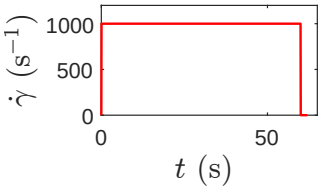

(1) As in the previous protocol, after being loaded in the rheometer cell, the sample is fully fluidized by applying a strong shear $\dot{\gamma} = 1000$ s^{-1} during 60 s, ensuring a reproducible initial state.

(2) The shear is stopped at $t = 0$, which defines the origin of time. We further measure the time evolution of the viscoelastic properties of the sample at different frequencies using time-resolved mechanical spectroscopy [Mours and Winter, 1994]. As described in Sec. 2.A.2, in order to obtain a high enough time resolution, we apply a multiwave signal that allows us to measure the viscoelastic properties of our sample at five frequencies simultaneously, every few seconds, over a duration of 5000 to 50000 s. This multiwave signal is a small amplitude periodic strain or torque signal, which results from the sum of five sinusoidal signals of different frequencies, as illustrated in Fig. 3.13. A Fourier transform of the resulting stress signal, directly performed by the software controlling the rheometer, allows us to obtain a measurement of the elastic modulus G', the viscous modulus G'' and the loss factor $\tan\delta$ at five different frequencies simultaneously, every interval time δt_{exp}. The data are averaged over two periods of the strain signal. We use two variations of this recovery step depending on the CNC weight fraction in the sample. (1) For "weak" suspensions containing less than 3.2 wt % CNC, the torque was set to Γ = 5, 4, 3, 2, 1 μN.m for frequencies f = 0.3, 0.6, 0.9, 1.2, 1.5 Hz respectively, corresponding to angular frequencies $\omega = 2\pi f$ = 1.88, 3.77, 5.65, 7.54, 9.42 rad.s^{-1}, leading to δt_{exp} = 5 s. The decrease of the torque amplitude with the frequency ensures that the maximum strain amplitude resulting from the whole multiwave signal remains smaller than γ_{NL}, the onset of the non-linear deformation regime. (2) For "stronger" suspensions containing 3.2 wt % CNC or more, the strain $\gamma \in [0.2; 2]$ % was imposed and kept constant for frequencies f = 0.3, 0.6, 1.2, 3, 6 Hz, corresponding to angular frequencies $\omega = 2\pi f$ = 1.88, 3.77, 7.54, 18.85, 37.70 rad.s^{-1}, leading to δt_{exp} = 8 s. The strain amplitude γ was adjusted for each suspension in order to stay in the linear deformation regime ($\gamma \ll \gamma_{NL}$). In both cases, the set of frequencies were chosen to ensure (i) that the sample properties do not evolve significantly over the measurement time-scale, i.e., its mutation number N_{mu} remains small: $N_{\text{mu}} = (\delta t_{\text{exp}}/G')\,(\partial G'/\partial t) \ll 1$ [Winter et al., 1988, Mours and Winter, 1994], and (ii) that there is no effect of inertia neither from the rheometer geometry, nor from the sample, impacting our data at large frequencies. The equivalence between the two protocols was checked on a suspension containing 3.2 wt % CNC and 12 mM of NaCl where both methods gave the same results (see Fig. 3.14)

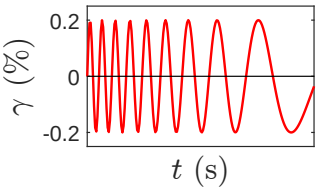

(3) Following this recovery period, we measure a complete viscoelastic spectrum G' and G'' versus ω by imposing an oscillatory strain of amplitude $\gamma \ll \gamma_{NL}$ and of angular frequency ω decreasing from 20 to 0.1 rad.s^{-1} with 10 points per decade. Each frequency is applied for six periods, and the recorded data are averaged over the last five periods.

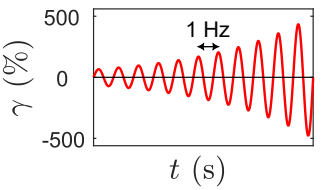

(4) Finally, like in the previous protocol, we estimate the onset of the non-linear regime of deformation γ_{NL} by imposing an oscillatory strain of frequency 1 Hz and of amplitude ramping up logarithmically from 0.01 to 1000 %. Each strain amplitude is applied for 6 s, and the recorded data are averaged over the last 3 s.

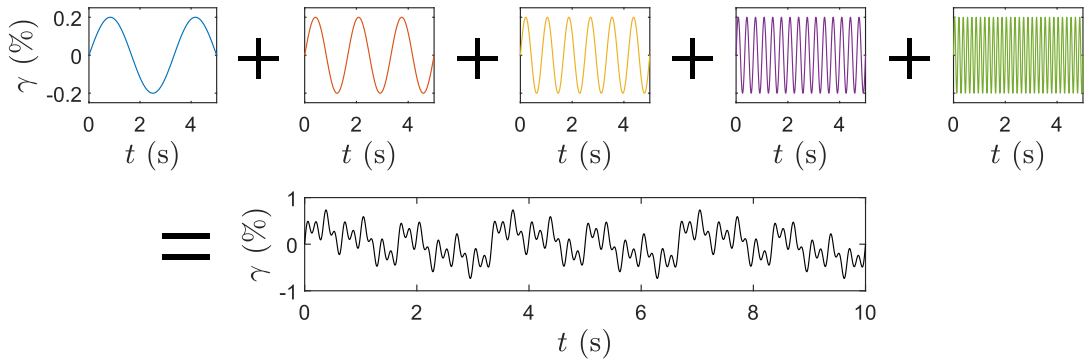

Figure 3.13: Construction of a multiwave signal, in the case where a strain of amplitude $\gamma = 0.2$ % is applied for the five angular frequencies $\omega = 1.88,\ 3.77,\ 7.54,\ 18.85,\ 37.70$ rad.s^{-1}. The first line shows the five individual strain signals of various angular frequencies, and the second line shows the resulting multiwave periodic strain signal, made of the sum of the five above signals.

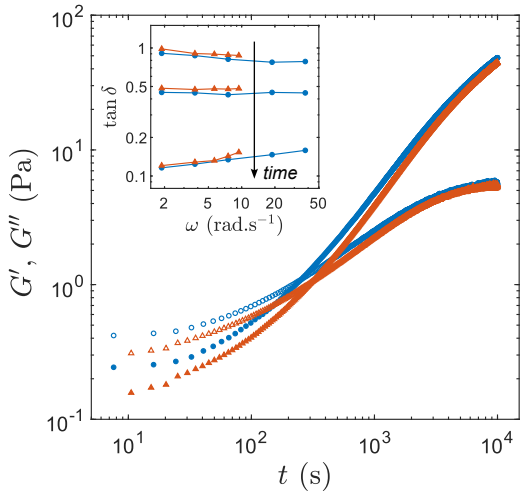

Figure 3.14: Comparison of the two recovery measurements used for step (2) of the rheological protocol described above: by imposing the torque (orange ▲) or by imposing the strain (blue •). Experiments performed on a suspension containing 3.2 wt % CNC and 12 mM NaCl. time evolution of the elastic modulus G' and of the viscous modulus G'' measured at $\omega = 1.88$ rad.s^{-1} following shear cessation. Inset: Viscoelastic spectra for the loss factor $\tan\delta$ versus frequency ω, extracted from both measurements at time $t = 330$ s, 1330 s and 10000 s following shear cessation.

B.2 Time-connectivity superposition

a Determination of the gelation time

As recalled above, the gelation time t_g is defined as the time when both the elastic modulus G' and the viscous modulus G'' have the same power-law dependence with frequency: $G' \sim G'' \sim \omega^{\beta}$. In practice, as previously done in Sec. 3.A.3 for the elastic spectra, both $G'(\omega, t)$ and $G''(\omega, t)$ spectra are fitted, for each measurement time, by two distinct power-laws, yielding two exponents, β' and β'' respectively [see Fig. 3.15(a)]. The time series $\beta'(t)$ and $\beta''(t)$ are then smoothed using a moving average over ten successive points in time, and plotted as a function of time in Fig. 3.15(b) for a sample containing 3.2 wt % CNC and 12 mM NaCl. The time at which both exponents become equal defines the gelation time t_g, and the corresponding exponent $\beta = \beta' = \beta''$ is defined as the "critical exponent". In this example, $t_g = 1330 \pm 20$ s and $\beta = 0.25 \pm 0.015$. This first estimation of t_g is then verified by plotting the loss factor $\tan\delta$ as a function of time for each frequency, as shown in Fig. 3.15(c). The time at which the five curves, corresponding to the five measurement frequencies, cross-over is the gelation time: $\tan\delta \sim \omega^0$.

Now that we have precisely identified the gelation time, let us investigate how the viscoelastic spectra of CNC suspensions evolve through time. Figures 3.16(a) and (d) show the time evolu-

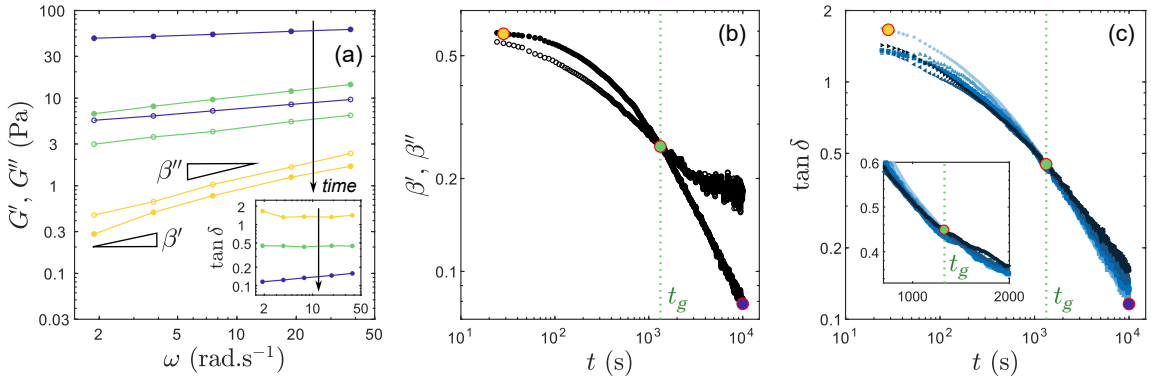

Figure 3.15: (a) Dependence of the elastic modulus G' (•) and the viscous modulus G'' (◦) on the frequency ω at different points in time (t =28 s, 1330 s and 10000 s, from yellow to dark blue) across the sol-gel transition. The corresponding times are highlighted with a red circle in (b) and (c). Inset: Dependence of the loss factor $\tan\delta$ on the frequency ω at the same points in time. (b) Temporal evolution of the exponents β' (•) and β'' (◦) from the power-law fit of the viscoelastic spectra $G'(\omega,t)$ and $G''(\omega,t)$ respectively. The raw data are smoothed using a moving average over ten successive points in time. (c) Temporal evolution of the loss factor at the five frequencies used in the multiwave signal: ω = 1.88 rad.s^{-1} (•), 3.77 rad.s^{-1} (▲), 7.54 rad.s^{-1} (■), 18.85 rad.s^{-1} (◂) and 37.70 rad.s^{-1} (▸). Data extracted from time-resolved spectroscopy measurements during the recovery of a sample containing 3.2 wt % CNC and 12 mM NaCl. The green vertical dashed lines in (b) and (c) highlight the gelation time t_g = 1330 ± 20 s.

tion of the viscoelastic properties of a sample containing 3.2 wt % CNC and 12 mM NaCl, at five different frequencies, from 8 s (yellow curves) to 10000 s (dark blue curves) after shear cessation. At a given frequency, we observe that both the elastic and the viscous moduli increase with time [see Fig. 3.16(d)]. Yet, the elastic modulus increases faster than the viscous modulus, inducing the loss factor $\tan\delta$ to decrease with time at a given frequency. Both the elastic and the viscous moduli increase as a power-law of the frequency at every point in time, yet with different exponents, except at the gel point when $G'(\omega)$ and $G''(\omega)$ become parallel in a logarithmic representation. Consequently, the loss factor also evolves as a power-law of the frequency, but it shows two opposite trends on each side of the gel point: $\tan\delta(\omega)$ decreases with ω for $t < t_g$ due to $\beta' > \beta''$, with an exponent $\beta'' - \beta'$ that decreases with time, while $\tan\delta(\omega)$ increases with ω for $t > t_g$, due to $\beta'' > \beta'$, with an exponent $\beta'' - \beta'$ that increases with time. At the gel point, $\beta' = \beta''$ and the loss factor becomes independent of the frequency, as highlighted by the horizontal gray dashed line at $\tan\delta$ = 0.44 in Fig. 3.16(a): this is characteristic of a critical gel, and the corresponding time t_g = 1330 s is the gelation time. In Sec. 3.A, we have shown that CNC suspensions undergo a liquid to solid transition at time t_c. The data in Fig. 3.16 additionally demonstrate that this CNC suspension undergoes a sol-gel transition at time t_g when recovering from a strong shear.

Remarkably, it appears very clearly that this sol-gel transition occurs much later than the liquid to solid transition, as reflected by the evolution of $\tan\delta$ with time. Indeed, at short time, 8 s after the cessation of shear, the viscous modulus is larger than the elastic modulus over the range of frequencies considered here [see the lowest yellow spectra in Fig. 3.16(d)], and the loss factor is greater than one for all frequencies [see the top yellow spectrum in Fig. 3.16(a)]: the sample is therefore in a liquid-like state. At longer times, here for $t \geq t_c \approx 210$ s depending on the frequency at which it is probed, the elastic modulus becomes larger than the viscous modulus and the loss factor becomes smaller than one over the whole range of measurement frequencies: the sample is therefore now in a solid-like state. This decoupling between the gelation time t_g and the G'-G'' crossover time t_c, over the range of frequencies considered here, appears as a distinctive feature of

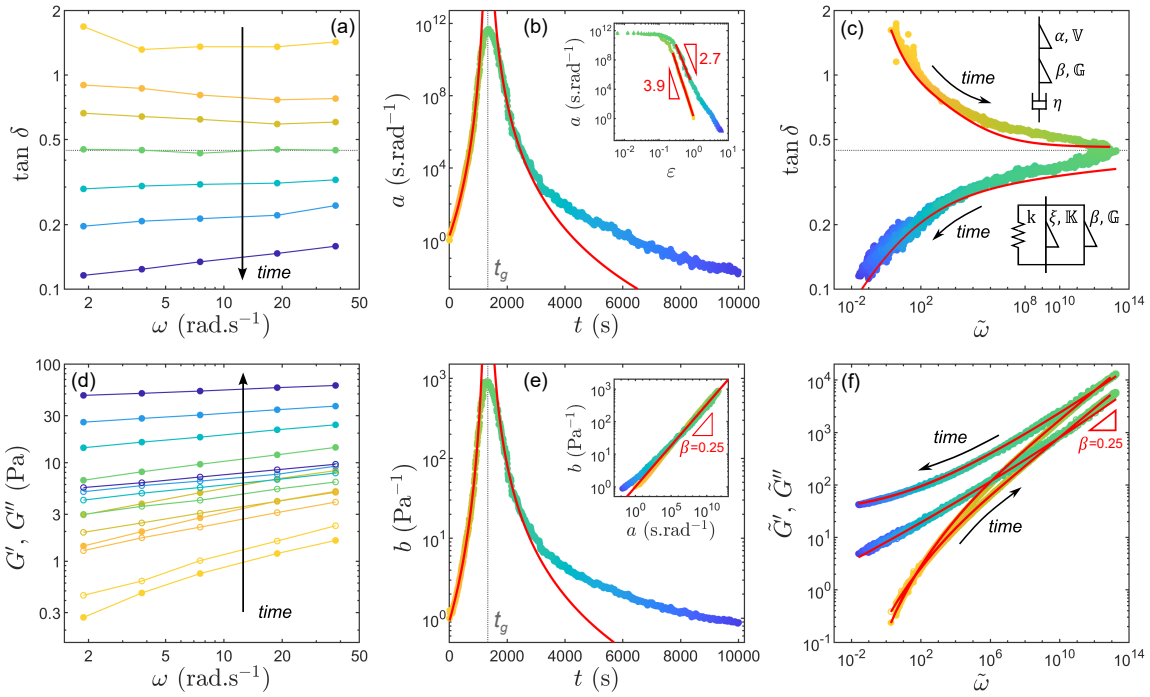

Figure 3.16: Time-resolved mechanical spectroscopy of the sol-gel transition in a 3.2 wt % CNC suspension containing 12 mM of NaCl. (a) Dependence of the loss factor $\tan\delta$ on the frequency ω at different points in time (t =8 to 10000 s, from yellow to dark blue) across the sol-gel transition. The gel point is highlighted by the horizontal dashed line. (b) Time dependence of the horizontal shift factor a. The initial value is arbitrarily taken as $a(0) = 1$ s.rad^{-1}. The vertical dashed line highlights the gelation time $t_g = 1330$ s. The red curves show the best power-law fits of the data near the gel point, $a \sim \varepsilon^{-y}$, with $\varepsilon = |t - t_g|/t_g$, with exponents $y_l = 14.4$ for $t < t_g$ and $y_g = 11.6$ for $t > t_g$. (c) Master curve for the loss factor $\tan\delta$ vs reduced frequency $\tilde{\omega} = a(t)\omega$. The horizontal dashed line highlights the gel point. The red curves show the best fits of the data respectively by a fractional Maxwell model for $t < t_g$ (upper curve) and by a fractional Kelvin-Voigt model for $t > t_g$ (lower curve). (d) Dependence of the elastic modulus G' (•) and the viscous modulus G'' (◦) on the frequency ω at different points in time (t =8 s to 10000 s, from yellow to dark blue) across the sol-gel transition. (e) Time dependence of the vertical shift factor b. The initial value is arbitrarily taken as $b(0) = 1$ Pa^{-1}. The vertical dashed line highlights the gelation time $t_g = 1330$ s. The red curves show the best power-law fits of the data near the gel point, $b \sim \varepsilon^{-z}$, with exponents $z_l = 3.9$ for $t < t_g$ and $z_g = 2.7$ for $t > t_g$. Inset: The vertical shift factor $b(t)$ as a function of the horizontal shift factor $a(t)$. The red curve shows a power-law of exponent $\beta = 0.25$: $y = x^{\beta}$. (f) Master curve for the rescaled elastic modulus $\tilde{G}'$ and viscous modulus $\tilde{G}''$ vs reduced frequency $\tilde{\omega} = a(t)\omega$. The red curves show the best fits of the data respectively by a fractional Maxwell model for $t < t_g$ (lower curve) and by a fractional Kelvin-Voigt model for $t > t_g$ (upper curve).

the recovery dynamics of CNC suspensions compared to other colloidal systems where t_c (1 Hz) $\approx t_g$ [Keshavarz et al., 2021, Suman and Joshi, 2020].[3]

[3]This result explains the observation made in Sec. 3.A.2 that $\beta' = \beta''$ at $t_w \approx t_g \approx 10t_c$.

b Evidence for a time-connectivity superposition principle

The continuous evolution of the exponent for $\tan\delta$ vs ω from negative to positive [see Fig. 3.16(a)] prompts us to shift each spectrum along the horizontal axis, towards large frequencies for $t < t_g$, and towards small frequencies for $t > t_g$, in order to collapse the $\tan\delta(\omega)$ spectrum measured at different times onto a single master curve. The time-dependent shift factor $a(t)$ used to realize this frequency shift $\tilde{\omega} = a(t)\omega$ is plotted in Fig. 3.16(b), and the resulting master curve is plotted in Fig. 3.16(c). Considering the viscoelastic spectra, we first shift $G'(\omega)$ and $G''(\omega)$ horizontally by applying the same time-dependent multiplicative factor $a(t)$ as for $\tan\delta$ to the frequency ω: $\tilde{\omega} = a(t)\omega$. Then, we vertically shift each spectrum, towards large moduli for $t < t_g$ and towards small moduli for $t > t_g$, by applying the same time-dependent multiplicative factor $b(t)$ to both moduli: $\tilde{G}' = b(t)G'$ and $\tilde{G}'' = b(t)G''$. This time-dependent multiplicative factor $b(t)$ is plotted in Fig. 3.16(e), and the two resulting master curves obtained for the viscoelastic moduli are plotted in Fig. 3.16(f).

In practice, the shift factors $a(t)$ and $b(t)$ are determined using an open-source code provided by Lennon *et al.* [Lennon et al., 2023]. This code determines the best set of parameters to horizontally or vertically shift the input data onto a single master curve, taking as a reference the first spectrum measured after the cessation of shear, at time $t = 8.0$ s. This is achieved by describing the data by statistical models determined using a Gaussian process regression, and then superimposing the resulting descriptions by maximizing their overlap. After using this code to determine $a(t)$ by horizontally shifting the loss factor spectra $\tan\delta(\omega)$, we apply it to vertically shift independently both the viscoelastic spectra rescaled in frequency $G'(\tilde{\omega})$ and $G''(\tilde{\omega})$, with $\tilde{\omega} = a(t)\omega$. As expected, the resulting time-dependent shift factors $b'(t)$ and $b''(t)$ (corresponding to G' and G'' measurements, respectively) are very similar. Therefore, we construct a single time-dependent vertical shift factor $b(t)$ by considering the mean value of both b' and b'' shift factors at each point in time.

Interestingly, both time-dependent multiplicative factors $a(t)$ and $b(t)$ diverge as power-laws of the time to gelation close to the gel point:

$$\begin{cases} a(t) \sim \varepsilon^{y_i} & (3.13) \\ b(t) \sim \varepsilon^{z_i} & (3.14) \end{cases}$$

with $\varepsilon = |t - t_g|/t_g$, and with exponents $y_l = 14.4 \pm 0.8$ and $z_l = 3.9 \pm 0.2$ respectively for $t < t_g$, and exponents $y_g = 11.6 \pm 0.7$ and $z_g = 2.7 \pm 0.15$ respectively for $t > t_g$ [see red curves in Figs. 3.16(b) and (e)][4]. Such a critical-like behavior has been observed for the gelation dynamics of other colloidal systems such as aluminosilicate spherical particles [Keshavarz et al., 2021], Laponite disks [Suman and Joshi, 2020] and polyamide rods [He et al., 2021], reflecting the critical behavior of the liquid-to-solid phase transition [Winter and Mours, 1997]. However, it is important to notice that, in our system, this divergence is not symmetrical with respect to the gel point, unlike what has been assumed and observed in other polymer and colloidal systems [Adolf and Martin, 1990, Suman and Joshi, 2020, Larsen and Furst, 2008, Scanlan and Winter, 1991, He et al., 2021]. In other words, the exponents characterizing the power-law divergence of $a(t)$ and $b(t)$ at t_g, respectively noted y_i and z_i, where $i = l$ for $t < t_g$ and $i = g$ for $t > t_g$, differ on each side of t_g, i.e., $y_l \neq y_g$ and $z_l \neq z_g$.

The resulting master curves, presented in Figs. 3.16(c) and (f), are composed of more than 1600 spectra and span over 5 orders of magnitude in rescaled viscoelastic moduli, and over 16 orders of magnitude in rescaled dimensionless frequency on both sides of the gel point, describing the entire gelation process. The fact that CNC suspensions allow us to resolve both the pre-gel and the post-gel dynamics, at least for a range of CNC weight fractions and salt concentrations, is quite remarkable as time-resolved mechanical spectroscopy on other colloidal systems usually

[4]The subscripts l and g respectively stand for "liquid" (for $t < t_g$, i.e., the pre-gel state) and "gel" (for $t > t_g$, i.e., the post-gel state)

gives access to the determination of the gel point and to the subsequent aging dynamics only, gelation being too fast to be able to resolve its dynamics before the gel point [Keshavarz et al., 2021, Chen et al., 2010]. To our knowledge, only three other studies on colloidal gels have reported pre-gel measurements, two on Laponite suspensions [Suman and Joshi, 2020, Rich et al., 2011] and one on monodisperse polyamide rods [He et al., 2021].

The possibility to construct such master curves on both sides of the gel point points to the existence of a time-connectivity superposition principle in CNC suspensions, which remains valid both before and after the gel point. Such a principle has been previously established in polymers [Adolf and Martin, 1990, Suman and Joshi, 2020, Larsen and Furst, 2008, Martin et al., 1990, Hong et al., 2018] and colloidal gels [Keshavarz et al., 2021, Suman and Joshi, 2020, Chen et al., 2010, He et al., 2021, Bantawa et al., 2023], and suggests that CNC particles organize in a self-similar way on each side of the gel point.

c Fractional models for capturing the broad relaxation dynamics

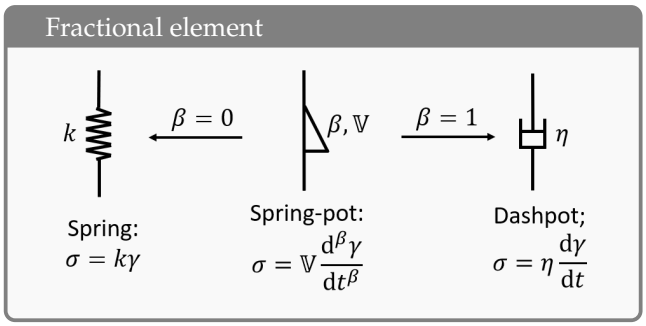

The very broad relaxation dynamics illustrated in Figs. 3.16(c) and (f) reflect a very wide range of time-scales in a CNC gel recovery, indicating a wide range of distinct relaxation processes in the sample microstructure. Such a broad relaxation spectrum is often compactly described by fractional models [Bonfanti et al., 2020, Keshavarz et al., 2021, Geri et al., 2018, Bouzid et al., 2018], which introduce "spring-pots" as key rheological elements.

A spring-pot is defined by a constitutive equation that relates the stress σ and the strain γ through a fractional derivative [Blair and Coppen, 1943, Jaishankar and McKinley, 2013]:

$$\sigma = \mathbb{G}\frac{d^{\beta}\gamma}{dt^{\beta}} \tag{3.15}$$

where $\mathbb{G}$ is a "quasi-property" with dimension Pa.s$^{\beta}$, and $\beta \in [0,1]$ is the order of the derivative. In the limit $\beta \to 0$ (resp. $\beta \to 1$), the spring-pot corresponds to a purely elastic (resp. viscous) response. For $0 < \beta < 1$, it displays a power-law viscoelastic spectrum $G' \sim G'' \sim \omega^{\beta}$, or equivalently a power-law relaxation modulus $G(t) \sim t^{-\beta}$, and a frequency-independent phase angle $\delta = \beta\pi/2$. Such power-law rheology is common to all "critical gels" that form self-similar percolated networks at the gel point [Winter and Chambon, 1986, Zaccone et al., 2014], and for which the exponent β is referred to as the *critical relaxation exponent* [Winter, 1987, Suman and Joshi, 2020]. Therefore, the fractional approach is ideally suited to characterize the mechanical response of colloidal gels, from their critical gel point and beyond [Geri et al., 2018, Bouzid et al., 2018, Keshavarz et al., 2021, Aime et al., 2018].

Here, we fit the master curves on each side of the gel point by two five-parameter fractional models, respectively a fractional Maxwell model for $t < t_g$, which captures the liquid-like viscoelasticity of the CNC suspension prior to the gel point, and a fractional Kelvin-Voigt model for $t > t_g$, which captures the solid-like viscoelastic behavior past the gel point [see, respectively, lower and upper sketches in Fig. 3.16(c)]. See Sec. 3.C in Appendix for a detailed mathematical interpretation of those models. A crucial result is that both models share a common spring-pot element $(\mathbb{G}, \beta)$, which is alone responsible for capturing the gel point, here with a critical relaxation exponent $\beta = 0.25$ that corresponds to a value of $\tan(\beta\pi/2) = 0.41$, which is fully consistent with the value of $\tan\delta$ observed at the gel point in Fig. 3.16(a). In practice, the value of the critical

exponent β is determined by fitting the viscoelastic moduli spectra at the gelation time t_g by a power-law of the frequency, using the definition of a gel point [Mours and Winter, 1994] given in Eq. (3.11): $G'(\omega, t_g) \sim G''(\omega, t_g) \sim \omega^{\beta}$. The value of this critical exponent β being set, only 4 free parameters are left for each model, with the constraints that (i) $\mathcal{G}$ must keep the same value in both models, and (ii) both models must correctly capture the recovery dynamics illustrated by the loss factor and by both viscoelastic moduli master curves, with a single set of parameters. The set of parameters determined for the sample containing 3.2 wt % CNC and 12 mM NaCl is reported in Table 3.3. The fits by the two models are shown with red lines in Fig. 3.16(f) for the rescaled viscoelastic moduli, and in Fig. 3.16(c) for the corresponding loss factor. The agreement between theory and experiment is excellent, which provides strong support for interpreting the gelation dynamics in terms of two consecutive fractional mechanical behaviors separated by a critical gel point.

B.3 Influence of the CNC weight fraction on the recovery dynamics

In order to refine our understanding of the impact of a change in the CNC weight fraction of a suspension on its recovery dynamics, we have performed the same time-resolved mechanical spectroscopy experiments, to which we have applied the same data processing as described above in Sec. 3.B.2, for suspensions containing between 0.75 wt % and 5.5 wt % of CNC. To be able to compare the different samples, we have chosen to adjust the NaCl concentration so that the gelation time t_g is always of the same order of magnitude, long enough to be able to resolve the recovery dynamics both before and after the gel point while avoiding evaporation and drying effects. Table 3.3 gathers the characteristics of the various suspensions that we have used, together with their composition and the corresponding gelation time, which ranges from 1150 s to 3330 s with a median of 1370 s, an average of 1700 s and a standard deviation of 675 s.

a Robustness of the time-connectivity superposition principle

Figure 3.17 shows the results obtained for four samples containing different CNC weight fractions: 1 wt %, 2.6 wt %, 4 wt %, and 5.5 wt % CNC. First, we note that, whatever the CNC weight fraction, we can always construct master curves for the time evolution of the loss factor and for both viscoelastic moduli. These master curves are similar to the ones presented in Fig. 3.16 for a gel containing 3.2 wt % CNC. This observation reveals that the time-connectivity superposition principle remains valid over the range of CNC weight fractions explored here. Moreover, for every CNC weight fraction, the gel point is always well defined: the loss factor plateaus [see gray dashed lines in Fig. 3.17(a)-(c)] and the rescaled viscoelastic moduli become parallel.

Second, we observe that the scaling factors a and b have the same time-dependence with a non-symmetrical power-law divergence at the gel point (see insets in Fig. 3.17). However, the critical exponents depend on the CNC content. For each CNC weight fraction, we have fitted the master curves by the two fractional models presented in the previous section: a Maxwell fractional model for $t < t_g$ and a Kelvin-Voigt fractional model for $t > t_g$, with the critical exponent β, common to both models, being extracted from the power-law frequency-dependence of the viscoelastic moduli at the gel point. Both models capture remarkably well the recovery dynamics of CNC gels over the whole range of CNC weight fractions explored here (see red curves in Fig. 3.17). However, it is important to note that the constraint of imposing the prefactor $\mathcal{G}$, associated to the exponent β, to keep the same value in both models, on both sides of the gel point, has to be relaxed for CNC weight fractions above 3.2 wt %. This suggests that the gel properties undergo a change of regime for $w_{CNC} \gtrsim 3.2$ wt %, as will be confirmed below in Sec. 3.B.3.c. It is also worth noting that the value of the critical exponent β varies with the CNC content. The full set of parameters corresponding to both models used to fit the various master curves are reported in Table 3.3.

In the following, we extract several observables of interest from the above time-resolved mechanical spectroscopy measurements, in order to characterize in more details how the recovery

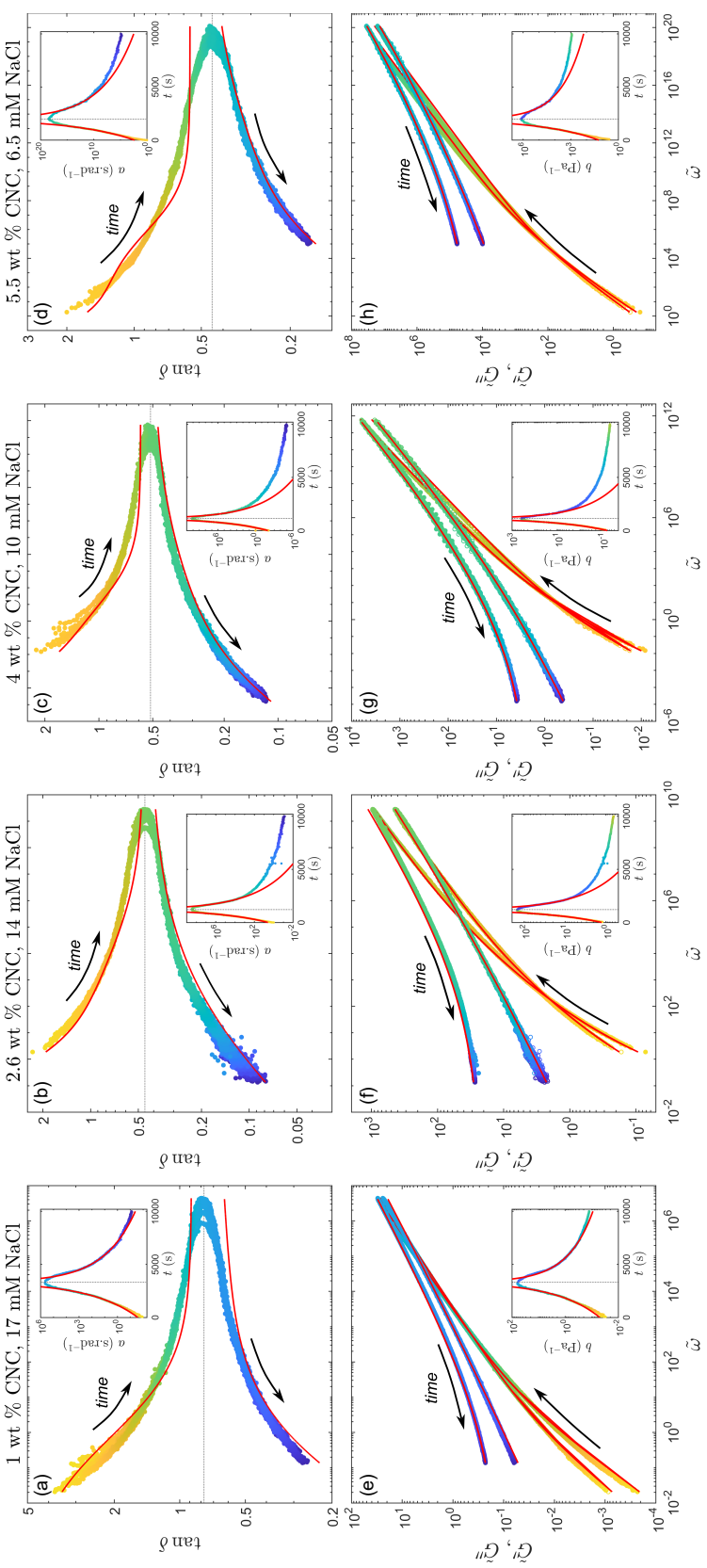

Figure 3.17: Time-resolved mechanical spectroscopy of the sol-gel transition in samples containing various CNC and salt concentrations: 1 wt % CNC and 17 mM NaCl, 2.6 wt % CNC and 14 mM NaCl, 4 wt % CNC and 10 mM NaCl, and 5.5 wt % CNC and 6.5 mM NaCl from left to right. The sample composition was tuned so that the gelation time t_g remains similar for all samples, with a median value of 1370 s (see Table 3.3). (a),(b),(c),(d) Master curves for the loss factor $\tan\delta$ vs reduced frequency $\tilde{\omega} = a(t)\omega$. The horizontal dashed line highlights the gel points. The red curves show the best fits of the data respectively by a fractional Maxwell model for $t < t_g$ (upper curve) and by a fractional Kelvin-Voigt model for $t > t_g$ (lower curve). Insets: Time dependence of the horizontal shift factors a. The initial value is arbitrarily taken as $a(0) = 1$ s.rad^{-1}. The vertical dashed line highlights the gelation time t_g. The red curves show the best power-law fits of the data near the gel point, $a \sim \varepsilon^{-y}$, with $\varepsilon = |t - t_g|/t_g$, and with exponents y_l for $t < t_g$ and y_g for $t > t_g$. (e),(f),(g),(h) Master curves for the rescaled elastic modulus $\tilde{G}'$ (•) and viscous modulus $\tilde{G}''$ (○) vs reduced frequency $\tilde{\omega} = a(t)\omega$. The red curves show the best fits of the data respectively by a fractional Maxwell model for $t < t_g$ (upper curve) and by a fractional Kelvin-Voigt model for $t > t_g$ (lower curve). Insets: Time dependence of the vertical shift factors b. The initial value is arbitrarily taken as $b(0) = 1$ Pa^{-1}. The vertical dashed line highlights the gelation time t_g. The red curves show the best power-law fits of the data near the gel point, $b \sim \varepsilon^{-z}$, with exponents z_l for $t < t_g$ and z_g for $t > t_g$.

Table 3.3: Parameters of the fractional Maxwell and Kelvin-Voigt models used to fit the viscoelastic moduli and $\tan\delta$ master curves obtained from the time evolution of the viscoelastic spectra during the recovery following a strong shear of aqueous suspensions containing various CNC weight fractions and various NaCl concentrations. The sample composition was tuned so that the gelation time t_g remains similar for all samples, with a median value of 1370 s. The constraint of imposing the prefactor $\mathbb{G}$, associated to the exponent β, to keep the same value in both models, on both sides of the gel point, has been relaxed for CNC weight fractions above 3.2 wt %. The bold text highlights the samples whose recovery dynamics are plotted in Fig. 3.17.

	t_g (s)	η	$\mathbb{V}$	α	$\mathbb{G}\,(t<t_g)$	$\mathbb{G}\,(t>t_g)$	β	$\mathbb{K}$	ξ	k
0.75 wt% CNC, 20 mM NaCl	1309.5	N.A.	N.A.	N.A.	N.A.		N.A.	N.A.	N.A.	N.A.
1 wt% CNC, 17 mM NaCl	3334.7	2.0	0.025	0.87	0.035		0.41	0.17	0.31	0.14
2 wt% CNC, 15 mM NaCl	1818.6	0.13	0.14	0.63	0.95		0.30	5.4	0.23	17
2.6 wt% CNC, 14 mM NaCl	1220.5	0.27	0.23	0.55	2.5		0.27	9.0	0.17	21
3.2 wt% CNC, 12 mM NaCl	1329.8	0.69	0.51	0.53	3.5		0.25	25.7	0.17	29.41
3.6 wt% CNC, 11 mM NaCl	1406.3	1.0	0.35	0.63	2.6	6.4	0.30	37.5	0.18	42.3
4 wt% CNC, 10 mM NaCl	1150.5	8.7	0.36	0.63	0.82	2.4	0.29	9.13	0.17	2.31
4.5 wt% CNC, 9 mM NaCl	1231.9	9.0	0.15	0.67	5.5	37.5	0.31	798	0.18	2318
5 wt% CNC, 7 mM NaCl	2104.2	10	0.15	0.65	6.1	160	0.29	9500	0.18	1.35×10^5
5.5 wt% CNC, 6.5 mM NaCl	2058.5	1.2	0.30	0.60	11	113	0.27	5422	0.16	2.51×10^4

dynamics of CNC gels depend on the CNC weight fraction.

b Comparison of the gelation time and the crossover time

We first consider the characteristic times of the recovery dynamics. Two distinct characteristic times in this system have been introduced so far: the gelation time t_g, which is independent of the frequency (see Sec. 3.B.2), and the G'-G'' crossover time t_c, which depends on the frequency (see Sec. 3.A.2). The ratio of those two characteristic times is plotted in Fig. 3.18(a) as a function of the CNC weight fraction, for the three frequencies that are common to both time-resolved spectroscopy protocols: ω = 1.88, 3.77, 7.54 rad.s^{-1}. Interestingly, for the suspension containing 0.75 wt % CNC, the gelation time t_g is slightly shorter than the crossover time t_c, while for concentrations equal or larger than 1 wt % CNC, the gelation time t_g is always longer than the crossover time t_c, at the three frequencies considered here. The point where $t_g = t_c$ corresponds to the transition from (i) a regime where CNC particles are not concentrated enough to overlap: $w_{CNC} < w^{ov}_{CNC}$ = 1 wt %, where w^{ov}_{CNC} is the overlap threshold roughly estimated by assimilating CNCs to equivalent spheres of diameter equal to their length, in the random close packing limit (see Sec. 3.C in Appendix for the detailed calculations) to (ii) a regime where they do overlap ($w_{CNC} \geq w^{ov}_{CNC}$ = 1 wt %). In the latter regime, CNCs cannot be assimilated to spherical particles anymore, as they may interact with each other on multiple points along a single CNC particle, therefore inducing some steric hindrance effects.

Moreover, the ratio t_g/t_c increases as the CNC weight fraction increases: the gelation time t_g gets as much as 8 times larger than the crossover time t_c in the range of frequencies used here. This is quite unusual as the crossover time is often taken to be the gelation time, and it has been shown that this assumption is valid for many different colloidal systems, constituted of both isotropic and anisotropic particles, such as weak aluminosilicate gels [Keshavarz et al., 2021], Laponite disk-like colloids [Suman and Joshi, 2020], and carbon nanotubes [Chen et al., 2010]. In Sec. 3.A, we have introduced another characteristic time which is the inflection time t^* when the time evolution of the elastic modulus G' presents an inflection point in logarithmic scales [see Fig. 3.4(b)]. The inset of Fig. 3.18(a) shows that this inflection time t^* actually coincides with the gelation time t_g, hereby giving a physical interpretation of this phenomenological characteristic time. Moreover, this result is quite remarkable as it proves that a simple "time-sweep" experiment, i.e., measuring the time evolution of the elastic modulus during the gel recovery by applying a small amplitude oscillatory strain at a single frequency, as often done to characterize a soft material, is enough to determine the gel point of a CNC suspension. Yet not from the crossover between $G'(t)$ and $G''(t)$ but rather from the mere shape of $G'(t)$.

c Viscoelastic parameters at the gel point

The values of the elastic and viscous moduli and of the loss factor at the gel point are plotted against the CNC weight fraction in Fig. 3.18(b). For the suspension containing 0.75 wt % CNC, the elastic modulus is smaller than the viscous modulus at the gel point, while suspensions with a larger CNC weight fraction show $G'(t_g) > G''(t_g)$. This is also highlighted by $\tan\delta(t_g) > 1$ for the smallest CNC content [see inset in Fig. 3.18(b)].

Both the elastic and the viscous moduli measured at the gel point increase as power-laws with w_{CNC}, with a change of exponent observed at $w_{CNC} \approx 3.4$ wt % [see red fits in Fig. 3.18(b)]. At small CNC weight fractions, for $w_{CNC} < 3.4$ wt %, the exponents for $G'(t_g)$ and $G''(t_g)$ versus w_{CNC} are different, as highlighted by the decrease of the loss factor measured at the gel point with w_{CNC} [see inset in Fig. 3.18(b)]. However, for $w_{CNC} > 3.4$ wt %, both exponents are similar, as highlighted by $\tan\delta(t_g)$ which remains roughly constant when varying w_{CNC}. As mentioned above, $\tan\delta(t_g) = G''(t_g)/G'(t_g)$ is much smaller than 1 for $w_{CNC} > 1$ wt %, which is consistent with $t_g/t_c > 1$: at the gel point, the elastic modulus is already much larger than the viscous modulus.

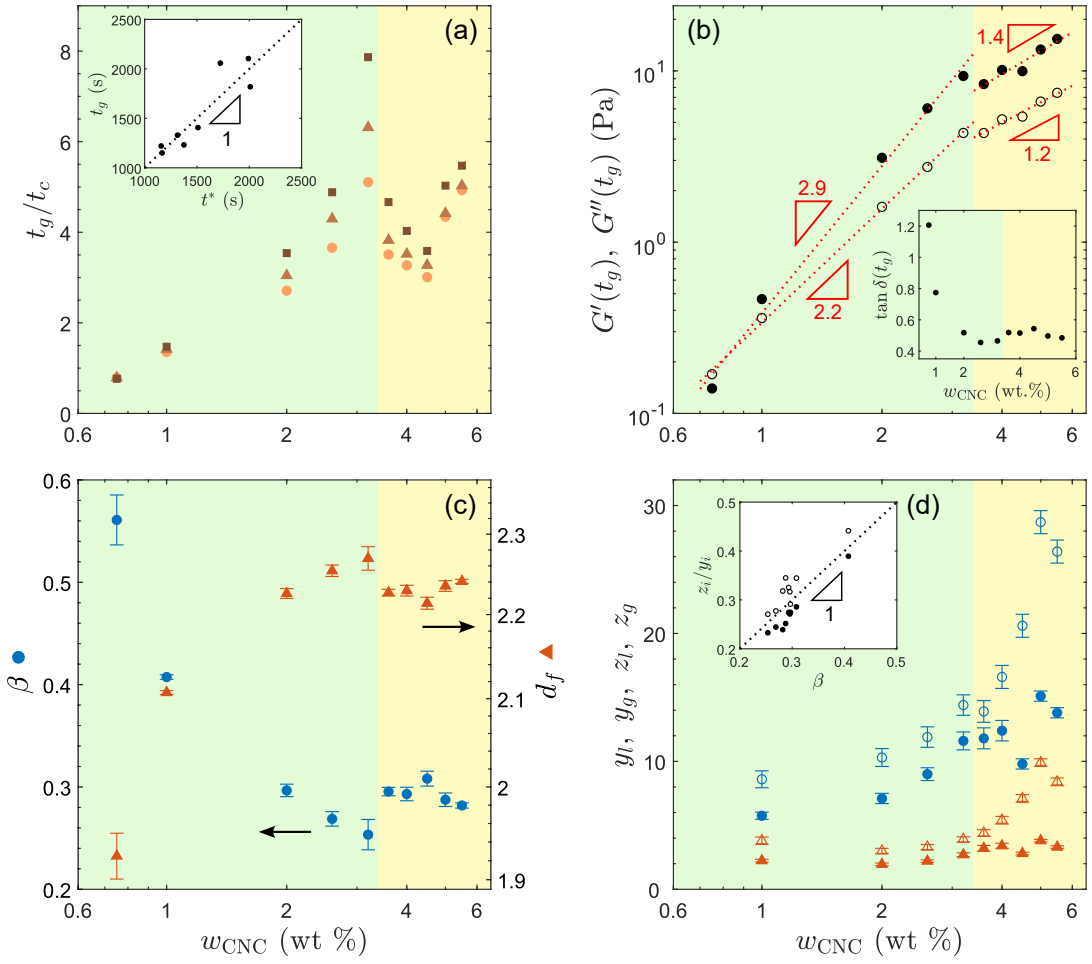

Figure 3.18: Gelation dynamics parameters of a series of suspensions containing various CNC weight fractions, and an NaCl concentration adjusted so that the gelation time t_g remains similar for all samples, with a median value of 1370 s (see Table 3.3). (a) Ratio of the gelation time t_g over the crossover time t_c measured at three different frequencies (1.88 rad.s^{-1} •, 3.77 rad.s^{-1} ▲, 7.54 rad.s^{-1} ■) versus CNC weight fraction w_{CNC}. Inset: Gelation time t_g determined through time-resolved mechanical spectroscopy as a function of the inflection time t^* introduced in Sec. 3.A.3. The dashed line denotes $t_g = t^*$. (b) Elastic modulus G' (•) and viscous modulus G'' (◦) at the gel point, measured at 7.54 rad.s^{-1}, as a function of w_{CNC}. The red dashed lines show the best fits of the data to power-laws of exponent 2.9 and 1.4 for $G'(t_g)$ and of exponent 2.2 and 1.2 for $G''(t_g)$, for $w_{CNC} < 3.4$ wt % and for $w_{CNC} > 3.4$ wt % respectively. Inset: Loss factor $\tan\delta$ at the gel point, measured at 7.54 rad.s^{-1} as a function of w_{CNC}. (c) Critical exponent β (•) at the gel point, and the corresponding fractal dimension d_f (▲), as a function of w_{CNC}. (d) Power-law exponents for the time evolution of the horizontal shift factor a and the vertical shift factor b, before the gel point, y_l (◦) and z_l (△) respectively, and after the gel point, y_g (•) and z_g (▲) respectively, as a function of w_{CNC}. Inset: Ratio z_i/y_i of the power-law exponent of the vertical shift factor b to that of the horizontal shift factor a both before the gel point, $i = l$ (◦), and after the gel point, $i = g$ (•), as a function of the critical exponent β at the gel point. The dashed line denotes $z_l/y_l = z_g/y_g = \beta$. The two regions in the four graphs delineate two different regimes depending on the CNC weight fraction: the green region corresponds to a gel phase and the orange one to an attractive glass phase.

This observation has already been made in polymeric gels [Winter et al., 1988], as discussed later in Sec. 3.B.5, but to our knowledge, it is the first time that it is reported in colloidal gels.

Muthukumar relationship

$$d_f = \frac{5}{2}\frac{(3-2\beta)}{(3-\beta)}$$

At the gel point, the loss factor $\tan\delta$ is independent of the frequency. This means that the viscoelastic properties of the suspension at this particular point in time are the same for all length-scales associated to the range of frequencies explored here. This self-similarity suggests that at the gel point, CNC particles are organized into a fractal network.

The fractal dimension d_f characterizing this fractal network can be linked to the exponent β of the power-law behavior of $G'(\omega)$ and $G''(\omega)$ at the gel point. Indeed, d_f can be calculated using the relationship proposed by Muthukumar in Ref. [Muthukumar, 1989] for polymers, in the limit of fully screened hydrodynamic and excluded-volume interactions in three dimensions, introduced previously in Sec. 1.C.1.b in the Introduction and in Sec. 3.A.6.d (see the gray box for a reminder of the relationship). Over the range of CNC weight fractions explored here, we obtain values for the critical exponent β decreasing from 0.56 to 0.25 with w_{CNC}, leading to a fractal dimension of the CNC network at the gel point that increases from 1.92 to 2.27 [see Fig. 3.18(c)]. Those values of d_f are consistent with the ones extracted from SANS and SAXS measurements and from TEM image analysis for suspensions at small CNC weight fraction (up to 1.5 wt %) [Moud et al., 2019, Moud et al., 2020, Phan-Xuan et al., 2016, Cherhal et al., 2015]. Nevertheless, to the best of our knowledge, no measurement of the fractal dimension of suspensions at larger CNC weight fraction has been reported yet.

d Critical exponents for the shift factors $a(t)$ and $b(t)$

Finally, for each CNC content, we extract the power-law exponents y_i and z_i from the divergence of the time-dependent shift factors a and b respectively, on both sides of the gel point $i = l$ for $t < t_g$ and $i = g$ for $t > t_g$ [see Fig. 3.18(d)]. Surprisingly, contrary to what has been reported in the literature, the divergence of the shift factors is always non-symmetrical with respect to the gel point, confirming the observation made previously in Sec. 3.B.2 on a sample containing 3.2 wt % CNC and 12 mM NaCl. Indeed, we note that, for all CNC suspensions, the exponents characterizing the divergence of both shift factors from the pre-gel state ($i = l$) are larger than the exponents characterizing the divergence of both shift factors from the post-gel state ($i = g$), over the whole range of CNC weight fractions explored.

Moreover, the exponents y_i for the divergence of the frequency shift factor a around the gel point are always larger than the exponents z_i characterizing the divergence of the viscoelastic moduli shift factor b around the gel point, which is similar to what has been reported for the gelation dynamics of other colloidal systems [Suman and Joshi, 2020, He et al., 2021], and consistent with the fact that $z_i/y_i = \beta$ with $\beta < 1$ as highlighted later in Sec. 3.B.3.f.

Finally, in our case, we find exponents that are quite large compared to the literature. Here, y_i vary between 5.7 and 28.7, compared to up to 6.24 in the literature. Moreover, our values of z_i range from 1.9 to 9.9, compared to up to 4.78 in the literature.

e Rheological evidence from a transition from a gel to an attractive glass

Interestingly, in all four graphs in Fig. 3.18, we can distinguish the same cutoff at $w_{CNC} \approx 3.4$ wt % CNC, separating two regimes for the dependence of the gelation dynamics parameters with the CNC weight fraction. The effect of the CNC weight fraction on the internal structure of a CNC suspension has already been studied. In particular, a generalized two dimensions phase diagram for CNC suspensions in the presence of NaCl has been established, which is supposed to remain valid whatever the CNC source [see Fig. 1.31 in Sec. 1.D.3 in the Introduction] [Xu et al., 2020].

Relying on this phase diagram, our suspensions are expected to show a transition from a gel to an attractive glass when the CNC weight fraction is increased and the NaCl concentration is slightly decreased to keep a gelation time about constant. Therefore, we hypothesize that the cutoff that we observe at $w_{CNC} \approx 3.4$ wt % CNC corresponds to the boundary in the w_{CNC} versus [NaCl] phase diagram between the gel phase at small CNC weight fraction, here for $w_{CNC} \lesssim 3.4$ wt % CNC, and the attractive glass phase at large CNC weight fraction, here for $w_{CNC} \gtrsim 3.4$ wt % CNC. Nevertheless, interestingly, independently on the type of phase, the suspension always goes through a critical gel point during its recovery dynamics.

The change of regime in the evolution of the critical gelation dynamics parameters with w_{CNC} between the gel and the attractive glass phase evidenced in Fig. 3.18 can be interpreted as follows. On the one hand, the more CNCs in the suspension, the more steric hindrance, leading to a significant decrease of the particles rotational diffusion, and therefore a more pronounced influence of the particles anisotropy. As a consequence, the ratio t_g/t_c increases with the CNC content. Indeed, increasing the amount of particles leads to faster aggregation (t_c decreases) as the distance between particles decreases. However, it also becomes more difficult for CNC particles to rotate and thus to percolate, leading to a slower decrease of t_g when compared to the decrease of t_c. Moreover, when increasing the CNC weight fraction, more matter is contained in a fixed solvent volume, inducing the formation of denser clusters, which is consistent both with the increase of the fractal dimension at the gel point, linked to the decrease of the critical exponent β [see Fig. 3.18(c)], and to the increase of both the elastic and the viscous moduli at the gel point [see Fig. 3.18(b)]. Interestingly, the decrease of the loss factor measured at the gel point with an increasing CNC weight fraction for $w_{CNC} < 3.4$ wt % suggests that, in the gel phase, the CNC network capacity to store energy through elasticity, reflected by G', increases faster than the dissipation through viscous effects, reflected by G''.

On the other hand, in the attractive glass phase, adding more particles to a suspension that is already quite concentrated does not change the global microstructural arrangement of CNC particles. Indeed, once the concentration threshold separating the gel phase from the attractive glass phase is reached, CNC particles are arranged into densely packed clusters, and when adding more particles into the suspension, it becomes impossible to densify even more the clusters due to an equilibrium between attractive forces (like hydrogen bonding or van der Waals interactions) and repulsive forces (like electrostratic or steric repulsion). Instead, the additional particles incorporate into the dense microstructure, not by creating new bonds in the CNC network, as in the gel phase, but by aligning with already existing bonds, hence creating thicker and stronger links between the network nodes. Therefore, we propose that instead of a network made of single CNC particles like in the gel phase, the CNC attractive glass would be constituted of a network made of bundles of CNC particles. This hypothesis is consistent with the observation that the fractal dimension of the CNC network, estimated through our rheological measurements and using the Muthukumar relationship, remains constant when increasing the CNC weight fraction in the glass phase [see Fig. 3.18(c)], and that both the elastic and the viscous moduli at the gel point increase at a slower rate than in the gel phase [see Fig. 3.18(b)]. This scenario for the CNC aggregation in the attractive glass phase is also compatible with the observation that the ratio t_g/t_c does not evolve much with the CNC weight fraction for $w_{CNC} > 3.4$ wt % [see Fig. 3.18(a)]. Indeed, in the gel phase, as previously explained, an increase in the t_g/t_c ratio might be due to a sensitivity of the system to the geometrical anisotropy of the CNC particles. However, this anisotropy does not play much role anymore in the aggregation scenario in the attractive glass phase, as the global microstructure of the network does not change. The fluctuations of t_g/t_c observed in the attractive glass phase might be due to the fact that the gelation time was not strictly the same for all samples (see Table 3.3). Indeed, for suspensions with a large CNC weight fraction, a small variation in the NaCl concentration has a strong impact on the gelation time and on the recovery dynamics, as will be described in more details in Sec. 3.B.4. Nevertheless, those interpretations need to be verified through microstructural measurements.

Finally, the power-law exponents y and z, respectively from the divergence of the time-dependent

shift factors a and b, also contain information about the difference between the gel and the attractive glass phase. In the gel phase, the exponents increase weakly with the CNC weight fraction, whereas in the glass phase, this increase is much sharper [see Fig. 3.18(d)]. This change of behavior can be interpreted as follows. In the gel phase, the suspension is dilute and CNC particles are far away from each other: the mean inter-particle distance d is about $1/\phi_{CNC}^{1/3} \approx 4$ to 6 times the particle length when decreasing the CNC weight fraction from 3.2 wt % to 2 wt % (ϕ_{CNC} is the CNC volume fraction), while it is about 3 times the particle length in the glass phase, for $w_{CNC} = 5.5$ wt %. Therefore, in order to build a connected network, CNCs need to diffuse on up to twice longer distances in the gel phase compared to the glass phase before they reach a neighboring particle, which takes up to four times longer. Consequently, a small change in the local CNC weight fraction, corresponding to a small time displacement around the gel point during particle aggregation, have a smaller impact on the local network properties in the gel phase than in the attractive glass phase, leading to small values of y and z on both sides of the gel point, and a weak dependence of these values on the CNC weight fraction. On the contrary, in the attractive glass phase the suspension is more concentrated and CNC particles have many close neighboring particles at all times. Therefore, the system is much more sensitive to a small translation in time around the gel point that now corresponds to a large local change in the sample microstructure, hence leading to larger values of the exponents y and z on both sides of the gel point, and to a stronger dependence on the CNC content.

f Dynamic critical exponents and hyperscaling relations

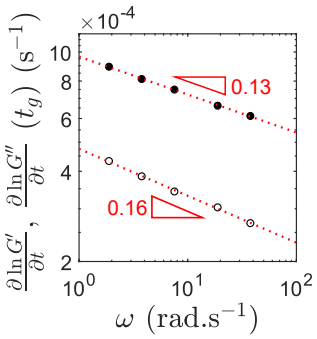

Figure 3.19: Time derivative of the logarithm of G' (•) and G'' (○) at the gelation time t_g as a function of the frequency. The red dashed lines show the best fits of the data with power-laws of exponents $\kappa' = 0.13 \pm 0.01$ and $\kappa'' = 0.16 \pm 0.02$ respectively. The error bars are estimated from the error on t_g. Data for a suspension containing 3.2 wt % CNC and 12 mM NaCl.

From the recovery data, it is possible to extract another critical exponent characteristic of the gelation dynamics, referred to as the dynamic critical exponent κ, introduced by Scanlan and Winter [Scanlan and Winter, 1991] and defined by:

$$\frac{\partial \ln G'}{\partial t}(\omega, t_g) = C \frac{\partial \ln G''}{\partial t}(\omega, t_g) \sim \omega^{-\kappa}, \tag{3.16}$$

where C is a proportionality factor. This relationship has been deduced from experimental observations (see Fig. 3.19), and suggests that, as the system approaches the critical gel point, the rates of change of both the elastic and the viscous moduli decrease in a similar way with frequency.

In practice, for every sample, we extract exponents from the time evolution of both the elastic and the viscous moduli separately, noted κ' and κ'' respectively. The resulting exponents are plotted in Fig. 3.20(a) as a function of the CNC weight fraction. We observe that, except for the most dilute sample, both exponents have very similar values in the gel phase, for $w_{CNC} < 3.4$ wt %, as stated by Eq. (3.16). However, κ' and κ'' differ clearly from each other in the attractive glass phase, for $w_{CNC} > 3.4$ wt %, and we cannot assume $\kappa' = \kappa''$ anymore. In the following, in order to compute a proportionality constant C as in Eq. (3.16), we shall impose $\kappa = \kappa'$, which is less noisy than κ''. Based on the comparison of experimental data obtained from different systems, Suman and Joshi [Suman and Joshi, 2020] have hypothesized that both the exponent κ and the proportionality factor C display some universality with $\kappa = 0.2$ and $C = 2$ for systems in which mechanical percolation and thus gelation is observed. While the physical interpretation for the value of κ is unclear, $C = 2$ means that, at the critical gel point, the growth rate of $G'(t)$ is typically twice the one of $G''(t)$.

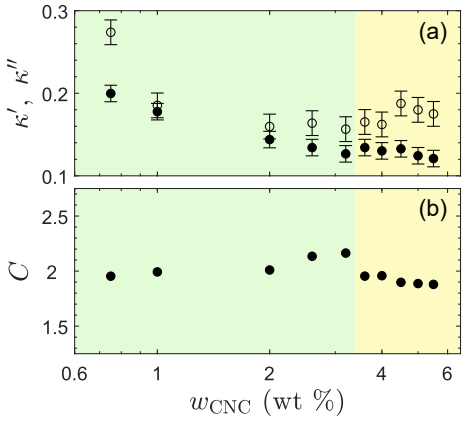

Figure 3.20: (a) Dynamic critical exponents κ' (•) and κ'' (◦) extracted from the time evolution of G' and G'' respectively, as a function of the CNC weight fraction w_{CNC}. (b) The constant of proportionality C, calculated by setting $\kappa = \kappa'$ for both the G' and G'' time evolutions, as a function of w_{CNC}. Experiments performed on a series of suspensions containing various CNC weight fractions, and an NaCl concentration adjusted so that the gelation time t_g remains similar for all samples, with a median value of 1370 s (see Table 3.3).

In our suspensions of CNC particles, we verify $C \approx 2$ for the range of CNC weight fractions studied [see Fig. 3.20(b)]. However, we report values for the dynamic critical exponent κ in the range $[0.12; 0.2]$, i.e., slightly smaller than expected [see Fig. 3.20(a)]. Actually, it seems that $\kappa' \approx 0.2$ only holds for $w_{CNC} < 2$ wt %, while it becomes significantly smaller than 0.2 for larger weight fractions. Therefore, our data refutes the hypothesis of a universal value for the exponent κ.

As shown in the literature, the various critical exponents characterizing the gelation dynamics around the gel point can be linked together using mathematical relationships called hyperscaling relations [Winter, 1987, Stauffer et al., 1982]. First, by connecting the power-law frequency dependence of the non-rescaled viscoelastic moduli $G'(\omega, t_g) \sim G''(\omega, t_g) \sim \omega^\beta$ to the rescaled ones at the gel point $\tilde{G}'(\tilde{\omega}, t_g) \sim \tilde{G}''(\tilde{\omega}, t_g) \sim \tilde{\omega}^\beta$, and using the definitions of the rescaled parameters $\tilde{\omega} = a(t)\omega$ and $\tilde{G}','' = b(t)G',''$, and the time evolution of the shift factors $a \sim \varepsilon^{y_i}$ and $b \sim \varepsilon^{z_i}$, with $\varepsilon = |t - t_g|/t_g$, one can demonstrate a first hyperscaling relation:

$$\beta = z_i/y_i, \tag{3.17}$$

with $i = l$ for $t < t_g$ and $i = g$ for $t > t_g$. The insets of Fig. 3.18(d) and of Fig. 3.16(e) shows that this hyperscaling relation is valid for all the CNC weight fractions explored here, both before and after the gel point.

Furthermore, Scanlan and Winter [Scanlan and Winter, 1991] have shown that, if we assume that the relaxation modulus evolves as a stretched exponential of exponent κ in the vicinity of the gel point, for $t < t_g$, one can establish a second hyperscaling relation, which holds only before the gel point:

$$\kappa_p = (1 - \beta)/(y_l - z_l). \tag{3.18}$$

Now, if one assumes the symmetry of the recovery dynamics with respect to the gel point, i.e., a symmetry of the exponents y and z on both sides of the gel point, one gets a similar hyperscaling relation for the dynamics after the gel point:

$$\kappa_p = \beta/z_g. \tag{3.19}$$

Finally, combining the hyperscaling relations given by Eq. (3.18) and by Eq. (3.19) with the one

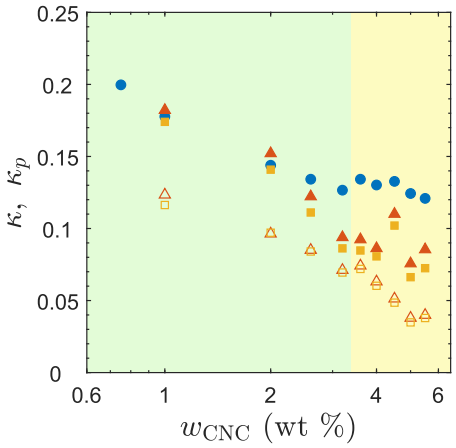

Figure 3.21: Dynamic critical exponent extracted from experimental data $\kappa = \kappa'$ (•), compared to the dynamic critical exponent κ_p calculated using the hyperscaling relations $\kappa_p = (1-\beta)/(y_l - z_l)$ (△), $\kappa_p = \beta/z_g$ (▲), $\kappa_p = 1/y_l$ (□), $\kappa_p = 1/y_g$ (■), as a function of the CNC weight fraction w_{CNC} for samples containing various CNC weight fractions, and an NaCl concentration adjusted so that the gelation time t_g remains similar for all samples, with a median value of 1370 s (see Table 3.3).

given by Eq. (3.17), for $t < t_g$ and $t > t_g$ separately, we get:

$$\kappa_p = \begin{cases} 1/y_l & \text{for } t < t_g \\ 1/y_g & \text{for } t > t_g \end{cases} \tag{3.20}$$

Figure 3.21 compares the exponent κ extracted from the data to the exponents κ_p predicted from the four hyperscaling relations given by Eqs. (3.18)–(3.20), as a function of the CNC weight fraction. First, as expected, the exponents predicted from the dynamics before the gel point (empty symbols) do not coincide with the ones predicted from the dynamics after the gel point (filled symbols), since our system does not verify the assumption of symmetry with respect to the gel point, as previously discussed. Moreover, we demonstrate once again that the hyperscaling relation given by Eq. (3.17) is valid in our system for all CNC weight fractions explored, since both the exponents predicted from the dynamics before the gel point given by Eqs. (3.18) and (3.20) coincide, as well as both the exponents predicted from the dynamics after the gel point given by Eqs. (3.19) and (3.20). Interestingly, the exponents predicted from the post-gel dynamics are in good agreement with the exponents κ' extracted from the data at small CNC weight fraction, for $w_{\mathrm{CNC}} < 3.4$ wt %. However, this prediction fails when the CNC weight fraction is increased above 3.4 wt %, i.e., when the sample lies in the attractive glass region of the phase diagram. Finally, for all CNC weight fractions, the exponents predicted from the pre-gel dynamics differ significantly from our data.

In this section, we have studied the recovery dynamics of suspensions containing various CNC weight fractions, in which we have adjusted the NaCl concentration in order to keep a constant gelation time t_g. We may now wonder how this recovery dynamics is affected by a change of salt concentration, at fixed CNC weight fraction, i.e. moving horizontally in the CNC versus NaCl phase diagram. In the previous Sec. 3.A.3, we have studied such an influence of the salt concentration on the recovery dynamics of CNC suspensions containing 3.2 wt % CNC, but at a single frequency.

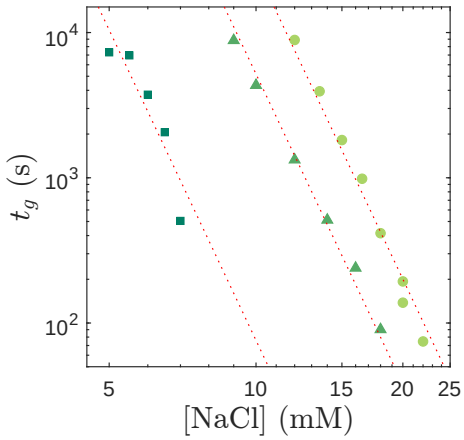

Figure 3.22: Gelation time t_g as a function of the NaCl concentration for three series of suspensions containing different CNC weight fractions: w_{CNC} = 2 wt % (•), 3.2 wt % (▲) and 5.5 wt % (■). The red dashed lines show power-law fits of exponent γ = 7.1.

B.4 Influence of the ionic strength on the recovery dynamics

In order to refine our understanding of the impact of the salt content on the recovery dynamics of CNC suspensions, we now apply the time-resolved mechanical spectroscopy protocol described in Sec. 3.B.1 to samples containing various NaCl concentrations. In particular, we focus on three series of samples containing w_{CNC} = 2 wt %, 3.2 wt %, and 5.5 wt %. For each CNC content, the range of NaCl concentrations explored was chosen to give measurable gelation times t_g, between 100 and 9000 s. The CNC weight fractions were precisely chosen in order to better understand the difference between the gel and the attractive glass phase from a rheological point of view.

a Robustness of the time-connectivity superposition

Similarly to what we have observed in Fig. 3.17 when varying the CNC weight fraction at a given NaCl concentration, whatever the CNC weight fraction and the salt concentration, we can always construct master curves for the time evolution of the loss factor and for both viscoelastic moduli. These master curves are similar to the ones presented in Fig. 3.16 for a gel containing 3.2 wt % CNC and 12 mM NaCl. This shows that the time-connectivity superposition principle remains valid over the whole range of NaCl and CNC concentrations explored here. Moreover, for each NaCl content at a given CNC weight fraction, the gel point is always well defined: at intermediate times, the loss factor plateaus and the rescaled viscoelastic moduli evolve as a power-law with the rescaled frequency, with the same exponent. Second, the scaling factors a and b have the same time-dependence with a non-symmetrical power-law divergence at the gel point. Finally, the above fractional approach provides very good fits for the data, both before and after the gel point, whatever the salt concentration. Yet it is important to note that, here again, the constraint of imposing the prefactor $\mathcal{G}$, associated to the exponent β, to keep the same value in both models, on both sides of the gel point, has to be relaxed for w_{CNC} = 5.5 wt %. The full set of parameters corresponding to both models used to fit the master curves are reported in Table 3.5 in Sec. 3.C in Appendix.

In the following, similarly to what we have done in Sec. 3.B.3, we extract several observables of interest from the above time-resolved mechanical spectroscopy measurements, in order to characterize in more details how the recovery dynamics of CNC gels depend on the salt concentration depending on the position in the phase diagram.

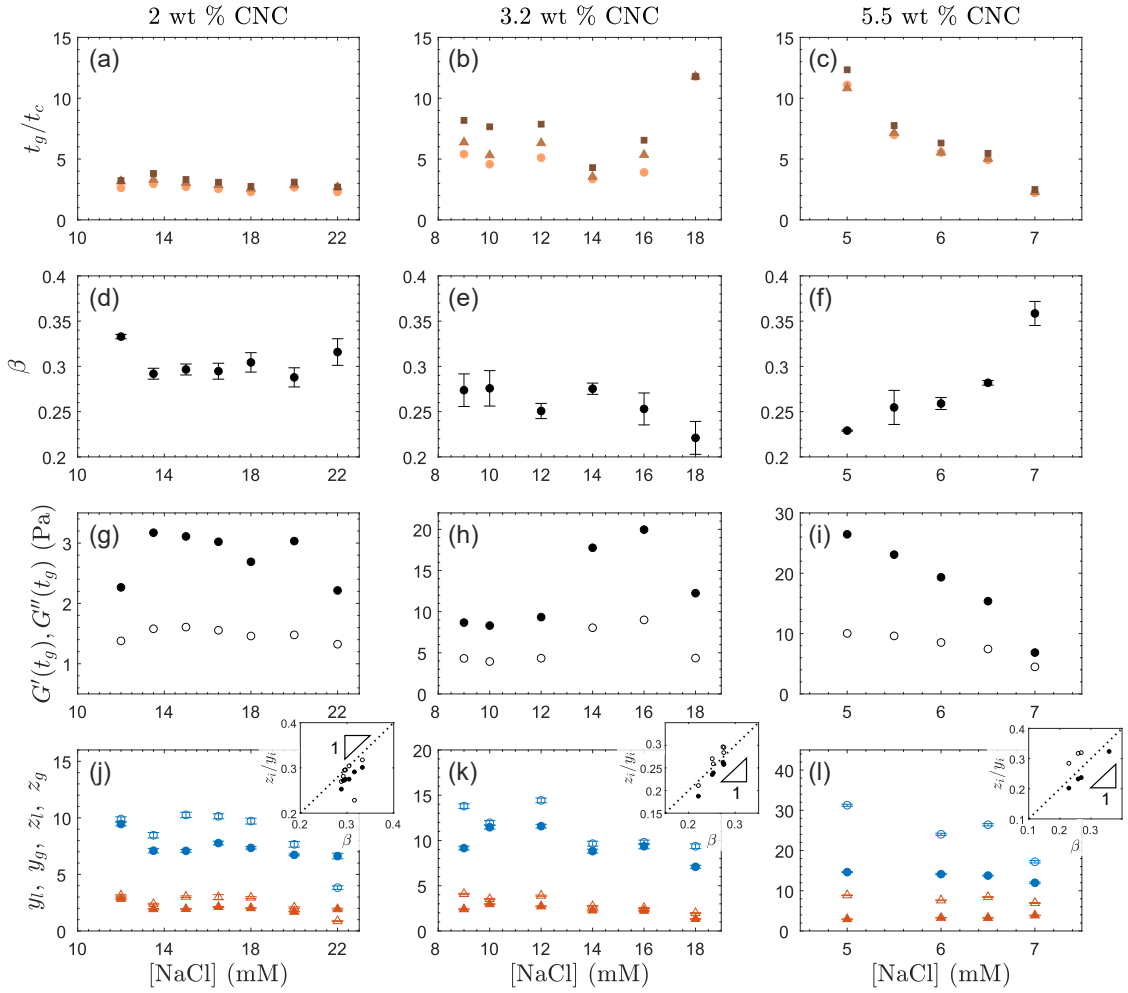

Figure 3.23: Gelation dynamics parameters of three series of suspensions of different CNC weight fraction (2 wt %, 3.2 wt % and 5.5 wt % from left to right), in which the NaCl concentration is varied. (a),(b),(c) Ratio of the gelation time t_g over the crossover time t_c measured at three different frequencies (1.88 rad.s^{-1} •, 3.77 rad.s^{-1} ▲, 7.54 rad.s^{-1} ■) versus NaCl concentration. (d),(e),(f) Dependence of the critical exponent β with the NaCl concentration. (g),(h),(i) Elastic modulus G' (•) and viscous modulus G'' (◦) at the gel point, measured at 7.54 rad.s^{-1}, versus NaCl concentration. (j),(k),(l) NaCl concentration dependence of the power-law exponents for the time evolution of the horizontal shift factor a and the vertical shift factor b, before the gel point y_l (◦) and z_l (△) respectively, and after the gel point y_g (•) and z_g (▲) respectively. Inset: Ratio of the power-law exponent for the time-dependence of the vertical shift factor b over the power-law exponent for the time-dependence of the horizontal shift factor a both before the gel point z_l/y_l (◦) and after the gel point z_g/y_g (•), as a function of the critical exponent β at the gel point. The dashed lines show $z_i/y_i = \beta$ [as in the inset of Fig. 3.18(d)].

b Dependence of the gelation kinetics on the salt content

Figure 3.22 shows the gelation time for the three series of samples containing 2 wt %, 3.2 wt %, and 5.5 wt % CNC, as a function of the NaCl concentration. As seen previously in Sec. 3.A.4 for the inflection time t^*, for all series, the gelation time decreases sharply with increasing salt concentration, showing that the gelation kinetics accelerate. As already mentioned, this behavior can be interpreted as follows: when increasing the salt content in a CNC suspension, the screening of the CNC surface charges is more efficient, facilitating and thus accelerating particle aggregation and percolation. Interestingly, all three series present a power-law dependence of the gelation time on the salt content:

$$t_g \propto [\mathrm{NaCl}]^{-\gamma} \tag{3.21}$$

with the same exponent $\gamma = 7.1 \pm 0.4$, which is consistent with the exponent $\gamma = 8.7 \pm 0.2$ evidenced in the previous Sec. 3.A.4. Note that the range of accessible salt concentrations is more restricted here than in Sec. 3.A.4 as t_g must remain reasonably small to be measured directly. Let us now investigate more precisely how the recovery dynamics depends on the salt concentration by focusing more particularly on the critical gel point, around the gelation time t_g.

c Influence of the salt content on the gel point across the phase diagram

As done in the previous Section 3.B.3, we extract various variables of interest from the time-resolved spectroscopy data, and explore how they depend on the NaCl concentration for each series at constant CNC weight fraction. First, we observe that the ratio of the two characteristic times t_g/t_c, plotted in Fig. 3.23(a-c), is roughly independent of the NaCl concentration for $w_{\mathrm{CNC}} = 2$ wt % and for $w_{\mathrm{CNC}} = 3.2$ wt %, while it decreases from $t_g/t_c = 12$ to 2 for $w_{\mathrm{CNC}} = 5.5$ wt %. Similarly, the critical exponent β is about constant for both $w_{\mathrm{CNC}} = 2$ wt % and $w_{\mathrm{CNC}} = 3.2$ wt %, while it significantly increases for $w_{\mathrm{CNC}} = 5.5$ wt %, from $\beta = 0.23$ to 0.36 [see Fig. 3.23(d-f)]. Furthermore, the values of the elastic and viscous moduli at the gel point, plotted in Fig. 3.23(g-i), are about constant for $w_{\mathrm{CNC}} = 2$ wt %, while they evolve non-monotonically with the salt content for $w_{\mathrm{CNC}} = 3.2$ wt %, varying by more than a factor of 2 over the range of NaCl concentration explored. For $w_{\mathrm{CNC}} = 5.5$ wt %, both the elastic and the viscous moduli measured at the gel point decrease with the NaCl concentration, but the elastic modulus decreases at a much faster rate, by almost a factor of 4, while the viscous modulus only decreases by a factor of about 2 over the same range of NaCl concentrations. Finally, the exponents y_i and z_i appear to be independent of the salt concentration for all three series of samples [see Fig. 3.23(j-l)].

The change of behavior with the salt content when increasing the CNC weight fraction from 2 wt % to 5.5 wt % confirms the existence of the critical concentration $w^*_{\mathrm{CNC}} \approx 3.4$ wt % CNC marking the transition between two phases, a gel and an attractive glass, associated with two different gelation scenarios. As described in Sec. 3.B.3.e, above this critical weight fraction, CNC particles are sufficiently close to each other so that they do not need to translate to aggregate. Rotation is enough to induce gelation. In this case, the system is very sensitive to the presence of salt: an increase in the salt content leads to an enhanced screening of the CNC surface charges, allowing particles to stick faster to each other, resulting in the formation of a more open structure at the gel point, hereby justifying the decrease of the fractal dimension, or equivalently the increase of the exponent β, with the salt concentration. For samples with a CNC weight fraction smaller than this critical concentration, CNC particles are far from each other in the dispersed state, so they need to translate to meet their neighbors and percolate, therefore following a diffusion-limited colloid aggregation (DLCA) dynamics [Gado et al., 2016]. In this case, the screening of the short range electrostatic repulsion forces does not have much influence on the microstructure of the network formed upon recovery. This most probably explains the independence on the salt concentration of the various parameters at the gel point for $w_{\mathrm{CNC}} = 2$ wt %. The suspensions containing $w_{\mathrm{CNC}} = 3.2$ wt % show a dependence on the NaCl concentration only at large NaCl concentration, for [NaCl]> 13 mM. Such a change of behavior is most likely due to the proximity to the

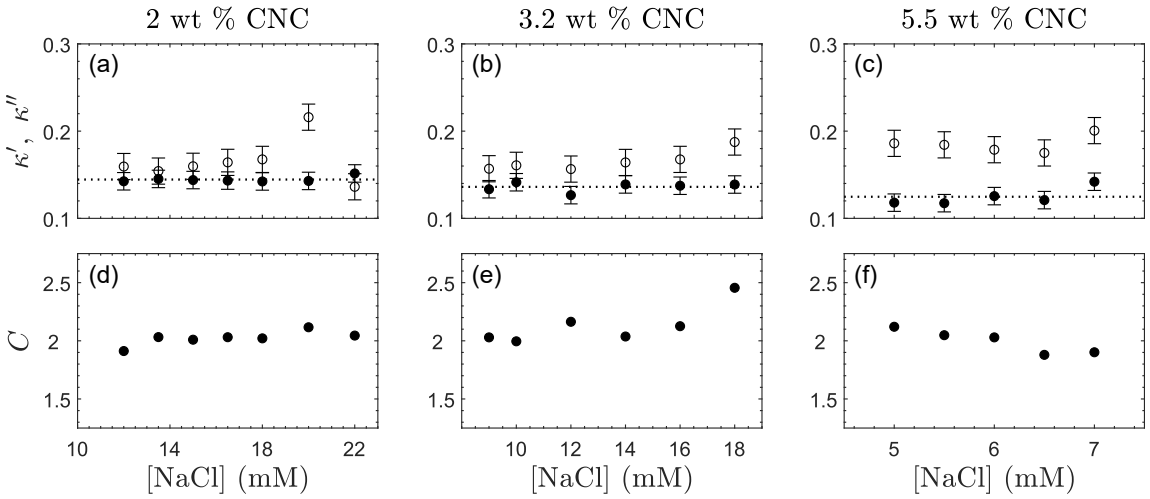

Figure 3.24: Dynamic critical exponents κ' (•) and κ'' (◦), extracted using the time evolution of G' and G'' respectively, and of constant of proportionality C, calculated by setting κ as the mean value of κ' over the range of NaCl concentration (see the horizontal gray dashed lines) as a function of NaCl concentration, for the three series of samples containing (a),(d) 2 wt % CNC, (b),(e) 3.2 wt % CNC, (c),(f) 5.5 wt % CNC.

gel/attractive glass boundary in the phase diagram, which might not be perfectly vertical.

d Robustness of the hyperscaling relations towards variations of the salt content

Figure 3.24(a-c) shows that the dynamic critical exponents κ' and κ'' are independent of the salt concentration for w_{CNC} = 2 wt %, 3.2 wt % and 5.5 wt %. Moreover, we observe $\kappa' \approx \kappa''$ for w_{CNC} = 2 wt% and for w_{CNC} = 3.2 wt% for all salt concentrations explored, although the difference between κ' and κ'' seems to increase with the CNC weight fraction. The two exponents become significantly different, $\kappa' \neq \kappa''$, for w_{CNC} = 5.5 wt%. These results are consistent with the observation made in Sec. 3.B.3.f for different w_{CNC} at similar values of t_g. In order to calculate the proportionality factor C, similarly to the analysis made in Sec. 3.B.3.f and using the fact that κ' and κ'' are independent of [NaCl], we set κ as being the mean value of κ' over the range of NaCl concentrations explored for every CNC weight fraction [see the horizontal dashed lines in Fig. 3.24(a-c)].

Interestingly, C is also independent of the salt concentration for w_{CNC} = 2 wt %, 3.2 wt % and 5.5 wt % [see Fig. 3.24(d-f)]. However, while C is equal to 2 for the three series of samples as predicted by Suman *et al.* [Suman and Joshi, 2020], κ' is always smaller than the expected value of 0.2, what hints to a non-universality of the dynamic critical exponent κ, as already suggested in Sec. 3.B.3.f.

The insets of Fig. 3.23(j-l) show that the hyperscaling relation given by Eq. (3.17), connecting the critical exponent β to the power-law exponents of the rescaling parameters y_i and z_i, still holds for the three series of samples, whatever the salt content, both before the gel point ($i = l$) and after the gel point ($i = g$). Figure 3.25, comparing the dynamic exponents κ estimated from the data and κ_p predicted from the hyperscaling relations given by Eqs. (3.18)-(3.20), shows that the observations made in the previous section hold over the whole range of salt content explored: for w_{CNC} = 2 wt % [see Fig. 3.25(a)], the hyperscaling relations using post-gel exponents predict quite well the dynamic exponent κ extracted from the data, while this prediction fails for w_{CNC} = 5.5 wt % [see Fig. 3.25(c)]. For the intermediate CNC weight fraction w_{CNC} = 3.2 wt % [see Fig. 3.25(b)], the predictions from the post-gel dynamics are in relatively good agreement with the

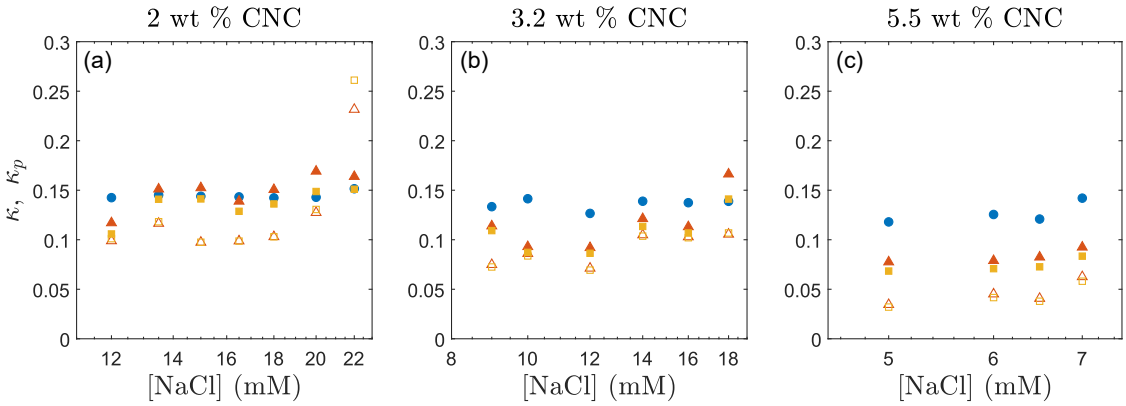

Figure 3.25: Comparison of the dynamic critical exponents extracted from experimental data $\kappa = \kappa'$ (•) to the dynamic critical exponents calculated using the hyperscaling relations $\kappa = (1-\beta)/(y_l - z_l)$ (△), $\kappa = \beta/z_g$ (▲), $\kappa = 1/y_l$ (□), $\kappa = 1/y_g$ (■) as a function of NaCl concentration, for the three series of samples containing (a) 2 wt % CNC, (b) 3.2 wt % CNC, and (c) 5.5 wt % CNC.

data, but a deviation becomes noticeable. In any case, the predictions made through hyperscaling relations using pre-gel exponents are not consistent with the estimations of the dynamic exponent from the data, as previously pointed out for every CNC weight fraction explored in this study (see Sec. 3.B.3.f). This is a consequence of the asymmetry of the pre-gel and post-gel exponents, which is observed whatever the sample [see Fig. 3.23(j)-(l)].

e Time-composition-connectivity superposition

The weak dependence of β with the salt concentration for suspensions containing 2 wt % CNC and 3.2 wt % CNC, together with the fact that the fractional derivative orders α and ξ of the two other spring-pots involved in the fractional models do not significantly depend on the salt content either (see Table 3.5 in Sec. 3.C in Appendix), prompt us to further rescale the master curves for the samples at a given w_{CNC} and various NaCl concentrations, onto two single general master curves for the pre-gel and the post-gel dynamics respectively. In fact, while β controls the frequency viscoelastic behavior at the critical gel point, α and ξ respectively control the small-frequency viscoelastic behavior of the viscoelastic liquid for $t < t_g$ and of the soft solid for $t > t_g$.

To do so, we consider the pre-gel dynamics, for $t < t_g$, and the post-gel dynamics, for $t > t_g$ separately. For $t < t_g$, we rescale the $\tan\delta(\tilde{\omega})$, $\tilde{G}'(\tilde{\omega})$ and $\tilde{G}''(\tilde{\omega})$ master curves, corresponding to various salt concentrations but to the same CNC content, by the point $(\tilde{\omega}_l, \tilde{G}_l)$ where the rescaled moduli $\tilde{G}'(\tilde{\omega})$ and $\tilde{G}''(\tilde{\omega})$ cross-over. The resulting rescaled master curves $\tilde{G}'/\tilde{G}_l(\tilde{\omega}/\tilde{\omega}_l)$ and $\tilde{G}''/\tilde{G}_l(\tilde{\omega}/\tilde{\omega}_l)$ obtained for the series of suspensions containing 2 wt %, 3.2 wt % and 5.5 wt % CNC are shown in Figs. 3.26(a)-(c). The corresponding rescaled parameters $\tilde{G}_l$ and $\tilde{\omega}_l$ are plotted as a function of one another in the upper insets, while the lower insets show the rescaled master curves for the loss factor $\tan\delta$ as a function of $\tilde{\omega}/\tilde{\omega}_l$). For $t > t_g$, we first collapse all loss factor master curves $\tan\delta$ $(\tilde{\omega})$ obtained for various NaCl concentrations at fixed w_{CNC}, by translating each of them along the horizontal direction by a factor $\tilde{\omega}_g$, which depends on the salt concentration, maximizing their overlap [see lower insets in Figs. 3.26(d)-(f)]. Then, we vertically shift both rescaled viscoelastic moduli $\tilde{G}'$ $(\tilde{\omega}_g/\tilde{\omega}_g)$ and $\tilde{G}''$ $(\tilde{\omega}_g/\tilde{\omega}_g)$ by a factor $\tilde{G}_g$, which depends on the salt concentration, in order to maximize their overlap. The resulting rescaled master curves $\tilde{G}'/\tilde{G}_g$ $(\tilde{\omega}/\tilde{\omega}_g)$ and $\tilde{G}''/\tilde{G}_g$ $(\tilde{\omega}/\tilde{\omega}_g)$ are displayed in Figs. 3.26(d)-(f). The corresponding rescaled parameters $\tilde{G}_g$ and $\tilde{\omega}_g$ are plotted versus one another in the upper insets, while the lower insets show the rescaled master curves for the loss factor.

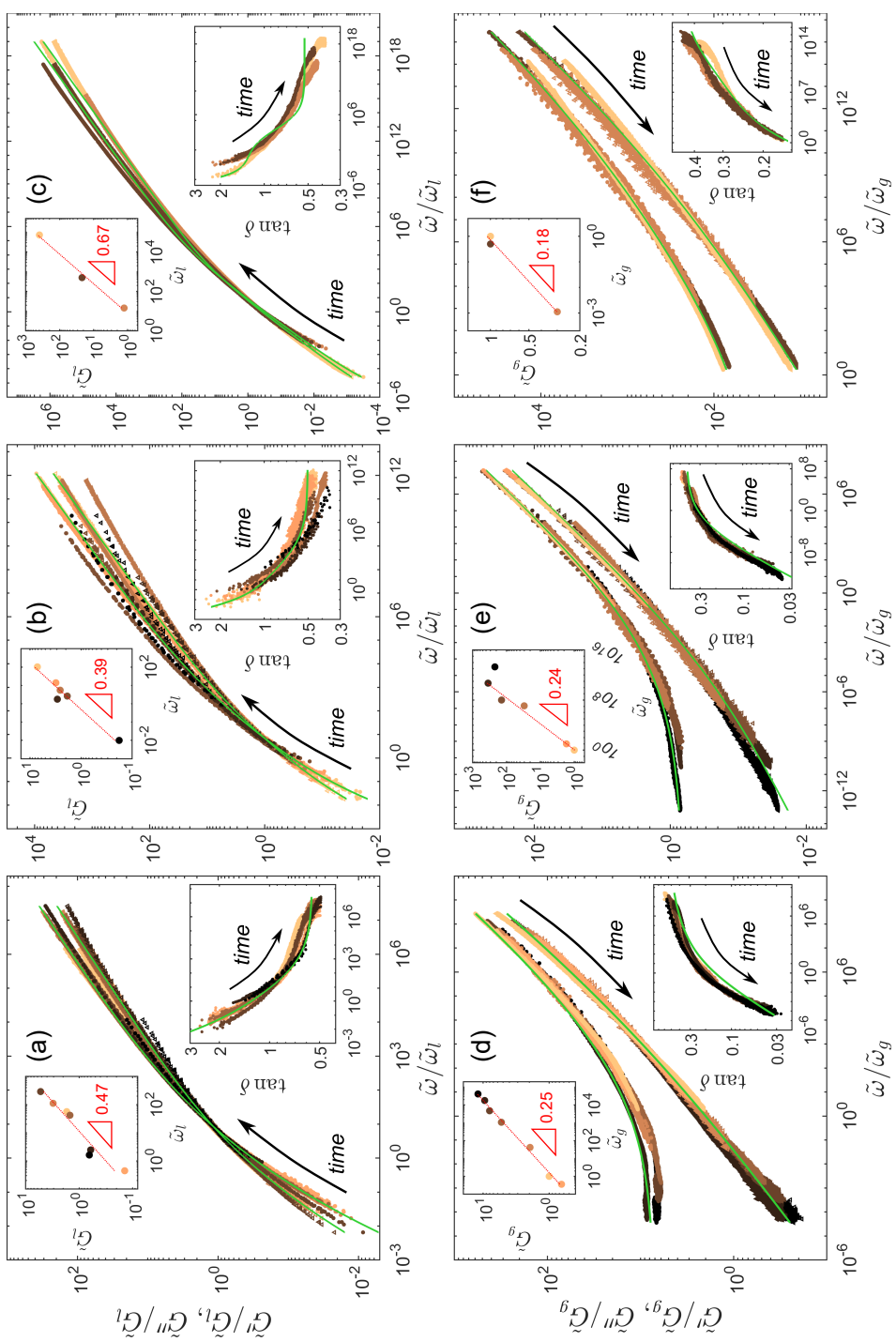

Figure 3.26: Rescaled master curves for the viscoelastic spectra measured (a),(b),(c) before and (d),(e),(f) after the gel point on CNC suspensions (a),(d) containing 2 wt % CNC and salt concentrations ranging between 12 mM and 22 mM NaCl, (b),(e) containing 3.2 wt % CNC and salt concentrations ranging between 9 mM and 18 mM NaCl, and (c),(f) containing 5.5 wt % CNC and salt concentrations ranging between 5 mM and 7 mM NaCl. Elastic and viscous moduli are shown with • and △ respectively. The color scales for the salt concentration: from orange for the smallest salt concentration, to black for the largest. Lower insets: $\tan\delta = \tilde{G}''/\tilde{G}' = G''/G'$ vs $\tilde{\omega}/\tilde{\omega}_i$. The x-axis are the same as the x-axis of the main plots. Upper insets: shift factors $\tilde{G}_i$ vs $\tilde{\omega}_i$ for the various salt concentrations, together with their best power-law fits (red dotted lines). The indices $i = l$ and $i = g$ respectively denote the pre-gel liquid state in (a),(b),(c) and the post-gel solid state in (d),(e),(f). The green curves show the best fits of the data with a fractional Maxwell model for $t < t_g$ in (a),(b),(c) and with a fractional Kelvin-Voigt model for $t > t_g$ in (d),(e),(f). The corresponding fit parameters are reported in Table 3.4. For each CNC weight fraction, the data with the smallest salt concentration were chosen as a reference to construct the general master curves.

Table 3.4: Parameters for the fit of the general master curves plotted in Fig. 3.26 by a Maxwell fractional model for the dynamics prior to the gel point, and by a Kelvin-Voigt fractional model for the dynamics following the gel point.

CNC (wt %)	η	$\mathbb{V}$	α	$\mathbb{G}$ ($t < t_g$)	$\mathbb{G}$ ($t > t_g$)	β	$\mathbb{K}$	ξ	k
2	5.1	0.83	0.64	1.7	0.84	0.32	5.5	0.19	7
3.2	4.7	0.69	0.56	2.8	6.3	0.26	3.6	0.12	0.65
5.5	100	0.53	0.59	4.6	1.6	0.28	40	0.15	28

Remarkably, the master curves for each of the three series of samples at a given CNC weight fraction collapse nicely onto single universal master curves, both for the gelation dynamics before the gel point, $t < t_g$, and after the gel point, $t > t_g$. The collapse appears to be better for the dynamics after the gel point than before the gel point, which might be due to the fact that at large salt concentration, the recovery dynamics is fast, leading to (i) an ill-defined $\tilde{G}'(\tilde{\omega})$-$\tilde{G}''(\tilde{\omega})$ crossover point, and (ii) fewer data points to construct the individual master curves for $t < t_g$ for a given salt content, inducing a larger error on the shape of the resulting master curve.

Nevertheless, general master curves for both the dynamics before and after the gel point can be well accounted for by the same Maxwell and Kelvin-Voigt fractional models introduced in Sec. 3.B.2. More precisely, each general master curve can be fitted using a single set of parameters for each model, reported in Table 3.4. While β is kept constant both before and after the gel point, the constraint of also keeping $\mathbb{G}$ constant needs to be relaxed, as previously done in Sec. 3.B.3.a to fit the master curves obtained for w_{CNC} = 5.5 wt %. As expected, the critical exponent β decreases with the CNC weight fraction, which is consistent with the previous description given in Sec. 3.B.3.c [see also Fig. 3.18(c)]. Interestingly, the parameters for the Maxwell fractional model fitting the dynamics prior to the gel point show a clear trend with the CNC weight fraction: $\mathbb{V}$ and α decrease with w_{CNC} while $\mathbb{G}$ increases. However, the parameters for the Kelvin-Voigt fractional model fitting the dynamics following the gel point, do not show any clear trend.

The shift factors $\tilde{G}_l$ and $\tilde{\omega}_l$, and $\tilde{G}_g$ and $\tilde{\omega}_g$ respectively, appear to be linked by two different non-trivial power-laws with exponents varying between 0.39 and 0.67 in the pre-gel state and decreasing from 0.25 to 0.18 with increasing w_{CNC} in the post-gel state (see upper insets in Fig. 3.26).

All in all, the existence of such general master curves for the recovery dynamics probed at several frequencies of CNC suspensions containing various salt concentrations highlights the robustness of the time-composition superposition principle detailed in Sec. 3.A.3, for both the dynamics before and after the gel point. This generalized time-composition-connectivity superposition principle supports our previous hypothesis that, at a given CNC weight fraction, a CNC suspension recovers following shear cessation by forming a similar microstructure whatever the salt concentration. Furthermore, the experiments performed on suspensions containing 2 wt % CNC and 5.5 wt % CNC allow us to extend this hypothesis to a wider range of CNC weight fractions.

(1) The recovery dynamics of a CNC suspension in the presence of salt follow a time-connectivity superposition principle, where the system goes through a critical gel point at a time t_g which coincides with the inflection point introduced in Sec. 3.A.3.

(2) These dynamics are well captured by a Maxwell fractional model before the gel point, and a Kelvin-Voigt fractional model after the gel, with one common fractional element characterizing the gel point.

(3) The time-connectivity principle is robust to changes in the salt and CNC concentrations.

(4) The time-composition superposition can be generalized to a time-composition-connectivity superposition valid over a wide range of CNC weight fractions when varying the salt concentration.

(5) A detailed dynamical characterization of the gel point allows us to evidence a transition from a gel phase to an attractive glass phase upon increasing the CNC weight fraction.

B.5 Discussion and open questions

We have studied how a suspension of cellulose nanocrystals recovers its solid-like properties in the presence of salt, after being fluidized by the application of a strong shear. Using time-resolved mechanical spectroscopy, we have shown that this recovery follows a time-connectivity superposition principle, as previously observed in other polymer and colloidal systems [Adolf and Martin, 1990, Keshavarz et al., 2021, Suman and Joshi, 2020, Larsen and Furst, 2008, Scanlan and Winter, 1991, Chen et al., 2010, Martin et al., 1990, Hong et al., 2018, He et al., 2021], by going through a critical gel as defined by Winter and Chambon [Winter and Chambon, 1986] at time t_g, called the gelation time. Our results raise the following questions.

a How may one rationalize the difference between the G'-G'' crossover time and the gelation time?

Remarkably, the gelation time t_g differs from the G'-G'' crossover time t_c measured at various frequencies, between 1.88 rad.s^{-1} and 7.54 rad.s^{-1}, as soon as the CNC weight fraction is larger than 1 wt %. In particular, the gelation time t_g can get as much as 8 times longer than the crossover time t_c in the range of CNC weight fractions explored here. This decoupling between those two characteristic time-scales is quite unexpected and highlights the necessity to perform time-resolved spectroscopy. Winter *et al.* [Winter et al., 1988] have established that a polymeric gel with a small amount of cross-linkers also displays a gap between t_c and t_g, but with $t_g < t_c$. Moreover, they have shown that, when the cross-linker content is increased, this decoupling disappears and t_g becomes equal to t_c, but without exceeding t_c. In the case of colloidal gels, including rod-like colloids other than CNCs, it has always been reported that $t_c \approx t_g$. Interestingly, we recover this limit in the dilute regime, for $w_{CNC} \leq 1$ wt %, but as soon as $w_{CNC} \geq 1$ wt %, t_c measured between 1.88 rad.s^{-1} and 7.54 rad.s^{-1} becomes much shorter than t_g. Whether this discrepancy is due to the particularly large aspect ratio of CNC particles, to their polydispersity, or to some particular interactions involved between CNC particles is still to be determined. In particular, steric interactions could slow down the emergence of the self-similar network at the origin of the critical-like behavior at t_g, while the system already shows some elasticity with $G' > G''$ (at frequencies between 0.3 and 1.2 Hz) at much earlier times. Such hypothesis is supported by the fact that the evolution of t_g/t_c with the salt concentration radically changes upon entering the attractive glass region of the phase diagram, where steric hindrance becomes predominant.

b What is the origin of the rescaling parameters asymmetry with respect to the gel point, and what sets the value of the corresponding exponents y and z?

By constructing master curves for the time evolution of the viscoelastic spectra, we have shown that the recovery dynamics of a CNC suspension following a strong shear follows a time-connectivity superposition principle. The validity of such a principle suggests that the suspension viscoelastic properties evolve in a self-similar way through time during the network reconstruction. Moreover, we have demonstrated that this time-connectivity superposition principle is robust to a change of CNC content and to a change of salt content, both in the gel and in the attractive glass phases, in the range of concentrations explored here. Such a superposition principle has already been established in many chemical [Adolf and Martin, 1990, Scanlan and Winter, 1991, Martin et al., 1990] and physical polymer gels [Suman and Joshi, 2020, Larsen and Furst, 2008, Hong et al., 2018], as well as in colloidal gels made of isotropic [Keshavarz et al., 2021] and anisotropic particles [Suman and Joshi, 2020, Chen et al., 2010, He et al., 2021]. However, the specificity of our system lies in the fact that the dynamics is non-symmetrical with respect to the gel point: the exponents y and z for the power-law divergence around the gel point of the horizontal and vertical shift factors $a(t)$ and $b(t)$ are different before and after the gel point. This asymmetry has been reported for only one other system: a gelatin solution [Hong et al., 2018] for which a difference of more than a factor of 2 between the pre-gel and the post-gel exponents for the vertical shift is observed. Another specificity of our system are the values of the exponents y and z which are much larger than those reported in the literature for polymeric and colloidal gels: the largest value found in the literature for y, which is always larger than z, is 6.24 for a suspension of polydisperse hydrogenated castor oil colloidal rods [Wehrman et al., 2016], while our values for y range between 6 and 28, depending on CNC and salt concentrations. Theories, such as the Flory-Stockmayer theory, also referred to as classical theory, and the percolation theory [Stauffer et al., 1982], have been developed to predict critical exponents for polymer gels. For instance, the Flory-Stockmayer theory predicts an exponent z_g that is equal to z_l, of value 3, and the percolation theory predicts a value of 1.7 in three dimensions. However, no theory has yet been established in the case of colloidal gels. The percolation theory can help us to understand the physical meaning of this discrepancy [Adolf and Martin, 1990, Winter and Mours, 1997, Larsen and Furst, 2008, Winter, 1987, Suman and Joshi, 2020, De Gennes, 1976, Adam et al., 1981, Stauffer et al., 1982, Axelos and Kolb, 1990, Hodgson and Amis, 1990, Rouwhorst et al., 2020]: on the one hand, the divergence of the shift factor a at the gel point reflects the divergence of the longest relaxation time in the system as the largest clusters grow. Therefore, a large value of the exponent y suggests that the system is very sensitive to the proximity of the sol-gel transition, and that its microstructure and the corresponding relaxation dynamics evolve rapidly upon approaching the critical gel point. On the other hand, the divergence of the shift factor b at the gel point reflects the emergence of the elastic modulus of the system in the limit of zero frequency. Therefore, a large value of the exponent z suggests, once again, that the system is very sensitive to the proximity of the sol-gel transition, and that the elastic modulus of the global network increases fast when approaching the critical gel point.

Nevertheless, despite the unexpected asymmetry of the recovery dynamics and the uncommonly large values of the y and z exponents, the hyperscaling relation $\beta = z/y$ holds for both the pre-gel and the post-gel dynamics separately, reflecting the continuous evolution of the viscoelastic spectra around the critical gel point, which ensures a constant value for β on both sides of this gel point.

Regarding the critical exponent β, we have interpreted its variations with the CNC and salt concentrations in terms of the fractal dimension of the CNC network at the gel point, using the relationship given by Muthukumar [Muthukumar, 1989]. However, one can wonder if this relationship, which has been established for branched polymers [Winter and Mours, 1997, Ng and McKinley, 2008], is valid in our system. To verify this assumption, we could deduce the fractal dimension of CNC suspensions of various compositions from light or X-ray scattering experiments.

c How does the gel versus attractive glass boundary evidenced through rheological measurements compare to the literature?

Finally, we have shown that by dynamically characterizing the critical gel point, we can identify a transition from a gel to an attractive glass when increasing the CNC weight fraction of a suspension. This transition is evidenced by a change of behavior of some rheological parameters towards the CNC content in both regimes. In their study, Xu *et al.* [Xu et al., 2020] have drawn the gel/attractive glass boundary as the continuity of the liquid crystal/repulsive glass boundary, without considering any experimental data points, and stating that the distinction between a gel and an attractive glass cannot be evidenced through rheology, but only using microstructural characterization. Yet, in our study, we propose to precisely identify the position of this boundary through rheology as the CNC weight fraction associated with a change of regime in the characteristics of the critical gel point. Interestingly, when calculating the dimensionless concentration $c_{\text{glass}} = \phi r$ corresponding to this boundary, with ϕ the CNC volume fraction and $r = L/D$ the CNC aspect ratio ($L \approx 120$ nm the length of an individual CNC, and $d \approx 10$ nm its diameter), we find $c_{\text{glass}} \approx 0.26$ instead of 0.8 as proposed by Xu *et al.* Such a discrepancy stands out as an open issue and deserves more investigations.

Finally, the gel to attractive glass phase transition associated to an increase of the CNC weight fraction [Solomon and Spicer, 2010] could be confirmed by getting some insight into the microscopic organization of CNCs. For this purpose, we could monitor the gelation dynamics at a smaller scale, using light, X-ray or neutron scattering, X-ray photon correlation spectroscopy (XPCS), as well as simulations. Moreover, conductivity measurements could provide information about electric percolation, to be compared to the mechanical percolation determined by rheology measurements.

C Appendix

C.1 Sample preparation protocol using dried CNCs

The suspensions of CNCs dispersed in D_2O were prepared from dried CNCs (CelluForce) that come in the form of a white powder. The following protocol was used in order to prepare homogeneous CNC suspensions containing 3.2 wt % CNC and various NaCl concentrations:

1. Preparation a 4.0 wt % CNC dispersion by progressively adding 0.4 g of dried CNCs in 9.6 g of deuterated water D_2O under mechanical shear using a magnetic bar. Continue mixing for one hour.

2. Application of high energy ultrasounds in order to break the CNC clusters. The energy applied per unit of CNC mass and per unit of suspension volume is E_m = 651 kJ.g^{-1}.L^{-1}, with a power P = 400 W [Girard et al., 2021]. The suspension is immersed in an ice bath and the ultrasounds are applied sequentially in order to avoid over-heating.

3. Progressive addition of 2.5 g of a solution of D_2O and NaCl under mechanical shear using a magnetic bar. Continue mixing for one hour.

4. Storage of the sample in the refrigerator for at least 24 hours.

Figure 3.27 shows a comparison of the rheological properties of aqueous CNC suspensions containing 3.2 wt % CNC and various NaCl concentrations, ranging between 5 mM and 100 mM, prepared from the commercial suspension, using the protocol described in Sec. 2.C (brown colorscale), or prepared from the dried CNCs, using the protocol described in this section, by replacing D_2O by H_2O. We observe no major discrepancy, neither in the linear nor in the non-linear regime of deformation. This observation shows that both protocols lead to suspensions with similar rheological properties. Therefore, the rheological properties of suspension prepared using one protocol or the other can be compared.

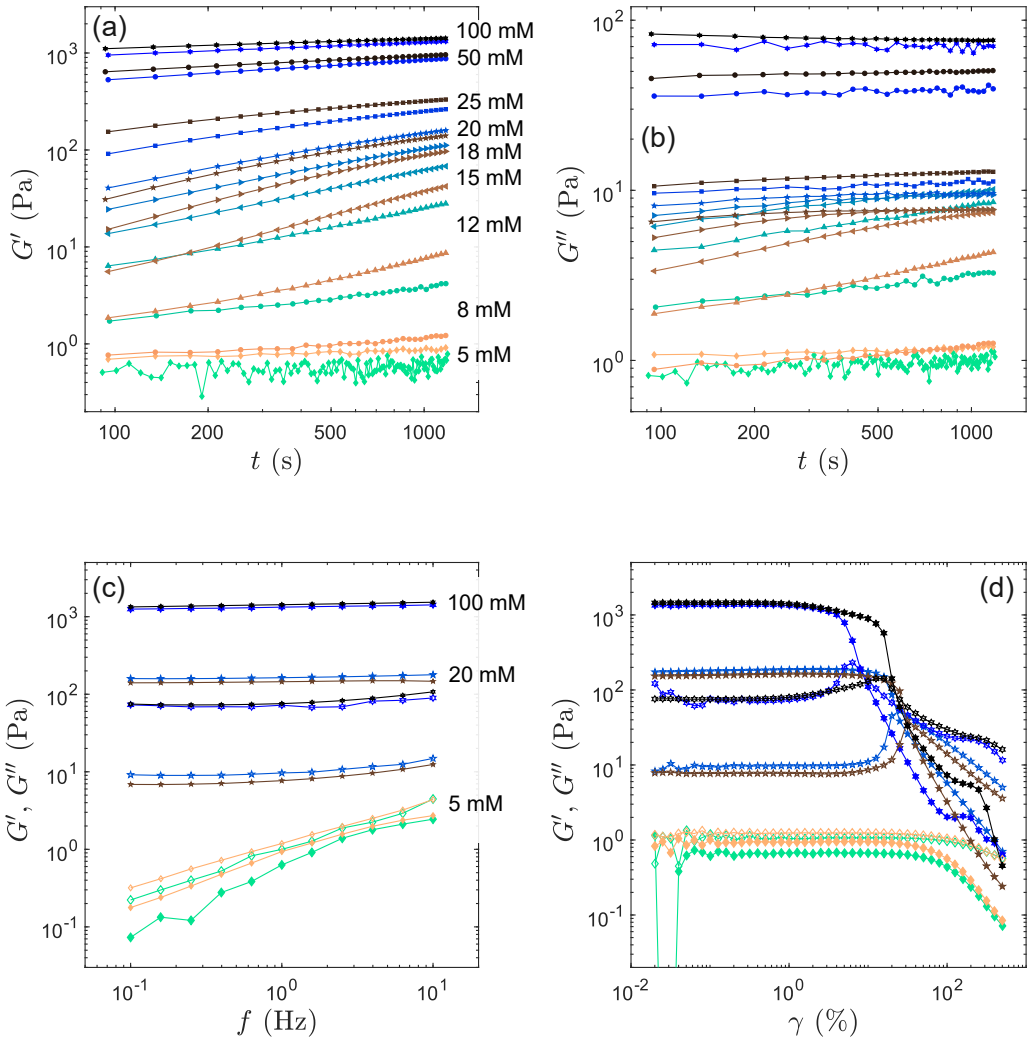

Figure 3.27: Comparison of the rheological properties of CNC suspensions containing 3.2 wt % CNC and various NaCl concentrations, prepared from the commercial suspension using the protocol described in Sec. 2.C (brown colorscale), or prepared from the dried CNCs using the protocol described in this section, by replacing D_2O by H_2O. (a) Elastic modulus and (b) viscous modulus as a function of time during the sample recovery following pre-shear, measured by applying an oscillatory strain signal of amplitude γ = 0.2 % and frequency f = 1 Hz. (c) Elastic modulus (filled symbols) and viscous modulus (empty symbols) as a function of frequency measured following the 1200 s of recovery, by applying an oscillatory strain signal of amplitude γ = 0.2 %. (d) Elastic modulus (filled symbols) and viscous modulus (empty symbols) as a function of strain amplitude measured following the 1200 s of recovery and the frequency sweep measurement, by applying an oscillatory strain signal of frequency f = 1 Hz.

C.2 Calculation of the overlap CNC weight fraction

The CNC weight fraction from which CNCs begin to overlap can be roughly estimated by assimilating CNCs to equivalent spheres of volume:

$$V_{eq} = \frac{4}{3}\pi\left(\frac{L}{2}\right)^3 \tag{3.22}$$

where L is the length of a CNC particle.

Using the random close packing limit, the critical number of CNCs N^*_{CNC} for particles to overlap is given by:

$$0.64 V_{tot} = N^{ov}_{\text{CNC}} \times V_{eq} \tag{3.23}$$

with $V_{tot} = V_{\text{CNC}} + V_w$ the suspension volume. V_{CNC} is the real volume occupied by CNCs, and V_w is the volume of water.

This suspension volume can be written:

$$\begin{aligned} V_{tot} &= \frac{m_{\text{CNC}}}{\rho_{\text{CNC}}} + \frac{m_w}{\rho_w} = \frac{m_{\text{CNC}}(\rho_w - \rho_{\text{CNC}}) + \rho_{\text{CNC}}(m_w + m_{\text{CNC}})}{\rho_w \rho_{\text{CNC}}} \\ &= \frac{N_{\text{CNC}} L\pi(D/2)^2(\rho_w - \rho_{\text{CNC}}) + (m_w + m_{\text{CNC}})}{\rho_w} \end{aligned} \tag{3.24}$$

with ρ_{CNC} the CNC density, ρ_w the water density, m_{CNC} the mass of CNCs in the suspension, m_w the mass of water in the suspension and $L\pi(D/2)^2$ the real volume of a CNC for length L and diameter D.

Combining Eq. (3.23) and Eq. (3.24), we obtain:

$$N^{ov}_{\text{CNC}} = \frac{m_{\text{CNC}} + m_w}{(1/0.64)\rho_w(4/3)\pi(L/2)^3 + L\pi(D/2)^2(\rho_{\text{CNC}} - \rho_w)}, \tag{3.25}$$

leading to the overlap CNC weight fraction w^{ov}_{CNC}:

$$\begin{aligned} w^{ov}_{\text{CNC}} &= \frac{m^{ov}_{\text{CNC}}}{m_{\text{CNC}} + m_w} = \frac{N^{ov}_{\text{CNC}} \rho_{\text{CNC}} L\pi(D/2)^2}{m_{\text{CNC}} + m_w} \\ &= \frac{\rho_{\text{CNC}} D^2}{(1/0.64)\rho_w(4/3)(L^2/2) + D^2(\rho_{\text{CNC}} - \rho_w)}. \end{aligned} \tag{3.26}$$

C.3 Fractional rheological models

As discussed in the main text, we take advantage of fractional mechanical approaches to model the rescaled viscoelastic moduli $\tilde{G}'(\tilde{\omega})$ and $\tilde{G}''(\tilde{\omega})$ of CNC suspensions obtained across the sol-gel transition following flow cessation. Building upon a first spring-pot element ($\mathbb{G}$, β) that accounts for the sample power-law response at the critical gel point, the liquid-like response of the CNC suspension for $t < t_g$ is described by a fractional Maxwell model (see lower sketch in Fig. 2 in the main text) composed of two additional elements in series with the spring-pot ($\mathbb{G}$, β), namely a purely viscous dashpot (defined by its viscosity η) and a second spring-pot ($\mathbb{V}$, α) with $0 < \beta < \alpha < 1$. The corresponding complex viscoelastic modulus reads [Jaishankar and McKinley, 2013]:

$$\tilde{G}^*(\tilde{\omega}) = \tilde{G}'(\tilde{\omega}) + i\tilde{G}''(\tilde{\omega}) = \frac{\mathbb{V}\mathbb{G}\eta(i\tilde{\omega})^{\alpha}}{\mathbb{G}\eta + \mathbb{V}\eta(i\tilde{\omega})^{\alpha-\beta} + \mathbb{V}\mathbb{G}(i\tilde{\omega})^{\alpha-1}}\,. \tag{3.27}$$

Past the gel point, i.e., for $t > t_g$, the solid-like response of the CNC gel is captured by a fractional Kelvin-Voigt model (see upper sketch in Fig. 2 in the main text) composed of the spring-pot ($\mathbb{G}$, β) characterizing the gel point, in parallel with a purely elastic spring (defined by its elastic modulus k) and a second spring-pot ($\mathbb{K}$, ξ) with $0 < \xi < \beta < 1$. The complex viscoelastic modulus for this model reads [Jaishankar and McKinley, 2013]:

$$\tilde{G}^*(\tilde{\omega}) = \tilde{G}'(\tilde{\omega}) + i\tilde{G}''(\tilde{\omega}) = k + \mathbb{G}(i\tilde{\omega})^{\beta} + \mathbb{K}(i\tilde{\omega})^{\xi}\,. \tag{3.28}$$

In order to get more physical insight into these two models, let us examine their large and small-frequency limits. First, at large rescaled frequencies, since $0 < \beta < \alpha < 1$ and $0 < \xi < \beta < 1$, both the fractional Maxwell model and the fractional Kelvin-Voigt model lead to a power-law evolution of the complex viscoelastic modulus with exponent β, $\tilde{G}^*(\tilde{\omega}) = \mathbb{G}(i\tilde{\omega})^{\beta}$, so that $\tilde{G}'(\tilde{\omega}) \sim \tilde{G}''(\tilde{\omega}) \sim \mathbb{G}\tilde{\omega}^{\beta}$. This corresponds to the power-law rheology observed at the critical gel point, i.e., to the frequency-independent plateau of $\tan\delta(\tilde{\omega}) = \beta\pi/2$ at $t = t_g$.

Second, considering the recovery dynamics in the liquid-like state prior to the gel point, the limit of small rescaled frequencies in the fractional Maxwell model corresponds to short times after flow cessation. There, to leading order in $\tilde{\omega} \to 0$, the fractional Maxwell model given by Eq. (3.27) yields a linear, viscous scaling for the viscous modulus, $\tilde{G}'' = \eta\tilde{\omega}$, and a power-law evolution of the elastic modulus, $\tilde{G}' = \frac{\eta^2}{\mathbb{V}}\cos(\alpha\pi/2)\tilde{\omega}^{2-\alpha}$.

Third, by construction of our rescaled data, long times after the gel point, i.e., late rebuilding dynamics of the solid-like state, correspond to the limit of small rescaled frequencies of the fractional Kelvin-Voigt model. For $\tilde{\omega} \to 0$, Eq. (3.28) leads to a frequency-independent elastic modulus, $\tilde{G}' = k$, and to a power-law evolution of the viscous modulus, $\tilde{G}'' = \mathbb{K}\sin(\xi\pi/2)\tilde{\omega}^{\xi}$.

C.4 Parameters for the fits by Maxwell and Kelvin-Voigt fractional models

Table 3.5 shows the parameters used to fit the viscoelastic moduli and $\tan\delta$ master curves, obtained from the time evolution of the viscoelastic spectra, by a fractional Maxwell model for $t < t_g$ and by a Kelvin-Voigt models for $t > t_g$, of aqueous suspensions containing 2 wt %, 3.2 wt % and 5.5 wt % CNC and various NaCl concentrations.

Table 3.5: Parameters of the fractional Maxwell and Kelvin-Voigt models used to fit the viscoelastic moduli and tan δ master curves obtained from the time evolution of the viscoelastic spectra during the recovery following a strong shear of aqueous suspensions containing 2 wt %, 3.2 wt % and 5.5 wt % CNC and various NaCl concentrations. The constraint of imposing the prefactor $\mathbb{G}$, associated to the exponent β, to keep the same value in both models, on both sides of the gel point, has been relaxed for w_{CNC} = 3.2 wt %.

w_{CNC}	[NaCl]	t_g (s)	η	$\mathbb{V}$	α	$\mathbb{G}$ ($t < t_g$)	$\mathbb{G}$ ($t > t_g$)	β	$\mathbb{K}$	ξ	k
2 wt% CNC	12 mM NaCl	8888	0.17	0.13	0.68	0.54		0.33	2.40	0.20	3.00
2 wt% CNC	13.5 mM NaCl	3939	1.00	0.19	0.60	0.35		0.29	0.60	0.18	0.49
2 wt% CNC	15 mM NaCl	1818	0.13	0.14	0.63	0.95		0.30	5.40	0.23	17.00
2 wt% CNC	16.5 mM NaCl	985	0.15	0.14	0.60	1.10		0.29	3.00	0.20	8.00
2 wt% CNC	18 mM NaCl	415	0.23	0.14	0.63	1.21		0.30	5.90	0.19	12.00
2 wt% CNC	20 mM NaCl	193	0.52	0.34	0.59	0.85		0.29	2.90	0.18	4.60
2 wt% CNC	22 mM NaCl	75	0.52	11410	0.70	0.40		0.32	1.10	0.20	0.32
3.2 wt% CNC	9 mM NaCl	8824	0.44	0.34	0.58	3.79		0.28	16.80	0.24	300.00
3.2 wt% CNC	10 mM NaCl	4334	1.00	0.40	0.58	4.50		0.30	0.16	0.19	38.11
3.2 wt% CNC	12 mM NaCl	1330	0.69	0.51	0.53	3.50		0.25	25.70	0.17	29.41
3.2 wt% CNC	14 mM NaCl	512	0.67	1.14	0.47	22.40		0.23	9.50	0.12	7.13
3.2 wt% CNC	16 mM NaCl	239	2.40	2.03	0.46	17.40		0.23	9.95	0.13	6.50
3.2 wt% CNC	18 mM NaCl	90	2.50	2.27	0.48	3.63		0.23	19.50	0.13	20.00
5.5 wt% CNC	5 mM NaCl	7306	0.28	0.64	0.51	189	189	0.23	3.03×10^4	0.18	2.58×10^6
5.5 wt% CNC	5.5 mM NaCl	6963	N.A.	N.A.	N.A.	N.A.	N.A.	N.A.	N.A.	N.A.	N.A.
5.5 wt% CNC	6 mM NaCl	3735	0.33	0.32	0.57	14.50	95.80	0.26	1.93×103	0.15	4.00×10^3
5.5 wt% CNC	6.5 mM NaCl	2059	1.20	0.30	0.60	11.00	113.00	0.27	5422	0.16	2.51×10^4
5.5 wt% CNC	7 mM NaCl	505	5.79×10^3	2.00	0.78	0.52	1.90	0.36	5.21	0.17	0.23

CHAPTER

4

SHEAR-INDUCED YIELDING AND FLOW

Contents

In the previous chapter, we have studied the rheological properties of CNC suspensions in the presence of salt in the linear regime of deformation. More precisely, we have extracted two characteristic times from the recovery dynamics following a strong shear, namely the G'-G'' crossover time t_c and the gelation time t_g, which were used to rationalize the time evolution of the viscoelastic properties during the suspension reconstruction.

In this chapter, we focus on the rheological behavior of CNC suspensions in the non-linear regime of deformation. In particular, we study how CNC suspensions yield and flow under shear, and how such properties are related to the characteristic times determined in the previous chapter. There are several ways of studying the solid-to-liquid transition in a soft material. We begin by studying the flow properties of CNC gels by measuring their flow curve through ramping up and down in shear rate. Then, we focus on two experimental techniques to study the solid-to-liquid transition: (i) by performing shear start up experiments consisting on applying a constant shear rate from rest, (ii) by performing LAOS measurements, consisting on applying an oscillatory strain of increasing amplitude.

In the first section, Sec. 4.A, we show that CNC suspensions present complex flow curves, with the presence of an hysteresis when ramping down and up in shear rate, which are the signature of a complex flowing scenario. From the flow curves, we show that the viscosity of a CNC suspension increases with the salt concentration, or equivalently with a decreasing gelation time. The viscosity saturates both at small and large salt concentration, corresponding respectively to the limit with no salt, and to the limit where all the accessible CNC surface charges are screened, as reported in the previous chapter. Finally, this measurement being a transient measurement, we show that the shape of the flow curves strongly depends on the measurement time. In particular, we show that the hysteresis area presents a maximum at a given measurement time interval, which is characteristic of time-dependent fluids. Such a hysteresis is due to a competition between the suspension reconstruction and its failure under shear.

In Sec. 4.B, using shear start up experiments, we evidence a stress overshoot, as introduce in Sec. 1.B.3 in the Introduction, when increasing strain by continuously shearing a CNC suspension. This overshoot is associated with a brittle-like to ductile-like yielding transition in CNC suspensions upon varying the applied shear rate or the sample age at the beginning of shear. By varying the suspension composition, and using its gelation time t_g, we highlight some universality in the yielding behavior of CNC suspensions. Finally, we show that for the suspensions with the largest salt concentration, memory effects, most likely due to CNCs orientation in the direction of shear, affect its yielding transition.

Some insight into the local fluidization scenario for both types of experiments is given in Sec. 4.C using ultrasound velocimetry. In particular, we evidence the development of a shear band during the flow curves measurements, and the existence of an elastic recoil during the suspension yielding, in the case of a brittle-like failure.

Finally, in Sec. 4.D, instead of applying a continuous shear, we study yielding of CNC suspensions using LAOS measurements. In particular, we evidence an overshoot of the viscous modulus near the yield point. Interestingly, the amplitude of this overshoot evolves non-monotonically with the salt concentration, with a maximum reached for a composition coinciding with the inflection point on the $G(\tilde{t})$ master curve presented in Sec. 3.A.3. Varying the suspension composition, we highlight a robustness of the yielding transition behavior of CNC suspensions under LAOS, which extends the generalized time-composition superposition principles established in the first chapter for the suspensions recovery dynamics, to the non-linear regime of deformation.

A Flow behavior under ramps of shear rate

In this section, we study the flow behavior of CNC suspensions by applying steps of shear rates of given duration, ramping down and up in amplitude. From the stress response to the various shear rates, we plot the suspensions flow curves $\sigma(\dot{\gamma})$. Such flow curves result from inherently out-of-

equilibrium and transient measurements. Such measurements are the most commonly used to characterize the flow behavior of a soft material.

A.1 Rheological protocol

To perform such measurements, we have used the stress-controlled rheometer (MCR 302, Anton Paar), equipped with a cone-and-plate geometry. The cone is sand-blasted, with a surface roughness of 30 μm as provided by the manufacturer, in order to avoid slip of the sample on its surface. It has a 40.0 mm diameter, a 2° angle, and a 176.0 μm truncation. The smooth plate is connected to a Peltier module, which controls the sample temperature to $T = 23.0 \pm 0.1$ °C for all the experiments described in this section. In order to avoid evaporation, we use a home-made solvent trap made of a Plexiglas cylindrical dome covering the geometry, and we saturate the atmosphere surrounding the sample with water.

The flow curves are measured in the last two steps of the rheological protocol detailed below[1], following the first four steps used to study the recovery dynamics of CNC suspensions, presented in Sec. 3.A.

(1) We strongly shear the sample in order to fully fluidize it and break down its microstructure by imposing a shear rate $\dot{\gamma} = 500\ \mathrm{s}^{-1}$ during 20 s. This pre-shear step allows us to obtain a reproducible initial state by minimizing the influence of previous mechanical history, including the loading of the sample into the shear cell.

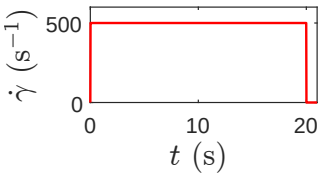

(2) The pre-shear is stopped abruptly by setting $\dot{\gamma} = 0$ and we subsequently measure the linear viscoelastic moduli, i.e., the elastic modulus G' and the viscous modulus G'', every second for 1200 s by imposing small-amplitude oscillatory shear (SAOS) with a strain amplitude $\gamma = 0.2$ % at a frequency $f = \omega/2\pi = 1$ Hz.

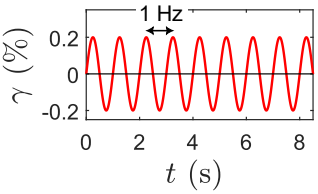

(3) The viscoelastic spectrum G' and G'' versus f is measured 1200 s after cessation of shear through a SAOS measurement, consisting of applying an oscillatory strain signal of amplitude $\gamma = 0.2$ % and sweeping down logarithmically the frequency f from 10 Hz to 0.1 Hz with 5 points per decade over a total duration of 270 s. Each frequency is applied for six periods, and the recorded data are averaged over the five last periods.

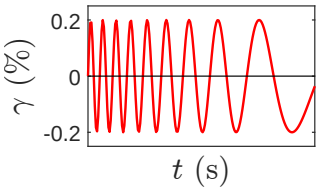

(4) Starting 1470 s following shear cessation, we determine the yielding properties of the sample through a large-amplitude oscillatory shear (LAOS) measurement, consisting in sweeping up logarithmically the oscillatory strain amplitude from $\gamma = 0.02$ % to 500 % at $f = 1$ Hz, with 10 points per decade and a waiting time of 18 s per point, leading to a total duration of 790 s. For each strain amplitude, the recorded data are averaged over the last 9 s of application of the given strain amplitude.

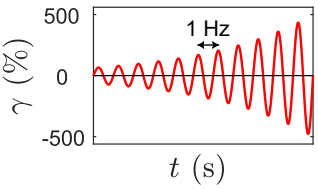

[1] In this protocol, we have not pre-sheared our sample right before measuring the flow curve. Therefore, the first two points measured in the flow curves at $\dot{\gamma} = 500\ \mathrm{s}^{-1}$ and $400\ \mathrm{s}^{-1}$ might be biased due to the transient flow initiation.

(5) We apply steps of continuous shear rate of amplitude decreasing logarithmically from $\dot{\gamma}$ = 500 s^{-1} to $\dot{\gamma}$ = 0.005 s^{-1}, with 10 points per decade. For each step of $\dot{\gamma}$, the constant shear rate is applied during a time interval δt. For all the experiments, δt = 10 s, resulting in a total duration of 510 s for this ramping down phase, except for the set of experiments presented in Sec. 4.A.3 for which δt is varied between 1 s and 60 s. The recorded data are averaged over the last 5 s of application of each shear rate step, except for the experiments with δt < 10 s. In this case, the recorded data are averaged over the last $\delta t/2$ seconds of application of each shear rate step.

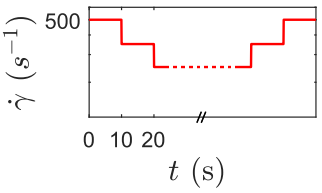

(6) We then apply steps of continuous shear rate of amplitude increasing logarithmically from $\dot{\gamma}$ = 0.005 s^{-1} to $\dot{\gamma}$ = 500 s^{-1}, with 10 points per decade. Each shear rate $\dot{\gamma}$ is applied during the same time interval δt as in step (5), with the same conditions of data recording.

A.2 General phenomenology

a Flow curves at various NaCl concentrations

Figure 4.2 presents the flow curves measured for suspensions containing 3.2 wt % CNC and various NaCl concentrations ranging from 5 mM to 240 mM. Strikingly, the shape of those flow curves depends strongly on the NaCl concentration. First, we note that a hysteresis appears when ramping down and up in shear rate for suspensions containing more than 5 mM NaCl. While the stress response when ramping up σ_{up} presents larger values than the stress measured when ramping down σ_{down} over the whole range of shear rates for suspensions at small salt concentrations, the reverse is observed at small shear rates, for $\dot{\gamma} \leq 0.15\ s^{-1}$, for the suspension containing 20 mM NaCl [see Fig. 4.2(e)]. This transition from $\sigma_{up} > \sigma_{down}$ to $\sigma_{up} < \sigma_{down}$ shifts towards larger shear rates when increasing the salt content, until a point where σ_{up} remains smaller than σ_{down} for all shear rates, as observed for suspensions containing 50 and 240 mM NaCl [see Figs. 4.2(g) and (h)]. Second, we observe that while the flow curves are monotonic at small salt content upon ramping down in shear rate, non-monotonic behaviors appear for [NaCl]= 20 mM and 25 mM [see Figs. 4.2(e) and (f)]. Above this concentration, the shapes of the stress responses are very different, which might be due to partial slip of the sample near the geometries surfaces, preventing us from shearing the bulk of the sample at the target shear rate, which may affect the stress response [Cloitre and Bonnecaze, 2017]. When ramping up in shear rate, non-monotonicity in the stress response appears at salt concentrations smaller than when ramping down, for [NaCl]≥ 18 mM NaCl [see Fig. 4.2(d)]. The development of such non-monotonic behaviors are the signature of the various complex mechanisms that can occur during the solid to liquid transition along the upward sweep, including the presence of lubrication layers leading to wall slip, the development of shear bands where part of the material is sheared while the rest of the sample remains solid, and the interplay with viscoelasticity under the form of a stress overshoot (see Sec. 4.B and Sec. 1.B.3 in the Introduction) [Radhakrishnan et al., 2017, Puisto et al., 2015, Bonn et al., 2017, Divoux et al., 2016].

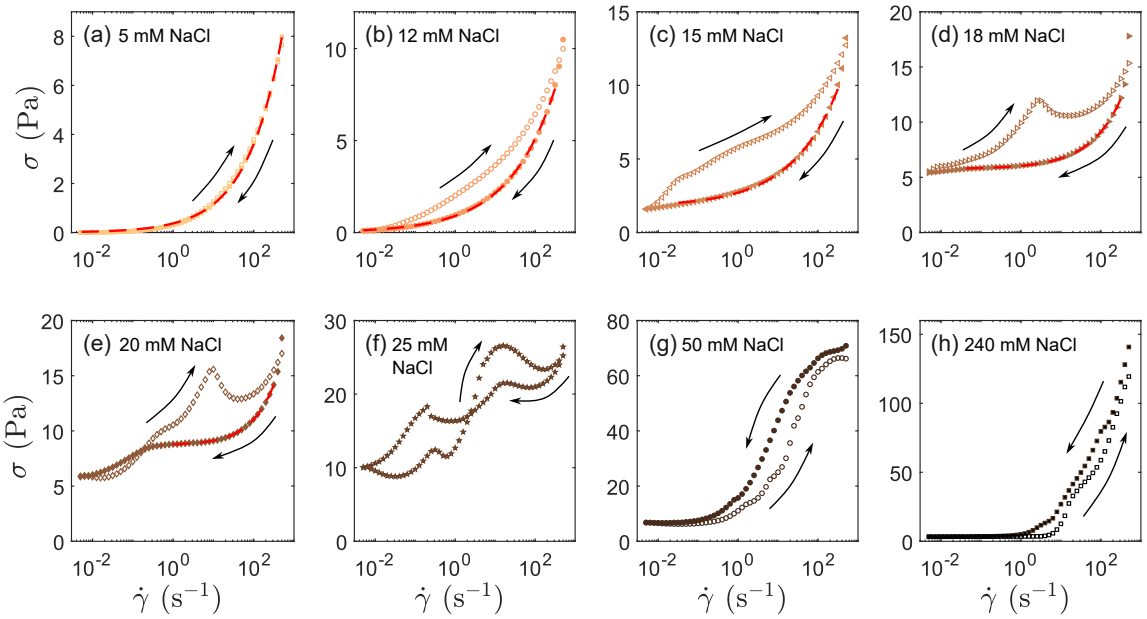

Figure 4.2: Stress as a function of the applied shear rate when ramping down (filled symbols) and then up (empty symbols). Flow curves measured using the rheological protocol described in Sec. 4.A.1 on suspensions containing 3.2 wt % CNC and 5, 12, 15, 18, 20, 25, 50, 240 mM NaCl. The red dashed lines show the best fit of the data with an Herschel-Bulkley model, whose parameters are reported in Table 4.1. See Sec. 4.A.1 for the detailed rheological protocol.

Herschel-Bulkley Model

Empirical model accounting for the stress response of a non-Newtonian fluid to the application of shear.

$$\sigma = \sigma_c + K\dot{\gamma}^n \tag{4.1}$$

- If $n = 1$ and $\sigma_c = 0 \Rightarrow$ Simple Newtonian fluid: $\sigma = \eta\dot{\gamma}$, with $K = \eta$.
- If $\sigma_c = 0 \Rightarrow$ Ostwald model.
- If $n > 1 \Rightarrow$ Shear-thickening fluid.
- If $n < 1 \Rightarrow$ Shear-thinning fluid.

At small salt concentration, for smooth flow curves presenting no non-monotonic stress response when ramping down in shear rate, i.e., for suspensions containing less than 20 mM NaCl, we can fit the stress versus shear rate data by a Herschel-Bulkley model given by Eq. (4.1), where σ_c is the yield stress and represents the minimum amount of stress that needs to be applied to the sample in order to fluidize it, K is a consistency index and n is a dimensionless exponent.

The resulting fits are represented by the red dashed lines in Fig. 4.2(a)-(d), and the corresponding parameters are reported in Table 4.1. We note that for the suspensions containing 5 mM to 12 mM NaCl, we recover the Ostwald model for which $\sigma_c = 0$, and which characterizes the flow behavior of shear-thinning ($n < 1$) power-law fluids. Above 12 mM NaCl, the simple power-law evolution of σ with $\dot{\gamma}$ is incomplete: a stress threshold appears and needs to be added to the power-law evolution, leading to the Herschel-Bulkley model. The existence of such a stress threshold results from the solid-like behavior of the suspension at rest (or at vanishing small shear rates). In fact, in the presence of salt, CNCs form aggregates. At large shear rates, most of those aggregates are broken down and the suspension of well dispersed individual particles is a liquid

Table 4.1: Parameters for the fits of the flow curves plotted in Figs. 4.2(a)-(d) by a Herschel-Bulkley model, when it is relevant. Suspensions containing 3.2 wt % CNC and various NaCl concentrations [2].

[NaCl] (mM)	σ_c (Pa)	K (Pa.s^n)	n
5	0	0.37	0.49
8	0	0.34	0.49
12	3.3×10^{-3}	0.90	0.38
15	1.8	0.96	0.37
18	5.8	0.26	0.55
20	8.7	0.08	0.74

that flows under shear. As the shear rate decreases, the CNC aggregates reform and induce a resilience to flowing, leading to a non-zero measured stress when the shear rate tends to zero. In agreement with this statement, we observe that such a yield stress σ_c is observed only for suspensions whose gelation time t_g is shorter than the total duration of the ramping down phase of the protocol (step (5)), i.e., for suspensions with a recovery dynamics that would be fast enough to form a percolated network of CNC particles at rest, over the 510 s of measurement. Interestingly, we do not observe any yield stress for suspensions whose G'-G'' crossover time t_c is shorter than the total duration of 510 s of the ramping down phase. For example, the suspension containing 12 mM NaCl has a crossover time $t_c = 96 < 510$ s and $\sigma_c = 0$. This result indicates that even if the suspension is in a solid-like state with $G' > G''$, the inter-particle bonds already formed are not sufficient to prevent the suspension from flowing even at very small shear rate. Moreover, we observe that the exponent n is always smaller than one. Therefore, we deduce that a CNC suspension behaves like a power-law shear-thinning fluid as long as no percolated network is formed.

Finally, we observe that the yield stress σ_c increases with the salt concentration. This result is consistent with the measurements of the viscoelastic moduli at rest presented in Sec. 3.A.3, and indicating that at a given point in time, the larger the salt concentration, the larger the suspension elastic modulus G', hence the more "solid" the suspension.

b Viscosity at fixed shear rate for various suspension compositions

Because of the complex shapes of the flow curves at intermediate to large salt concentrations, from which we cannot extract properly the yield stress σ_c, we have chosen to consider another parameter to quantify the sample flowing properties depending on its composition: the viscosity $\eta = \sigma/\dot{\gamma}$ extracted from the flow curves, for $\dot{\gamma} = 10$ s^{-1} and for $\dot{\gamma} = 100$ s^{-1}. For both shear rates, the viscosity value results from an average over the last 5 s of application of $\dot{\gamma}$.

Figure 4.3 shows the results for suspensions containing 3.2 wt % CNC and various NaCl concentrations. As expected from the measurements of the viscous modulus G'' as a function of time reported in Fig. 3.5, the viscosity of the suspension increases with the salt concentration. Interestingly, at both shear rates, the viscosity seems to plateau for [NaCl]$\geq$ 50 mM, coinciding with the plateau observed in the previous chapter for τ or $t^\star = t_g$ versus [NaCl] [see inset of Fig. 3.4(b) and orange points in Figs. 3.7(c) and (d)]. Moreover, we observe that, for both shear rates, the viscosity of the suspension with the smallest salt concentration, i.e., [NaCl]=5 mM, is much larger than the viscosity of a suspension with the same CNC content and containing no salt: about four times larger for $\dot{\gamma} = 10$ s^{-1}, and about twice larger for $\dot{\gamma} = 100$ s^{-1} (see the horizontal gray dashed lines in Fig. 4.3). Now that we have verified that both the viscosity measured at $\dot{\gamma} = 10$ s^{-1} and the one measured at $\dot{\gamma} = 100$ s^{-1} behave similarly when varying the salt content, and considering the

[2] The flow curve for the suspension containing 3.2 wt % CNC and 8 mM NaCl is not represented in Fig. 4.2. It is very similar to the one measured for the suspension containing 5 mM NaCl plotted in Fig. 4.2(a)

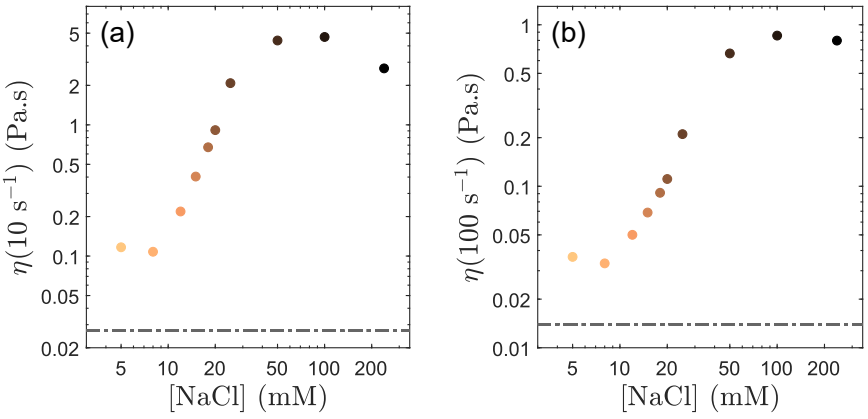

Figure 4.3: Viscosity extracted from the flow curves for a shear rate (a) $\dot{\gamma} = 10\ \mathrm{s}^{-1}$ and (b) $\dot{\gamma} = 100\ \mathrm{s}^{-1}$ as a function of the NaCl concentration in CNC suspensions containing 3.2 wt % CNC. The horizontal dashed lines show the viscosity extracted from the flow curve of a suspension containing 3.2 wt % CNC, without any salt, for a shear rate (a) $\dot{\gamma} = 10\ \mathrm{s}^{-1}$ and (b) $\dot{\gamma} = 100\ \mathrm{s}^{-1}$.

complex behaviors that occur at small shear rates (see the flow curves presented in Fig. 4.2), we will consider only the viscosity measured at $\dot{\gamma} = 100\ \mathrm{s}^{-1}$ in the following.

Figure 4.4 compares the value of the viscosity extracted from the flow curves for $\dot{\gamma} = 100\ \mathrm{s}^{-1}$, averaged over the last 5 s of the corresponding shear step, for suspensions of various compositions. Once again, we observe a plateau of the viscosity at short gelation times, or equivalently at large salt concentrations, coinciding with the plateau observed for $t^* = t_g$ versus I in the previous chapter [see Figs. 3.7(c) and (d) and 3.10(b)]. This observation suggests that once all the accessible CNC surface charges are screened by the salt cations, further addition of salt does not modify the flow behavior of the suspension, and hence its viscosity.

Furthermore, as observed for $t^* = t_g$ versus I, the viscosity of suspensions containing different salt cations all collapse remarkably well onto a single curve when plotted as a function of the gelation time [see Fig. 4.4(a)]. Interestingly, besides the plateau at short gelation times, corresponding to large salt concentrations, a second plateau at small viscosity and long gelation time seems to appear. This second plateau corresponds to the regime where CNCs are mostly in the form of well dispersed individual colloids due to the small amount of salt cations which cannot effectively screen the CNCs surface charges and lead to the formation of aggregates. At $t_g \to \infty$, i.e., $[\mathrm{salt}] \to 0$, the viscosity $\eta(100\ \mathrm{s}^{-1})$ should reach the viscosity of a CNC suspension containing the same CNC weight fraction $w_{\mathrm{CNC}} = 3.2$ wt % and no salt, highlighted by the horizontal dashed line in Fig. 4.4(a). We observe that the smallest value of $\eta(100\ \mathrm{s}^{-1})$ that we record, for suspensions containing 5 mM NaCl or KCl, is about twice larger than the limit value of $\eta(100\ \mathrm{s}^{-1})$ without any salt. This comparison attests that only a very small amount of salt has a great influence on the suspension viscosity.

When varying the CNC weight fraction, the data are more scattered and seem to deviate from a general master curve as the gelation time increases, corresponding to a decreasing NaCl concentration [see Fig. 4.4(b) and (c)]. This is due to the fact that the viscosity of a CNC suspension without any salt is larger for an increased CNC concentration, as highlighted by the horizontal dashed lines in Fig. 4.4(b). Indeed, at $\dot{\gamma} = 100\ \mathrm{s}^{-1}$, the viscosity of a suspension containing 4.8 wt % CNC without any salt is about three times larger than the viscosity of a suspension containing 3.2 wt % CNC without any salt. This result is consistent with the fact that an increased number of CNC particles induces more drag.

Similarly to what we have done in the previous chapter, we can also change the solvent nature

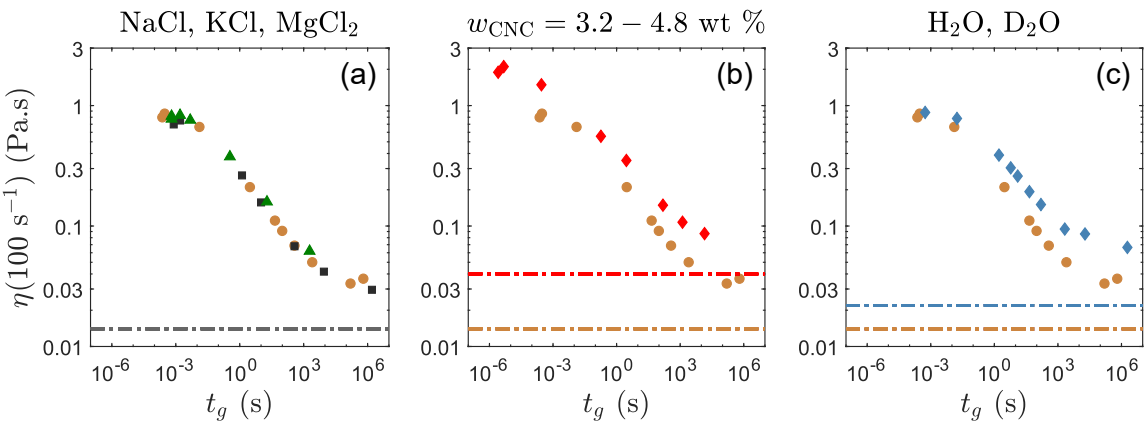

Figure 4.4: Viscosity extracted from the flow curves for a shear rate $\dot{\gamma} = 100\ s^{-1}$ as a function of the gelation time for suspensions of various composition. (a) Variation of the salt cation: suspensions containing 3.2 wt % CNC and and various concentrations of NaCl (orange •), KCl (black ■) or $MgCl_2$ (green ▲). The horizontal dashed line shows the viscosity extracted from the flow curve of a suspension containing 3.2 wt % CNC, without any salt, for a shear rate $\dot{\gamma} = 100\ s^{-1}$. (b) Variation of the CNC weight fraction: suspensions containing 3.2 wt % CNC (orange •) or 4.8 wt % CNC (red ⧫) and various NaCl concentrations. The horizontal dashed lines show the viscosity extracted from the flow curve of suspensions containing 3.2 wt % CNC (orange) and 4.8 wt % CNC (red) respectively, without any salt, for a shear rate $\dot{\gamma} = 100\ s^{-1}$. (c) Variation of the solvent nature: suspensions containing 3.2 wt % CNC and various NaCl concentrations, dispersed in H_2O (orange •) or D_2O (blue ⧫). The horizontal dashed lines show the viscosity extracted from the flow curve of suspensions containing 3.2 wt % CNC dispersed in H_2O (orange) and in D_2O (blue) respectively, without any salt, for a shear rate $\dot{\gamma} = 100\ s^{-1}$.

in order to vary the inter-particle interactions. When switching from hydrogenated to deuterated water [see Fig. 4.4(c)], the data do not collapse onto a general master curve, as also reported for $t^* = t_g$ versus [NaCl] in the previous chapter [see Fig. 3.10(b)]. Moreover, the plateau at long t_g seems to shift towards larger viscosity, what cannot be simply explained by a larger viscosity of D_2O, which is only 0.25 mPa.s larger than the one of water at 20°C ($\eta_{D_2O} = 1.25$ mPa.s, compared to $\eta_{H_2O} = 1.00$ mPa.s). Indeed, at $\dot{\gamma} = 100\ s^{-1}$, the viscosity of a suspension containing 3.2 wt % CNC dispersed in D_2O without any salt is about 1.6 times larger than the one of a similar suspension with H_2O [see the horizontal dashed lines in Fig. 4.4(c)]. This difference of viscosity is consistent with the one measured for the two suspensions containing 5 mM NaCl, dispersed in D_2O and in H_2O. Those results suggest once again that D_2O induces inter-particle interactions or a CNC organization that is different from the one induced by H_2O.

A.3 Effect of the ramping rate

The flow curves presented above are intrinsically measured in the transient regime. Indeed, we have arbitrarily chosen to apply each shear rate value during a time interval $\delta t = 10$ s, as detailed in the rheological protocol presented in Sec. 4.A.1. In this section, we focus on how the time interval δt impacts the flow curves and therefore our estimation of the flow properties of CNC suspensions.

To do so, we consider a suspension containing 3.2 wt % CNC and 15 mM NaCl for which the flow curve presents an hysteresis, yet with a monotonic downward response. We repeat the same rheological protocol as the one described in Sec. 4.A.1 by varying the time interval δt during which we apply each shear rate step. The values for the time interval δt are varied in a random order

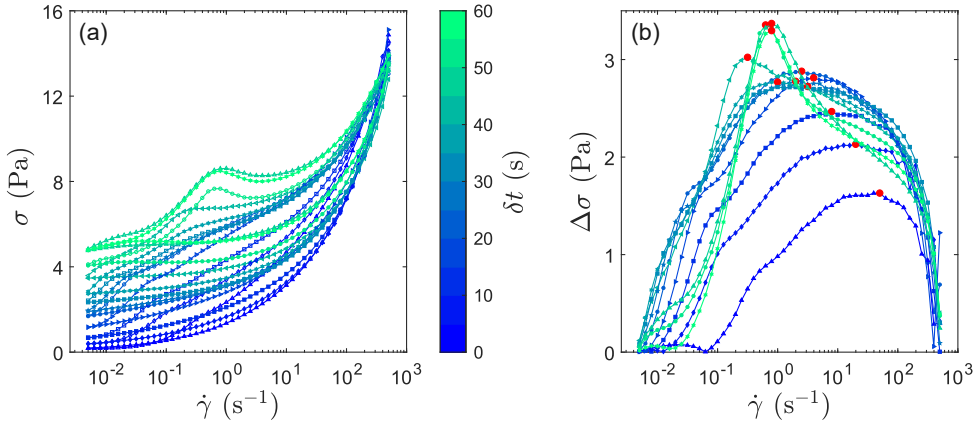

Figure 4.5: (a) Stress as a function of the applied shear rate when ramping down (filled symbols) and up (open symbols), with δt = 1 s (blue) to 60 s (green). (b) Stress difference between the ramping up and the ramping down response as a function of the shear rate for the various δt. The red dots highlight the maximum of $\Delta\sigma$, of coordinates $(\max(\Delta\sigma), \dot{\gamma}_m)$. Experiments performed on a suspension containing 3.2 wt % CNC and 15 mM NaCl.

between 1 s and 60 s in order to minimize the effects of a potential drift of the material properties due to successive repetitions of the protocol on a single loading. In between each repetition of the protocol, we let the sample recover during 180 s while measuring its viscoelastic properties in order to detect the appearance of drying effects.

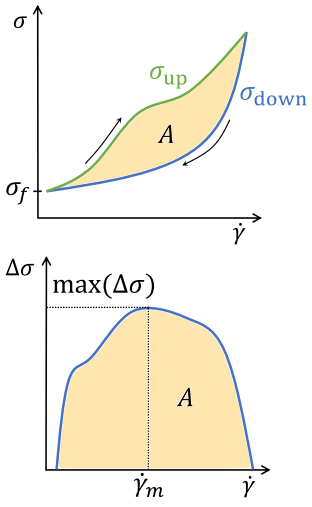

Figure 4.5(a) presents the resulting flow curves. We observe that the shape of the flow curves is significantly influenced by δt. First, we note that while the stress responses at large shear rates are superimposed, the stress measured at the smallest shear rate $\sigma_f = \sigma(\dot{\gamma} = 0.005\ \mathrm{s}^{-1})$ increases with δt, indicating an increase of the suspension dynamic yield stress. This observation is consistent with the fact that for long δt, the suspension has more time to rebuild under shear, leading to a more solid-like behavior which requires a larger stress to break and fluidize. However, a suspension can rebuild under shear only at small enough shear rate, when CNCs have enough time to re-arrange in response to the induced deformation. Therefore, this time-dependent effect is not present at large shear rates, hence the superposition of the data. The values of σ_f are plotted in Fig. 4.7(a) as a function of δt. We observe that σ_f increases as a power-law of exponent 0.82. Second, we note that while the stress response when decreasing the shear rate keeps a similar monotonic shape when varying δt, the stress response when increasing the shear rate is widely impacted by δt. Indeed, the response becomes non-monotonic at large δt with the development of a stress maximum at intermediate shear rates. Changes in the flow curves shape is easier to capture by getting rid of the variations of the yield stress, i.e., by considering the stress difference $\Delta\sigma$ between the ramping up and the ramping down responses:

$$\Delta\sigma(\dot{\gamma}) = \sigma_{\mathrm{up}}(\dot{\gamma}) - \sigma_{\mathrm{down}}(\dot{\gamma}) \tag{4.2}$$

as plotted in Fig. 4.5(b). First, we note that $\Delta\sigma$ always presents a maximum which becomes sharper when increasing δt, and which amplitude and position vary with δt. Furthermore, we observe that the difference between the ramping up and the ramping down responses increases with δt until δt = 10 s. From δt = 10 s to δt = 25 s, we observe no significant difference in $\Delta\sigma(\dot{\gamma})$. For δt = 30 s,

the shape of $\Delta\sigma(\dot{\gamma})$ changes and we observe the development of a sharp maximum for $\Delta\sigma$ which corresponds to the appearance of a local stress maximum in the σ vs $\dot{\gamma}$ response when ramping up in $\dot{\gamma}$. For $\delta t > 30$ s, we observe no strong impact of δt on the difference between the ramping up and the ramping down responses anymore.

In order to quantify the effect of δt on the difference of the stress responses when ramping up or down in shear rate, we have plotted the hysteresis area A defined as [Divoux et al., 2013]:

$$A = \int_{\dot{\gamma}_{\min}}^{\dot{\gamma}_{\max}} \Delta\sigma(\dot{\gamma})\, d(\log\dot{\gamma}) \tag{4.3}$$

as well as the coordinates $(\dot{\gamma}_m, \max(\Delta\sigma))$ of the maximum of $\Delta\sigma(\dot{\gamma})$ as a function of δt in Fig. 4.7(b), (c) and (d) respectively. The hysteresis area presents a maximum reached for $\delta t = \delta t^* \approx 15$ s. Interestingly, this characteristic time δt^* coincides with the crossover time $t_c \approx 13$ s of this suspension, containing 3.2 wt % CNC and 15 mM NaCl, while the total experimental time of 765 s for ramping down in shear rate at δt^* is about twice the gelation time $t_g \approx 370$ s. Such a non-monotonic behavior has already been reported in Carbopol microgels, suspensions of carbon black particles, and suspensions of disk-like clay particles of Laponite [Divoux et al., 2013]. Numerical modeling of yield stress fluids has shown that such a non-monotonic evolution of the hysteresis area A is characteristic of time-dependent fluids and emerges with the development of shear bands, due to a competition between the suspension reconstruction and its failure under shear [Radhakrishnan et al., 2017]. In fact, over the interval time δt during which shear is applied, the suspension may reconstruct. This reconstruction being more "efficient" at small shear rate, where the suspension failure is less pronounced, the state of the sample and therefore its properties are different when ramping down or up in shear rate. This difference gets more pronounced at longer δt, as the sample has more time to reconstruct, hence the increase of the hysteresis area A. However, at large δt, the sample properties are measured in a quasi-static state at every shear step, resulting in a reduced influence of the sweeping direction. At very large δt, the sweeping down and the sweeping up responses should eventually superimpose so that A should tend to zero, if no other effects come into play, such as CNCs alignment under shear.

While the hysteresis area evolves non-monotonically with the time interval δt during which each step shear is applied, both coordinates of the $\Delta\sigma(\dot{\gamma})$ maximum present a strong monotonic dependence on δt. On the one hand, the position of this maximum $\dot{\gamma}_m$ is proportional to $1/\delta t$, as highlighted by the constant value of $\dot{\gamma}_m \times \delta t$ and by the fit of $\dot{\gamma}_m$ versus δt with a power-law of exponent -1 [see inset of Fig. 4.7(c)]. This observation suggests that, the ramping rate $1/\delta t$ sets a characteristic shear rate $\dot{\gamma}_m = 37/\delta t$, where the interplay between sample reconstruction and failure under shear is "optimum", i.e., $\Delta\sigma$ is maximum. Moreover, the amplitude of the maximum of the stress difference $\max(\Delta\sigma)$ increases with δt. In first approximation, this increase can be captured by a logarithmic law of prefactor 0.90 Pa. Overall, the power-law decrease of $\dot{\gamma}_m$ combined with the logarithmic increase of $\max(\Delta\sigma)$ leads to the bell-shaped curve for the hysteresis area A versus δt, with a maximum at δt^*. A better understanding of the various features of the hysteresis area, including the location of the maximum of the stress difference, requires both local measurements of the velocity field in the bulk material (see Sec. 4.C.1), and further modeling [Radhakrishnan et al., 2017].

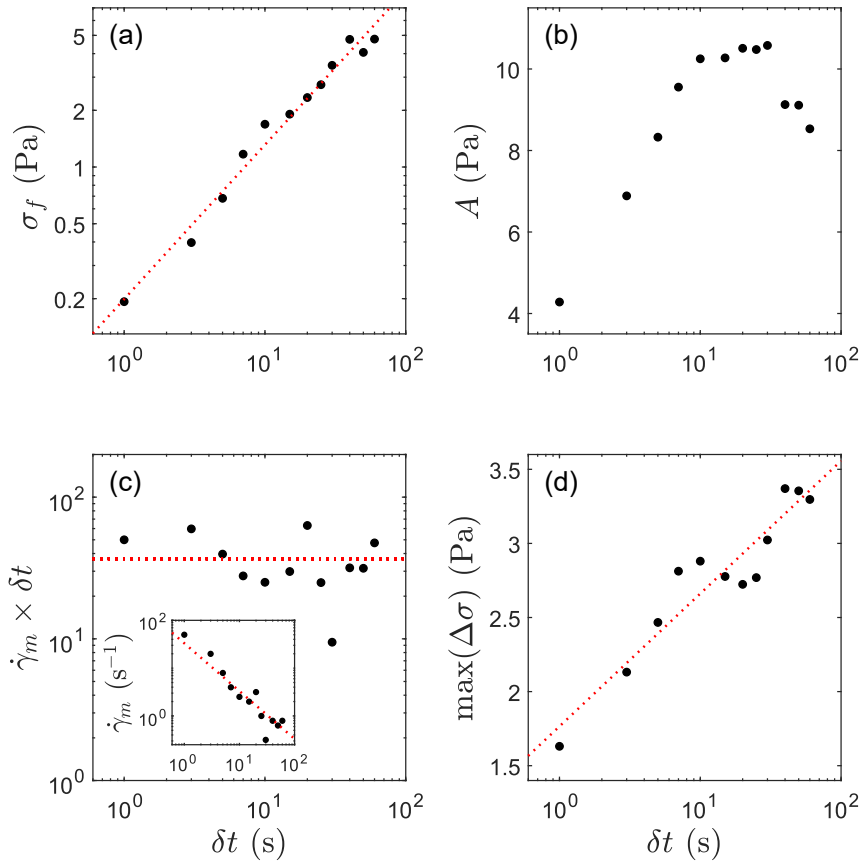

Figure 4.7: Parameters extracted from the flow curves measured at various δt. (a) Stress σ_f measured at the smallest shear rate $\dot{\gamma}$ = 0.005 $^{-1}$ as a function of the measuring time per shear step δt. The red dashed line represents the best power-law fit of the data with a power-law of exponent 0.82. (b) Hysteresis area A as a function of δt. (c) Product of the shear rate $\dot{\gamma}_m$ corresponding to the position of the maximum of $\Delta\sigma$ versus $\dot{\gamma}$ with the interval time δt as a function of δt. The horizontal red dashed line shows the mean value of $\dot{\gamma}_m \times \delta t$ over the range of δt. Inset: Position $\dot{\gamma}_m$ of the $\Delta\sigma$ maximum versus δt. The red dashed line shows the best fit of the data with a power-law of exponent set to −1. (d) Amplitude of the maximum of $\Delta\sigma$ versus $\dot{\gamma}$ as a function of δt. The red dashed line show the best fit of the data with a logarithmic law of prefactor 0.90 Pa.

(1) CNC suspensions present complex flow curves:

- presence of a yield stress
- hysteresis between the ramping down and the ramping up responses
- non-monotonic stress response.

→ Signature of complex flowing scenarios (shear bands, slip on the geometry surfaces, etc).

(2) At a given shear rate, the viscosity of a CNC suspension decreases with the gelation time or equivalently with a decreasing salt concentration.

(3) The shapes of the flow curves strongly depend on the time interval δt during which each shear rate is imposed.

→ The dynamical yield stress increases: $\sigma_f \propto \delta t^{0.82}$.

→ The difference between the ramping up and ramping down stress responses $\Delta\sigma$ presents a maximum whose coordinates vary with δt.

→ The hysteresis area A depends on δt and presents a maximum for δt^* coinciding with the suspension crossover time t_c.

Those flow curves being complicated to interpret due to their complex shapes inherent to the complex flowing scenarios at stake during their measurement when ramping in shear rate, we now investigate the mechanical response of CNC suspensions to the application of a continuous shear.

B Yielding upon start-up of shear

In order to understand the yielding properties of CNC suspensions, without any complex effects of ramping rates, we now perform shear start up experiments, i.e., we continuously shear a CNC suspension at a fixed shear rate, starting from rest, and during a time long enough for the sample to fail and flow. We explore the interplay between the sample age and its failure and flow behavior under shear, through studying both the influence of the sample recovery time prior to the start of the experiment, and of the magnitude of the applied shear rate. Indeed, we have seen in the previous chapter that the viscoelastic properties of a CNC suspension strongly depend on its age t_w, what most certainly influences the suspension yielding properties.

B.1 Phenomenology of yielding

a Rheological protocol

For this set of experiments, in order to apply the target shear rate as soon as possible, we use a strain-controlled rheometer (ARES G2, TA Instrument), equipped with a cone-and-plate geometry, which ensures an homogeneous shear rate in the sample volume. The upper cone is smooth, and the bottom plate is sand-blasted, with a surface roughness of 1 μm as provided by the manufacturer, in order to avoid the sample from slipping on its surface during measurements. The bottom plate is connected to a Peltier module that sets the sample temperature to $T = 23.0 \pm 0.1$ °C. Both geometries have a diameter of 40.0 mm, and the cone has a 2.0° angle, and a 46.0 μm truncation. In order to avoid evaporation, we use a solvent trap covering the geometry, and we saturate the atmosphere surrounding the sample with water.

For the experiments involving the longest time-scales (for t_w = 10000 and 20000 s), for which solvent evaporation becomes non-negligible in the cone-and-plate geometry, we use a smooth Taylor-Couette geometry of height 58 mm, inner rotating cylinder of radius 24 mm, outer fixed cylinder of radius 25 mm, and gap e = 1 mm. In order to prevent the sample from drying, we cover the geometry with a solvent trap. We have verified that a change of geometry has no influence on the suspension shear-induced yielding behavior (see Fig. 4.36 and Fig. 4.46 in Sec. 4.E in Appendix)

The rheological protocol is as follows:

(1) We strongly shear the sample in order to fluidize it by breaking its microstructure and to obtain a reproducible initial state. This "pre-shear" step consists of imposing a shear rate $\dot{\gamma}_p = 500$ s^{-1} during 20 s (during 60 s when using the Taylor-Couette geometry).

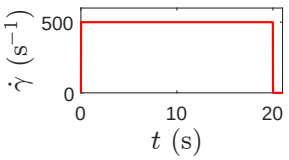

(2) Immediately after step (1), we measure the flow curve of the sample by sweeping down logarithmically the shear rate from $\dot{\gamma} = 500$ s^{-1} to $\dot{\gamma} = 0.01$ s^{-1}, with 7 points per decade and 10 s per point, for a total of 34 points. The data are recorded over the last 5 s of application of each shear rate step.

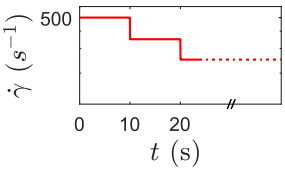

(3) We strongly shear the sample again to re-fluidize it and recover a reproducible initial state. This "pre-shear" step is the same as step (1): we impose a shear rate $\dot{\gamma}_p = 500$ s^{-1} during 20 s (during 60 s when using the Taylor-Couette geometry).

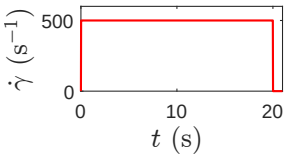

(4) Pre-shear is stopped abruptly by setting the shear rate to zero. We subsequently let the sample rest for a time t_w, ranging between 6 s and 20000 s, while measuring its linear viscoelastic moduli, i.e., the elastic modulus G' and the viscous

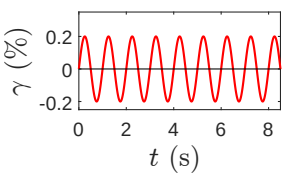

modulus G'', every second by imposing small-amplitude oscillatory shear (SAOS) with strain amplitude $\gamma = 0.2$ % and frequency $f = \omega/2\pi = 1$ Hz. The elastic modulus at the end of this recovery period, for $t = t_w$, is denoted G'_0. Note that t_w is often referred to as the "aging time" in the literature.

(5) We impose a zero stress $\sigma = 0$ Pa during 0.3 s in order to relax any residual stress that could remain in the sample from the rest period. The rheometer used for this set of experiments being a strain-controlled rheometer, we measure the stress as a function of time to ensure that we reach $\sigma = 0$ at the end of this step. An example of the time-evolution of the stress during this step is plotted in Fig. 4.9.

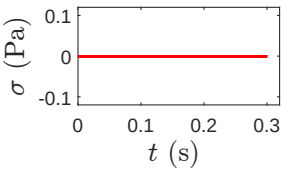

(6) We continuously shear the sample by imposing a constant shear rate $\dot{\gamma}$, chosen between 0.01 s^{-1} and 100 s^{-1}, during $\Delta t = 10/\dot{\gamma}$. The data are recorded as fast as possible in a logarithm time-scale. The initiation of shear defines the origin of time $t = 0$. This step is referred to as a "shear-start up experiment". Whatever its value, the target shear rate is reached as soon as 10^{-2} s after shear initiation (see Fig. 4.45 in Sec. 4.E in Appendix).

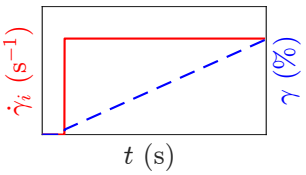

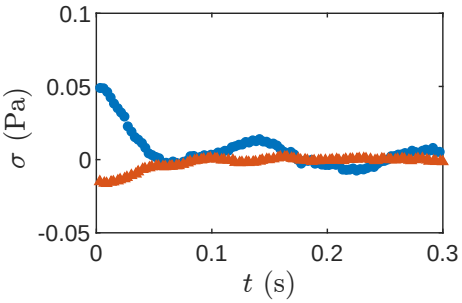

Figure 4.9: Stress as a function of time during step (5) in the rheological protocol detailed above, following the suspension recovery. Results obtained for a suspension containing 3.2 wt % CNC and 18 mM NaCl, after a recovery period of duration $t_w = 6$ s (blue •) and $t_w = 20000$ s (orange ▲).

b Typical yielding response of a CNC suspension

Figure 4.10 presents the typical response of a CNC suspension to the continuous shear $\dot{\gamma}$ imposed during step (6) of the protocol described above, for a suspension containing 3.2 wt % CNC and 18 mM NaCl, a recovery time $t_w = 600$ s and an applied shear rate $\dot{\gamma} = 0.5$ s^{-1}. Before shearing the sample, the internal stress is zero, $\sigma = 0$ Pa, thanks to step (5) of the protocol. Then, shearing the suspension induces an elastic-like response of the material microstructure. Fig. 4.10(a) presents the evolution of the stress as a function of the shearing time t. Yet, a more physically meaningful quantity is the total strain applied to the sample since shear initiation at $t = 0$ [see Fig. 4.10(b)]. This total strain is defined as the integral of the shear rate over the shearing time:

$$\gamma(t) = \int_0^t \dot{\gamma}(t')dt' \tag{4.4}$$

At short times, corresponding to small strains, the stress increases linearly with time and with the strain, and perfectly follows the prediction from Hooke's law using the value of the elastic modulus G'_0 measured at the end of the rest period [see the red lines in Figs. 4.10(a) and (b)]:

$$\sigma(t) = G'_0 \times \gamma(t) \tag{4.5}$$

This great correspondence shows that, at short times, or equivalently, at small strains, a CNC suspension deforms like a perfect elastic solid of shear modulus G'_0. After about 0.28 s of shear

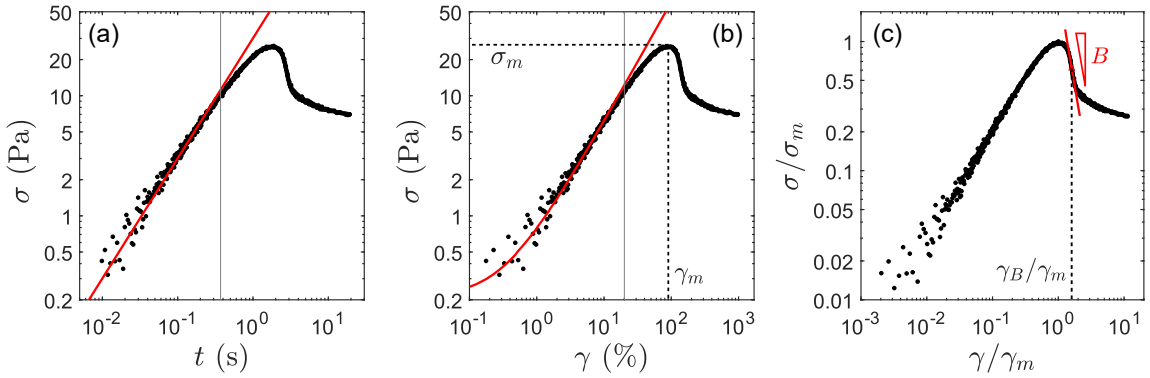

Figure 4.10: Typical stress response during yielding of a CNC suspension during a shear start up experiment. (a) Stress as a function of shearing time. The red line shows the perfect elastic response of the sample based on the elastic modulus G_0' at the end of the recovery period: $\sigma = G_0'\dot{\gamma}t$. (b) Stress as a function of strain, related to the shear rate and to the shearing time through Eq. (4.4). The red line shows the perfect elastic response given by Eq. (4.5), and the black dashed lines highlight the coordinates (γ_m, σ_m) of the stress overshoot. The gray continuous lines in (a) and (b) highlight the deviation from the perfect elastic response. (c) Stress as a function of strain normalized by the coordinates of the stress overshoot. The red line shows the slope of the steepest stress decrease following the stress maximum, defining the brittleness parameter B (B = 3.0 here). The red point defines the position γ_B/γ_m of the inflection point in log scales, where the parameter B is estimated. Experiment performed on a suspension containing 3.2 wt % CNC and 18 mM NaCl, by applying a shear rate $\dot{\gamma}$ = 0.5 s^{-1}, after a recovery time t_w = 600 s.

and $\gamma \approx 8$ %, the stress increase slows down and deviates from Hooke's law, suggesting that the sample does not deform as a perfect elastic solid anymore, but that some plastic deformations are induced. Part of the sample or the whole sample might also flow at larger strains. In this regime, the stress response of the material to the imposed shear is not linear anymore. At even longer times, or equivalently at larger strains, around $t \approx 2$ s ($\gamma \approx 87$ %), the stress goes through a maximum and subsequently decreases quite abruptly. This stress overshoot is the signature of the microstructure failure, which could not support anymore the large amount of stress it was subjected to. The more abrupt the transition, the more brittle-like the failure of the suspension, as previously established in Sec. 1.B.3 in the Introduction. After this sharp decrease, the stress continues to decrease with the shearing time, equivalently with the strain, but more slowly. The existence of similar stress overshoots under continuous shear of a colloidal gel has already been reported for polystyrene [Mohraz and Solomon, 2005] and polymethylmethacrylate [Koumakis and Petekidis, 2011] spheres, silica [Persello et al., 1994] and fumed silica particles [Wei et al., 2019], or synthetic hectorite clay (Laponite) [Suman and Joshi, 2019] for example.

In order to characterize more quantitatively the failure of a CNC suspension, we extract several parameters quantifying its stress response. First, we extract the coordinates (γ_m, σ_m) of the stress maximum [see Fig. 4.10(b)]. Then, we normalize the σ versus γ response by these coordinates, as plotted in Fig. 4.10(c). In order to quantify the brittleness of the failure of a CNC suspension under shear, we introduce an additional parameter B called the "brittleness parameter", which evaluates the maximum slope following the stress maximum in logarithmic scales, in the σ/σ_m versus γ/γ_m normalized representation:

$$B = \max\left(-\frac{\mathrm{d}\log(\sigma/\sigma_m)}{\mathrm{d}\log(\gamma/\gamma_m)}\right) \tag{4.6}$$

From the results plotted in Fig. 4.10(c) for a suspension containing 3.2 wt % CNC and 18 mM NaCl, sheared at $\dot{\gamma}$ = 0.5 s^{-1} after a recovery time t_w = 600 s, we obtain B = 3.0. Finally, we also

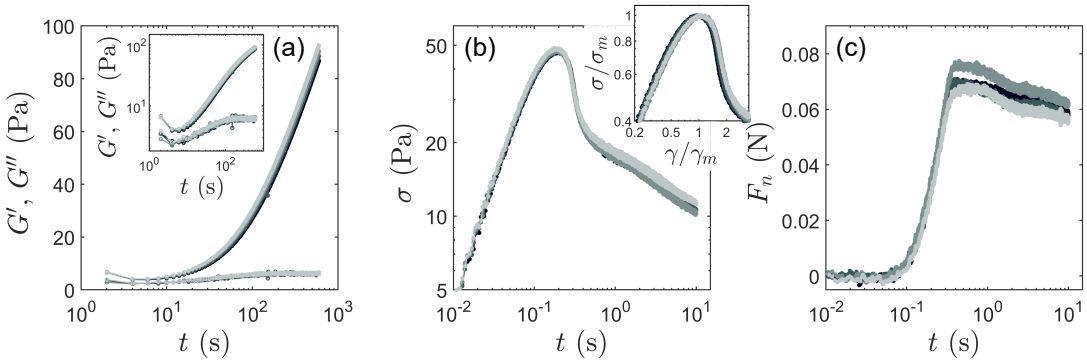

Figure 4.11: Repeatability of the measurements for four consecutive repetitions of the same protocol on the same loading, from dark to light gray. (a) Elastic modulus G' (•) and viscous modulus G'' (◦) as a function of time during the sample recovery following pre-shear. Inset: Same data plotted in logarithmic scales. (b) Stress σ as a function of time during the shear start up experiment following the recovery period. The inset shows an enlargement of the data, normalized by the coordinates of the stress maximum. (c) Normal force F_n induced by the sample on the upper geometry as a function of time during the shear start up experiment. Experiments performed on a suspension containing 3.2 wt % CNC and 18 mM NaCl, with t_w = 600 s and $\dot{\gamma}$ = 5 s^{-1}.

extract the position γ_B/γ_m where this maximum slope is reached [see the red line and the red dot in Fig. 4.10(c)]. The way a CNC suspension fails under shear most certainly depends both on the experimental conditions and on the composition of this suspension. This is the subject of the rest of this section.

c Repeatability and effect of shear direction

First, we check that the shear start up experiments after a given recovery time t_w and shear rate $\dot{\gamma}$ are reproducible. Figure 4.11 shows the results for a suspension containing 3.2 wt % CNC and 18 mM of NaCl, to which we have applied four times successively, the rheological protocol detailed in Sec. 4.B.1.a, with t_w = 600 s and $\dot{\gamma}$ = 5 s^{-1}. We observe that the four responses are very well super-imposed, with only a small discrepancy in the time evolution of the viscoelastic moduli during the recovery period [see Fig. 4.11(a)]. This small discrepancy does not impact the shear start up results [see Fig. 4.11(b)]: both the position of the stress overshoot, its amplitude and the slope during the suspension failure are very similar. Indeed, the mean coordinates of the stress overshoot are γ_m = 93.97 % and σ_m = 47.39 Pa, with a standard deviation of 2.19 % and 0.66 Pa respectively ; and the mean value of the brittleness parameter is B = 1.98 with a standard deviation of 0.09. Moreover, the normal forces induced by the sample on the upper geometry during the shear start up step are very similar. This further confirms the reproducibility of the measurements [see Fig. 4.11(c)]. Interestingly, we note that the normal force overshoot is synchronized with the stress overshoot. However, the amplitude of these forces being only about one order of magnitude larger than the sensor limitation (of 0.001 N), we will not further interpret this quantity in the following sections.

Figure 4.12 compares the responses of the same suspension to the application of shear start up in the same direction as the pre-shear, $\dot{\gamma}$ = +5 s^{-1}, referred to as a "positive shear" (blue curves), and the response of another sample of the same suspension to the application of a shear in the opposite direction as the pre-shear, $\dot{\gamma}$ = −5 s^{-1}, referred to as a "negative shear" (red curves). We observe that the recovery dynamics of the two samples are very similar [see Fig. 4.12(a)], and that the yielding responses to the application of a positive or a negative shear are very similar too, with only slight differences [see Fig. 4.12(b)]. Indeed, the linear response at short times and the

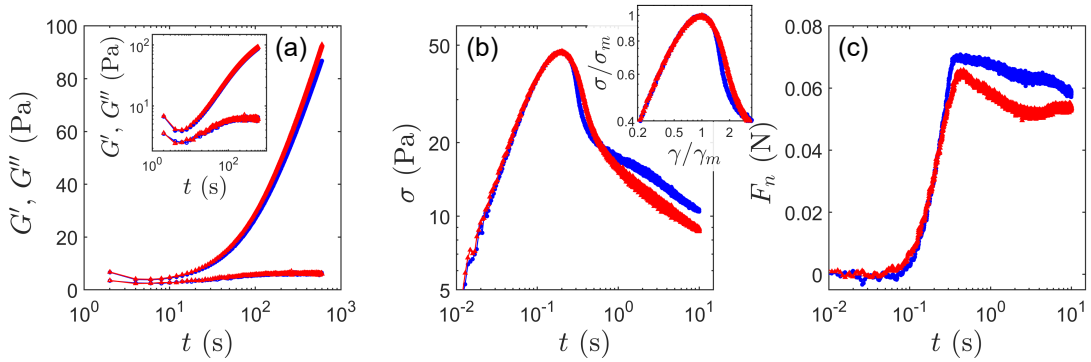

Figure 4.12: Reproductibility of the measurements towards a change of the shear orientation during the shear start up experiment: $\dot{\gamma}$ = +5 s^{-1} (blue •) and $\dot{\gamma}$ = −5 s^{-1} (red ▲). (a) Elastic modulus G' (filled symbols) and viscous modulus G'' (empty symbols) as a function of time during the sample recovery following pre-shear. Inset: Same data plotted in logarithmic scales. (b) Stress σ as a function of time during the shear start up experiment following the recovery period. The inset shows an enlargement of of the data, normalized by the coordinates of the stress maximum. (c) Normal force F_n induced by the sample on the upper geometry as a function of time during the shear start up experiment. Experiments performed on a suspension containing 3.2 wt % CNC and 18 mM NaCl, with t_w = 600 s and $\dot{\gamma}$ = ±5 s^{-1}.

coordinates of the stress maximum are unchanged: γ_m = 97.01 % and σ_m = 46.86 Pa for the positive shear, and γ_m = 98.11 % and σ_m = 46.79 Pa for the negative shear. Moreover, the slope of the stress decreasing following this maximum is almost the same: B = 2.08 for the positive shear and B = 1.35 for the negative shear. However, the response at longer time differs. Once again, the normal forces measured during the shear start up step are very similar in both cases [see Fig. 4.12(c)].

From those two sets of results, we deduce that a CNC suspension containing 3.2 wt % CNC and 18 mM NaCl does not keep any memory of the shear history (pre-shear and previous shear start up experiments), as long as this shear has been applied always in the same direction: the yielding behavior is independent of the total amount of deformation that the sample has undergone. However, a weak memory effect appears at long-time when changing the direction of shear. Therefore, we have decided to apply only positive values of shear, both during the pre-shear and the continuous shear steps corresponding to steps (1), (3) and (6) in the protocol described in Sec. 4.B.1.a. Moreover, in order to ensure that no memory effect affects our data, we vary randomly the shear rate $\dot{\gamma}$ of step (6) and the recovery time t_w of step (4), based on a list of predefined reasonable values.

We will study in more details memory effects in Sec. 4.B.6, where we will see that, at large salt concentration or large CNC weight fraction, both the repeatability of the same protocol and the direction of shear actually have a strong influence on the rupture scenario.

B.2 Influence of the shear rate on the yielding behavior

In this section, we study the influence of the shear rate applied during shear start up on the yielding behavior of a CNC suspension. To do so, we repeat the six step protocol described in Sec. 4.B.1.a on a same suspension, keeping the recovery time constant, t_w = 600 s, but varying the shear rate $\dot{\gamma}$ of step (6) between 0.01 s^{-1} and 100 s^{-1} in a random order, in order to minimize the effects of a potential drift of the material properties due to successive repetitions of the protocol on a single loading.

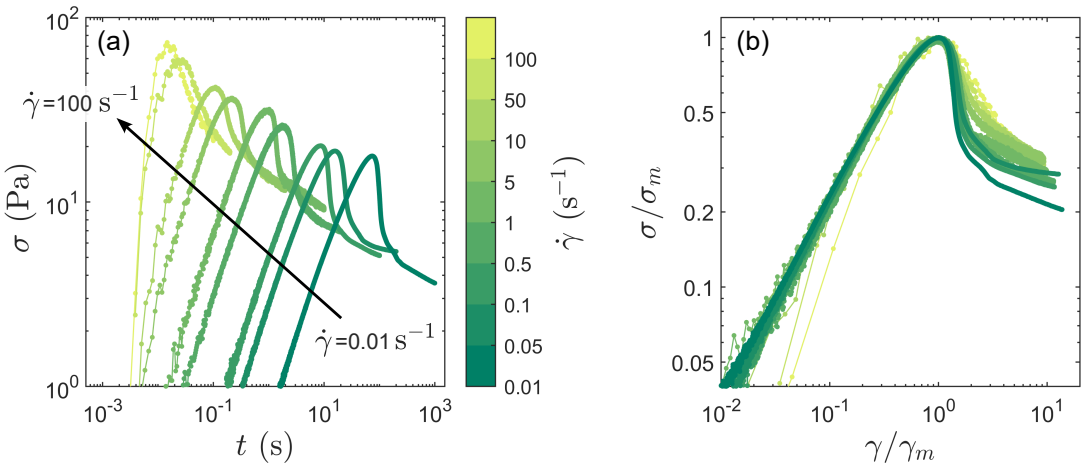

Figure 4.13: Yielding transition of a CNC suspension induced at various shear rates, from $\dot{\gamma}$ = 0.01 s^{-1} in dark green to $\dot{\gamma}$ = 100 s^{-1} in light green. (a) Stress σ as a function of time during the shear start up experiment. (b) Stress σ as a function of strain γ normalized by the coordinates of the stress overshoot for each $\dot{\gamma}$. Experiments performed on a suspension containing 3.2 wt % CNC and 18 mM NaCl with a recovery time t_w = 600 s.

a A representative example

Figure 4.13(a) shows the resulting stress responses versus shearing time for a sample containing 3.2 wt % CNC and 18 mm NaCl. We observe that whatever the shear rate, the stress always presents an overshoot. Therefore, we can convert each $\sigma(t)$ curve into a $\sigma(\gamma)$ curve normalized by the coordinates (γ_m, σ_m) of the stress overshoot, as previously described in Sec. 4.B.1.b. The resulting σ/σ_m versus γ/γ_m curves are plotted in Fig. 4.13(b). Interestingly, all the curves corresponding to different shear rates $\dot{\gamma}$ rescale onto a single curve in the linear regime of deformation and until the stress maximum, i.e., for $\gamma/\gamma_m \leq 1$. However, this rescaling does not hold at larger strains, for $\gamma/\gamma_m > 1$. More precisely, we observe that the decrease of the stress following its maximum becomes less abrupt when the shear rate increases. This observation indicates a transition from a brittle-like to a ductile-like yielding of the suspension when increasing the shear rate.

In order to quantify the failure of a CNC suspension, we first consider the coordinates of the stress overshoot (γ_m, σ_m). Figure 4.15(a) shows the position of the stress overshoot γ_m as a function of the shear rate, while Fig. 4.15(b) shows normalized distance $\sigma_m/\sigma_c - 1$ between the stress maximum σ_m and the suspension yield stress σ_c extracted from the flow curve measured in step (2) of the rheological protocol detailed in Sec. 4.B.1.a, and plotted in Fig. 4.14. The position of the stress maximum γ_m only weakly depends on the shear rate, and one cannot distinguish between a weak power-law:

$$\gamma_m \propto \dot{\gamma}^{\zeta} \tag{4.7}$$

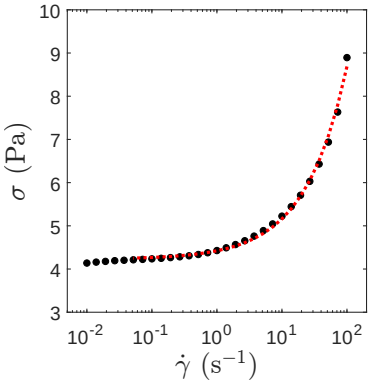

Figure 4.14: Flow curve of a suspension containing 3.2 wt % CNC and 18 mM NaCl measured by ramping down the shear rate, as described in step (2) of the protocol detailed in Sec. 4.B.1.a. The red dashed line show the best fit of the data with an Herschel-Bulkley model of parameters σ_c = 4.2 Pa, n = 0.7 and k = 0.2 Pa.s^n.

with $\zeta = 0.06$ [see red dashed line in Fig. 4.15((a)], indistinguishable from a logarithmic dependence [see the blue dashed line in Fig. 4.15(a)]. Such a weak dependence of γ_m on the shear rate has already been reported in a colloidal gel of polymethylmethacrylate hard spheres [Koumakis and Petekidis, 2011], and in Carbopol microgels [Divoux et al., 2011].

The distance between the stress maximum and the yield stress $\sigma_m/\sigma_c - 1$ depends more strongly on the shear rate, and in this case, only a power-law increase with $\dot{\gamma}$ can capture properly our data [see the red dashed line compared to the blue one in Fig. 4.15(b)]:

$$\sigma_m/\sigma_c - 1 \propto \dot{\gamma}^{v} \tag{4.8}$$

with $v = 0.17$ for the suspension considered in Fig. 4.15. Note that a power-law increase of the maximum stress with the shear rate has already been reported in a colloidal gel of polymethylmethacrylate hard spheres [Koumakis and Petekidis, 2011], yet without considering the distance to the yield stress. The σ_m versus $\dot{\gamma}$ dependence has been studied in more details in colloidal glasses. In particular, numerical simulations report both a logarithmic behavior [Varnik et al., 2004, Rottler and Robbins, 2005] and a power-law behavior [Derec et al., 2003, Whittle and Dickinson, 1997], while experiments report a power-law behavior [Derec et al., 2003, Divoux et al., 2011]. Yet, recently, Benzi *et al.* [Benzi et al., 2021a, Benzi et al., 2021b] proposed to rather focus on $\sigma_m/\sigma_c - 1$. Assuming a Herschel-Bulkley flow behavior with an exponent n [see Eq. (4.1)], they predict the following scalings:

$$\begin{cases} \sigma_m/\sigma_c - 1 \propto \dot{\gamma}^{2n/3} & \text{at small } \dot{\gamma} \quad (4.9) \\ \sigma_m/\sigma_c - 1 \propto \dot{\gamma}^{4n/(9-n)} & \text{at large } \dot{\gamma} \quad (4.10) \end{cases}$$

In this framework, for the suspension containing 3.2 wt % CNC and 18 mM NaCl whose data are shown in Fig. 4.15, we find $\sigma_c = 4.2$ Pa and $n = 0.7$ [see the red dashed line in Fig. 4.14]. Using Eqs. (4.9) and (4.10), we calculate exponents of values $2n/3 = 0.48$ and $4n/(9-n) = 0.35$, which are very different from the exponent $v = 0.17$ found by fitting our data. Therefore, although $\sigma_m/\sigma_c - 1$ indeed follows a power-law with $\dot{\gamma}$, the quantitative prediction for the exponent v by Benzi *et al.* does not hold for this CNC suspension. The validity of this model for our CNC suspensions will be further discussed in Sec. 4.B.2.b.

In order to quantify the brittleness of the gel failure, we now consider the dependence of the brittleness parameter B, defined above in Eq. (4.6), with the shear rate, as plotted in Fig. 4.15(c). We observe that as the shear rate increases, B decreases, indicating a shift from a brittle-like to a more ductile-like failure of the gel. This brittle to ductile transition upon increasing the shear rate is quite unexpected. Indeed, a soft material is generally expected to fail more abruptly when subjected to a faster deformation, as observed in fumed silica colloidal gels [Wei et al., 2019] or in gels of polymethylmethacrylate hard spheres [Koumakis and Petekidis, 2011], as well as in glassy colloidal suspensions such as carbopol microgels [Benzi et al., 2023] and silica suspensions [Derec et al., 2003], and in glasses of polymethylmethacrylate hard spheres [Koumakis and Petekidis, 2011]. Nevertheless, this counter-intuitive behavior of CNC gels can be understood assuming that the gel continues to rebuild under shear during the shear start up experiment, at least for small enough shear rates. Indeed, at small shear rate $\dot{\gamma}$, the experiment time $\Delta t = 10/\dot{\gamma}$ is long compared to the typical time-scale of evolution of a CNC suspension viscoelastic properties at rest: for $\dot{\gamma} = 0.01$ s^{-1}, the shear start up experiment lasts $\Delta t = 1000$ s, and the typical evolution of the elastic modulus over this time interval, at rest and after a recovery period $t_w = 600$ s, is $\Delta G'/G' \approx 60$ %, for the suspension considered in Fig. 4.13. Even though the recovery dynamics of a CNC suspension are most certainly different at rest and under shear, such a long shearing time associated to small shear rates must allow for a non-negligible evolution of the sample viscoelastic properties by increasing its effective recovery time. Therefore, the CNC network formed at such an increased effective sample age is tougher, and should fail more abruptly, hence in a more brittle-like way. On the contrary, at larger shear rate $\dot{\gamma}$, the experiment time $\Delta t = 10/\dot{\gamma}$ is much shorter: for $\dot{\gamma} = 100$ s^{-1}, the

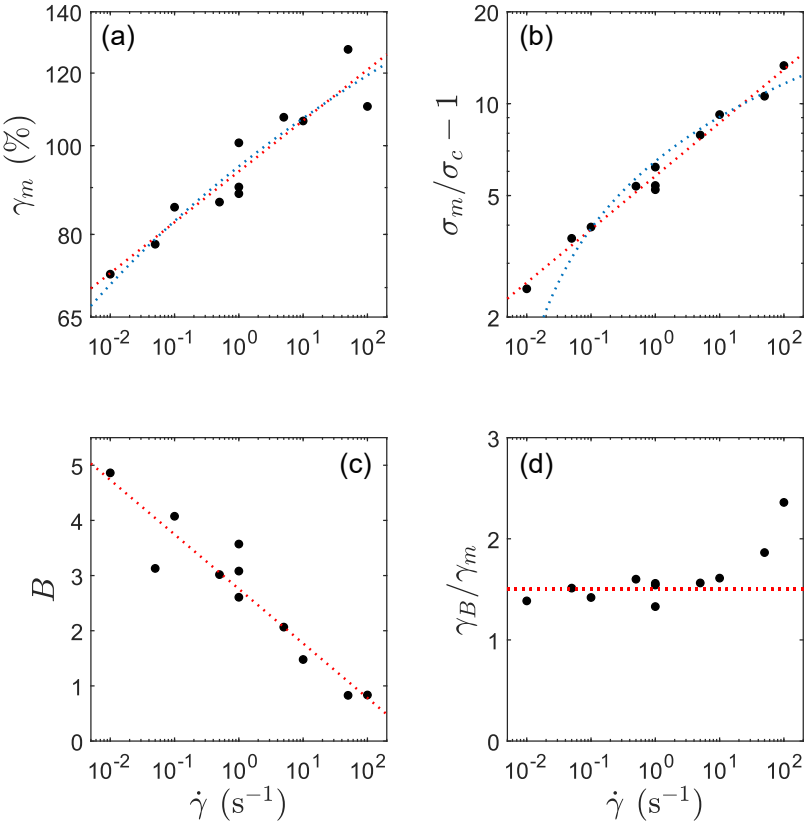

Figure 4.15: Parameters quantifying the impact of the shear rate on the shear-induced yielding transition of a CNC suspension. (a) Strain γ_m corresponding to the stress maximum during the stress overshoot, (b) normalized distance $\sigma_m/\sigma_c - 1$ between the stress maximum σ_m and the suspension yield stress σ_c, (c) brittleness parameter B and (d) strain γ_B where B is estimated, normalized by γ_m, as a function of the applied shear rate. Experiments performed on a suspension containing 3.2 wt % CNC and 18 mM NaCl, at fixed t_w = 600 s. The red dashed lines in (a) and (b) show the best fits of the data by power-laws of exponent 0.06 and 0.17, respectively, while the blue dashed lines show the best fits of the data by a logarithmic law. The red dashed line in (c) shows the best fit of the data by Eq. (4.11), while the one in (d) shows the mean value of γ_B/γ_m, equal to 1.5, over the range of shear rates.

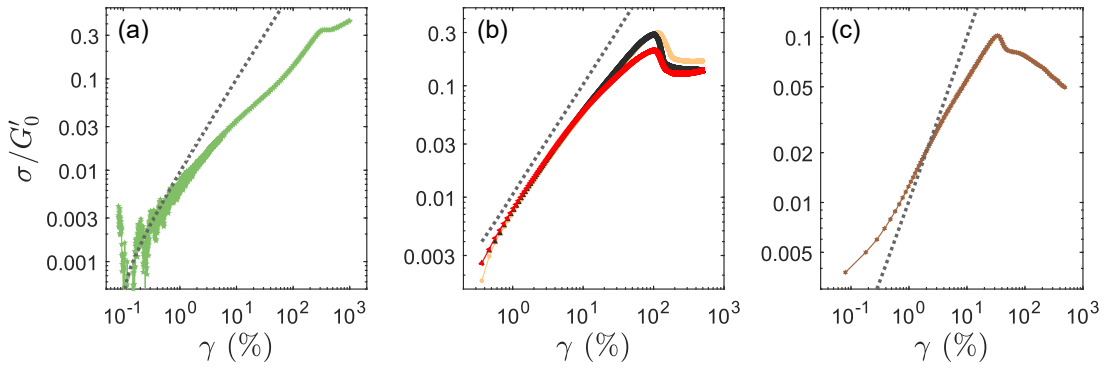

Figure 4.16: Stress response during shear start up of suspensions of various gelation times, corresponding to various positions along the $G'(\tilde{t})$ master curve for the suspension recovery. The gelation time is varied by changing the suspension composition. Stress normalized by the elastic modulus G_0' measured at time t_w at the end of the recovery period versus strain (a) for t_g = 800 s, for a suspension containing 5.5 wt % CNC and 7 mM NaCl ; (b) for t_g = 371, 372, 154 s, and various compositions, for suspensions containing respectively 3.2 wt % CNC and 15 mM NaCl (orange), 3.2 wt % CNC and 12 mM KCl (black) and 4.8 wt % CNC and 12 mM NaCl (red) ; (c) for $t_g = 3 \times 10^{-4}$ s, for a suspension containing 3.2 wt % CNC and 100 mM NaCl. The black dashed lines represent the linear elastic response given by $\sigma = G_0'\gamma$. Experiments performed by shearing the samples at $\dot{\gamma}$ = 0.01 s^{-1} after a recovery period of (a) t_w = 350 s or (b),(c) t_w = 600 s.

shear start up experiment lasts Δt = 0.1 s, and the elastic modulus does not evolve significantly over this time interval. The sample has therefore almost no additional time to rebuild following the t_w = 600 s rest period. Therefore, such a smaller effective sample age leads to a weaker CNC network, which should break less abruptly, hence in a more ductile-like way. A decrease of the brittleness parameter B with the applied shear rate has been predicted in numerical modeling of glassy systems [Barlow et al., 2020].

Figure 4.15(c) further shows that the brittleness parameter B decreases logarithmically with the shear rate, i.e.:

$$B - B_0 = -\lambda \log(\dot{\gamma}) \tag{4.11}$$

with λ = 1 for the suspension considered in Figs. 4.13 and 4.15. Moreover, we show that the position where we observe the maximum of slope in the stress decrease during the gel failure does not depend on the shear rate: $\gamma_B/\gamma_m \approx 1.5$ whatever the shear rate [see Fig. 4.13(d)].

b Impact of the suspension composition

We now study how the composition of a CNC suspension impacts its response to shear start up. To do so, we consider suspensions where we vary simultaneously the salt concentration, its nature, and the CNC weight fraction while keeping a gelation time in between 154 and 370 s. For comparison, we have also considered a suspension with a much shorter gelation time, i.e., $t_g = 3 \times 10^{-4}$ s, and a suspension with a longer gelation time, i.e., t_g = 800 s. Varying the gelation time t_g is equivalent to moving along the $G'(\tilde{t})$ master curve established at f = 1 Hz for the recovery dynamics of CNC suspensions (see Sec. 3.A). We have applied the same series of experiments as described in the previous section to all samples [3].

Figure 4.16 shows the stress responses of the different samples considered in this section, for a shear rate $\dot{\gamma}$ = 0.01 s^{-1}. We note that the stress response during the suspension yielding strongly

[3] We have used t_w = 600 s for all samples, except for the suspension with t_g = 800 s for which we have used t_w = 350 s in order to have $t_w < t_g$. See Sec. 4.B.5 for a representation of the data taking into account this change in t_w.

Table 4.2: Parameters for the fits of γ_m, $\sigma_m/\sigma_c - 1$ and B versus $\dot{\gamma}$ plotted in Fig. 4.17, for suspensions of various gelation times.

Suspension composition	t_w (s)	t_g (s)	ζ	υ	$2n/3$	$4n/(9-n)$	λ
3.2 wt % CNC, 15 mM NaCl	600	371	0.024	0.27	0.28	0.19	0.2581
3.2 wt % CNC, 12 mM KCl	600	372	0.007	0.21	0.14	0.09	1.0805
4.8 wt % CNC, 12 mM NaCl	600	154	0.031	0.29	0.20	0.14	0.4172
3.2 wt % CNC, 100 mM NaCl	600	3×10^{-4}	0	0.02			0.0080
5.5 wt % CNC, 7 mM NaCl	350	800	0.027	0.21	0.24	0.17	

depends on the value of the gelation time t_g relative to the recovery time t_w. Indeed, the stress responses for the suspensions of similar gelation time are very well superimposed at small strains, and only differ when approaching the stress overshoot, whose overall shape is very similar for the three suspensions [see Fig. 4.16(b)]. At large strains, for the suspension with $t_g \approx 2t_w$, the stress overshoot is hardly visible, and the stress continues to increase for $\gamma > \gamma_m$ [see Fig. 4.16(a)]. On the contrary, for the suspension with $t_g \ll t_w$, the stress decreases for $\gamma > \gamma_m$ [see Fig. 4.16(c)]. Such an absence of steady state is the signature of the strong time dependence of the suspension over the duration of the start up experiment.

In order to quantify more precisely the differences in the stress responses of the five suspensions, we extract the various parameters γ_m, σ_m, B and γ_B/γ_m defined above and we explore how they depend on the shear rate. The coordinates of the stress overshoot are plotted in Figs. 4.17(a) and (b) as a function of the shear rate. Interestingly, irrespective of the suspension composition, both parameters can always be fitted by a power-law (see the red dashed lines), as stated in the previous section, with exponents ζ and υ that depend on t_g, i.e., on the sample age. Indeed, for a gelation time t_g ranging between 154 and 800 s, both ζ and υ remain of the same order of magnitude: $\zeta \approx 0.02$ and $\upsilon \approx 0.25$ (see Table 4.2). However, for a fully recovered sample, with $t_g \ll t_w$, both γ_m and $\sigma_m/\sigma_c - 1$ become almost independent of the shear rate for such short gelation time. This is consistent with our hypothesis that the dependence of the yielding properties of a suspension with the shear rate at least partly comes from a change in the effective sample age, due to the sample reconstruction under shear. Indeed, at large salt concentration, corresponding to fast gelation time, the sample recovers its viscoelastic properties following shear cessation in only a few seconds, after which those viscoelastic properties continue to evolve but very slowly. Therefore, the effective sample age does not vary significantly during the shear start up experiments, leading to a very weak dependence of the suspension yielding properties with the shear rate. Interestingly, at small salt concentrations and long gelation times, i.e., for young samples, we recover ζ and υ exponents that are comparable to the ones found for the three samples with a gelation time about twice shorter. This is quite remarkable as, for this sample, $t_w < t_g$, meaning that the CNC network is not percolated yet at the beginning of the shear start up experiments. The solid-like failure that we observe in this case comes from the fact that the recovery time t_w = 350 s is larger than the G'-G'' crossover time t_c, which is of about 50 s at f = 1 Hz, ensuring that the suspension has a solid-like behavior when we begin the shear start up experiments. However, the experiments were performed on a suspension that contains a large CNC weight fraction, w_{CNC} = 5.5 wt %, and whose viscoelastic properties still evolve significantly in a short time-interval due to a gelation time that is not long enough, hence the large ζ and υ exponent values. Therefore, it would be interesting to complete this study by performing experiments on suspensions with a much larger gelation time while keeping $t_w > t_c$. The viscoelastic properties of such suspensions do not evolve much during the shear start up experiments, and we could compare the resulting ζ and υ exponents to the ones obtained on the opposite end of the master curve.

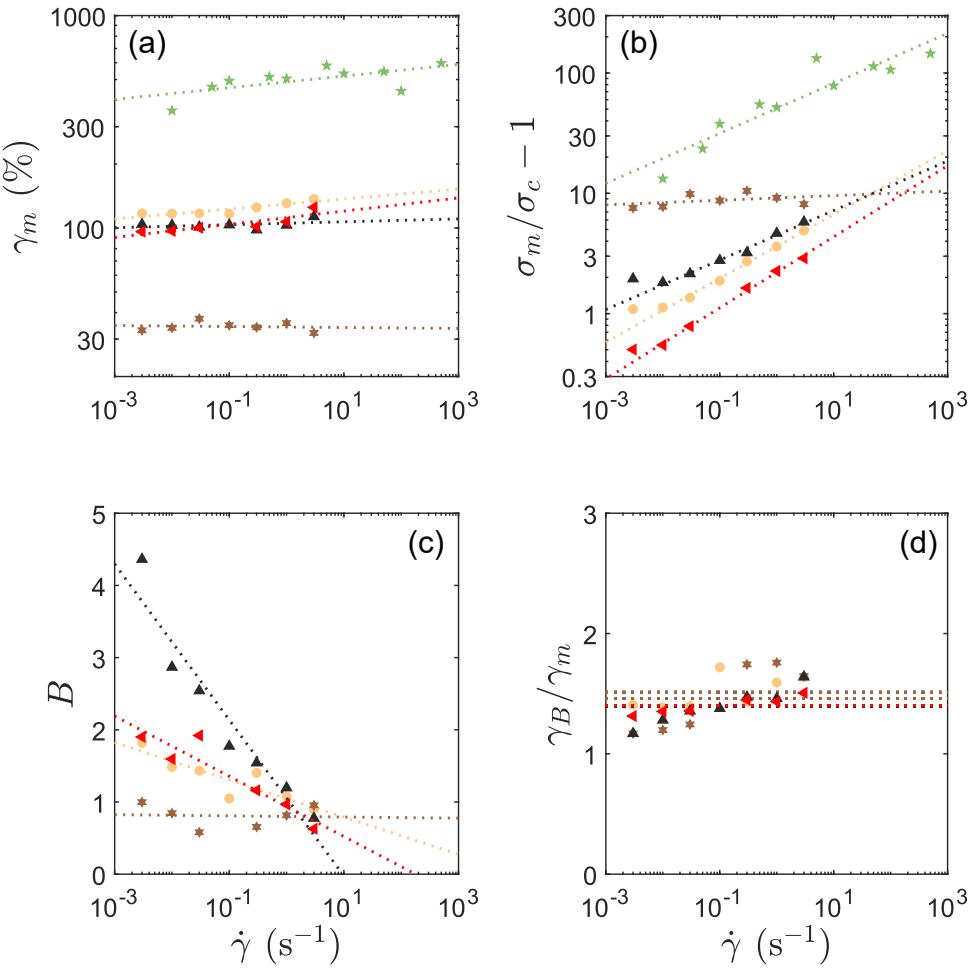

Figure 4.17: Parameters quantifying the shear-induced yielding response of suspensions of various gelation times, corresponding to various positions on the $G'(\tilde{t})$ master curve for the suspension recovery. The gelation time is varied by changing the suspension composition. (a) Strain γ_m corresponding to the stress maximum and (b) normalized distance $\sigma_m/\sigma_c - 1$ between the stress maximum σ_m and the suspension yield stress σ_c ; (c) brittleness parameter B and (d) strain γ_B where B is estimated, normalized by γ_m, as a function of the applied shear rate. The dashed lines in (a) and (b) show the best fits of the data by power-laws of exponents ζ and υ respectively. The dashed lines in (c) show the best fit of the data by a logarithmic law of prefactor λ. The dashed lines in (d) highlight the mean value of the data over the range of $\dot{\gamma}$ for each suspension. The values of the various fitting parameters are reported in Table 4.2. Experiments performed on suspensions of gelation time t_g = 800 s containing 5.5 wt % CNC and 7 mM NaCl (green ⋆), t_g = 371 s containing 3.2 wt % CNC and 15 mM NaCl (orange •), t_g = 372 s containing 3.2 wt % CNC and 12 mM KCl (black ▲), t_g = 154 s containing 4.8 wt % CNC and 12 mM NaCl (red ◂) and $t_g = 3 \times 10^{-4}$ s containing 3.2 wt % CNC and 100 mM NaCl (brown ✶).

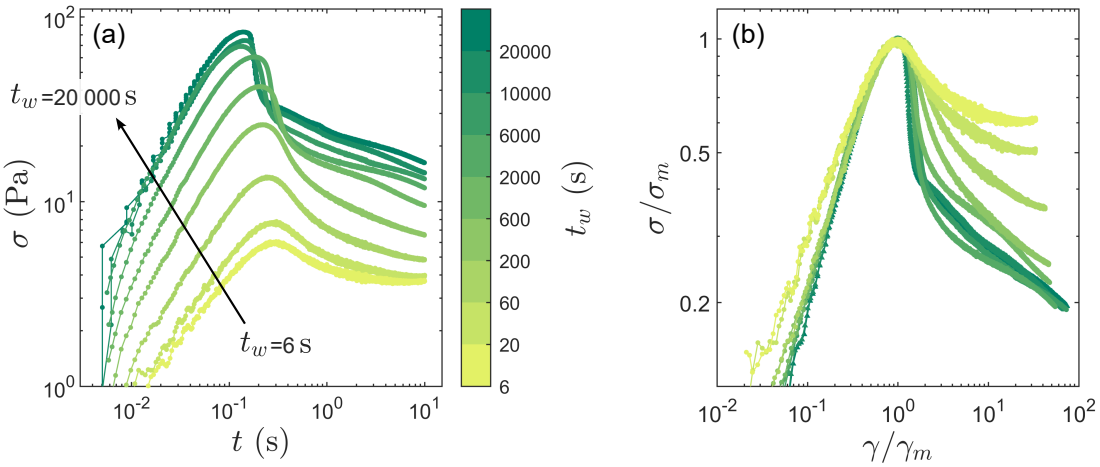

Figure 4.18: Yielding transition of a CNC suspension induced at fixed shear rate $\dot{\gamma}$ = 5 s^{-1}, after various recovery times t_w = 6, 20, 60, 200, 600, 2000, 6000, 10000, 20000 s from light green to dark green. (a) Stress σ as a function of time. (b) Stress σ as a function of strain γ normalized by the coordinates of the stress overshoot for each t_w. Experiments performed on a suspension containing 3.2 wt % CNC and 18 mM NaCl, of gelation time t_g = 90 s.

Comparing our v exponents to the ones predicted by Benzi *et al.* [Benzi et al., 2021a, Benzi et al., 2021b] [see Eq. (4.10)], reported in Table 4.2, we note that the prediction does not apply in our system, except maybe at large CNC weight fraction, for w_{CNC} = 5.5 wt %. This discrepancy is expected as the prediction has been established for repulsive glasses, while CNC suspensions at the considered weight fractions in the presence of salt form attractive gels or attractive glasses. However, it is the only prediction that we are aware of for the yielding transition of colloidal suspensions. It would be interesting to test it further on samples containing 5.5 wt % CNC, which may form attractive glasses. The exponents from the prediction of Benzi *et al.* could not be calculated for the suspension containing 100 mM NaCl as the flow curve at such a large salt concentration cannot be fitted by a Herschel-Bulkley model (see Sec. 4.A).

Finally, we observe that the brittleness parameter B becomes independent of the shear rate at short gelation times t_g, for $t_w \gg t_g$ [see Fig. 4.17(c) and Table 4.2][4]. This observation suggests a balance between the time-evolution of the sample properties during the start up experiment, and the evolution of the brittleness of the yielding transition with the shear rate. For samples near the inflection point, with an intermediate gelation time, we observe no systematic trend for the prefactor λ accounting for the logarithmic decrease of B with $\dot{\gamma}$, defined in Eq. (4.11): B decreases with $\dot{\gamma}$ for all sample compositions, but the rate of this decrease varies.

B.3 Influence of the recovery time on the yielding behavior

In order to further test our hypothesis that the brittle to ductile transition of the gel failure upon increasing the shear rate is due to an increasing effective recovery time, we now consider a series of experiments where the shear rate is fixed to $\dot{\gamma}$ = 5 s^{-1}, and the sample "age" t_w following pre-shear cessation is varied between 6 s and 20000 s in a random order to minimize the effects of a potential drift of the material properties due to successive repetitions of the protocol on a single loading.

[4]The brittleness parameter B could not be estimated for the sample with the longest t_g, for which the stress does not decrease but rather plateaus for $\gamma > \gamma_m$, before increasing again [see] Fig. 4.16(a)].

Figure 4.18(a) shows the resulting stress responses versus time for the same sample as in the previous section, i.e., a CNC suspension containing 3.2 wt % CNC and 18 mM NaCl, of gelation time t_g = 90 s. Once again, we observe that whatever the recovery time t_w, the stress always presents an overshoot, even for recovery times that are shorter than the gelation time, i.e., for $t_w < t_g$. This observation suggests that even if CNC particles do not form a percolated network, the suspension does fail like a viscoelastic solid at the time-scale associated to $\dot{\gamma} = 5\ s^{-1}$. This solid-like behavior is consistent with the fact that $t_w > t_c$ even for the smallest sample age, ensuring that $G' > G''$ at the beginning of the shear start up experiment. As previously described, we can convert each $\sigma(t)$ curve into a $\sigma(\gamma)$ curve that we can normalize by the coordinates (γ_m, σ_m) of the stress overshoot. The resulting σ/σ_m versus γ/γ_m curves are plotted in Fig. 4.18(b). Here again, similarly to what we have observed when varying the shear rate, all the curves obtained after different recovery times t_w rescale onto a single curve in the linear regime of deformation, before the stress maximum, for $\gamma/\gamma_m < 1$, yet with a small discrepancy for the two shortest recovery times t_w = 6 – 20 s. Once again, this rescaling fails at larger strains, in the non-linear regime of deformation, for $\gamma/\gamma_m > 1$. We further observe that in this regime, the decrease of the stress following its maximum becomes less abrupt when the recovery time t_w decreases, similarly to what we have observed when increasing the shear rate. Therefore, for fixed gelation time and shear rate, increasing the "age" of the system leads to a ductile to brittle transition. This transition is consistent with the fact that the longer we let the sample recover, the tougher the CNC network, and the more brittle this network fails under shear. This transition is similar to the behavior reported from simulations where a deeper annealing leads to a brittle-like yielding [Barlow et al., 2020]. The brittle to ductile transition upon increasing the sample age has also been reported experimentally for several colloidal glasses [Koumakis and Petekidis, 2011], and only few colloidal gels, such as a gel of fumed silica particles [Wei et al., 2019], a gel of waxy crude oil [Dimitriou and McKinley, 2014], and a gel of polymethylmethacrylate hard spheres [Koumakis and Petekidis, 2011]. However, to our knowledge, no quantitative study characterizing this brittle to ductile yielding transition upon varying the sample age has been reported yet.

We now extract parameters characterizing the stress overshoot in order to quantify the CNC suspension failure. Figures 4.19(a) and (b) show the coordinates of the stress overshoot γ_m and σ_m as a function of the sample age t_w, the maximum stress being normalized by the elastic modulus G'_0 measured at time t_w at the end of the recovery period corresponding to step (4) in the rheological protocol detailed in Sec. 4.B.1.a. We observe that while γ_m does not depend much on the shear rate over the range explored [see Fig. 4.13(a)], it decreases by a factor of 2.5 when varying the sample age between 6 s and 20000 s for a fixed shear rate. Concomitantly, σ_m/G'_0 decreases by a factor of about 7 over the range of sample ages [see Fig. 4.13(b)]. This could be indicative of a more brittle behavior as t_w increases. This is confirmed in Fig. 4.19(c) which presents the dependence of the brittleness parameter B with the sample age t_w. We observe that as the sample age increases, B strongly increases by a factor 5, indicating a more brittle failure of the gel. An increase of the brittleness with the degree of annealing has been predicted for soft glassy materials through numerical modeling [Barlow et al., 2020]. More precisely, our results show that B depends logarithmically on the age of the system, as it was shown for its dependence on the shear rate in Sec. 4.B.2. Strikingly, B points to a change of regime on both sides of the gelation time [see Fig. 4.19(c)]. Such a change of regime can also be detected in σ_m/G'_0 versus t_w [see Fig. 4.19(b)]. However, Fig. 4.19(d) suggests that, as already highlighted when varying the shear rate, the position where we observe the steepest stress decrease during the gel failure does not depend on the recovery time: $\gamma_B/\gamma_m \approx 1.5$ for all t_w.

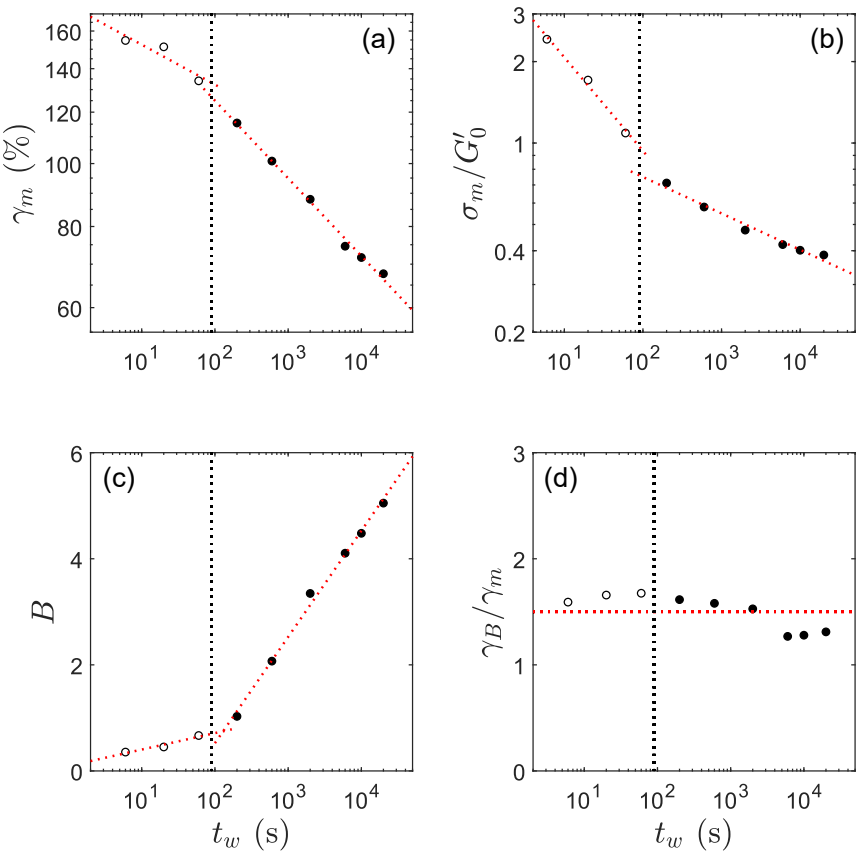

Figure 4.19: Parameters quantifying the impact of the sample age on the shear-induced yielding transition of a CNC suspension. (a) Strain γ_m corresponding to the stress maximum during the stress overshoot, (b) stress maximum σ_m normalized by the elastic modulus G_0' measured right prior to the start up experiment, (c) brittleness parameter B and (d) strain γ_B where B is estimated, normalized by γ_m, as a function of the recovery time, or sample age, t_w. The empty symbols correspond to $t_w < t_g$, while the filled symbols correspond to $t_w > t_g$. Experiments performed on a suspension containing 3.2 wt % CNC and 18 mM NaCl, at fixed $\dot{\gamma}$ = 5 s^{-1}. The black vertical dashed lines highlight the suspension gelation time t_g = 90 s. The red dashed lines in (a) and (b) show the best fits of the data by power-laws of exponent 0.06 and 0.35 respectively for $t_w < t_g$, and of exponents 0.13 and 0.20 respectively for $t_w > t_g$. The red dashed line in (c) shows the best fit of the data by logarithmic laws of prefactor 0.31 for $t_w < t_g$ and 2.00 for $t_w > t_g$. The horizontal red dashed line in (d) shows the mean value of γ_B/γ_m over the range of recovery times, equal to 1.5.

B.4 Influence of the salt concentration on the yielding behavior

In the previous sections, we have identified that a relevant parameter for controlling the brittleness of a CNC suspension failure under continuous shear, is the "age" of the system t_w. Therefore, in order to test the robustness of our observations concerning the dependence of this yielding behavior on t_w, we now reproduce the same shear start up experiments as in Sec. 4.B.3, at fixed shear rate and various recovery times t_w, on CNC suspensions of various compositions.

To do so, we have repeated the protocol detailed in Sec. 4.B.1.a by applying the same shear rate $\dot{\gamma} = 5\ s^{-1}$ and randomly varying the recovery time between 6 s and 20000 s, on a single sample loading. We have repeated this series of experiments on a series of suspensions containing the same CNC weight fraction, $w_{CNC} = 3.2$ wt %, and a salt concentration varying between 18 mM and 50 mM NaCl.

First, we note that for all salt concentrations, the stress response to continuous shear is very similar to the one described in Secs. 4.B.1.b, 4.B.2 and 4.B.3: the stress presents an overshoot, and the σ/σ_m versus γ/γ_m responses collapse onto a single curve in the linear regime of deformation, but not in the non-linear regime of deformation (see Fig. 4.47 in Sec. 4.E in Appendix).

Second, as previously detailed in Sec. 4.B.3, we extract the various parameters characterizing the yielding transition, and we report them in Fig. 4.20 as a function of the normalized sample age t_w/t_g. Remarkably, the coordinates of the stress overshoot γ_m and σ_m, normalized by the elastic modulus G'_0 measured at time t_w at the end of each recovery period, follow a similar trend with the normalized sample age [see Figs. 4.20(a) and (b)]. However, interestingly, this is not the case for the brittleness parameter B. Indeed, we rather observe that the increase of B with the normalized sample age becomes weaker upon increasing the salt concentration [see Fig. 4.20(c)]. This result suggests that the brittleness of the suspension is less sensitive to the recovery time, and so to the network toughness, at large salt content, when t_w/t_g increases, i.e., further way from the critical gel point. This result suggests that, as t_w/t_g increases, the re-arrangements in the CNC network formed at the critical gel point become slower and less prominent, resulting in a slowing down of the time evolution of the suspension elastic properties, therefore leading to a weaker dependence of the suspension yielding behavior upon t_w, for a fixed shear rate. Furthermore, we observe that at a given normalized sample age, B decreases with the NaCl concentration. Therefore, the CNC suspension yields in a more ductile way at larger salt content. This is quite counter-intuitive, as we would expect that a CNC suspension containing more salt and therefore having a larger elastic modulus, as evidenced by the time-composition superposition principle, would form a tougher network, which would break in a more brittle way, as observed when varying the recovery time at a given salt content. Interestingly, despite the discrepancies in the brittleness parameter, we observe that the position γ_B/γ_m where we estimate this parameter seems to be independent of the NaCl concentration: whatever the normalized sample age and the corresponding salt content, we observe $\gamma_B/\gamma_m \approx 1.5$ [see Fig. 4.20(d)].

Besides varying the salt concentration, we have also explored the effect of the CNC weight fraction on the suspension yielding behavior, as detailed in Sec. 4.E in Appendix.

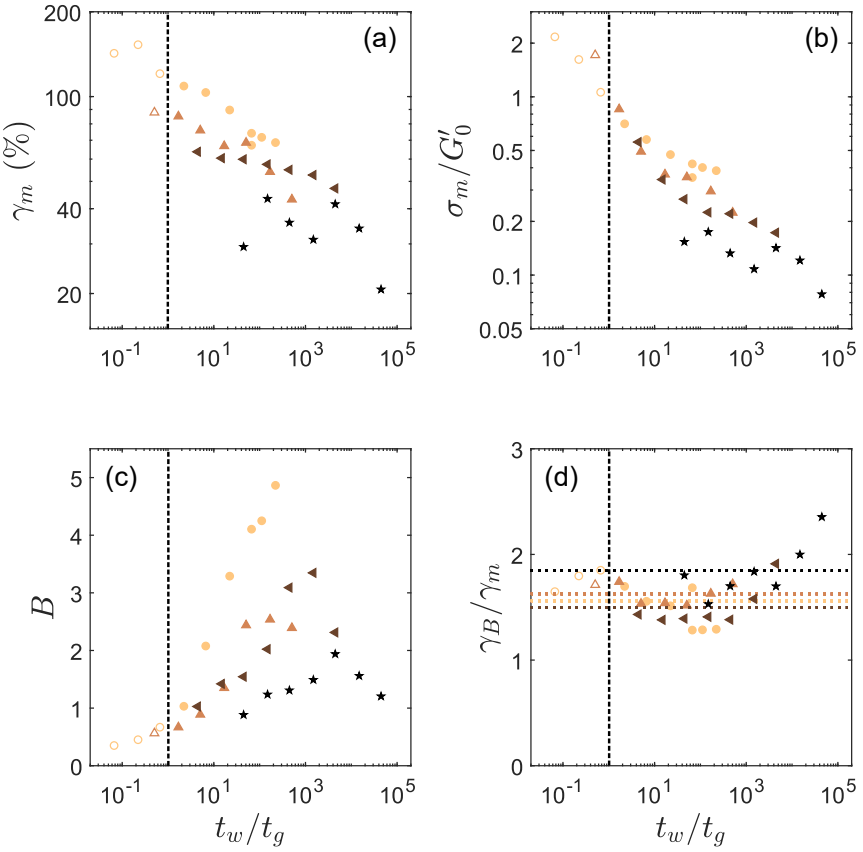

Figure 4.20: Parameters quantifying the impact of the sample age on the shear-induced yielding transition of CNC suspensions containing various NaCl concentrations. (a) Strain γ_m corresponding to the stress maximum during the stress overshoot, (b) stress maximum σ_m normalized by the elastic modulus G_0' measured right prior to the start up experiment, (c) brittleness parameter B, and (d) strain γ_B where B is estimated, normalized by γ_m, as a function of the normalized sample age t_w/t_g, with t_g the suspension gelation time. The empty symbols correspond to $t_w < t_g$, while the filled symbols correspond to $t_w > t_g$. Experiments performed on suspensions containing 3.2 wt % CNC and 18 mM (yellow •), 25 mM (light brown ▲), 35 mM (brown ◂) and 50 mM NaCl (black ⋆), sheared at fixed $\dot{\gamma}$ = 5 s^{-1}. The horizontal dashed lines in (d) show the mean value of γ_B/γ_m over the range of normalized sample ages, for each NaCl concentration.

(1) CNC suspensions show a stress overshoot under continuous shear, irrespective of the experimental parameters and the suspension composition.

(2) The coordinates of this overshoot evolve as a power-law with the applied shear rate $\dot{\gamma}$:

$$\begin{cases} \gamma_m \propto \dot{\gamma}^{\zeta} \\ \sigma_m/\sigma_c - 1 \propto \dot{\gamma}^{\upsilon} \end{cases}$$

(3) The exponents ζ and υ depend on the suspension gelation time t_g, whatever its composition.

(4) The suspension shows a brittle to ductile transition when:

- increasing the recovery time t_w
- decreasing the shear rate $\dot{\gamma}$.

(5) The brittleness parameter B evolves logarithmically with $\dot{\gamma}$ and t_w, with a prefactor that depends on the suspension composition.

(6) The normalized position of the steepest stress decrease, where B is estimated, is independent of $\dot{\gamma}$, of t_w, and of the sample composition: $\gamma_B/\gamma_m \approx 1.5$.

B.5 Rescaling of the parameters quantifying the yielding behavior

In order to rationalize the effects of both the shear rate and the recovery time on the yielding transition of CNC suspensions, we construct a dimensionless parameter from the various characteristic times involved in our system. There are three time-scales to consider in shear start up experiments: one time-scale that is specific to our system, which is the gelation time t_g, and two that arise from the rheological protocol, which are the sample age, or recovery time, t_w and the inverse of the shear rate $1/\dot{\gamma}$. First, a natural thing to do is to compare each of the experimental characteristic times to the gelation time, leading to the dimensionless parameter t_w/t_g for the set of experiments at various t_w, and to the dimensionless parameter $\dot{\gamma}t_g$ for the set of experiments at various $\dot{\gamma}$. Combining those two dimensionless parameters without getting rid of any of the three characteristic times, in order to be able to gather the data from both sets of experiments, we can construct the following dimensionless parameter:

$$\left(\frac{t_w}{t_g}\right)^{\alpha} \times \left(\frac{1}{\dot{\gamma}t_g}\right)^{\delta} \tag{4.12}$$

Adjusting our data, we find a good rescaling for $\alpha = 2$ and $\delta = 1$, leading to[5]:

$$\left(\frac{t_w}{t_g}\right)^{2} \times \left(\frac{1}{\dot{\gamma}t_g}\right)^{1} = \frac{t_w^2}{\dot{\gamma}t_g^3} \tag{4.13}$$

Figure 4.21 shows the yielding parameters extracted from the experiments at various $\dot{\gamma}$ and at various t_w presented in Secs. 4.B.2 and 4.B.3, and in Figs. 4.15 and 4.19 respectively, for a suspension containing 3.2 wt % CNC and 18 mM NaCl. Once plotted as a function of this dimensionless parameter, the data from the two sets of experiments rescale remarkably well for all four parameters, demonstrating an equivalence between an increasing recovery time and a decreasing shear rate, and therefore confirming our statement indicating that decreasing the shear rate leads to a longer effective recovery time.

[5]See Fig. 4.52 in Sec. 4.E in Appendix for tests with other values of α and δ

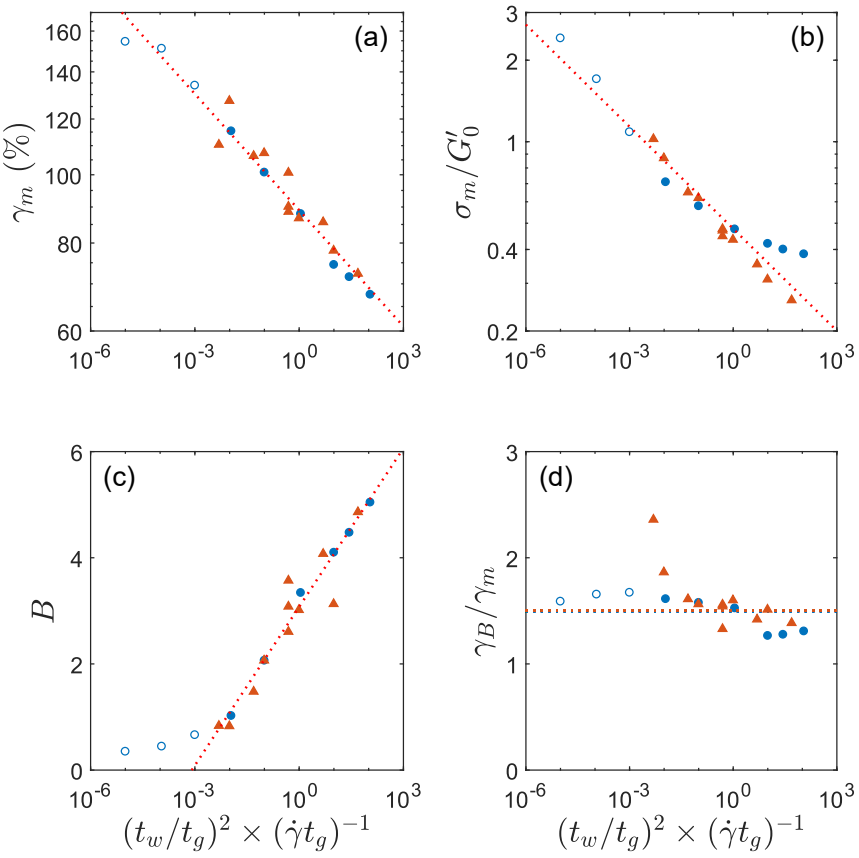

Figure 4.21: Rescaling of the parameters quantifying the shear-induced yielding transition of a CNC suspension when varying both the recovery time (blue •) and the shear rate (orange ▲). Data from Fig. 4.15 and Fig. 4.19. (a) Strain γ_m corresponding to the stress maximum during the stress overshoot, (b) stress maximum σ_m normalized by the elastic modulus G'_0 measured right prior to the start up experiment, (c) brittleness parameter B and (d) strain γ_B where B is estimated, normalized by γ_m, as a function of the dimensionless parameter $\left(\frac{t_w}{t_g}\right)^2 \times \left(\frac{1}{\dot{\gamma}t_g}\right)$. The empty symbols correspond to $t_w < t_g$, while the filled symbols correspond to $t_w > t_g$. Experiments performed on a suspension containing 3.2 wt % CNC and 18 mM NaCl. The red dashed lines in (a) and (b) show the best fits of the data by power-laws given by Eqs. (4.14) and (4.15), with exponents $\xi = 0.05 \pm 0.01$ and $\chi = 0.14 \pm 0.03$ respectively. The red dashed line in (c) shows the best fit of the data, for $t_w > t_g$, by a logarithmic law given by Eq. (4.16), with prefactor $\psi = 1.0 \pm 0.2$. The horizontal red dashed line in (d) shows the mean value of γ_B/γ_m over the range of dimensionless parameter, equal to 1.5.

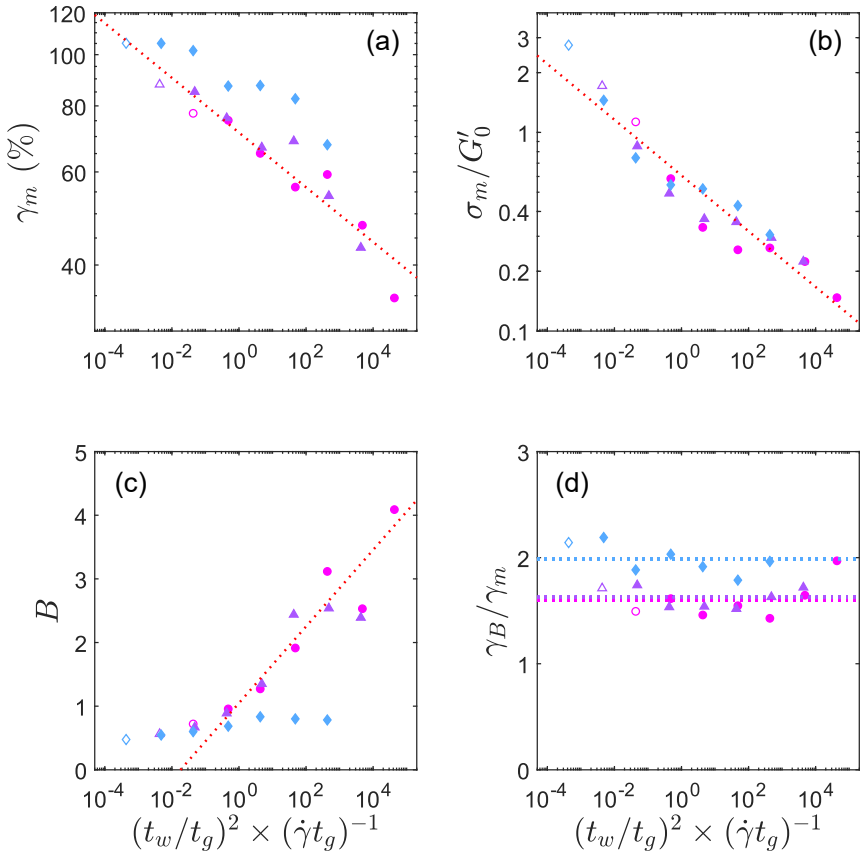

Figure 4.22: Rescaling of the parameters quantifying the shear-induced yielding transition of a CNC suspension when varying the sample age t_w, between 6 s and 6000 s, for three different shear rates: $\dot{\gamma}$ = 0.5 s^{-1} (pink •), $\dot{\gamma}$ = 5 s^{-1} (purple ▲), $\dot{\gamma}$ = 50 s^{-1} (blue ⧫). Data from Fig. 4.51 in Sec. 4.E in Appendix. (a) Strain γ_m corresponding to the stress maximum during the stress overshoot, (b) stress maximum σ_m normalized by the elastic modulus G'_0 measured right prior to the start up experiment, (c) brittleness parameter B, and (d) strain γ_B where B is estimated, normalized by γ_m, as a function of the dimensionless parameter $\left(\frac{t_w}{t_g}\right)^2 \times \left(\frac{1}{\dot{\gamma} t_g}\right)$. Experiments performed on a suspension containing 3.2 wt % CNC and 25 mM NaCl. The red dashed lines in (a) and (b) show the best fits of the data by power-laws given by Eqs. (4.14) and (4.15), with exponents $\xi = 0.05 \pm 0.02$ and $\chi = 0.14 \pm 0.07$ respectively. The red dashed line in (c) shows the best fit of the data, for $t_w > t_g$, by a logarithmic law given by Eq. (4.16), with prefactor $\psi = 0.6 \pm 0.2$. The horizontal dashed lines in (d) show the mean values of γ_B/γ_m over the range of the dimensionless time-scales, for each series of experiments at fixed $\dot{\gamma}$.

Figure 4.22 shows that this rescaling is also well verified for a suspension containing 3.2 wt % CNC and 25 mM NaCl, on which we have performed a series of experiments at various recovery times t_w, ranging between 6 s and 6000 s, for three different shear rates, $\dot{\gamma} = 0.5\ \text{s}^{-1}$, $5\ \text{s}^{-1}$ and $50\ \text{s}^{-1}$ (see Figs. 4.50 and 4.51 in Sec. 4.E in Appendix for the non-rescaled data). The deviations that we observe correspond to the set of data obtained by applying the largest shear rate, i.e., $\dot{\gamma} = 50\ \text{s}^{-1}$, which are more noisy due to the short experimental time interval $\Delta t = 10/\dot{\gamma}$, resulting in a lower resolution around the stress overshoot.

Interestingly, for both suspensions, both γ_m and σ_m/G_0' evolve as a power-law with the dimensionless parameter $\left(\frac{t_w}{t_g}\right)^2 \times \left(\frac{1}{\dot{\gamma} t_g}\right)$:

$$\begin{cases} \gamma_m \propto \left[\left(\dfrac{t_w}{t_g}\right)^2 \times \left(\dfrac{1}{\dot{\gamma} t_g}\right)\right]^{-\xi} & (4.14) \\ \sigma_m/G_0' \propto \left[\left(\dfrac{t_w}{t_g}\right)^2 \times \left(\dfrac{1}{\dot{\gamma} t_g}\right)\right]^{-\chi} & (4.15) \end{cases}$$

with exponents $\xi = 0.05 \pm 0.02$ and $\chi = 0.14 \pm 0.07$, respectively, which seem independent of the salt concentration [see the red fits in Figs. 4.21(a),(b) and in Figs. 4.22(a),(b)]. However, while B is proportional to the logarithm of $\left(\frac{t_w}{t_g}\right)^2 \times \left(\frac{1}{\dot{\gamma} t_g}\right)$ for both salt concentrations, for $t_w > t_g$:

$$B - B_0 = \psi \log\left[\left(\frac{t_w}{t_g}\right)^2 \times \left(\frac{1}{\dot{\gamma} t_g}\right)\right], \tag{4.16}$$

the proportionality factor ψ does depend on the salt concentration. Indeed, it decreases from 1.0 to 0.6 when the salt concentration is increased from 18 mM to 25 mM, at constant CNC weight fraction $w_{\text{CNC}} = 3.2$ wt %.

Figure 4.23 shows the data from Sec. 4.B.4 for suspensions containing 3.2 wt % CNC and various NaCl concentrations, plotted as a function of the dimensionless parameter $\left(\frac{t_w}{t_g}\right)^2 \times \left(\frac{1}{\dot{\gamma} t_g}\right)$. First, we note that the overshoot coordinates γ_m and σ_m/G_0' rescale well with this dimensionless parameter, as expected from the previous observation that both evolve as a power-law with $\left(\frac{t_w}{t_g}\right)^2 \times \left(\frac{1}{\dot{\gamma} t_g}\right)$ with exponents ξ and χ respectively which are independent of the salt concentration. Interestingly, the exponent ξ for the evolution of γ_m seems to be also independent of the CNC weight fraction. However, it is less clear whether the exponent χ for the evolution of σ_m/G_0' does depend on the CNC concentration [see Figs. 4.53(a) and (b) and Figs. 4.54(a) and (b) in Sec.4.E in Appendix]. Nevertheless, the yielding transition around γ_m is a highly dynamical process, involving a cascade of bond break-up events [Masschaele et al., 2009], and the fluidization scenario is likely to involve spatially heterogeneous dynamics, such as shear bands or wall slip [Persello et al., 1994, Perge et al., 2014, Gibaud et al., 2016, Gibaud et al., 2022], which could partially account for the dispersion that we observe in the data.

Finally, the parameter B estimated for various salt concentrations does not rescale when plotted as a function of the dimensionless parameter $\left(\frac{t_w}{t_g}\right)^2 \times \left(\frac{1}{\dot{\gamma} t_g}\right)$. It was expected from the previous observation that the proportionality factor ψ does depend on the salt concentration. The origin of the failure of this rescaling of the brittleness parameter can be understood from Fig. 4.24. Fig. 4.24(a) shows the stress responses of a suspension containing 3.2 wt % CNC and 18 mM NaCl to which we have applied either $\dot{\gamma} = 5\ \text{s}^{-1}$ after a recovery time $t_w = 2000$ s, or $\dot{\gamma} = 0.5\ \text{s}^{-1}$ after a recovery time $t_w = 600$ s. Both experimental conditions correspond to the same value of the dimensionless parameter: $\left(\frac{t_w}{t_g}\right)^2 \times \left(\frac{1}{\dot{\gamma} t_g}\right) = 1.0$. We observe that both stress responses are perfectly superimposed.

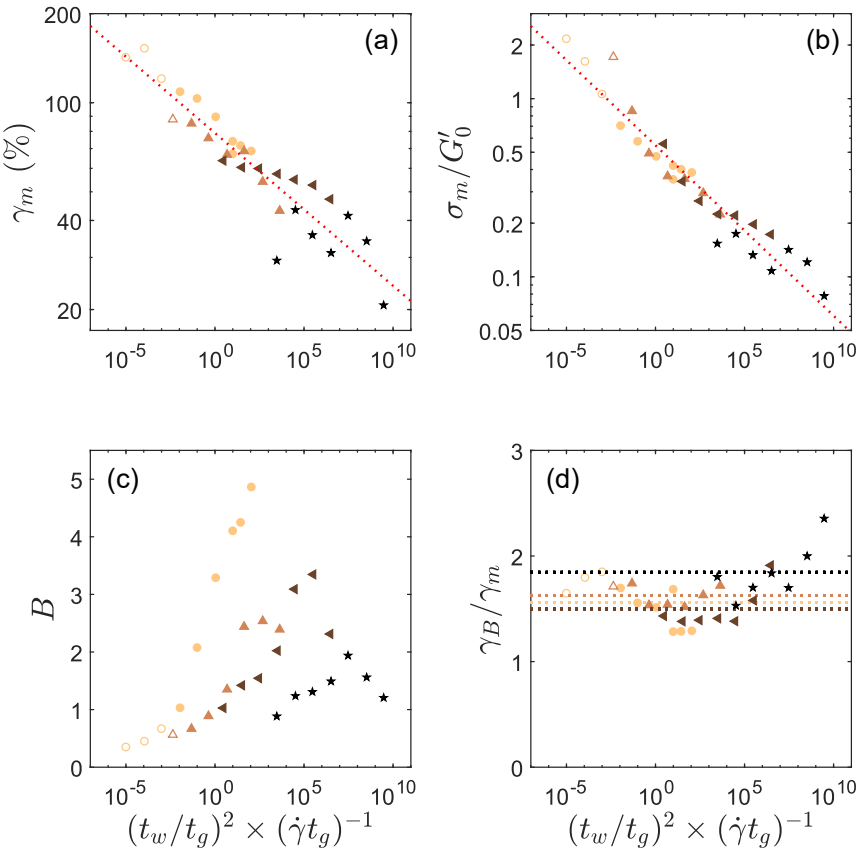

Figure 4.23: Rescaling of the parameters quantifying the shear-induced yielding transition of CNC suspensions containing various NaCl concentrations, when varying the sample age t_w, between 6 s and 6000 s, at a given shear rate $\dot{\gamma}$ = 5 s^{-1}. Data from Fig. 4.20. (a) Strain γ_m corresponding to the stress maximum during the stress overshoot, (b) stress maximum σ_m normalized by the elastic modulus G_0' measured right prior to the start up experiment, (c) brittleness parameter B, and (d) strain γ_B where B is estimated, normalized by γ_m, as a function of the dimensionless parameter $\left(\frac{t_w}{t_g}\right)^2 \times \left(\frac{1}{\dot{\gamma} t_g}\right)$. Experiments performed on suspensions containing 3.2 wt % CNC and 18 mM (yellow •), 25 mM (light brown ▲), 35 mM (brown ◂) and 50 mM NaCl (black ⋆). The red dashed lines in (a) and (b) show the best fits of the data by power-laws given by Eqs. (4.14) and (4.15), with exponents ξ = 0.05 ± 0.02 and χ = 0.10 ± 0.05 respectively. The horizontal dashed lines in (d) show the mean values of γ_B/γ_m over the range of the dimensionless time-scales, for each NaCl concentration.

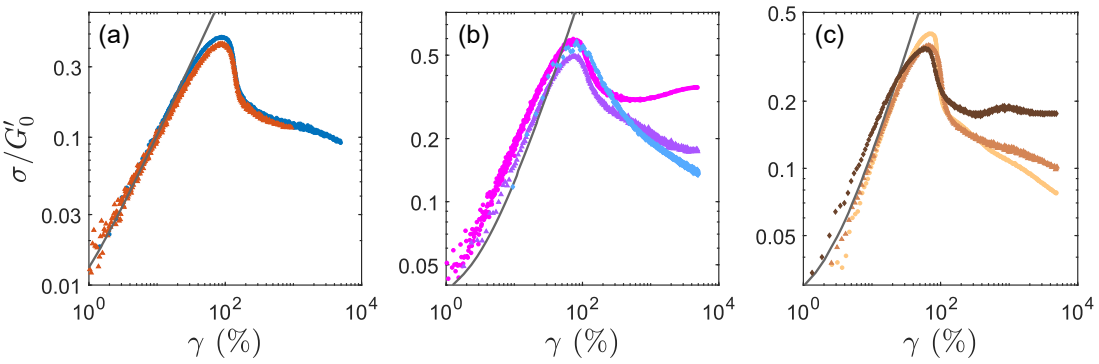

Figure 4.24: Shear-induced yielding transition of CNC suspensions with experimental parameters t_w and $\dot{\gamma}$ adjusted in order to keep a constant value for the rescaling parameter $\left(\frac{t_w}{t_g}\right)^2 \times \left(\frac{1}{\dot{\gamma} t_g}\right)$. Stress σ normalized by the elastic modulus G_0' measured right prior to the start up experiment as a function of strain γ. Data from Figs. 4.13 and 4.18, from Fig. 4.50 in Sec. 4.E in Appendix, and from Fig. 4.47 in Sec. 4.E in Appendix respectively. (a) For a suspension containing 3.2 wt % CNC and 18 mM NaCl, with t_w = 2000 s and $\dot{\gamma}$ = 5 s^{-1}, leading to $\left(\frac{t_w}{t_g}\right)^2 \times \left(\frac{1}{\dot{\gamma} t_g}\right)$ = 1.1 (blue •), and with t_w = 600 s and $\dot{\gamma}$ = 0.5 s^{-1}, leading to $\left(\frac{t_w}{t_g}\right)^2 \times \left(\frac{1}{\dot{\gamma} t_g}\right)$ = 1.0 (orange ▲). (b) For a suspension containing 3.2 wt % CNC and 25 mM NaCl, with t_w = 20 s and $\dot{\gamma}$ = 0.5 s^{-1}, leading to $\left(\frac{t_w}{t_g}\right)^2 \times \left(\frac{1}{\dot{\gamma} t_g}\right)$ = 0.48 (pink •), with t_w = 60 s and $\dot{\gamma}$ = 5 s^{-1}, leading to $\left(\frac{t_w}{t_g}\right)^2 \times \left(\frac{1}{\dot{\gamma} t_g}\right)$ = 0.89 (purple ▲), and with t_w = 200 s and $\dot{\gamma}$ = 50 s^{-1}, leading to $\left(\frac{t_w}{t_g}\right)^2 \times \left(\frac{1}{\dot{\gamma} t_g}\right)$ = 0.48 (blue ⧫). (c) For a suspension containing 3.2 wt % CNC and 18 mM (yellow •), 25 mM (light brown ▲), and 35 mM NaCl (dark brown ⧫), with $\dot{\gamma}$ = 5 s^{-1}, and t_w = 10000 s, 600 s, and 20 s respectively, leading to $\left(\frac{t_w}{t_g}\right)^2 \times \left(\frac{1}{\dot{\gamma} t_g}\right)$ = 27.3, 43.1, and 32.6 respectively. The gray lines represent the linear elastic response given by $\sigma = G_0'\gamma$.

In particular, the shape of the stress overshoot and the steepness of the stress decrease are very comparable, indicating similar values for the coordinates of the stress overshoot, and more particularly for the parameter B. Indeed, consistently, we measure B = 3.01 for $\dot{\gamma}$ = 0.5 s^{-1} and t_w = 600 s [see the orange ▲ in Fig. 4.24(a)], and B = 3.35 for $\dot{\gamma}$ = 5 s^{-1} and t_w = 2000 s [see the blue • in Fig. 4.24(a)], and the brittleness parameter of both sets of experiments rescale very well with $\left(\frac{t_w}{t_g}\right)^2 \times \left(\frac{1}{\dot{\gamma} t_g}\right)$ [see Fig. 4.21(c)]. This observation support the fact that the parameter $\left(\frac{t_w}{t_g}\right)^2 \times \left(\frac{1}{\dot{\gamma} t_g}\right)$ is a good candidate to properly rescale data from shear start up experiments performed under various parameters.

The relevance of this parameter is strengthen by Fig. 4.24(b), which shows the stress responses of a suspension containing 3.2 wt % CNC and 25 mM NaCl to which we have applied either $\dot{\gamma}$ = 0.5 s^{-1} after a recovery time t_w = 20 s, $\dot{\gamma}$ = 5 s^{-1} after a recovery time t_w = 60 s, or $\dot{\gamma}$ = 50 s^{-1} after a recovery time t_w = 200 s. Here again, the experimental conditions correspond to very similar values of the dimensionless parameter: $\left(\frac{t_w}{t_g}\right)^2 \times \left(\frac{1}{\dot{\gamma} t_g}\right)$ = 0.48, 0.43, and 0.48 respectively. As for the previous set of experiments, we observe that the stress overshoot shapes and steepness are very similar (for γ < 300 %). Consistently, we measure very similar values for the stress overshoot coordinates, and for the brittleness parameter: B = 0.96, 0.89, and 0.69. This last result further supports the relevance of the rescaling parameter $\left(\frac{t_w}{t_g}\right)^2 \times \left(\frac{1}{\dot{\gamma} t_g}\right)$.

Finally, Fig. 4.24(c) shows the stress responses of suspensions containing 3.2 wt % CNC and 18 mM, 25 mM, and 35 mM NaCl, to which we have applied $\dot{\gamma} = 5\ s^{-1}$ after a recovery time t_w = 10000 s, 600 s, and 20 s respectively. These experimental conditions lead to values of the dimensionless parameter: $\left(\frac{t_w}{t_g}\right)^2 \times \left(\frac{1}{\dot{\gamma} t_g}\right)$ = 27.3, 43.1, and 32.6 respectively. We observe that the stress responses of the three samples are quite similar, yet with a notable difference in the shape of the stress overshoots, and more particularly in the steepness of the stress decrease. Indeed, we measure different value for the brittleness parameter: B = 4.24, 2.44, and 1.42 respectively. The fact that B decreases with the salt concentration, while $\left(\frac{t_w}{t_g}\right)^2 \times \left(\frac{1}{\dot{\gamma} t_g}\right)$ does not follow any monotonic evolution, confirms that the brittleness parameter B does not rescale with this dimensionless parameter. Actually, since B is defined using the stress response normalized by the coordinates of the stress overshoot (γ_m, σ_m) [see Eq. (4.6)], it already contains a dependence on t_w, t_g and $\dot{\gamma}$. This specific definition of B might be responsible for the failure to rescale the brittleness parameter of suspensions containing various the salt concentrations, when plotted as a function of $\left(\frac{t_w}{t_g}\right)^2 \times \left(\frac{1}{\dot{\gamma} t_g}\right)$ [see Fig. 4.23(c)]. In any case, the expression for such a phenomenological rescaling parameter remains to be justified from physical modeling.

The dimensionless parameter $\left(\frac{t_w}{t_g}\right)^2 \times \left(\frac{1}{\dot{\gamma} t_g}\right)$ allows one to rescale:

→ the data from experiments at various $\dot{\gamma}$ and at various t_w for a given suspension composition.

→ the data for suspensions of various composition, when varying both the CNC and the salt contents, ***except*** for B, most likely due to its specific definition involving the coordinates of the stress overshoot.

B.6 Shear-induced memory effects

In the previous Sec. 4.B.1.c, we have shown that there was only a very weak effect of shear memory on the yielding behavior of a suspension containing 3.2 wt % CNC and 18 mM NaCl. However, we have observed that this effect can be much more pronounced for suspensions containing more salt. In this section, we study the impact of shear memory on the yielding transition of suspensions where this effect is the most pronounced, i.e., for suspensions with the largest salt concentrations.

a Impact of the accumulation of shear

To begin with, we study the effect of the accumulation of shear, or equivalently strain, resulting from the repetition of start up flows, on the yielding behavior of CNC suspensions. To do so, we repeat four times in a row the rheological protocol detailed in Sec. 4.B.1.a on a single sample loading, with t_w = 100 s and $\dot{\gamma} = 5\ s^{-1}$. Then, we reproduce this set of experiments on a second sample of the same suspension to confirm the reproducibility of the results.

Figures 4.25 and 4.26 show the results obtained for suspensions containing 2 wt % CNC and 50 mM NaCl, 3.2 wt % CNC and 50 mM NaCl, and 5.5 wt % CNC and 14 mM NaCl, where γ_{tot} is the total strain accumulated through each repetition of the protocol during steps (1) to (3), (5) and (6). For every CNC weight fraction, the recovery dynamics are similar for each repetition of the protocol, but we observe a vertical shift of the data [see Figs. 4.25(a)-(c)]. In particular, the elastic modulus at the end of the recovery period G_0' decreases with the accumulation of strain, corresponding to each repetition of the protocol, for suspensions containing 2 wt % CNC and 3.2 wt % CNC, while it increases for the suspension containing 5.5 wt % CNC [see Figs. 4.26(a)-(c)]. Yet, the overshoot coordinates γ_m and σ_m/G_0' and the brittleness parameter B always decrease

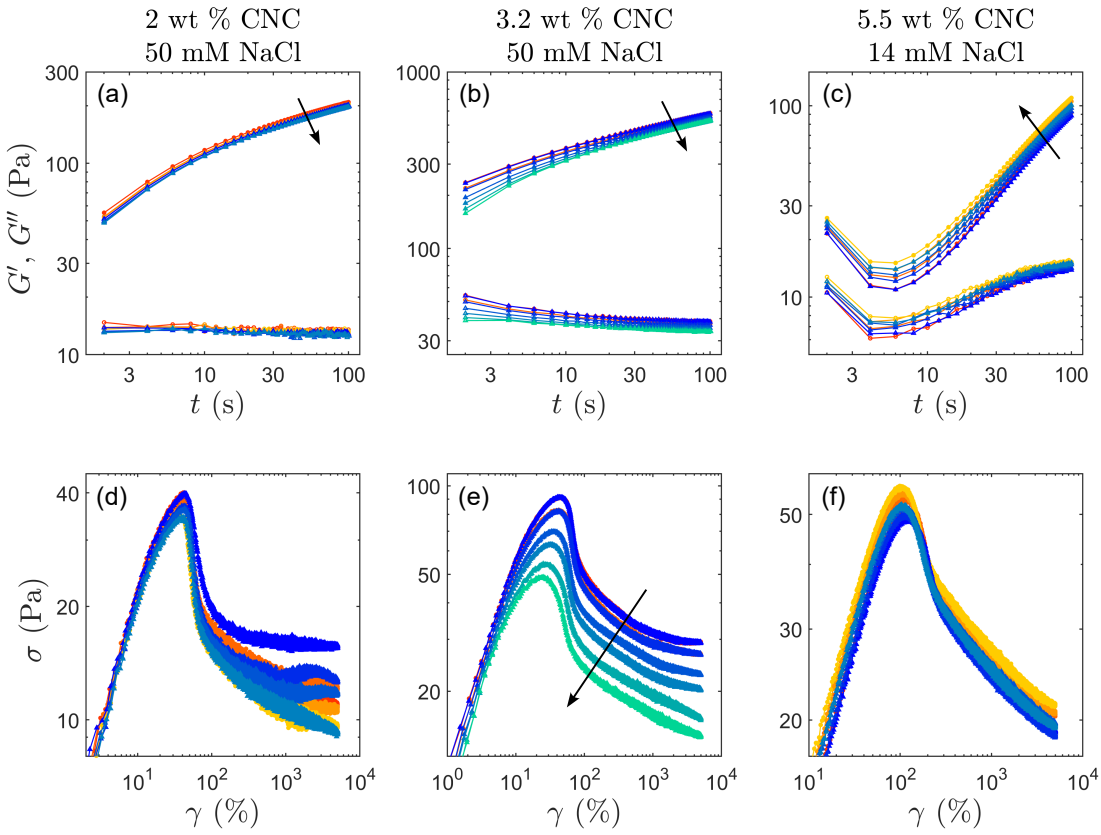

Figure 4.25: Impact of the accumulation of shear on the shear-induced yielding of CNC suspensions of various compositions: (a),(d) 2 wt % CNC and 50 mM NaCl, (b),(e) 3.2 wt % CNC and 50 mM NaCl and (c),(f) 5.5 wt % CNC and 14 mM NaCl. (a),(b),(c) Elastic modulus G' (filled symbols) and viscous modulus G'' (empty symbols) as a function of time during the recovery period of duration t_w = 100 s prior to shear start up. (d),(e),(f) Stress as a function of strain during shear start up experiments at $\dot{\gamma}$ = 5 s^{-1}. The blue to green colorscale (▲) codes for the repetition of the experiment on a first sample loading, and the red to yellow colorscale (•) codes for a second sample loading.

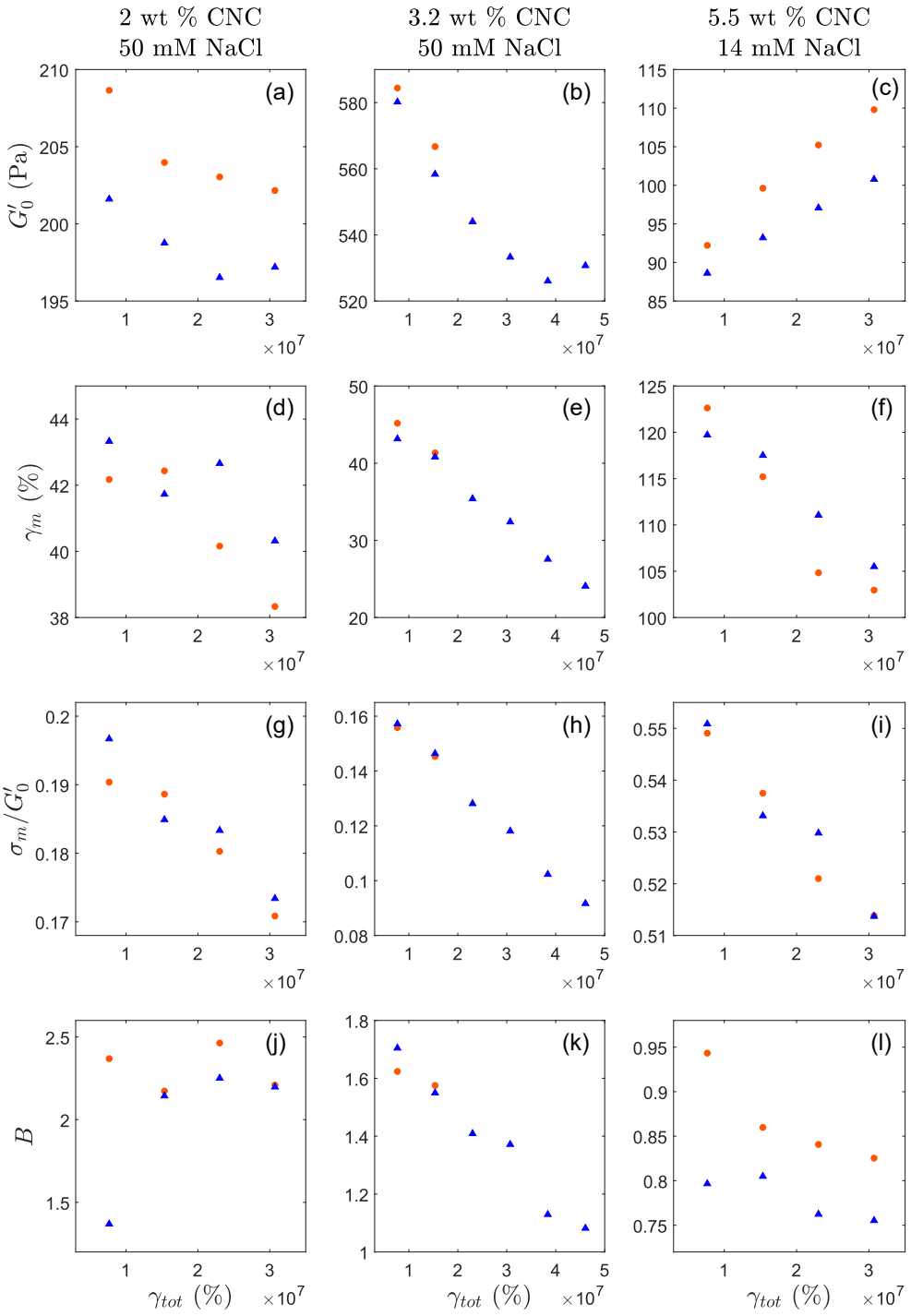

Figure 4.26: Parameters quantifying the impact of the accumulation of shear on the shear-induced yielding transition of suspensions of various compositions: 2 wt % CNC and 50 mM NaCl (first row), 3.2 wt % CNC and 50 mM NaCl (second row) and 5.5 wt % CNC and 14 mM NaCl (third row). Data from Fig. 4.25. (First line) Elastic modulus G_0' measured at time t_w, at the end of the recovery period, right prior to the start up experiment, (Second line) strain γ_m corresponding to the stress maximum during the stress overshoot, (Third line) stress maximum σ_m normalized by G_0' and (Forth line) brittleness parameter B as a function of the total strain γ_{tot} underwent by the sample along the four repetitions of the experiment. The two symbols and associated colors correspond to the data obtained for two distinct loadings of a same suspension. Experiments performed with a fixed recovery time t_w = 100 s, and a fixed shear rate $\dot{\gamma}$ = 5 s^{-1}.

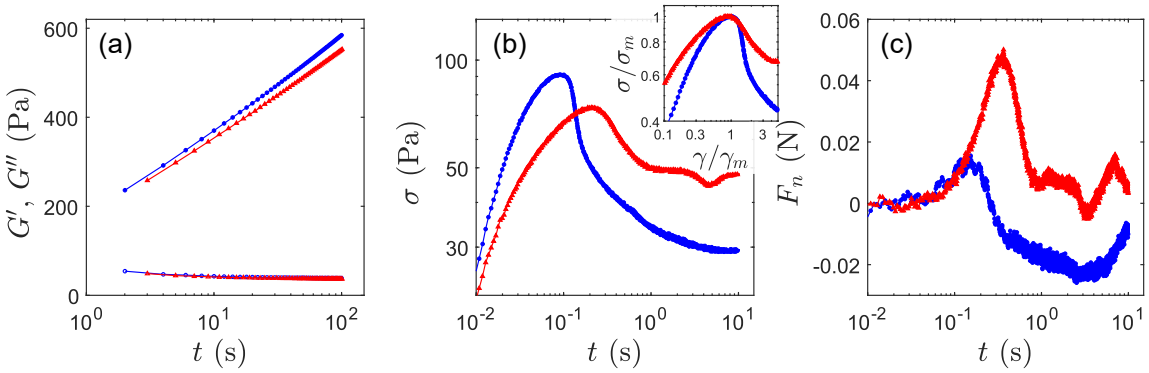

Figure 4.27: Effect of the shear direction relative to pre-shear on the yielding transition: $\dot{\gamma} = +5\ \mathrm{s}^{-1}$ (blue •) and $\dot{\gamma} = -5\ \mathrm{s}^{-1}$ (red ▲). (a) Elastic modulus G' (filled symbols) and the viscous modulus G'' (empty symbols) as a function of time during the sample recovery following pre-shear. (b) Stress σ as a function of time during the shear start up experiment following the recovery period. The inset shows an enlargement of the data, normalized by the coordinates of the stress maximum. (c) Normal force F_n as a function of time during the shear start up experiment. Experiments performed on two distinct loadings of the same suspension containing 3.2 wt % CNC and 50 mM NaCl, with a fixed recovery time $t_w = 100$ s.

with the accumulation of strain. Moreover, the variations of G'_0 are generally smaller than the variations induced by the accumulation of strain on the overshoot coordinates γ_m and σ_m/G'_0 [see Figs. 4.25(d)-(f) and Figs. 4.26(d)-(f) and (g)-(i) respectively], and on the brittleness parameter B [see Figs. 4.26(j)-(l)]: while G'_0 decreases by about 3 % and 8 % for the suspensions containing 2 wt % CNC and 3.2 wt % CNC respectively, and increases by about 12 % for the suspension containing 5.5 wt % CNC, γ_m decreases by about 6 %, 27 % and 13 %, σ_m/G'_0 by about 13 %, 25 % and 6 % and B by about 6 %, 19 % and 6 % respectively. This observation demonstrates that the changes in the yielding behavior of the suspension cannot be simply explained by the change in the elastic modulus. These results highlight a memory effect in CNC suspensions, whose yielding properties do depend on their shear history, or at least on the total strain they have undergone. This memory effect might be due to some alignment of the CNC particles or clusters in the direction of shear. In fact, it has already been evidenced, for a two dimensional colloidal gel, that clusters of particles orient and deform during yielding under continuous shear [Masschaele et al., 2009]. Moreover, it has been shown that CNC particles do align under shear, with a more pronounced overall alignment at larger shear rate [Hausmann et al., 2018, Shafiei-Sabet et al., 2014]. Interestingly, this memory effect is not visible in the linear regime of deformations, as highlighted by the superposition of all the σ versus γ curves before the stress overshoot, for $\gamma < \gamma_m$, for all suspensions.

In order to verify the robustness of this effect, we have applied the same series of experiments to a second sample for each suspension (see the red to yellow curves in Fig. 4.25 and the red points in Fig. 4.26). We observe the same memory effect with the same intensity for all suspensions. Moreover, we notice that our yielding experiments are quite repeatable as both the $\sigma(\gamma)$ curves and the corresponding parameters superimpose for each sample of the same suspension.

b Influence of the shear direction relative to pre-shear

In order to test our hypothesis that this memory effect might be due to some alignment of the CNC particles or clusters parallel to the shear direction, we apply the same rheological protocol as detailed in Sec. 4.B.1.a to two samples of the same suspension, but we change the orientation of the shear $\dot{\gamma}$ during the shear start up step, as previously done in Sec. 4.B.1.c.

Figure 4.27 shows the results for a suspension containing 3.2 wt % CNC and 50 mM NaCl for

which this memory effect is quite pronounced, and to which we have applied a positive shear rate $\dot{\gamma} = +5\ s^{-1}$ (blue curves) or a negative shear rate $\dot{\gamma} = -5\ s^{-1}$ (red curves), following the same pre-shear step at $\dot{\gamma} = +500\ s^{-1}$ and the same recovery step for $t_w = 100$ s. We observe that depending on the direction of shear with respect to that of the pre-shear, the yielding response of the sample is very different [see Fig. 4.27(b)]. Indeed, the stress overshoots in both cases, but this overshoot is much less pronounced when we shear the sample in the direction opposite to pre-shear. The position of this overshoot γ_m as well as the maximum stress σ_m are also impacted: γ_m increases from 44.7 % to 116.4 % while σ_m/G_0' decreases from 0.16 to 0.13 when the shear rate goes from positive to a negative. Furthermore, the stress overshoot is more spread in time and in strain when a negative shear rate is applied [see the inset of Fig. 4.27(b)], and the brittleness parameter B decreases from 1.64 to 0.42, therefore indicating a less abrupt failure of the suspension. Interestingly, the effect of the shear orientation also appears at short times, before the stress overshoot: as soon as the continuous shear is applied, the stress responses differ. Such a transition from to a more ductile yielding when reversing the shear direction between pre-shear and shear start up has already been reported in jammed suspensions of polyelectrolyte microgels [Di Dio et al., 2022].

Finally, the normal forces measured during the sample yielding, plotted in Fig. 4.27(c), show a great difference between the two experiments. Such a difference was not observed in Sec. 4.B.1.c for a suspension containing a smaller salt concentration, 18 mM NaCl compared to 50 mM NaCl, and in which no memory effect was observed (see Fig. 4.11). In particular, we note a change of sign of the normal force, corresponding to a change of orientation of this force (pulling on the upper geometry corresponds to $F < 0$, and pushing on the upper geometry corresponds to $F > 0$). Such a difference in the normal force responses is a signature for a different failure scenario. We note a small vertical shift of the elastic modulus during the recovery step of each sample [see Fig. 4.27(a)]. However, this discrepancy is too small to be responsible for the great differences observed in the yielding transition of both samples. Such a strong sensitivity to shear orientation suggests that CNC particles indeed orient under shear to form an anisotropic microstructure. Due to this anisotropy, the microstructure does not deform and fail similarly depending on the direction in which it is sheared, hereby inducing differences both in the linear and in the yielding responses of the suspension. Such an effect of shear on the rheological properties of a colloidal gel of anisotropic particles has already been reported in a study of the impact of pre-shear on the mechanical properties of gels of silica rods [Das and Petekidis, 2022].

c Modification of the pre-shear step to reduce CNC orientation and memory effects

In order to reduce the shear memory effect induced by the orientation of CNC particles or clusters along the shear direction, we modify the pre-shear step corresponding to step (3) in the rheological protocol detailed in Sec. 4.B.1.a. Indeed, the alignment of CNC particles might mainly come from the application of a strong shear for 20 s during the pre-shear step. Therefore, instead of applying a constant shear in a single direction, we now apply an oscillatory strain of frequency $f = 1$ Hz and amplitude about 40 % larger than the suspension yield strain γ_c, determined through a LAOS measurement, as detailed in the next Sec. 4.D, during 600 s. Indeed, it has been shown that a strain amplitude of 40 % γ_c is optimum to minimize the anisotropy induced by shear in the sample microstructure [Di Dio and Cloitre, 2024].

We test the efficiency of this new pre-shear step to minimize anisotropy on the same suspension as in the previous section, containing 3.2 wt % CNC and 50 mM NaCl, for which memory effects are particularly pronounced. Figure 4.28 shows the results obtained by applying four times in a row the same pre-shear/recovery/shear start up protocol on three different samples of the same suspension: two samples for which we apply a positive shear rate $\dot{\gamma} = 5\ s^{-1}$ during the shear start up step (see the curves encoded in the blue and gray color scales) and one sample for which we apply a negative shear rate $\dot{\gamma} = -5\ s^{-1}$ during the shear start up step (see the curves encoded in the orange color scale). Figure 4.29 shows the various parameters that we extract from the rheological response of the three samples, as a function of the total strain they have undergone prior to each

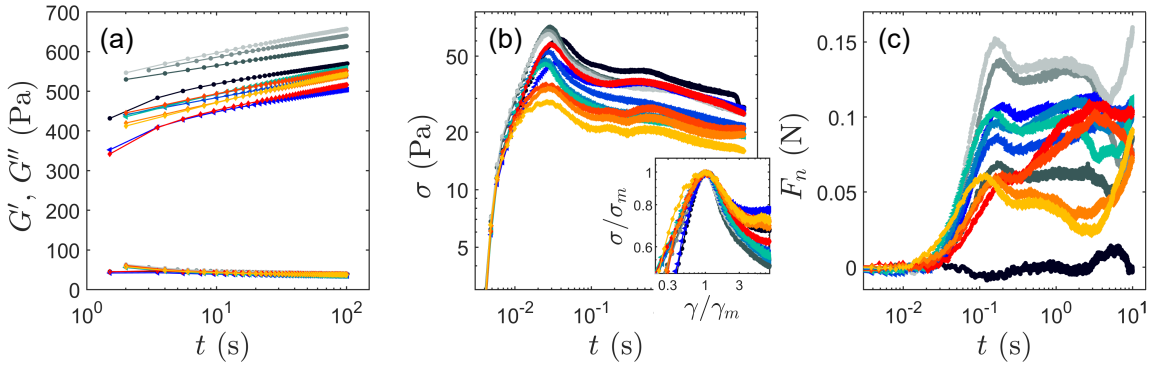

Figure 4.28: Impact of the accumulation of shear and effect of the shear direction on the shear-induced yielding transition, in the case of an oscillatory pre-shear at large amplitude. (a) Elastic modulus G' (filled symbols) and viscous modulus G'' (empty symbols) as a function of time during the sample recovery following pre-shear. (b) Stress σ as a function of time during the shear start up experiment. The inset shows an enlargement of the data, normalized by the coordinates of the stress maximum. (c) Normal force F_n as a function of time during the shear start up experiment. Experiments performed on three distinct loadings of the same suspension containing 3.2 wt % CNC and 50 mM NaCl, with an oscillatory pre-shear at γ = 70 % and f = 1 Hz during 600 s, followed by a t_w = 100 s recovery period. The same experiment is repeated four times in a row on each loading. In blue (▲) and gray (●) colorscales: application of a positive shear rate $\dot{\gamma} = +5\ \mathrm{s}^{-1}$, on two different loadings. In orange colorscale (♦): application of a negative shear rate $\dot{\gamma} = -5\ \mathrm{s}^{-1}$.

shear start up step.

First, we note that for all three samples, the first repetition of the protocol leads to rheological responses which differ slightly from the three following repetitions, both for the recovery step and for the yielding step. This difference might come from some memory of the deformations induced in the sample during loading. This loading memory has not been erased by the oscillatory pre-shear, but it is erased later by the application of the continuous shear at $\dot{\gamma} = 5\ \mathrm{s}^{-1}$ during the shear start up step. For the following three repetitions of the protocol, both the stress and the normal force responses are quite similar for each repetition, and for both shear orientations. However, when looking more precisely the overshoot coordinates and the brittleness parameter, both show a significant effect of the shear direction on the yielding properties of the suspension: γ_m and B vary by a factor about 1.5, and σ_m/G'_0 by a factor of 2. The discrepancy in the values of those parameters can be attributed to variations of the elastic modulus G'_0 for the two samples to which we have applied a positive shear rate. However, this argument cannot hold for justifying the discrepancy observed when changing the shear orientation, as G'_0 takes the same value for both samples (see the blue and red data in Fig. 4.29). This observation suggests that the sample might keep a memory of the orientation of shear during the last half-period of the oscillating pre-shear, which might induce partial alignment of CNC particles along the deformation direction.

Although memory effects are less pronounced when using this oscillatory pre-shear compared to using a strong continuous pre-shear, both on the repeatability and on the shear direction perspectives, this rheological protocol still needs to be improved. The effect of shear orientation could be tackled by applying an oscillatory strain pre-shear of decreasing amplitude [Das and Petekidis, 2022]. However, the fact that some memory from the sample loading is not erased by this oscillatory pre-shear is a matter of concern for controlling the initial state of the sample microstructure, and therefore its final state depending on the rheological protocol. It might not be possible to get rid of this loading memory effect without applying a larger oscillation amplitude or a continuous shear, which might also induce partial alignment of CNC particles and

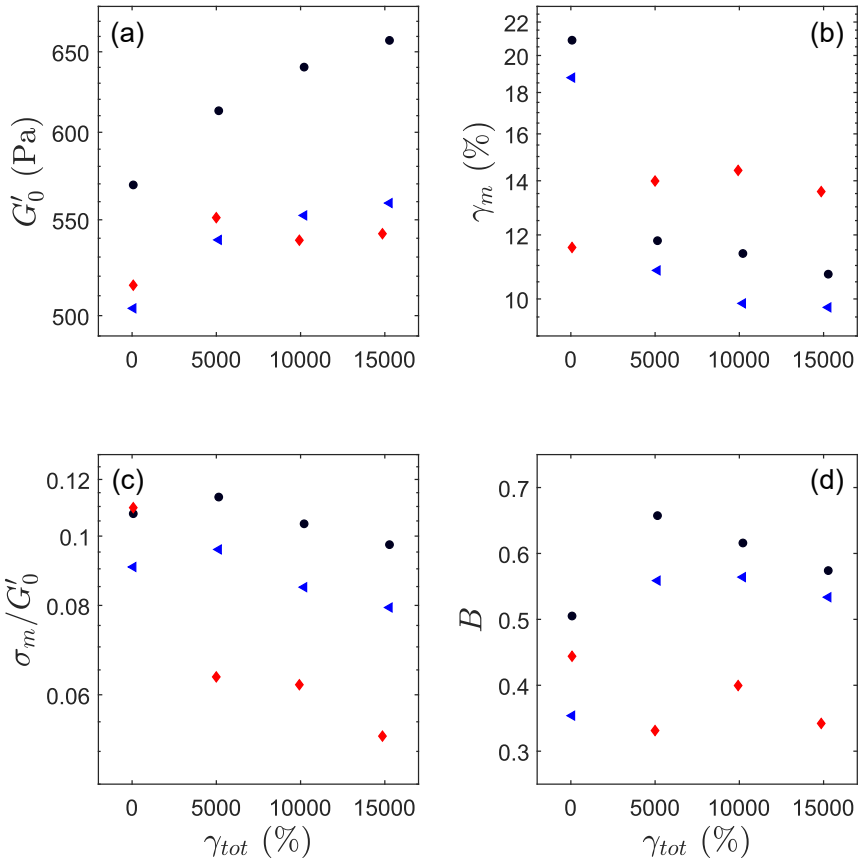

Figure 4.29: Parameters quantifying the impact of the shear direction and of the accumulation of shear on the shear-induced yielding transition of suspensions which have been pre-sheared using large amplitude oscillatory stain. Data from Fig. 4.28. (a) Elastic modulus G_0' measured at time t_w at the end of the recovery period, right prior to the start up experiment (b) strain γ_m corresponding to the stress maximum, (c) stress maximum σ_m normalized by G_0' and (d) brittleness parameter B as a function of the total strain γ_{tot} underwent by the sample along the four repetitions of the same protocol. Experiments performed on three distinct loadings of the same suspension containing 3.2 wt % CNC and 50 mM NaCl, pre-sheared using large amplitude oscillatory strain at γ = 70 %, f = 1 Hz during 600 s, followed by a t_w = 100 s recovery period. In blue (▲) and black (●): application of a positive shear rate $\dot{\gamma}$ = +5 s^{-1}, on two different loadings. In red (⧫): application of a negative shear rate $\dot{\gamma}$ = –5 s^{-1}.

orientation memory effects in return.

Finally, it is important to note that the memory effects due to particle orientation, differing from one pre-shear protocol to the other, only impact the rheological properties of CNC suspensions in their non-linear regime of deformation. Therefore, the results presented in the previous Chapter 3 in the linear regime of deformation are not influenced by the choice of pre-shear protocol.

(1) CNC suspensions at large salt concentration keep a memory of their shear history. Their yielding behavior varies with:

- the accumulation of strain
- the direction of shear.

⇒ Most likely due to CNCs alignment along the shear direction.

(2) Changing the pre-shear protocol from continuous shear to oscillatory shear at large strain amplitude, we observe that:

→ the sample loading memory is not erased

→ the effect of the accumulation of strain is still present.

C Insight into the local fluidization scenario through ultrasound velocimetry

In order to get some insight into the local scenario during fluidization of CNC suspensions under shear, we use the two dimensional ultrasound velocimetry technique developed by Sébastien Manneville [Manneville et al., 2004] and described in Sec. 2.A.3 in Materials and Methods, on a suspension containing 3.2 wt % CNC and 18 mM NaCl, to which we have added 1 wt % of polyamide beads of diameter 30 μm (Orgasol, Arkema) for the shear steps experiments presented in Sec. 4.C.1, and 1 wt % of polystyrene beads of diameter 20 μm (Dynoseeds, Microbeads) for the shear start up experiments presented in Sec. 4.C.2. We have shown in Sec. 2.A.3 that the addition of these beads, which serve as ultrasound contrast agents, do not modify significantly the rheological properties of the CNC suspensions. The resulting suspensions are loaded in a smooth cylindrical Taylor-Couette geometry of height 59 mm, inner rotating cylinder of radius R_{int} = 23 mm, outer fixed cylinder of radius R_{ext} = 25 mm, and gap e = 2 mm, connected to a stress-controlled rheometer (ARG2, TA instrument). In order to prevent evaporation, the cell is closed by a home-made lid, and the temperature is controlled to $T = (23.0 \pm 0.1)$ °C, thanks to a water circulation around the cell.

C.1 Flow curves

We first focus on the flow behavior during steps of constant shear rates, ramping up or down in shear rate. To do so, we impose steps of shear rate of amplitude (1) decreasing logarithmically from $\dot{\gamma}$ = 500 s^{-1} to $\dot{\gamma}$ = 0.01 s^{-1}, with a total of 16 points, and (2) increasing logarithmically from $\dot{\gamma}$ = 10 s^{-1} to $\dot{\gamma}$ = 500 s^{-1}, with a total of 9 points. However, contrary to the experiments performed in Sec. 4.A, step (1) and step (2) are performed on a different sample of the same suspension. Therefore both steps begin with a sample which is in a solid-like initial state. Each shear rate step is applied during δt = 60 s before the start of the ultrasound velocimetry measurements. Those measurements were performed only for $\dot{\gamma}$ varying between 250 s^{-1} and 0.05 s^{-1} for step (1). For each measurement at a given $\dot{\gamma}$, 500 ultrasound pulses are sent with a frequency $f = 40 \times \dot{\gamma}$, except for the step at $\dot{\gamma}$ = 0.05 s^{-1}, which is the slowest, for which 100 pulses are sent. The resulting measurement time interval varies between 0.025 s at large shear rate, to 125 s at small shear rate. We observe that 60 s after the beginning of shear, for any shear rate, the sample flowing behavior does not evolve in time during the ultrasound velocimetry measurement (see the real-time measurements from the links provided in the captions of Figs. 4.30 and 4.34). Therefore, in order to reduce noise, the measurements were averaged in time over the 500 or 100 pulses.

a Ramping down in shear rate

Figure 4.30 shows the results obtained from ultrasound velocimetry, averaged in time, on a CNC suspension containing 3.2 wt % CNC and 18 mM NaCl, sheared at $\dot{\gamma}$ = 10 s^{-1} during the ramping down experiments. Both the intensity map and the velocity map allows us to conclude that the suspension flows uniformly over the geometry height, with no tracers migration induced by shear or by sedimentation [Saint-Michel et al., 2017]. Therefore, in the following, we only consider velocity profiles $v(r)$ that are averaged both in time and over the height of the Taylor-Couette geometry, like the one represented in Fig. 4.30(f). We observe that this velocity profile is curved and does not follow the Newtonian linear prediction represented by the dashed line. This discrepancy shows that this CNC suspension is a non-Newtonian, shear-thinning fluid, as previously deduced from the measurements presented in Sec. 4.A. Furthermore, we observe that at the rotor surface, the sample flows with a velocity $v(r = 0)$ = 15.5 mm.s^{-1} which is smaller than the 18.5 mm.s^{-1} corresponding to the application of a shear rate $\dot{\gamma}$ = 10 s^{-1}. This deviation shows that the sample partially slips on the rotor surface.

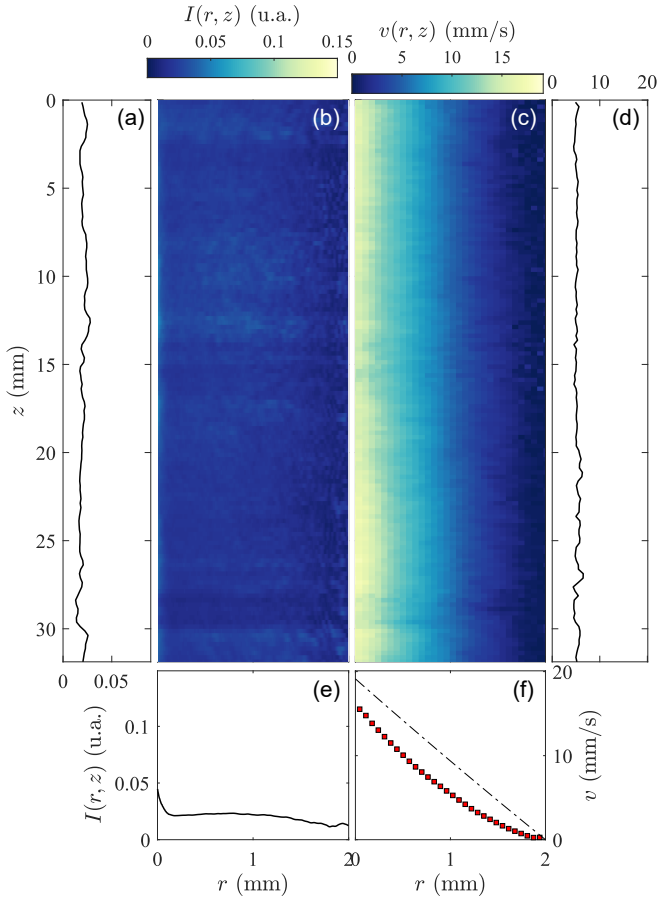

Figure 4.30: (b) Map of the intensity $I(r,z)$ of the ultrasound recorded by the receiver, and (c) map of the calculated velocity $v(r,z)$, in the region of interest. (a) Intensity, and (d) velocity as a function of the gap height z, averaged over the gap depth. (e) Intensity, and (f) velocity as a function of the gap depth r, averaged over the gap height. The dashed line in (f) represents the velocity profile of a Newtonian fluid sheared under the same conditions. Data obtained when shearing a CNC suspension containing 3.2 wt % CNC, 18 mM NaCl and 1 wt % polyamide beads, with a shear rate $\dot{\gamma}$ = 10 s^{-1}, averaged over the 1.23 s of ultrasound measurements, performed 60 s after the beginning of shear (see the video for the non-averaged real-time measurements).

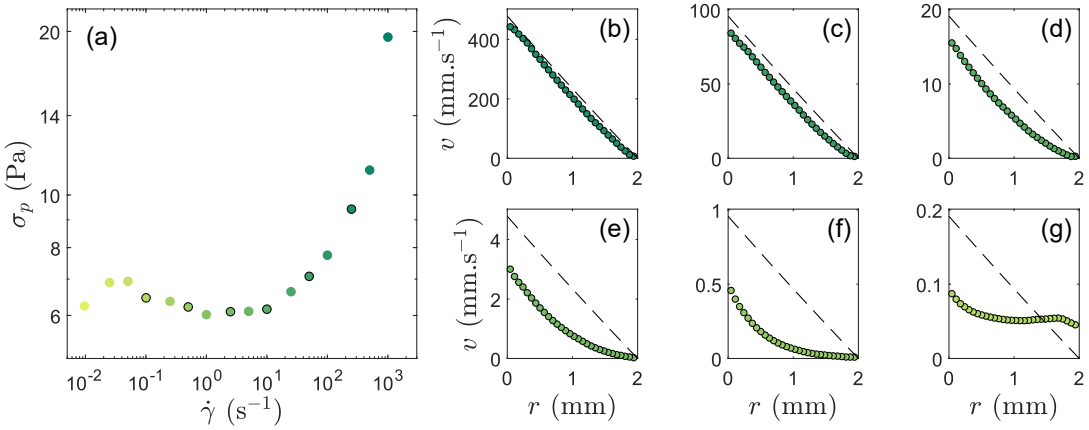

Figure 4.31: (a) Stress σ_p measured 60 s after the start of each shear step, as a function of the imposed shear rate $\dot{\gamma}$. (b)-(g) Velocity profiles corresponding to the dots highlighted in black in (a), averaged over time and over the height of the gap volume: velocity v as a function of the depth r in the gap volume for $\dot{\gamma}$ = 250, 50, 10, 2.5, 0.5, 0.1 s^{-1} respectively. Experiments performed on a suspension containing 3.2 wt % CNC, 18 mM NaCl and 1 wt % polyamide beads.

C. INSIGHT INTO THE LOCAL FLUIDIZATION SCENARIO THROUGH ULTRASOUND VELOCIMETRY

We now explore how the velocity profiles evolve when decreasing the shear rate. Figure 4.31 shows the stress σ_p measured 60 s after the beginning of shear for each shear step, as a function of the imposed shear rate $\dot{\gamma}$, and the velocity profiles corresponding to the data points highlighted in black in the flow curve[6]. We observe that at large shear rate, for $\dot{\gamma} = 500$ s^{-1}, the sample is homogeneously sheared in the volume of the geometry and flows like a Newtonian fluid. When the shear rate decreases, we observe that the velocity profiles deviate from the Newtonian prediction. At $\dot{\gamma} = 0.1$ s^{-1}, the velocity measured at the position of the stator $v(r = 2\text{ mm})$ is not zero, and the velocity measured in the sample volume is almost constant over the gap depth, indicating that the sample slips on both surfaces and shows a plug-like flow, with only two thin lubrication layers near both geometry surfaces, in which the sample is sheared. Moreover, when decreasing the shear rate, the velocity of the sample measured at the rotor surface, for $r = 0$, is smaller than the velocity of the rotor surface v_0, set by $\dot{\gamma}$ through $v_0 = \frac{R_{ext}^2 - R_{int}^2}{R_{ext}^2 + R_{int}^2} R_{int} \times \dot{\gamma}$, hence indicating that the sample slips on the rotor surface. The deviation from the rotor velocity increases when decreasing the shear rate, as well as the normalized slip velocity defined as:

$$v_s/v_0 = \frac{v(r = e) + v_0 - v(r = 0)}{v_0} \tag{4.17}$$

and depicted in Fig. 4.32. This observation, together with the final solid rotation of the sample at small shear rate, suggests that the suspension builds up under shear when the shear rate is small enough, as previously pointed out in Sec. 4.A.

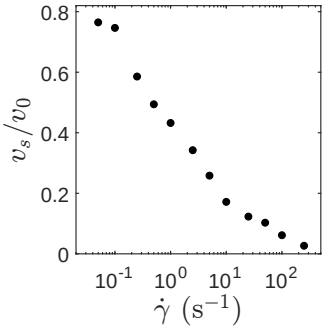

Figure 4.32: Velocity v_s measured in the material at the rotor surface, i.e., at $r = 0$, normalized by the velocity of the rotor surface v_0, as a function of the imposed shear rate $\dot{\gamma}$. Experiments performed on a suspension containing 3.2 wt % CNC, 18 mM NaCl and 1 wt % polyamide beads.

Figure 4.33(a) compares the flow curve of the suspension measured during the ultrasound velocimetry experiments, i.e., using a Taylor-Couette configuration, to the one measured in the same experimental conditions as in Sec. 4.A, i.e., using a cone-and-plate configuration. The two flow curves are very well superimposed for $\dot{\gamma} > 1$ s^{-1}. This result suggests that the overall fluidization scenario at long times are quite similar in both geometries, therefore allowing us to extend our conclusions to the experiments described in Sec. 4.A.

From the velocity profiles, we can correct the flow curve measured by the rheometer by taking into account the sample slip on the geometry surfaces. The corrected flow curve is obtained by plotting the stress as a function of the actual shear rate applied to the bulk sample. In the presence of slip, this shear rate is different from the shear rate imposed to the rotor, and it is given by:

$$\dot{\gamma} = \frac{v(r = 0) - v(r = e)}{e} \tag{4.18}$$

The corrected flow curve is plotted in red symbols in Fig. 4.33(b). We observe that the corrected flow curve is shifted towards smaller shear rates, as expected. For each profile, corresponding to each $\dot{\gamma}$ imposed to the rotor, we can also calculate the local stress $\sigma(r)$ and the local shear rate $\dot{\gamma}(r)$ for every position across the gap r. Indeed, the torque Γ imposed on the rotor in order to apply a shear rate $\dot{\gamma}$, induces the stress distribution $\sigma(r)$ across the sample volume given by:

$$\sigma(r) = \frac{\Gamma}{2\pi h x^2} \tag{4.19}$$

[6]The stress versus time response corresponding to each shear step is plotted in Fig. 4.55(a) in Sec. 4.E in Appendix

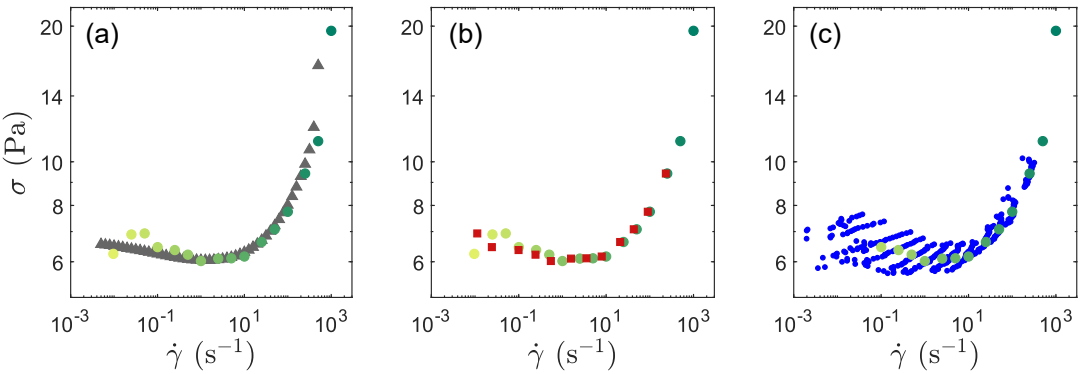

Figure 4.33: Comparison of the flow curves of a suspension containing 3.2 wt % CNC and 18 mM NaCl, obtained through different measurements upon decreasing the shear rate. (a) Stress σ_p measured by the rheometer 60 s after the start of each shear step in a Taylor-Couette geometry (green •), and stress σ measured by the rheometer in a cone-and-plate geometry (gray ▲), as a function of the imposed shear rate $\dot{\gamma}$. (b) Stress σ_p measured by the rheometer 60 s after the start of each shear step, as a function of the imposed shear rate (green •), and as a function of the actual shear rate applied to the sample, corrected taking into account the sample slip using Eq. (4.18) (red ■). (c) Stress σ_p measured by the rheometer 60 s after the start of each shear step as a function of the imposed shear rate (green •), and local stress $\sigma(r)$ as a function of the local shear rate $\dot{\gamma}(r)$ in the sample volume, computed using Eqs. 4.19 and 4.20 (small blue •).

where h is the height of the moving cylinder, and $x = R_{int} + r$ with R_{int} the radius of the moving cylinder. Then, the velocity profile yields the local shear rate $\dot{\gamma}(r)$ using the relationship:

$$\dot{\gamma}(r) = -x\frac{\partial}{\partial r}\frac{v(r)}{x}. \tag{4.20}$$

The resulting local flow curves are plotted in blue symbols in Fig. 4.33(c) and compared to the global flow curve measured by the rheometer. We observe that as soon as the shear rate decreases below 30 s^{-1}, the local flow curves deviate strongly from the global one. This result indicates that, as we ramp down in shear rate, the rheology of our suspension changes. This observation confirms our previous statement that the suspension recovers under shear, at small enough shear rate.

b Ramping up in shear rate

We now focus on the second step of the protocol, i.e., inducing yielding and fluidization of a CNC suspension by applying shear steps of increasing amplitude. Similarly to Fig. 4.30, Fig. 4.34 shows the intensity and the velocity map of the same suspension, containing 3.2 wt % CNC, 18 mM NaCl and 1 wt % polystyrene beads, sheared at $\dot{\gamma} = 40$ s^{-1} for 60 s during the ramping up experiment. Interestingly, this map is very different from the one presented above: contrary to what we have observed in Fig. 4.30, even though the shear rate is four times larger, part of the sample has not been fluidized yet and does not flow. Indeed the high level of noise for $r > 0.6$ mm indicates that no beads displacement is recorded, and therefore that $v = 0$ in this part of the sample. Nevertheless, as observed in Fig. 4.30, the velocity profile is uniform over the volume height z. Therefore, we can here again only consider profiles that are averaged both over the measurement time and the cylinder height z. An example of such a velocity profile is presented in Fig. 4.34(f). Once again, we observe that the velocity profile does not follow the Newtonian prediction: the sample slips

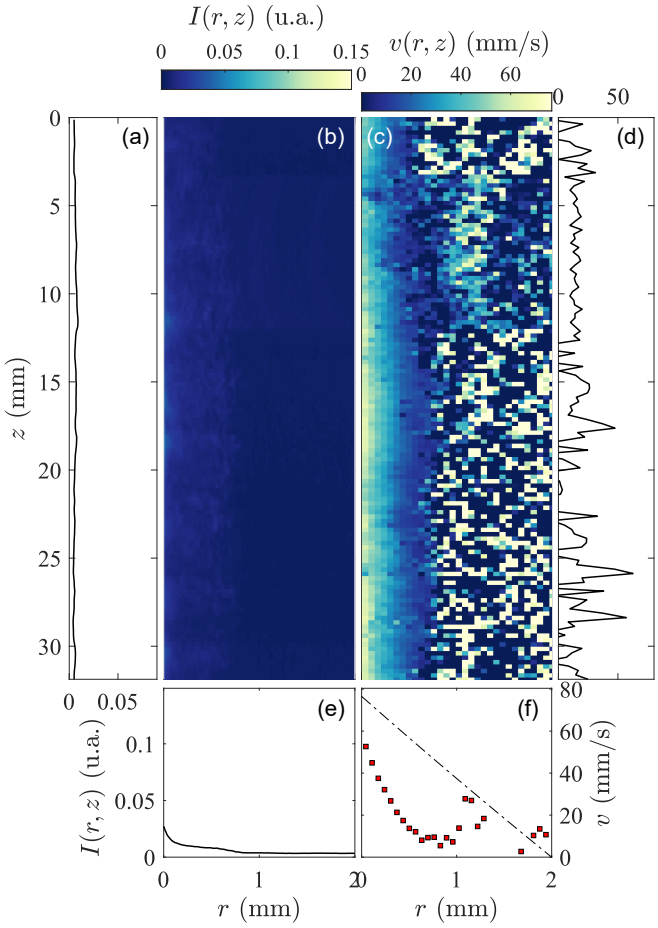

Figure 4.34: (b) Map of the intensity $I(r,z)$ of the ultrasound recorded by the receiver, and (c) map of the calculated velocity $v(r,z)$, in the region of interest. (a) Intensity, and (d) velocity as a function of the gap height z, averaged over the gap depth. (e) Intensity, and (f) velocity as a function of the gap depth r, averaged over the gap height. The dashed line in (f) represents the velocity profile of a Newtonian fluid sheared under the same conditions. Data obtained when shearing a CNC suspension containing 3.2 wt % CNC, 18 mM NaCl and 1 wt % polyamide beads, with a shear rate $\dot{\gamma} = 40$ s^{-1}, averaged over the 0.06 s of ultrasound measurements, performed 60 s after the beginning of shear (see the video for the non-averaged real-time measurements).

on the rotor surface, as the velocity measured at $r = 0$ is smaller than the one of the rotor, and an arrested band is present between $r = 0.6$ mm and $r = 2$ mm, corresponding to the rotor position.

Figure 4.35 presents the stress measured after the 60 s of shear for each step, as a function of the shear rate, and the velocity profiles corresponding to some of the shear steps, highlighted in black on the ramping up flow curve[7]. Looking at the velocity profiles, we observe that at small shear rate, only a small volume of the sample near the rotor surface is sheared and flows, but also slips on the rotor surface, as described in the previous paragraph. Interestingly, when the shear rate increases, the volume of sheared sample does not increase, and the size of the arrested band remains about constant. Indeed, in this arrested band, the sample is not sheared. Therefore, the suspension can continue to age and to solidify, so that the CNC network becomes stronger and does not break when the shear rate is increased. However, when the imposed shear rate is large enough, the whole sample is fluidized, without any slip on the geometry surfaces, and it flows following the Newtonian prediction.

[7]The stress versus time response corresponding to each shear step is plotted in Fig. 4.55(b) in Sec. 4.E in Appendix

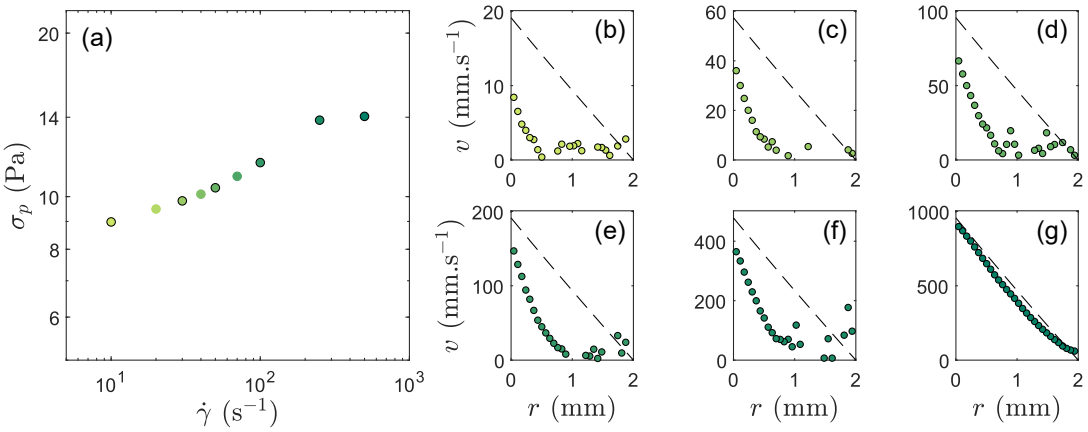

Figure 4.35: (a) Stress σ_p measured 60 s after the start of each shear step, as a function of the imposed shear rate $\dot{\gamma}$. (b)-(g) Velocity profiles corresponding to the dots highlighted in black in (a), averaged over time and over the height of the gap volume: velocity v as a function of the depth r in the gap volume for $\dot{\gamma}$ = 10, 30, 50, 100, 250, 500 s^{-1} respectively. Experiments performed on a suspension containing 3.2 wt % CNC, 18 mM NaCl and 1 wt % polyamide beads.

(1) Starting from a large shear rate where the whole suspension is fluidized, the bulk of the suspension progressively stops flowing when decreasing the shear rate as the suspension reconstructs under shear and slips on the geometry surfaces.

(2) Starting from a small shear rate and a solid-like suspension, only a small volume of the suspension is fluidized near the rotor, while the rest of the suspension is not sheared and continues to age. A very large shear rate $\dot{\gamma} > 250$ s^{-1} is necessary for the suspension to be fully fluidized.

(3) The local flow scenario presents strong differences depending on whether the shear rate is decreased or increased. This is consistent with the strong hysteresis in the flow curves, and with their dependence on the measurement interval time δt revealed in Sec. 4.A.

C.2 Yielding under continuous shear: shear start up experiments

The experiments described in this section are performed using a rheological protocol similar to the one detailed in Sec. 4.B.1.a for the shear start up experiments, on a suspension containing 3.2 wt % CNC and 18 mM NaCl. First, the sample is strongly pre-sheared in order to fluidize it and obtain a reproducible initial state, by applying $\dot{\gamma}_p$ = 1000 s^{-1} during 60 s. Then, we let it recover during a time t_w while measuring its viscoelastic properties by applying a small amplitude oscillatory strain of frequency f = 1 Hz and amplitude γ = 0.2 %. Finally, we continuously shear the sample by imposing a constant shear rate $\dot{\gamma}$, and we simultaneously measure the velocity profiles resolved in time and in space across the bulk sample, by applying pulses of ultrasound at a frequency $f = 40 \times \dot{\gamma}$, and for a time long enough for the sample to yield.

It is expected that the yielding behavior of a soft material might depend on the geometry in which it is loaded. In order to verify the equivalence between configurations, and ensure that we can compare the results presented in this sections using a smooth Taylor-Couette geometry, to the one presented in the above Sec. 4.B using a sand blasted cone-and-plate geometry, we compare sets of data obtained in both configurations, using the same rheological protocol, detailed in

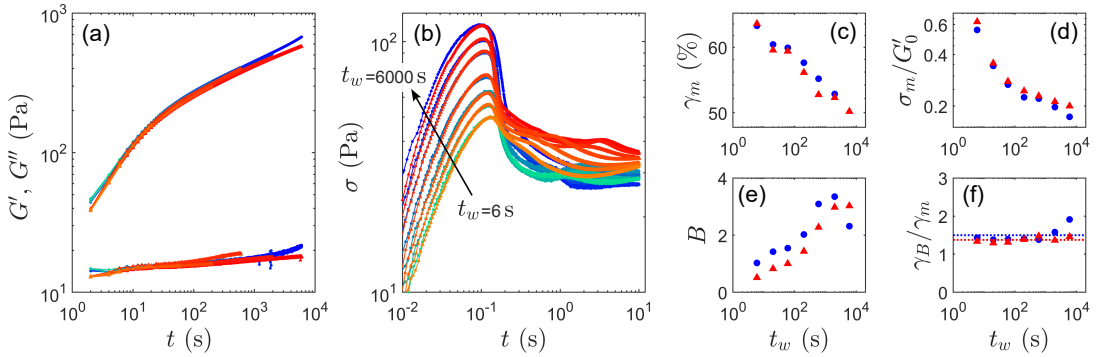

Figure 4.36: Effect of the geometry on the shear-induced yielding of a CNC suspension. Comparison of shear start up experiments made with a cone-and-plate geometry (blue to green colorscale •) and with a Taylor-Couette geometry (red to orange colorscale ▲). Experiments performed on a suspension containing 3.2 wt % CNC and 35 mM NaCl, varying the recovery time t_w from 6 s to 6000 s (green to blue and orange to red respectively), and keeping a constant value for the shear rate $\dot{\gamma} = 5\ s^{-1}$ (see the protocol detailed in Sec. 4.B.1.a). (a) Elastic modulus G' (filled symbols) and viscous modulus G'' (empty symbols) as a function of time during the sample recovery following pre-shear, and preceding the start up experiment. (b) Stress σ as a function of time during the shear start up experiment. (c) Strain γ_m corresponding to the stress maximum, (d) stress maximum σ_m normalized by the elastic modulus G'_0 measured right prior to the start up experiment, (e) brittleness parameter B and (f) strain γ_B where B is estimated, normalized by γ_m, as a function of the sample age t_w for the two series of experiments.

Sec. 4.B.1.a, and the same rheometer (ARES G2, TA Instrument). To carry out this comparison, we use two samples in which the memory effects described in Sec. 4.B.6 are the most pronounced, and therefore for which we could expect a greater sensitivity to the boundary conditions, and therefore to the configuration used: a suspension containing 3.2 wt % CNC and 35 mM NaCl, and a suspension containing 5.5 wt % CNC and 14 mM NaCl.

Figure 4.36 shows the results for the suspension containing 3.2 wt % CNC and 35 mM NaCl, with t_w varying between 6 s and 6000 s, and a constant shear rate $\dot{\gamma} = 5\ s^{-1}$. The results for the suspension containing 5.5 wt % CNC and 14 mM NaCl are quite similar and are presented in Fig. 4.46 in Sec. 4.E in Appendix. We observe that both the recovery and the yielding of the suspension are very similar in both configurations, whatever the recovery time. Indeed, the dependence of all the yielding parameters with the recovery time t_w are all very well superimposed. This result allows us to conclude that the geometry does not play a significant role on the suspension yielding. Therefore, we can compare the results presented in this section to the ones presented in the previous Sec. 4.B.

For both sets of experiments at fixed recovery time t_w or at fixed shear rate $\dot{\gamma}$, we observe that, as in the previous section, the sample yields uniformly over the gap height (see the real-time measurements from the links provided in the captions of Figs. 4.37 and 4.38). Therefore, in the following, we shall only consider velocity profiles that are averaged over the gap height z. Moreover, the ultrasound measurements are averaged over time using a moving average over five measurements corresponding to five consecutive ultrasound pulses.

We perform two sets of experiments on the suspension containing 3.2 wt % CNC, 18 mM NaCl and 1 wt % polyamide beads, of gelation time $t_g = 90.2$ s: one where the recovery time is fixed to $t_w = 600$ s and the shear rate is varied between 0.05 s^{-1} and 10 s^{-1}, and another where the recovery time t_w is varied between 60 s and 6000 s and the shear rate is fixed to $\dot{\gamma} = 0.5\ s^{-1}$. Figure 4.37 presents the data from the first set of experiments, for two different shear rates, $\dot{\gamma} = 0.5\ s^{-1}$ and

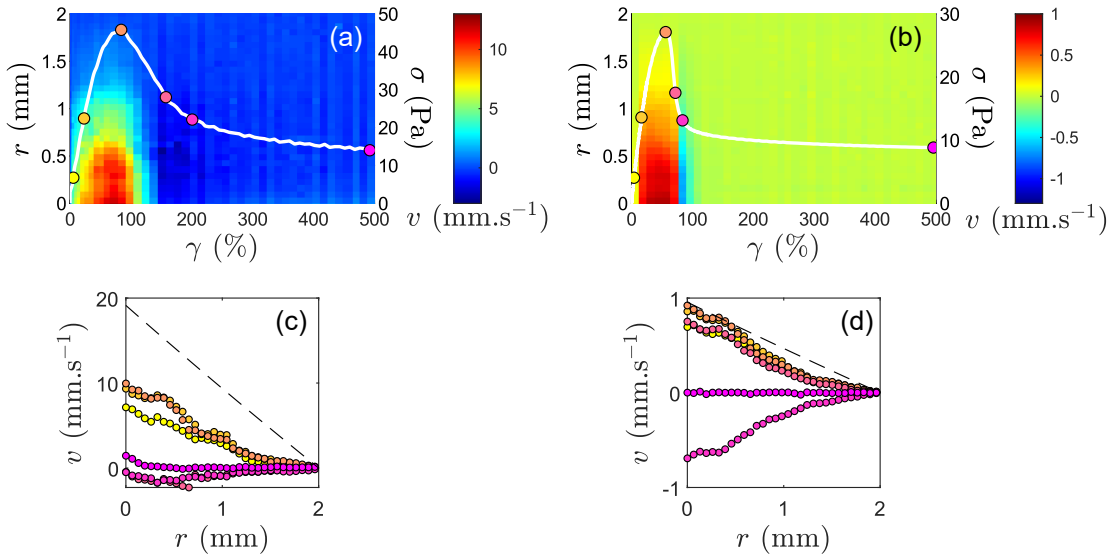

Figure 4.37: Comparison of the local scenario during shear-induced yielding of a CNC suspension, sheared at (a),(c) $\dot{\gamma}$ = 10 s^{-1} (B = 1.15) and (b),(d) $\dot{\gamma}$ = 0.5 s^{-1} (B = 3.36), after a t_w = 600 s recovery period, using ultrasound velocimetry measurements. (a),(b) Velocity v measured along the radial direction r as a function of the imposed strain γ during the shear start up experiment (blue to red colorscale), and stress σ measured by the rheometer as a function of the imposed strain γ (white curve). Data averaged over the height of the gap volume. (c),(d) Velocity profiles corresponding to the positions marked by the colored dots in (a) and (b): at 15 % of the stress maximum σ_m, at 50 % of σ_m, at the stress maximum (γ_m, σ_m), at γ_B, at the minimum (negative) velocities, and at γ = 500 %. The black dashed line represent the velocity profile of a perfect Newtonian fluid sheared at $\dot{\gamma}$. Experiments performed on a suspension containing 3.2 wt % CNC, 18 mM NaCl and 1 wt % polystyrene beads. See the real-time measurements in videos for $\dot{\gamma}$ = 10 s^{-1} and for $\dot{\gamma}$ = 0.5 s^{-1}.

$\dot{\gamma}$ = 10 s^{-1}, while Fig. 4.38 presents the data from the second set of experiments, for the two extreme recovery times t_w = 60 s and t_w = 6000 s.

In all cases, we observe that the sample gradually gets dragged by the rotation of the inner cylinder at small strains, or equivalently, at short times. The strain at which the maximum velocity is reached is slightly smaller than the strain at which the maximum of stress is reached [see Figs. 4.37(a),(b) and Figs. 4.38(a),(b)]. Moreover, we observe that there is always some slip of the sample on the rotor surface, except for the experiment at $\dot{\gamma}$ = 0.5 s^{-1} and t_w = 600 s [see Fig. 4.37(d)].

At larger strains, following the stress maximum, we observe an elastic recoil in the case of the brittle-like yielding, at small shear rate and long recovery time: negative velocities are recorded following the stress overshoot [see Fig. 4.37(d) and Fig. 4.38(d)]. Such negative velocities indicate that after the sample fails, it rotates in the direction opposite to the shear rate due to some remaining internal elastic forces in its microstructure. Such a phenomenon has already been reported in Carbopol microgels [Divoux et al., 2011]. Interestingly, the strain at which this elastic recoil is observed is larger than the strain at which we observe the fastest stress decrease following the stress maximum, where the parameter B is estimated. It is also important to note that this elastic recoil is absent from the response in the case of a ductile-like yielding, at large shear rate and short recovery time [see Fig. 4.37(c) and Fig. 4.38(c)].

Finally, surprisingly, contrary to what one would expect, the bulk sample is not sheared at large strains, or equivalently, at long times, whatever the shear rate and the recovery time. Indeed, we

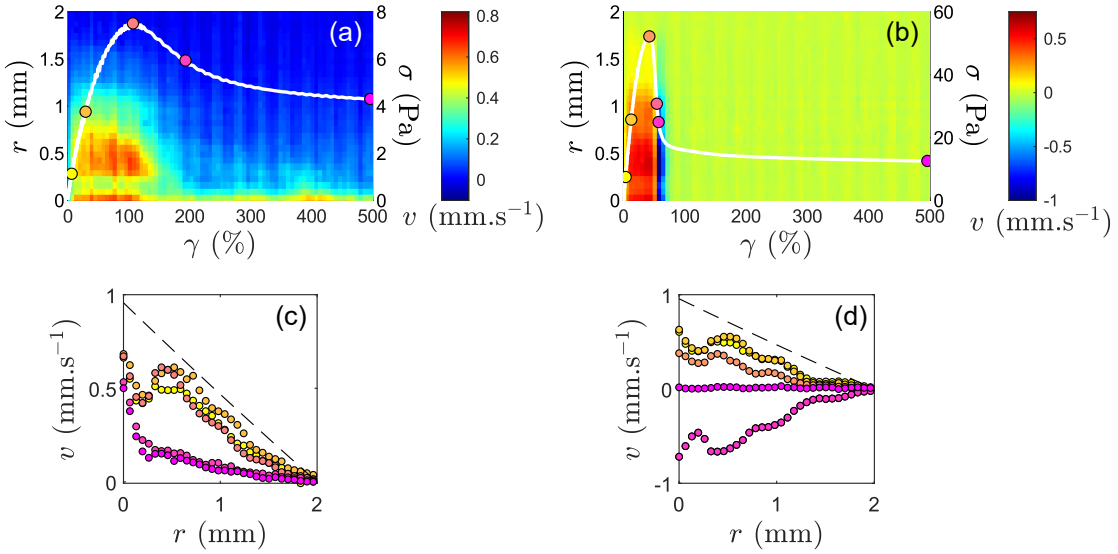

Figure 4.38: Comparison of the local scenario during shear-induced yielding of a CNC suspension, sheared at $\dot{\gamma}$ = 0.5 s^{-1}, after a recovery period of (a),(c) t_w = 60 s (B = 0.58) and (b),(d) t_w = 6000 s (B = 4.74), using ultrasound velocimetry measurements. (a),(b) Velocity v measured along the radial direction r as a function of the imposed strain γ during the shear start up experiment (blue to red colorscale), and stress σ measured by the rheometer as a function of the imposed strain γ (white curve). Data averaged over the height of the gap volume. (c),(d) Velocity profiles corresponding to the positions marked by the colored dots in (a) and (b): at 15 % of the stress maximum σ_m, at 50 % of σ_m, at the stress maximum (γ_m, σ_m), at γ_B, at the minimum (negative) velocities (in (d) only), and at γ = 500 %. The black dashed line represent the velocity profile of a perfect Newtonian fluid sheared at $\dot{\gamma}$. Experiments performed on a suspension containing 3.2 wt % CNC, 18 mM NaCl and 1 wt % polystyrene beads. See the real-time measurements in videos for t_w = 60 s and for t_w = 6000 s.

observe that the sample fully slips on the rotor surface, and zero velocities are measured over the whole gap volume, except for the experiment at $\dot{\gamma}$ = 0.5 s^{-1} and t_w = 60 s [see Figs. 4.38(a) and (c)]. In this case, we observe a shear band at large strains, where the sample is highly sheared over about 0.2 mm close to the rotor, while the rest of the volume is sheared at a much lower shear rate. The fact that the bulk sample does not flow, even at large strains has also been observed in Carbopol microgels [Divoux et al., 2011]. Moreover, this observation is consistent with the measurements made when ramping up in shear rate during the flow curves experiments described in the previous Sec. 4.C.1, where we observe that, by applying 60 s shear steps, the suspension does not flow in its whole volume until a shear rate larger than 250 s^{-1} is applied. However, the suspension might begin to partially flow if we would keep shearing it for a longer time.

(1) The suspension slips on the rotor surface after yielding, whatever the recovery time and the imposed shear rate.

(2) An elastic recoil is present following the suspension failure in the case of a brittle-like yielding transition. This elastic recoil is absent from a ductile-like yielding transition.

(3) After failure, the bulk sample does not flow in bulk. It is either sheared only in a small shear band close to the rotor, or it is totally arrested and fully slips on the rotor surface.

D Yielding under oscillatory shear

In order to make the connection between chapter 3, where all the measurements were performed in the linear regime of deformation, and the previous measurements under flow, we now investigate the gel response to large-amplitude oscillatory shear (LAOS) and ask whether time-composition superposition also holds for non-linear viscoelastic parameters.

D.1 Rheological protocol

To do so, we focus on the LAOS measurements realized during step (4) of the rheological protocols described in Sec. 3.A.1 and in Sec. 3.B.1, and recalled below. As a reminder, those experiments are performed using either a stress-controlled rheometer (MCR 302, Anton Paar) equipped with a cone-and-plate geometry, or a stress-controlled rheometer (ARG G2, TA Instrument) equipped with a Taylor-Couette geometry.

(1) We strongly shear the sample in order to fluidize it and break down its microstructure by imposing a shear rate $\dot{\gamma} = 500$ s^{-1} during 20 s in the cone-and-plate geometry, and a shear rate $\dot{\gamma} = 1000$ s^{-1} during 60 s in the Taylor-Couette geometry. This pre-shear step allows us to obtain a reproducible initial state by minimizing the influence of previous mechanical history, including the loading of the sample into the shear cell.

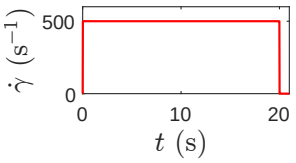

(2) Pre-shear is stopped abruptly by setting $\dot{\gamma} = 0$, which defines the time origin $t = 0$ s, and we subsequently let the sample rest while measuring its linear viscoelastic moduli, i.e., the elastic modulus G' and the viscous modulus G'', every second by imposing small amplitude oscillatory shear (SAOS) at $f = 1$ Hz, or through time-resolved mechanical spectroscopy (see Sec. 3.B.1 in chapter 3).

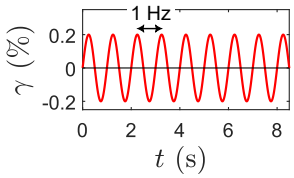

(3) The viscoelastic spectrum G' and G'' versus f is measured through a SAOS measurement consisting on applying an oscillatory strain signal of amplitude $\gamma = 0.2$ % and sweeping down logarithmically the frequency f from 10 Hz to 0.1 Hz with 5 points per decade for the cone-and-plate configuration, and from 20 Hz to 0.1 Hz with 10 points per decade for the Taylor-Couette configuration. In both cases, each frequency is applied for six periods, and the recorded data are averaged over the five last periods.

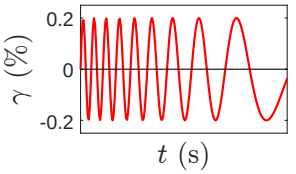

(4) Finally, starting at time t_w following shear cessation, we determine the yielding properties of the sample through a LAOS measurement, consisting on sweeping up logarithmically the oscillatory strain amplitude from $\gamma = 0.02$ % to 500 % at $f = 1$ Hz, with 10 points per decade and a waiting time of 18 s per point, leading to a total duration of 790 s in the case of the cone-and-plate configuration. For each strain amplitude, the recorded data are averaged over the last 9 s of application of the given strain amplitude. In the case of the Taylor-Couette configuration, the strain amplitude is increased from $\gamma = 0.01$ % to 500 % at $f = 1$ Hz, with 10 points per decade and a waiting time of 6 s per point, leading to a total duration of 337 s. In this case, the recorded data are averaged over the last 3 s of application of the given strain amplitude.

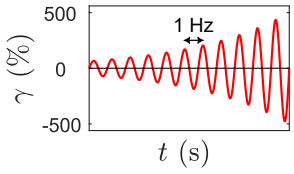

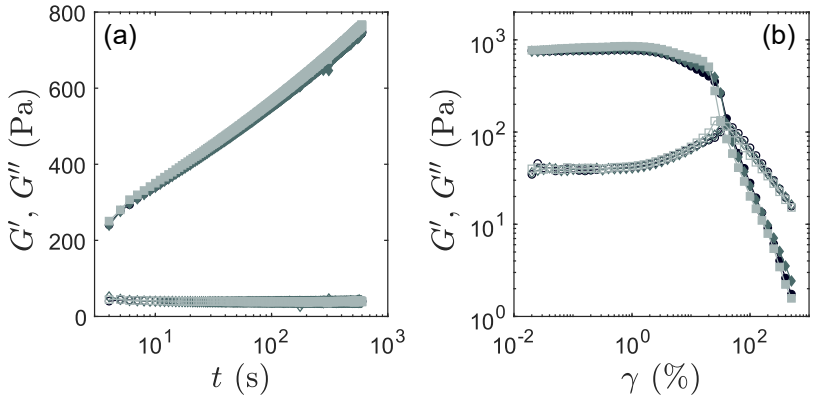

Figure 4.40: Effect of the sweeping rate. (a) Elastic modulus G' (filled symbols) and viscous modulus G'' (empty symbols) as a function of time during the recovery period. (b) Elastic modulus G' (filled symbols) and viscous modulus G'' (empty symbols) versus strain amplitude γ following a 600 s recovery period. Experiments performed on a suspension containing 3.2 wt % CNC and 50 mM NaCl, with a strain amplitude sweeping rate of 9 s per point (black •), 18 s per point (gray ⧫) and 36 s per point (light gray ■).

In order to get some insight into the effect of the ramping rate on the yielding properties of CNC suspensions, we apply three times consecutively the above protocol on a single loading of a suspension containing 3.2 wt % CNC and 50 mM NaCl, of gelation time $t_g \approx 0.01$ s. For every repetition, we vary the measurement duration for the application of each strain amplitude: 9 s per point for the first repetitions, 18 s per point for the second one, and 36 s per point for the last one. We observe from Fig. 4.40(a) that the linear viscoelastic properties of the suspension are superimposed for all repetitions of the protocol. This ensures that the suspension is in a reproducible state at the beginning of the LAOS measurement. Figure 4.40(b) further shows that the yielding behavior of the suspension is similar for the three measurement durations: they present a G'' overshoot and the $G'(\gamma)$ and $G''(\gamma)$ decrease following yielding are superimposed. Yet, we observe a small decrease of the strain amplitude γ_c at which G' and G'' cross-over when increasing the measurement duration: γ_c = 43.5 %, 41 % and 31.5 % respectively for measurements at 9 s per point, 18 s per point and 36 s per point respectively. Such a decrease of γ_c is most likely due to "fatigue" of the suspension [Perge et al., 2014]. It is therefore the signature of a time-dependent yielding. This time-dependence most likely depend on the suspension, and more particularly on its gelation time t_g. In the following, we chose to perform the measurements with 18 s per point in the case of the cone-and-plate configuration, and with 6 s per point in the case of the Taylor-Couette configuration.

D.2 Influence of the salt concentration on the yielding behavior

Examples of the evolution of the elastic modulus G' and viscous modulus G'' as a function of the strain amplitude γ during a LAOS measurement are shown in Fig. 4.41 for suspensions containing 3.2 wt % CNC and NaCl concentrations ranging between 5 mM and 100 mM (see Fig. 4.56 in Sec. 4.E in Appendix for the other NaCl concentrations).

First, we notice that the suspension with the smallest salt concentration presents a yielding behavior which differs from suspensions containing more salt [see Fig. 4.41(a) to be compared to Figs. 4.41(b) and (c)]. Indeed, at the beginning of the LAOS test, t_w = 1470 s after the cessation of shear, the suspension containing 5 mM NaCl is still in a viscoelastic liquid state as $G'' > G'$ at the smallest strain amplitude, while the suspensions containing 20 mM and 100 mM NaCl are in

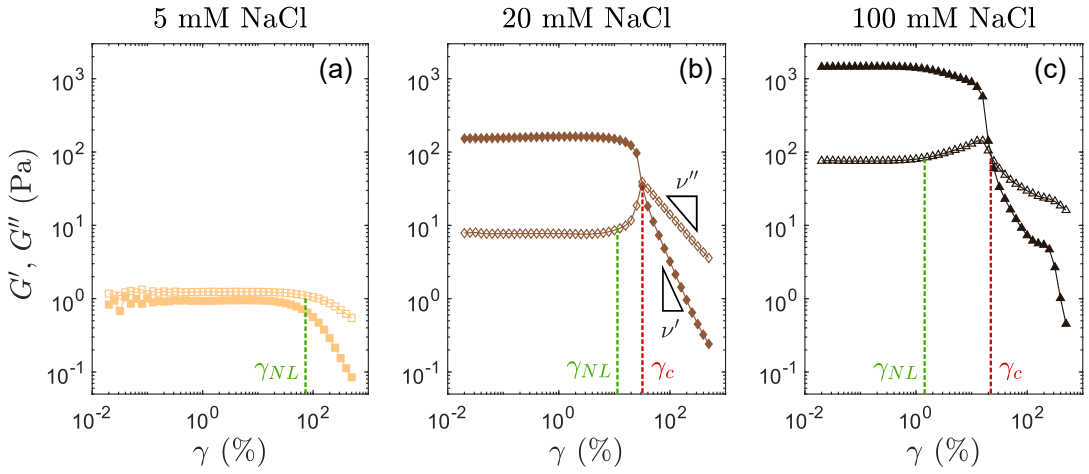

Figure 4.41: Elastic modulus G' (filled symbols) and viscous modulus G'' (empty symbols) versus strain amplitude γ, measured t_w = 1470 s following shear cessation. Experiments performed on samples containing 3.2 wt % CNC and (a) 5 mM NaCl, (b) 20 mM NaCl and (c) 100 mM NaCl. The green dashed line highlights the characteristic strain $\gamma_{\rm NL}$ defining the onset of the non-linear response, corresponding to a deviation of 10 % of $G''(\gamma_{\rm NL})$ with respect to G''_0, the plateau value of the viscous modulus at small strain amplitudes. The red dashed line defines the yield strain $\gamma_{\rm c}$ at which $G' = G''$. ν' and ν'' are the exponents for the power-law dependence of the elastic and viscous moduli respectively versus strain amplitude γ, at large strain amplitudes, defined in Eq. (4.22).

a viscoelastic solid state, with $G' > G''$ at the smallest strain amplitude. This is consistent with the fact that t_w = 1470 s is much shorter than the G'-G'' crossover time t_c for the suspension containing 5 mM NaCl ($t_c \ll$ 1500 s), while $t_w \gg t_c$ for the two other suspensions. In both cases, for those samples, t_c cannot be measured experimentally because it is either too short or too long. For all NaCl concentrations, at small strain amplitudes, both the elastic and the viscous moduli remain constant upon increasing the strain amplitude γ. We define G''_0 as the value of the viscous modulus plateau. The moderate increase in G' observed for suspensions containing between 12 mM and 18 mM NaCl [see Figs. 4.56(c) to (e) in Sec. 4.E in Appendix], is due to the aging of the sample while the strain is being ramped up over 337 s to 790 s. Such an increase is in agreement with the master curve of Fig. 3.4(b), and justifies our choice to rely on the viscous modulus instead of the elastic modulus to determine the onset of the non-linear regime of deformations.

At larger strain amplitudes, for the sample with the smallest salt concentration, both the elastic and the viscous moduli decrease upon increasing the strain amplitude, while for the samples containing a larger NaCl concentration, the viscous modulus increases to reach a maximum before decreasing. The presence of such an overshoot for G'' proves that CNC suspensions with large enough salt concentrations, yield following a so-called "type III" yielding scenario [Hyun et al., 2002, Hyun et al., 2011]. This is consistent with recent observations on CNC gels prepared in a similar concentration range [Danesh et al., 2021]. This specific "type III" fluidization scenario is reminiscent of the yielding transition reported in soft glasses made of hard-sphere colloids or jammed emulsions [Mason et al., 1995, Rogers et al., 2018, Pham et al., 2006], and in weak polymer gels involving stiff or charged molecules [Hyun et al., 2002]. The overshoot in G'', known as the Payne effect in the context of rubber, has been associated with the increased dissipation due to irreversible, plastic deformations [Mason et al., 1996, Rogers et al., 2018], and has been recently interpreted in terms of a combination of recoverable and unrecoverable strains [Donley et al., 2020]. Moreover, a microscopic interpretation of the G'' overshoot in CNC gels has been proposed re-

cently based on the intracycle analysis of LAOS measurements [Moud et al., 2020]: the increase in strain amplitude would reduce the interparticle distance, thus allowing the formation of "shear-induced networks" which increase the viscous dissipation when dragged along by shear. Time-resolved structural measurements under LAOS in our systems would be necessary to confirm such an interpretation.

Finally, at even larger strain amplitudes, the elastic modulus is smaller than the viscous modulus, and both moduli decrease as power-laws of the strain amplitude:

$$\begin{cases} G' \sim \gamma^{-\nu'} & (4.21) \\ G'' \sim \gamma^{-\nu''} & (4.22) \end{cases}$$

with $\nu' > \nu''$.

For all samples, the point at which the elastic and viscous moduli cross defines the yield strain γ_c beyond which the sample behaves as a viscoelastic liquid, with $G'' > G'$. This parameter can only be defined for samples for which $t_c < t_w$, i.e. for which $G' > G''$ at the beginning of the LAOS measurement. Moreover, as explained above, we chose to define the onset of the non-linear regime of deformations as the strain amplitude γ_{NL} where the viscous modulus deviates by 10 % from its plateau value G''_0 defined at small strain amplitudes. Finally, we quantify the G'' overshoot by comparing the value of the maximum reached by the viscous modulus during the overshoot, to its plateau value G''_0 at small strain amplitudes:

$$\Delta G''/G''_0 = \frac{G''_{max} - G''_0}{G''_0} \quad (4.23)$$

Figure 4.42 shows the dependence of the yielding parameters introduced above with the NaCl concentration, for CNC suspensions containing 3.2 wt % CNC. Figure 4.42(a) reports the exponents ν' and ν'' associated to the power-law decrease of G' and G'' with the strain amplitude beyond the yield point [see Eq. (4.22) and Fig 4.41 for their definition]. We observe that these two exponents seem to be independent of the NaCl concentration and related to one another by a factor 2: $\nu' \simeq 1.57$ and $\nu'' \simeq 0.74 \simeq \nu'/2$, consistently with previous works in colloidal gels [Sudreau et al., 2022, Laurati et al., 2011].

Remarkably, contrary to ν' and ν'', the amplitude of the viscous modulus overshoot at the yield point strongly depends on the salt content, as deduced from Fig. 4.42(b). At small NaCl concentration, there is no overshoot in G'' and the sample is barely solid-like when the LAOS test is performed [see Fig. 4.41(a)]. The G'' overshoot only appears beyond a salt concentration of 12 mM. Upon increasing the salt concentration, $\Delta G''/G''_0$ reaches a maximum for an NaCl concentration of about 18 to 20 mM, before decreasing and possibly leveling off at salt concentrations larger than 240 mM. Interestingly, the development of the G'' overshoot for [NaCl]> 12 mM perfectly corresponds to the transition between a sample whose gelation time t_g is larger than the sample age t_w, i.e., the time interval between shear cessation and the beginning of the LAOS measurement, to a sample for which $t_g < t_w$. Indeed, for this series of experiments, t_w = 1470 s, and the suspensions containing 3.2 wt % CNC and 12 mM NaCl and 15 mM NaCl have a gelation time t_g = 1330 s and t_g = 371 s respectively. Therefore, the presence of a G'' overshoot seems to be correlated to the existence of a percolated network constituting the suspension microstructure. This observation prompts us, in the following (in Fig. 4.43), to plot $\Delta G''/G''_0$ as a function of the normalized sample age t_w/t_g. The non-monotonic behavior of $\Delta G''/G''_0$ with NaCl is an outstanding feature of the G'' overshoot in CNC suspensions. Although a decrease of $\Delta G''/G''_0$ for increasing salt concentration has been reported in a dense assembly of microgels [Shao et al., 2013], this is, to our knowledge, the first time that such a non-monotonic dependence is reported. Notably, the salt concentrations at which we observe the largest overshoots in G'', for an NaCl concentration of about 20-25 mM, coincide with the compositions for which a fast increase of the viscous modulus $G''(t)$ appears at short times, during the suspension recovery following shear cessation [see Fig. 3.5 in chapter 3].

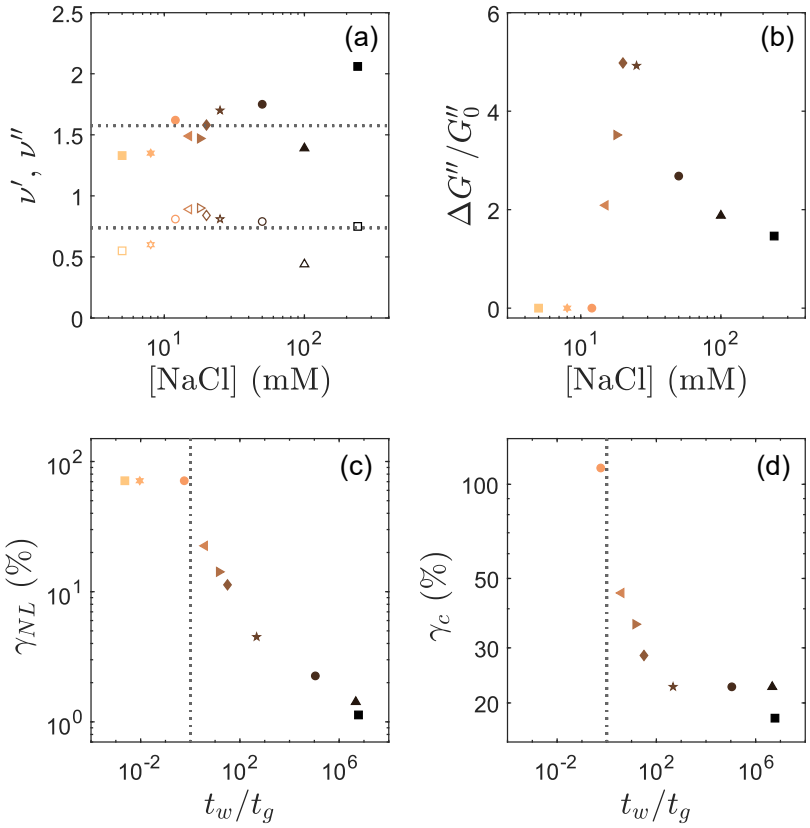

Figure 4.42: (a) Exponents ν' (filled symbols) and ν'' (empty symbols) for the power-law dependence of the elastic and viscous moduli respectively with strain amplitude, at large strain amplitudes [see Eq. (4.22) and Fig. 4.41], versus NaCl concentration. The dashed lines highlight the mean values of ν' and ν'' over the range of salt concentrations. (b) Dimensionless amplitude of the viscous modulus overshoot $\Delta G''/G''_0$ [defined in Eq. (4.23)] versus NaCl concentration. (c) Characteristic strain $\gamma_{\rm NL}$ for the onset of non-linearity and (d) yield strain $\gamma_{\rm c}$ versus the normalized sample age t_w/t_g at the beginning of the LAOS test. The vertical dashed lines in (c) and (d) highlight $t_w = t_g$. Experiments performed on a series of suspensions containing 3.2 wt % CNC and various NaCl concentrations ranging between 5 mM to 100 mM.

Figure 4.42(c) and (d) show respectively the strain amplitude γ_{NL} at the onset of the non-linear regime and the yield strain γ_c as a function of the sample age normalized by its gelation time t_w/t_g. Interestingly both parameters show a similar evolution at short normalized sample age, or equivalently at small NaCl concentrations: they both decrease when moving along the $G'(\tilde{t})$ master curve. However, while γ_{NL} continues to decrease at larger t_w/t_g, or equivalently at larger salt concentrations, γ_c seems to reach a plateau for $t_w/t_g \approx 5 \times 10^2$ corresponding to [NaCl]= 20 mM. Interestingly, this critical concentration is the same as the one observed for the maximum of the G'' overshoot amplitude.

D.3 Robustness of the yielding behavior to changes in salt nature, CNC concentration and solvent nature

In this section, we study the robustness of the yielding properties versus salt concentration, or normalized sample age, to a change of salt nature, CNC concentration and solvent nature.

Figures 4.43(a)-(c) report the exponents ν' and ν'' associated with the power-law decrease of G' and G'' with the strain amplitude beyond the yield point, as a function of the salt concentration, or the ionic strength I (defined in Sec. 3.A.4), for three series of samples containing respectively different type of salts [NaCl, KCl and $MgCl_2$, see Fig. 4.43(a)], different CNC weight fractions [2 wt %, 3.2 wt %, 4.8 wt % and 5.5 wt % CNC, see Fig. 4.43(b)], and different solvents [H_2O and D_2O, see Fig. 4.43(c)]. Interestingly, the values of the exponents ν' and ν'' seem to be independent of the salt nature, the CNC weight fraction and the solvent nature: in all three series, $\nu' \approx 1.6 \pm 0.05$ and $\nu'' \approx 0.8 \pm 0.02$. Moreover, we always verify $\nu'/\nu'' \approx 2$, as predicted by a simple Maxwell model with a power-law dependence of the characteristic time with the shear rate [Miyazaki et al., 2006].

Figures 4.43(d)-(f) show the dimensionless G'' overshoot amplitude $\Delta G''/G''_0$ as a function of the normalized sample age t_w/t_g for the three series of samples. In all cases, the G'' overshoot begins to appear for samples for which $t_w > t_g$, and the amplitude of the overshoot presents a maximum that corresponds to samples where a fast increase of the viscous modulus appears at short times during its recovery following shear cessation [see Fig. 3.8 and Fig. 3.11]. Remarkably, for the three series of samples, the non-monotonic behaviors fall onto a single curve when plotted against the normalized sample age t_w/t_g, suggesting a universal behavior of the G'' overshoot amplitude. Moreover, this observation confirms that the generalized time-composition superposition principle established in the previous Secs. 3.A.4 and 3.A.5, also holds in the non-linear regime of deformations, as previously deduced from the shear start up measurements in Sec. 4.B.5.

To further confirm the robustness of the generalized time-composition superposition principle in the non-linear regime of deformations, Fig. 4.44 shows the two characteristic strains γ_{NL} and γ_c as a function of the normalized sample age t_w/t_g at the beginning of the LAOS test, for the three series of samples. Here again, whatever the nature of the salt cation, the CNC weight fraction or the solvent nature, both the strain amplitude γ_{NL} at the onset of the non-linear regime of deformation and the yield strain γ_c show the same decreasing trend when moving along the master curves of Figs. 3.7(a) and (b) and 3.10(a), and rescale onto a universal curve when plotted as a function of the normalized sample age. From this observation, we conclude that the generalized time-composition superposition principle remains valid for the non-linear viscoelastic properties of CNC suspensions, over the range of concentrations explored.

Nevertheless, we note that the yield strain data are more scattered, more particularly when varying the CNC weight fraction [see Fig. 4.44(e)]. This observation suggests that the CNC content may have some non-negligible impact on the scaling of the yield point. Yet, the yielding transition around γ_c is a highly dynamical process and the fluidization scenario is likely to involve spatially heterogeneous dynamics, such as shear bands or wall slip [Perge et al., 2014, Gibaud et al., 2016, Gibaud et al., 2022]. Therefore, a complex interplay between the sweep rate of the strain amplitude, the total duration of the test, and the yielding scenario most probably accounts for the larger dispersion around a single curve in Fig. 4.44(e).

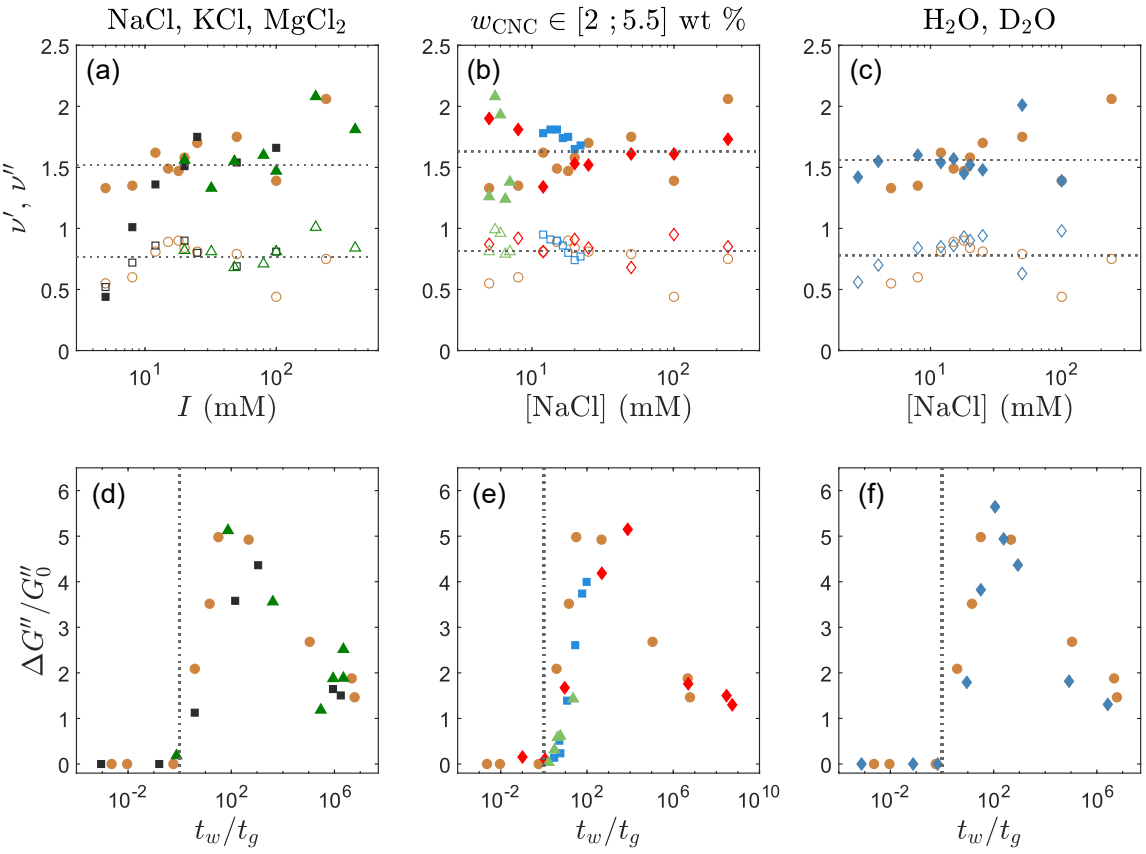

Figure 4.43: (a),(b),(c) Exponents ν' (•) and ν'' (◦) for the power-law dependence of the elastic and viscous moduli respectively with strain amplitude, at large strain amplitudes, versus ionic strengths and NaCl concentrations. The dashed lines highlight the mean values of ν' and ν'' for all series of samples, over the range of ionic strengths or salt concentrations. (d),(e),(f) Dimensionless amplitude of the viscous modulus overshoot $\Delta G''/G''_0$ versus the normalized sample age t_w/t_g at the beginning of the LAOS test. The vertical dashed lines highlight $t_w = t_g$. Experiments performed on series of suspensions (a),(d) containing 3.2 wt % CNC and various NaCl (orange •), KCl (green ▲) or $MgCl_2$ (black ■) concentrations ; (b),(e) containing 2 wt % CNC (blue ■), 3.2 wt % CNC (orange •), 4.8 wt % CNC (red ⧫) and 5.5 wt % CNC (green ▲) and various NaCl concentrations ; (c),(f) containing 3.2 wt % CNC dispersed in H_2O (orange •) or D_2O (blue ⧫) and various NaCl concentrations.

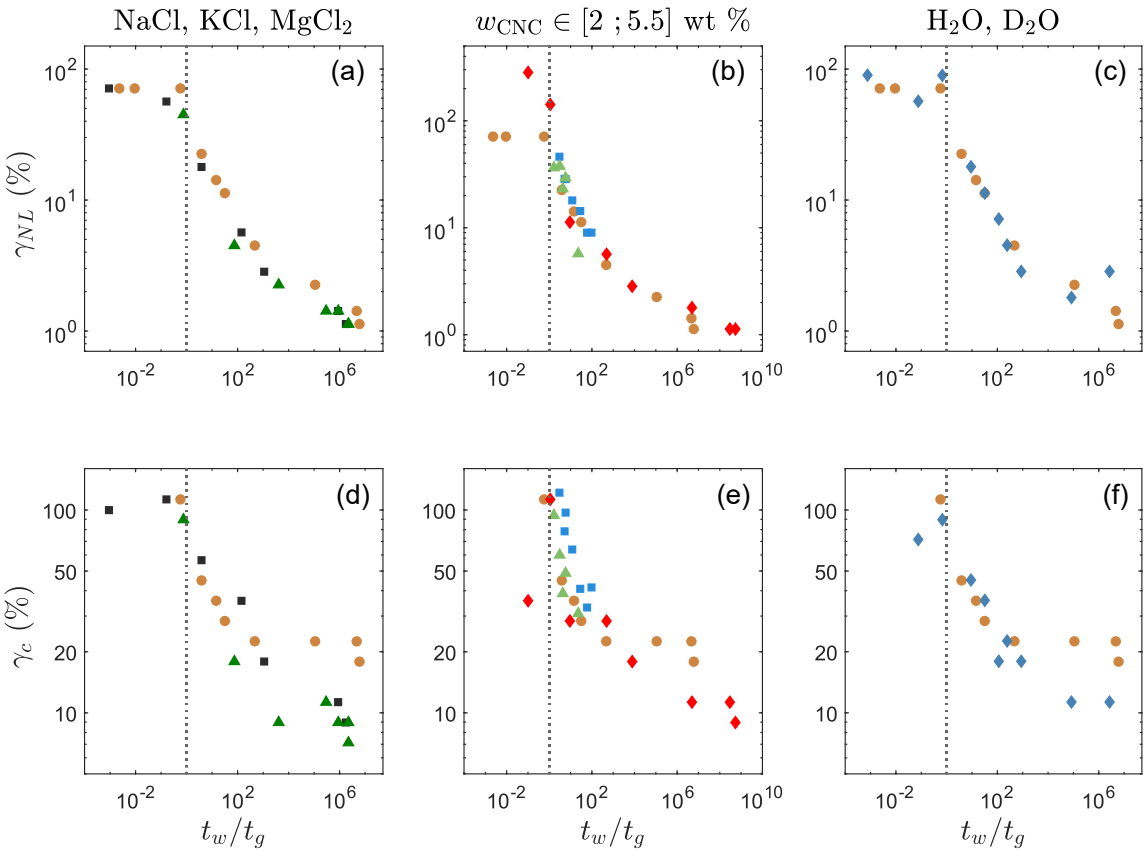

Figure 4.44: (a),(b),(c) Characteristic strain γ_{NL} for the onset of non-linearity and (d),(e),(f) yield strain γ_c versus the normalized sample age t_w/t_g at the beginning of the LAOS test. The vertical dashed lines highlight $t_w = t_g$. Experiments performed on series of suspensions (a),(d) containing 3.2 wt % CNC and various NaCl (orange •), KCl (green ▲) or $MgCl_2$ (black ■) concentrations ; (b),(e) containing 2 wt % CNC (blue ■), 3.2 wt % CNC (orange •), 4.8 wt % CNC (red ♦) and 5.5 wt % CNC (green ▲) and various NaCl concentrations ; (c),(f) containing 3.2 wt % CNC dispersed in H_2O (orange •) or D_2O (blue ♦) and various NaCl concentrations.

(1) The generalized time-composition superposition principle established for the time evolution of the linear viscoelastic properties of CNC suspensions following a strong shear remains valid for the suspensions yielding properties, in the non-linear regime of deformation.

(2) The onset of the non-linear regime of deformation γ_{NL}, and the yield strain γ_c decrease with the normalized sample age t_w/t_g, or equivalently with the salt concentration.

(3) CNC suspensions switch from a type I to a type III yielding behavior, with the development of a G'' overshoot, as soon as the sample age t_w before starting the LAOS test is long enough for CNCs to organize into a percolated network, i.e. for $t_w > t_g$.

(4) The amplitude of the G'' overshoot evolves non-monotonically with the normalized sample age t_w/t_g, or equivalently with the salt concentration, with a maximum for suspension compositions coinciding with the development of a fast G'' increase at short times during their recovery following shear cessation.

E Appendix

E.1 Time evolution of the shear rate during shear start up experiments

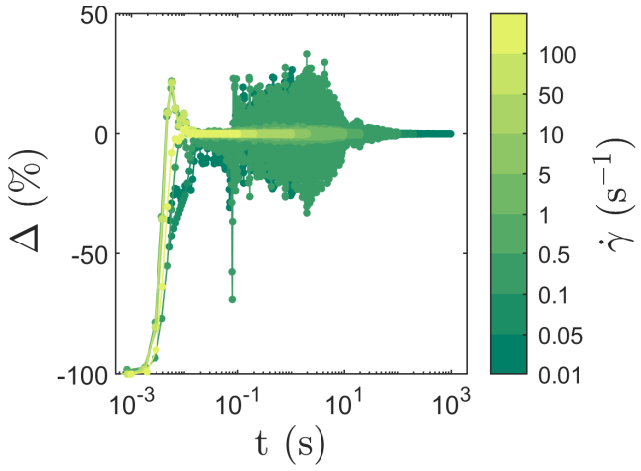

Figure 4.45: Deviation $\Delta(t) = (\dot{\gamma}(t) - \dot{\gamma})/\dot{\gamma}$ of the shear rate imposed by the rheometer $\dot{\gamma}(t)$, from the targeted shear rate $\dot{\gamma}$ as a function of time, for targeted shear rates varying from $\dot{\gamma} = 0.01$ s^{-1} (dark green) to $\dot{\gamma} = 100$ s^{-1} (light green). Experiments performed using the cone-and-plate geometry, on a suspension containing 3.2 wt % CNC and 18 mM NaCl.

E.2 Effect of the geometry on the shear-induced yielding behavior

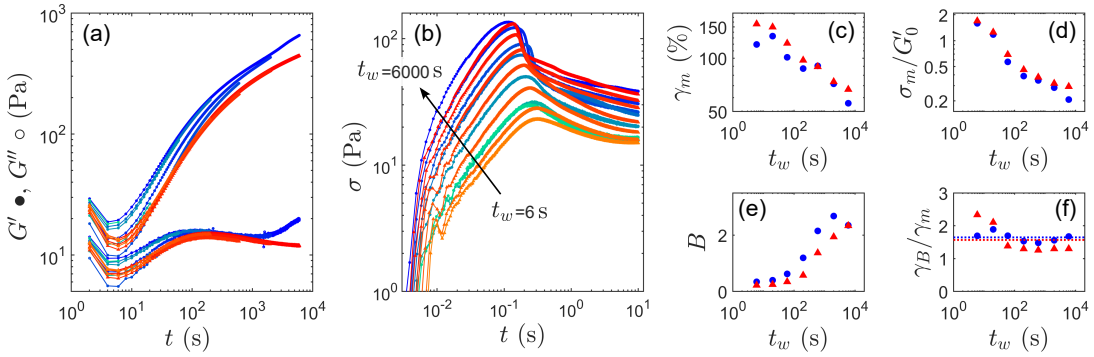

Figure 4.46: Comparison of shear start up experiments made with a cone-and-plate geometry (blue to green colorscale •) and with a Taylor-Couette geometry (red to orange colorscale ▲). Experiments performed on a suspension containing 5.5 wt % CNC and 14 mM NaCl, varying the recovery time t_w from 6 s to 6000 s (green to blue and orange to red respectively), and keeping a constant value for the shear rate $\dot{\gamma}$ = 5 s^{-1} (see the protocol detailed in Sec. 4.B.1.a). (a) Elastic modulus G' (filled symbols) and viscous modulus G'' (empty symbols) as a function of time during the sample recovery following pre-shear, and preceding the start up experiment. (b) Stress σ as a function of time during the shear start up experiment. (c) Strain γ_m corresponding to the stress maximum, (d) stress maximum σ_m normalized by the elastic modulus G'_0 measured right prior to the start up experiment, (e) brittleness parameter B and (f) strain γ_B where B is estimated, normalized by γ_m, as a function of the sample age t_w for the two series of experiments.

E.3 Influence of the salt concentration on the shear-induced yielding behavior

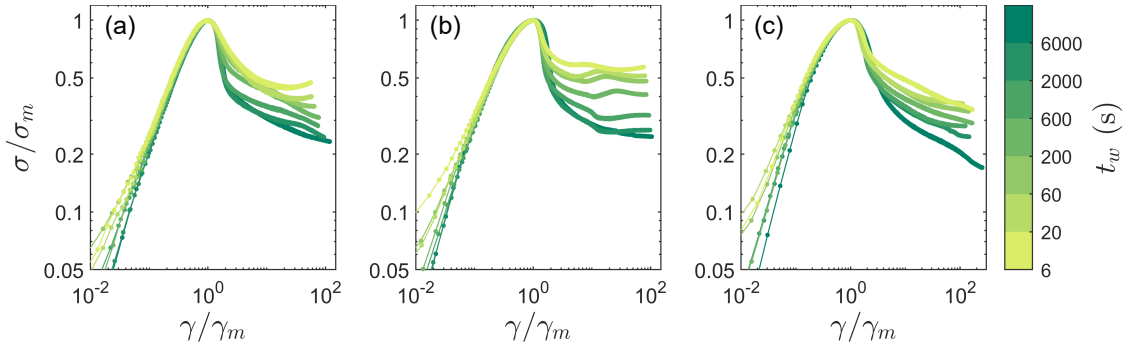

Figure 4.47: Yielding transition of CNC suspensions sheared at fixed shear rate $\dot{\gamma}$ = 5 s^{-1} after various recovery times t_w = 6, 20, 60, 200, 600, 2000, 6000, 10000, 20000 s from light green to dark green. Stress σ as a function of strain γ normalized by the coordinates of the stress overshoot for each t_w. Experiments performed on suspensions containing 3.2 wt % CNC and (a) 25 mM NaCl of gelation time t_g = 11.9 s, (b) 35 mM NaCl of gelation time t_g = 1.3 s, and (c) 50 mM NaCl of gelation time t_g = 0.1 s.

E.4 Influence of the CNC weight fraction on the shear-induced yielding behavior

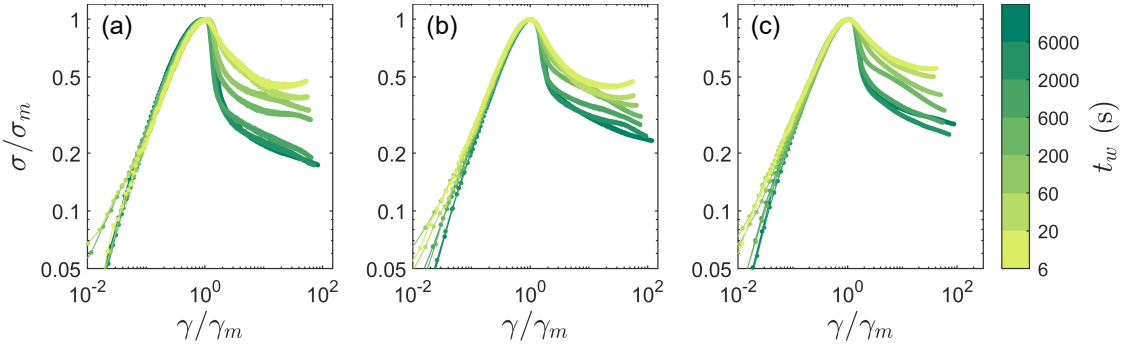

Figure 4.48: Yielding transition of CNC suspensions sheared at fixed shear rate $\dot{\gamma}$ = 5 s^{-1} after various recovery times t_w = 6, 20, 60, 200, 600, 2000, 6000, 10000, 20000 s from light green to dark green. Stress σ as a function of strain γ normalized by the coordinates of the stress overshoot for each t_w. Experiments performed on suspensions containing (a) 2 wt % CNC and 30 mM NaCl of gelation time t_g = 11.1 s, (b) 3.2 wt % CNC and 25 mM NaCl of gelation time t_g = 11.9 s, and (c) 5.5 wt % CNC and 14 mM NaCl of gelation time t_g = 14.0 s.

Besides varying the salt concentration in the suspension, we may also vary its CNC weight fraction, and explore the effect on its yielding behavior. In particular, we can verify if the dependence of the yielding behavior of suspensions with the normalized sample age t_w/t_g, rationalized in Sec. 4.B.4 when varying the salt concentration at a given CNC weight fraction, holds both in the gel and in the attractive glass phases. To do so, we have considered a series of samples containing 2 wt % CNC and 20 mM, 30 mM, and 50 mM NaCl, and a series of samples containing 5.5 wt % CNC and 7 mM and 14 mM NaCl. Similarly to what is done in Sec. 4.B.4, we have repeated the protocol detailed in Sec. 4.B.1.a on all series of samples, by applying the same shear rate $\dot{\gamma}$ = 5 s^{-1} and randomly varying the recovery time between 6 s and 20000 s, on a single sample loading.

For every sample composition, the stress response to a continuous shear presents an overshoot. Moreover, similarly to what we have observed in the previous Secs. 4.18 and 4.B.4, the stress responses upon varying the recovery time t_w at a given sample composition, all collapse onto a single curve in the linear regime of deformation, while this rescaling fails in the non-linear regime of deformation (see Fig. 4.48).

For each series of samples at fixed CNC weight fraction and various salt concentration, γ_m and σ_m/G_0' decrease and follow a same trend as a function of the normalized sample age t_w/t_g, similarly to what we have observed in Figs. 4.20(a) and (b) for suspensions containing 3.2 wt % CNC. The same trend persists when varying the CNC weight fraction, yet with a larger dispersion [see Figs. 4.49(a) and (b)], and except for the suspension containing 5.5 wt % CNC and 7 mM NaCl. Indeed, for this suspension, γ_m versus t_w/t_g differs significantly from the other responses: γ_m takes larger values and does not seem to depend as a power-law of the normalized sample age. The brittleness parameter B increases with the normalized sample age for every suspension composition. However, as described in Sec. 4.B.4 for the series of samples at w_{CNC} = 3.2 wt %, B does not rescale when varying the salt concentration at a given CNC weight fraction [see Fig. 4.49(c)]. Finally, we observe that, here again, the position of the steepest decrease of the stress γ_B/γ_m seems to be independent of both the salt concentration and the CNC weight fraction [see Fig. 4.49(d)]. The robustness of this parameter value $\gamma_B/\gamma_m \approx 1.5$ raises the question of whether it is a universal constant, and of its physical meaning.

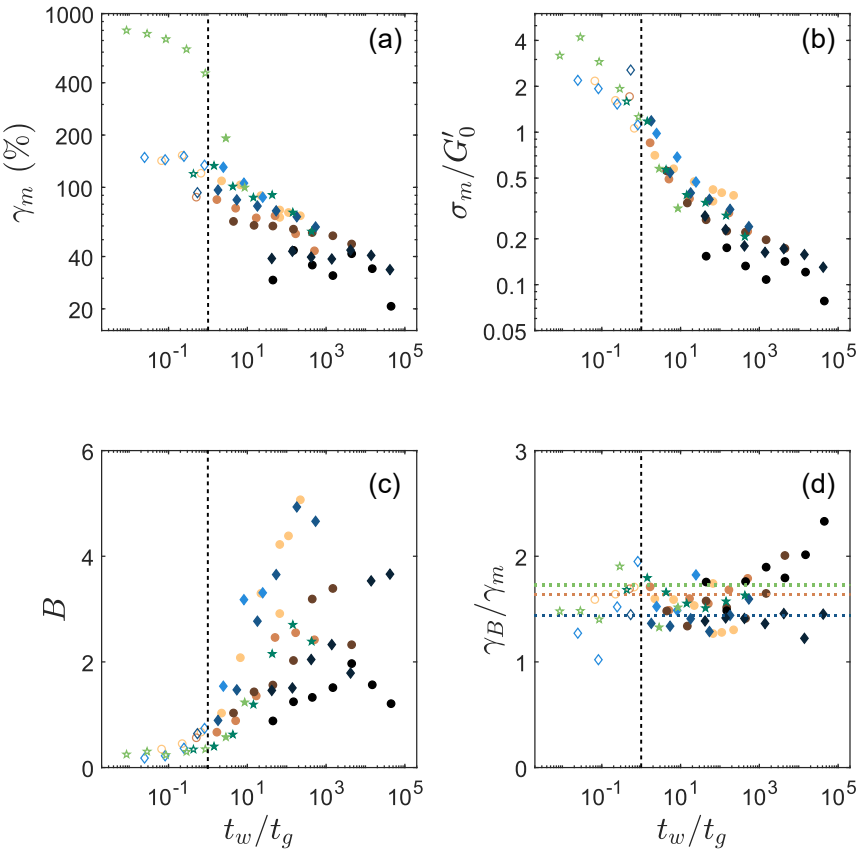

Figure 4.49: Parameters quantifying the impact of the sample age on the shear-induced yielding transition of CNC suspensions of various compositions. (a) Strain γ_m corresponding to the stress maximum during the stress overshoot, (b) stress maximum σ_m normalized by the elastic modulus G'_0 measured right prior to the start up experiment, (c) brittleness parameter B and (d) strain γ_B where B is estimated, normalized by γ_m, as a function of the normalized sample age t_w/t_g, with t_g the gelation time of each suspension. The empty symbols correspond to $t_w < t_g$, while the filled symbols correspond to $t_w > t_g$. Experiments performed at fixed shear rate $\dot{\gamma} = 5$ s^{-1}, on a series of suspensions containing 2 wt % CNC (blue ♦) and 20 mM (lightest blue), 30 mM, or 50 mM NaCl (darkest blue) ; containing 3.2 wt % CNC (orange •) and 18 mM (lightest orange), 25 mM, 35 mM or 50 mM NaCl (darkest brown) ; or containing 5.5 wt % CNC (green ⋆) and 7 mM (light green) or 14 mM NaCl (dark green). The horizontal dashed lines in (d) show the mean value of γ_B/γ_m over the range of normalized sample ages for each series of suspensions at fixed CNC weight fraction.

E.5 Shear-induced yielding behavior of a suspension containing 3.2 wt % CNC and 25 mM NaCl

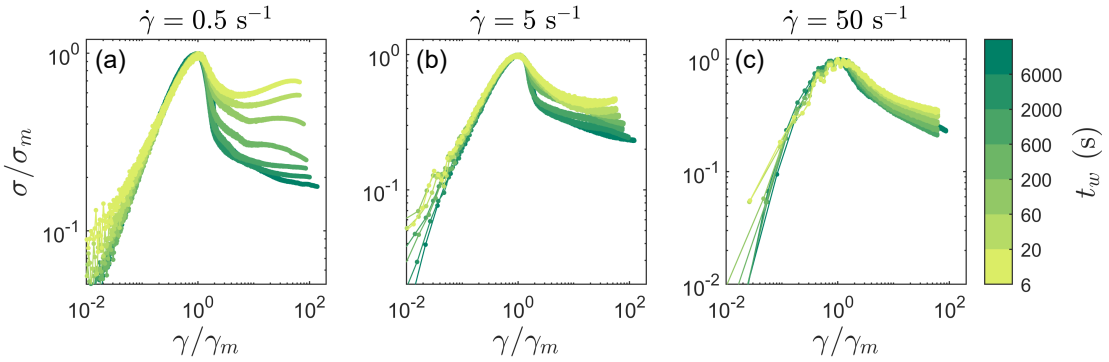

Figure 4.50: Yielding transition of a CNC suspension after various recovery times t_w = 6, 20, 60, 200, 600, 2000, 6000 s from light green to dark green, sheared at fixed shear rate (a) $\dot{\gamma}$ = 0.5 s^{-1}, (b) $\dot{\gamma}$ = 5 s^{-1}, and (c) $\dot{\gamma}$ = 50 s^{-1}. Stress σ as a function of strain γ normalized by the coordinates of the stress overshoot for each t_w. Experiments performed on a suspension containing 3.2 wt % CNC and 25 mM NaCl of gelation time t_g = 11.9 s.

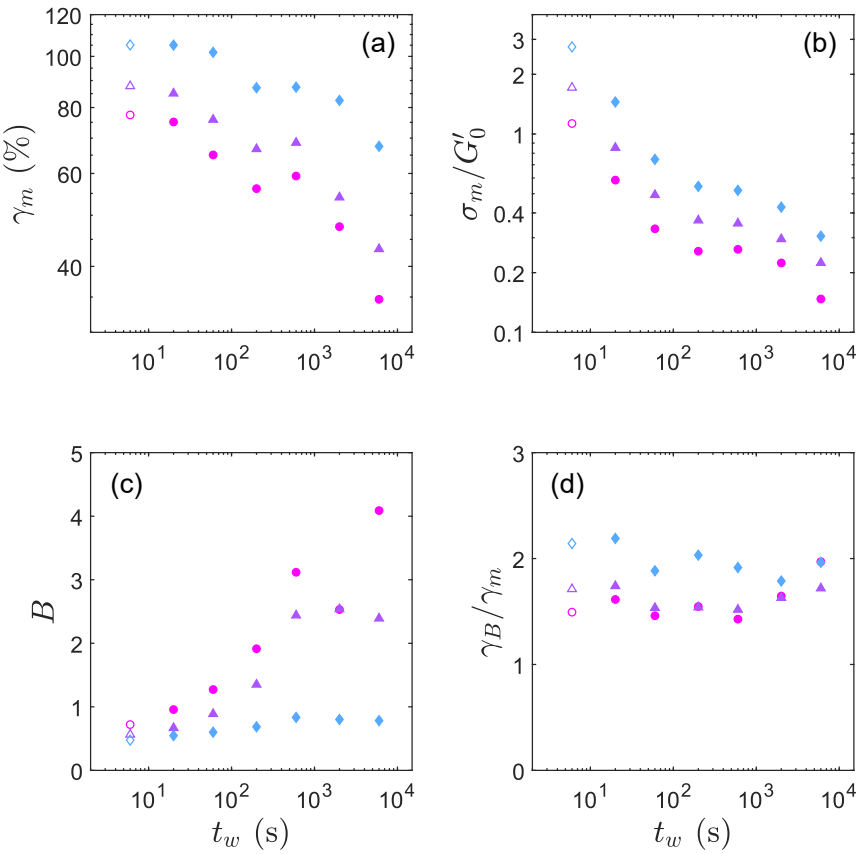

Figure 4.51: Parameters quantifying the impact of the sample age on the shear-induced yielding transition of a CNC suspension, for three different shear rates: $\dot{\gamma}$ = 0.5 s^{-1} (blue •), $\dot{\gamma}$ = 5 s^{-1} (purple ♦), $\dot{\gamma}$ = 50 s^{-1} (pink ▲). Data from Fig. 4.50. (a) Strain γ_m corresponding to the stress maximum during the stress overshoot, (b) stress maximum σ_m normalized by the elastic modulus G_0' measured right prior to the start up experiment, (c) brittleness parameter B, and (d) strain γ_B where B is estimated, normalized by γ_m, as a function of the recovery time, or sample age, t_w. Experiments performed on a suspension containing 3.2 wt % CNC and 25 mM NaCl.

E.6 Rescaling of the parameters quantifying the yielding behavior

Figure 4.52 shows the rescaling of parameters quantifying the shear-induced yielding transition of a CNC suspension, when varying both the recovery time and the shear rate, using the dimensionless parameter given by Eq. (4.12), with either $\alpha = \delta = 1$ or with $\alpha = 1$ and $\delta = 2$.

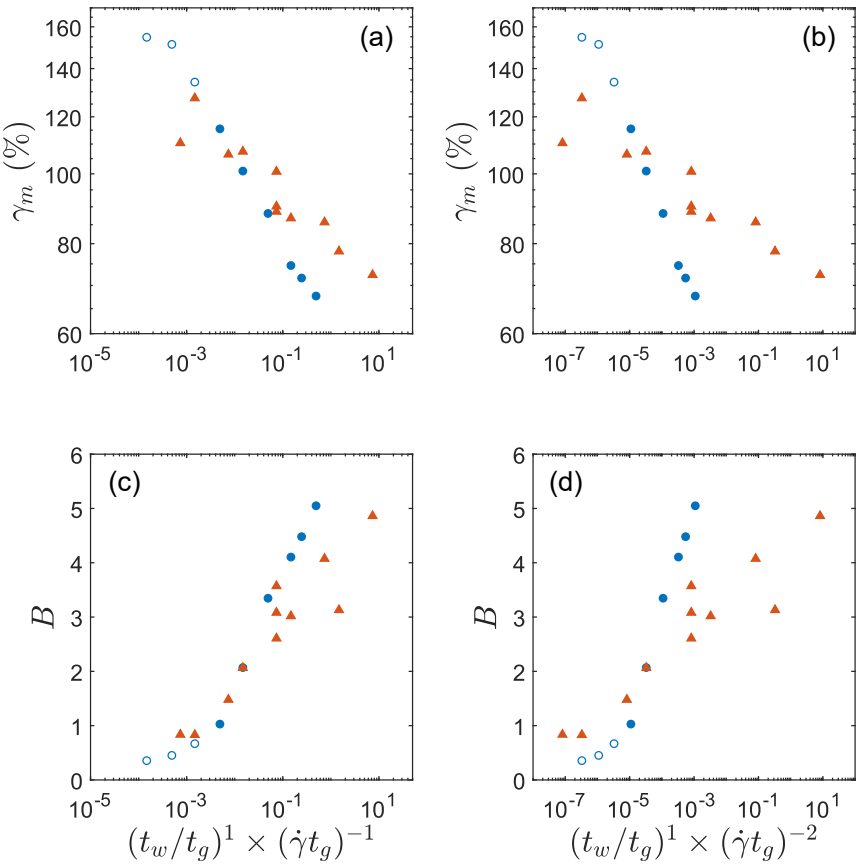

Figure 4.52: Rescaling of the parameters quantifying the shear-induced yielding transition of a CNC suspension when varying both the recovery time (blue •) and the shear rate (orange ▲), using (a),(c) $\alpha = \delta = 1$ or (b),(d) $\alpha = 1$ and $\delta = 2$. Data from Fig. 4.15 and Fig. 4.19. (a),(c) Strain γ_m corresponding to the stress maximum σ_m during the stress overshoot, and (b),(d) brittleness parameter B as a function of a dimensionless parameter. The empty symbols correspond to $t_w < t_g$, while the filled symbols correspond to $t_w > t_g$. Experiments performed on a suspension containing 3.2 wt % CNC and 18 mM NaCl.

Figures 4.53 and 4.54 show the rescaling of parameters quantifying the shear-induced yielding transition of CNC suspensions containing various CNC weight fractions and various NaCl concentrations, using the dimensionless parameter $\left(\frac{t_w}{t_g}\right)^2 \times \left(\frac{1}{\dot{\gamma} t_g}\right)$, given by Eq. (4.12) with $\alpha = 2$ and $\delta = 1$.

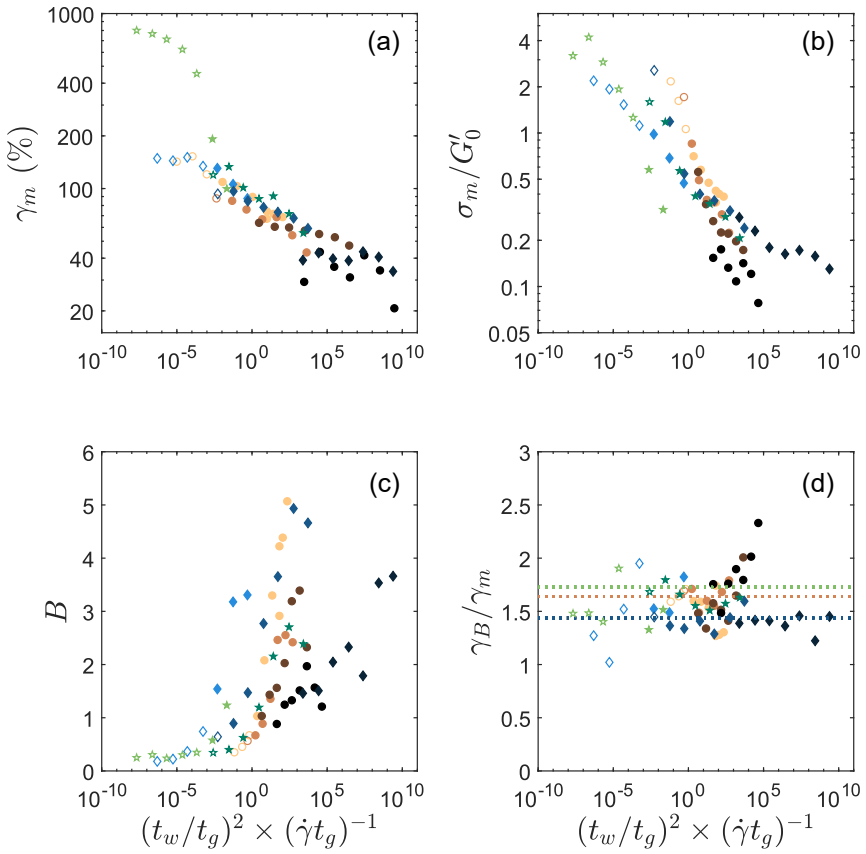

Figure 4.53: Rescaling of the parameters quantifying the impact of the sample age on the shear-induced yielding transition of CNC suspensions of various compositions. Data from Fig. 4.49. (a) Strain γ_m corresponding to the stress maximum during the stress overshoot, (b) stress maximum σ_m normalized by the elastic modulus G'_0 measured right prior to the start up experiment, (c) brittleness parameter B and (d) strain γ_B where B is estimated, normalized by γ_m, as a function of the dimensionless parameter $\left(\frac{t_w}{t_g}\right)^2 \times \left(\frac{1}{\dot{\gamma}t_g}\right)$. The empty symbols correspond to $t_w < t_g$, while the filled symbols correspond to $t_w > t_g$. Experiments performed at fixed shear rate $\dot{\gamma} = 5$ s^{-1}, on a series of suspensions containing 2 wt % CNC (blue ♦) and 20 mM (lightest blue), 30 mM, or 50 mM NaCl (darkest blue) ; containing 3.2 wt % CNC (orange •) and 18 mM (lightest orange), 25 mM, 35 mM or 50 mM NaCl (darkest brown) ; or containing 5.5 wt % CNC (green ⋆) and 7 mM (light green) or 14 mM NaCl (dark green). The horizontal dashed lines in (d) show the mean value of γ_B/γ_m over the range of normalized sample ages for each series of suspensions at fixed CNC weight fraction.

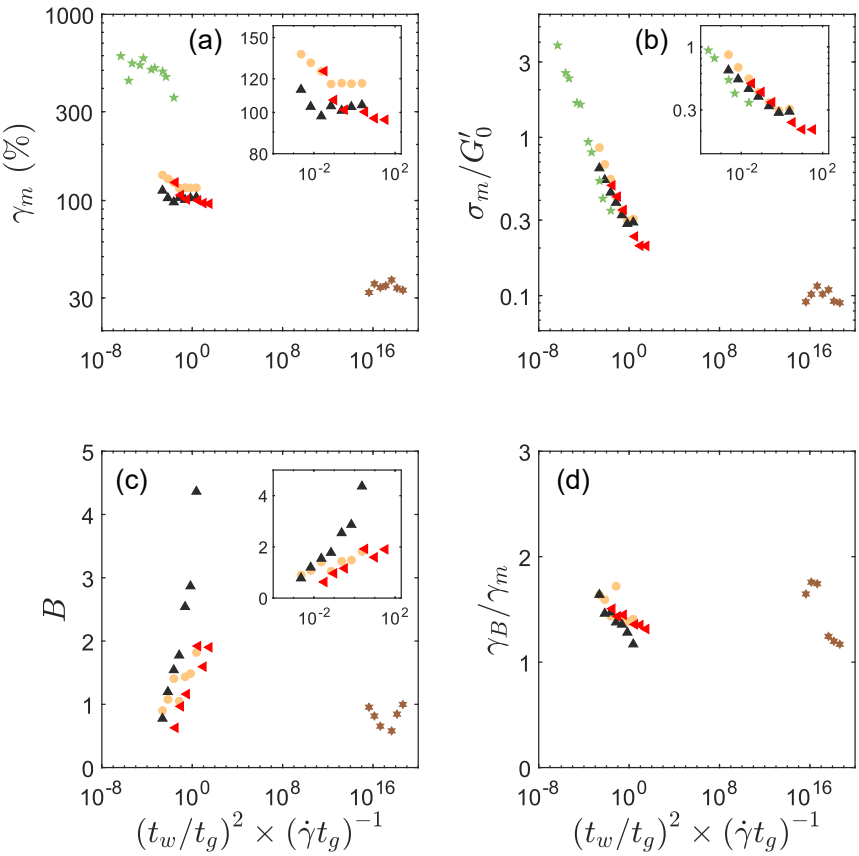

Figure 4.54: Rescaling of the parameters quantifying the impact of the shear rate on the shear-induced yielding transition of CNC suspensions of various gelation times, corresponding to various positions on the $G'(\tilde{t})$ master curve for the suspension recovery. Data from Fig. 4.17. (a) Strain γ_m corresponding to the stress maximum during the stress overshoot, (b) stress maximum σ_m normalized by the elastic modulus G'_0 measured right prior to the start up experiment, (c) brittleness parameter B and (d) strain γ_B where B is estimated, normalized by γ_m, as a function of the dimensionless parameter $\left(\frac{t_w}{t_g}\right)^2 \times \left(\frac{1}{\dot{\gamma} t_g}\right)$. The insets in (a), (b) and (c) show an enlargement around the data of the three suspensions of similar gelation time. Experiments performed on suspensions of gelation time t_g = 800 s containing 5.5 wt % CNC and 7 mM NaCl (green ⋆), t_g = 371 s containing 3.2 wt % CNC and 15 mM NaCl (orange •), t_g = 372 s containing 3.2 wt % CNC and 12 mM KCl (black ▲), t_g = 154 s containing 4.8 wt % CNC and 12 mM NaCl (red ◂) and $t_g = 3 \times 10^{-4}$ s containing 3.2 wt % CNC and 100 mM NaCl (brown ✶).

E.7 Stress responses during shear steps used for ultrasound velocimetry

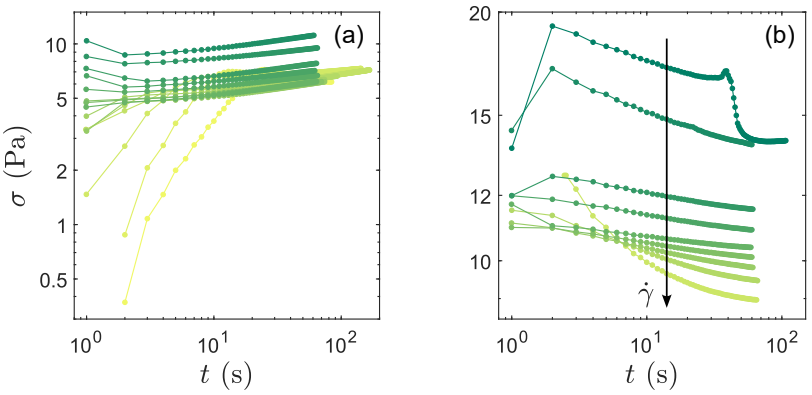

Figure 4.55: Stress σ as a function of time during ultrasound velocimetry experiments associated to the flow curve measurements. (a) When ramping down the applied shear rate from $\dot{\gamma}$ = 500 s^{-1} (dark green) to $\dot{\gamma}$ = 0.01 s^{-1} (light green). (b) When ramping up the applied shear rate from $\dot{\gamma}$ = 10 s^{-1} (light green) to $\dot{\gamma}$ = 500 s^{-1} (dark green).

E.8 Influence of the salt concentration on the yielding behavior under oscillatory shear

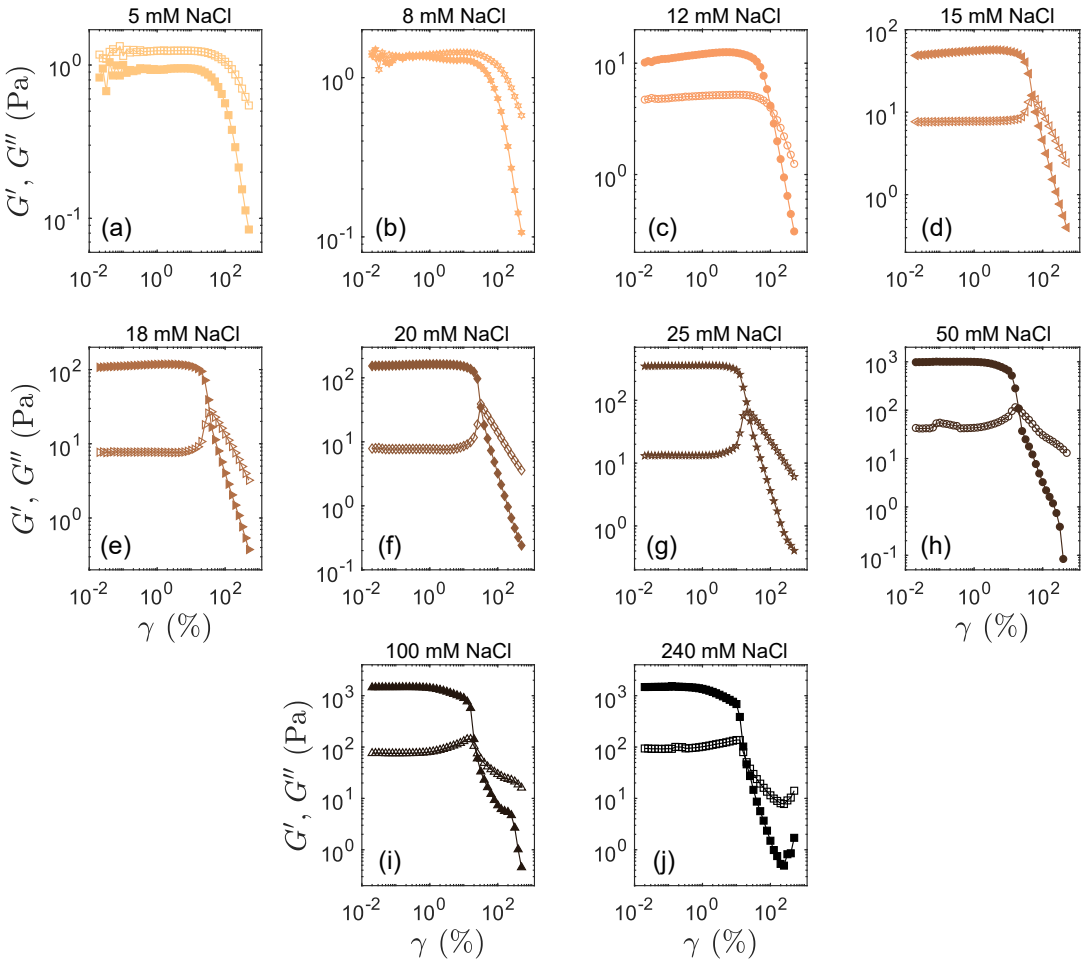

Figure 4.56: Elastic modulus G' (filled symbols) and viscous modulus G'' (empty symbols) versus strain amplitude γ, measured t_w = 1470 s following shear cessation. Experiments performed on samples containing 3.2 wt % CNC and (a) 5 mM NaCl, (b) 8 mM NaCl, (c) 12 mM NaCl, (d) 15 mM NaCl, (e) 18 mM NaCl, (f) 20 mM NaCl, (g) 25 mM NaCl, (h) 50 mM NaCl, (i) 100 mM NaCl, and (j) 240 mM NaCl.

CHAPTER

5

CONCLUSION AND PERSPECTIVES

Contents

In this thesis, we have studied in detail the rheological properties of water-based suspensions of cellulose nanocrystals in the presence of salt. In particular, we have studied the gelation and aging dynamics of such suspensions, as well as their shear-induced failure and their flow properties. In this conclusive chapter, after summing up the main results of this thesis, we explore some perspectives for extending the current study.

A Summary of the main results

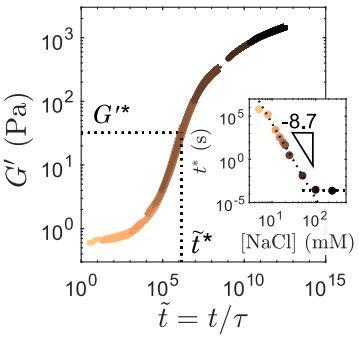

In chapter 3, we have studied the recovery dynamics of CNC suspensions following shear cessation. First, by rescaling the time evolution of the viscoelastic properties measured at a single frequency of suspensions containing various salt concentrations, we have evidenced a time-composition superposition principle in CNC suspensions. Varying the salt nature and the CNC content, and further rescaling the data into two general master curves, we have shown that this superposition principle remains valid and can be generalized upon a change of salt nature and of CNC weight fraction. However, while a change of solvent isotope from H_2O to D_2O does not affect the validity of the time-composition superposition principle, we have shown that this principle cannot be generalized. Indeed, data obtained from CNC suspended in H_2O do not superimpose with data obtained from CNC suspended in D_2O. The sigmoidal shape, in logarithmic scale, of the elastic modulus versus time response at a single frequency, allows one to extract a characteristic time scale: the time t^* defined by the coordinates of the inflection point. Using time-resolved mechanical spectroscopy, we have shown that, in the range of CNC and salt concentrations explored, CNC suspensions always present a critical gel point, associated with a gelation time t_g. Furthermore, we have shown that t_g coincides with the inflection time t^*, thereby providing a simple experimental method for determining the gelation time of a CNC suspension. Interestingly, this gelation time can be as much as eight times larger than the G'-G'' crossover time t_c, which is often used as a first approximation for the gelation time of a colloidal suspension. Finally, we have shown that this gelation time strongly depends on the salt concentration and decreases as a power-law of exponent 8.7, which is independent of both the salt nature and the CNC weight fraction. Here again, a change of solvent isotope has a significant impact on the results, for the exponent drops from 8.7 in H_2O to 5.9 in D_2O.

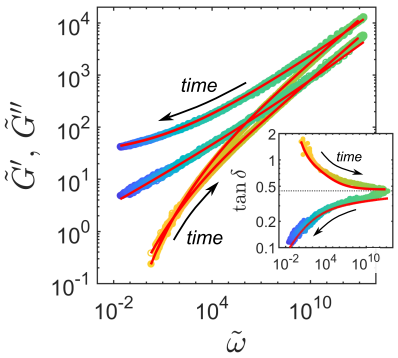

Second, by constructing master curves for the evolution of the viscoelastic spectra measured across the sol-gel transition by time-resolved mechanical spectroscopy, we have evidenced a time-connectivity superposition principle in CNC suspensions. We have established two fractional models to capture the very broad relaxation dynamics highlighted by the master curves: a fractional Maxwell model for the dynamics prior to the critical gel point, and a fractional Kelvin-Voigt model for the dynamics following the critical gel point. Moreover, we verify that the hyperscaling relations established in polymer suspensions from the dynamics close to the critical gel point, are verified in this anisotropic colloidal system, yet with a major discrepancy: in CNC suspensions, the gelation and aging dynamics are not symmetrical with respect to the gel point, i.e., the exponents characterizing the critical gel point are different for $t < t_g$ and for $t > t_g$. Then, we have shown that the

time-connectivity superposition principle, the fractional models, and the hyperscaling relations remain valid when varying the salt and the CNC concentrations. In particular, by further rescaling the master curves obtained for various salt concentrations at a given CNC weight fraction, we have shown that both the time-composition and the time-connectivity superposition principles can be generalized into a time-composition-connectivity superposition principle, where each general master curve, on each side of the gel point, is well captured by a single set of parameters for the fractional Maxwell model and for the fractional Kelvin-Voigt model respectively. Finally, by dynamically characterizing the critical gel point, using rheology only, we have evidenced a change of regime upon increasing the CNC weight fraction of a suspension, that we have proposed to identify to the gel to attractive glass boundary in the CNC versus NaCl phase diagram.

In chapter 4, we have focused on the non-linear rheological properties of CNC suspensions. More precisely, we have studied their failure and flow behaviors under different types of solicitations. First, we have evidenced the presence of a hysteresis in the suspensions flow curves, between the ramping down and the ramping up responses, whose characteristics depend on the ramping rate. Indeed, we have shown that the hysteresis area presents a maximum for a ramping rate which coincides with the inverse of the crossover time t_c. Moreover, we have determined a correlation between the ramping rate and the position where the maximum difference between the ramping down and the ramping up stress responses is observed.

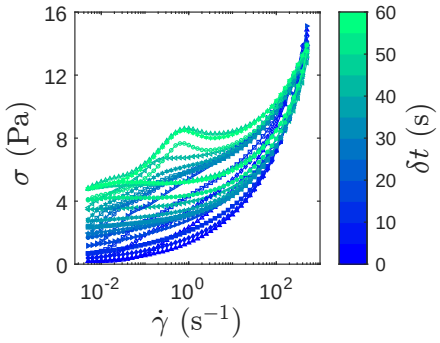

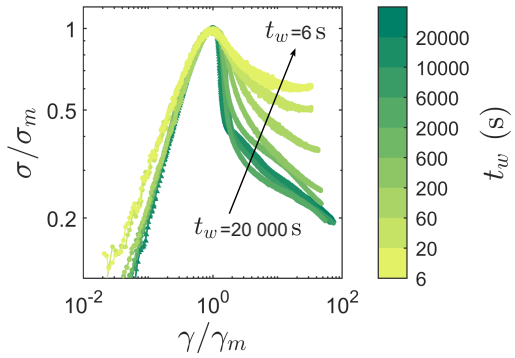

Second, focusing on the stress response under continuous shear, we have evidenced a ductile to brittle transition for the yielding behavior of CNC suspensions upon either decreasing the shear rate or increasing the sample age. We have quantitatively characterized this transition by using a parameter referred to as the "brittleness parameter" B. We have shown that, while the brittleness parameter evolves as a logarithmic law with either the shear rate or the sample age, the coordinates of the stress overshoot (γ_m, σ_m) evolve as power-laws with the shear rate or the sample age. Remarkably, we have shown that, whatever the suspension composition and the experimental parameters, the strain γ_B at which the steepest stress decrease is observed during the suspension failure, corresponding to the strain where B is estimated, is always 1.5 times larger than the strain γ_m at which the stress is maximum. Then, we have proposed a dimensionless number that allows one to account for both a change in shear rate and a change in sample age. All the parameters characterizing the shear-induced yielding transition under various conditions and for various sample compositions, can be rescaled using this dimensionless number, except the brittleness parameter, most likely due to its definition involving the coordinates of the stress overshoot. Yet, a physical understanding of this parameter remains to be uncovered. Finally, we have evidenced strong shear memory effects in suspensions containing large salt concentrations. Indeed, in such suspensions, the yielding behavior strongly depends both on the shear history of the suspension, and on the direction of shear relative to the pre-shear.

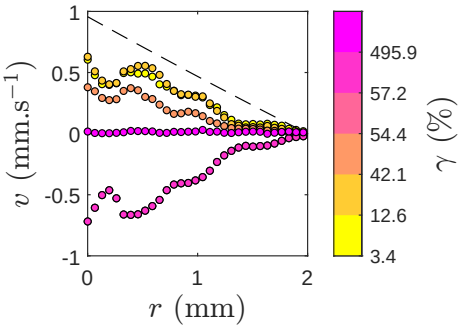

Third, ultrasound velocimetry coupled with rheometry has allowed us to get some insight into the local fluidization and failure scenarios in CNC suspensions. In particular, we have shown that, when shearing a suspension by applying shear steps of decreasing amplitude, the bulk of the suspension progressively stops flowing as it solidifies under shear and slips on the geometry surfaces. When ramping up in shear rate, shear bands are present, and a large shear rate is necessary for the suspension to be fully fluidized. By continuously shearing a suspension at a constant shear rate from a rested state, we have shown that the brittle yielding behavior observed at small shear rates or large sample ages coincides with the presence of an elastic recoil. This elastic recoil is absent from a ductile yielding at large shear rates or small sample ages. Moreover, we have demonstrated that following failure, at long shearing times, or equivalently at large strains, the bulk of the suspension does not flow. Rather, it is either totally arrested by slipping on the geometry surfaces, or it presents shear bands.

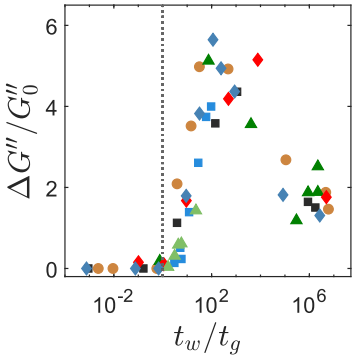

Finally, we have studied the yielding behavior of CNC suspensions under oscillatory shear of increasing strain amplitude. We have shown that when increasing the salt concentration, a CNC suspension transits from a type I to a type III yielding scenario with the growth of a viscous modulus overshoot. Interestingly, the relative amplitude of this overshoot $\Delta G''/G''$ reaches a maximum for a salt concentration coinciding with a change of behavior in the time evolution of G'' during the suspension recovery following shear cessation. We have further observed that both the yield strain γ_c and the strain γ_{NL} corresponding to the transition from the linear to the non-linear regime of deformation, decrease with the salt concentration, or equivalently with the suspension age normalized by its gelation time. Moreover, we have shown that when plotted as a function of this normalized suspension age, the three parameters $\Delta G''/G''$, γ_c, and γ_{NL} rescale quite well when varying the salt nature, the CNC weight fraction or the solvent isotope. This observation suggests that the generalized time-composition superposition principle established in the previous chapter for the linear viscoelastic properties of CNC suspensions remains valid for their yielding properties. Finally, we have shown that both the elastic and the viscous moduli decrease as power-laws of the strain amplitude beyond the yield point, with exponents of ratio equal to 2, that neither depends on the salt nature and concentration, nor on the CNC weight fraction and the solvent isotope.

B Perspectives

To conclude, we present in this final section a few perspectives opened by this thesis. We first detail key open questions regarding the microscopic origin of the macroscopic mechanical response of CNC suspensions evidenced through rheology, and we show some preliminary results probing the time evolution of the suspensions microstructure using various techniques. Moreover, since most applications of CNCs are concerned with the design of new solid materials [Lagerwall et al., 2014, Grishkewich et al., 2017], we then briefly investigate two solidification processes and present some preliminary results about the material structuration induced by such processes.

B.1 Short-term perspectives and their preliminary results

a Origin of the specificities of the gelation dynamics of CNC suspensions

The unique aspects of the gelation dynamics observed in the CNC suspensions studied in this thesis could stem from certain characteristics of the individual CNC particles. For instance, the large discrepancy between the crossover time t_c and the gelation time t_g, as well as the asymmetry of the recovery dynamics around the critical gel point, may be due to their large aspect ratio, as previously mentioned in Sec. 3.B.5 in chapter 3. Indeed, such structural anisotropy most likely enhances steric interactions that may slow down the formation of a percolated network, and lead to different local dynamics in the pre-gel state, where no percolated network is formed yet, and in the post-gel state, where the percolated network re-arranges. Furthermore, such specificities of the gelation dynamics might also come from the surface charge distribution on the CNCs. In order to test these assumptions, we could perform the same time-resolved mechanical spectroscopy experiments on suspensions of CNCs of different aspect ratios and different charge distributions, extracted from different sources [Li et al., 2021, Lahiji et al., 2010, Elazzouzi-Hafraoui et al., 2008, Battista, 1975], on the one hand, and on suspensions of other solid rod-like particles, either charged or not, such as bacteria or viruses [Zhang et al., 2009], on the other hand.

Moreover, the exponent for the dependence of the gelation time with the salt concentration might also be influenced by the charge density on the CNC surface. This assumption could be verified by performing experiments using CNCs extracted from different sources, or through different extraction processes. Yet, the dependence of this exponent on the solvent isotope suggests that interactions other than electrostatic interactions, such as hydrogen bonds, may be involved in the gelation dynamics of CNC suspensions. This hypothesis could be verified by either changing the surface sulfate groups to another group that does not interact through hydrogen bonds [Eyley and Thielemans, 2014, Rana et al., 2021], or by adding in the suspension an inhibitor of inter-CNCs hydrogen bonds, such as urea. We have performed preliminary recovery experiments with a suspension containing 3.2 wt % CNC, 20 mM of NaCl, and 3 M of urea. Figure 5.1 shows that both the elastic and the viscous moduli of the suspension are decreased by a factor 4 and by a factor 1.5 respectively, due to urea. This observation suggests the formation of a weaker CNC network in the presence of urea, most likely due to the substitution of the hydrogen bonds formed between CNCs, by hydrogen bonds formed between CNCs and urea [Vadillo et al., 2021, Fan et al., 2023].

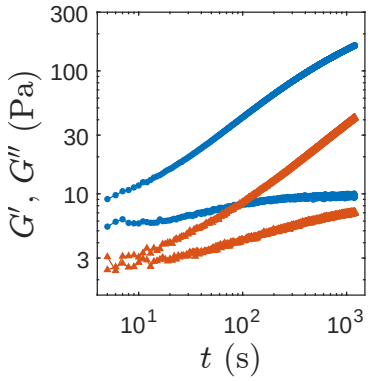

Figure 5.1: Elastic modulus G' (filled symbols) and viscous modulus G'' (open symbols) as a function of time during suspensions recovery following shear cessation, for suspensions containing 3.2 wt %, 20 mM NaCl and no urea (•) or 3 M urea (▲).

b Looking for a local scenario for gelation of CNC suspensions

To identify the local scenario underpinning the gelation dynamics of CNC suspensions, we have performed various experiments using a range of different techniques in order to get some insight into the microstructure of CNC suspensions and, more particularly, to evidence a microscopic signature of either the G'-G'' crossover time or of the gelation time. While our results show some promising leads, we did not find a definitive microscopic signature of the macroscopic sol-gel transition upon flow cessation. Here below are some preliminary results from the largest to the smallest length-scale explored.

Polarized light imaging during recovery.- We have looked for a signature of the time evolution of CNC suspensions during their recovery following shear cessation via direct optical imaging in the rheometer cell. Figure 5.2 shows bottom view images in polarized light of a suspension containing 4.8 wt % CNC and 8 mM NaCl, which has been loaded in between two transparent plates of diameter 40 mm, separated by a 0.1 mm gap. We observe that a birefringent texture appears during the recovery, indicating a microscopic organization of CNC particles, spreading over increasing length-scales over time. Such an evolution of the suspension structure is in phase with the evolution of the viscoelastic moduli monitored by rheometry.

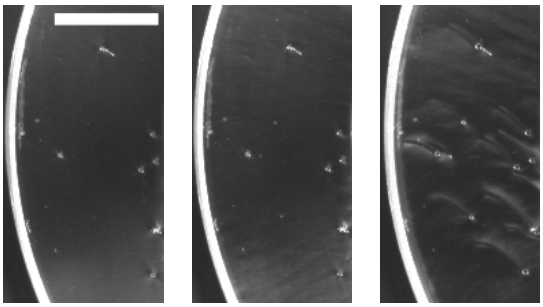

Figure 5.2: Bottom view under polarized light of a CNC suspension loaded in between two transparent plates, separated by a 0.1 mm gap. Pictures taken at time t = 1, 4, and 43 min during the suspension recovery following shear cessation. Experiment performed on a suspension containing 4.8 wt % CNC and 8 mM NaCl, of crossover time $t_c(1\text{ Hz})$ = 50 s and gelation time t_g = 1288 s ≈ 21.5 min. The scale bar on the first image corresponds to 5 mm.

Dynamic light scattering (DLS).- The aggregation and the formation of a percolated network affect the mobility of colloids and, hence, the relaxation times associated with the suspension microstructure. Indeed, as detailed in Sec. 1.B.2 in the Introduction, short relaxation times are associated with rearrangements over small length-scales, while longer relaxation times are associated with rearrangements over larger length-scales. Therefore, by performing DLS measurements over time during a CNC suspension recovery, from which we extract the relaxation times τ of the suspension microstructure [Liénard et al., 2022], we hoped to evidence clear signatures of the microstructural changes, coinciding either with the crossover time t_c or with the gelation time t_g. From the map of the relaxation times shown in Fig. 5.3 for a suspension containing 3.2 wt % CNC and 9 mM NaCl of crossover time $t_c(1\text{ Hz})$ = 23 min and gelation time t_g = 147 min, we distinguish two relaxation times: one of about 4×10^{-3} s, and one of about 6.5×10^{-4} s. Interestingly, these relaxation times are of the same order of magnitude as the estimation of the translation and rotation diffusion times of CNC particles ($\tau_t \approx 1.3 \times 10^{-4}$ s and $\tau_r \approx 2.7 \times 10^{-4}$ s respectively) given in Sec. 3.A.6.b in chapter 3, which also coincide with the plateau value of the inflection time t^* reached at large salt concentrations (about 4×10^{-4} s). Yet, these two relaxation times seem about constant throughout the entire sol-gel transition. The present technique might not be suitable to capture either the aggregation of CNCs, which may occur over a very short timescale following flow cessation, or the formation of a percolated network at the critical gel point. Future tests should be performed on more slowly gelling systems, and some attempts on more dilute samples might be worth a try too.

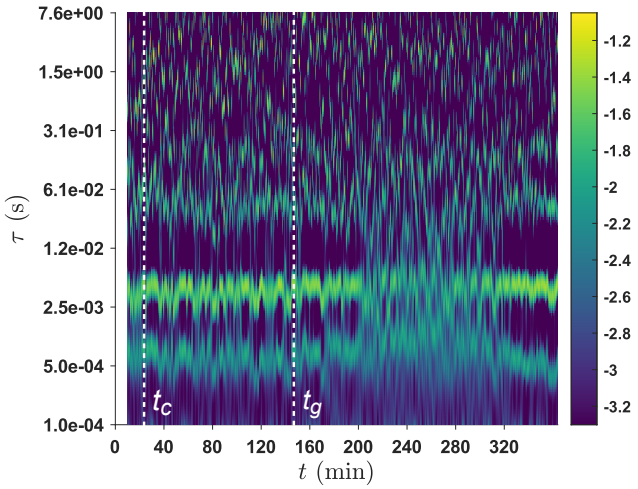

Figure 5.3: Map of the relaxation times τ, extracted from dynamic light scattering using the analysis detailed in [Liénard et al., 2022], as a function of time during the suspension recovery following shear cessation. The colors code for the contribution of the relaxation time τ in the spectrum of relaxation times. Experiment performed on a suspension containing 3.2 wt % CNC and 9 mM NaCl, of crossover time $t_c(1\text{ Hz})$ = 23 min, and of gelation time t_g = 147 min.

Rheo-X-ray scattering.- This technique allows to characterize the microstructure of a colloidal suspension at length-scales as small as the size of a particle [Narayanan, 2024]. The experiments were performed at the European Synchrotron Radiation Facility (ESRF, line ID02) in Grenoble. An example of the result that we have obtained is shown in Fig. 5.4, where the scattered intensity I is plotted as a function of the wave vector q at different points in time during the suspension recovery following shear cessation. Each wave vector q corresponds to a length scale $2\pi/q$ in the suspension microstructure. The experiment is performed on a suspension containing 3.2 wt % CNC and 12 mM NaCl, of crossover time $t_c(1\text{ Hz})$ = 90 s and of gelation time t_g = 1330 s. We observe no clear evolution of the spectrum over time and, therefore, no clear signature of a change in the CNC organization over the range 10^{-2} nm^{-1} to 6×10^{-1} nm^{-1}. Yet, changes in the CNC organization might take place at larger length-scales, i.e., at smaller q vectors, outside of the accessible window. Therefore, it would be interesting to perform the same type of experiments over a lower range of wave vectors q. Spectra of CNC suspensions of various compositions were measured at rest, in order to investigate variations in the microstructure induced by a change of salt concentration or salt nature, and of CNC weight fraction. The results are described in Sec. 5.C in Appendix.

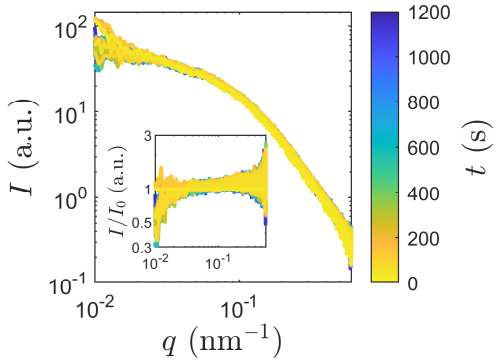

Figure 5.4: Scattered intensity I as a function of the wave vector q extracted from Rheo-SAXS measurements conducted on a CNC suspension during its recovery following pre-shear. The spectrum of the solvent, i.e., water, has been subtracted. Inset: I normalized by the scattered intensity I_0 at time t = 0 as a function of q. The color scale codes for the time. Experiment performed on a suspension containing 3.2 wt % CNC and 12 mM NaCl, of crossover time $t_c(1\text{ Hz})$ = 90 s and of gelation time t_g = 1330 s.

Raman spectroscopy.- Raman spectroscopy characterizes the vibrational modes of molecules, relying upon inelastic scattering of photons, known as "Raman scattering". It can be used to probe the formation or destruction of hydrogen bonds, which affect these vibrational modes [Burikov et al., 2010, Kolesov, 2021]. The experiments were performed with the help of A. Di Bitetto at the Thermo Fisher Scientific labs in Villebon-sur-Yvette (France). Fig. 5.5 shows a typical Raman spectrum we measured, similar to those reported in the literature for CNCs from various sources [Agarwal, 2017, Lewandowska et al., 2018, Sacui et al., 2014] (see Sec. 5.C in Appendix for an association of each peak to the various deformation modes in a cellulose molecule). It has been shown that the peaks centered at 900 cm^{-1} and at 1100 cm^{-1} shift towards smaller Raman shifts when CNCs form inter-particle hydrogen bonds [Lewandowska et al., 2018]. Measuring the time evolution of the Raman spectra of CNC suspensions during their recovery following pre-shear reveals some temporal evolution of the Raman shifts associated with these two particular peaks, yet with no systematic trend when repeating the experiment on suspensions of various compositions. More details on the results are given in Sec. 5.C in Appendix. A more careful analysis of the data by an expert on Raman spectroscopy applied to CNCs would be necessary to reach a definitive conclusion. Nevertheless, this technique is promising to provide a better understanding of the time evolution of the hydrogen bond network in a CNC suspension.

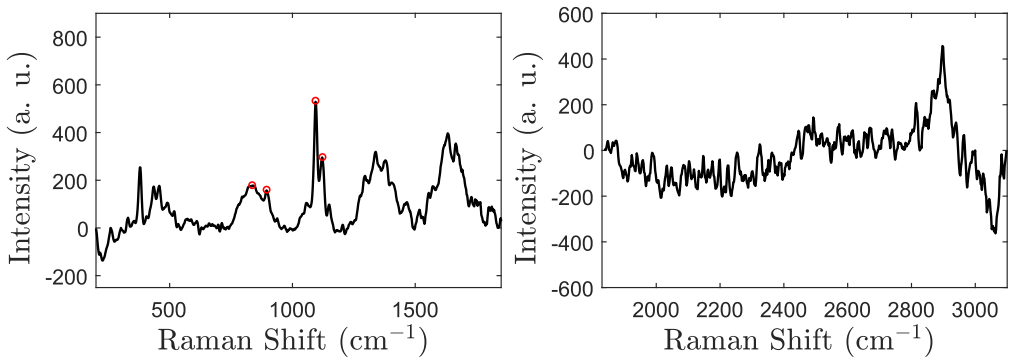

Figure 5.5: Raman spectrum of a suspension containing 3.2 wt % CNC and 10 mM NaCl, corrected from fluorescence effects. The red circles highlight the Raman shifts of interest to probe the formation of hydrogen bounds. See Fig. 5.10 and Table 5.1 in Sec. 5.C in Appendix for the attribution of the peaks.

B.2 Long-term perspectives: from soft precursors to solid materials

Another perspective to explore is the transition from a soft CNC gel to the formation of a solid material. Indeed, a solid material inherits part of the mechanical and optical properties of its soft precursor, and its structure often depends on the solidification process. Therefore, besides the study of the properties of the soft precursor, a better understanding of this soft-to-solid transition is of major concern for potential applications of CNCs to the design of solid materials. In this goal, we have started to investigate the solidification of CNC suspensions through two different processes: drying and freezing. These studies were conducted in collaboration with J.-B. Salmon from the Laboratoire du Futur in Pessac, and with S. Deville from the Institut Lumière Matière in Villeurbanne, respectively.

Structuration through drying.- We have shown that a drop of CNC suspension, confined between two transparent wafers, dries through water evaporation in the air following the same dynamics as a similar drop constituted of pure water. Yet, in order to properly capture the CNC concentration gradients induced by the solvent evaporation and the drop shrinkage, one needs to

take into account the coordinated motion of CNCs instead of restricting to the very dilute regime. Moreover, as the solvent evaporates and the drop shrinks, polarized light microscopy has allowed us to evidence a structuration of the suspension, as seen in Fig. 5.6. While birefringent domains, most likely cholesteric domains, can be clearly identified and tracked as the drop shrinks over the first 80 min of evaporation, a transition toward a much more homogeneous pattern occurs around 100 min, most probably indicative of a glassy state. Moreover, as expected, drying a CNC suspension through pervaporation in a microfluidic channel leads to a very different structuration of the solid material, where alignment of CNCs is induced both by the flow and by the channel geometry. In the final dry material, CNCs are organized into a well-defined microstructure showing strong birefringence, that spreads over the whole channel length, as shown in Fig. 5.7. More detailed analysis and further results are given in Sec. 5.C in Appendix for the drying of the drop, and in Sec. 5.C in Appendix for the pervaporation experiments.

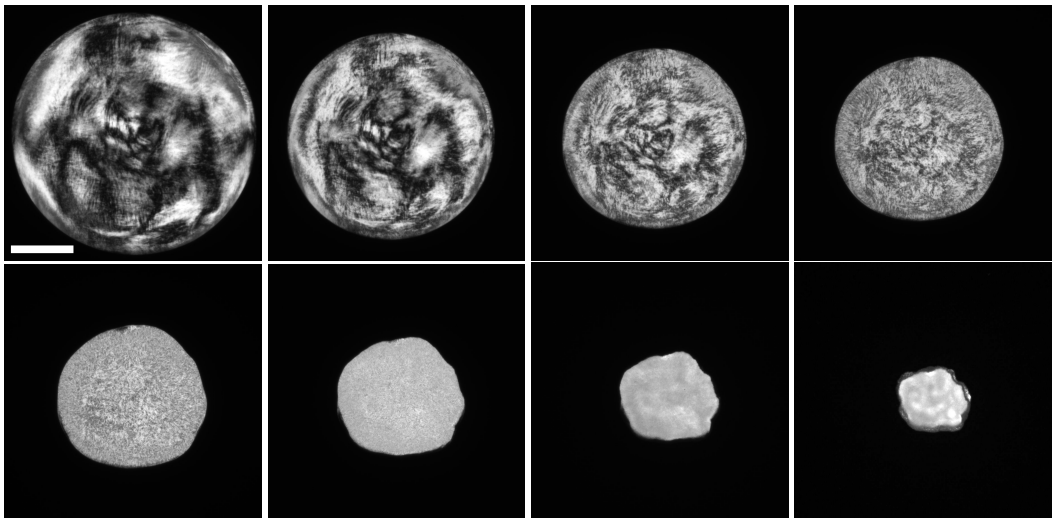

Figure 5.6: Polarized light microscopy images of a drop of a suspension initially containing 6.4 wt % CNC during drying (see the corresponding video). From left to right and top to bottom, the images are taken at t =3 min, 49 min, 79 min, 96 min, 116 min, 136 min, 160 min, and 236 min after the drop deposition and the beginning of solvent evaporation. The scale bar on the top left image corresponds to 500 μm.

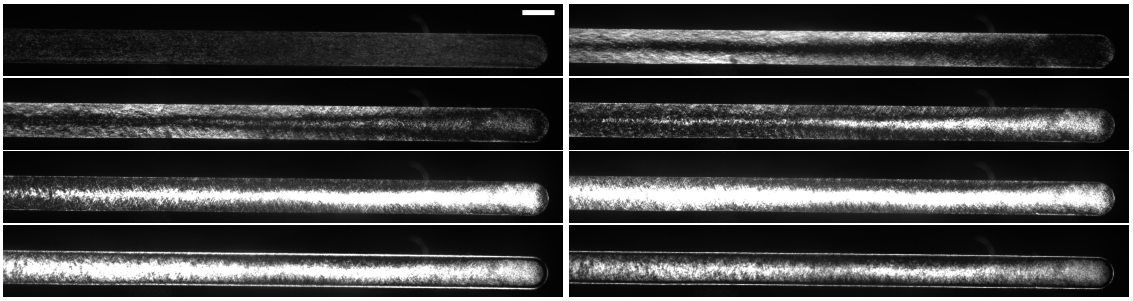

Figure 5.7: Polarized light microscopy images of a microfluidic channel filled with a suspension initially containing 6.4 wt % CNC, during drying through pervaporation (see the corresponding video). From top to bottom and left to right, the images are taken a time t = 15 min, 1 h 38 min, 2 h 50 min, 3 h 49 min, 4 h 59 min, 6 h 38 min, 8 h 52 min, and 13 h 25 min. The scale bar in the top left image corresponds to 400 μm.

Freeze-casting.- Another well-known technique to obtain a solid material with a specific microstructural organization is using freeze-casting, also referred to as freeze-templating. Indeed, as ice grows inside the suspension, it rejects all impurities, including the CNCs. As a result, CNCs are highly concentrated and confined in between the ice domains. When directionally freezing the suspension in a controlled way and imposing the right growth rate for the ice inside the suspension, a particularly interesting regime can be reached, where the ice grows forming elongated cells. An image of a CNC suspension containing 4 wt % CNC frozen in this particular regime is shown in Fig. 5.8a, where the ice appears in black and CNCs in red. After sublimation of the ice, the sample is transformed into a porous solid material (see Fig. 5.8b), where the shape and the size of the pores can be controlled by the experimental conditions and the suspension composition [Shao et al., 2020]. Further details are given in Sec. 5.C in Appendix. Future experiments could aim to better characterize (i) the dimensions of the pores depending on the experimental conditions and on the suspension composition, and (ii) the mechanical properties of the resulting material. Moreover, besides this interesting large scale structuration, further observations under polarized light microscopy during freezing, and further characterization of the solid material at the nanoscale, could allow one to determine the local organization of CNCs. More precisely, one could determine if confinement by the growing ice induces alignment of the particles.

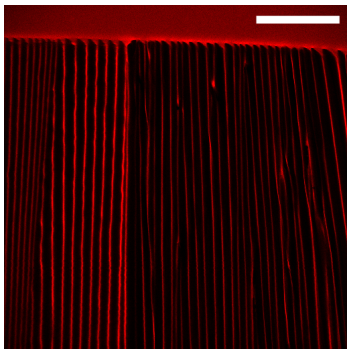

(a) Confocal microscopy image of a suspension containing 4 wt % CNC (and 0.1 mM rhodamine to increase contrast), frozen in a temperature gradient set by a temperature different ΔT = 30 °C, at a constant ice front velocity v = 30 μm.s^{-1} (see Sec. 5.C in Appendix for a description of the setup). The ice appears in black while the liquid suspension and the CNCs concentrated in between the glass cells appear in red. The scale bar corresponds to 150 μm.

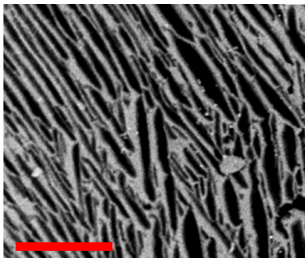

(b) Perpendicular cut, with respect to the image plane of Fig. 5.8a (and to the ice cells), of a solid CNC material obtained in similar freezing conditions, followed by ice sublimation, of a suspension containing 1.5 wt % CNC. The scale bar corresponds to 200 μm. Extracted from [Munier et al., 2016].

Figure 5.8: Freeze-casting of a CNC suspension.

C Appendix

C.1 X-ray scattering

In order to probe the effect of the composition on the microstructure of CNC suspensions, we have measured SAXS spectra of various CNC suspensions at rest. Figure 5.9 shows some of these spectra. We observe that all the spectra are superimposed for $q \geq 10^{-1}$ nm^{-1}. This range of wave vectors corresponding to the size of an individual CNC particle, this result is consistent with the fact that the shape of CNC particles is not affected when varying the suspension composition. At smaller q, i.e., when probing the microstructure at the scale of CNC aggregates and/or gel networks, we observe a strong influence of the salt concentration, for every type of salt nature and CNC weight fraction [see Figs. 5.9(a) to (d)]. Varying the CNC weight fraction at fixed salt concentration, an effect is observed only for a NaCl concentration of 25 mM [see Figs. 5.9(e) and (f)]. Whatever the salt concentration, a change of salt cation seems to have a weaker impact on the suspension microstructure [see Figs. 5.9(g) and (h)]. However, the origin of such an impact is difficult to rationalize, since the SAXS measurements were performed on samples prepared at various times, and without controlling precisely their age and thus their "position" relative to the gel point. As suggested in the previous paragraph, it would be necessary to perform measurements at smaller q values in order to better quantify the effect of the sample composition and of the salt nature on its microstructure.

Moreover, it would be interesting to compare these results to the ones obtained on CNC suspensions dispersed in D_2O. Indeed, we have evidenced in Sec. 3.A.5 in chapter 3 that a change from H_2O to D_2O induces significant changes in the recovery dynamics of CNC suspensions, most likely due to changes in the inter-particle interaction strength. Such experiments would allow us to determine if a change of solvent isotope induces only a change of gelation kinetics or if it also influences the microstructure of the suspension.

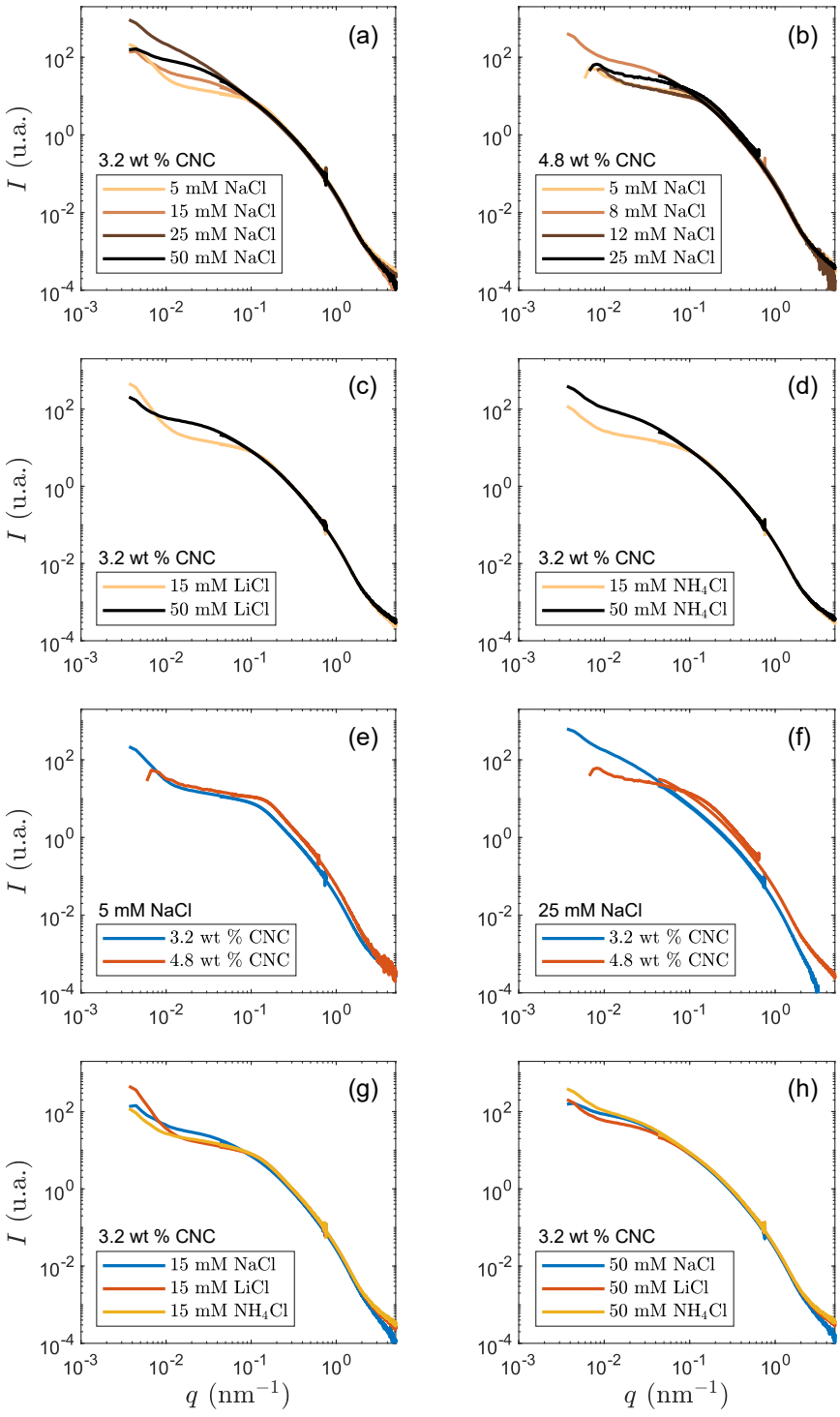

Figure 5.9: Scattered intensity I as a function of the wave vector q extracted from SAXS measurements on CNC suspensions of various compositions. The spectrum of the solvent, i.e., water, has been subtracted. The suspensions were loaded in borosilicate glass capillaries of diameter 2 mm.

C.2 Raman spectroscopy

In order to characterize the interactions between CNC particles, we have used Raman spectroscopy. This spectroscopic technique characterizes the vibrational modes of molecules, relying upon inelastic scattering of photons, known as "Raman scattering". The measurements were performed with the help of A. Di Bitetto at the Thermo Fisher Scientific labs in Villebon-sur-Yvette (France).

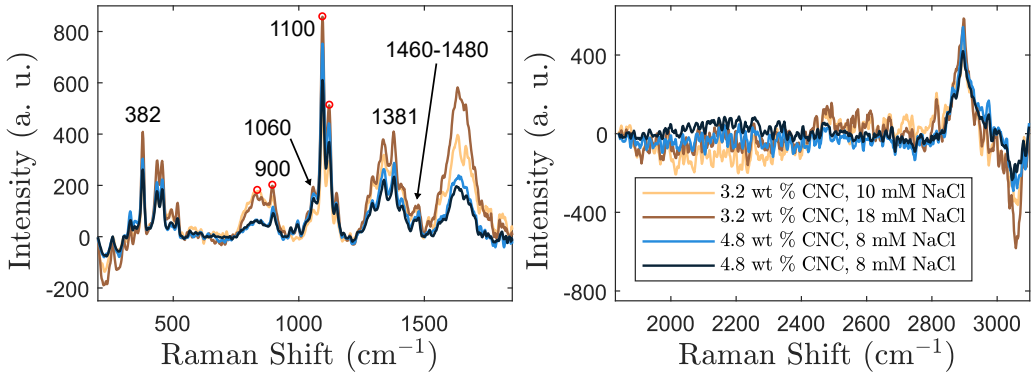

Figure 5.10: Raman spectra of suspensions of various compositions, corrected from fluorescence effects[1]. The red circles highlight the Raman shifts of interest to probe the formation of hydrogen bounds. The attribution of the labeled peaks is detailed in Table 5.1.

Figure 5.10 shows Raman spectra obtained for CNC suspensions of various compositions, corrected from fluorescence effects. These spectra are very similar to the ones reported in the literature for CNCs extracted from various sources [Agarwal, 2017, Lewandowska et al., 2018, Sacui et al., 2014], which allows us to associate each peak at a given Raman shift to the various deformation modes in a cellulose molecule, as reported in Table 5.1. While we observe no influence of the salt concentration on the peaks of the spectra that we could attribute, an increase in the CNC weight fraction leads to a change of shape of the peak at a Raman shift around 900 cm^{-1}. However, the physical interpretation of such a change remains to be determined.

Table 5.1: Raman shifts associated to the various peaks highlighted in the spectra showed in Fig. 5.10, and the corresponding deformation modes in the cellulose molecules constituting the CNCs.

Raman shift (cm $^{-1}$)	Attribution
382	Skeletal-bending modes involving C−C−C, C−O−C, O−C−C, O−C−O, and skeletal stretching modes of C−C and C−O bonds
900	Vibrational modes in the cellulose chain
1060	Sulfate esters groups
1100	Contribution from C−O of the ring, and C−O−C stretching between the glucose rings of the cellulose chains
1381	Bending modes involving the C−C−H, O−C−H and C−O−H moities
1460-1480	CH_2 bending

[1]The experiment on the suspension containing 4.8 wt % CNC and 8 mM NaCl has been performed twice.

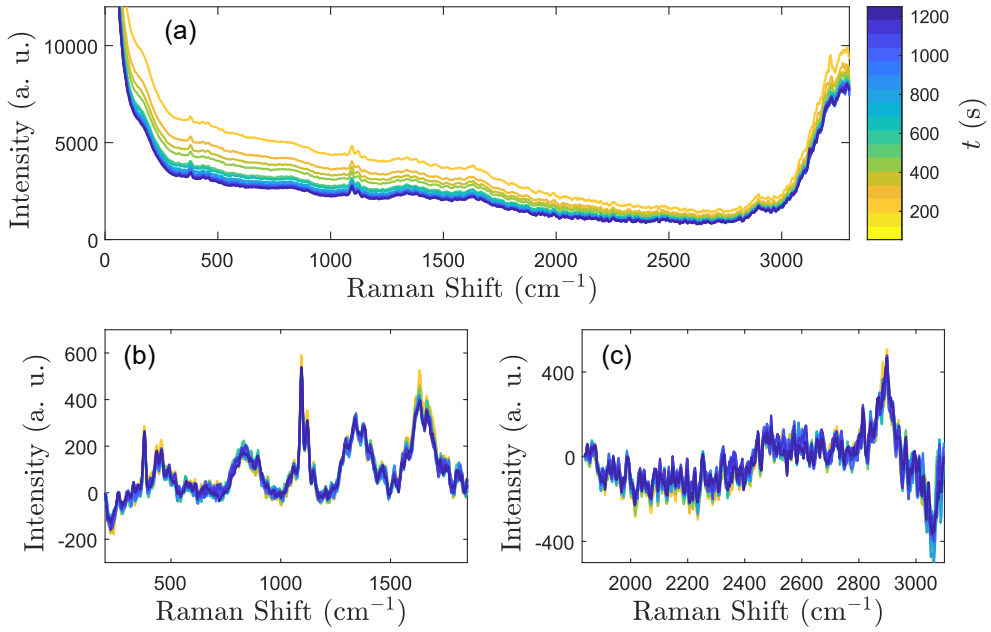

Figure 5.11: Raman spectra measured through time during a CNC suspension recovery following pre-shear. Experiment performed on a suspension containing 3.2 wt % CNC and 10 mM NaCl, of crossover time $t_c(1\text{ Hz}) \approx 300$ s and of gelation time $t_g = 4334$ s. (a) Raw data. (b),(c) Spectra corrected from fluorescence effects.

The formation or breakage of hydrogen bonds can influence the vibrational mode of some chemical bonds in a cellulose chain, hereby inducing a shift of the Raman peaks. In particular, it has been shown that the peaks centered at 900 cm^{-1} and at 1100 cm^{-1} shift towards smaller Raman shifts when CNCs form inter-particle hydrogen bonds, even though these peaks correspond to vibrational modes that are not directly involved in the formation of hydrogen bonds [Lewandowska et al., 2018]. In fact, the position of these peaks is sensitive to the deformations of the cellulose chains that may arise from the formation of inter-particle hydrogen bonds. Therefore, we have measured the time evolution of the Raman spectra of three CNC suspensions, containing respectively 3.2 wt % CNC and 10 mM NaCl, 3.2 wt % CNC and 18 mM NaCl, and 4.8 wt % CNC and 8 mM NaCl, during their recovery following shear cessation.

Figure 5.11 shows the Raman spectra measured through time for the suspension containing 3.2 wt % CNC and 10 mM NaCl, of crossover time $t_c(1\text{ Hz}) \approx 300$ s and of gelation time $t_g = 4334$ s. We observe that the fluorescence of the sample decreases with time [see Fig. 5.11(a)]. Such a decrease of the fluorescence was also observed on the two other suspensions, however it is less pronounced for the suspension containing a larger CNC weight fraction (4.8 wt % CNC). Moreover, for every suspension composition, we observe no major effect of the sample age on the spectra corrected from fluorescence [see Figs. 5.11(b) and (c) for the suspension containing 3.2 wt % CNC and 10 mM NaCl]. Further focusing on the time evolution of the Raman shifts of the two peaks around 900 cm^{-1} and of the two peaks around 1100 cm^{-1}, plotted in Fig. 5.12 for the three suspensions, we indeed observe a displacement of the Raman shifts associated to these peaks. However, this behavior is not systematic, and the peaks shift towards smaller or larger Raman shifts depending on the suspension. These preliminary results suggest an evolution of the number or of the intensity of inter-CNC hydrogen bonds during the suspension gelation and aging. However, a more precise analysis is required to identify more precise effects.

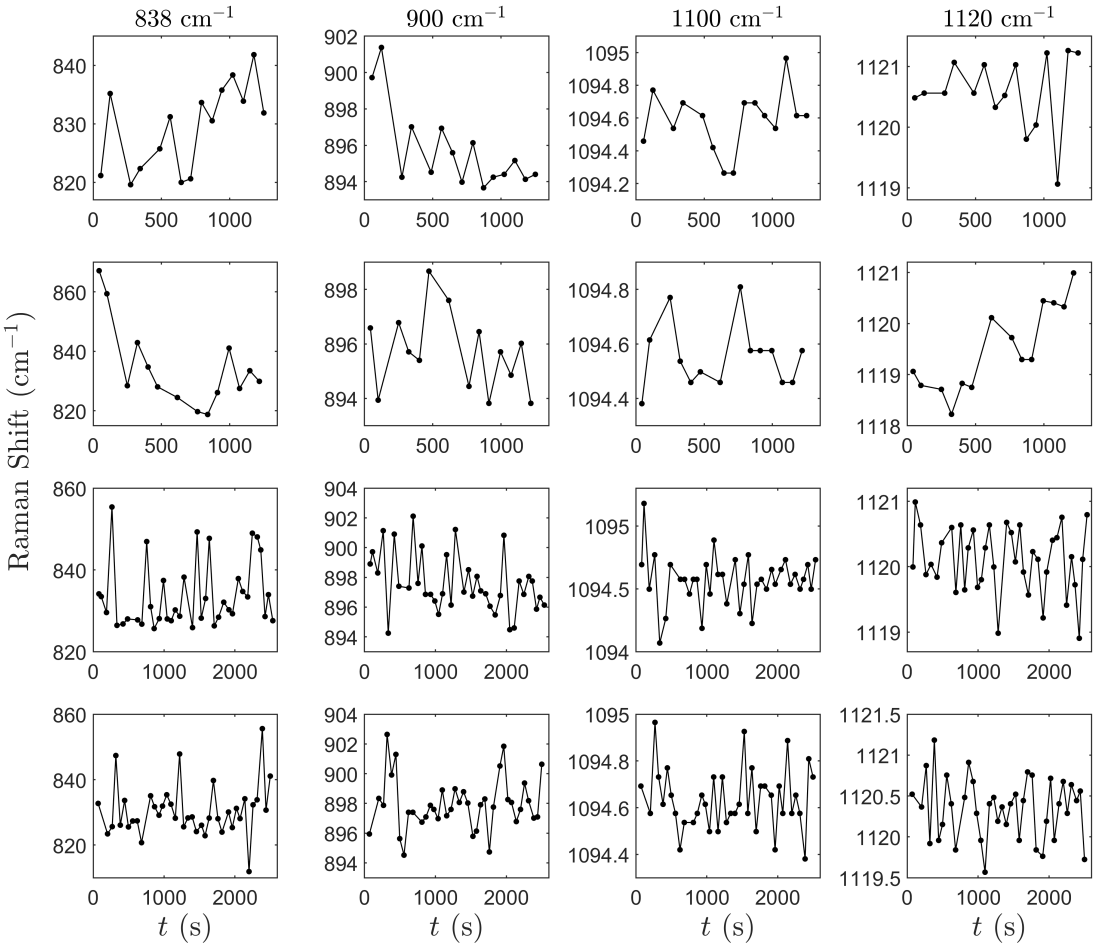

Figure 5.12: Raman shifts corresponding to the two peaks centered around 838 cm^{-1} and 900 cm^{-1} and to the two peaks centered around 1100 cm^{-1} and 1120 cm^{-1}, highlighted by red circles in Fig. 5.10, as a function of time during the suspension recovery, for suspensions containing (First line) 3.2 wt % CNC and 10 mM NaCl of crossover time t_c(1 Hz) = 300 s and gelation time t_g = 4334 s, (Second line) 3.2 wt % CNC and 18 mM NaCl of crossover time t_c(1 Hz) < 1 s and gelation time t_g = 90 s, and (Third and fourth lines) 4.8 wt % CNC and 8 mM NaCl of crossover time t_c(1 Hz) = 50 s and gelation time t_g = 1288 s.

C.3 Drying of a two-dimensional drop

To study how a CNC suspension solidifies through drying, we consider a first configuration where drying is induced through direct solvent evaporation (water here) in the air under ambient conditions. In this configuration, a drop of suspension is confined in between two surfaces, and the edges of the drop are in direct contact with the surrounding air.

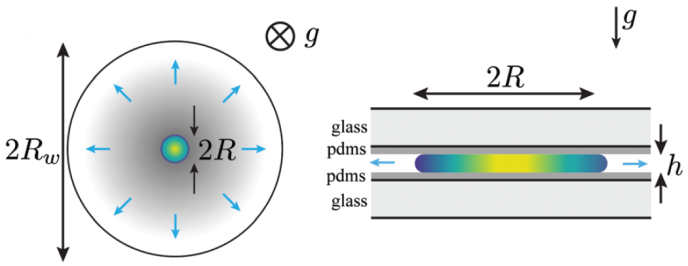

Figure 5.13: Sketch of the experimental setup. A two-dimensional drop of a CNC suspension evaporates in a confined cell made of two superimposed wafer disks separated by a distance h. The sketch on the right is an enlargement around the drop of the representation on the left. R defines the radius of the drop, and R_w defines the radius of the wafers. Extracted from [Sobac et al., 2020].

Experimental setup.- The experimental setup is schematically illustrated in Fig. 5.13. A drop of about 0.8 μL of a CNC suspension is confined between two circular transparent wafers, separated by a height h, and covered with a coating to prevent the contact line from sticking.

The coating is a mix of polydimethylsiloxane (PDMS) and of a silicone elastomer curing agent of ratio 10/1. This mix is poured over circular glass plates of diameter $2R_w$ = 7.62 cm, which are then rotated at 1500 rpm for 30 s in order to obtain an homogeneous layer of thickness about 50 μm. The wafers are then placed in a oven at 65 °C for two to three hours for the curing agent to polymerize the PDMS. This hydrophobic coating prevents the pinning of the receding meniscus, mainly constituted of water, during the drying of the drop. Spacers, consisting in small pieces, of few mm^2, of glass slides of thickness 150 μm, are positioned close to the edge of the bottom wafer. The drop of suspension is deposited at the center of the bottom wafer at time t = 0 s. Right after deposition, the second wafer is placed on top of the bottom one, at a height h = 150 μm defined by the spacers. The radius of the resulting confined drop R is much smaller than the radius of the wafers R_w. The drop dries by solvent evaporation through the meniscus of height h only, which is in direct contact with the surrounding air. The temperature T and relative humidity R.H. of the ambient air are measured at the beginning of an experiment, and remain roughly constant during the experiment.

The setup is placed under a microscope and the drying of the drop is observed from the top using either white light, polarized light or ultraviolet light. A camera placed on the microscope allows us to record the drying of the drop through time, taking one image every 45 s. The resulting images are analyzed to determine the radius $R(t)$ of the drying drop through time, and deduce several quantities such as the drop area, the drop volume, or the average CNC volume fraction in the drop, as detailed in the following.

Such an experiment enables to limit complex phenomena related to the free surfaces. Indeed, the axisymmetrical drying of the drop, combined with the small free surface ($\approx 2\pi hR$) prevents flows such as capillary-induced convection or Marangoni-induced convection.

Preliminary results.- As the solvent evaporates, the drop shrinks axisymmetrically. Only small deviations from a perfect disk are observed at long times (see Figs. 5.6, 5.15, 5.19 and 5.20). Therefore, by detecting the meniscus of the drop through time, we can extract the time evolution of the

radius of the drop $R(t)$. The water evaporation from an aqueous suspension being quasi-steady and limited by the diffusion of the vapor towards the edge of the cell of radius R_w, the radius of the drop varies as [Daubersies and Salmon, 2011]:

$$\frac{\mathrm{d}R}{\mathrm{d}t} = \frac{D_s V_s c_{sat}(1 - R.H.)}{R \ln(R/R_w)}, \tag{5.1}$$

with D_s the diffusion coefficient of water vapor in air, V_s the molar volume of liquid water, c_{sat} the concentration of the saturated vapor pressure, and $R.H.$ the external relative humidity. This equation holds for colloidal suspensions, even at large concentration, as the chemical activity of water remains close to unity even for strongly interacting colloids [Daubersies and Salmon, 2011]. Furthermore, Eq. (5.1) remains valid as long as the drop stays cylindrical and that $R(t) > h$. In practice, with the CNC suspensions that we have tested, we always verify $R(t) > h$, until the end of the experiment. Using the initial condition $R(t = 0) = R_0$, the analytical solution of Eq. (5.1) is given by:

$$\frac{t}{\tau_f} = 1 - \frac{\alpha(\ln(\beta\alpha) - 1)}{\ln\beta - 1}, \tag{5.2}$$

with $\alpha = (R(t)/R_0)^2$, $\beta = (R_0/R_w)^2$, and τ_f the drying time of a pure water drop of the same initial radius R_0, evaporating in the same conditions, given by:

$$\tau_f = \frac{R_0^2}{4D_s V_s c_{sat}(1 - R.H.)}(1 - \ln\beta). \tag{5.3}$$

Finally, using the colloid mass balance, the average CNC concentration in the drop $\langle\phi\rangle$ is given by:

$$\langle\phi\rangle(t) = \frac{\phi_0}{\alpha(t)}, \tag{5.4}$$

where $\phi_0 = \phi(r, t = 0)$ is the initial volume concentration of the drop.

Figure 5.14(a) and (b) show the time evolution of the ratio $\alpha = (R(t)/R_0)^2$ and of the average volume fraction $\langle\phi\rangle$ for a drop of suspension of initial CNC weight fraction 6.4 wt % and no salt. Interestingly, we observe that at the end of the experiment, the dry suspension reaches a volume fraction of about 80 %. This value is larger than the 64 % volume fraction obtained by random close packing of spheres. Indeed, it has been mathematically shown that ellipsoids can pack denser than spheres. In Fig. 5.14(c), the time t is plotted as a function of $\frac{\alpha(\ln(\beta\alpha)-1)}{\ln\beta-1}$. Linearly fitting this curve and using Eq. (5.2), we extract the value of the drying time τ_f [see the red line in Fig. 5.14(c)]. In this experiment, we obtain $\tau_f = 196.6$ min. Using this value of τ_f, combined with Eq. (5.3), we can calculate the value of the diffusion coefficient D_s of water vapor in air, and compare it to the tabulated one. For this experiment, we obtain $D_s = 2.92 \times 10^{-5}$ m^2.s^{-1}, which is in good agreement with the tabulated value of 2.49×10^{-5} m^2.s^{-1}. This comparison enables us to confirm that a drop of a CNC suspension dries following the same dynamics as a drop of pure water. To further confirm the validity of this theory based on the evaporation dynamics of pure water, we verify that Eq. (5.1) holds during solvent evaporation. To do so, we have plotted in Fig. 5.14(d) the time derivative $\frac{\mathrm{d}R}{\mathrm{d}t}$ as a function of time, extracted from the image analysis, that we superimpose to the time evolution of $\frac{D_s V_s c_{sat}(1-R.H.)}{R\ln(R(t)/R_w)}$, where $R(t)$ is extracted from the image analysis, and D_s is the value estimated from the experiment. We observe that the data superimpose quite well until about 170 min, when the shape of the drop strongly deviates from a perfect cylindrical shape ([]see Fig. 5.6).

From the value of τ_f, we can calculate the Peclet number Pe which compares the characteristic time-scale of diffusion of the colloids across the drop to the drying time τ_f:

$$Pe = \frac{R_0^2}{D_0 \tau_f}, \tag{5.5}$$

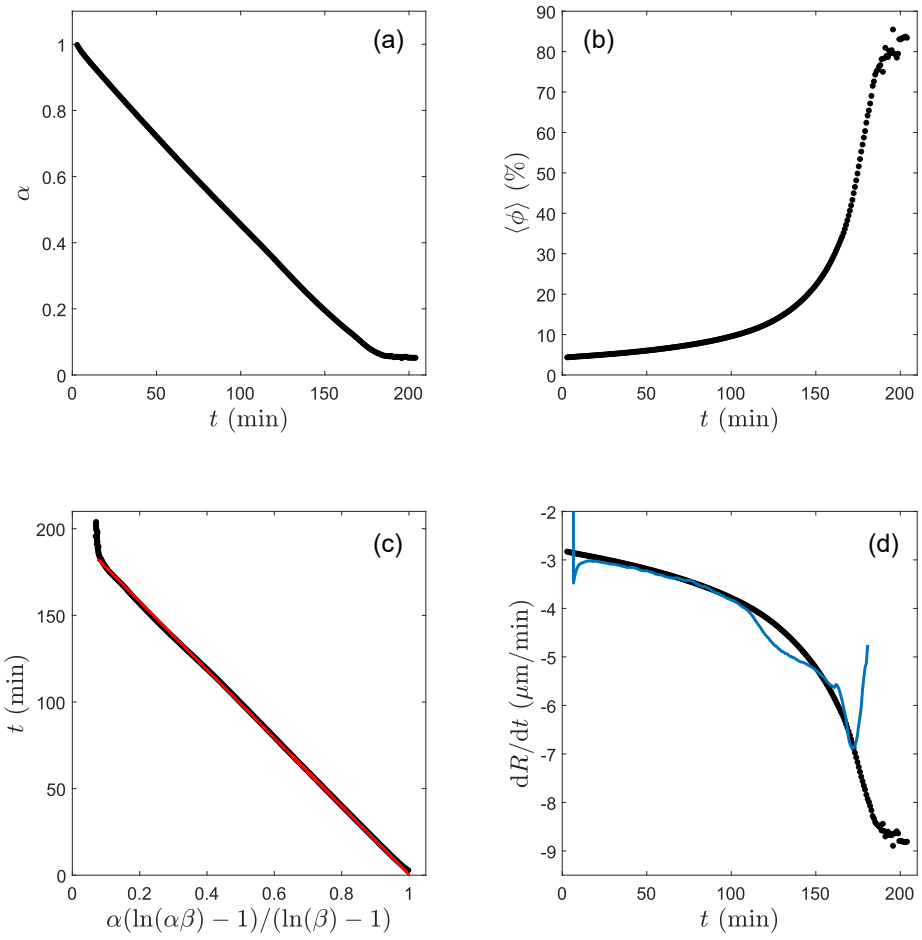

Figure 5.14: Data extracted from the image analysis of a drying drop of a suspension initially containing 6.4 wt % CNC (some of the corresponding images are shown in Fig. 5.6). (a) Drop area normalized by the initial drop area $\alpha = (R(t)/R_0)^2$, and (b) averaged volume fraction $\langle\phi\rangle$ as a function of time. (c) Time as a function of the right member of Eq. (5.2). The red line shows the best fit by a linear function of slope τ_f = 196.6 min. (d) Time derivative of the radius of the drop dR/dt as a function of time. The black data points correspond to the right member of Eq. 5.1, and the blue line corresponds to the left member of Eq. 5.1.

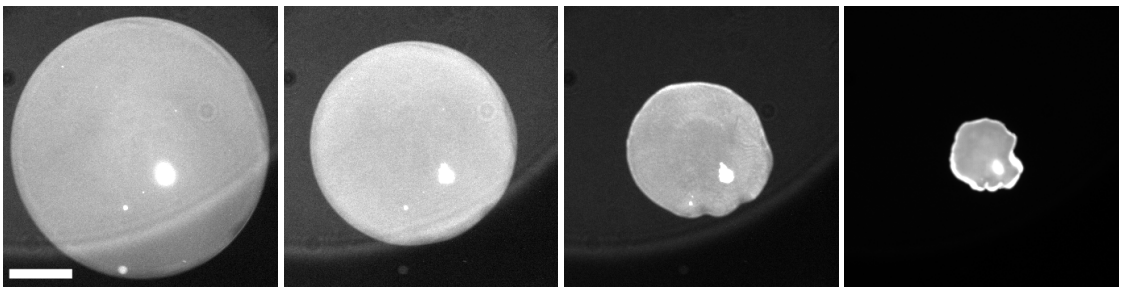

Figure 5.15: Fluorescence images of a drop of a suspension containing 6.4 wt % CNC during drying (see the corresponding video). From left to right, the images are taken at t =1 min, 56 min, 113 min, and 170 min after the drop deposition and the beginning of solvent evaporation. The scale bar on the left image corresponds to 500 μm.

where D_0 is the diffusion coefficient of the colloids in water, in the very dilute regime. For elongated ellipsoids, such as CNCs, of aspect ratio $r = a/b$, with a the semi major axis and b the semi minor axis, this diffusion coefficient is given by [Perrin, 1936]:

$$D_0 = \frac{k_B T}{6\pi\eta a\sqrt{1-r^{-2}}} \log\left[r\left(1+\sqrt{1-r^{-2}}\right)\right], \tag{5.6}$$

with k_B the Boltzmann's constant and η the viscosity of water. For the CNCs used in this thesis, of length $L \approx 131$ nm, i.e., $a \approx 65.5$ nm, and of diameter $D \approx 4$ nm, , i.e., $b \approx 2$ nm, we obtain $D_0 = 1.45 \times 10^{-11}$ m^2.s^{-1}. The resulting Peclet number that we calculate for this experiment is $Pe = 5.68$.

The fact that $Pe > 1$ means that the diffusion of CNC particles in the drop is slower than the drying of the drop. Therefore, $Pe > 1$ implies the existence of concentration gradients along the radial direction of the drop. Figure 5.16 shows a numerical computation of the CNC concentration profiles $\phi(r,t)$ along the radial direction in the drop r, through time, calculated using the same experimental conditions as for the experiment presented in Fig. 5.14, with $Pe = 5.68$. We observe that sharp concentration gradients develop at long times. Cellulose nanocrystals being fluorescent, we have observed the drying of a drop of a CNC suspension lightened at a wavelength of 360 nm, where the fluorescence is maximum. Figure 5.15 shows images at various times of this drying drop, containing an initial CNC weight fraction of 6.4 wt %. We observe that the fluorescence is almost homogeneous on the drop surface, indicating that no sharp concentration gradients, such as the ones calculated in the numerical computation, develop. This discrepancy originates from a wrong estimation of the Peclet number. Indeed, the small concentration gradients actually observed in the experiments show that the actual Peclet number should be smaller than the estimated one. This over-estimation of Pe comes from an underestimation of the CNCs diffusion coefficient. Indeed, as mentioned above, Eq. (5.6) used to calculate the diffusion coefficient D_0 is valid in the very dilute regime. At an initial weight fraction of 6.4 wt % CNC, corresponding to an initial volume fraction $\phi_0 = 4.4$ % CNC, we are not in the very dilute regime anymore, and CNCs interact with each other. In particular, coordinated motion is

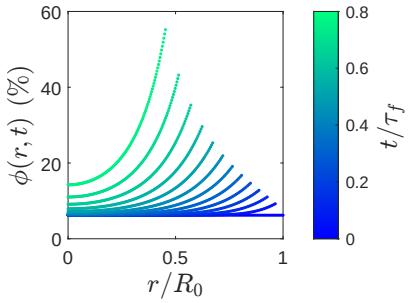

Figure 5.16: Numerical computation of the time evolution of the CNC volume fraction profile $\phi(r,t)$ along the radial direction in the drop during drying, normalized by the initial radius R_0 of the drop, in the experimental conditions corresponding to the data plotted in Fig. 5.14 with $Pe = 5.68$.

Table 5.2: Parameters extracted from the image analysis of drying drops of suspensions of various initial compositions. The experiment on the suspension initially containing 6.4 wt % CNC has been performed twice (under polarized light, and using the fluorescence of CNCs).

Suspension composition	ϕ_0 (%)	τ_f (min)	D_s ($m^2.s^{-1}$)	Pe
6.4 wt % CNC	4.35	196.6	2.92×10^{-5}	5.68
6.4 wt % CNC	4.35	74.53	2.69×10^{-5}	8.80
3.2 wt % CNC	2.15	171.83	3.40×10^{-5}	8.77
1.6 wt % CNC	1.07	150.91	2.83×10^{-5}	8.12
3.2 wt % CNC, 5 mM NaCl	2.15	170.3	3.03×10^{-5}	6.34
3.2 wt % CNC, 100 mM NaCl	2.15	109.6	2.95×10^{-5}	5.8

induced and the resulting collective diffusion coefficient D_{coll} is larger than the self-diffusion coefficient D_0 related to Brownian motion only. Therefore, using D_{coll} instead of D_0 lowers the Peclet number, and leads to computations of weaker CNC concentration gradients, that are more realistic. In most cases, the approximation $D_{coll} \approx D_0$ is acceptable to properly capture the concentration gradients in the drop during drying. However, in the case of CNC suspensions, this approximation fails, most likely due to their anisotropic shape. Indeed, assimilating CNCs to equivalent spheres of diameter their length L, the effective volume fraction becomes much larger, hereby accounting for the appearance of steric interactions at smaller CNC concentrations than in the case of spherical colloids.

We have performed the same drying experiment on drops of suspensions containing various initial CNC weight fractions, and various salt concentrations. The values of the parameters obtained for each experiment are reported in Table 5.2. For every experiments, we obtain values for the diffusion coefficient of water vapor D_s that are very close to the tabulated value of 2.49×10^{-5} $m^2.s^{-1}$. Moreover, we observe that the values of the Peclet number are always quite large, ranging between 5.68 and 8.80, indicating that even at the smallest CNC weight fraction considered here, i.e., for w_{CNC} = 1.6 wt %, the diffusion coefficient of CNCs in water is under-estimated, hereby revealing that collective effects are non-negligible.

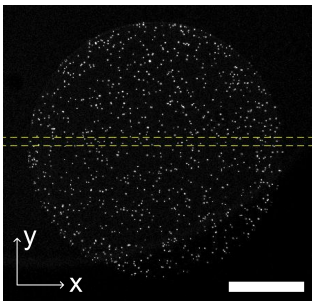

Figure 5.17: Drop of a suspension containing 1.6 wt % CNC and less than 0.01 % fluorescent tracers. The horizontal yellow lines define the region of the drop over which the intensity is averaged to construct the space-time plots showed in Fig. 5.18. The scale bar corresponds to 500 μm.

In order to get some insight into the local flows inside the drop, induced by solvent evaporation and by the drop shrinkage over time, we add some fluorescent tracers (Fluospheres, 500 μm diameter, at ϕ < 0.01 %) to the CNC suspension. We have performed such experiments on three suspensions of initial CNC weight fractions 6.4 wt %, 3.2 wt % and 1.6 wt %, respectively, without any salt. From each image, at a given point in time, we calculate the intensity $\langle I(x,t)\rangle_y$ averaged along the vertical axis y over a height of 40 pixels, centered around the drop horizontal median line (see the region defined by the yellow horizontal lines in Fig. 5.17). Then, we plot this averaged intensity $\langle I(x,t)\rangle_y$ for each time t as a function of the horizontal position x. Figure 5.18 shows the resulting space-time plots for the three initial CNC weight fractions. We observe that at large initial CNC weight fraction, for w_{CNC} = 6.4 wt % or equivalently ϕ_0 = 4.4 %, the tracers follow straight trajectories, with no visible Brownian motion, indicating that the fluorescent colloids are tightly trapped into the CNC network. At smaller initial weight fractions, w_{CNC} = 3.2 wt % and 1.6 wt %, the

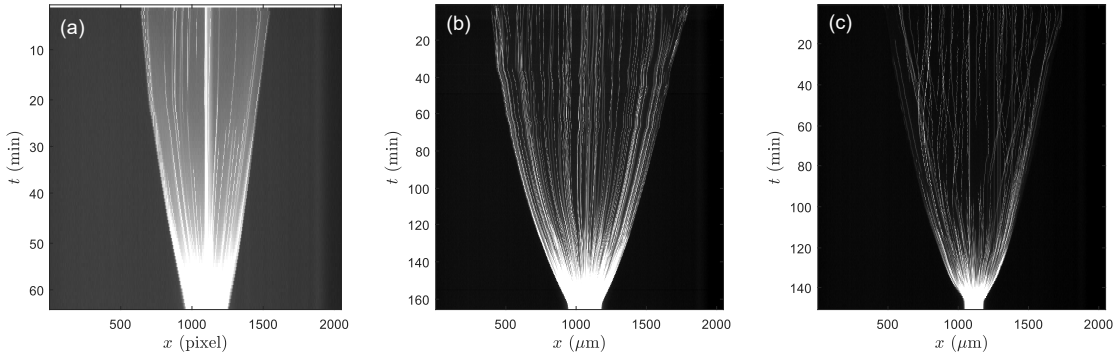

Figure 5.18: Space-time plots showing the trajectories of the fluorescent tracers inside the drop during drying. Suspensions initially containing (a) 6.4 wt % CNC, (b) 3.2 wt % CNC, and (c) 1.6 wt % CNC, and less than 0.01 % tracers. See the corresponding videos of the drying drops of initial CNC weight fractions of 6.4 wt %, 3.2 wt % and 1.6 wt %.

trajectories are not straight anymore, and we observe Brownian motion. Consistently, this observation indicates that as we decrease the CNC weight fraction, the tracers are less tightly trapped into the CNC network, as this network becomes less dense. At the smallest initial CNC weight fraction considered here, i.e., for w_{CNC} = 1.6 wt % or equivalently ϕ_0 = 1.1 %, we observe typical recirculating flows in the vicinity of the meniscus [Loussert et al., 2016]. Such flows are buoyancy-driven flows that are induced by concentration gradients of CNC particles. In fact, at such a small initial CNC weight fraction, at least at short times, the CNCs are not concentrated enough to form a dense network that would trap the tracers, and that would hinder the motion of CNCs. Therefore, more pronounced CNC concentration gradients may develop. Interestingly, such recirculating flows are evidenced at much larger colloid volume fractions in the case of isotropic colloids. For example, recirculating flows are observed for ϕ_0 = 24 % in a suspension of silica particles [Bouchaudy and Salmon, 2019]. Once again, this discrepancy is most likely due to the rod-like shape of the CNC colloids.

Finally, in order to investigate the global organization of CNCs induced by the increased concentration during the drop drying, we perform experiments under polarized light. Figure 5.6 shows some images obtained through time for a drop of initial CNC weight fraction w_{CNC} = 6.4 wt %. We observe that at all time, the drop is birefringent. Initially, large birefringent domains are observed, of maximum dimension up to about 500 μm, and these domains are either bright or dark. This texture indicates local organization of CNCs into larger-scale liquid crystal domains, most likely cholesteric domains, whose orientation varies from one domain to the other. As the solvent evaporates and the CNC weight fraction increases inside the drop, the size of the domains decreases, until we observe only a uniform gray drop, most likely indicative of a glassy state. Interestingly, this "homogeneization" of the CNCs organization seems to originate from the sides of the drop, and to progressively propagate towards the center of the drop.

We have performed the same type of experiment under polarized light on drops of suspensions of initial CNC weight fraction 3.2 wt % and initial salt concentrations 5 mM and 100 mM (see Figs. 5.19 and 5.20). In both experiments, we also observe that the drop is birefringent from t = 0 s until the end of the experiment. Yet, the birefringent patterns are slightly different, and the time-evolution of these patterns differs slightly. In the case of the suspension containing 5 mM NaCl, as the solvent evaporates and the drop shrinks, we observe that bright domains grow in size, indicating a global CNC alignment over the drop surface, before observing a more homogeneous intensity, again suggesting the appearance of a glassy state with no birefringent domains. All along drying, we observe that at a given position on the drop surface, domains alternate between

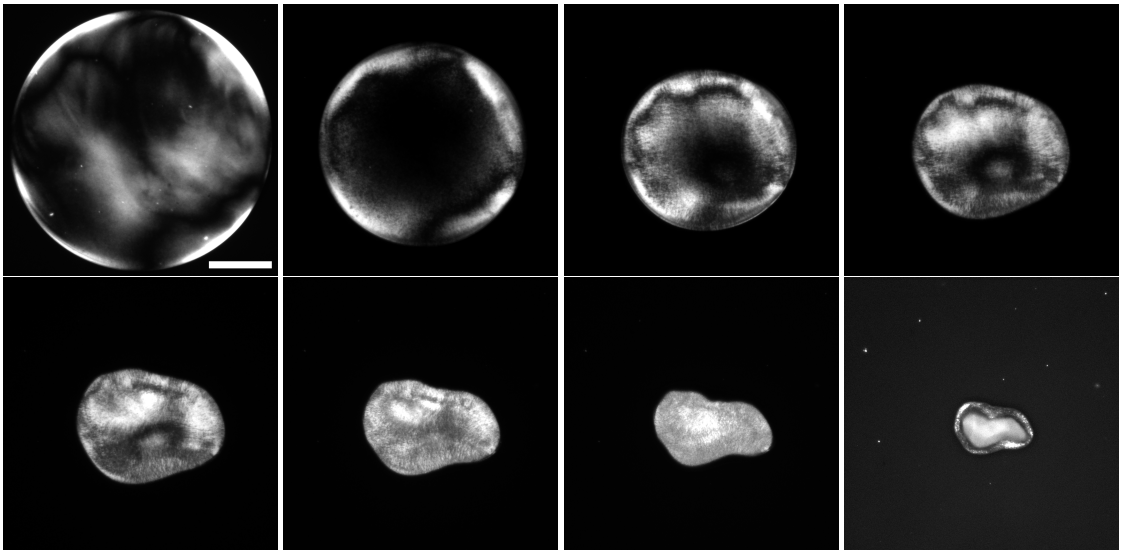

Figure 5.19: Polarized light microscopy images of a drop of a suspension initially containing 3.2 wt % CNC and 5 mM NaCl during drying (see the corresponding video). From left to right and top to bottom, the images are taken at t =4 min, 57 min, 91 min, 105 min, 116 min, 126 min, 138 min, and 170 min after the drop deposition and the beginning of solvent evaporation. The scale bar on the top left image corresponds to 500 μm.

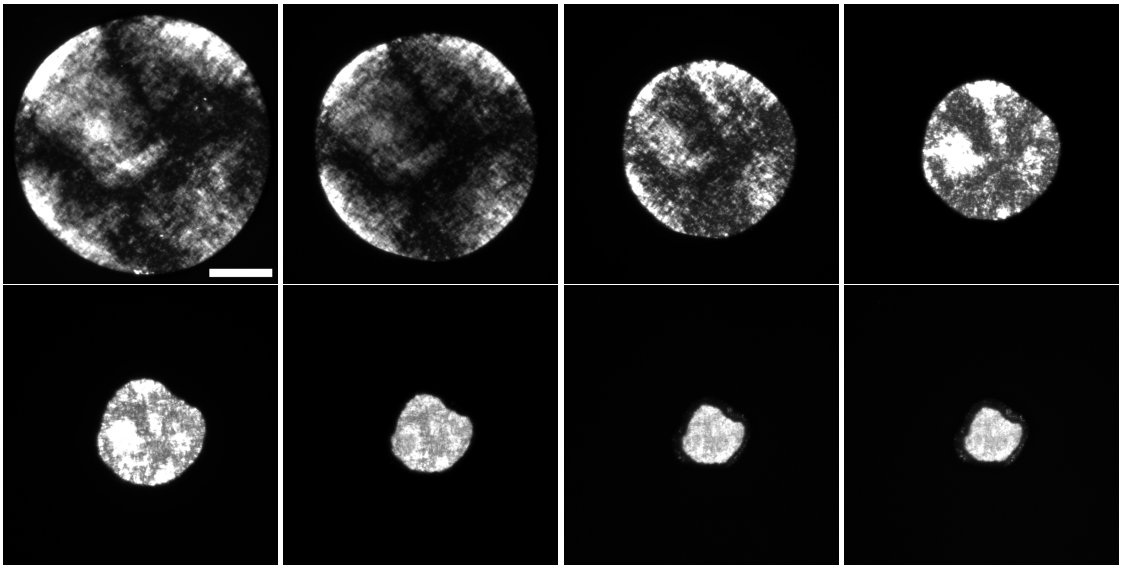

Figure 5.20: Polarized light microscopy images of a drop of a suspension initially containing 3.2 wt % CNC and 100 mM NaCl during drying (see the corresponding video). From left to right and top to bottom, the images are taken at t =4 min, 35 min, 59 min, 75 min, 87 min, 96 min, 103 min, and 144 min after the drop deposition and the beginning of solvent evaporation. The scale bar on the top left image corresponds to 500 μm.

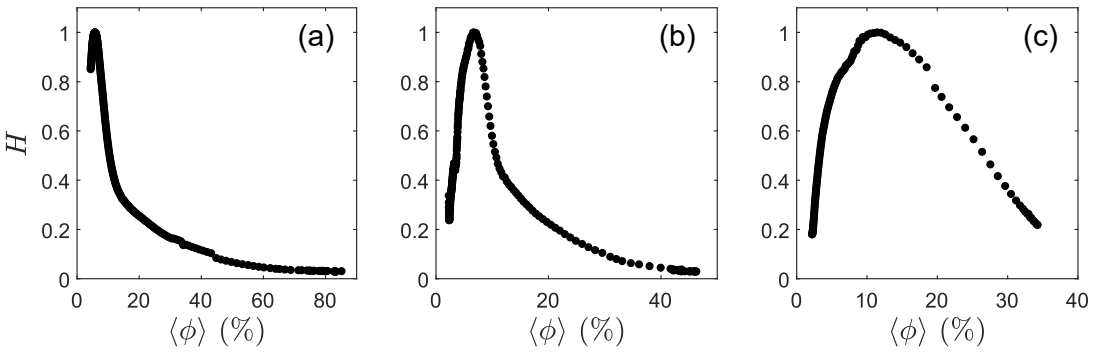

Figure 5.21: heterogeneity parameter H as a function of the averaged CNC volume fraction during the drop drying, for drops of suspensions initially containing (a) 6.4 wt % CNC (see the corresponding video), (b) 3.2 wt % CNC and 5 mM NaCl (see the corresponding video), and (c) 3.2 wt % CNC and 100 mM NaCl (see the corresponding video).

bright and dark, indicating a variation of the local CNCs orientation. Moreover, these domains seem to be easily deformed by the edges of the drop and by some convection inside the drop volume. Such motion is absent from the experiments with suspensions initially containing either 6.4 wt % CNC and no salt, or 3.2 wt % CNC and 100 mM NaCl. Indeed, in both conditions, CNCs displacements are hindered by steric hindrance in one case, and by attractive interactions in the other. For the suspension containing initially 3.2 wt % CNC and 100 mM NaCl, similarly to the previous experiment at 3.2 wt % CNC and 5 mM NaCl, we observe that bright domains grow in size from short to intermediate drying times. Yet, in this case, the domains which are not near the drop meniscus are not influenced by the drop shrinkage over this time interval, and this effect seems to be due to the "concentration", along the radial direction of the drop, of the domains of similar alignment. At longer times, as the radius of the drop decreases, all the domains are affected by the drop shrinkage, and we observe here again a decrease in the size of the domains, until the birefringence image becomes almost homogeneous.

In order to better quantify the time evolution of the CNCs orientation and of the size of the birefringent domains, we use the heterogeneity parameter $H(t)$ which we define as follows. At each given time t, and for every vertical position y over a height of 80 pixels around the drop center, we calculate the standard deviation $\sigma_I(y,t)$ of the pixels intensity along the drop width. Then, $H(t)$ is given by the mean value $\langle\sigma_I(t)\rangle_y$ of the standard deviations calculated for every y position, normalized by the maximum value of $\langle\sigma_I(t)\rangle_y$ calculated over the experiment time interval. Figure 5.21 shows the evolution of this heterogeneity parameter H, plotted as a function of the CNC average volume fraction $\langle\phi\rangle$, for the three suspensions considered in the previous paragraph. We observe that in every case, H increases at small volume fractions corresponding to the beginning of the drying experiments, reaches a maximum and then decreases at larger volume fractions. This non-monotonic evolution is consistent with the observations made in the previous paragraph. Interestingly, the volume fraction corresponding to the maximum of H, i.e., where the birefringent domains are the largest, is different in the three experiments, and increases by almost a factor of two, from 6.6 % to 11.5 %, when varying the initial salt concentration from 5 mM to 100 mM [see Fig. 5.21(b) and (c)].

Further experiments and analysis would be necessary to get a better understanding of the dynamics and CNC organization induced by the suspension drying.

C.4 Pervaporation

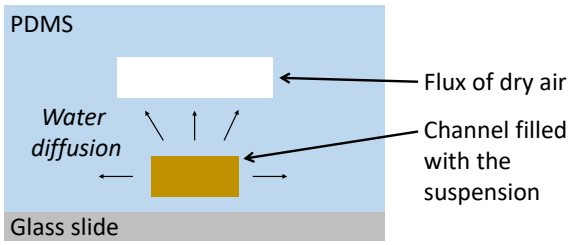

Figure 5.22: Vertical cut of the microfluidic setup. The microfluidic channel containing the suspension is connected to a reservoir filled with this suspension. In this experiment, the channel containing the suspension has a 3 cm length, 50 μm height and 400 μm width, and a 200 μm thick PDMS layer separates the microfluidic channel from the air channel.

In order to further explore the CNCs macroscopic organization induced by the solvent evaporation and by the resulting increase of the suspension CNC weight or volume fraction, we consider another configuration to dry the CNC suspensions. In this configuration, sketched in Fig. 5.22, we fill a microfluidic channel with a CNC suspension initially containing 6.4 wt % CNC, connected to a reservoir filled with the same suspension, and we impose a flow of dry air in an channel positioned just above the microfluidic channel in order to accelerate drying. Both the microfluidic channel and the air channel are made of PDMS, which is permeable to water. The water from the CNC suspension solubilizes at the interface between the suspension and PDMS, then diffuses into the PDMS layer, and finally evaporates at the interface between PDMS and air. This process is called pervaporation. Contrary to the 2D drop configuration, there is no free surface here. Therefore, as the solvent pervaporates, the CNC suspension concentrates, and a flux of suspension is induced from the reservoir into the microfluidic channel. As a result, at the end of the experiment, the channel is fully filled with the dry material, which contains only CNCs, at a concentration of about 100 %. In this experiment, the microfluidic channel is straight, of length 3 cm, width 400 μm and height 50 μm. In order not to induce plugs in the microfluidic channel, we previously filter the commercial CNC suspension using a filter of pore size 800 nm.

Figure 5.7 shows images taken from above at different times during pervaporation, under polarized light. Note that for this experiment, there was no dry air flow in the air channel, hence the long drying times. Initially, just after the filling of the microchannel, the suspension is homogeneously gray. Then, as soon as the suspension begins to concentrate at the end of the channel, inducing a flow of the CNC suspension, we observe that CNCs orient along the flow. This orientation gets more pronounced as the flow gets established for longer times. Interestingly, the white regions near the channel walls and the black one at the center indicate a 180 °rotation of the CNCs orientation over the width of the channel. The flow rates induced by the solvent pervaporation are very small. Therefore, the flow induced in the microchannel is most likely similar to a Poiseuille flow, where the shear rate is maximum (in absolute value) near the channel walls, and zero at the center. If CNCs tend to align with the shear rate, this observation suggests that CNCs are parallel to the channel walls close to the walls, and perpendicular to the channel walls at the center. At the end of the channel, the CNCs orientation begins to appear later, after about 2 h 30 min. Interestingly, we observe a similar 180°rotation of the CNCs orientation over the width of the channel, yet, with a 90°rotation compared to the opposite side of the channel, as indicated by the reversed colors. If our previous statement is true, this observation indicates that, at this time and position in the channel, CNCs are perpendicular to the channel walls near the walls, and parallel to the walls at the center. This reversed configuration might originate from an interaction between PDMS and the individual CNC particles, resulting in a minimization of their interaction surfaces for example, or an anchoring of the CNC particles in this preferred orientation. Remarkably, at longer times,

when the flow slows down in this part of the microchannel and the shear rates become smaller, this second preferred orientation spreads across the channel length, towards the reservoir end. At even longer times, when the material is highly concentrated, and no flow is observed, and hence no solvent pervaporation occurs anymore, we observe that the strong CNC orientation persists. Moreover, we observe that the material delaminates from the microchannel walls at the very end of the drying process.

To further investigate the orientation of CNC particles induced by solvent pervaporation in a microfluidic channel, we could first image the resulting material using atomic force microscopy (AFM) in order to determinate the orientation of the CNC particles. Moreover, we could investigate the effect of the channel geometry and of the drying speed on the induced orientation. Finally, it would be interesting to characterize the mechanical properties of the resulting solid. To do so, we could use nanoindentation and other techniques in order to measure the Young modulus of the material in various directions and under various deformation modes.

C.5 Freeze-casting

Finally, instead of drying the soft precursor, another well-known technique to obtain a solid material with a specific microstructural organization is to use freeze-casting, also referred to as ice-templating.

Experimental setup.- The experimental setup used for this experiment is represented in Fig. 5.23. The suspension is placed in between two glass slides separated by a distance e = 100 μm, using tape strips, and sealed using nail-polish in order to avoid solvent evaporation. The cell is then placed above two Peltier modules, under the objective of a confocal microscope, and linked to a motor. The Peltier modules allow one to impose a positive temperature T_h on one side and a negative temperature T_c on the other side ($t_c < 0$ °C), hereby inducing a temperature gradient ΔT along the cell length, in the x direction. The position of the Peltier modules is adjusted so that the position of the ice front, corresponding to the middle of the temperature gradient, is vertically aligned with the objective of the microscope. The Peltier modules are then kept fixed, and only the cell containing the suspension is mobile. The motor pulls on the cell and induces its translation along the x direction at a given velocity v. As a result, the ice front progresses across the cell, while remaining aligned with the microscope objective.

Rhodamine is added to the CNC suspensions, at a concentration of 0.1 mM, in order to increase the contrast between the ice and the liquid suspension. Indeed, rhodamine is miscible with water. Yet, ice has very low solubility for solutes and hence rejects the rhodamine molecules as well as the CNCs. As a result, when illuminating the sample using a blue laser, of wavelength λ = 488 nm, ice appears black, while the liquid suspension fluoresces. CNCs are fluorescent, but the intensity of the fluorescence of the samples confined between the two glass slides is too weak to be able to record images with a good enough time and spatial resolution. Yet, this property of CNCs has allowed us to verify that the rhodamine was spatially segregated similarly to the CNCs in between the ice, hereby ensuring that rhodamine is a good tracer for our experiments.

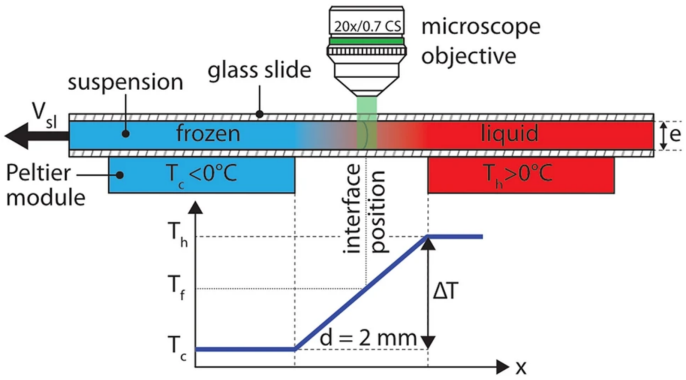

Figure 5.23: Experimental setup used for freezing CNC suspensions. Extracted from [Tyagi et al., 2021].

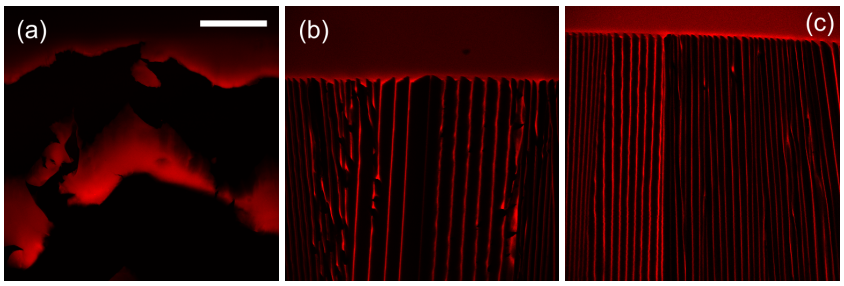

Figure 5.24: Confocal microscopy images of a suspension containing 4 wt % CNC (and 0.1 mM rhodamine to increase contrast), frozen in a temperature gradient set by a temperature different ΔT = 30 °C, at a constant ice front velocity v, with (a) v = 5 μm.s^{-1}, (b) v = 20 μm.s^{-1}, and (c) v = 30 μm.s^{-1}. The ice appears in black while the liquid suspension and the CNCs concentrated in between the glass cells appear in red. The scale bar in the left image corresponds to 150 μm.

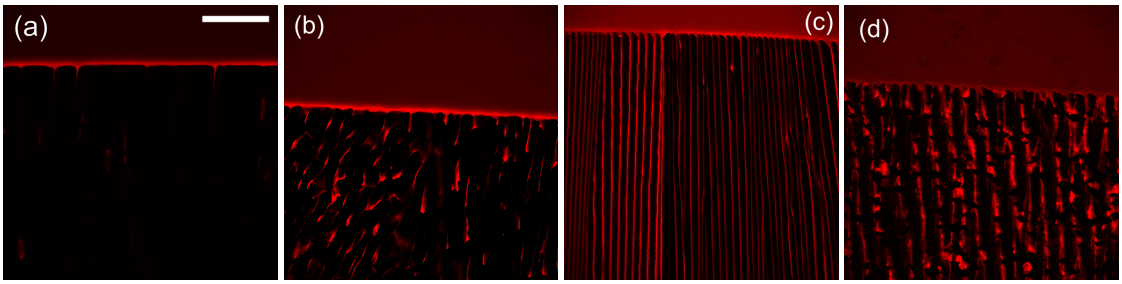

Figure 5.25: Confocal microscopy images of suspensions containing respectively (a) 0.04 wt % CNC, (b) 1 wt % CNC, (c) 4 wt % CNC and (d) 10 wt % CNC (and 0.1 mM rhodamine to increase contrast), frozen in a temperature gradient set by a temperature different ΔT = 30 °C, at a constant ice front velocity v = 530 μm.s^{-1}. The ice appears in black while the liquid suspension and the CNCs concentrated in between the glass cells appear in red. The scale bar in the left image corresponds to 150 μm.

Preliminary results.- Ice has extremely low solubility for dissolved solutes, as well as for dispersed colloids, and rejects them in the remaining liquid as solidification progresses. Depending on the velocity of the ice front, the segregation is more or less efficient. Indeed, four general regimes can be distinguished depending on the velocity of the ice front v [Shao et al., 2020]. These regimes involve a critical velocity v_{cr} that depends on many controlled parameters. In particular, it depends on the suspension composition, i.e., in our case, on both the salt and the CNC concentrations, as well as on the colloids themselves, and more precisely on their drag coefficient and on their interaction with the ice front. These four regimes are schematically represented in Fig. 5.26, and illustrated in Fig. 5.24, at fixed CNC weight fraction w_{CNC} = 4 wt %, i.e., fixed v_{cr}, and various velocities v, ranging from 5 μm.s^{-1} to 30 μm.s^{-1}, and in Fig. 5.25, at fixed velocity v = 30 μm.s^{-1}, and various CNC weight fraction ranging from 0.04 wt % to 10 wt %, i.e., various v_{cr}. In both sets of experiments, the ratio v/v_{cr} varies, and allows us to switch between the four regimes.

At very small solidification velocities, for $v \ll v_{cr}$, the ice-growth proceeds as a planar front, displacing the colloids and increasing their concentration in the liquid region, close to the ice front. Such a phenomenon is evidenced by the rhodamine gradient induced near the ice front [see the more intense red region in Fig. 5.25(a)]. However, as the ice front progresses in the suspension, CNCs accumulate, until their concentration becomes too large to be rejected by the ice. At this point, an instability appears and the ice encapsulates the CNCs particles that were accumulated

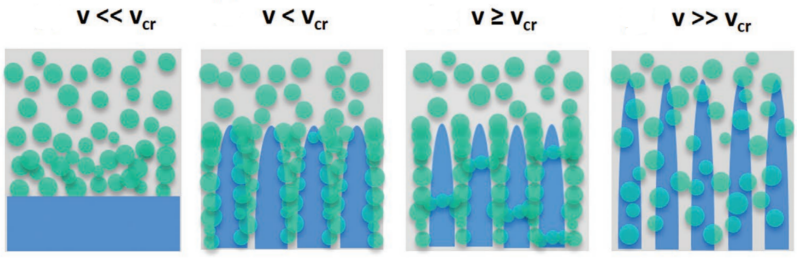

Figure 5.26: Schematic representation of the four regimes of freeze-casting depending on the ice front velocity v with respect to a critical velocity v_{cr}. Extracted from [Shao et al., 2020].

at the front in the form of large patches, as visible in Fig. 5.24(a). In this regime, if one sublimates the ice in order to keep only the structure formed by the colloids, the resulting material is very disorganized.

For $v < v_{cr}$, colloids are generally rejected by the ice, and form lamellar walls within the final freeze-cast scaffold. This regime is also referred to as the cellular regime, where, in a 2D image of an horizontal cut of the sample, theses lamellar walls appear as lines separated by elongated cells of ice [see Fig. 5.25(c) and Figs. 5.24(b) and (c)]. In this regime, after ice sublimation, the resulting material is porous. Figure 5.8b shows an image of a cut, perpendicular to the lamellar walls, of such material, obtained by freezing a CNC suspension containing 1.5 wt % [Munier et al., 2016]. Depending on the ratio v/v_{cr}, the ice cells are more or less well defined, as highlighted by Fig. 5.25(b), taken in a regime intermediate to the cellular regime and to the $v \ll v_{cr}$ regime. Also, as v increases in this cellular regime, the distance separating the lamellar walls of colloids decreases. As a result, the size of the pores of the final solid material decreases.

At ice front velocities larger than the critical velocity, for $v \geq v_{cr}$, a certain fraction of the colloids is generally entrapped by the solid phase, creating bridges between lamellar walls, and leading to a fine-scale porosity throughout the resulting freeze cast structure, in between the larger pores constituted by the ice cells [see Fig. 5.25(d)]. Finally, at very large velocities, for $v \gg v_{cr}$, the colloids do not have enough time to segregate, and they are totally and continuously encapsulated by the ice front.

We have observed that the structures induced by the ice growth inside a CNC suspension also depend on the salt concentration. Thus, depending on the geometry, on the freezing process, and on the suspension composition, many different structures and pore shapes can be obtained, as illustrated in Fig. 5.27. Thereby, freeze-casting offers a great potential for the design of solid materials with well-controlled and innovative properties, from colloidal suspension precursors.

An additional parameter that CNCs offer, and which most likely has an effect on the resulting solid material, is their orientation in the structure. Indeed, CNCs may align in the lamellar walls where they are highly confined and concentrated, as represented in Fig. 5.28. In order to investigate on the orientation of CNCs during the suspension freezing, depending on the experimental conditions, we would like to reproduce the experiments under polarized light.

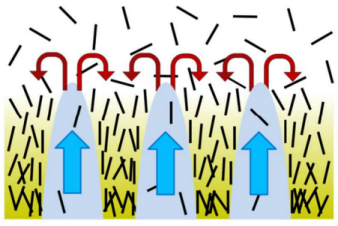

Figure 5.28: Orientation of CNCs induced by the growth of the ice inside the suspension. Extracted from [Munier et al., 2016].

Finally, another interesting point would be to determine if the CNC aggregation induced by the ice-growth is reversible or not when de-freezing the sample. Such a study is important to consider for applications in the food industry for instance, where CNCs can be used as thickening agents.

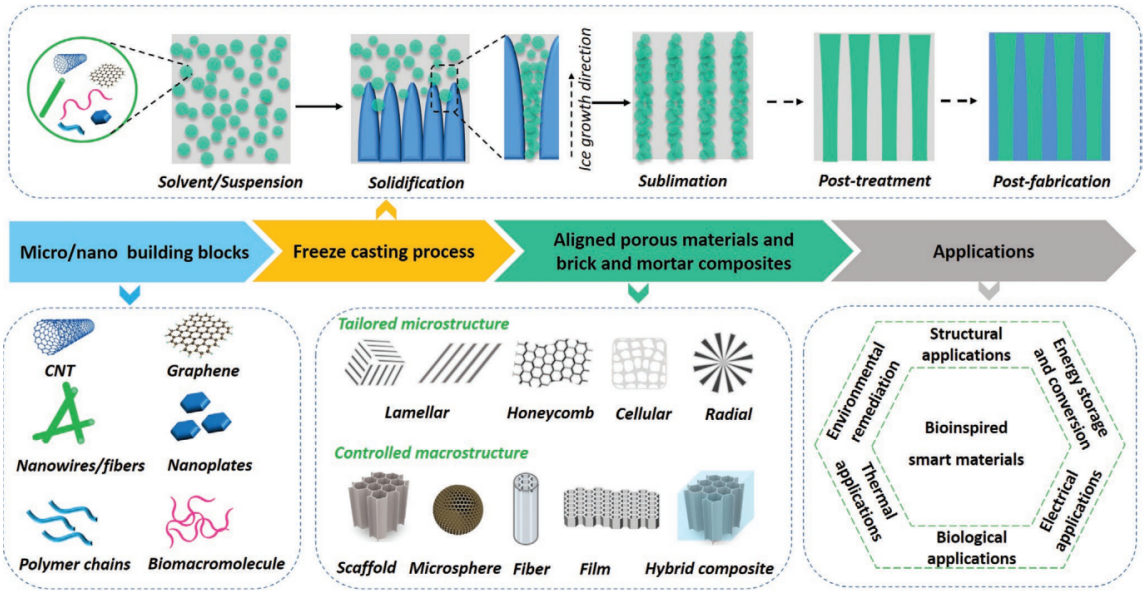

Figure 5.27: Examples of solid material structures obtained through freeze-casting, and their applications. Extracted from [Shao et al., 2020].

BIBLIOGRAPHY

[Abitbol et al., 2013] Abitbol, T., Kloser, E., and Gray, D. (2013). Estimation of the surface sulfur content of cellulose nanocrystals prepared by sulfuric acid hydrolysis. *Cellulose*, 20:785–794.

[Adam et al., 1981] Adam, M., Delsanti, M., Durand, D., Hild, G., and Munch, J. (1981). Mechanical properties near gelation threshold, comparison with classical and 3d percolation theories. *Pure and Applied Chemistry*, 53(8):1489–1494.

[Adolf and Martin, 1990] Adolf, D. and Martin, J. E. (1990). Time-cure superposition during crosslinking. *Macromolecules*, 23(15):3700–3704.

[Agarwal, 2017] Agarwal, U. P. (2017). Raman spectroscopy of cnc-and cnf-based nanocomposites. *Handbook of Nanocellulose and Cellulose Nanocomposites*, 2:609–625.

[Aime et al., 2018] Aime, S., Cipelletti, L., and Ramos, L. (2018). Power law viscoelasticity of a fractal colloidal gel. *Journal of Rheology*, 62(6):1429–1441.

[Aragon and Flamik, 2009] Aragon, S. R. and Flamik, D. (2009). High precision transport properties of cylinders by the boundary element method. *Macromolecules*, 42(16):6290–6299.

[Arrigo et al., 2020] Arrigo, R., Mascia, L., Clarke, J., and Malucelli, G. (2020). Structure evolution of epoxidized natural rubber (enr) in the melt state by time-resolved mechanical spectroscopy. *Materials*, 13(4):946.

[Axelos and Kolb, 1990] Axelos, M. and Kolb, M. (1990). Crosslinked biopolymers: Experimental evidence for scalar percolation theory. *Physical Review Letters*, 64(12):1457.

[Aziz et al., 2021] Aziz, M. A., Zubair, M., and Saleem, M. (2021). Development and testing of cellulose nanocrystal-based concrete. *Case Studies in Construction Materials*, 15:e00761.

[Bantawa et al., 2023] Bantawa, M., Keshavarz, B., Geri, M., Bouzid, M., Divoux, T., McKinley, G. H., and Del Gado, E. (2023). The hidden hierarchical nature of soft particulate gels. *Nature Physics*, pages 1–7.

[Barlow et al., 2020] Barlow, H. J., Cochran, J. O., and Fielding, S. M. (2020). Ductile and brittle yielding in thermal and athermal amorphous materials. *Physical Review Letters*, 125(16):168003.

[Barrett, 2021] Barrett, C. J. (2021). Introduction to Liquid Crystals. http://barrett-group.mcgill.ca/tutorials/liquid_crystal/LC03.htm?fbclid=IwAR043SesR5dDtwmXBZ95-7KtnUd5q0EaVman0e58GsJMX3BfPJZRGfDfj-I.

[Barthelat et al., 2016] Barthelat, F., Yin, Z., and Buehler, M. J. (2016). Structure and mechanics of interfaces in biological materials. *Nature Reviews Materials*, 1(4):1–16.

[Battista, 1975] Battista, O. (1975). Colloidal microcrystalline celluloses. In *Cellulose Technology Research*, pages 1–8. ACS Publications.

[Beck-Candanedo et al., 2005] Beck-Candanedo, S., Roman, M., and Gray, D. G. (2005). Effect of reaction conditions on the properties and behavior of wood cellulose nanocrystal suspensions. *Biomacromolecules*, 6(2):1048–1054.

[Benzi et al., 2021a] Benzi, R., Divoux, T., Barentin, C., Manneville, S., Sbragaglia, M., and Toschi, F. (2021a). Continuum modeling of shear startup in soft glassy materials. *Physical Review E*, 104(3):034612.

[Benzi et al., 2021b] Benzi, R., Divoux, T., Barentin, C., Manneville, S., Sbragaglia, M., and Toschi, F. (2021b). Stress overshoots in simple yield stress fluids. *Physical Review Letters*, 127(14):148003.

[Benzi et al., 2023] Benzi, R., Divoux, T., Barentin, C., Manneville, S., Sbragaglia, M., and Toschi, F. (2023). Continuum modeling of soft glassy materials under shear. *Europhysics Letters*, 141(5):56001.

[Bertsch et al., 2018] Bertsch, P., Diener, M., Adamcik, J., Scheuble, N., Geue, T., Mezzenga, R., and Fischer, P. (2018). Adsorption and interfacial layer structure of unmodified nanocrystalline cellulose at air/water interfaces. *Langmuir*, 34(50):15195–15202.

[Blair and Coppen, 1943] Blair, G. S. and Coppen, F. (1943). The estimation of firmness in soft materials. *The American Journal of Psychology*, pages 234–246.

[Boltzmann, 1874] Boltzmann, L. (1874). Zur theorie der elastischen nachwirkung, sitzber. kaiserl. akad. wiss. wien, math. *Naturwissenschaftliche Klasse*, 70:275–300.

[Bonfanti et al., 2020] Bonfanti, A., Kaplan, J. L., Charras, G., and Kabla, A. (2020). Fractional viscoelastic models for power-law materials. *Soft Matter*, 16:6002–6020.

[Bonn et al., 2017] Bonn, D., Denn, M. M., Berthier, L., Divoux, T., and Manneville, S. (2017). Yield stress materials in soft condensed matter. *Reviews of Modern Physics*, 89(3):035005.

[Bouchaudy and Salmon, 2019] Bouchaudy, A. and Salmon, J.-B. (2019). Drying-induced stresses before solidification in colloidal dispersions: In situ measurements. *Soft Matter*, 15(13):2768–2781.

[Bouzid et al., 2017] Bouzid, M., Colombo, J., Barbosa, L., and Del Gado, E. (2017). Elastically driven intermittent microscopic dynamics in soft solids. *Nature Communications*, 8:15846.

[Bouzid et al., 2018] Bouzid, M., Keshavarz, B., Geri, M., Divoux, T., Del Gado, E., and McKinley, G. H. (2018). Computing the linear viscoelastic properties of soft gels using an optimally windowed chirp protocol. *Journal of Rheology*, 62:1037–1050.

[Brenner, 1974] Brenner, H. (1974). Rheology of a dilute suspension of axisymmetric brownian particles. *International Journal of Multiphase Flow*, 1(2):195–341.

[Buffa et al., 2019] Buffa, J. M., Casado, U., Mucci, V., and Aranguren, M. I. (2019). Cellulose nanocrystals in aqueous suspensions: rheology of lyotropic chiral liquid crystals. *Cellulose*, 26:2317–2332.

[Burikov et al., 2010] Burikov, S., Dolenko, T., Patsaeva, S., Starokurov, Y., and Yuzhakov, V. (2010). Raman and ir spectroscopy research on hydrogen bonding in water–ethanol systems. *Molecular physics*, 108(18):2427–2436.

[Cao and Elimelech, 2021] Cao, T. and Elimelech, M. (2021). Colloidal stability of cellulose nanocrystals in aqueous solutions containing monovalent, divalent, and trivalent inorganic salts. *Journal of Colloid and Interface Science*, 584:456–463.

[Cao et al., 2010] Cao, X. J., Cummins, H. Z., and Morris, J. F. (2010). Structural and rheological evolution of silica nanoparticle gels. *Soft Matter*, 6:5425–5433.

[Chau et al., 2015] Chau, M., Sriskandha, S. E., Pichugin, D., Thérien-Aubin, H., Nykypanchuk, D., Chauve, G., Méthot, M., Bouchard, J., Gang, O., and Kumacheva, E. (2015). Ion-mediated gelation of aqueous suspensions of cellulose nanocrystals. *Biomacromolecules*, 16(8):2455–2462.

[Chen et al., 2010] Chen, D., Chen, K., Hough, L., Islam, M., and Yodh, A. (2010). Rheology of carbon nanotube networks during gelation. *Macromolecules*, 43(4):2048–2053.

[Cherhal et al., 2015] Cherhal, F., Cousin, F., and Capron, I. (2015). Influence of charge density and ionic strength on the aggregation process of cellulose nanocrystals in aqueous suspension, as revealed by small-angle neutron scattering. *Langmuir*, 31(20):5596–5602.

[Cipelletti and Ramos, 2002] Cipelletti, L. and Ramos, L. (2002). Slow dynamics in glasses, gels and foams. *Current Opinion in Colloid & Interface Science*, 7(3):228–234.

[Cipelletti et al., 2003] Cipelletti, L., Ramos, L., Manley, S., Pitard, E., Weitz, D. A., Pashkovski, E. E., and Johansson, M. (2003). Universal non-diffusive slow dynamics in aging soft matter. *Faraday Discussions*, 123:237–251.

[Cloitre and Bonnecaze, 2017] Cloitre, M. and Bonnecaze, R. T. (2017). A review on wall slip in high solid dispersions. *Rheologica Acta*, 56:283–305.

[Clough et al., 1973] Clough, S. A., Beers, Y., Klein, G. P., and Rothman, L. S. (1973). Dipole moment of water from stark measurements of h2o, hdo, and d2o. *The Journal of Chemical Physics*, 59(5):2254–2259.

[Colombo and Del Gado, 2014] Colombo, J. and Del Gado, E. (2014). Stress localization, stiffening, and yielding in a model colloidal gel. *Journal of Rheology*, 58(5):1089–1116.

[Curtis et al., 2013] Curtis, D. J., Williams, P. R., Badiei, N., Campbell, A. I., Hawkins, K., Evans, P. A., and Brown, M. R. (2013). A study of microstructural templating in fibrin–thrombin gel networks by spectral and viscoelastic analysis. *Soft Matter*, 9(19):4883–4889.

[Dagès, 2021] Dagès, N. (2021). *Matériaux rhéo-acoustiques*. PhD Thesis, Université de Lyon.

[Danesh et al., 2021] Danesh, M., Moud, A. A., Mauran, D., Hojabr, S., Berry, R., Pawlik, M., and Hatzikiriakos, S. G. (2021). The yielding of attractive gels of nanocrystal cellulose (cnc). *Journal of Rheology*, 65(5):855–869.

[Danial et al., 2015] Danial, W. H., Majid, Z. A., Muhid, M. N. M., Triwahyono, S., Bakar, M. B., and Ramli, Z. (2015). The reuse of wastepaper for the extraction of cellulose nanocrystals. *Carbohydrate Polymers*, 118:165–169.

[Das and Petekidis, 2022] Das, M. and Petekidis, G. (2022). Shear induced tuning and memory effects in colloidal gels of rods and spheres. *The Journal of Chemical Physics*, 157(23):234902.

[Daubersies and Salmon, 2011] Daubersies, L. and Salmon, J.-B. (2011). Evaporation of solutions and colloidal dispersions in confined droplets. *Physical Review E*, 84:031406.

[Davidson, 1943] Davidson, G. (1943). 9—the rate of change in the properties of cotton cellulose under the prolonged action of acids. *Journal of the Textile Institute Transactions*, 34(10):T87–T96.

[De Gennes, 1976] De Gennes, P.-G. (1976). On a relation between percolation theory and the elasticity of gels. *Journal de Physique Lettres*, 37(1):1–2.

[de Gennes, 1992] de Gennes, P.-G. (1992). Soft matter (nobel lecture). *Angewandte Chemie International Edition in English*, 31(7):842–845.

[Derakhshandeh et al., 2013] Derakhshandeh, B., Petekidis, G., Shafiei Sabet, S., Hamad, W. Y., and Hatzikiriakos, S. G. (2013). Ageing, yielding, and rheology of nanocrystalline cellulose suspensions. *Journal of Rheology*, 57(1):131–148.

[Derec et al., 2003] Derec, C., Ducouret, G., Ajdari, A., and Lequeux, F. (2003). Aging and nonlinear rheology in suspensions of polyethylene oxide–protected silica particles. *Physical Review E*, 67(6):061403.

[Di Dio and Cloitre, 2024] Di Dio, B. and Cloitre, M. (2024). Private communication 2024.

[Di Dio et al., 2022] Di Dio, B. F., Khabaz, F., Bonnecaze, R. T., and Cloitre, M. (2022). Transient dynamics of soft particle glasses in startup shear flow. part ii: Memory and aging. *Journal of Rheology*, 66(4):717–730.

[Dimitriou and McKinley, 2014] Dimitriou, C. J. and McKinley, G. H. (2014). A comprehensive constitutive law for waxy crude oil: A thixotropic yield stress fluid. *Soft Matter*, 10(35):6619–6644.

[Divoux et al., 2023] Divoux, T., Agoritsas, E., Aime, S., Barentin, C., Barrat, J.-L., Benzi, R., Berthier, L., Bi, D., Biroli, G., Bonn, D., et al. (2023). Ductile-to-brittle transition and yielding in soft amorphous materials: perspectives and open questions. *arXiv preprint arXiv:2312.14278*.

[Divoux et al., 2011] Divoux, T., Barentin, C., and Manneville, S. (2011). Stress overshoot in a simple yield stress fluid: An extensive study combining rheology and velocimetry. *Soft Matter*, 7(19):9335–9349.

[Divoux et al., 2016] Divoux, T., Fardin, M. A., Manneville, S., and Lerouge, S. (2016). Shear banding of complex fluids. *Annual Review of Fluid Mechanics*, 48:81–103.

[Divoux et al., 2013] Divoux, T., Grenard, V., and Manneville, S. (2013). Rheological hysteresis in soft glassy materials. *Physical Review Letters*, 110(1):018304.

[Doi and Edwards, 1988] Doi, M. and Edwards, S. (1988). *The theory of polymer dynamics*, volume 73. Oxford University Press, USA.

[Donley et al., 2020] Donley, G. J., Singh, P. K., Shetty, A., and Rogers, S. A. (2020). Elucidating the g" overshoot in soft materials with a yield transition via a time-resolved experimental strain decomposition. *Proceedings of the National Academy of Sciences*, 117(36):21945–21952.

[Du et al., 2019] Du, H., Liu, W., Zhang, M., Si, C., Zhang, X., and Li, B. (2019). Cellulose nanocrystals and cellulose nanofibrils based hydrogels for biomedical applications. *Carbohydrate Polymers*, 209:130–144.

[Eberle et al., 2012] Eberle, A. P., Castañeda Priego, R., Kim, J. M., and Wagner, N. J. (2012). Dynamical arrest, percolation, gelation, and glass formation in model nanoparticle dispersions with thermoreversible adhesive interactions. *Langmuir*, 28(3):1866–1878.

[Eichhorn et al., 2010] Eichhorn, S., Dufresne, A., Aranguren, M., Marcovich, N., Capadona, J., Rowan, S., et al. (2010). Current international research into cellulose nanofibres and nanocomposites. *Journal of Materials Science*, 45:1–33.

[Elazzouzi-Hafraoui et al., 2008] Elazzouzi-Hafraoui, S., Nishiyama, Y., Putaux, J.-L., Heux, L., Dubreuil, F., and Rochas, C. (2008). The shape and size distribution of crystalline nanoparticles prepared by acid hydrolysis of native cellulose. *Biomacromolecules*, 9(1):57–65.

[Ewoldt et al., 2015] Ewoldt, R. H., Johnston, M. T., and Caretta, L. M. (2015). Experimental challenges of shear rheology: How to avoid bad data. *Complex Fluids in Biological Systems: Experiment, Theory, and Computation*, pages 207–241.

[Eyley and Thielemans, 2014] Eyley, S. and Thielemans, W. (2014). Surface modification of cellulose nanocrystals. *Nanoscale*, 6(14):7764–7779.

[Fan et al., 2023] Fan, X., Zhang, L., Dong, F., Liu, H., and Xu, X. (2023). Room-temperature self-healing polyurethane–cellulose nanocrystal composites with strong strength and toughness based on dynamic bonds. *Carbohydrate Polymers*, 308:120654.

[Fazilati et al., 2021] Fazilati, M., Ingelsten, S., Wojno, S., Nypelö, T., and Kádár, R. (2021). Thixotropy of cellulose nanocrystal suspensions. *Journal of Rheology*, 65(5):1035–1052.

[Filippone et al., 2015] Filippone, G., Carroccio, S., Mendichi, R., Gioiella, L., Dintcheva, N. T., and Gambarotti, C. (2015). Time-resolved rheology as a tool to monitor the progress of polymer degradation in the melt state–part i: Thermal and thermo-oxidative degradation of polyamide 11. *Polymer*, 72:134–141.

[Forrest and Witten Jr, 1979] Forrest, S. R. and Witten Jr, T. A. (1979). Long-range correlations in smoke-particle aggregates. *Journal of Physics A: Mathematical and General*, 12(5):L109.

[Franks, 2002] Franks, G. V. (2002). Zeta potentials and yield stresses of silica suspensions in concentrated monovalent electrolytes: isoelectric point shift and additional attraction. *Journal of Colloid and Interface Science*, 249(1):44–51.

[Frka-Petesic et al., 2014] Frka-Petesic, B., Jean, B., and Heux, L. (2014). First experimental evidence of a giant permanent electric-dipole moment in cellulose nanocrystals. *Europhysics Letters*, 107(2):28006.

[Gado et al., 2016] Gado, E. D., Fiocco, D., Foffi, G., Manley, S., Trappe, V., and Zaccone, A. (2016). *Colloidal Gelation*, chapter 14, pages 279–291. John Wiley & Sons, Ltd.

[Gallot et al., 2013] Gallot, T., Perge, C., Grenard, V., Fardin, M.-A., Taberlet, N., and Manneville, S. (2013). Ultrafast ultrasonic imaging coupled to rheometry: Principle and illustration. *Review of Scientific Instruments*, 84(4):045107.

[George and Sabapathi, 2015] George, J. and Sabapathi, S. (2015). Cellulose nanocrystals: synthesis, functional properties, and applications. *Nanotechnology, science and applications*, pages 45–54.

[Geri et al., 2018] Geri, M., Keshavarz, B., Divoux, T., Clasen, C., Curtis, D. J., and McKinley, G. H. (2018). Time-resolved mechanical spectroscopy of soft materials via optimally windowed chirps. *Physical Review X*, 8:041042.

[Ghiringhelli et al., 2012] Ghiringhelli, E., Roux, D., Bleses, D., Galliard, H., and Caton, F. (2012). Optimal fourier rheometry: Application to the gelation of an alginate. *Rheologica acta*, 51(5):413–420.

[Gibaud et al., 2022] Gibaud, T., Divoux, T., and Manneville, S. (2022). Nonlinear mechanics of colloidal gels: Creep, fatigue, and shear-induced yielding. In *Statistical and Nonlinear Physics*, pages 313–336. Springer.

[Gibaud et al., 2016] Gibaud, T., Perge, C., Lindström, S. B., Taberlet, N., and Manneville, S. (2016). Multiple yielding processes in a colloidal gel under large amplitude oscillatory stress. *Soft Matter*, 12(6):1701–1712.

[Girard et al., 2021] Girard, M., Vidal, D., Bertrand, F., Tavares, J. R., and Heuzey, M.-C. (2021). Evidence-based guidelines for the ultrasonic dispersion of cellulose nanocrystals. *Ultrasonics Sonochemistry*, 71:105378.

[Giubertoni et al., 2023] Giubertoni, G., Bonn, M., and Woutersen, S. (2023). D2o as an imperfect replacement for h2o: Problem or opportunity for protein research? *The Journal of Physical Chemistry B*, 127(38):8086–8094.

[Grishkewich et al., 2017] Grishkewich, N., Mohammed, N., Tang, J., and Tam, K. C. (2017). Recent advances in the application of cellulose nanocrystals. *Current Opinion in Colloid & Interface Science*, 29:32–45.

[Gu et al., 2009] Gu, X., Poon, S., Shiflet, G., and Lewandowski, J. (2009). Ductile-to-brittle transition in a ti-based bulk metallic glass. *Scripta Materialia*, 60(11):1027–1030.

[Guo et al., 2011] Guo, H., Ramakrishnan, S., Harden, J. L., and Leheny, R. L. (2011). Gel formation and aging in weakly attractive nanocolloid suspensions at intermediate concentrations. *The Journal of Chemical Physics*, 135(15):154903.

[Guo et al., 2007] Guo, H., Wilking, J., Liang, D., Mason, T., Harden, J., and Leheny, R. (2007). Slow, nondiffusive dynamics in concentrated nanoemulsions. *Physical Review E*, 75(4):041401.

[Habibi et al., 2010] Habibi, Y., Lucia, L. A., and Rojas, O. J. (2010). Cellulose nanocrystals: chemistry, self-assembly, and applications. *Chemical Reviews*, 110(6):3479–3500.

[Hausmann et al., 2018] Hausmann, M. K., Ruhs, P. A., Siqueira, G., Lauger, J., Libanori, R., Zimmermann, T., and Studart, A. R. (2018). Dynamics of cellulose nanocrystal alignment during 3d printing. *ACS nano*, 12(7):6926–6937.

[He and Thorpe, 1985] He, H. and Thorpe, M. F. (1985). Elastic properties of glasses. *Physical Review Letters*, 54(19):2107.

[He et al., 2021] He, S., Pascucci, D. R., Caggioni, M., Lindberg, S., and Schultz, K. M. (2021). Rheological properties of phase transitions in polydisperse and monodisperse colloidal rod systems. *AIChE Journal*, 67(11):e17401.

[Heyes et al., 1994] Heyes, D., Mitchell, P., Visscher, P., and Melrose, J. (1994). Brownian dynamics simulations of concentrated dispersions: Viscoelasticity and near-newtonian behaviour. *Journal of the Chemical Society, Faraday Transactions*, 90(8):1133–1141.

[Hirai et al., 2009] Hirai, A., Inui, O., Horii, F., and Tsuji, M. (2009). Phase separation behavior in aqueous suspensions of bacterial cellulose nanocrystals prepared by sulfuric acid treatment. *Langmuir*, 25(1):497–502.

[Hodgson and Amis, 1990] Hodgson, D. F. and Amis, E. J. (1990). Dynamic viscoelastic characterization of sol-gel reactions. *Macromolecules*, 23(9):2512–2519.

[Hong et al., 2018] Hong, W., Xu, G., Ou, X., Sun, W., Wang, T., and Tong, Z. (2018). Colloidal probe dynamics in gelatin solution during the sol–gel transition. *Soft Matter*, 14(19):3694–3703.

[Hyun et al., 2002] Hyun, K., Kim, S. H., Ahn, K. H., and Lee, S. J. (2002). Large amplitude oscillatory shear as a way to classify the complex fluids. *Journal of Non-Newtonian Fluid Mechanics*, 107:51–65.

[Hyun et al., 2011] Hyun, K., Wilhelm, M., Klein, C. O., Cho, K. S., Nam, J. G., Ahn, K. H., Lee, S. J., Ewoldt, R. H., and McKinley, G. H. (2011). A review of nonlinear oscillatory shear tests: Analysis and application of large amplitude oscillatory shear (laos). *Progress in Polymer Science*, 36(12):1697–1753.

[Ikeda, 2003] Ikeda, S. (2003). Heat-induced gelation of whey proteins observed by rheology, atomic force microscopy, and raman scattering spectroscopy. *Food Hydrocolloids*, 17(4):399–406.

[Ikeda and Nishinari, 2001] Ikeda, S. and Nishinari, K. (2001). On solid-like rheological behaviors of globular protein solutions. *Food Hydrocolloids*, 15(4-6):401–406.

[Imhof et al., 1994] Imhof, A., Van Blaaderen, A., Maret, G., Mellema, J., and Dhont, J. (1994). A comparison between the long-time self-diffusion and low shear viscosity of concentrated dispersions of charged colloidal silica spheres. *The Journal of Chemical Physics*, 100(3):2170–2181.

[Israelachvili and Wennerström, 1996] Israelachvili, J. and Wennerström, H. (1996). Role of hydration and water structure in biological and colloidal interactions. *Nature*, 379(6562):219–225.

[Jaishankar and McKinley, 2013] Jaishankar, A. and McKinley, G. H. (2013). Power-law rheology in the bulk and at the interface: quasi-properties and fractional constitutive equations. *Physical and Engineering Sciences in Medicine*, 469(2149):20120284.

[Jiang et al., 2010] Jiang, F., Esker, A. R., and Roman, M. (2010). Acid-catalyzed and solvolytic desulfation of h2so4-hydrolyzed cellulose nanocrystals. *Langmuir*, 26:17919–17925.

[Johnson et al., 2019] Johnson, L. C., Zia, R. N., Moghimi, E., and Petekidis, G. (2019). Influence of structure on the linear response rheology of colloidal gels. *Journal of Rheology*, 63(4):583–608.

[Kádár et al., 2020] Kádár, R., Fazilati, M., and Nypelö, T. (2020). Unexpected microphase transitions in flow towards nematic order of cellulose nanocrystals. *Cellulose*, 27:2003–2014.

[Keshavarz et al., 2021] Keshavarz, B., Rodrigues, D. G., Champenois, J.-B., Frith, M. G., Ilavsky, J., Geri, M., Divoux, T., McKinley, G. H., and Poulesquen, A. (2021). Time-connectivity superposition and the gel/glass duality of weak colloidal gels. *Proceedings of the National Academy of Sciences*, 118(15):e2022339118.

[Keyvani et al., 2021] Keyvani, P., Nyamayaro, K., Mehrkhodavandi, P., and Hatzikiriakos, S. G. (2021). Cationic and anionic cellulose nanocrystalline (cnc) hydrogels: A rheological study. *Physics of Fluids*, 33(4):043102.

[Kjaersgaard et al., 2020] Kjaersgaard, A., Vogt, E., Christensen, N. F., and Kjaergaard, H. G. (2020). Attenuated deuterium stabilization of hydrogen-bound complexes at room temperature. *The Journal of Physical Chemistry A*, 124(9):1763–1774.

[Klemm et al., 2018] Klemm, D., Cranston, E. D., Fischer, D., Gama, M., Kedzior, S. A., Kralisch, D., Kramer, F., Kondo, T., Lindström, T., Nietzsche, S., et al. (2018). Nanocellulose as a natural source for groundbreaking applications in materials science: Today's state. *Materials Today*, 21(7):720–748.

[Kolesov, 2021] Kolesov, B. A. (2021). Hydrogen bonds: Raman spectroscopic study. *International journal of molecular sciences*, 22(10):5380.

[Koumakis et al., 2012] Koumakis, N., Laurati, M., Egelhaaf, S., Brady, J., and Petekidis, G. (2012). Yielding of hard-sphere glasses during start-up shear. *Physical Review Letters*, 108(9):098303.

[Koumakis and Petekidis, 2011] Koumakis, N. and Petekidis, G. (2011). Two step yielding in attractive colloids: transition from gels to attractive glasses. *Soft Matter*, 7(6):2456–2470.

[Kruse and Wagner, 2016] Kruse, M. and Wagner, M. H. (2016). Time-resolved rheometry of poly (ethylene terephthalate) during thermal and thermo-oxidative degradation. *Rheologica Acta*, 55:789–800.

[Kunz et al., 2004a] Kunz, W., Henle, J., and Ninham, B. W. (2004a). 'zur lehre von der wirkung der salze'(about the science of the effect of salts): Franz hofmeister's historical papers. *Current Opinion in Colloid & Interface Science*, 9(1-2):19–37.

[Kunz et al., 2004b] Kunz, W., Nostro, P. L., and Ninham, B. W. (2004b). The present state of affairs with hofmeister effects. *Current Opinion in Colloid & Interface Science*, 9(1-2):1–18.

[Kurokawa et al., 2015] Kurokawa, A., Vidal, V., Kurita, K., Divoux, T., and Manneville, S. (2015). Avalanche-like fluidization of a non-brownian particle gel. *Soft Matter*, 11(46):9026–9037.

[Lagerwall et al., 2014] Lagerwall, J. P. F., Schütz, C., Salajkova, M., Noh, J., Hyun Park, J., Scalia, G., and Bergström, L. (2014). Cellulose nanocrystal-based materials: from liquid crystal self-assembly and glass formation to multifunctional thin films. *NPG Asia Mater.*, 6:e80.

[Lahiji et al., 2010] Lahiji, R. R., Xu, X., Reifenberger, R., Raman, A., Rudie, A., and Moon, R. J. (2010). Atomic force microscopy characterization of cellulose nanocrystals. *Langmuir*, 26(6):4480–4488.

[Larsen et al., 2008] Larsen, T., Schultz, K., and Furst, E. M. (2008). Hydrogel microrheology near the liquid-solid transition. *Korea-Australia Rheology Journal*, 20(3):165–173.

[Larsen and Furst, 2008] Larsen, T. H. and Furst, E. M. (2008). Microrheology of the liquid-solid transition during gelation. *Physical Review Letters*, 100(14):146001.

[Laurati et al., 2011] Laurati, M., Egelhaaf, S., and Petekidis, G. (2011). Nonlinear rheology of colloidal gels with intermediate volume fraction. *Journal of Rheology*, 55(3):673–706.

[Lee and Cognet, 2020] Lee, A. and Cognet, L. (2020). Length measurement of single-walled carbon nanotubes from translational diffusion and intensity fluctuations. *Journal of Applied Physics*, 128(22):224301.

[Lennon et al., 2023] Lennon, K. R., McKinley, G. H., and Swan, J. W. (2023). A data-driven method for automated data superposition with applications in soft matter science. *Data-Centric Engineering*, 4:e13.

[Lewandowska et al., 2018] Lewandowska, A. E., Inai, N. H., Ghita, O. R., and Eichhorn, S. J. (2018). Quantitative analysis of the distribution and mixing of cellulose nanocrystals in thermoplastic composites using raman chemical imaging. *RSC Advances*, 8(62):35831–35839.

[Li et al., 2021] Li, M., Wu, Q., Moon, R. J., Hubbe, M. A., and Bortner, M. J. (2021). Rheological aspects of cellulose nanomaterials: Governing factors and emerging applications. *Advanced Materials*, 33(21):2006052.

[Li et al., 2015] Li, M.-C., Wu, Q., Song, K., Lee, S., Qing, Y., and Wu, Y. (2015). Cellulose nanoparticles: structure–morphology–rheology relationships. *ACS Sustainable Chemistry & Engineering*, 3(5):821–832.

[Li et al., 2017] Li, V. C.-F., Dunn, C. K., Zhang, Z., Deng, Y., and Qi, H. J. (2017). Direct ink write (diw) 3d printed cellulose nanocrystal aerogel structures. *Scientific Reports*, 7(1):8018.

[Lidon, 2016] Lidon, P. (2016). *Effet d'ultrasons de puissance sur les matériaux mous: vers des matériaux " acousto-rhéologiques"*. PhD Thesis, Université de Lyon.

[Liénard et al., 2022] Liénard, F., Freyssingeas, É., and Borgnat, P. (2022). A multiscale time-laplace method to extract relaxation times from non-stationary dynamic light scattering signals. *The Journal of Chemical Physics*, 156(22).

[Lin et al., 1989] Lin, M., Lindsay, H., Weitz, D., Ball, R., Klein, R., and Meakin, P. (1989). Universality in colloid aggregation. *Nature*, 339(6223):360–362.

[Lopez and Richtering, 2019] Lopez, C. G. and Richtering, W. (2019). Influence of divalent counterions on the solution rheology and supramolecular aggregation of carboxymethyl cellulose. *Cellulose*, 26:1517–1534.

[Loussert et al., 2016] Loussert, C., Bouchaudy, A., and Salmon, J.-B. (2016). Drying dynamics of a charged colloidal dispersion in a confined drop. *Physical Review Fluids*, 1(8):084201.

[Lu et al., 2003] Lu, J., Ravichandran, G., and Johnson, W. L. (2003). Deformation behavior of the zr41. 2ti13. 8cu12. 5ni10be22. 5 bulk metallic glass over a wide range of strain-rates and temperatures. *Acta Materialia*, 51(12):3429–3443.

[Lu et al., 2024] Lu, S., Hu, X., Xu, B., Bai, C., Wang, T., Ma, T., and Song, Y. (2024). Effects of different salt ions on the structure and rheological behavior of sulfated cellulose nanocrystal hydrogel. *Food Hydrocolloids*, 151:109799.

[Lyklema, 2009] Lyklema, J. (2009). Simple hofmeister series. *Chemical Physics Letters*, 467(4-6):217–222.

[Madsen et al., 2010] Madsen, A., Leheny, R. L., Guo, H., Sprung, M., and Czakkel, O. (2010). Beyond simple exponential correlation functions and equilibrium dynamics in x-ray photon correlation spectroscopy. *New Journal of Physics*, 12(5):055001.

[Mahmoudi and Stradner, 2017] Mahmoudi, N. and Stradner, A. (2017). Structural arrest and dynamic localization in biocolloidal gels. *Soft Matter*, 13(26):4629–4635.

[Manneville et al., 2004] Manneville, S., Bécu, L., and Colin, A. (2004). High-frequency ultrasonic speckle velocimetry in sheared complex fluids. *The European Physical Journal Applied Physics*, 28(3):361–373.

[Martin et al., 1990] Martin, J. E., Adolf, D., and Odinek, J. (1990). Relaxation phenomena near the sol-gel transition. In *Makromolekulare Chemie. Macromolecular Symposia*, volume 40, pages 1–21. Wiley Online Library.

[Mason et al., 1995] Mason, T., Bibette, J., and Weitz, D. (1995). Elasticity of compressed emulsions. *Physical Review Letters*, 75(10):2051.

[Mason et al., 1996] Mason, T., Bibette, J., and Weitz, D. (1996). Yielding and flow of monodisperse emulsions. *Journal of Colloid and Interface Science*, 179(2):439–448.

[Mason and Weitz, 1995a] Mason, T. G. and Weitz, D. A. (1995a). Linear viscoelasticity of colloidal hard sphere suspensions near the glass transition. *Physical Review Letters*, 75:2770–2773.

[Mason and Weitz, 1995b] Mason, T. G. and Weitz, D. A. (1995b). Optical measurements of frequency-dependent linear viscoelastic moduli of complex fluids. *Physical Review Letters*, 74(7):1250.

[Masschaele et al., 2009] Masschaele, K., Fransaer, J., and Vermant, J. (2009). Direct visualization of yielding in model two-dimensional colloidal gels subjected to shear flow. *Journal of Rheology*, 53(6):1437–1460.

[Maxwell, 1867] Maxwell, J. C. (1867). Iv. on the dynamical theory of gases. *Philosophical Transactions of the Royal Society of London*, 157:49–88.

[Meyers et al., 2006] Meyers, M. A., Lin, A. Y., Seki, Y., Chen, P.-Y., Kad, B. K., and Bodde, S. (2006). Structural biological composites: an overview. *Jom*, 58:35–41.

[Miyashiro et al., 2020] Miyashiro, D., Hamano, R., and Umemura, K. (2020). A review of applications using mixed materials of cellulose, nanocellulose and carbon nanotubes. *Nanomaterials*, 10(2):186.

[Miyazaki et al., 2006] Miyazaki, K., Wyss, H. M., Weitz, D. A., and Reichman, D. R. (2006). Nonlinear viscoelasticity of metastable complex fluids. *Europhysics Letters*, 75(6):915.

[Mohraz and Solomon, 2005] Mohraz, A. and Solomon, M. J. (2005). Orientation and rupture of fractal colloidal gels during start-up of steady shear flow. *Journal of Rheology*, 49(3):657–681.

[Morlet-Decarnin et al., 2022] Morlet-Decarnin, L., Divoux, T., and Manneville, S. (2022). Slow dynamics and time–composition superposition in gels of cellulose nanocrystals. *The Journal of Chemical Physics*, 156(21):214901.

[Morlet-Decarnin et al., 2023] Morlet-Decarnin, L., Divoux, T., and Manneville, S. (2023). Critical-like gelation dynamics in cellulose nanocrystal suspensions. *ACS Macro Letters*, 12(0):1733–1738.

[Moud et al., 2019] Moud, A. A., Arjmand, M., Liu, J., Yang, Y., Sanati-Nezhad, A., and Hejazi, S. H. (2019). Cellulose nanocrystal structure in the presence of salts. *Cellulose*, 26:9387–9401.

[Moud et al., 2020] Moud, A. A., Kamkar, M., Sanati-Nezhad, A., Hejazi, S. H., and Sundararaj, U. (2020). Nonlinear viscoelastic characterization of charged cellulose nanocrystal network structure in the presence of salt in aqueous media. *Cellulose*, 27(10):5729–5743.

[Moud and Moud, 2023] Moud, A. A. and Moud, A. A. (2023). Flow and assembly of cellulose nanocrystals (cnc): A bottom-up perspective-a review. *International Journal of Biological Macromolecules*, 232:123391.

[Moud et al., 2021] Moud, A. A., Nezhad, A. S., and Hejazi, S. H. (2021). Confocal analysis of cnc based hydrogels and suspensions.

[Mours and Winter, 1994] Mours, M. and Winter, H. (1994). Time-resolved rheometry. *Rheologica Acta*, 33:385–397.

[Mu et al., 2019] Mu, R., Hong, X., Ni, Y., Li, Y., Pang, J., Wang, Q., Xiao, J., and Zheng, Y. (2019). Recent trends and applications of cellulose nanocrystals in food industry. *Trends in Food Science & Technology*, 93:136–144.

[Munier et al., 2016] Munier, P., Gordeyeva, K., Bergstrom, L., and Fall, A. B. (2016). Directional freezing of nanocellulose dispersions aligns the rod-like particles and produces low-density and robust particle networks. *Biomacromolecules*, 17(5):1875–1881.

[Muthukumar, 1989] Muthukumar, M. (1989). Screening effect on viscoelasticity near the gel point. *Macromolecules*, 22(12):4656–4658.

[Narayanan, 2024] Narayanan, T. (2024). Recent advances in synchrotron scattering methods for probing the structure and dynamics of colloids. *Advances in Colloid and Interface Science*, page 103114.

[Negi and Osuji, 2010] Negi, A. S. and Osuji, C. O. (2010). Physical aging and relaxation of residual stresses in a colloidal glass following flow cessation. *Journal of Rheology*, 54(5):943–958.

[Negi et al., 2014] Negi, A. S., Redmon, C. G., Ramakrishnan, S., and Osuji, C. O. (2014). Viscoelasticity of a colloidal gel during dynamical arrest: evolution through the critical gel and comparison with a soft colloidal glass. *Journal of Rheology*, 58:1557.

[Neto et al., 2013] Neto, W. P. F., Silvério, H. A., Dantas, N. O., and Pasquini, D. (2013). Extraction and characterization of cellulose nanocrystals from agro-industrial residue–soy hulls. *Industrial Crops and Products*, 42:480–488.

[Ng and McKinley, 2008] Ng, T. S. and McKinley, G. H. (2008). Power law gels at finite strains: The nonlinear rheology of gluten gels. *Journal of Rheology*, 52(2):417–449.

[Nickerson and Habrle, 1947] Nickerson, R. and Habrle, J. (1947). Cellulose intercrystalline structure. *Industrial & Engineering Chemistry*, 39(11):1507–1512.

[Nikoumanesh and Poling-Skutvik, 2023] Nikoumanesh, E. and Poling-Skutvik, R. (2023). The effect of thixotropy on the yield transition in reversible, colloidal gels. *The Journal of Chemical Physics*, 159(4):044905.

[Nyamayaro et al., 2023] Nyamayaro, K., Mehrkhodavandi, P., and Hatzikiriakos, S. G. (2023). Impact of counterion valency on the rheology of sulfonated cellulose nanocrystal hydrogels. *Carbohydrate Polymers*, 302:120378.

[Oguzlu et al., 2017] Oguzlu, H., Danumah, C., and Boluk, Y. (2017). Colloidal behavior of aqueous cellulose nanocrystal suspensions. *Current Opinion in Colloid & Interface Science*, 29:46–56.

[Okazaki and Kawaguchi, 2008] Okazaki, K. and Kawaguchi, M. (2008). Influence of monovalent electrolytes on rheological properties of gelled colloidal silica suspensions. *Journal of Dispersion Science and Technology*, 29(1):77–82.

[Ozawa et al., 2018] Ozawa, M., Berthier, L., Biroli, G., Rosso, A., and Tarjus, G. (2018). Random critical point separates brittle and ductile yielding transitions in amorphous materials. *Proceedings of the National Academy of Sciences*, 115(26):6656–6661.

[Pant and Levinger, 1999] Pant, D. and Levinger, N. E. (1999). Polar solvation dynamics of h2o and d2o at the surface of zirconia nanoparticles. *The Journal of Physical Chemistry B*, 103(37):7846–7852.

[Park and Ahn, 2013] Park, J. D. and Ahn, K. H. (2013). Structural evolution of colloidal gels at intermediate volume fraction under start-up of shear flow. *Soft Matter*, 9(48):11650–11662.

[Parker et al., 2018] Parker, R. M., Guidetti, G., Williams, C. A., Zhao, T., Narkevicius, A., Vignolini, S., and Frka-Petesic, B. (2018). The self-assembly of cellulose nanocrystals: Hierarchical design of visual appearance. *Advanced Materials*, 30(19):1704477.

[Parton et al., 2022] Parton, T. G., Parker, R. M., van de Kerkhof, G. T., Narkevicius, A., Haataja, J. S., Frka-Petesic, B., and Vignolini, S. (2022). Chiral self-assembly of cellulose nanocrystals is driven by crystallite bundles. *Nature Communications*, 13(1):2657.

[Peddireddy et al., 2016] Peddireddy, K. R., Capron, I., Nicolai, T., and Benyahia, L. (2016). Gelation kinetics and network structure of cellulose nanocrystals in aqueous solution. *Biomacromolecules*, 17(10):3298–3304.

[Perge et al., 2014] Perge, C., Taberlet, N., Gibaud, T., and Manneville, S. (2014). Time dependence in large amplitude oscillatory shear: A rheo-ultrasonic study of fatigue dynamics in a colloidal gel. *Journal of Rheology*, 58(5):1331–1357.

[Perrin, 1936] Perrin, F. (1936). Mouvement brownien d'un ellipsoide (ii). rotation libre et dépolarisation des fluorescences. translation et diffusion de molécules ellipsoidales. *Journal de Physique et Le Radium*, 7(1):1–11.

[Persello et al., 1994] Persello, J., Magnin, A., Chang, J., Piau, J., and Cabane, B. (1994). Flow of colloidal aqueous silica dispersions. *Journal of Rheology*, 38(6):1845–1870.

[Perumal et al., 2022] Perumal, A. B., Nambiar, R. B., Moses, J., and Anandharamakrishnan, C. (2022). Nanocellulose: Recent trends and applications in the food industry. *Food Hydrocolloids*, 127:107484.

[Peterlik et al., 2006] Peterlik, H., Roschger, P., Klaushofer, K., and Fratzl, P. (2006). From brittle to ductile fracture of bone. *Nature Materials*, 5(1):52–55.

[Pham et al., 2006] Pham, K., Petekidis, G., Vlassopoulos, D., Egelhaaf, S., Pusey, P., and Poon, W. (2006). Yielding of colloidal glasses. *Europhysics Letters*, 1975:624–630.

[Phan-Xuan et al., 2016] Phan-Xuan, T., Thuresson, A., Skepö, M., Labrador, A., Bordes, R., and Matic, A. (2016). Aggregation behavior of aqueous cellulose nanocrystals: the effect of inorganic salts. *Cellulose*, 23:3653–3663.

[Podlubny, 1999] Podlubny, I. (1999). *Fractional differential equations*.

[Ponton et al., 2002] Ponton, A., Warlus, S., and Griesmar, P. (2002). Rheological study of the sol–gel transition in silica alkoxides. *Journal of Colloid and Interface Science*, 249(1):209–216.

[Prathapan et al., 2016] Prathapan, R., Thapa, R., Garnier, G., and Tabor, R. F. (2016). Modulating the zeta potential of cellulose nanocrystals using salts and surfactants. *Colloids and Surfaces A: Physicochemical and Engineering Aspects*, 509:11–18.

[Puisto et al., 2015] Puisto, A., Mohtaschemi, M., Alava, M. J., and Illa, X. (2015). Dynamic hysteresis in the rheology of complex fluids. *Physical Review E*, 91(4):042314.

[Purnomo et al., 2006] Purnomo, E. H., van den Ende, D., Mellema, J., and Mugele, F. (2006). Linear viscoelastic properties of aging suspensions. *Europhysics Letter*, 76(1):74–80.

[Qiao et al., 2016] Qiao, C., Chen, G., Zhang, J., and Yao, J. (2016). Structure and rheological properties of cellulose nanocrystals suspension. *Food Hydrocolloids*, 55:19–25.

[Radhakrishnan et al., 2017] Radhakrishnan, R., Divoux, T., Manneville, S., and Fielding, S. M. (2017). Understanding rheological hysteresis in soft glassy materials. *Soft Matter*, 13(9):1834–1852.

[Rahmawati et al., 2021] Rahmawati, C., Aprilia, S., Saidi, T., and Aulia, T. B. (2021). Current development of geopolymer cement with nanosilica and cellulose nanocrystals. In *Journal of Physics: Conference Series*, volume 1783, page 012056. IOP Publishing.

[Rana et al., 2021] Rana, A. K., Frollini, E., and Thakur, V. K. (2021). Cellulose nanocrystals: Pretreatments, preparation strategies, and surface functionalization. *International Journal of Biological Macromolecules*, 182:1554–1581.

[Rao et al., 2019] Rao, A., Divoux, T., McKinley, G. H., and Hart, A. J. (2019). Shear melting and recovery of crosslinkable cellulose nanocrystal–polymer gels. *Soft Matter*, 15:4401–4412.

[Rao et al., 2022] Rao, A., Divoux, T., Owens, C. E., and Hart, A. J. (2022). Printable, castable, nanocrystalline cellulose-epoxy composites exhibiting hierarchical nacre-like toughening. *Cellulose*, 29(4):2387–2398.

[Reerink and Overbeek, 1954] Reerink, H. and Overbeek, J. T. G. (1954). The rate of coagulation as a measure of the stability of silver iodide sols. *Discussions of the Faraday Society*, 18:74–84.

[Reid et al., 2017] Reid, M. S., Villalobos, M., and Cranston, E. D. (2017). Benchmarking cellulose nanocrystals: From the laboratory to industrial production. *Langmuir*, 33:1583–1598.

[Revol et al., 1992] Revol, J.-F., Bradford, H., Giasson, J., Marchessault, R., and Gray, D. (1992). Helicoidal self-ordering of cellulose microfibrils in aqueous suspension. *International Journal of Biological Macromolecules*, 14(3):170–172.

[Rich et al., 2011] Rich, J. P., McKinley, G. H., and Doyle, P. S. (2011). Size dependence of microprobe dynamics during gelation of a discotic colloidal clay. *Journal of Rheology*, 55(2):273–299.

[Rogers et al., 2018] Rogers, M. C., Chen, K., Pagenkopp, M. J., Mason, T. G., Narayanan, S., Harden, J. L., and Leheny, R. L. (2018). Microscopic signatures of yielding in concentrated nanoemulsions under large-amplitude oscillatory shear. *Physical Review Materials*, 2:095601.

[Rottler and Robbins, 2005] Rottler, J. and Robbins, M. O. (2005). Unified description of aging and rate effects in yield of glassy solids. *Physical Review Letters*, 95(22):225504.

[Rouwhorst et al., 2020] Rouwhorst, J., Ness, C., Stoyanov, S., Zaccone, A., and Schall, P. (2020). Nonequilibrium continuous phase transition in colloidal gelation with short-range attraction. *Nature Communications*, 11(1):3558.

[Rowland and Roberts, 1972] Rowland, S. P. and Roberts, E. J. (1972). The nature of accessible surfaces in the microstructure of cotton cellulose. *Journal of Polymer Science Part A-1: Polymer Chemistry*, 10(8):2447–2461.

[Rueb and Zukoski, 1997] Rueb, C. and Zukoski, C. (1997). Viscoelastic properties of colloidal gels. *Journal of Rheology*, 41(2):197–218.

[Sacui et al., 2014] Sacui, I. A., Nieuwendaal, R. C., Burnett, D. J., Stranick, S. J., Jorfi, M., Weder, C., Foster, E. J., Olsson, R. T., and Gilman, J. W. (2014). Comparison of the properties of cellulose nanocrystals and cellulose nanofibrils isolated from bacteria, tunicate, and wood processed using acid, enzymatic, mechanical, and oxidative methods. *ACS Applied Materials & Interfaces*, 6(9):6127–6138.

[Saint-Michel et al., 2017] Saint-Michel, B., Bodiguel, H., Meeker, S., and Manneville, S. (2017). Simultaneous concentration and velocity maps in particle suspensions under shear from rheo-ultrasonic imaging. *Physical Review Applied*, 8(1):014023.

[Scanlan and Winter, 1991] Scanlan, J. C. and Winter, H. H. (1991). The evolution of viscoelasticity near the gel point of end-linking poly (dimethylsiloxane) s. In *Makromolekulare Chemie. Macromolecular Symposia*, volume 45, pages 11–21. Wiley Online Library.

[Scheiner and Čuma, 1996] Scheiner, S. and Čuma, M. (1996). Relative stability of hydrogen and deuterium bonds. *Journal of the American Chemical Society*, 118(6):1511–1521.

[Schuh et al., 2007] Schuh, C. A., Hufnagel, T. C., and Ramamurty, U. (2007). Mechanical behavior of amorphous alloys. *Acta Materialia*, 55(12):4067–4109.

[Segre et al., 1995] Segre, P., Meeker, S., Pusey, P., and Poon, W. (1995). Viscosity and structural relaxation in suspensions of hard-sphere colloids. *Physical Review Letters*, 75(5):958.

[Shafiei-Sabet et al., 2014] Shafiei-Sabet, S., Hamad, W., and Hatzikiriakos, S. (2014). Ionic strength effects on the microstructure and shear rheology of cellulose nanocrystal suspensions. *Cellulose*, 21:3347–3359.

[Shao et al., 2020] Shao, G., Hanaor, D. A., Shen, X., and Gurlo, A. (2020). Freeze casting: from low-dimensional building blocks to aligned porous structures - a review of novel materials, methods, and applications. *Advanced Materials*, 32(17):1907176.

[Shao et al., 2013] Shao, Z., Negi, A. S., and Osuji, C. O. (2013). Role of interparticle attraction in the yielding response of microgel suspensions. *Soft Matter*, 9:5492–5500.

[Shim and Rogers, 2023] Shim, Y. H. and Rogers, S. A. (2023). Understanding the yielding behavior of graphene oxide colloids via experimental strain decomposition. *Physics of Fluids*, 35(6):063117.

[Shojaeiarani et al., 2020] Shojaeiarani, J., Bajwa, D., and Holt, G. (2020). Sonication amplitude and processing time influence the cellulose nanocrystals morphology and dispersion. *Nanocomposites*, 6(1):41–46.

[Shopsowitz et al., 2010] Shopsowitz, K. E., Qi, H., Hamad, W. Y., and MacLachlan, M. J. (2010). Free-standing mesoporous silica films with tunable chiral nematic structures. *Nature*, 468(7322):422–425.

[Sinko and Keten, 2014] Sinko, R. and Keten, S. (2014). Effect of moisture on the traction-separation behavior of cellulose nanocrystal interfaces. *Applied Physics Letters*, 105(24):243702.

[Sinko et al., 2015] Sinko, R., Qin, X., and Keten, S. (2015). Interfacial mechanics of cellulose nanocrystals. *Mrs Bulletin*, 40(4):340–348.

[Sobac et al., 2020] Sobac, B., Dehaeck, S., Bouchaudy, A., and Salmon, J.-B. (2020). Collective diffusion coefficient of a charged colloidal dispersion: Interferometric measurements in a drying drop. *Soft Matter*, 16(35):8213–8225.

[Solomon and Spicer, 2010] Solomon, M. J. and Spicer, P. T. (2010). Microstructural regimes of colloidal rod suspensions, gels, and glasses. *Soft Matter*, 6(7):1391–1400.

[Soper and Benmore, 2008] Soper, A. and Benmore, C. (2008). Quantum differences between heavy and light water. *Physical Review Letters*, 101(6):065502.

[Stauffer et al., 1982] Stauffer, D., Coniglio, A., and Adam, M. (1982). *Gelation and critical phenomena*, pages 103–158. Springer Berlin Heidelberg.

[Sudreau, 2022] Sudreau, I. (2022). *Dispersions de boehmite sous cisaillement: anisotropie structurale, rhéologie et effets mémoire*. PhD Thesis, Ecole normale supérieure de lyon.

[Sudreau et al., 2022] Sudreau, I., Manneville, S., Servel, M., and Divoux, T. (2022). Shear-induced memory effects in boehmite gels. *Journal of Rheology*, 66(1):91–104.

[Suman and Joshi, 2019] Suman, K. and Joshi, Y. M. (2019). Analyzing onset of nonlinearity of a colloidal gel at the critical point. *Journal of Rheology*, 63(6):991–1001.

[Suman and Joshi, 2020] Suman, K. and Joshi, Y. M. (2020). On the universality of the scaling relations during sol-gel transition. *Journal of Rheology*, 64(4):863–877.

[Sumari et al., 2013] Sumari, S., Roesyadi, A., and Sumarno, S. (2013). Effects of ultrasound on the morphology, particle size, crystallinity, and crystallite size of cellulose. *Scientific Study & Research. Chemistry & Chemical Engineering, Biotechnology, Food Industry*, 14(4):229.

[Tortora et al., 2020] Tortora, M. M., Mishra, G., Prešern, D., and Doye, J. P. (2020). Chiral shape fluctuations and the origin of chirality in cholesteric phases of dna origamis. *Science Advances*, 6(31):eaaw8331.

[Trache et al., 2020] Trache, D., Tarchoun, A. F., Derradji, M., Hamidon, T. S., Masruchin, N., Brosse, N., and Hussin, M. H. (2020). Nanocellulose: From fundamentals to advanced applications. *Frontiers in Chemistry*, 8:392.

[Tschoegl, 2012] Tschoegl, N. W. (2012). *The phenomenological theory of linear viscoelastic behavior: an introduction*. Springer Science & Business Media.

[Turowski et al., 2003] Turowski, M., Yamakawa, N., Meller, J., Kimata, K., Ikegami, T., Hosoya, K., Tanaka, N., and Thornton, E. R. (2003). Deuterium isotope effects on hydrophobic interactions: the importance of dispersion interactions in the hydrophobic phase. *Journal of the American Chemical Society*, 125(45):13836–13849.

[Tyagi et al., 2021] Tyagi, S., Monteux, C., and Deville, S. (2021). Multiple objects interacting with a solidification front. *Scientific Reports*, 11(1):3513.

[Vadillo et al., 2021] Vadillo, J., Larraza, I., Calvo-Correas, T., Gabilondo, N., Derail, C., and Eceiza, A. (2021). Role of in situ added cellulose nanocrystals as rheological modulator of novel waterborne polyurethane urea for 3d-printing technology. *Cellulose*, 28:4729–4744.

[van der Linden et al., 2015] van der Linden, M., Conchúir, B. O., Spigone, E., Niranjan, A., Zaccone, A., and Cicuta, P. (2015). Microscopic origin of the hofmeister effect in gelation kinetics of colloidal silica. *The Journal of Physical Chemistry Letters*, 6(15):2881–2887.

[Varnik et al., 2004] Varnik, F., Bocquet, L., and Barrat, J.-L. (2004). A study of the static yield stress in a binary lennard-jones glass. *The Journal of Chemical Physics*, 120(6):2788–2801.

[Voigt, 1890] Voigt, W. (1890). Ueber die innere reibung der festen körper, insbesondere der krystalle. *Abhandlungen der Koeniglichen Gesellschaft der Wissenschaften in Goettingen*, 36:3–48.

[Wade, 1999] Wade, D. (1999). Deuterium isotope effects on noncovalent interactions between molecules. *Chemico-Biological Interactions*, 117(3):191–217.

[Wagner and Mewis, 2021] Wagner, N. J. and Mewis, J. (2021). *Theory and applications of colloidal suspension rheology*. Cambridge University Press.

[Wehrman et al., 2016] Wehrman, M. D., Lindberg, S., and Schultz, K. M. (2016). Quantifying the dynamic transition of hydrogenated castor oil gels measured via multiple particle tracking microrheology. *Soft matter*, 12(30):6463–6472.

[Wei et al., 2019] Wei, Y., Solomon, M. J., and Larson, R. G. (2019). Time-dependent shear rate inhomogeneities and shear bands in a thixotropic yield-stress fluid under transient shear. *Soft Matter*, 15(39):7956–7967.

[Wei et al., 2018] Wei, Z., Sinko, R., Keten, S., and Luijten, E. (2018). Effect of surface modification on water adsorption and interfacial mechanics of cellulose nanocrystals. *ACS Applied Materials & Interfaces*, 10(9):8349–8358.

[Weitz and Oliveria, 1984] Weitz, D. and Oliveria, M. (1984). Fractal structures formed by kinetic aggregation of aqueous gold colloids. *Physical Review Letters*, 52(16):1433.

[Whalley, 1957] Whalley, E. (1957). The difference in the intermolecular forces of h2o and d2o. *Transactions of the Faraday Society*, 53:1578–1585.

[Whitaker et al., 2019] Whitaker, K. A., Varga, Z., Hsiao, L. C., Solomon, M. J., Swan, J. W., and Furst, E. M. (2019). Colloidal gel elasticity arises from the packing of locally glassy clusters. *Nature Communications*, 10(1):2237.

[Whittle and Dickinson, 1997] Whittle, M. and Dickinson, E. (1997). Stress overshoot in a model particle gel. *The Journal of Chemical Physics*, 107(23):10191–10200.

[Winter, 1987] Winter, H. (1987). Evolution of rheology during chemical gelation. *Progress in Colloid and Polymer Science*, 75:104–110.

[Winter and Mours, 1997] Winter, H. and Mours, M. (1997). Rheology of polymers near liquid-solid transitions. *Advances in Polymer Science*, 134:165–230.

[Winter and Chambon, 1986] Winter, H. H. and Chambon, F. (1986). Analysis of linear viscoelasticity of a crosslinking polymer at the gel point. *Journal of Rheology*, 30(2):367–382.

[Winter et al., 1988] Winter, H. H., Morganelli, P., and Chambon, F. (1988). Stoichiometry effects on rheology of model polyurethanes at the gel point. *Macromolecules*, 21(2):532–535.

[Wohlert et al., 2021] Wohlert, M., Benselfelt, T., Wågberg, L., Furó, I., Berglund, L. A., and Wohlert, J. (2021). Cellulose and the role of hydrogen bonds: not in charge of everything. *Cellulose*, pages 1–23.

[Wojno et al., 2023] Wojno, S., Sonker, A. K., Feldhusen, J., Westman, G., and Kádár, R. (2023). Isotropic gels of cellulose nanocrystals grafted with dialkyl groups: Influence of surface group topology from nonlinear oscillatory shear. *Langmuir*, 39(18):6433–6446.

[Wu et al., 2013] Wu, H., Xie, J.-j., and Morbidelli, M. (2013). Kinetics of colloidal gelation and scaling of the gelation point. *Soft Matter*, 9(17):4437–4443.

[Wu et al., 2014] Wu, Q., Meng, Y., Wang, S., Li, Y., Fu, S., Ma, L., and Harper, D. (2014). Rheological behavior of cellulose nanocrystal suspension: Influence of concentration and aspect ratio. *Journal of Applied Polymer Science*, 131(15):40525.

[Xie et al., 2018] Xie, S., Zhang, X., Walcott, M. P., and Lin, H. (2018). Applications of cellulose nanocrystals: a review. *Engineered Science*, 2(16):4–16.

[Xu et al., 2024] Xu, J., Wang, P., Yuan, B., and Zhang, H. (2024). Rheology of cellulose nanocrystal and nanofibril suspensions. *Carbohydrate Polymers*, 324:121527.

[Xu et al., 2019] Xu, Y., Atrens, A. D., and Stokes, J. R. (2019). Structure and rheology of liquid crystal hydroglass formed in aqueous nanocrystalline cellulose suspensions. *Journal of Colloid and Interface Science*, 555:702–713.

[Xu et al., 2020] Xu, Y., Atrens, A. D., and Stokes, J. R. (2020). A review of nanocrystalline cellulose suspensions: Rheology, liquid crystal ordering and colloidal phase behaviour. *Current Opinion in Colloid & Interface Science*, 275:102076.

[Yu et al., 2021] Yu, S., Sun, J., Shi, Y., Wang, Q., Wu, J., and Liu, J. (2021). Nanocellulose from various biomass wastes: Its preparation and potential usages towards the high value-added products. *Environmental Science and Ecotechnology*, 5:100077.

[Zaccone et al., 2013] Zaccone, A., Crassous, J. J., and Ballauff, M. (2013). Colloidal gelation with variable attraction energy. *The Journal of Chemical Physics*, 138(10):104908.

[Zaccone et al., 2014] Zaccone, A., Winter, H., Siebenbürger, M., and Ballauff, M. (2014). Linking self-assembly, rheology, and gel transition in attractive colloids. *Journal of Rheology*, 58(5):1219–1244.

[Zhang et al., 2019] Zhang, S., Zhang, L., Bouzid, M., Rocklin, D. Z., Del Gado, E., and Mao, X. (2019). Correlated rigidity percolation and colloidal gels. *Physical Review Letters*, 123(5):058001.

[Zhang et al., 2009] Zhang, Z., Krishna, N., Lettinga, M. P., Vermant, J., and Grelet, E. (2009). Reversible gelation of rod-like viruses grafted with thermoresponsive polymers. *Langmuir*, 25(4):2437–2442.

[Zia et al., 2014] Zia, R. N., Landrum, B. J., and Russel, W. B. (2014). A micro-mechanical study of coarsening and rheology of colloidal gels: Cage building, cage hopping, and smoluchowski's ratchet. *Journal of Rheology*, 58(5):1121–1157.

Résumé

Les nanocristaux de cellulose (CNC) sont des particules solides en forme de bâtonnets, chargées négativement en surface. Suspendus dans de l'eau salée, les CNC s'agrègent pour former des gels qui peuvent servir de précurseurs mous à la fabrication de matériaux solides biosourcés, auxquels ils transmettent en partie leurs propriétés mécaniques remarquables.

Le but de cette thèse est, tout d'abord, de comprendre les propriétés mécaniques des gels de CNC par mesures rhéologiques. L'étude de la dynamique de gélification de ces gels et l'établissement de principes de superposition temps-connectivité et temps-composition, nous a permis de montrer, d'une part, l'existence d'un scénario universel pour la formation et le vieillissement de gels de CNC, et d'autre part, l'équivalence d'un point de vue structural entre la concentration en sel et l'âge d'un gel. Nous avons ensuite étudié la rupture et la fluidification induite par cisaillement de ces gels de CNC. Nous avons notamment montré que cette rupture peut être abrupte (« fragile ») ou graduelle (« ductile ») selon l'âge du gel et le taux de cisaillement appliqué, et que cette transition présente certains traits universels vis-vis de la composition des gels.

Enfin, nous avons commencé à étudier le passage d'un matériau mou à un matériau solide, à travers deux processus de solidification différents : le séchage et la congélation. Nous avons montré que ces deux processus induisent la formation de structures bien particulières au sein du matériau solide, en partie dues à l'alignement des CNC, et dont les caractéristiques peuvent être contrôlées par les conditions aux bords ou encore par la vitesse de solidification.

Abstract

Cellulose nanocrystals (CNC) are solid rod-like particles with a large negative surface charge. When suspended in water in the presence of salt, CNCs aggregate and form gels. Such gels can be used as soft precursors in the design of biosourced solid materials, to which they transmit part of their remarkable mechanical properties.

The goal of the present thesis is, first, to probe the mechanical properties of CNC gels using rheology. The study of the gelation dynamics of such gels and the establishment of time-connectivity and time-composition superposition principles have allowed us to show (i) the existence of a universal scenario for the formation and aging of CNC gels, and (ii) the structural equivalence between the salt concentration of a gel and its age. Then, we have studied the shear-induced failure and fluidization of CNC gels. In particular, we have shown that the failure can be abrupt ("fragile") or gradual ("ductile") depending on the gel age and on the applied shear rate.

Finally, we have performed a preliminary study of the transition from a soft material to a solid material, through two different solidification processes: drying and freezing. We have shown that the two processes induce the formation of specific microscopic structures inside the solid material, partially due to CNCs alignment, whose characteristics can be controlled by the boundary conditions or by the solidification speed.